ISSN 1580-2949
UDK 669+666+678+53 MTAEC9, 50(5)637–834(2016)

MATER. TEHNOL.	LETNIK VOLUME 50	ŠTEV. NO. 5	STR. P. 637–834	LJUBLJANA SLOVENIJA	SEP.–OKT. SEP.–OCT. 2016

VSEBINA – CONTENTS

STROKOVNI ČLANKI – PROFESSIONAL ARTICLES

EDITOR'S PREFACE

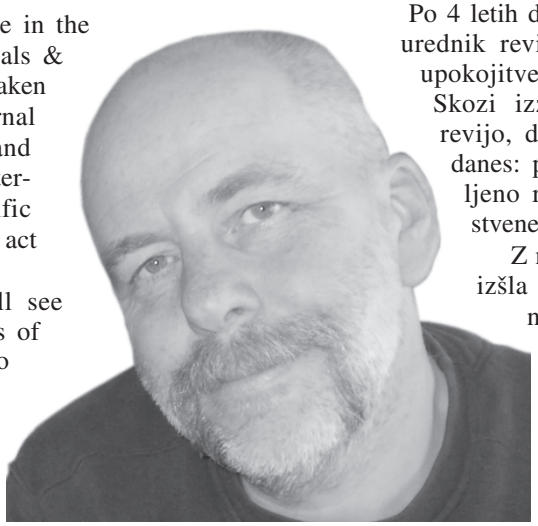

After 4 years of great service in the job as Editor-in-Chief of Materials & Technology, Matjaž Torkar has taken retirement. He saw the journal through some difficult times and established it as an important international record of scientific achievements. He will be a tough act to follow.

The next issue, 6/2016, will see some changes. After many years of being both open access and free to publish, we will have to acknowledge the economic realities of the situation and start to charge for each published paper. In line with other Slovenian journals we will introduce a publication fee of €300, payable on acceptance of the manuscript, with a reduced fee of €150 for those people presenting at the annual International Conference on Materials & Technology, held annually in Portorož, Slovenia. This fee will be applied to manuscripts submitted after 30 Sept. 2016.

A second change, which we feel is in line with the progress the journal has been making over the past decade, is to publish original and review scientific articles. From now on we will not have a separate section for professional articles. As the number of submissions in the past years has soared, from 120 in 1995 to near 400 in 2015, our selection criteria have had to become stricter. So, in order to help authors get their articles published we have re-written the Instructions for Authors, introduced a template for manuscript submission and now require a mandatory check-list to accompany all new manuscripts. For the time being we will still be accepting submissions by e-mail to mit@imt.si, where they will be handled first by the journal's new Technical Editor, Erika Nared, who will be checking each manuscript's eligibility, before they are assessed by myself or members of the Editorial Board. However, we expect to be switching to a web-based submission procedure in next few years.

The journal is becoming increasingly international, with manuscripts being submitted from all over the world. It is very gratifying to see that Materials & Technology is now such a familiar and respected journal in places outside of Slovenia, but we would still like to receive more submissions from researchers from Slovenia.

PREDGOVOR UREDNIKA

Po 4 letih delovanja kot glavni in odgovorni urednik revije je dr. Matjaž Torkar zaradi upokojitve prenehal z urednikovanjem. Skozi izzivov polno obdobje je vodil revijo, da je postala to, kar predstavlja danes: pomembno mednarodno uveljavljeno revijo, ki objavlja mnoge znanstvene dosežke.

Z naslednjo številko (6/2016), ki bo izšla v decembru 2016, bomo uvedli nekaj sprememb. Po mnogih letih, tako odprtega dostopa revije kot brezplačne objave člankov, bomo zaradi ekonomske situacije začeli zaračunavati objavo člankov v naši reviji. Tako kot to počne že prenekatera slovenska znanstvena revija. Za običajne članke bo cena 300 €, za tiste članke, ki bodo predstavljeni na letni Mednarodni konferenci o materialih in tehnologijah, ki poteka vsako leto v Portorožu, pa 150 €. Za članke, ki jih bomo prejeli od 30. septembra 2016 dalje, bo potrebno plačilo za objavo.

Druga sprememba, za katero menimo, da je dobrodošla in nujna za nadaljnji razvoj revije, je objavljanje izvirnih znanstvenih in preglednih člankov. Od sedaj naprej tako ne bo več sekcije za strokovne članke. Ker je v zadnjem času število oddaje člankov izredno naraslo, od nekaj 120 v letu 1995 na blizu 400 v letu 2015, smo mnenja, da je potrebno kriterije za izbiro člankov zaostriti. Tako smo, v pomoč avtorjem, posodobili Navodila za avtorje, predstavili bomo vzorec oz. predlogo, kako naj bo članek napisan in poleg oddaje članka bomo zahtevali obvezno oddajo kontrolnega seznama, ki ga bo moral izpolniti avtor. Oddaja člankov bo tako še vedno potekala preko e-pošte: mit@imt.si, kjer jih bo najprej obravnavala nova tehnična urednica, Erika Nared, preden bodo posredovani v pregled meni ali članom uredniškega odbora. Nadalje, v bodoče načrtujemo prehod na spletno oddajanje člankov za objavo v reviji.

Revija postaja vse bolj mednarodna, saj so članki poslani iz različnih delov sveta. V čast nam je, da je revija Materiali in tehnologije danes tako znana in ugledna tudi izven Slovenije, vendar si želimo, da bi v naši reviji objavljalo večje število strokovnjakov in raziskovalcev iz Slovenije.

Naše osnovno prizadevanje ostaja še naprej: da je revija Materiali in tehnologije znanstvena revija, ki je posvečena izvirnim znanstvenim člankom in člankom, ki

Our basic remit remains the same: we are a scientific journal, devoted to original scientific papers and articles relating to fundamental and applied science and technology. Topics of particular interest to the journal include metallic materials, inorganic materials, polymers, vacuum techniques and nanomaterials. In response to requests by authors we will be making a lot of effort over the next year to reduce the waiting period for publication to 4–6 months, so as to provide a better service to both authors and readers. In addition, we welcome constructive comments from anyone with an interest in the journal and are happy to discuss new ideas.

I would like to thank you for your interest in Materials & Technology journal and look forward to working with you in the future.

Paul McGuiness,
Editor-in-Chief

obravnavajo tematiko temeljne in aplikativne znanosti ter tehnologije. Tematike, ki so posebnega pomena za revijo vključujejo kovinske materiale, anorganske materiale, polimere, vakuumsko tehniko in nanomateriale. Glede na želje in zahteve mnogih avtorjev, se bomo v naslednjem letu trudili skrajšati obdobje čakanja na objavo članka (na 4–6 mesecev) in tako stopiti naproti tako avtorjem, kot tudi bralcem. Veseli bomo vsake vaše konstruktivne kritike, predlogov ali novih idej, ki nam bodo pomagale narediti revijo še boljšo.

Zahvaljujem se vam za vaše zanimanje in prebiranje revije Materiali in tehnologije ter se veselim prihodnjega sodelovanja z vami.

Paul McGuiness,
Glavni in odgovorni urednik

UDK 621.762:669.293:669.71:67.017
Review article/Pregledni članek

ISSN 1580-2949
MTAEC9, 50(5)641(2016)

EFFECT OF THE ADDITION OF NIOBIUM AND ALUMINIUM ON THE MICROSTRUCTURES AND MECHANICAL PROPERTIES OF MICRO-ALLOYED PM STEELS

VPLIV DODATKA NIOBIJA IN ALUMINIJA NA MIKROSTRUKTURO IN MEHANSKE LASTNOSTI MIKROLEGIRANIH PM JEKEL

Süleyman Gündüz[1], Mehmet Akif Erden[2], Hasan Karabulut[3], Mustafa Türkmen[4]

[1]Karabük University, Faculty of Technology, Department of Manufacturing Engineering, 78050 Karabük, Turkey
[2]Karabük University, Institute of Science and Technology, Department of Manufacturing Engineering, 78050 Karabük, Turkey
[3]Karabük University, Karabük Vocational School, 78050 Karabük, Turkey
[4]Kocaeli University, Hereke Vocational School, Department of Metallurgy, Kocaeli, Turkey
hasankarabulut@karabuk.edu.tr

Prejem rokopisa – received: 2015-08-08; sprejem za objavo – accepted for publication: 2015-09-04

doi:10.17222/mit.2015.248

In this work, the effects of the addition of Nb and Al on the microstructures and tensile behaviours of micro-alloyed powder metallurgy (PM) steels were investigated. The microstructure of the micro-alloyed PM steels was examined by light microscope, SEM, XRD, XRF and EDS. The results indicated that the addition of (0.1, 0.15 or 0.2) % of Nb-Al increases the yield strength (*YS*) and the ultimate tensile strength (*UTS*) of the PM sintered steels. Elongation also tends to improve with an increasing Nb and Al content. In addition, the Nb and Al limit the grain growth during austenitization.

Keywords: powder metallurgy, micro-alloyed steels, microstructure

V delu je bil preiskovan vpliv dodatka Nb in Al na mikrostrukturo in na natezno trdnost mikrolegiranih PM jekel, izdelanih iz prahov. Mikrostruktura mikrolegiranih PM jekel je bila preiskovana s svetlobnim mikroskopom ter s SEM, XRD, XRF in EDS. Rezultati so pokazali, da dodatek (0,1, 0,15 ali 0,2) % Nb-Al poveča mejo plastičnosti (*YS*) in natezno trdnost (*UTS*) sintranih PM jekel. Tudi raztezek se izboljša s povečano vsebnostjo Nb in Al. Ugotovljeno je še, da dodatek Nb in Al omejuje rast zrn med avstenitizacijo.

Ključne besede: metalurgija prahov, mikrolegirana jekla, mikrostruktura

1 INTRODUCTION

Steels with a minimal strength high toughness and excellent weldability are required in a wide range of applications. This combination of properties is achieved by optimizing the chemical composition and by thermo-mechanical processing (TMP). The addition of micro-alloying elements such as Nb, V, Ti and Al contribute to an increase in strength, both directly, through micro-structural refinement and precipitation strengthening, and indirectly, through enhanced hardenability and an associated modification of the transformation micro-structure.[1–3]

Niobium forms nitrides and carbides, but it is the carbide that is the most important. In steels it precipitates at a temperature just below 1000 °C and prevents austenite recrystallization. Niobium carbide particles are very effective in preventing austenite recrystallization and the formation of "pancake" grains that transform to fine ferrite grains.[4–6] Thus, the precipitation of niobium carbide particles plays a major role in controlling the final microstructure and the product properties. Besides increasing the non-recrystallization temperature, the presence of precipitates also increases the austenite grain-coarsening temperature[7], which is important through controlled reheating.[8] Niobium is widely used in this way for the production of fined-grained pipeline and other structural steels.

A large volume of work was spent investigating the effect of niobium on the recrystallization and growth of austenite grains,[5,6,9,10] and it was found that a minor addition of niobium to the steel was sufficient to inhibit the static recrystallization of austenite and to achieve the final microstructure.[11] Similar effects were observed in titanium, and vanadium steels were found generally less marked.[12]

Aluminium only forms nitride precipitates, which are stable at temperatures above 900 °C. It forms during reheating to heat-treatment temperatures and at the expense of the vanadium nitride, if present. At normalising temperatures it is stable, pins grain boundaries and is effective in refining the grain size.[12] Aluminium nitride forms only with a hexagonal crystal lattice and it was not found in any substantial solid solution in the face-centred-cubic micro-alloy carbonitrides.[4]

AlN precipitation occurs at both grain boundaries and dislocations. It has been shown that the precipitation kinetics depends on the content of nitrogen and alumi-

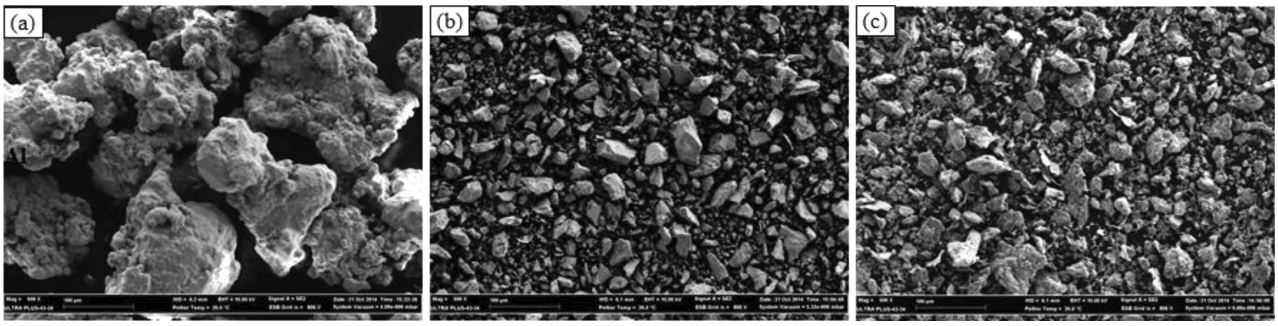

Figure 1: SEM micrographs of Fe, Nb and Al powders: a) Fe ≤180 μm, b) Nb <45 μm and c) Al <75 μm
Slika 1: SEM-posnetki prahov Fe, Nb in Al: a) Fe ≤180 μm, b) Nb <45 μm in c) Al <75 μm

nium in the steel and also on the grain size and the annealing temperature.[13] In the austenite region, the precipitation occurs predominantly at the grain boundaries because of the considerable volumetric misfit of the AlN precipitates and the steel matrix,[14] and the increased diffusion rate of both elements at the grain boundaries, as compared to the grains.[15]

The rising costs and disposition volatility of metals has led to the development of new PM steels. In particular, PM steels with the addition of copper, nickel and molybdenum to compete with wrought grades. Recently, due to cost constraints and availability, PM steels have also included chromium and manganese as the alloying elements. These material systems are categorized as alloy steels, since significant levels of these elements are required to achieve changes in the mechanical properties.[16] The demand for cheaper but high-strength structural steels forced powder metallurgists to seek newer compositions with wider applications, and such steels found applications in the automotive industry, aerospace, and power tools.[17]

Micro-alloyed steels contain small amounts of niobium, vanadium or titanium, generally at levels between 0.02 and 0.2 % of mass fractions. Despite the low alloy content, micro-alloying can lead to a major increase in the strength and toughness as a result of carbonitride particles, which led to precipitation strengthening and grain refinement.[16] The production of micro-alloyed steels is estimated to be around 12 % of the total world steel production and are used in every major steel market sector. In many parts of the world their development has played an important role in the expansion of some key industries, such as oil and gas extraction, construction, and transportation.[18] The present study was undertaken to examine the effect of Nb and Al on the microstructure and mechanical properties of sintered PM steels. The mechanical properties were determined and the microstructures were investigated in the sintered condition to assess the role of precipitation strengthening and grain refinement.

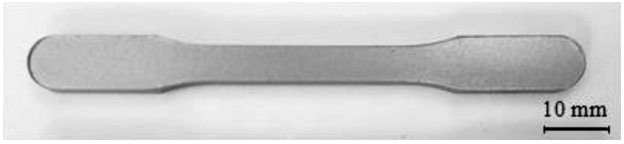

Figure 2: General view of tensile test specimen sintered at 1350 °C for 1 h
Slika 2: Izgled preizkušanca za natezni preizkus, 1 h sintranega na 1350 °C

2 MATERIALS AND EXPERIMENTAL PROCEDURE

In this investigation, Fe, Nb and Al powders of ≤180 μm, <45 μm, and <75 μm supplied by Aldrich were used, with purities of 99.9 %, 99.8 % and 93 %, respectively. Electron micrographs of the powders presented in **Figure 1** reveal an irregular shape of the powder particles for all the studied samples. The required mass of Fe-0.25C (Alloy 1), Fe-0.25C-0.05Nb-0.05Al (Alloy 2), Fe-0.25C-0.075Nb-0.075Al (Alloy 3) and Fe-0.25C-0.1Nb-0.1Al (Alloy 4) powders was accurately weighed and mixed in an industrial conic mixer for 1 h. A total of 0.45 of graphite was added to reach a carbon content of 0.25 % in the sintered test pieces. Zn-stearate was added as a lubricant. The mixed powder mass was then compacted into dog-bone tensile specimens using a hydraulic press with a capacity of 100 tons and a compaction pressure of 700 MPa. Standard cross-section tensile-test specimens were produced in accordance with the standard of ASTM E8/E8M [19] as shown in **Figure 2**. The specimen has two large shoulders with a smaller cross-section gauge in between. The shoulders are large so they can be readily gripped, whereas the gauge section has a smaller cross-section.

The test pieces were sintered in a tube furnace with an argon atmosphere. The sintering cycle was: heating to 1350 °C at a rate of 5 °C/min, holding at this temperature for 1 h, cooling to room temperature at a rate of 5 °C/min. The sintered density was determined by Archimedes' principle using pure water according to ASTM B 328-96.[20] Four measurements were made for each composition and the variation of those values was less than 1 %. A tensile test at room temperature was performed using a Schimadzu tensile-testing machine at a crosshead speed of 1 mm min^{-1} and perfect alignment of the specimens in the pull direction and no slippage.

Three specimens of each alloy were tested and the mean value was used.

The examination of the microstructure was carried out using optical and scanning electron microscopy (SEM), and energy-dispersive spectrometry (EDS) was used to provide elemental analyses of the particles. The average elemental composition of alloys was determined with the X-ray fluorescence technique (XRF). The chemical composition of the produced PM steels is presented in **Table 1**. The specimens were mechanically polished using a standard metallographic procedure and etched with 2 % Nital solution. The microstructures were examined in a Nikon ECLIPSE L150 microscope with a magnification of 50× to 1000×. An electrochemical extraction technique was used to characterise the precipitates in the examined specimens. This procedure involves the electrochemical dissolution of tensile specimen in the electrolyte (10 % HCl in methanol) and filtering to separate the precipitate from the solution. The dissolution time of 8 hours sufficed for the dissolution of around two grams of the specimen. For the filtering, cellulose acetate filters were used with a pore size of 0.4 μm and X-ray diffraction (XRD) analysis of the collected residues with precipitates was carried out. The XRD data were obtained using Cu-K_α radiation, a scan step of 4°, a step time of 1 min and 2θ range from 20° to 90°.

Table 1: Chemical composition of PM steel and microalloyed PM steels

Tabela 1: Kemijska sestava PM jekla in mikrolegiranih PM jekel

	Fe	C	Mn	Al	Nb
Alloy 1	99.232	0.249	0.2110	0.0000	0.0000
Alloy 2	98,5174	0.2355	0.2316	0.0514	0.0468
Alloy 3	99.0191	0.2624	0.2223	0.0752	0.0740
Alloy 4	99.0452	0.2653	0.2223	0.0974	0.0918

The grain size measurement was carried out using the mean linear intercept (mli) method, with the line inclined by 45°. At least 500 grains cut by the intersecting line were counted for each sample. From the results the mean linear intercept grain sizes[21,22] was determined. The statistical errors for the assessment of the mean linear intercept were examined by Woodhead and reviewed by J. R. Blank and T. Gladman,[23] and it was suggested that the relative error of the individual intercept value (σ_i/i) = 0.7 is almost constant for a variety of regular and space-filling polyhedrals. The relative error, ϕ, of the mean linear intercept based on the measurement of n grains (SE_i/i) is deduced as shown in Equation (1):

$$f = \frac{SE_i}{i} = \frac{\frac{\sigma_i}{\iota}}{\sqrt{n}} = \frac{0.7}{\sqrt{n}} \quad (1)$$

where σ_i is the standard deviation of the assessment of the intercept lengths.

The volume fraction of ferrite or pearlite was also calculated using the systematic point-count method.[24,25] According to this method, when the grid points intersect the ferrite boundary, they are counted as half. Errors in the point counting were also calculated by T. Gladman and J. Woodhead[26] in Equation (2):

$$\sigma = \sqrt{\frac{f(1-f)}{N}} \quad (2)$$

where σ is the standard deviation, f is the measured volume fraction of ferrite or pearlite and N is the total number of points counted. All the volume fractions were expressed ± σ (standard deviation)

3 RESULTS AND DISCUSSION

The light micrographs of the Fe-0.25C (Alloy 1), Fe-0.25C-0.05Nb-0.05Al (Alloy 2), Fe-0.25C-0.075Nb-0.075Al (Alloy 3) and Fe-0.25C-0.1Nb-0.1Al (Alloy 4) PM steel in **Figure 3** show that the microstructures of the examined steels consist of ferrite and pearlite grains of varying sizes. In **Table 2** the relative density, phase volume fractions and mean linear intercept grain sizes of the specimens are listed.

Figure 3 and the data in **Table 2** indicate the grain sizes decreasing with an increasing content of Nb-Al, from 0.1, 0.15 or 0.2 %. A major benefit of micro-alloying is the decrease of the grain growth rate during

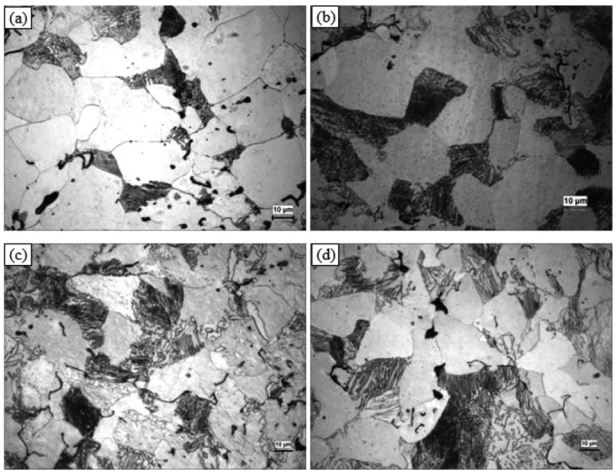

Figure 3: Microstructures of sintered PM steel and microalloyed PM steels: a) Alloy 1, b) Alloy 2, c) Alloy 3, and d) Alloy 4

Slika 3: Mikrostrukture sintranega PM jekla in mikrolegiranih PM jekel: a) zlitina 1, b) zlitina 2, c) zlitina 3 in d) zlitina 4

Table 2: Relative density, mean linear intercept grain sizes and volume fractions of ferrite and pearlite phases in the PM steel and microalloyed PM steels

Tabela 2: Relativna gostota, srednja velikost zrn pri linearni intercepciji in volumenski delež ferita in perlita v PM jeklu in v PM mikrolegiranem jeklu

Alloy	Relative density (%)	Grain size (μm)	Ferrite (%)	Pearlite (%)
Alloy 1	92	29.7±0.93	78.4±0.018	21.6±0.018
Alloy 2	94	27.2±0.85	75±0.019	25±0.019
Alloy 3	94	23.4±0.73	74±0.02	26±0.019
Alloy 4	94	22.9±0.71	73±0.02	27±0.02

austenitizing, and if fine precipitates exist during austentizing the growth of grains is restricted and a finer grain size is obtained after quenching.[16,27] Niobium has a low solubility product that allows the substantial dissolution of niobium carbonitrides only at elevated temperatures. At low temperatures in the austenite range, the carbonitride shows such low solubility and the dispersion strengthening is not generally observed. The undissolved carbonitride at these temperatures acts mostly as an effective grain refiner. The marked change in carbonitride dissolution between the high and low temperatures (1300 °C and 900 °C) in the austenite temperature range allows substantial strain-accelerated precipitation at temperatures below about 1000 °C, and produces what is arguably the most obvious distinctive effect of niobium, i.e., the marked retardation of recrystallization at these temperatures.[4,28–30]

Aluminium only forms a nitride that is stable at low temperatures in the austenite range, but will dissolve progressively as the temperature is increased. The extent of the dissolution at high temperatures in the austenite range (e.g. 1350 °C) depends upon the content of aluminium and nitrogen, but the solubility product for aluminium nitride is low and the only common micro-alloy nitride having a lower solubility product is titanium nitride. Aluminium nitride has the distinction of forming a separate nitride, which has a hexagonal crystal structure and forms no solid solution with the face-centred-cubic micro-alloy carbonitrides.[12]

Table 3 shows the yield strength (*YS*), ultimate tensile strength (*UTS*) and elongation of the examined PM steels, and **Figure 4** shows typical examples of the stress-strain curves obtained with the tensile test and a general increase of *YS* and *UTS* of steel with the addition of Nb and Al. Elongation tends to improve with increasing Nb-Al content. These changes are a consequence of the differences in the precipitation distribution.[31] High strength and good toughness in micro-alloyed steels are achieved by a combination of micro-alloying and controlled rolling. During sintering and slow cooling from the sintering temperature NbC(N) or AlN precipitates form in the austenite and the ferrite during the austenite-ferrite transformation or after transformation, as suggested by M. A. Erden at al.[32] These lead to an increase in the strength compared with the titanium-free alloy.

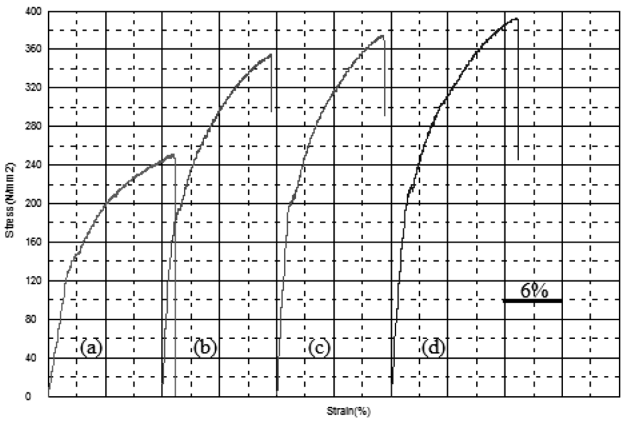

Figure 4: Variation of stress–strain curves of the PM steel and microalloyed PM steels at different percentages of Nb and Al content: a) Alloy 1, b) Alloy 2, c) Alloy 3, and d) Alloy 4

Slika 4: Spreminjanje krivulj napetost-raztezek PM jekla in mikrolegiranih PM jekel pri različnih vsebnostih Nb in Al: a) zlitina 1, b) zlitina 2, c) zlitina 3 in d) zlitina 4

Table 3: Mechanical properties of sintered PM steel and microalloyed PM steels

Tabela 3: Mehanske lastnosti sintranega PM jekla in mikrolegiranih PM jekel

Alloy	Yield strength (MPa)	Ultimate tensile strength (MPa)	Elongation (%)
Alloy 1	144	252	13
Alloy 2	198	356	12
Alloy 3	209	375	12
Alloy 4	220	394	13

The alloying elements have widely differing effects due to the different solubilities of their carbides and nitrides in both austenite and ferrite as well as their different precipitation kinetics. The strength is increased by grain refinement and precipitation hardening, by a sufficient content of carbon and nitrogen in the steel.[33,34] In modern micro-alloyed steels, the requirements for specific properties may call for the use of more than one micro-alloying element. An example are Al-Nb steels, where aluminium is used for the grain refinement and niobium for controlling the hot-rolled microstructure and dispersion strengthening. The behaviour of the micro-alloying elements can be modified by the presence of another of them and changes dependent on the particular elements. In principle, it depends on their mutual insolubility or mutual solubility. AlN has a close-packed-hexagonal structure, with little or no solubility for niobium and the NbN has a cubic structure with little or no solubility for aluminium. Under these conditions, the two separate nitrides can co-exist in the austenite according to their own solubility products.[35]

In the present experimental work, the solubility product of AlN, NbN and NbC at 1350 °C was calculated using the equations given by K. Narita.[36] At 1350 °C the solubility products of AlN, NbN and NbC are 2.3×10^{-3}, 3.7×10^{-3} and 3.6×10^{-2}. It is clear that the solubility of NbC is higher than NbN and AlN, and therefore niobium and carbon atoms should be present in the solid solution during sintering at 1350 °C. The dissolved Nb will precipitate as NbC(N) in austenite or ferrite, depending on the cooling rate. The strength increment in micro-alloyed PM steels is mainly due to precipitation hardening, resulting in the formation of AlN and NbC(N).

The steel's mechanical properties and toughness were analysed in terms of the influence of grain size. Traditionally, the approaches developed by E. O. Hall[37], based on experimental observations, and by N. S. Petch,[38] based on both experimental and theoretical approaches.

The relation between the yield strength and the grain size is now commonly known as the Hall-Petch equation (3):

$$\sigma_y = \sigma_0 + k_y d^{-1/2} \quad (3)$$

where σ_y is the lower yield stress, σ_o is the friction stress, k_y is the strengthening coefficient and d is the grain size. To study the influence of precipitates and clusters on the strength of micro-alloyed PM steel it is necessary to calculate the value of σ_p, which represents the strength obtained from precipitates and clusters in the micro-alloyed PM steel containing a different weight percentage of Nb-Al. This was done using the F. B. Pickering and T. Gladman[39] equation (4):

$$\sigma_y = 54 + 17.4 d^{-1/2} + \sigma_p \quad (4)$$

where d is the grain diameter in mm, and σ_p is the strength obtained from precipitates and clusters. In the present study the σ_p values were calculated using equation (2) for micro-alloyed PM steels. A value for the level of σ_p was derived by subtracting the predicted yield strength from the actual yield strength. The values of σ_p are given in **Table 4** and vary from -10 to 51 MPa for the Nb-Al-free and Nb-Al-added micro-alloyed PM steels tensile tested at room temperature.

As seen in **Table 4**, different values for σ_p were observed in the PM steel and microalloyed PM steels. For example, the additions (0.1, 0.15 and 0.2) of Nb-Al increased the precipitation contribution (σ_p). This is a result of the formation of carbonitrides after sintering at 1350 °C, which led to both precipitation strengthening and grain refinement. Alloy 1 without Nb-Al does not show any measurable precipitation strengthening. The role of niobium in sintered PM steels was investigated by several investigators.[40–43] To examine this effect a simple iron-carbon system was investigated by 0.16 % of mass fractions of Nb and carbon contents from 0.10 to 0.50 % of mass fractions and transverse rupture strength and apparent hardness were measured in the sintered condition. At low carbon there is an increase in the transverse rupture strength, presumably due to the precipitation of NbC(N). The precipitation of nitrides, as AlN may also occur during sintering and/or cooling after sintering, since nitrogen cannot be completely avoided in PM steels using current sintering technologies, such as sintering under an argon atmosphere. It has been shown that the $\gamma \rightarrow \gamma + \alpha$ transformation in isothermal conditions accelerates the precipitation kinetics of AlN, due to the lower solubility of nitrogen in ferrite.[44]

Table 4: Structure-property analyses of PM steel and microalloyed PM steels tensile tested at room temperature

Tabela 4: Analiza lastnosti PM jekla in mikrolegiranih PM jekel pri nateznem preizkusu na sobni temperaturi

Alloy	σ_o (MPa)	d (μm)	$k_y d^{-1/2}$ (MPa)	$\sigma_y$total (MPa)	σ_y test (MPa)	σ_p (MPa)
Alloy 1	54	29.7±0.93	100	154	144	–10
Alloy 2	54	27.2±0.85	106	160	198	38
Alloy 3	54	23.4±0.73	113	167	209	42
Alloy 4	54	22.9±0.71	115	169	220	51

σ_o: the friction stress, d: grain size, k_y: strengthening coefficient, σ_y total: predicted yield strength, σ_y test: actual yield strength, σ_p: difference between predicted yield strength and actual yield strength (strength obtained from precipitates)

The density is also expected to significantly affect the properties of PM steel and micro-alloyed PM steels because the pores are potential crack-initiation sites, and can also guide and propagate cracks through the material. This reduces the strength as well as the heat-transfer and cooling rates after sintering.[45] A strong microstructure may be obtained by incorporating small amounts of alloying elements to compensate for the effect of pores.[46]

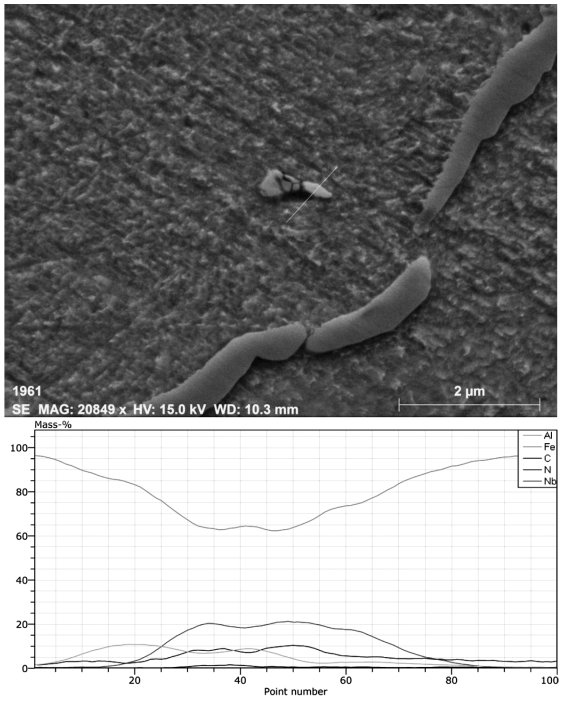

Figure 5: SEM micrograph for Alloy 2 and EDS line scan of the indicated particle

Slika 5: SEM-posnetek zlitine 2 in EDS-analiza preko označenega delca

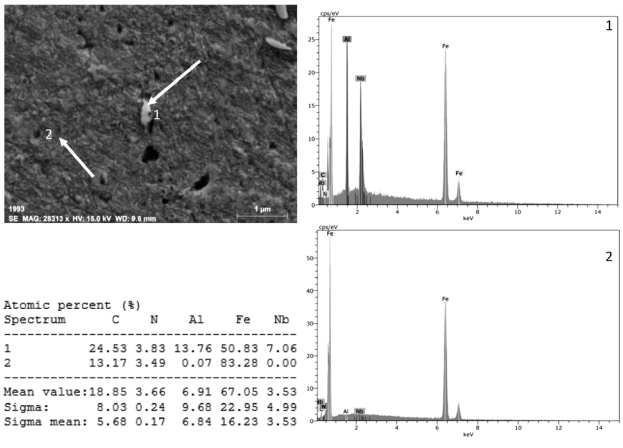

Figure 6: SEM micrograph for Alloy 4 and corresponding EDS of the indicated points

Slika 6: SEM-posnetek zlitine 4 in EDS-analiza označenih točk

In the present work PM steel and micro-alloyed PM steels showed a similar relative density, i.e., 92 % and 94 %, for the as-sintered condition. This may explain that the strength increase is the effect of the different content of NbC(N), AlN in micro-alloyed PM steel.

Figure 5 illustrates EDS Fe, Nb and C line analysis of the cross-section of the matrix and precipitate particle in Alloy 2 (Fe-0.25C-0.05Nb-0.05Al). Two distinct constituents are detectable: a Fe-rich matrix and a Nb-rich phase depicted a sharp increase from the Fe-rich matrix to the particle and inverse Fe behaviour. **Figure 6** also shows EDS analyses at points of 1 (precipitate particles) and 2 (matrix) marked in the micrograph of Alloy 4 (Fe-0.25C-0.1Nb-0.1Al). As seen in **Figure 6**, at point 1 the Fe, C, N, Al, Nb and at point 3 the Fe, C, N contents are detected. Concerning the literature and the current results, some NbC(N) and AlN particles probably did not dissolve during sintering. The results of the EDS analysis agree with the precipitates visible on the SEM micrograph of the fracture of micro-alloyed PM steels (Alloys 2 and 4).

Past studies to characterize precipitation in micro-alloyed steels have been mainly carried out using the transmission electron microscopy (TEM) of extraction replicas and thin foils.[47–50] However, quantitative chemical analysis is also helpful to determine the amounts of micro-alloying elements in solid solution and precipitates. Such investigations can be performed using a chemical or electrochemical procedure, selectively dissolving the steel matrix, and separating the undissolved particles from the matrix by filtration.[51] **Figure 7** shows the XRD precipitate peaks of the filter residue of Alloy 3 (Fe-0.25C-0.075Nb-0.075Al). The diffraction peaks in this **Figure 7** match well with NbC(N) and AlN. Therefore, the precipitates rich in Nb and Al observed in **Figure 7** correspond to these two types of precipitates.

In an alloy containing aluminium and without titanium or niobium, AlN precipitation occurs in the austenitic or ferritic regions. Several investigations report a fine precipitation («1 μm) with a large number density of nitride particles for steels containing between 29.96 mg/L and 299 mg/Lnitrogen.[15] This precipitation is known to have significant effects upon recrystallization and austenite grain growth.[52] The strengthening effect of Nb micro-alloying on steels also occurs with ferrite grain refinement due to austenite grain-boundary pinning, retardation of recrystallization and precipitation strengthening with an increase of the steel's strength.[53]

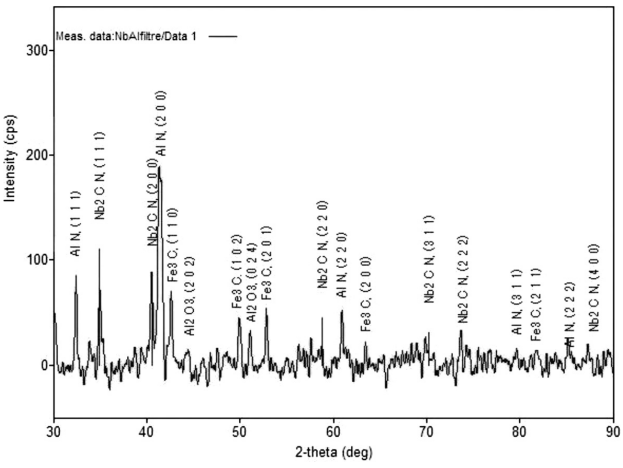

Figure 7: X-ray diffraction pattern of residues collected in the filter for Alloy 3
Slika 7: Rentgenogram ostankov zbranih na filtru pri zlitini 3

The elemental composition of the micro-alloyed powder metallurgy steels was performed using the X-ray fluorescence technique (XRF), which has many advantages: it is fast, accurate, non destructive and has a limit of detection in the range of few ppm for most elements.[54] For these reasons, the XRF analysis method is widely used in many fields such as metallurgy, geology and mineralogy, the food industry and environmental management. However, most routine steel analyses involve standard wet-chemical methods or inductively coupled plasma atomic emission. These methods are destructive and require dissolution of the alloy and a long sample-preparation time. The use of the X-ray fluorescence technique is very attractive in many fields and especially for metal and alloy analyses.[55] The sample preparation for XRF is relatively simple, so that it requires less time and work. For example, when the solid sample is homogeneous, then it only needs polishing to be ready for analysis.[56] In this experimental work, micro-alloyed PM steels were analysed using the XRF technique to determine their elemental compositions. The chemical composition in % of mass fractions of Alloy 4 (Fe-0.25C-0.1Nb-0.1Al) are presented in **Table 5**. It can be noted from Table 5 that most elemental compositions obtained conform to the values claimed by micro-alloyed steels.

Table 5: Chemical composition of Alloy 4 obtained by XRF analysis
Tabela 5: Kemijska sestava zlitine 4, dobljene z XRF analizo

No.	Component	Result	Unit	El. line	Intensity	*w*/% normal	Analyzing depth
1	Fe	99.0452	*w*/%			99.0452	
2	C	0.2653	*w*/%	C-KA	0.0400	0.2653	
3	Mn	0.2223	*w*/%	Mn-KA	0.7588	0.2223	0.0281
4	Al	0.0974	*w*/%	Al-KA	0.1224	0.0974	0.0009
5	Nb	0.0918	*w*/%	Nb-KA	1.1323	0.0918	0.0658

Figure 8 shows the tensile-testing fracture surfaces of Alloy 1 and Alloy 3. The changes were observed on the fracture surface of the PM steel and micro-alloyed PM steels sintered at 1350 °C with respect to the micro-voids' size, shape and depth. The mode of fracture for Alloy 1 (**Figure 8a**) is purely ductile. This is evident from the presence of numerous dimples along with fine and rounded pores. The mechanisms of the fracture were void formation and coalescence in the necks between adjoining fracturing microvolumes. Some microvoids pre-existed in the material, others nucleated and grew from defects or inclusions. The microvoids nucleate at strain discontinuities, such as those associated with

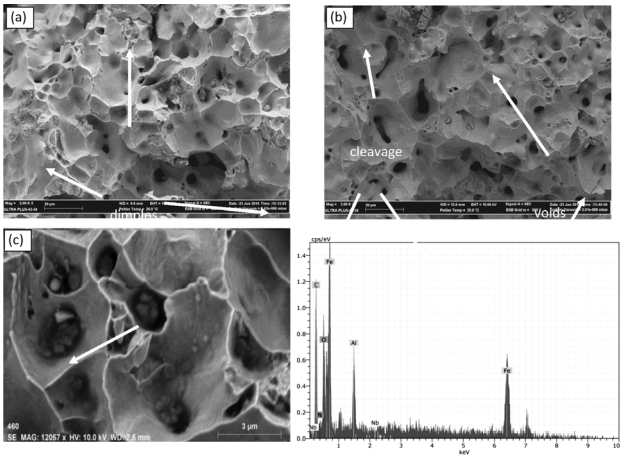

Figure 8: Fracture surfaces of: a) Alloy 1, b) Alloy 3 and c) EDS results from indicated particle of Alloy 3

Slika 8: Površine preloma: a) zlitina 1, b) zlitina 3 in c) EDS-analiza označenega delca v zlitini 3

a-priori defects (pores, microcracks), second-phase particles, inclusions, grain boundaries, dislocations pile-up. As the strain increases, the microvoids grow, coalesce, which involves plastic deformation, and eventually form a continuous fracture surface.[57]

However, Alloy 3 showed dimples and cleavage facets (**Figure 8b**) indicating that the fracture is of the mixed type. Large voids were also observed in the alloy. These voids are an indication of the removal of NbC or AlN particulates in the minor fracture surfaces. The pull-out of the NbC or AlN particulates on the crack faces indicates a possible mechanism for crack-tip bridging in the micro-alloyed PM steel, as well M. Hajisafari et al.[58] showed that void nucleation and growth in micro-alloyed steel are a function of the shape factor of second-phase particles and the mismatch between the second-phase particle and the metal matrix. Voids firstly nucleate around second-phase particles and consequently grow.

The Al-N-based particle inside the large microvoids of micro-alloyed PM steel is clearly shown in the SEM fractograph and the corresponding EDS results in **Figure 8c**. M. A. Erden et al.[32] investigated the tensile behaviour of sinter-forged Ti-alloyed PM steel and they observed a mixed (ductile-brittle) type of fracture in the micro-alloyed PM steel with Ti due to the formation of carbides and the carbide pull-off during heavy deformation.

4 CONCLUSIONS

Micro-alloyed PM steels with three different volume fractions of Nb-Al were processed through cold pressing and sintering in an argon atmosphere. The important findings obtained can be summarised as follows:

Micro-alloyed PM steels were analysed using the XRF technique to determine their elemental compositions. The results show that most elemental compositions obtained confirm to the values claimed by micro-alloyed steels.

Micro-alloying with Nb and Al requires high-temperature sintering to dissolve the Nb and Al in the austenite. The relative density of the sintered Nb-Al micro-alloyed PM steels can reach 94 % after sintering at 1350 °C.

The addition of Nb-Al can improve the strength of micro-alloyed PM steel through precipitation hardening and microstructure refining. The NbC(N) and AlN precipitates inhibit the grain growth during the sintering step, leading to enhanced strength.

The EDS and XRD analyses of the micro-alloyed PM steels revealed Nb- and Al-rich particles in micro-alloyed PM steel. The presence of Nb and Al elements in the particles indicates that NbC(N) and AlN formed during sintering and/or precipitate during the cooling after sintering.

The analysis of the fracture surface indicated that PM steel without micro-alloying addition exhibited ductile fracture. In the case of the micro-alloyed PM steels the mode of fracture is the mixed type with ductile and brittle regions. This could be attributed to the pull-out of NbC or AlN particles during deformation, indicating the possible mechanism for crack tip is bridging in the micro-alloyed PM steels.

Acknowledgements

The authors gratefully acknowledge financial support from TÜBİTAK, the Research Project of The Scientific and Technological Research Council of Turkey with the NO: 113M350.

5 REFERENCES

[1] Y. Li, D. N. Crowther, P. S. Mitchell, T. N. Baker, The Evolution of Microstructure during Thin Slab Direct Rolling Processing in Vanadium Microalloyed Steels, ISIJ International, 42 (**2002**) 6, 636–644, doi:10.2355/isijinternational.42.636

[2] B. A. Graville, Proc. Int. Conf. Welding of HSLA Structure Steels ASM, Metals Park, Ohio 1978, 85–101

[3] M. Olasolo, P. Uranga, J. M. Rodriguez-Ibabe, B. López, Effect of austenite microstructure and cooling rate on transformation characteristics in a low carbon Nb–V microalloyed steel, Mater. Sci. Eng. A, 528 (**2011**) 6, 2559–2569, doi:10.1016/j.msea.2010.11.078

[4] A. M. Sage, HSLA Steels: Processing, Properties and Applications, G. Tither, Z. Shouhua (Eds.), 1992, 51–61

[5] G. Y. Qiao, F. R. Xiao, X. B. Zhang, Y. B. Cao, B. Liao, Effects of contents of Nb and C on hot deformation behaviors of high Nb X80 pipeline steels, Trans. Nonferrous Met. Soc., 19 (**2009**) 6, 1395–1399, doi:10.1016/S1003-6326(09)60039-X

[6] J. C. Cao, Q. Y. Liu, Q. L. Yong, X. J. Sun, Effect of Niobium on Isothermal Transformation of Austenite to Ferrite in HSLA Low-Carbon Steel, J.Iron and Steel Res. Int., 14 (**2007**) 3, 52–56, doi:10.1016/S1006-706X(07)60043-0

[7] E. J. Palmiere, C. I. Garcia, A. J. DeArdo, Compositional and microstructural changes which attend reheating and grain coarsening in steels containing niobium, Mater. Metall. Trans. A, 25A (**1994**) 2, 277–286, doi:10.1007/BF02647973

[8] S. Vervynckt, K. Verbeken, P. Thibaux, Y. Houbaert, Recrystallization–precipitation interaction during austenite hot deformation of a Nb microalloyed steel, Mater. Sci. Eng. A, 528 (**2011**) 16-17, 5519–5528, doi:10.1016/j.msea.2011.03.087

[9] T. Siwecki, Modelling of Microstructure Evolution during Recrystallization Controlled Rolling, ISIJ Int., 32 (**1992**) 3, 368–376, doi:10.2355/isijinternational.32.368

[10] M. G. Mecozzi, J. Sietsma, S. Van der Zwaag, Analysis of $\gamma \rightarrow \alpha$ transformation in a Nb micro-alloyed C–Mn steel by phase field modelling, Acta. Mater., 54 (**2006**) 5, 1431–1440, doi:10.1016/j.actamat.2005.11.014

[11] M. Gómez, S. F. Medina, A. Quispe, P. Valles, Static Recrystallization and Induced Precipitation in a Low Nb Microalloyed SteeI, SIJ Int., 42 (**2002**) 4, 423–431, doi:10.2355/isijinternational.42.423

[12] T. Gladman, The Physical Metallurgy of Microalloyed Steels, The institute of Materials, London, 1997, 102–104

[13] G. Jeanmaire, M. Dehmas, A. Redjaïmia, S. Puech, G. Fribourg, Precipitation of aluminum nitride in a high strength maraging steel with low nitrogen content, Mater. Charac., 98 (**2014**) 4, 193–201, doi:10.1016/j.matchar.2014.11.001

[14] L. M. Cheng, E. B. Hawbolt, T. R. Meadowcroft, Dissolution and Coarsening oF Aluminum Nitride Precipitates in Low Carbon Steel – Distribution, Size and Morphology, Can. Metall. Q., 39 (**2000**), 73–85, doi:10.1179/000844300794388930

[15] R. Radis, E. Kozeschnik, Kinetics of AlN precipitation in microalloyed steel, Model Simul. Mater. Sci. Eng., 18 (**2010**) 5, 605–611, doi:10.1088/0965-0393/18/5/055003

[16] C. Schade, T. Murphy, A. Lawley, R. Doherty, Int. J. of Powder Metall., 48 (**2012**) 3, 51–59

[17] R. Chandramouli, T. K. Kandavel, D. Shanmugasundaram, T. Ashok Kumar, Deformation, densification, and corrosion studies of sintered powder metallurgy plain carbon steel preforms, Mater. Des., 28 (**2007**), 2260–2264, doi:10.1016/j.matdes.2006.05.018

[18] W. B. Morrison, The Proceedings of the Vanitec Symposium Guilin, China 2000, 25–35

[19] ASTM E8/E8M, Standard Test Methods for Tension Testing of Metallic Materials, ASTM International, West Conshohocken, PA 2013

[20] ASTM B328-96, Standard Test Method for Density, Oil Content, and Interconnected Porosity of Sintered Metal Structural Parts and Oil-Impregnated Bearings, ASTM International, Philadelphia, USA 2004

[21] S. Sankaran, S. Sangal, K. A. Padmanabhan, Microstructural evolution and tensile behaviour of medium carbon microalloyed steel processed through two thermomechanical routes, Mater. Sci. Technol., 21 (**2005**) 10, 1152–1160, doi:10.1179/174328405X51767

[22] Y. Pu, B. Guo, J. Zhou, S. Zhang, H. Zhou, J. Chen, Microstructure and tribological properties of in situ synthesized TiC, TiN, and SiC reinforced Ti3Al intermetallic matrix composite coatings on pure Ti by laser cladding, Appl. Surf. Sci., 255 (**2008**) 5, 2697–203, doi:10.1016/j.apsusc.2008.07.180

[23] J. R. Blank, T. Gladman, Quantitative Metallography, Tools and Technique in Physical Metallurgy, F. Weinberg, M. Dekker (Eds.), New York 1970, 265–327

[24] S. Gündüz, A. Çapar, Influence of forging and cooling rate on microstructure and properties of medium carbon microalloy forging steel, J. of Mater Sci Letters, 41 (**2006**) 2, 561–564, doi:10.1007/s10853-005-4239-y

[25] A. M. Sage, HSLA Steels: Processing, Properties and Applications, G. Tither, Z. Shouhua (Eds.), 1992, 51–61

[26] T. Gladman, J. Woodhead, J. of Iron and Steel Inst., 194 (**1960**), 189–193

[27] C. Schade, T. Murphy, A. Lawley, R. Doherty, Int. J. of Powder Metall., 48 (**2012**) 6, 41–48

[28] S. S. Campos, H. J. Kestenbach, E. V. Morales, On strengthening mechanisms in commercial Nb-Ti hot strip steels, Metall. Mater. Trans. A, 32 (**2001**), 1245–1248, doi:10.1007/s11661-001-0133-7

[29] B. Dutta, C. M.Sellars, Mater. Sci. Technol., 2 (**1986**) 2, 146–153

[30] J. G. Jung, J. S. Park, J. Kim, Y. K. Lee, Carbide precipitation kinetics in austenite of a Nb–Ti–V microalloyed steel, Mater. Sci. Eng. A., 528 (**2011**) 16, 5529–5535, doi:10.1016/j.msea.2011.03.086

[31] H. Karabulut, S. Gündüz, Effect of vanadium content on dynamic strain ageing in microalloyed medium carbon steel, Mater. Des., 25 (**2004**), 521–527, doi:10.1016/j.matdes.2004.01.005

[32] M. A. Erden, S. Gündüz, M. Türkmen, H. Karabulut, Microstructural characterization and mechanical properties of microalloyed powder metallurgy steels, Mater. Sci. Eng. A., 616 (**2014**), 201–206, doi:10.1016/j.msea.2014.08.026

[33] D. T. Llewellyn, R. C. Hudd, Steels: Metallurgy and Applications, Reed Educational and Professional Publishing Ltd, Oxford 1998, 153–154

[34] L. C. Cuddy, J. C. Raley, Metall. Trans. A., 14 (**1983**) 10, 1989–1995

[35] T. Gladman, The Minerals, G. Tither, Z. Shouhua (Eds.), Metals and Materials Society, (**1992**) 3, 267–271

[36] K. Narita, Transact ISIJ, 15 (**1975**), 145–152

[37] E. O. Hall, Process Physical Society, 64B (**1951**), 747–755

[38] N. J. Petch, J. Iron and Steel Inst., 174 (**1953**), 25–28

[39] F. B. Pickering, T. Gladman, Iron and Steel Inst, Special Report No: 81, (**1963**), 10–20

[40] R. Oberacker, F. Thummler, Metal Powder Report, 44 (**1989**), 120–124

[41] R. Oberacker, F. Thummler, Proceedings of the International Powder Metallurgy Conference, 1986, 647–648

[42] M. Orban, R. L. Orban, Sintered Structural Cu-Ni-Mo-C Low Alloyed Steels with Small Niobium Additions, Mater. Sci. Forum, 534 (**2007**), 725–728, doi:10.4028/www.scientific.net/MSF.534-536.725

[43] T. Tsutsui, K. Ishii, M. Yoshida, Proceedings of the Powder Metallurgy World Congress, 2 (**1994**) 1, 883–886

[44] G. Jeanmaire, M. Dehmas, A. Redjaïmia, S. Puech, G. Fribourg, Mater. Charac., 98 (**2014**), 193–201

[45] F. Changnon, Y. Trudel, International Conference on Powder Metallurgy & Particulate Material, Las Vegas, Nevada 1998, 1–8

[46] A. Bergmark, L. Alzati, Fatigue crack path in Cu-Ni-Mo alloyed PM steel, Fatigue Fract. Eng. Mater. Struct., 28 (**2005**), 229–235, doi:10.1111/j.1460-2695.2004.00841.x

[47] A. L. Rivas, D. M. Michal, M. E. Burnett, C. F. Musolff, Collection Papers 2nd Int. Symp. Microalloyed Bar and Forging Steels, C. J. Van Tyne, G. Krauss, D. K. Matlock (Eds.), The Minerals, Metals & Materials Society, Golden, Colorado, U.S.A. 1996, 159–172

[48] H. J. Kestenbach, E. V. Morales, Acta Microsc., 7 (**1998**), 22–33

[49] R. F. Morais, A. Reguly, L. H. de Almeida, Transmission Electron Microscopy Characterization of a Nb Microalloyed Steel for Carburizing at High Temperatures, J. Mater. Eng. Perform, 15 (**2006**) 4, 494–498, doi:10.1361/105994906X124596

[50] J. Strid, K. E. Easterling, Acta Metal., 33 (**1985**), 2057–2074

[51] A. L. Rivas, E. Vidal, D. K. Matlock, J. G. Speer, Electrochemical extraction of microalloy carbides in Nb-steel, Revista De Metalurgia, 44 (**2008**), 447–456, doi:10.3989/revmetalm.0771

[52] K. J. Irvine, F. B. Pickering, J. Iron Steel Inst., 201 (**1963**), 944–959

[53] A. G Kostryzhev, A. Al Shahrani, C. Zhu, J. M. Cairney, S. P. Ringer, C. R. Killmore et al., Effect of niobium clustering and precipitation on strength of an NbTi-microalloyed ferritic steel, Mater. Sci. Eng. A, 607 (**2014**), 226–235, doi:10.1016/j.msea.2014.03.140

[54] M. A. Al-Eshaikh, A. Kadachi, Proceedings of the 12th International Conference on Machine Design and Protection, Kusadasi, Turkey 2006

[55] G. J. Steven, S. L. Dale, Adv. X-ray Anal, 45 (**2002**), 457–463

[56] M. A. Al-Eshaikh, A. Kadachi, Elemental analysis of steel products using X-ray fluorescence (XRF) technique, J. of King Saud Uni–Engi Sci., 23 (**2011**) 2, 75–79, doi:10.1016/j.jksues.2011.03.002

[57] E. Dudrová, M. Kabátová, Powder Metall Prog, 8 (**2008**) 2, 59–75

[58] M. Hajisafari, S. Nategh, H. Yoozbashizadeh, A. Ekrami, Fatigue Properties of Heat-Treated 30MSV6 Vanadium Microalloyed Steel, J. Iron and Steel Res. Int., 20 (**2013**) 5, 66–73, doi:10.1007/s11665-012-0324-y

UDK 67.017:620.3:621.383.51
Original scientific article/Izvirni znanstveni članek

ISSN 1580-2949
MTAEC9, 50(5)649(2016)

CHARACTERISTICS OF DYE-SENSITIZED SOLAR CELLS WITH CARBON NANOMATERIALS

ZNAČILNOSTI NA FIKSIRANO BARVO OBČUTLJIVIH SOLARNIH CELIC Z OGLJIKOVIMI NANOMATERIALI

Leszek Adam Dobrzański, Agnieszka Mucha, Marzena Prokopiuk vel Prokopowicz, Marek Szindler, Aleksandra Drygała, Krzysztof Lukaszkowicz

Silesian University of Technology, Konarskiego St. 18A, 44-100, Gliwice, Poland
krzysztof.lukaszkowicz@polsl.pl

Prejem rokopisa – received: 2014-07-30; sprejem za objavo – accepted for publication: 2015-09-21

doi:10.17222/mit.2014.134

Dye-sensitized photovoltaic cells consisting of a layered structure have been developed for 20 years and they are a basis for the new development trend of photovoltaics. One of the examined aspects of their application is building-integrated photovoltaics. Dye-sensitized photovoltaic cells (DSSCs) were developed by Michael Grätzel and Brian O'Regan in 1991 and have been intensively examined ever since. Because of their low production costs, easy transfer, the relatively high efficiency of the photon conversion to the current and an easy production technology, dye-sensitized cells might represent an alternative to silicon cells. Basically, a dye-sensitized photovoltaic cell consists of five elements: a mechanical base covered with a layer of transparent conductive oxides (TCOs), a semiconductor film, e.g., TiO_2, dye absorbed on the semiconductor's surface, an electrolyte including a redox carrier, and a counter electrode suitable to regenerate a redox carrier, e.g., platinum. As part of this work we produced dye-sensitized solar cells. First, the glass with transparent conductive oxides was thoroughly cleaned. Then, the glass with TCO was coated with a layer of TiO_2 using the doctor-blade technique, and fired in a furnace at 450 °C. The plate prepared in this way was then sensitized in a ruthenium-based dye. The counter electrode was obtained by applying it on the glass with TCO carbon nanomaterials, including graphite, carbon black and carbon nanotubes. The photo-anode and the counter electrode were combined and between them was injected the redox electrolyte. This paper provides an analysis of the microstructure and electrical properties of nanostructural coatings with the carbon nano-element of the integrated dye-sensitized photovoltaic cells.

Keywords: dye-sensitized solar cell, carbon elements, counter electrode

Na fiksirano barvo občutljive fotovoltaične celice sestojijo iz plastovite strukture in so zadnjih dvajset let tematika razvoja na tem področju, predstavljajo namreč nov razvojni trend v fotovoltaiki. Eden od raziskovanih vidikov njihove uporabe je fotovoltaika, integrirana v zgradbe. Na fiksirano barvo občutljive fotovoltaične celice (DSSC), sta razvila Michael Grätzel in Brian O'Regan leta 1991 in so od tedaj pogost predmet raziskav. Zaradi nizkih stroškov njihove proizvodnje, enostavne prenosljivosti, relativno visoko učinkovite konverzije fotonov v tok in enostavne proizvodnje, so na fiksirano barvo občutljive celice lahko nadomestek silicijevim celicam. V osnovi na fiksirano barvo občutljive fotovoltaične celice sestojijo iz 5 elementov: mehanska podlaga je prekrita s plastjo prosojnih, prevodnih oksidov TCO, polprevodnega sloja, npr. TiO_2, fiksne barve absorbirane na površini polprevodnika, elektrolita z vključno redoks nosilcem nasprotna elektroda, ki je sposobna regeneracije redoks nosilca, kot je npr. platina. Kot del tega dela, so bile izdelane na fiksirano barvo občutljive solarne celice. Najprej je bilo steklo s presevnimi prevodnimi oksidi dobro očiščeno. Nato je bilo steklo s TCO, z uporabo tehnike kirurških nožev, prekrito s plastjo TiO_2 in žgano v peči pri 450 °C. Tako pripravljena plošča je bila občutljiva za barve na osnovi rutenija. Nasprotna elektroda je bila dobljena z nanosom TCO ogljikovih nanomaterialov, vključno z grafitom, črnim ogljikom in ogljikovimi nanocevkami na steklu. Fotoanoda in nasprotna elektroda sta bili kombinirani in med njiju je bil vbrizgan redoks elektrolit. Članek predstavlja analizo mikrostrukture in električnih lastnosti prevlek z nano strukturo, z ogljikovimi nanoelementi integrirane fotovoltaične celice, občutljive na fiksirano barvo.

Ključne besede: solarna celica, občutljiva na fiksirano barvo, ogljikovi elementi, nasprotna elektroda

1 INTRODUCTION

The increasing rate of energy consumption in the world is directly related to the increase in the human population. The progress of civilization is associated with an increase in the demand for energy, and particularly the most useful of its forms – electricity. Nowadays, mankind consumes 13,500 GW of power. The solar power reaching the Earth is 170,000,000 GW. If even a part of this energy could be used it could reduce environmental problems involving atmospheric pollution, arising as a result of the excessive use of conventional energy sources. Photovoltaics is an alternative and environmentally friendly technology for electricity production. Photovoltaic cells (also known as solar cells or PV cells) are used to convert solar energy into electricity, and this phenomenon is called the photovoltaic effect. The main advantage that enhances the development of organic photovoltaics is the potentially several times lower price of energy production per unit cell area than conventional solar cells based on silicon. Other advantages include [1–4] much better aesthetics compared to silicon solar cells, low toxicity, high transparency, possibility to choose the colour, flexibility, low dead-weight, low power loss due to the unfavourable angle of incidence of the sunlight, which is used in BIPV (Building Integrated Photovoltaics), working under reduced radiation (cloudy, darkening), where these cells

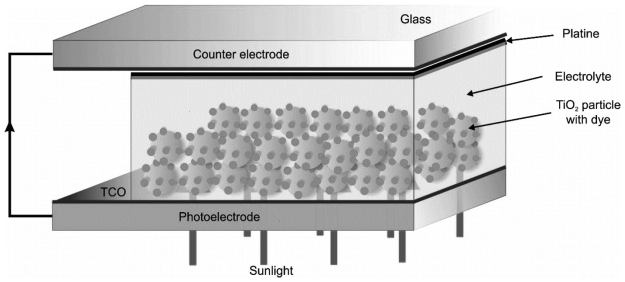

Figure 1: Construction of dye-sensitized solar cell[6]
Slika 1: Zgradba solarne celice občutljive na fiksirano barvo[6]

have a much better performance than silicon solar cells, a low production price due to the use of small amounts of material and the simplicity of production technologies, and the performance is independent of temperature changes in the range of 25–65 °C.

The construction of a dye-sensitized solar cell is based on a layered structure, which consists of two transparent glass plates with a Transparent Conductive Oxide (TCO) on it, placed parallel to each other and spaced about 40 μm apart (**Figure 1**). On one of the plates is applied a nanocrystalline titanium oxide layer coated organometallic photosensitive dye (photosensitizer) – this system retrieve in the cell function photo-anode (illuminated anode). On the surface of the second plate glass with TCO is usually nanoplatinum, which is a catalytic layer – this system is in the cell cathode. The space between the plates is filled with an electrolyte containing a redox system I^-/I^{3-}. Each component shows the dependence between many other materials. If at least one element in dye-sensitized solar cells is changed, e.g., the dye, the particle size of the TiO_2, the film thickness, or the composition of the electrolyte, the DSSC cell requires adjustment to ensure optimal system performance.[5,6]

The operating principle of a dye-sensitized solar cell is shown in **Figure 2**. The dye and the electrolyte are essential components of the cell.

The task of the counter electrode is to gather electrons flowing from the outer current and to catalyse the reduction of the triiodide ions. Platinum is the most common material used as a counter electrode. Despite the fact that platinum shows a high catalytic activity, its shortage in resources, high costs and corrosion possibility through a triiodide solution, inhibit its application on a large scale in the future.[7] For this reason, there is a need for research on alternative materials that are characterized by electrochemical activity and chemical stability. So far platinum[8], carbon,[9,10] conductive plastics,[11] CoS,[12] WO_2,[13], Mo_2C and WC,[14] TiN,[15] have been used as the counter electrodes. There are many publications about the methods of shaping the surface and structure of materials to improve their properties.[16–18]

Carbon nanotubes conduct electricity. They are almost transparent, flexible and strong, which makes them the ideal material for transparent electrodes for DSSC. The only drawback is that photo-generated charge carriers in the nanotube may recombine with ions in the dye, which reduces the power-conversion efficiency of the solar cell.

In the present work inexpensive and available carbon materials such as carbon black, graphite, and carbon nanotubes have been used as alternative materials to platinum because of their high corrosive resistance, high reactivity for triiodide reduction and low costs.[7,9,10,19–25] The disadvantages in catalytic activity in comparison to platinum may be compensated for by increasing the active surface of a catalytic layer using the porous structure.[7,25] Forming high-quality carbon bands on a substrate gives us prospects for using carbon as a counter electrode.

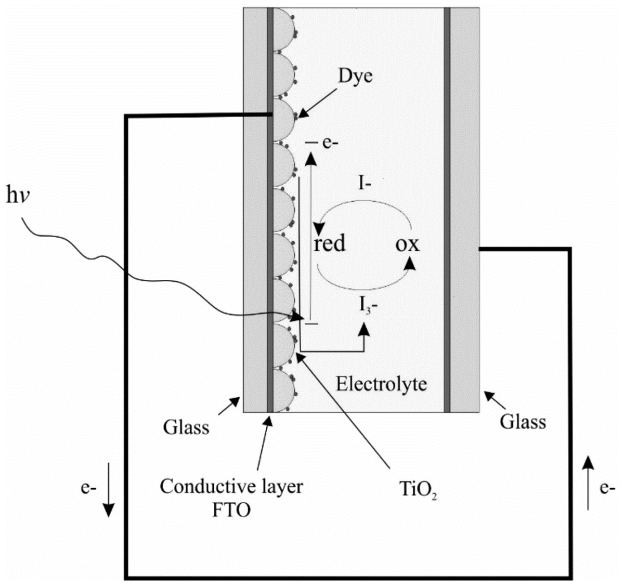

Figure 2: The operating principle of dye-sensitized solar cells[6]
Slika 2: Princip delovanja solarnih celic, občutljivih na fiksirano barvo[6]

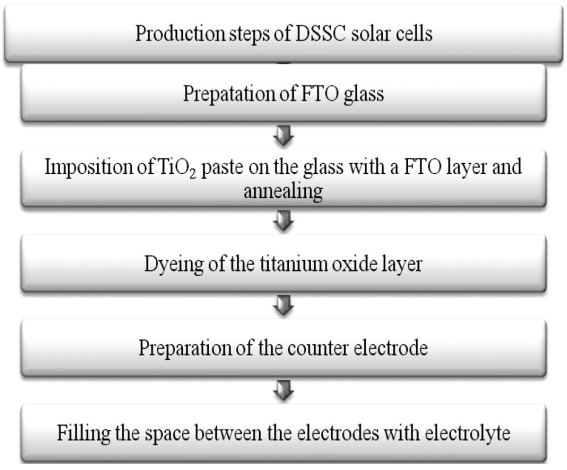

Figure 3: The production steps of dye-sensitized solar cells
Slika 3: Proizvodni koraki pri solarnih celicah, občutljivih na fiksirano barvo

2 EXPERIMENTAL PROCEDURE

The production steps for dye-sensitized solar cells were shown in **Figure 3**. As the counter electrodes we used three carbon materials: carbon black, graphite and carbon nanotube. The dye-sensitized solar cells have the following arrangement of layers (**Figure 4**):

- FTO glass/TiO_2/dye/electrolyte/carbon black/FTO glass,
- FTO glass/TiO_2/dye/electrolyte/graphite/FTO glass,
- FTO glass/TiO_2/dye/electrolyte/nanotube/FTO glass,

where:
FTO glass is glass with a layer of fluorine-doped tin oxide (FTO).

2.1 Fabrication of the photoanode

Glass plates with dimensions 30 mm × 30 mm (10Ω/sq.) were used. In order to remove any surface contamination and to degrease, the FTO glasses were dipped and held in an ultrasonic, deionized water, acetone, ethanol and isopropanol. In order to reduce the active surface of the dye-sensitized solar cells the FTO glass was covered with a layer of tape (**Figure 5**). In order to obtain a TiO_2 paste nitric acid with pH 3–4 was mixed with ethanol.[26–28] To the solution was added titanium oxide nanopowder. This solution was stirred until a uniform paste was obtained. A drop of TiO_2 paste was applied to the FTO glass and then it was uniformly spread over the glass surface using the doctor-blade technique (**Figure 6**). After removing the tape, the glass plate with the titanium paste was annealed in a furnace at 450 °C in air and then air-cooled. In order to sensitize the electrode it was immersed in the dye solution with absolute ethanol for 24 h at room temperature, without access to light. Once removed, the electrode was washed with ethanol to remove any excess dye and allowed to dry. A glass plate with a layer of titanium oxide, with and without dye, is shown in **Figure 7.**

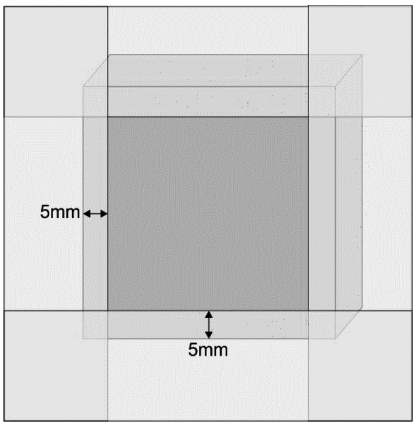

Figure 5: FTO glass covered with a layer of tape
Slika 5: FTO-steklo, prekrito s plastjo traku

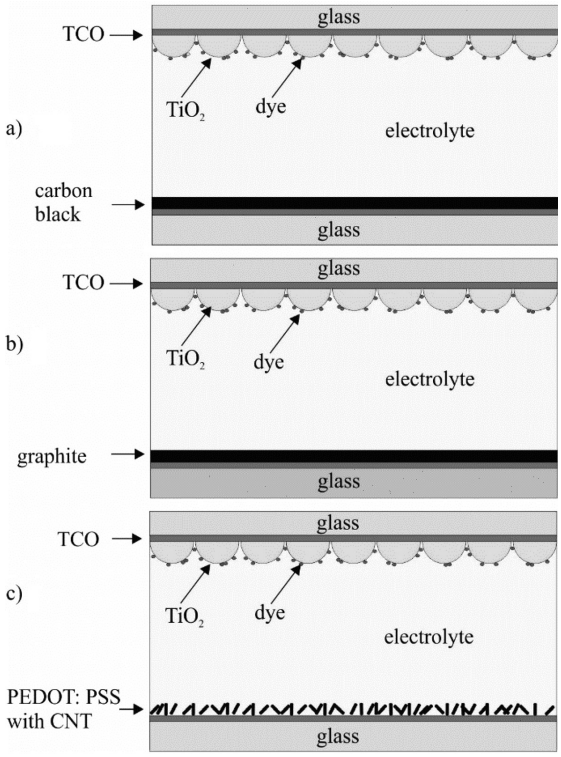

Figure 4: Schema of DSSC with: a) carbon black, b) graphite, c) carbon nanotube
Slika 4: Shema DSSC z: a) črnim ogljikom, b) grafitom, c) ogljikovimi nanocevkami

2.2 Fabrication of the counter electrode

The preparation of the carbon nanotubes' surface layers on the silicon substrates was performed using EasyTube®2000. During the process the default settings were used. EasyTube®2000 is an advanced, turnkey, thermal catalytic chemical vapor deposition CVD process tool for the synthesis of a wide variety of nanostructured materials. The catalyst needed for the CNT growth was a transition metal plus iron, and the catalyst was introduced to the process together with the CNT precursor.

It this case the counter electrodes were prepared by spring carbon nanotubes on the FTO glass. The CNT solution was prepared by direct mixing of the acid highly conductive PEDOT:PSS and applied on the glass surface with FTO. The second electrode that was used for this experiment was the electrode with carbon black. The

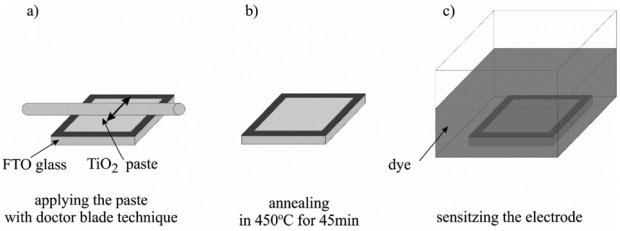

Figure 6: Photo-anode preparation
Slika 6: Priprava fotoanode

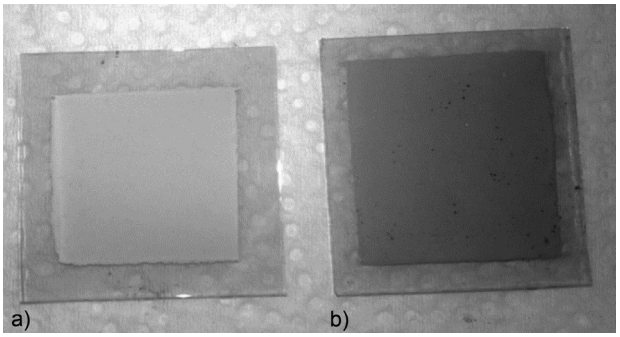

Figure 7: FTO glass with TiO_2 layer: a) before dying, b) after dying
Slika 7: FTO steklo s plastjo TiO_2: a) pred sušenjem, b) po sušenju

carbon black is cheap in industrial mass production. Ti is also used in printing toners, so we can easily spray it on to FTO glass.

A thin layer of carbon materials, i.e., carbon black (**Figure 8a**), graphite (**Figure 8b**), carbon nanotube (**Figure 8c**), were deposited on the FTO glass that was previously cleared of impurities.

2.3 Fabrication of the DSSC

An anode and a cathode were combined with the sealing strip, which simultaneously serves as a separator. Careful electrode bonding is a very important step in the preparation of DSSC cells. It prevents the leakage and evaporation of the electrolyte.

The last step was the placement the electrolyte, which is a solution of iodine and iodide in an organic solvent containing a redox couple I^-/I^{3-}, between the photo-anode and a counter electrode.

2.4 Measurements

Because the used carbon elements and titanium oxide consist of nano-metric structural units or single carbon layers, modern research equipment was used. First of all, an Atomic Force Microscope, a High Resolution Transmission Electron Microscope and a Scanning Electron Microscope.

Atomic force microscopy (AFM, XE-100, Park Systems) was used to observe the surface morphology of the TiO_2 layer with and without the dye.

The counter electrodes' morphology was observed using the scanning electron microscope (SEM; SUPRA 35, ZEISS).

The High Resolution Transmission Electron Microscope S/TEM (TITAN 80-300, FEI) was used to observe the surface morphology of the carbon nanotubes.

The voltages of the DSSCs were recorded using a multimeter (Meter Link Extech EX845) as a source measure unit, which was connected between the FTO glass and the counter electrode.

3 RESULTS AND DISCUSSION

Figure 9 shows the AFM images of the TiO_2 layer and the dye-adsorbed TiO_2 layer. The size and the dis-

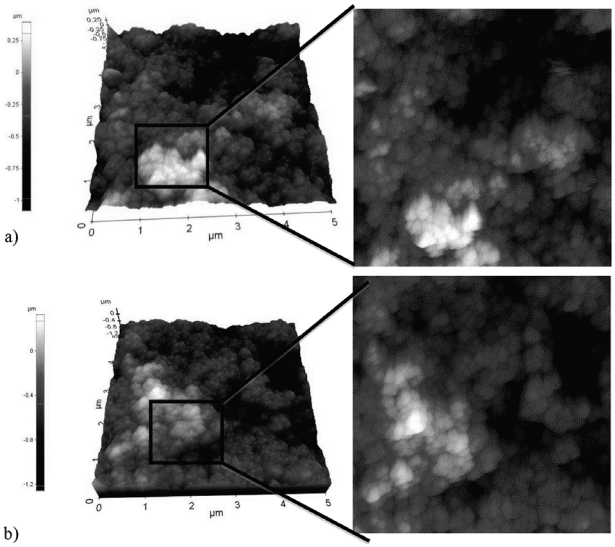

Figure 9: AFM images of the: a) TiO_2 layer and b) dye-adsorbed TiO_2 layer
Slika 9: AFM-posnetek: a) plast TiO_2 in b) s fiksirano barvo adsorbirana plast TiO_2

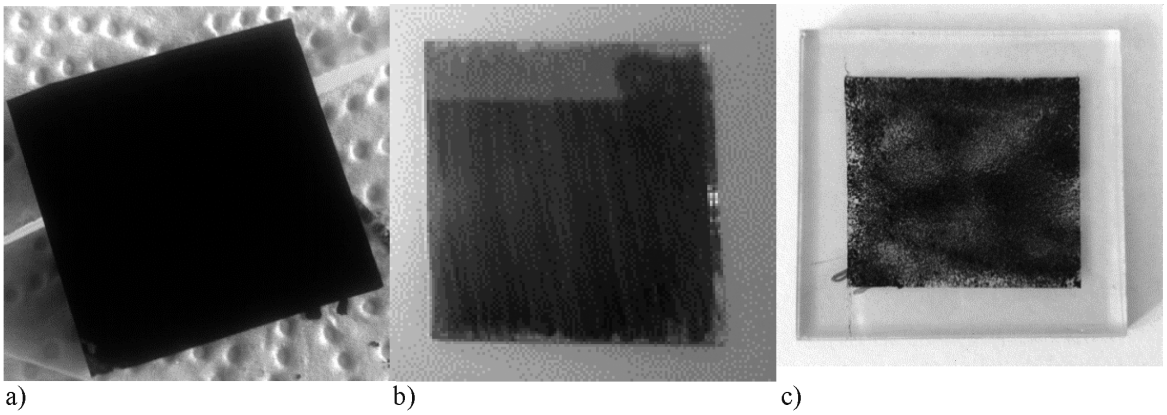

Figure 8: Counter electrode with a layer of: a) carbon black, b) graphite, c) PEDOT: PSS with carbon nanotubes
Slika 8: Nasprotna elektroda s plastjo: a) črnega ogljika, b) grafita, c) PEDOT: PSS z ogljikovimi nanocevkami

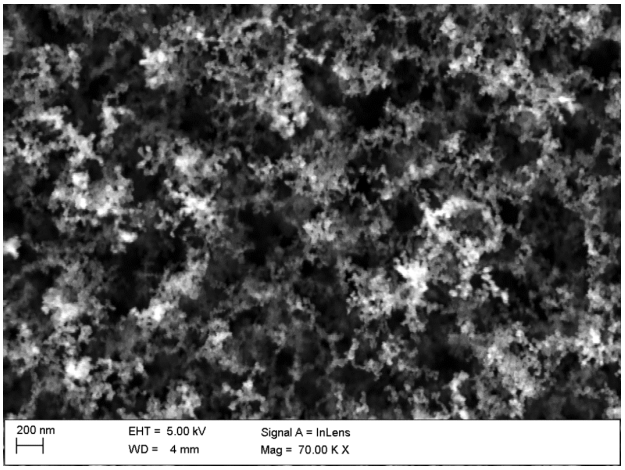

Figure 10: SEM image of carbon black
Slika 10: SEM-posnetek črnega ogljika

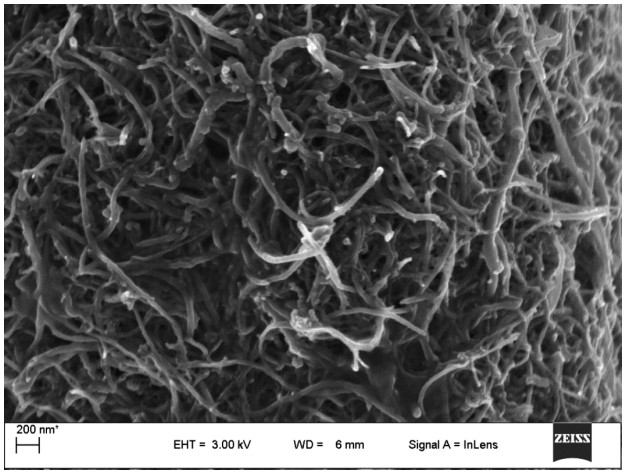

Figure 12: SEM images of carbon nanotubes
Slika 12: SEM-posnetek ogljikovih nanocevk

tribution of the particles characterize the dye-absorbed surface of the photo-anode. The SEM images show that TiO_2 surface with the absorbed dye is smoother than the surface without the dye.

Figures 10 to **12** show the SEM surface images of various counter electrodes on the FTO glass. **Figure 10** shows the microstructure of the carbon black, where a rectangular atomic arrangement can be observed. Because the fluorine-doped tin oxide film deposited on the glass has a rough surface, in **Figure 11** where the graphite is shown, we can also observe the rough pyramid microstructure. **Figure 12** shows the microstructure of the carbon nanotubes' electrode, where severely agglomerated CNTs are observable. We can see that the surface with the CNT and the highly conductive PEDOT:PSS has a uniform structure and fewer pores were generated in the structure compared with the microstructure of the carbon black or the graphite.

By adding carbon nanotubes to the electrode it is possible to obtain a larger surface area and therefore a larger contact surface than the graphite and carbon black counter electrode.

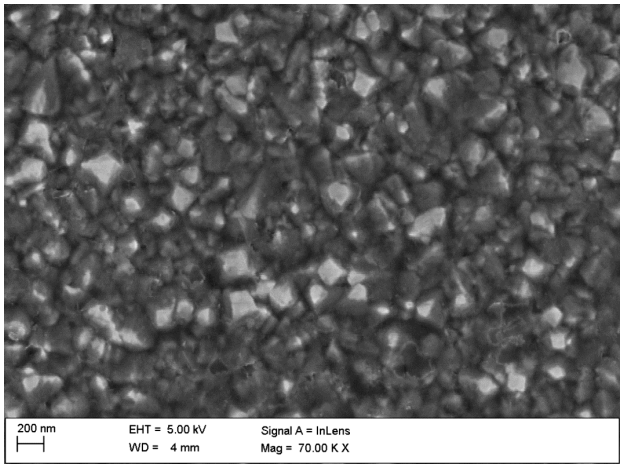

Figure 11: SEM image of graphite
Slika 11: SEM-posnetek grafita

Table 1 shows the electrical parameters by means of voltage for the three dye-sensitized solar cells with three different counter electrodes. As was expected after the SEM images, the highest voltage comes from the DSSC with carbon nanotubes as a counter electrode.

Table 1: Electrical properties of the investigated DSSCs
Tabela 1: Električne lastnosti preiskovane DSSC

Type of counter electrode	Voltage (mV)
carbon black	40
graphite	35
carbon nanotubes	52

4 CONCLUSIONS

In this study, for the purpose of decreasing the cost of dye-sensitized solar cells (DSSCs), we investigated the effect of carbon materials, i.e., carbon nanotubes, graphite and carbon black, added as a counter electrode. Three different low-cost DSSCs (CNT-counter electrode DSSC, carbon black-counter electrode DSSC, graphite-electrolyte DSSC) were fabricated.

The costly platinum electrode is able to be replaced by the modified counter electrode (using CNTs), with only little change in the efficiency of the cell. The effect of the carbon nanotubes on the performance of the DSSC showed that the DSSC fabricated with the CNT and PEDOT:PSS had the highest photovoltaic performances. These results are attributed to increasing the surface area of the counter electrode.

The conductivity of the carbon black is lower than carbon materials such as the graphite and carbon nanotubes, because those carbon nanotubes have a high conductivity and a large surface area. The literature proves that the carbon nanotubes with PEDOT:PSS layers have a good adhesion, so it can be used on the DSSC

electrodes. In the future it is planned to perform tests of the adhesion for the products' layers of low-cost DSSCs.

The investigated effect of the CNT counter electrodes on the efficiency of DSSC showed that these kinds of solar cells had the best efficiency for the counter electrodes.

Acknowledgment

The project was funded by the National Science Centre on the basis of the contract No. DEC-2013/09/B/ST8/02943.

5 REFERENCES

[1] J. Szlachta, S. Chrobak, DSCC cells – colorful future of photovoltaics, Green Energy, 9 (**2013**), 56–58

[2] B. I. Stiepanow, Fundamentals of chemistry and technology of organic dyes, Scientific and Technical Publishing, Warsaw 1980

[3] J. Godlewski, J. Kosk, M. Makowska, Dye sensitized solar cells, Green Energy, 3 (**2008**), 28–29

[4] A. Wrobel, J. Wasik, J. Godlewski, Trends in development of organic solar cells, Green Energy, 7-8 (**2010**), 22–23

[5] K. Siuzdak, Synthesis and properties of non-metals doped titanium dioxide as the active electrode material in visible light, PhD Thesis, Gdansk University of Technology, Gdansk, 2012

[6] H. Desilvestro, Y. Hebting, M. Khan, D. Milliken, Understanding and successfully applying materials for dye-sensitized solar cells, Materials Matters, 9 (**2014**) 1, 14–18

[7] S. Xu, Y. Luo, W. Zhong, Investigation of catalytic activity of glassy carbon with controlled crystallinity for counter electrode in dye-sensitized solar cells, Solar Energy, 85 (**2011**) 11, 2826–2832, doi:10.1016/j.solener.2011.08.014

[8] X. L. He, M. Liu, G. J. Yang, S. Q. Fan, C. J. Li, Correlation between microstructure and property of electroless deposited Pt counter electrodes on plastic substrate for dye-sensitized solar cells, Applied Surface Science, 258 (**2011**) 4, 1377–1384, doi:10.1016/j.apsusc.2011.09.070

[9] S. U. Lee, W. S. Choi, B. Hong, A comparative study of dye-sensitized solar cells added carbon nanotubes to electrolyte and counter electrodes, Solar Energy Materials & Solar Cells, 94 (**2010**) 4, 680–685, doi:10.1016/j.solmat.2009.11.030

[10] K. Li, Y. Luo, Z. Yu, M. Deng, D. Li, Q. Meng, Low temperature fabrication of efficient porous carbon counter electrode for dye-sensitized solar cells, Electrochemistry Communications, 11 (**2009**) 7, 1346–1349, doi:10.1016/j.elecom.2009.04.025

[11] J. Nei de Freitas, C. Longo, A. Flavia Nogueria, M. A. De Paoli, Solar module using dyesensitized solar cells with a polymer electrolyte, Solar Energy Materials & Solar Cells, 92 (**2008**) 9, 1110–1114, doi:10.1016/j.solmat.2008.03.022

[12] M. Wang, A. M. Anghel, B. Marsan, N. L. Cevey Ha, N. Pootrakulchote, S. M. Zakeeruddin, M. Grätzel, CoS supersedes Pt as efficient electrocatalyst for triiodide reduction in dyesensitized solar cells, Journal of the American Chemical Society, 131 (**2009**) 44, 15976–15977, doi:10.1021/ja905970y

[13] M. X. Wu, X. A. Lin, A. Hagfeldt, T. L. Ma, A novel catalyst of WO_2 nanorod for the counter electrode of dye-sensitized solar cells, Chem. Commun., 47 (**2011**), 4535–4537, doi:10.1039/c1cc10638d

[14] M. X. Wu, X. A. Lin, A. Hagfeldt, T. L. Ma, Low-cost molybdenum carbide and tungsten carbide counter electrodes fo rdye-sensitized solar cells, Angewandte Chemie International Edition, 50 (**2011**) 15, 3520–3524, doi:10.1002/anie.201006635

[15] Q. W. Jiang, G. R. Li, X. P. Gao, Highly ordered TiN nanotube arrays as counter electrodes for dye-sensitized solar cells, Chemical Communications, 44 (**2009**), 6720–6722, doi:10.1039/b912776c

[16] S. Lesz, R. Szewczyk, D. Szewieczek, A. Bieńkowski, The structure and magnetoelastic properties of the Fe-based amorphous alloy with Hf addition, Journal of Materials Processing Technology, 157–158 (**2004**), 743–748, doi:10.1016/j.jmatprotec.2004.07.133

[17] K. Lukaszkowicz, L. A. Dobrzański, A. Zarychta, Structure, chemical and phase compositions of coatings deposited by reactive magnetron sputtering onto the brass substrate, Journal of Materials Processing Technology, 157–158 (**2004**), 380–387, doi:10.1016/j.jmatprotec.2004.09.059

[18] L. A. Dobrzański, M. Kremzer, K. Golombek, Structure and properties of aluminum matrix composites reinforced by Al_2O_3 particles, Materials Science Forum, 591–593 (**2008**), 188–192, doi:10.4028/www.scientific.net/MSF.591-593.188

[19] K. Li, Y. Luo, Z. Yu, M. Deng, D. Li, Q. Meng, Low temperature fabrication of efficient porous carbon counter electrode for dye-sensitized solar cells, Electrochemistry Communications, 11 (**2009**) 7, 1346–1349, doi:10.1016/j.elecom.2009.04.025

[20] F. Miao, B. Tao, P. K. Chu, Enhancementof the efficiency of dye-sensitized solar cells with highly ordered Pt-decorated nanostructured silicon nanowires based counter electrodes, Electrochimica Acta, 96 (**2013**), 61–65, doi:10.1016/j.electacta.2013.02.059

[21] A. Kay, M. Grätzel, Low cost photovoltaic modules based on dye sensitized nanocrystalline titanium dioxide and carbon powder, Solar Energy Materials and Solar Cells, 44 (**1996**) 1, 99–117, doi:10.1016/0927-0248(96)00063-3

[22] K. Imoto, K. Takahashi, T. Yamaguchi, T. Komura, J. Nakamura, K. Murata, High-performance carbon counter electrode for dye-sensitized solar cells, Solar Energy Materials and Solar Cells, 79 (**2003**) 4, 459–469, doi:10.1016/S0927-0248(03)00021-7

[23] Z. Huang, X. Liu, K. Li, D. Li, Y. Luo, H. Li, W. Song, L. Q. Chen, Q. Meng, Application of carbon materials as counter electrodes of dye-sensitized solar cells, Electrochemistry Communications, 9 (**2007**) 4, 596–598, doi:10.1016/j.elecom.2006.10.028

[24] S. Peng, Y. Wu, P. Zhi, V. Thavasi, G. Mhaisalkar, S. Ramakrishna, Facile fabrication of polypyrrole/funcionalized multiwalled carbon nanotubes composite as counter electrodes in low-cost dye-sensitized solar cells, Journal of Photochemistry and Photobiology A: Chemistry, 223 (**2011**) 2-3, 97–102, doi:10.1016/j.jphotochem.2011.08.004

[25] H. Anwar, A. E. George, I. G. Hill, Vertically-aligned carbon nanotube counter electrodes for dye-sensitized solar cells, Solar Energy, 88 (**2013**), 129–136, doi:10.1016/j.solener.2012.11.013

[26] G. P. Smestad, Nanocrystalline Solar Cell Kit, Madison, The Institute for Chemical Education, Madison 2008

[27] A. Hagfeldt, M. Grätzel, Molecular Photovoltaics, Accounts of Chemical Research, 33 (**2000**) 5, 269–277, doi:10.1021/ar980112j

[28] N. J. Cherepy, G. P. Smestad, M. Grätzel, J. Z. Zhang, Ultrafast Electron Injection: Implications for Photoelectrochemical Cell Utilizing an Anthocyanin Dye-Sensitized TiO_2 Nanocrystalline Electrode, Journal of Physical Chemistry B, 101 (**1997**) 45, 9342–9351, doi:10.1021/jp972197w

UDK 621.791.92:669.018.25:678.742.3
Original scientific article/Izvirni znanstveni članek

ISSN 1580-2949
MTAEC9, 50(5)655(2016)

THE EFFECT OF THE WELDING PARAMETERS AND THE COUPLING AGENT ON THE WELDING OF COMPOSITES

VPLIV PARAMETROV VARJENJA IN SREDSTVA ZA SPAJANJE NA VARJENJE KOMPOZITOV

Selcuk Ertugrul Erdogan, Umit Huner

Trakya University, Faculty of Engineering, Department of Mechanical Engineering, 22050 Edirne, Turkey
umithuner@trakya.edu.tr

Prejem rokopisa – received: 2015-03-11; sprejem za objavo – accepted for publication: 2015-09-14

doi:10.17222/mit.2015.059

This paper presents an experimental investigation of the welding of a glass-fiber-reinforced PP composite. The goals of this paper are to investigate the issues of local changes of the welding strength that depend on the heating time and the coupling agent (MAPP). Composite samples were prepared by using an extruding (for mixing) process and a hot-press method. The PP matrix was reinforced by unidirectional short glass fibers. The welding process for the specimens was carried out using a non-contact heated tool butt welding process. Tensile and fatigue tests were conducted to investigate the effects of the heating time parameter and the coupling agent. The highest weld strength dependent on the heating time was achieved with 94 % relative to the base strength of the material. The fatigue behavior of short-fiber-reinforced thermoplastic composites (polypropylene/20 % of volume fractions of E-glass fiber) is presented in terms of stress versus the number of cycles to failure. The specimens were fatigue tested at various percentages of their static tensile strengths at a load ratio $R = 0.1$ and frequency f= 5 Hz. An indefinite fatigue life was obtained at 35 % of the static damage initiation load for glass-fiber-reinforced specimens. Then, these specimen's maximum welding strengths and fatigue properties that were dependent on the heating time were compared.

Keywords: plastic material, composite, heated tool, welding process, reinforcement, fatigue, polypropylene

Članek predstavlja preiskavo varjenja PP kompozita, ojačanega s steklenimi vlakni. Cilj članka je bil preiskati vpliv lokalnih sprememb na trdnost zvara, ki je odvisna od časa ogrevanja in sredstva za spajanje (MAPP). Kompozitni vzorci so bili pripravljeni z uporabo metode ekstruzije in vročega stiskanja. PP osnova je bila ojačana z usmerjenimi kratkimi steklenimi vlakni. Postopek čelnega varjenja vzorcev je bil izveden z brezkontaktno ogrevanim orodjem. Izvedeni so bili natezni preizkusi in preizkusi utrujenosti, da bi ugotovili vpliv časa ogrevanja in sredstva za spajanje. Največja trdnost zvara v odvisnosti od časa ogrevanja je bila 94 % trdnosti osnovnega materiala. Obnašanje pri utrujanju termoplastičnega kompozita (polipropilen/20 % prostorninskih deležev E-steklenih vlaken), ojačanega s kratkimi vlakni, je prikazano na krivulji utrujanja kot odvisnost napetosti od števila ciklov. Utrujenost vzorcev je bila preizkušana pri različnih odstotkih statične natezne trdnosti, pri hitrosti obremenjevanja $R = 0{,}1$ in frekvenci $f = 5$ Hz. Zdržljivost na utrujanje s steklenimi vlakni ojačanih vzorcev je bila dobljena pri 35 % nazivne statične obremenitve. Primerjane so bile maksimalne trdnosti zvarov, z obnašanjem pri utrujanju v odvisnosti od časa ogrevanja.

Ključne besede: plastični material, kompozit, ogrevano orodje, postopek varjenja, ojačanje, utrujenost, polipropilen

1 INTRODUCTION

In high-technology applications, a composite is suitably qualified due to the fact that it has a higher strength and a better stiffness-to-weight ratio. The vital properties of thermoplastic composites include higher damage tolerance, corrosion resistance, higher impact resistance and enhanced fatigue life. Due to their recyclable and re-formable natures, thermoplastic composites are selected for environmentally benign applications.[1–4]

The welding process is one of the preferred methods to realize the assembly structure of thermoplastic composites. This method eliminates disadvantages such as stress concentration and the galvanic corrosion of mechanical fastenings. Also, the thermoplastic matrix has its own specific welding parameters with much the same reinforcements. In the welding zone the dispersion of the reinforcement and orientation could be affected by the welding pressure, heating, heating time and some similar properties, which results in the corruption on unity for the reinforced thermoplastic.[5–7]

Some researchers have worked on different welding methods for thermoplastic composites. At present, there is still not enough literature available related to the process parameters and their influence on the joint's strength.

C. B. Bucknall et al.[8] reported that the weld strengths of glass-fiber-reinforced polypropylene were strongly affected by the hot-plate temperature, heating time, and melt flow during welding. K. V. Stokes[5] has studied the fatigue life of vibration-welded unreinforced polycarbonate (PC), polyetherimide (PEI), modified polyphenylene oxide resin (M-PPO) and poly (butylenes terephthalate) (PBT), under tension–tension loading at $R = 0.1$. The first three polymers are amorphous and PBT is semi-crystalline. K. V. Stokes[5] found that the ratio of the endurance limit stress to the tensile strength was 0.29 for PC, 0.34 for PEI, 0.22 for M-PPO and 0.31

Table 1: Thermoplastic materials and glass-fiber properties used in the experiments
Tabela 1: Lastnosti termoplastičnega materiala in steklenih vlaken, uporabljenih pri preizkusih

Material	Producer	Density	MFI (g/10min)	Melting temp.	Vicat soft. temp. (°C)	Tensile strength (MPa)
Polipropilen (S.R.L)	ROM Petrol	0.90	20	165	132	32
PP-g-MA	Sigma Aldrich	0.95	115	152	147	–
Material	Producer	Dimensions	Density (gr/cm^3)	Tensile strength (MPa)	Melting temp. (°C)	Annotations
Glass Fiber	Cam Elyaf A.Ş.	D: 10.5 μm L: 4.5 mm	2.54	3450	1722	treated 0.6 % silane

for PBT. T. T. Lin et al.[9] investigated the effect of welding parameters on the non-contact hot-plate butt welding of polypropylene. For a given hot-plate temperature, an optimum heating time and forging pressure were found. M. Watson et al.[10] investigated the parameters of heated tool welding. The heated tool temperature has been found to be a less critical parameter than either the heating pressure or time.

These studies mostly concentrate on the parameters of the welding process, such as the heating time, the tool temperature and the pressure. But they lack the comparison of composites that had a chemical treatment of a matrix material like maleic anhydride (MA). There is a need to better understand the influence of various processing parameters and the coupling agent (MAPP) on the joint properties of hot tool welded thermoplastic composites. In accordance with previous studies published in the literature about the fatigue life of SGFR thermoplastics, the fatigue scattering is small, especially in comparison with the fatigue of metallic materials.

The final goal of this study is to gain a better understanding of the effects of using a coupling agent (MAPP) and the heating time parameter on the welding properties of hot tool welded composites. For constant temperatures and reinforced MAPP with a different ratio, thermoplastic composite component's butt welded joint strength, failure strain, modulus of elasticity and fatigue properties that depend on the heating time and cyclic number were compared by using the tensile and the fatigue-tests method. Non-welded material data are also included as a reference. The results are analyzed using curves for the stress versus the number of cycles to failure (S–N) for the fatigue test.

2 MATERIALS AND EXPERIMENTAL PROCEDURES

2.1 Materials

The resins used in this study were commercially available, virgin-grade polypropylene (PP) S.R.L., polypropylene-grafted maleic anhydride (PP-*g*-MA (Sigma Aldrich), MA content = 1 % of mass fraction) chopped into strands of glass fiber PA2-4.5 (Cam Elyaf Inc.). **Table 1** lists the properties of the resins as provided by the resin producer. Glass-fiber-reinforced PP granules were prepared with a lab-type single-screw extruder (L/D: 28). And then the granules were shaped as 200×200 mm^2 plates using a hot press. The samples were obtained from the plates with a cutting press. ISO 527 tensile-test procedures were used in this investigation. Three identical samples of each composition (**Table 2**) were measured and the average values were reported.

Table 2: Thermoplastic composites used in the experiments
Tabela 2: Termoplastični kompoziti, uporabljeni za preizkuse

Material type	PP (*w*/%)	MA-g-PP (*w*/%)	GF (*w*/%)
PPv (virgin)	100	–	–
PP20GF	80	0	20
MA2.5PPGF	77.5	2.5	20
MA5PPGF	75	5	20

2.2 Welding method

In the non-contact hot-tool welding process, the parts being welded are placed near the hot tool separated from it by a distance referred to as the non-contact gap. The hot tool is removed during the change-over phase. Pressure is applied to hold the parts in close contact during weld cooling and solidification. The heat is transferred by thermal radiation and convection. The process is otherwise identical to hot-tool welding: the hot plate is removed in the changeover phase, and pressure is applied to achieve close contact as the weld cools and solidifies.[8] The non-contact hot-tool or hot-plate welding has processing parameters that influence the weld strength, which include the size of the non-contact gap, the platen temperature, heating time, change-over time, weld pressure and duration. A butt-type joint has a lower weld line strength at a low welding pressure.[11] The welding and tensile test steps are shown as an example in **Figure 1**.

During the welding process, the heat transfer raises the temperature of the part and the resulting thermal expansion causes a small rightward (away from the hot-tool surface) motion in the part and fixture. When the surface temperature reaches the melting point of the plastic the part surface begins to melt. The externally applied pressure causes the molten material to flow laterally outwards, thereby inducing a leftward motion of the part.[8]

In non-contact heated tool welding, the contamination of the weld surfaces is minimized, the heating is

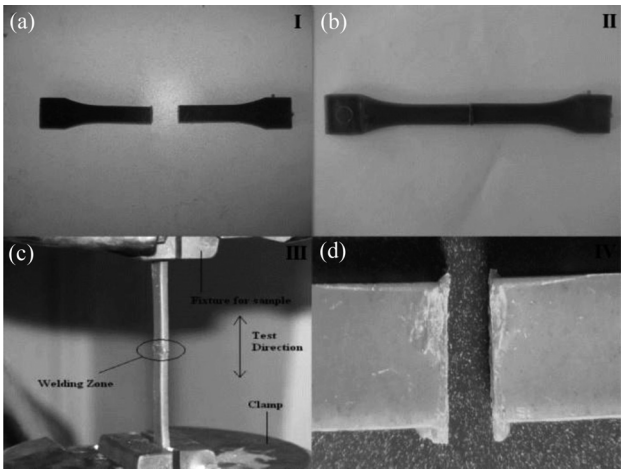

Figure 1: Welding and tensile test procedure of a sample: a) divide injection-molded sample into two parts, b) joint samples by welding, c) tensile testing of welded part, d) failure on welded parts after tensile test

Slika 1: Postopek varjenja in preizkušanja vzorca: a) dva dela razdeljenega tlačno litega vzorca, b) zvarjen vzorec, c) natezni preizkus zvara, d) porušen zvar po nateznem preizkusu

uniform, and a small weld bead is produced, providing good, consistent weld strengths.[11] An important aspect was the heat-soak time, which was influential in obtaining high joint strengths. Ideally, the stops should be as close to the joint interface as possible, consistent with bringing the joint interface into close contact with the heating element.

The experimental activity was carried out with the aim of evaluating the static and fatigue behavior under tension loadings of single lap welded joints in composite materials and to investigate the mechanics of damage evolution.

In this study the mechanical performance of the weld was obtained using rectangles of injection-molded samples that were welded together. The dimensions of the samples have enough tolerance for the welding process. Two parts were joined under heat that was generated by the stainless-steel hot-tool plate with dimensions of 40 mm × 2 mm × 100 mm. The weld line temperature was manually controlled with an InfraRed thermometer (CEM DT-8835, K-Type). The sets of these test samples and test parameters are given in **Table 3**. The weld area is equal to 40 mm^2. The welding pressure was held at constant values of 0.5 MPa and 4 MPa. For each type of thermoplastic composite a welding temperature of 260 °C was applied.[12] The non-contact gap was 1 mm. A constant heating displacement and weld displacement were maintained during the experiments. The heating temperature was chosen as an optimum value that is common to welding on all types of thermoplastic composite welding. The range for the heating time was 40 s to 70 s. The weld was always situated in the middle of the specimen, perpendicular to the load line.

2.3 Tensile test

In this study the tensile tests were performed using an Instron Universal Testing Machine Model 8501, equipped with a 500-kg load cell, a strain-gauge extensometer (Instron, model 2620, UK) after conditioning at 23±2 °C according to the ISO 527 standard. The cross-head speed used for the type IA tensile specimens was 5 mm/min. All the samples were 150 mm in length with a bonded butt (flat) type. The tests were performed in triplicate and the results reported are the arithmetic average of the parallel samples.

The dog-bone-shaped sample is routed down to a standard ISO 527 tensile test specimen with a butt joint at its center. The tensile sample, which has a transverse butt weld at mid-length, is then subjected to a constant-displacement-rate tensile test in which the strain across the weld is monitored with an extensometer. In this way the average failure strain across the weld over a 25 mm gauge length can be monitored.

2.4 Fatigue test

Load-controlled fatigue tests were performed in the tension-tension mode at ambient temperature (approximately 23 °C). The specimens were tested under a sinusoidal waveform at various loads between 35 % and 80 % of the static damage initiation load according to ASTM D 3479 (tension-tension fatigue behavior). The tests were conducted under a load ratio R = 0.1 and a frequency f = 5 Hz. No significant heating was noticed during the fatigue testing. When specimen failure could

Table 3: Some parameters of the experimental procedure for the study and sample codes (welding temp. 260 °C)
Tabela 3: Nekateri parametri preizkusov in oznake vzorcev (temperatura varjenja 260 °C)

Materials	Heating time (s)	Welding pressure (MPa) Part I/Part II	Materials	Heating time (s)	Welding pressure (MPa) Part I/Part II
PPv	40	0.5/4 MPa	MA2.5PPGF	40	0.5/4 MPa
	50	0.5/4 MPa		50	0.5/4 MPa
	60	0.5/4 MPa		60	0.5/4 MPa
	70	0.5/4 MPa		70	0.5/4 MPa
PP20GF	40	0.5/4 MPa	MA5PPGF	40	0.5/4 MPa
	50	0.5/4 MPa		50	0.5/4 MPa
	60	0.5/4 MPa		60	0.5/4 MPa
	70	0.5/4 MPa		70	0.5/4 MPa

not be obtained within 1 million cycles, the test was terminated and an indefinite fatigue life was reported. Between 10 and 15 specimens were tested for each material. The fracture surfaces of the broken specimens were observed visually and using scanning electron microscopy (SEM). The samples were first sputter coated with a fine layer of gold under vacuum for 60 s. An accelerating voltage of 20 kV was used to collect the SEM images.

3 RESULTS AND DISCUSSION

3.1 Tensile test results

The results of the static tests are presented in terms of both nominal tensile stress on the adherents and shear stress on the adhesive. The aim of this is to provide information on the load-carrying capability of the joints and the adhesive properties. It is a well-known fact that the welding quality is influenced by many processing factors, some of these being the welding time and the welding pressure. It is therefore important to explore the best combination of these factors to obtain the best welding result. Considering the used filler content, it was verified that for all the tested composites the tensile strength increases by the welding time and considering the shape of filler content, the type of fiber for the filler content achieved a relatively high strength compared to the other reinforced PP composites. This happens because the fiber adhesion to the matrix is enough, when compared with the others, to increase the matrix tension's transfer efficiency through the interface and that is essential to get an improvement of the mechanical properties in the composite.

For each time period (40 s, 50 s, 60 s, 70 s) three parallel samples were used and the results reported are the arithmetic average of the parallel samples. The joint

Table 4: Comparing the results of joint strength and failure strain for the welded samples
Tabela 4: Primerjava rezultatov trdnosti spojev in raztezek pri porušitvi zvarjenih vzorcev

Materials	Heating time(s)	Joint strength (MPa) I	S_d***	σ_w/σ_b* I	Joint strength (MPa) II	S_d	σ_w/σ_b II
PPv (Bulk strength 32 MPa)	40	17.84	7.55	0.55	14.53	5.86	0.45
	50	20.16	9.77	0.63	17.66	6.53	0.55
	60	23.42	8.02	5.73	20.45	7.94	0.63
	70	26.11	8.51	5.81	23.71	12.84	0.74
PP20GF (Bulk strength 41 MPa)	40	24.15	10.87	4.58	20.31	9.12	0.49
	50	26.34	11.14	7.55	22.59	6.35	0.55
	60	33.18	15.97	9.11	29.16	8.74	0.71
	70	37.77	16.23	8.92	33.94	10.81	0.82
MA2.5PPGF (Bulk strength 44 MPa)	40	30.24	10.88	1.68	27.76	8.54	0.63
	50	35.61	12.01	6.80	32.59	8.62	0.74
	60	38.22	14.11	5.77	38.93	10.88	0.88
	70	40.78	18.14	6.92	40.56	11.99	0.92
MA5PPGF (Bulk strength 48 MPa)	40	36.45	10.78	1.75	32.98	9.21	0.68
	50	39.27	12.28	4.81	35.26	10.54	0.73
	60	41.48	17.33	3.86	36.48	13.33	0.76
	70	46.25	19.71	6.96	40.58	10.27	0.92
Materials	Heating time(s)	Failure strain (%) I	S_d***	$\varepsilon_w/\varepsilon_b$** I	Failure strain (%) II	S_d	$\varepsilon_w/\varepsilon_b$ II
PPv (Bulk material strain ε_0 = 4.56%)	40	3.51	1.3	0.77	3.14	1.72	0.69
	50	3.76	0.7	0.82	3.05	2.02	0.67
	60	4.11	2.2	0.90	2.87	0.97	0.63
	70	4.18	2.4	0.92	2.56	1.12	0.56
PP20GF (Bulk material strain ε_0 = 0.58 %)	40	0.51	0.16	0.88	0.40	0.14	0.69
	50	0.45	0.04	0.78	0.34	0.12	0.59
	60	0.41	0.13	0.71	0.29	0.09	0.50
	70	0.36	0.08	0.62	0.26	0.11	0.45
MA2.5PPGF (Bulk material strain ε_0 = 0.35 %)	40	0.22	0.04	0.63	0.16	0.06	0.46
	50	0.17	0.04	0.49	0.11	0.08	0.31
	60	0.11	0.03	0.31	0.06	0.02	0.17
	70	0.08	0.01	0.23	0.04	0.02	0.11
MA5PPGF (Bulk material strain ε_0 = 0.24 %)	40	0.17	0.04	0.71	0.14	0.07	0.58
	50	0.15	0.06	0.63	0.11	0.03	0.46
	60	0.07	0.06	0.29	0.04	0.01	0.17
	70	0.05	0.02	0.21	0.02	0.01	0.08

* σ_w/σ_b (Relative strength),** $\varepsilon_w/\varepsilon_b$ (Relative strain),*** S_d (Standard deviation)

strength of the welded samples and the bulk strength of unwelded samples are compared in **Table 4**. All of the welded assemblies of virgin and reinforced polypropylene failed at the weld lines. All the glass-fiber-reinforced parts were found to fracture at the weld interfaces. The results suggested that the hot-plate-welded MA5PPGF composite parts exhibited the highest joint strength on 0.5 MPa weld pressure, followed by the MA2.5PPGF and PP20GF composites. The welded virgin polypropylene showed the lowest joint strengths.

It is clear that a weld does not represent just a discontinuity in the material, but is the source of an extended mechanical disturbance, which strongly influences the local material's behavior, even at a distance outside the weld.[13] It can be noticed that for the higher MA-g-PP/GF content the local strain (**Table 4**) in the accompanying zones is lower, which corresponds to the lower compliance of the reinforced material. Also, in this case the lower pressure results in a local strain super elevation at the weld. The range of fiber orientation inside the weld is only very low, so that the material showing a higher degree of deformation and damage at the same weld pressure governs the mechanical behavior for the whole weld range.

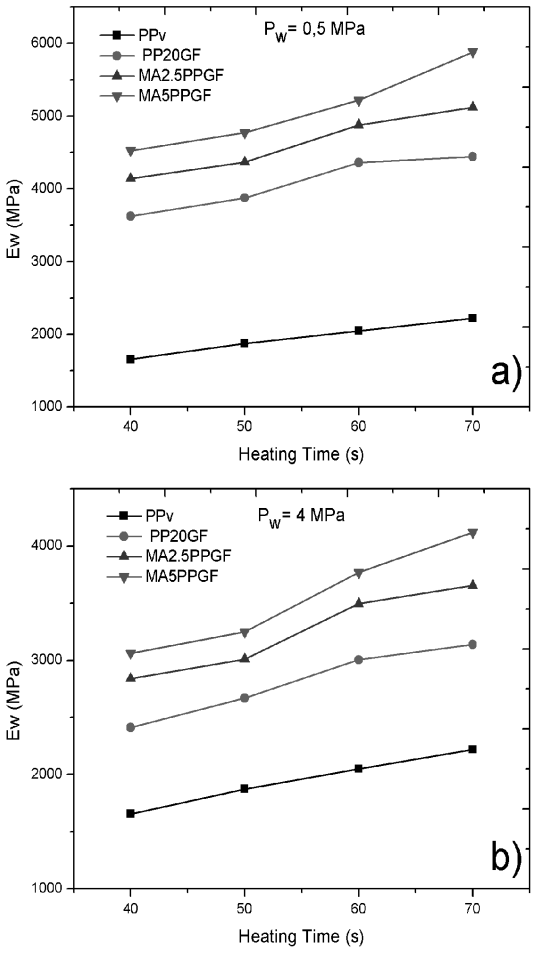

Figure 2: a) Modulus of welded samples under 0.5 MPa weld pressure, b) modulus of welded samples under 4 MPa weld pressure
Slika 2: a) Modul zvarjenih spojev pri 0,5 MPa tlaku zvara, b) modul zvarjenih vzorcev pri 4 MPa tlaku zvara

As the amount of MAPP increases the joint strength increases to a 0.5-MPa weld pressure as reported in Table 4, but the joint strength of the samples decreases with less than 4 MPa weld pressure. Similar results have been reported by J. S. Liu, H. F. Cheng[13] Under the influence of the welding pressure, the plasticized material in the weld zone flows. With increasing penetration, fibers push out of the surface. This fiber bridging causes a high weld strength. But increasing the welding pressure causes a high degree of orientation transverse to flow (injection) to the original fiber alignment. This in turn leads to a decrease in the joint strength.

The modulus (E) of the material is also reported in **Figure 2**. With respect to PPv, they have higher moduli and strengths, but they break at a lower strain. The differences in the E of the PP-based composites cannot be ascribed to their different composition because in that case, E should monotonically decrease with the welding pressure.

Increasing the hot-plate heating time increases the temperatures of the materials. The temperature provides the necessary movement of the melt flow, and time is needed for the diffusion to occur. A higher material temperature therefore aids increasing the weld strengths. Homogenous filler orientation such as fiber on the welding zone and matrix material dominates the stress behavior. Fiber reinforcements lead to an increase of the melting point of the matrix. The random orientation of glass fiber on the welding zone affects the welding strength depending on the heating time. Increasing the heating time thereby the melting length leads to increasing fiber orientation horizontal to the direction of the load. With the increasing melting length fibers move to the welding zone while the melt flows out. The results that depend on heating time have provided a comparison for a variety of filler-reinforced PP composites. M. Gehde et al.[14] have investigated the effect of melting length and joining length for different heating times (0 s, 60 s and 120 s) on the material reinforced PP with a random glass mat (PP-GM). PP-GM attains the highest strength at a low joining length. Varying the melting length does not affect the maximum strength of 28 MPa. In this study, 46.25 MPa, the highest strength value of the welding, was obtained for a low welding pressure, which means a low joining length. This strength was reached at a time of 60 s. The higher strength values from the literature can be said to be associated with the use of MA. MA-g-PP usage, increasing the fiber adhesion, also on the welding interface, has fulfilled its function of improving the strength in the basic structure. The MA-g-PP (5 %), approximately 20 % difference between using and not using the welding strength of the composite were determined at low/high weld pressures.

The SEM observation at the fracture surface suggests that the welded MA5PPGF materials have fewer fibers

that are oriented horizontal to the direction of load 0.5 MPa, when compared to that of the welded MA5PPGF composites (**Figure 3**) on the pressure load of 4 MPa. The joint strengths of the welded MA5PPGF at a 4-MPa weld pressure may thus be inferior to that of the MA5PPGF composites welded a 0.5-MPa weld pressure. Many transverse fibers were widely detached and sometimes fibers in longitudinal direction of the specimen were broken. Additionally, the squeezed-out plastic melt generates a flash, resulting in a sharp transition in the cross-section of the product.[8] For a welding pressure of 4 MPa, the SEM micrographs show that the fibers that bridge the weld zone are shorter than those at a pressure of 0.5 MPa. Therefore, the region with fibers protruding from the weld is smaller, and the fiber orientation in the direction of the flash increases.

3.2 Fatigue test results

There are many factors that govern the fatigue behavior of discontinuous fiber-reinforced polymer-matrix composites. Some of these include the processing conditions, the fiber length and the orientation with respect to the loading axis, the properties of the matrix, interfacial properties, and testing conditions. The fibers tend to orient along the flow direction, which leads to superior mechanical properties along the flow direction. As the degree of fiber disorientation with respect to the

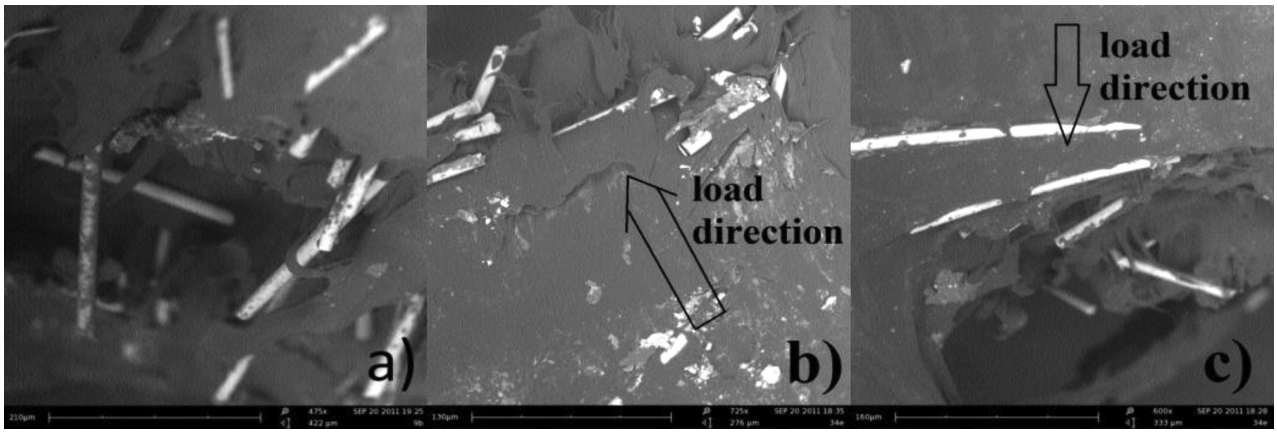

Figure 3: a) Increasing fiber orientations in the direction of the flash, b) MA5PPGF composite interface with fiber orientation at 4-MPa welding pressure, c) MA5PPGF composite interface, fibers oriented horizontal to the direction of load 0.5 MPa

Slika 3: a) Naraščanje usmerjenosti vlaken v smeri svetlobe, b) MA5PPGF stika kompozita z usmerjenostjo vlaken pri tlaku varjenja 4 MPa, c) MA5PPGF stik kompozita, vlakna so usmerjena horizontalno v smeri obremenitve z 0,5 MPa

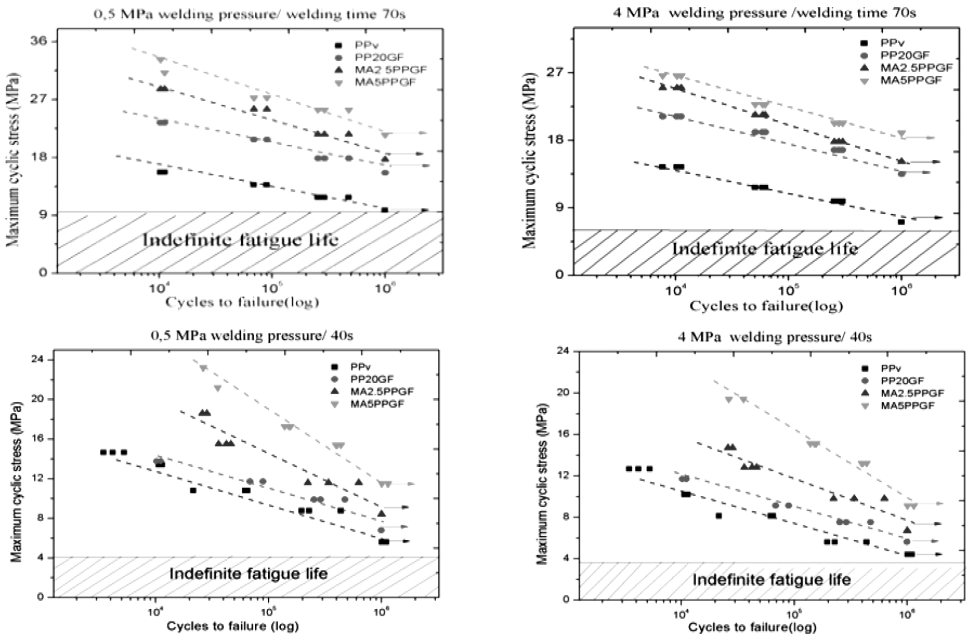

Figure 4: *S-N* curves at $R = 0.1$ for glass-fiber-reinforced PP with weld pressure of 0.5 MPa (LP), 4.0 MPa (HP) and PPv (unreinforced), (arrows indicate unbroken specimens)

Slika 4: *S-N* krivulje pri $R = 0,1$ za PP ojačan s steklenimi vlakni, pri tlaku varjenja 0,5 MPa (LP), 4 MPA (HP) in PP (neojačan), (puščice kažejo na neporušene vzorce)

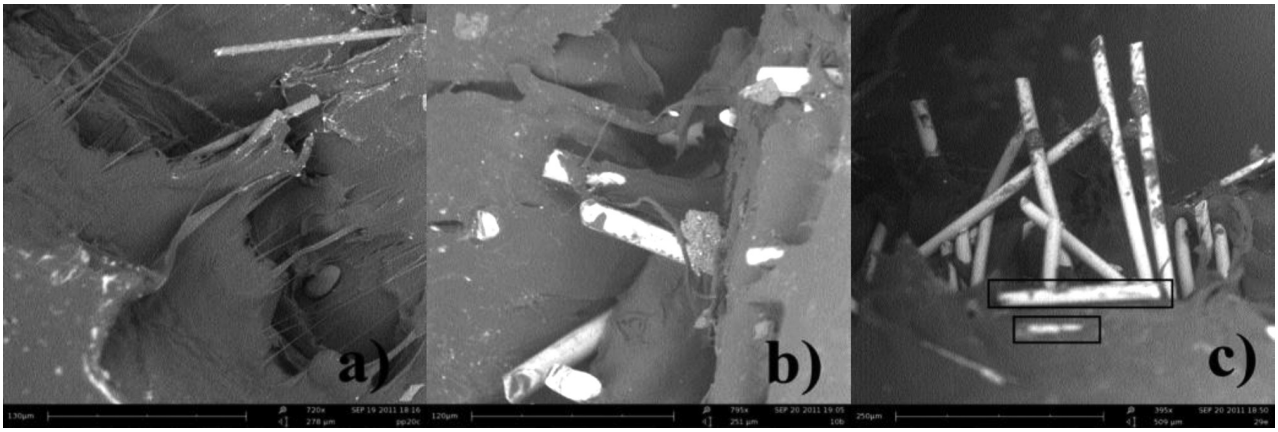

Figure 5: a) The matrix adhering to the fiber (at high pressure), b) matrix sticking to the fiber can be clearly seen and the orientation of the fibers perpendicular to the weld line. The sample exhibited a similar fracture surface as shown by the tensile specimen with the matrix sticking to the surface, c) fibers oriented to the center of the weld interface (rectangle area).

Slika 5: a) Matrica, ki se je prijela na vlakno (pri visokem tlaku), b) osnova, ki se je prijela na vlakno se dobro vidi in orientacija vlakna je pravokotna na linijo zvara. Vzorec kaže enako površino preloma kot pri nateznem preizkušancu, kjer se je osnova prilepila na površino, c) vlakna v sredini zvara (pravokotna področja).

loading axis increases, the strength of the composite is increasingly dominated by the matrix and interfacial properties.[15–20]

All the fatigue data were preliminarily analyzed using the classic stress-life approach and drawing the fatigue curves based on the nominal stress and the number of cycles to failure, identified as the complete separation of the joints. **Figure 4** presents the fatigue performance for all four materials as a plot of the maximum cyclic stress versus the number of cycles to failure, on a semi-log scale (S–N plot). **Figure 4** also reports the S-N curves of glass-fiber-filled polypropylene samples that were welded under a 0.5-MPa weld pressure and 4 MPa weld pressure. The vertical axis represents the maximum cyclic stress and the horizontal axis is the number of fatigue cycles to failure in this figure.

The stress-life approach allows the influence of the design parameters under investigation to be clearly identified.[21–23] In fact, an increase in the fatigue strength of the joints and therefore in their load capability can be observed when the welding pressure decreases for the joint process. Even the influence of the weld pressure itself can be easily identified in **Figure 4**. In terms of absolute stress, as could be expected from the static tests, MA5PPGF specimens exhibited better performance. Analyzing the fatigue diagrams, the low-pressure welding process led to a higher fatigue strength. At the welding pressure of 0.5 MPa, the highest strength values were achieved with the MA5PPGF material. Based on this result, in the welding zone, the fiber orientation is parallel to the applied force direction. The samples were welded under a pressure of 4 MPa, and the test results showed that the fatigue strength decreased. While MA5PPGF material strength again showed the highest fatigue strength of 26.88 MPa at about 9500 cycle, this load level represents 80 % of the static damage initiation load, which is similar to the findings of previous studies on the welding of thermoplastic composites.[15,16] K. J. Tsang et al.[16] also reported that the fatigue life of specimens welded at low pressure was 50 % greater than that of the specimens welded at high pressure, this study's results showed an 18 % fatigue life increase at low pressure. The low-weld-pressure condition shows more fibers oriented perpendicular to the weld plane, which may have increased the weld strength and resulted in a longer fatigue life. When the effects on the strength of the welding reinforcement by MAPP are analyzed, using MAPP material at a low rate (2.5 %) provided protection of the weld strength at a low weld pressure. The MAPP2,5PP material showed similar results (**Figure 5**) under a fatigue load, neither at a low welding pressure nor at a high welding pressure This tendency is also seen in the tensile-strength value (**Table 4**).

Figures 5a to **5c** show the fatigue fracture surfaces of reinforced PP specimens welded at low and high pressures. The low-weld-pressure condition shows more fibers oriented perpendicular to the weld plane (**Figure 5b**), which may have increased the weld strength and resulted in a longer fatigue life. This is consistent with the fracture surface observed in previous studies.[8] For reinforced material, the fatigue crack propagation process is more local and on a smaller scale compared with that of the unreinforced material due to the presence of glass fibers.

4 CONCLUSIONS

This study has examined the effect of different processing parameters on the joint strength of hot-plate welded thermoplastic composites, including the heating time, weld pressure and using MA-treated polypropylene. Four materials were used in the study: virgin polypropylene, 20 % glass fiber, 2.5 % MAPP (and 20 %

glass fiber), 5 % MAPP (and 20 % glass fiber) reinforced polypropylene composites.

With the increased welding time, the tensile strength increased and this was found to be reversed by correlating the welding pressure.

At a low welding pressure the MAPP material provides increased tensile strength of the glass-fiber-reinforced PP at about a rate of 50 %. Under a high welding pressure the MAPP increases the tensile strength, but it is seen that when using 2.5 % of that 5 % of any contribution when used.

The fatigue behavior gets worse and the fatigue limit of the tested material decreases when the weld pressure increases. As well as this, the welding time shows similar trends to the weld pressure. While contributing positively to the use of MAPP fatigue strength, the strength drop caused by the pressure increase was partially blocked.

5 REFERENCES

[1] M. Hou, Y. Ye, Y. W. Mai, An Experimental Study of Resistance Welding of Carbon Fiber Fabric Reinforced Polyetherimide (CF Fabric/PEI) Composite Material, Applied Composite Materials, 6 (**1999**) 1, 35–49, doi:10.1023/A:1008879402267

[2] M. Hou, M. Yang, B. Andrew, Y. W. Mai, L. Ye, Resistance Welding Of Carbon Fibre Reinforced Thermoplastic Composite Using Alternative Heating Element, Composite Structures, 47 (**1999**) 1, 667–672, doi:10.1016/S0263-8223(00)00047-7

[3] J. C. Caraschi, L. A. Leão, Woodflour as Reinforcement of Polypropylene, Materials Research, 5 (**2002**) 4, 405–409, doi:10.1590/S1516-14392002000400003

[4] H. G. Karian, Handbook of Polypropylene and Polypropylene Composites, 2nd ed., Marcel Dekker Inc. New York 2003, 653

[5] K. V. Stokes, K. R. Conway, A Phenomenological Study Of The Hot-Tool Welding Of Thermoplastics. Weld Strength Data For Several Blends, Polymer, 42 (**2001**) 17, 7477–7493, doi:10.1016/S0032-3861(01)00182-3

[6] M. Xanthos, Functional fillers for plastics, 2nd ed., Wiley-VCH Verlag Gmbh&Co. KGaA, Weinheim, 2010, 451

[7] William Andrew Publishing, Plastic Design Library, Chapter 1, Available from World Wide Web: http://www.Knovel.com, 1997

[8] C. B. Bucknall, I. C. Drinkwater, G. R. Smith Hot Plate Welding of Plastics: Factors Affecting Weld Strength, Polym. Eng. Sci., 20 (**1980**) 6, 432–440, doi:10.1002/pen.760200609

[9] T. T. Lin, S. Staicovici, A. Benatar, Non-Contact Hot Plate Welding of Polypropylene, ANTEC (1996), conference proceedings – Society of Plastics Engineers, Orlando, Philadelphia USA 1996

[10] M. Watson, M. Murch, Recent Developments in Hot Plate Welding of Thermoplastics, ANTEC (1989), conference proceedings – Society of Plastics Engineers, New York 1989

[11] J. Y. Nieh, L. J. Lee, Morphological characterization of the heat-affected zone (HAZ) in hot plate welding, ANTEC (1993), Conference proceedings, Society of Plastics Engineers, New Orleans, 1993

[12] K. Panneerselvam, S. Aravindan, A. Haq Noorul, Study On Resistance Welding Of Glass Fiber Reinforced Thermoplastic Composites, Materials and Design, 41 (**2012**), 453–459, doi:10.1016/j.matdes.2012.05.025

[13] J. S. Liu, H. F. Cheng, The Influence of Interface Geometry On The Joint Strength Of Hot Plate Welded Composites, Journal Of Reinforced Plastics and Composites, 29 (**2010**) 4, 497–509, doi:10.1177/0731684408099410

[14] M. Gehde, M. Giese, G. W. Ehrenstein, Welding of thermoplastics reinforced with random glass mat, Polymer Engineering and Science, 37 (**1997**) 4, 702–715

[15] A. Goel, K. Chawla, U. K. Vaidya, N. Chawla, M. Koopman, Characterization Of Fatigue Behavior Of Long Fiber Reinforced Thermoplastic (LFT) Composites, Materials Characterization, 60 (**2009**) 6, 537–544, doi:10.1016/j.matchar.2008.12.020

[16] K. Y. Tsang, D. L. DuQuesnay, P. J. Bates, Fatigue Properties of Vibration Welded Nylon 6 And Nylon 66 Reinforced With Glass Fiber, Composites: Part B: Engineering, 39 (**2008**) 29, 396–404, doi:10.1016/j.compositesb.2007.01.012

[17] K. V. Stokes, Experiments On The Hot-Tool Welding Of Three Dissimilar Thermoplastics, Polymer, 39 (**1998**) 12, 2469–2477, doi:10.1016/S0032-3861(97)00569-7

[18] P. Mitschang, R. Rudolf, M. Neitzel, Continuous Induction Welding Process, Modelling and Realisation, Journal of Thermoplastic Composite Materials, 15 (**2002**) 2, 127–153, doi:10.1177/0892705702015002451

[19] A. V. Kagan, J. R. Nichols, Benefits of Induction Welding of Reinforced Thermoplastics in High Performance Applications, Journal of Reinforced Plastics and Composites, 24 (**2005**) 13, 1345–1352, doi:10.1177/0731684405048846

[20] K. V. Stokes, A Phenomenological Study Of The Hot-Tool Welding Of Thermoplastics. Part:1 Polycarbonate, Polymer, 40 (**1999**) 23, 6235–6263, doi:10.1016/S0032-3861(98)00584-9

[21] M. J. Troughton, Handbook of Plastics Joining, A Practical Guide, 2nd. ed., William Andrew Inc., 2008, 577

[22] C. Bierogel, W. Grellmann, T. Fahnert, R. Lach, Material Parameters For The Evaluation Of PA Welds Using Laser Extensometry, Polymer Testing, 25 (**2006**) 8, 1024–1037, doi:10.1016/j.polymertesting.2006.07.001

[23] A. Yousefpour, M. Hojjati, J. P. Immarigeon, Fusion Bonding/Welding of Thermoplastic Composites, Journal of Thermoplastic Composite Materials, 17 (**2004**) 4, 303–341, doi:10.1177/0892705704045187

UDK 620.192.4:660.017:678.744.7
Original scientific article/Izvirni znanstveni članek

ISSN 1580-2949
MTAEC9, 50(5)663(2016)

CHEMICAL CROSS-LINKING OF CHITOSAN/POLYVINYL ALCOHOL ELECTROSPUN NANOFIBERS

KEMIJSKO ZAMREŽENJE ELEKTRO SPREDENIH NANOVLAKEN IZ HITOSAN/POLIVINIL ALKOHOLA

Sara Pouranvari[1], Firouz Ebrahimi[2], Gholamreza Javadi[1], Bozorgmehr Maddah[3]

[1]Islamic Azad University, Department of Biology, Science and Research Branch, Tehran, Iran
[2]IHU, Basic Sciences Faculty, Biology Research Center, Tehran, Iran
[3]IHU, Basic Sciences Faculty, Department of Chemistry, Tehran, Iran
febrhimi@ihu.ac.ir

Prejem rokopisa – received: 2015-04-17; sprejem za objavo – accepted for publication: 2015-07-08

doi:10.17222/mit.2015.083

Electrospun nanofibrous scaffolds have great potential for many biomedical applications. In the present study, we fabricated and characterized chitosan/polyvinyl alcohol (Chi/PVA) nanofibrous scaffolds through electrospinning. Cross-linking was performed using chemically with 5 % glutaraldehyde vapor. The morphology and chemical banding of the electrospun nanofibers before and after cross-linking were evaluated using scanning electron microscopy (SEM) and Attenuated Total Reflectance-Fourier Transform InfraRed (ATR-FTIR) spectroscopy. SEM micrographs and FTIR spectra showed that the cross-linking process was accomplished successfully. With the biocompatibility and non-toxicity of chitosan and PVA, it is expected that this electrospun nanofibrous scaffold could be an excellent candidate for biomedical applications.

Keywords: electrospinning, chitosan, polyvinyl alcohol, cross-linking

Mreže iz elektro spredenih nanovlaken imajo velik potencial za uporabo v biomedicini. V študiji smo izdelali in karakterizirali nanovlaknasto mrežo, izdelano z elektro predenjem nanovlaken iz hitosan/polivinil alkohola (Chi/PVA). Zamreženje je bilo izdelano s pomočjo kemijske metode s 5 % glutaraldehidne pare. Morfologija in kemijsko povezovanje elektro predenih nanovlaken, pred in po zamreženju, sta bila ocenjena z uporabo vrstičnega elektronskega mikroskopa (SEM) in z metodo z oslabljenim odbojem infrardeče spektroskopije s Fourierjevo transformacijo (ATR-FTIR). SEM-posnetki in FTIR-spekter sta pokazala, da je bil postopek zamreženja uspešno dosežen. Glede na biokompatibilnost in netoksičnost hitosana in PVA se pričakuje, da bodo mreže iz elektro spredenih nanovlaken odličen element za uporabo v biomedicini.

Ključne besede: elektro-predenje, hitosan, polivinil alkohol, zamreženje

1 INTRODUCTION

Electrospinning is a simple, versatile and cost effective method for forming non-woven fibrous scaffolds. Technically, the electrospinning process uses a high voltage source to draw a polymer fluid into fine fibers which are deposited on a collector.[1] In recent years, the use of electrospun nanofibers for biomedical applications such as tissue engineering[2], wound dressing[3], protein immobilization[4], materials for artificial blood vessels[5], barriers for the prevention of induced adhesion after operation[6], and vehicles for drug or gene delivery[7] has attracted a great deal of attention from scientists. Electrospinning of synthetic and natural polymers has been reported for collagen[8], gelatin[9], silk fibroin[10], polyglycolide (PGA)[11], polylactide (PLA)[12] and poly(ε-caprolactone) (PCL)[13], polyurethane[14], poly(vinylalcohol)[15], PEO[16], polydioxanone[17], and polyphosphazene derivatives.[18] Furthermore, the blending of two or more polymers and copolymerization are effective methods for the preparation of composites with new and desirable properties. Obviously, by adjusting the ratio of the components, structure and morphology of the nanofibers and the biological properties of the electrospun scaffolds can be tailored to the desired traits and functions.[1] For example PLGA[7], P(LA-CL) copolymers,[19] and mixtures of collagen with elastin,[20] gelatin with PCL,[9] chitosan with poly(ethylene oxide) (PEO)[21] and chitosan with PVA[22] have all been utilized to fabricate electrospun nanofibrous scaffolds for biomedical applications.

In biomedical applications, after electrospinning, different cross-linking methods can be uses to provide stabilization against aqueous environments for those scaffolds produced from aqueous soluble polymers (For example: PVA).

In the present study, electrospinning of a chitosan and PVA blend was performed. Chitosan was selected due to its cytocompatibility, biocompatibility, biodegradability and antibacterial activity.[23] PVA was used due to its biocompatibility, biodegradability, non-toxicity, chemical resistance, and good fiber-forming properties.[24]

2 MATERIALS AND METHODS

2.1 Materials

PVA (average molecular weight of 70000–100000 g/mol) and chitosan (medium molecular weight) were purchased from Sigma-Aldrich (St. Louis, MO). Acetic

acid and glutaraldehyde were obtained from Merck (Germany).

2.2 Preparation of the solutions

Chitosan and PVA were dissolved in 50 % aqueous solution of acetic acid at a concentration of 2 % mass fraction and 15 % mass fraction, respectively. The chitosan solution and PVA solution were mixed together with a weight ratio of 40/60 (Chi/PVA) under magnetic stirring at 60 °C.

2.3 Preparation of nanofibrous membranes

The optimal conditions for the electrospinning were as follows: 25 kV applied voltage, 15 cm tip-to-collector distance, and 1 ml/h flow rate. Moreover, a 5 ml syringe with a 21 gauge stainless-steel needle was used for the delivery of the polymer solution via a syringe pump.

2.4 Crosslinking of nanofibrous membranes

Samples were exposed to the 5 % glutaraldehyde (GA) vapor at room temperature for 48 h for cross-linking to stabilize them against aqueous media solubility and enhance their biomechanical properties biomedical applications. After crosslinking, the samples were carefully washed several times with 2 % glycine for the inactivation and removal of the GA.[25]

2.5 Characterization of nanofibrous membranes

The morphology and microstructure of the electrospun nanofibers before and after cross-linking were determined by Scanning Electron Microscopy (SEM). The average diameter of fibers were calculated using the ImageJ (US National Institute of Health, Bethesda, MD) image analysis program by analyzing at least 50 fibers in ten SEM micrographs. The chemical structures of the chitosan and PVA powders and Chi/PVA nanofiber membranes before and after cross-linking were investigated by Attenuated Total Reflectance-Fourier Transform InfraRed (ATR-FTIR) spectroscopy (Bruker Tensor 27, USA). FTIR spectra were obtained in the 4000 cm^{-1} to 400 cm^{-1} wavenumber range, with the data analyzed using OPUS software.

RESULTS AND DISCUSSION

3.1 Morphology of the nanofibrous scaffold

SEM images of Chi/PVA nanofibers before and after GA cross-linking are shown in **Figure 1**. As seen in **Figure 1a**, relatively fine, continuous, uniform fiber-structures (no bead), and randomly oriented fibers were obtained. The average fiber diameter was found to be 180±2.28 nm. In accordance with the relatively fine fibers fabricated, it is expected that a suitable porosity exists for biomedical applications.

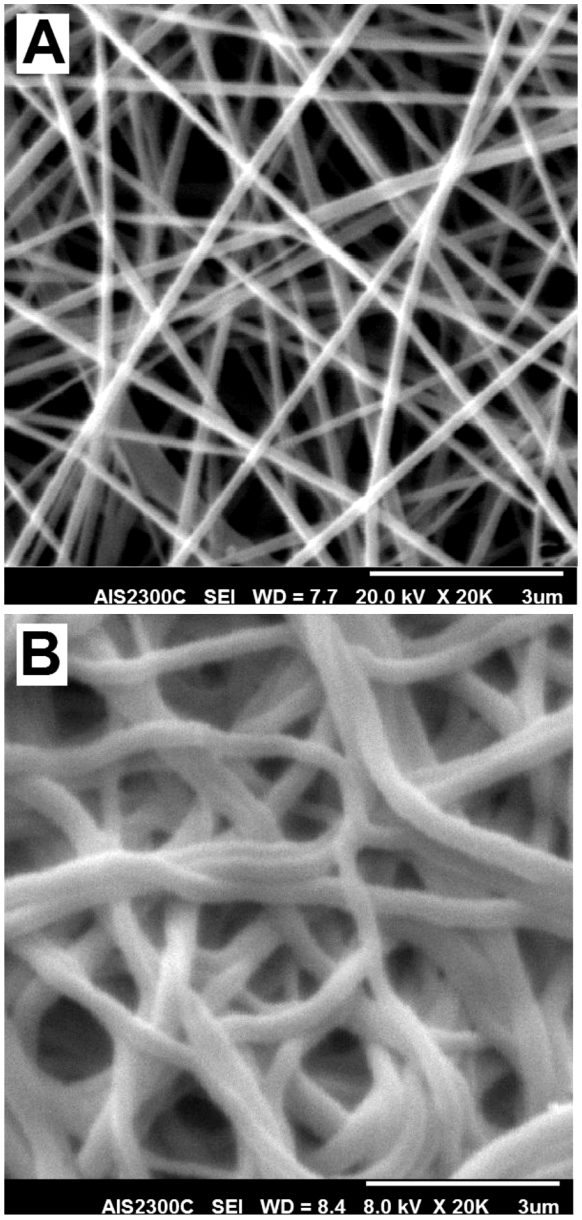

Figure 1: SEM micrographs of electrospun Chi/PVA nanofibers, after 48 h immersion in water at 37 °C: a) before GA cross-linking and b) after GA cross-linking

Slika 1: SEM posnetek elektro spredenih Chi/PVA nanovlaken, po 48 h namakanja v vodi s 37 °C: a) pred GA zamreženjem in b) po GA zamreženju

3.2 Crosslinking of nanofibrous scaffold

The SEM micrographs of the cross-linked nanofibers after immersion in water (at least 48 h) are shown in **Figure 1b**. As PVA is a water-soluble polymer, cross-linking should be performed for the use of Chi/PVA nanofibers in biomedical applications. Several studies have been reported on GA cross-linking for medical application. For example, Jafari et al. used a saturated vapor of a 25 % GA aqueous solution for cross-linking of chitosan-gelatin electrospun nanofibers.[26] In another study cross-linking of electrospun water-soluble carbo-

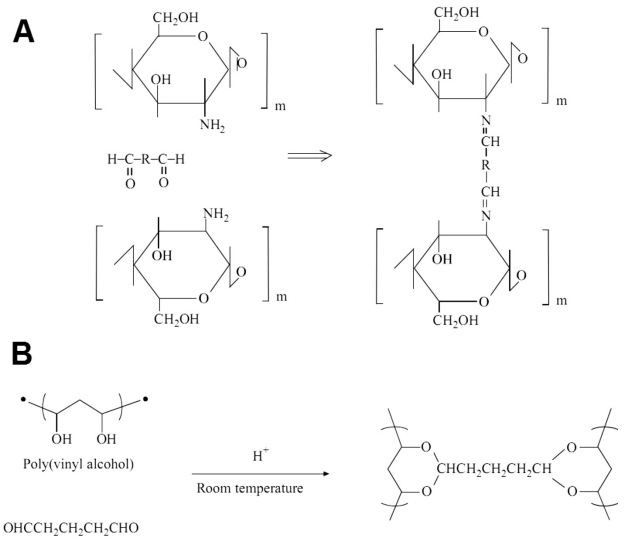

Figure 2: Schematic representation of cross-linking reaction of chitosan with GA and cross-linking reaction of PVA with GA [1,2]
Slika 2: Shematski prikaz reakcije zamreženja hitosana z GA in reakcije zamreženja PVA z GA[1,2]

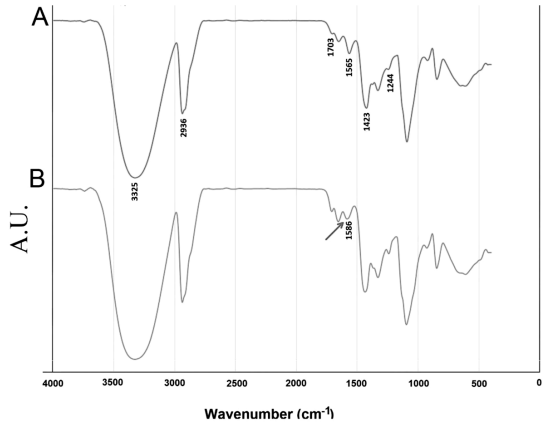

Figure 3: ATR-FTIR analysis of Chi/PVA electrospun samples: a) before chemical electrospinning and b) after electrospinning
Slika 3: ATR-FTIR analiza elektropredenih Chi/PVA vzorcev: a) pred kemijskim elektropredenjem in b) po elektropredenju

xyethyl chitosan/poly (vinyl alcohol) nanofibrous membrane towards wound dressings for skin regeneration was performed using a GA vapor.[27] Unlike the previous work, in the present study, the cross-linking was performed using a lower concentration of GA vapor (5 %). Despite using this low concentration, it was proved that the fabricated membranes' structure is stable in an aqueous solution. Moreover, according to the SEM micrographs shown in **Figure 1**, the porous structure of the fabricated membranes remained intact implying that they are insoluble in water. The cross-linking mechanism of chitosan and PVA with GA is shown in **Figure 2**.[28,29]

3.3 ATR-FTIR analysis

FTIR spectra were taken of the electrospun nanofibers before and after cross-linking, to assess their chemical groups. The FTIR spectrum of the Chi/PVA blended nanofibers before cross-linking, is shown in **Figure 3**. The two peaks at 1423 cm^{-1} and 1565 cm^{-1} arise fromcarboxylic acid and symmetric deformation of $^{-}NH3^{+}$ groups due to ionization of primary amino groups in the acidic medium, respectively. The peak at 1703 cm^{-1} is attributed to the carboxylic acid dimer.[22] In this study, this peak is due to the acetic acid utilized for dissolving the chitosan. The peak located at 1244 cm^{-1} is related to the C–O of the CH2OH chitosan group forming a hydrogen bond with the OH of PVA, confirming the fabrication of Chi/PVA blend nanofibers.[30] The FTIR spectra of the Chi/PVA blended nanofibers before cross-linking is given in **Figure 3**. Chemical crosslinking of the chitosan/PVA is verified by the peak located at 1586 cm^{-1} attributed to the C-N band. All chitosan-derived blends cross-linked with GA, have shown the presence of the imine (C=N) band. The imine band was formed by the nucleophilic reaction of the amine from chitosan with the aldehyde group of GA.[31] Due to imine band instability with temperature and pH, this group can transform to a C-N group.[32]

4 CONCLUSION

In this work, nanofibrous Chi/PVA was fabricated via electrospinning and stabilized by chemical cross-linking using 5 % GA. The porous structure of the electrospun scaffolds, antimicrobial properties of the chitosan and chemical resistant traits of PVA, make our fabricated electrospun scaffold an excellent candidate for biomedical applications. However, *in vitro* and *in vivo* experiments for evaluation of the biocompatibility of these Chi/PVA nanofiberous membranes is necessary.

5 REFERENCES

[1] D. Liang, B. S. Hsiao, B. Chu, Functional electrospun nanofibrous scaffolds for biomedical applications, Advanced drug delivery reviews, 59 (**2007**) 14, 1392–1412, doi:10.1016/j.addr.2007.04.021
[2] F.Yang, R. Murugan, S. Wang, S. Ramakrishna, Electrospinning of nano/micro scale poly(L-lactic acid) aligned fibers and their potential in neural tissue engineering, Biomaterials, 26 (**2005**) 15, 2603–2610, doi:10.1016/j.biomaterials.2004.06.051
[3] M. Gumusderelioglu, S. Dalkiranoglu, R. S. Aydin, S. Cakmak, A novel dermal substitute based on biofunctionalized electrospun PCL nanofibrous matrix, Journal of biomedical materials research Part A, 98 (**2011**) 3, 461–472, doi:10.1002/jbm.a.33143
[4] L. Wu, X. Yuan, J. Sheng, Immobilization of cellulase in nanofibrous PVA membranes by electrospinning, Journal of Membrane Science, 250 (**2005**) 1–2, 167–173, doi:10.1016/j.memsci.2004.10.024
[5] S. A. Sell, M. J. McClure, K. Garg, P. S. Wolfe, G. L. Bowlin, Electrospinning of collagen/biopolymers for regenerative medicine and cardiovascular tissue engineering, Advanced drug delivery reviews, 61 (**2009**) 12, 1007–1019, doi:10.1016/j.addr.2009.07.012
[6] Y. Wang, Y. L. Hsieh, Enzyme immobilization to ultra-fine cellulose fibers via amphiphilic polyethylene glycol spacers, Journal of Polymer Science Part A: Polymer Chemistry, 42 (**2004**) 17, 4289–4299, doi:10.1002/pola.20271

[7] D. S. Katti, K. W. Robinson, F. K. Ko, C. T. Laurencin, Bioresorbable nanofiber-based systems for wound healing and drug delivery: optimization of fabrication parameters, Journal of biomedical materials research Part B, Applied biomaterials, 70 (**2004**) 2, 286–296, doi:10.1002/jbm.b.30041

[8] K. J.Shields, M. J. Beckman, G. L. Bowlin, J. S. Wayne, Mechanical properties and cellular proliferation of electrospun collagen type II, Tissue engineering, 10 (**2004**) 9, 1510–1517, doi:10.1089/1076327042500373

[9] Y. Zhang, H. Ouyang, C. T. Lim, S. Ramakrishna, Z. M. Huang, Electrospinning of gelatin fibers and gelatin/PCL composite fibrous scaffolds, Journal of biomedical materials research Part B, Applied biomaterials, 72 (**2005**) 1, 156–165, doi:10.1002/jbm.b.30128

[10] B. M. Min,L. Jeong ,Y. S. Nam, J. M. Kim, J. Y. Kim, W. H. Park, Formation of silk fibroin matrices with different texture and its cellular response to normal human keratinocytes, International journal of biological macromolecules,34 (**2004**) 5, 281–288, doi:10.1016/j.ijbiomac.2004.08.004

[11] E. D. Boland, T. A. Telemeco, D. G. Simpson, G. E. Wnek, G. L. Bowlin, Utilizing acid pretreatment and electrospinning to improve biocompatibility of poly(glycolic acid) for tissue engineering, Journal of biomedical materials research Part B, Applied biomaterials, 71 (**2004**) 1, 144–152, doi:10.1002/jbm.b.30105

[12] F. Yang, C. Y. Xu, M. Kotaki, S. Wang, S. Ramakrishna, Characterization of neural stem cells on electrospun poly(L-lactic acid) nanofibrous scaffold, Journal of biomaterials science Polymer edition, 15 (**2004**) 12, 1483–1497, doi:10.1163/1568562042459733

[13] E. P. S. Tan, S. Y. Ng, C. T. Lim, Tensile testing of a single ultrafine polymeric fiber, Biomaterials, 26 (**2005**) 13, 1453–1456, doi:10.1016/j.biomaterials.2004.05.021

[14] G. Tetteh, A. S. Khan, R. M. Delaine-Smith, G. C. Reilly, I. U. Rehman, Electrospun polyurethane/hydroxyapatite bioactive Scaffolds for bone tissue engineering: The role of solvent and hydroxyapatite particles, Journal of the Mechanical Behavior of Biomedical Materials, 39 (**2014**), 95–110, doi:10.1016/j.jmbbm.2014.06.019

[15] L. Yao, T. W. Haas, A. Guiseppi-Elie, G. L. Bowlin, D. G. Simpson, G. E. Wnek, Electrospinning and Stabilization of Fully Hydrolyzed Poly(Vinyl Alcohol) Fibers, Chemistry of Materials, 15 (**2003**) 9, 1860–1864, doi:10.1021/cm0210795

[16] W. K. Son, J. H. Youk, T. S. Lee, W. H. Park, The effects of solution properties and polyelectrolyte on electrospinning of ultrafine poly(ethylene oxide) fibers, Polymer, 45 (**2004**) 9, 2959–2966, doi:10.1016/j.polymer.2004.03.006

[17] E. D. Boland, B. D. Coleman, C. P. Barnes, D. G.Simpson, G. E. Wnek, G. L. Bowlin, Electrospinning polydioxanone for biomedical applications, Acta biomaterialia, 1 (**2005**) 1, 115–123, doi:10.1016/j.actbio.2004.09.003

[18] L. S. Nair, S. Bhattacharyya, J. D. Bender, Y. E. Greish, P. W. Brown, H. R. Allcock et al., Fabrication and optimization of methylphenoxy substituted polyphosphazene nanofibers for biomedical applications, Biomacromolecules, 5 (**2004**) 6, 2212–2220, doi:10.1021/bm049759j

[19] I. K. Kwon, S. Kidoaki, T. Matsuda, Electrospun nano- to microfiber fabrics made of biodegradable copolyesters: structural characteristics, mechanical properties and cell adhesion potential, Biomaterials, 26 (**2005**) 18, 3929–3939, doi:10.1016/j.biomaterials.2004.10.007

[20] E. D. Boland, J. A. Matthews, K. J. Pawlowski, D. G. Simpson, G. E. Wnek, G. L. Bowlin, Electrospinning collagen and elastin: preliminary vascular tissue engineering, Frontiers in bioscience : a journal and virtual library, 9 (**2004**) 1–3, 1422–1432, doi:10.2741/1313

[21] B. Duan, C. Dong, X. Yuan, K. Yao, Electrospinning of chitosan solutions in acetic acid with poly(ethylene oxide), Journal of biomaterials science Polymer edition, 15 (**2004**) 6, 797–811, doi:10.1163/156856204774196171

[22] S. N. Alhosseini, F. Moztarzadeh, M. Mozafari, S. Asgari, M. Dodel, A. Samadikuchaksaraei et al., Synthesis and characterization of electrospun polyvinyl alcohol nanofibrous scaffolds modified by blending with chitosan for neural tissue engineering, International journal of nanomedicine, 7 (**2012**), 25–34, doi:10.2147/ijn.s25376

[23] E. Khor, L. Y. Lim, Implantable applications of chitin and chitosan, Biomaterials, 24 (**2003**) 13, 2339–2349, doi:10.1016/s0142-9612(03)00026-7

[24] I. Gibas, H. Janik, Review: synthetic polymer hydrogels for biomedical applications, Chemistry Chemical technol, 4 (**2010**) 4, 297–304

[25] S. S.Block, Disinfection, Sterilization and Preservation, Lea & Febiger, Philadelphia 1991

[26] J. Jafari, S. H. Emami, A. Samadikuchaksaraei, M. A. Bahar, F. Gorjipour, Electrospun chitosan-gelatin nanofiberous scaffold: fabrication and in vitro evaluation, Bio-medical materials and engineering, 21 (**2011**) 2, 99–112, doi:10.3233/BME-2011-0660

[27] Y. Zhou, D. Yang, X. Chen, Q. Xu, F. Lu, J. Nie, Electrospun water-soluble carboxyethyl chitosan/poly(vinyl alcohol) nanofibrous membrane as potential wound dressing for skin regeneration, Biomacromolecules, 9 (**2008**) 1, 349–54, doi:10.1021/bm7009015

[28] S. Nakatsuka, A. L. Andrady, Permeability of vitamin B-12 in chitosan membranes. Effect of crosslinking and blending with poly(vinyl alcohol) on permeability, Journal of Applied Polymer Science, 44 (**1992**) 1, 17–28, doi:10.1002/app.1992.070440103

[29] J. Jegal, K. H. Lee, Nanofiltration membranes based on poly(vinyl alcohol) and ionic polymers, Journal of Applied Polymer Science, 72 (**1999**), 1755–62, doi:10.1002/(sici)1097-4628(19990624)72:13<1755::aid-app11>3.0.co;2-r

[30] A. Gholipour, K. S. H. Bahrami, M. Nouri M, Chitosan-poly (vinyl alcohol) blend nanofibers: morphology, biological and antimicrobial properties, e-Polymers, 9 (**2009**) 1, 1580–1591, doi:10.1515/epoly.2009.9.1.1580

[31] U. Parida, A. Nayak, B. Binhani, P. Nayak, Synthesis and Characterization of Chitosan-Polyvinyl Alcohol Blended with Cloisite 30B for Controlled Release of the Anticancer Drug Curcumin, Journal of Biomaterials and Nanobiotechnology, 2 (**2011**) 4, 414–425, doi:10.4236/jbnb.2011.24051

[32] T. Wang, M.Turhan, S. Gunasekaran, Selected properties of pH-sensitive, biodegradable chitosan–poly (vinyl alcohol) hydrogel, Polymer International, 53 (**2004**) 7, 911–918, doi:10.1002/pi.1461

UDK 620.1:669.14.018.8:621.95
Original scientific article/Izvirni znanstveni članek

ISSN 1580-2949
MTAEC9, 50(5)667(2016)

INVESTIGATION OF HOLE PROFILES IN DEEP MICRO-HOLE DRILLING OF AISI 420 STAINLESS STEEL USING POWDER-MIXED DIELECTRIC FLUIDS

PREISKAVA PROFILOV LUKNJE PRI GLOBOKEM VRTANJU MIKRO LUKNJE V AISI 420 NERJAVNEM JEKLU S POMOČJO DIELEKTRIČNE TEKOČINE S PRIMEŠANIM PRAHOM

Volkan Yılmaz

Gazi University, Faculty of Technology, Manufacturing Engineering, Ankara, Turkey
volkan@gazi.edu.tr

Prejem rokopisa – received: 2015-05-18; sprejem za objavo – accepted for publication: 2015-07-13

doi:10.17222/mit.2015.100

A series of experiments were carried out to drill deep micro-holes, using Electrical Discharge Machining (EDM) with different concentrations of carbon powder/dielectric fluid mixture into, and varying machining parameters such as elecrode rotation speed and dielectric fluid spray pressure. Four dielectric fluid concentrations, three electrode rotation speeds, and three dielectric fluid spray pressure settings were tested; the resulting holes were investigated with respect to their average radial overcut and surface roughness (R_a) values. Study results indicate that as carbon powder concentrations, dielectric fluid spray pressure and electrode rotation speeds are increased, *ARO* values increased while R_a values are observed to decrease. It was determined that improvements in R_a and *ARO* values may be attained by the right configuration of machining parameters and the selection of the appropriate mixtures of carbon powder with dielectric fluid.

Keywords: AISI 420 stainless steel, deep micro-hole drilling, electro discharge machining, hole profile, surface roughness

Izvedena je bila vrsta eksperimentov vrtanja globokih mikroizvrtin s pomočjo EDM in različne koncentracije prahu ogljika, primešanega dielektrični tekočini pri spreminjanju parametrov obdelave, vključno s hitrostjo vrtenja elektrode in tlaka curka dielektrične tekočine. Preizkušene so bile štiri koncentracije dielektrične tekočine, tri hitrosti vrtenja elektrode in trije različni tlaki curka dielektrične raztopine; nastale luknje so bile preiskovane glede na povprečni radij preseka in vrednosti hrapavosti površine (R_a). Rezultati kažejo, da naraščanje koncentracije prahu ogljika, tlak curka tekočine in hitrost rotacije elektrode povečuje vrednosti *ARO*, medtem ko se vrednost R_a zmanjšuje. Bilo je ugotovljeno, da je mogoče izbolšanje vrednosti R_a in *ARO* mogoče doseči s konfiguracijo parametrov obdelave in z izbiro primerne količine prahu ogljika, ki je primešan dielektrični tekočini.

Ključne besede: AISI 420 nerjavno jeklo, vrtanje globokih mikroizvrtin, obdelava z elektroerozijo, profil luknje, hrapavost površine

1 INTRODUCTION

In recent years, the use of Electrical Discharge Machining (EDM) for drilling small diameter holes in very hard materials has gathered momentum, as the materials used in newly developed systems exhibit advanced mechanical properties and conventional drilling methods fall short in such materials. In EDM, there is no direct contact between the drilling tool and the workpiece, a significant benefit which eliminates the problems associated with physical contact.[1–8] The EDM method is based on principles of thermal and electrical conductivity whereby small regions on the workpiece surface are removed by melting and vaporization. EDM systems allow the drilling of specific diameter holes provided that the material is electrically conductive.[9] The EDM method is used for applications such as machine assembly points, fuel injection spray nozzles and aircraft engine cooling holes. EDM hole drilling has found applications at both the macroscale and microscale, with good surface quality and acceptable tapering.[10]

Due to electrode wear and lateral erosion, EDM holes exhibit some, albeit a small, amount of tapering. This is a complication for the EDM industry to overcome. Research is being conducted into reducing the tapering, and disparities between hole entry and exit diameters are reported to have been reduced to acceptable levels.[11] Additionally, it has been reported that the problem may be surmounted with the use of coating on the tool electrode.[12,13] The parameters used for EDM hole drilling have a significant effect on hole tapering and surface roughness.[14–16] Rotation of the electrode has enhanced hole drilling performance in EDM operations.[17,18] The type of dielectric fluid and the manner in which it is applied have improved the process.[19,20] In addition to the tapering of the holes in EDM hole drilling, the surface roughness of hole walls is also of importance. It has been reported that the electrode plunge action is facilitated by rotational movement, and that surface roughness is simultabneously improved.[21] Various types of electrodes are used in EDM and by changing their polarization, the surface roughness of holes have been reported to be

reduced.[22] It is also reported that ancillary equipment can achieve significant enhancements in surface roughness.[23] In EDM hole drilling in tandem with grinding, improved surface roughness results have been achieved.[24] Additionally, system hybridization has been implemented resulting in the process duration being decreased while quality has been enhanced.[25]

One factor affecting machining performance in EDM is the conductive powder mixed with the dielectric fluid. Thanks to the conducting particulate, EDM processing, including hole drilling, is improved. The presence of conductive particulates not only improves hole drilling performance, but also has positive effects on hole tapering and hole surface roughness.[26–28] However, despite the existence of several studies concerning hole drilling using powder-mixed dielectric fluids, the benefits and drawbacks of the method have yet to be established.

This study focuses on carbon (C) powder mixed with the dielectric fluid, as well as two specific EDM parameters, and attempts to determine their effect on hole profile and surface roughness. In a survey of the literature, no studies have been identified targeting hole profile and surface roughness properties of the EDM micro-hole drilling method using either classical or powder-mixed EDM in AISI 420 material; this study attempts to fill the gap.

2 EXPERIMENTAL SETUP

For machining, a Furkan brand EEI M50A model EDM machine was used. A custom attachment was mounted on the EDM tool head to allow for the rotation of the electrode at various min^{-1} (revolutions per minute) speeds and to provide for the dielectric fluid to be delivered through the tool, at the required pressure, to the area to be machined on the workpiece. The attachment is shown in **Figure 1**; the EDM machine and the testing set-up are shown in **Figure 2**.

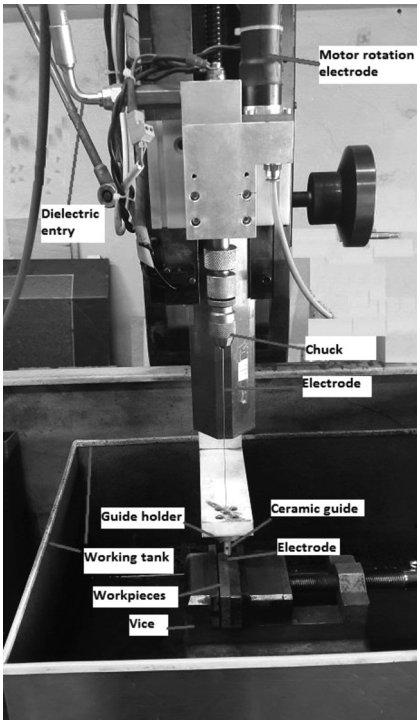

Figure 1: Custom attachment to enable electrode rotation
Slika 1: Prilagoditev, ki omogoča vrtenje elektrode

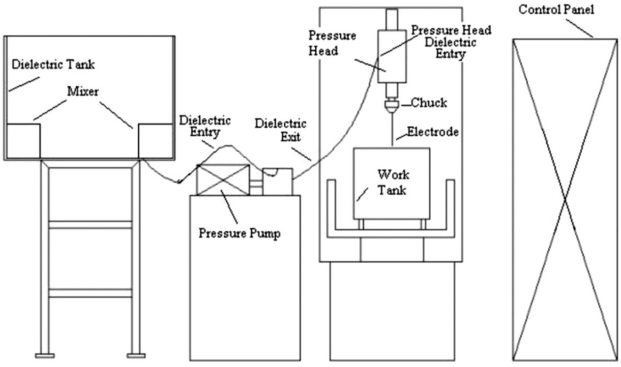

Figure 2: Experiment set-up
Slika 2: Eksperimentalni sestav

Single-hole brass pipe with diameter of 0.5 mm was used as tool electrode; AISI 420 stainless steel, commonly utilized in the manufacturing industry as hot work tool steel and also used for turbine blade construction, was selected as the workpiece; distilled water in pure form as well as distilled water mixed with carbon powder at three concentrations (2 g/L, 4 g/L and 8 g/L) were used as dielectric fluids. The chemical composition of AISI 420 is presented in **Table 1** and the workpiece, electrode and carbon powder physical characteristics in **Table 2**. **Table 3** shows the machining parameters used in the testing.

Table 1: Chemical composition of the AISI 420 material in mass fractions, (*w*/%)
Tabela 1: Kemijska sestava materiala AISI 420, v masnih deležih (*w*/%)

C	Mn	Si	P	S	Cr
0.1	1.00	1.00	0.04	0.030	12.0

The average radial overcut value is determined by taking the sum of the individual measurements of the hole diameter along the depth of the hole (**Figure 3**), averaging the sum, subtracting the result from the tool electrode diameter d_e, and dividing by 2:

$$\mathrm{ARO}(\mu\mathrm{m}) = \frac{\left[\left(\frac{d1+d2+d3+d4+d5+d6+d7}{7}\right) - d_e\right]}{2} \quad (1)$$

The surface roughness values were measured using a Mitutoyo Surftest SJ-210. The values were determined through an arithmetical averaging of several readings for each hole.

Table 2: Workpiece, electrode and carbon powder physical characteristics
Tabela 2: Fizikalne značilnosti obdelovanca, elektrode in prahu ogljika

Material	Density (gr/cm^3)	Specific heat capacity	Electrical resistivity	Thermal conductivity (W/m K)	Melting point (°C)
AISI 420	7.75	460 (J/kg K)	55 (μΩ-cm)	24.9	1450
Brass	8.25	0.380 (J/g °C)	6.39 (μΩ-cm)	159	900
C powder	2.25	–	12.2 (μΩ-m)	100	3527

Table 3: Machining parameters
Tabela 3: Obdelovalni parametri

Discharge current (*I*) (A)	6
Pulse duration (On-time) (μs)	200
Pulse interval (Off-time) (μs)	100
Electrode rotational speed (min^{-1})	100, 200, 400
Dielectric spray pressure (bar)	20, 40, 80
Polarity	Electrode (+), Workpiece (–)
Dielectric Fluid	Pure distilled water, pure distilled water with carbon powder
Workpiece	AISI 420
Electrode	Brass
Processing depth (mm)	20
Electrode diameter (mm)	0.5

3 RESULTS AND DISCUSSION

Using EDM, micro-holes with a diameter of 0.5 mm and depth of 20 mm were drilled into AISI 420 steel workpiece using four dielectric fluid concentrations (pure distilled water, and distilled water with carbon powder concentrations of 2 g/L, 4 g/L, and 8 g/L), three electrode rotation speeds (100 min^{-1}, 200 min^{-1} and 400 min^{-1}), three spray pressure settings for the dielectric fluid (20 bar, 40 bar, and 80 bar), with constant discharge current (6 A), pulse duration (200 μs) and pulse interval (100 μs). The effects of the machining parameters on the *ARO* values for hole profile and surface roughness have been investigated. Sample drillings are presented in **Figure 4**.

The study was designed to test the dielectric fluid mixes against dielectric fluid pressure and electrode rotation speed. Test numbers in the following description are described in **Table 3**: Four groups of dielectric fluid were used for testing (Di-0: pure distilled water with no powder mix, Di-1: distilled water with 2 g/L carbon powder mix, Di-2: with 4 g/L mix, Di-3: with 8 g/L mix). Three separate powder mixes were subjected to three groups of tests (A, B, and C), with three tests in each test group (1, 2, and 3). For the three test groups, the pressure setting of the dielectric fluid was varied (A: 20 bar, B: 40 bar and C: 80 bar). For each individual test within a test group, the electrode rotation speed was varied (1: 100 min^{-1}, 2: 200 min^{-1} and 3: 400 min^{-1}). For each individual test, the average radial overcut (*ARO*)

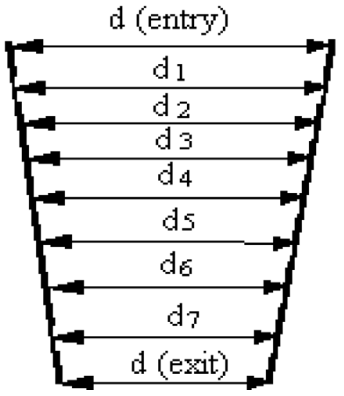

Figure 3: Measurements along hole profile
Slika 3: Meritve vzdolž profila izvrtine

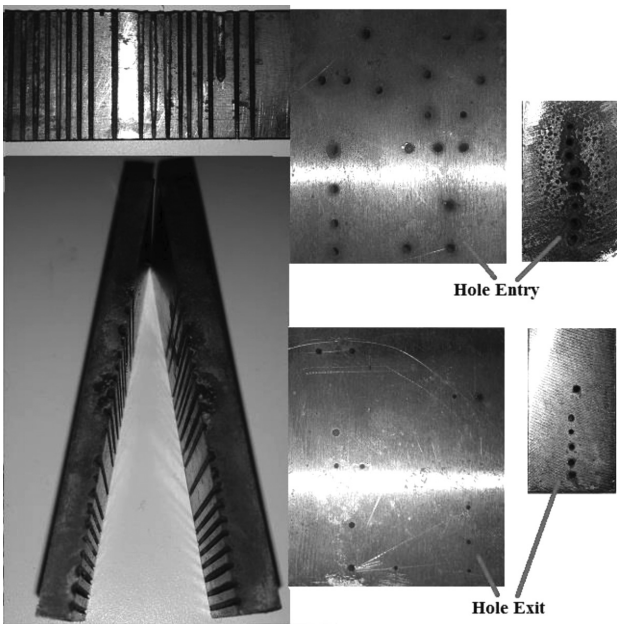

Figure 4: Sample drillings
Slika 4: Vzorčne izvrtine

Table 4: Test organization and results
Tabela 4: Zasnova preizkusov in rezultati

			Di-0 Pure distilled water (no powder mix)		Di-1 Distilled water with carbon (2 g/L)		Di-2 Distilled water with carbon (4 g/L)		Di-3 Distilled water with carbon (8 g/L)	
Test group	Dielectric fluid spray pressure (bar)	Electrode rotation (min^{-1})	Average radial overcut (μm)	Surface roughness R_a (μm)	Average radial overcut (μm)	Surface roughness R_a (μm)	Average radial overcut (μm)	Surface roughness R_a (μm)	Average radial overcut (μm)	Surface roughness R_a (μm)
A-1	20	100	42	3.25	62	2.46	77	2.14	81	1.92
A-2		200	48	2.98	65	2.24	79	2.06	88	1.87
A-3		400	51	2.79	77	2.06	84	1.92	93	1.75
B-1	40	100	53	3.04	71	2.35	82	2.05	92	1.85
B-2		200	59	2.82	78	2.18	86	1.95	98	1.82
B-3		400	64	2.70	83	2.02	94	1.85	104	1.63
C-1	80	100	65	2.66	86	2.26	91	1.92	101	1.81
C-2		200	72	2.62	88	2.11	94	1.88	105	1.74
C-3		400	76	2.51	94	1.96	102	1.73	112	1.68

and surface roughness (R_a) values were recorded. Results of the tests are presented in **Table 4**.

3.1 Examination of the results obtained for surface roughness (R_a)

Variations in R_a values in response to machining parameters and the concentration of carbon powder used in the dielectric fluid are presented graphically in **Figures 5** and **6**. A fundamental goal of EDM processing in manufacturing is to achieve low surface roughness (R_a) values. While having a direct relationship with the machining parameters, R_a values are also influenced by factors such as the workpiece itself, the type of dielectric fluid used, the dielectric application method and the type of electrode used.[1,7,29,30,31]

Figures 5 and **6** show the R_a values obtained for. **Figure 5** indicates that as the electrode rotation speed is increased, the R_a values decrease across all tests. This is a welcome outcome in terms of the overall industry goal of obtaining lower R_a values in general. A preliminary explanation offered for the decrease observed in R_a values is the easier electrode plunge action due to its rotation. Note that during testing, as the rotation speed was increased, the drilling duration was observed to decrease.

In tests conducted using the pure distilled water dielectric fluid (column Di-0) at 20 bar pressure (test group A), the R_a value decreased by 8% (from 3.25 μm to 2.98 μm) as the electrode rotation speed was increased from 100 min^{-1} to 200 min^{-1}, the R_a value decreasing by another 6% (from 2.98 μm to 2.79 μm) as electrode rotation speed increased from 200 min^{-1} to 400 min^{-1} (corresponding to surface roughness results for individual tests A-1, A-2, and A-3, under column Di-0). For tests conducted with dielectric fluid of distilled water mixed with 2 g/L carbon powder (column Di-1) at 20 bar pressure (test group A), the decreases were 9 % and 8 %, for rotation speed increases from 100 min^{-1} to 200 min^{-1}, and from 200 min^{-1} to 400 min^{-1}, respectively (corresponding to surface roughness results for individual tests A-1, A-2, and A-3, under column Di-1). For the same

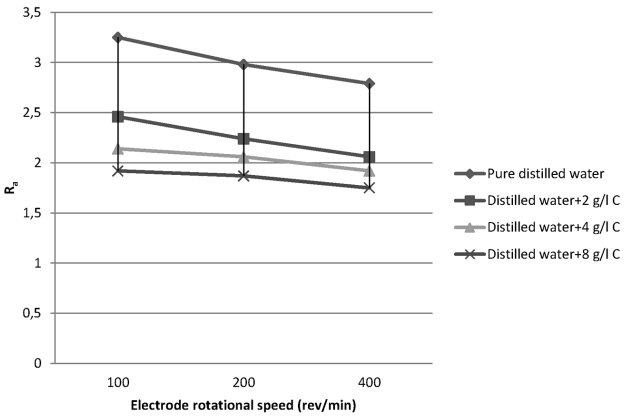

Figure 5: Electrode rotation speed vs. R_a (constant spray pressure at 20 bar)
Slika 5: Odvisnost hitrosti vrtenja elektrode od hrapavosti R_a (konstanten tlak curka 20 bar)

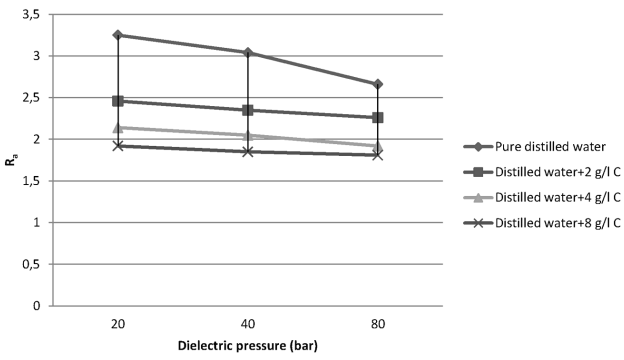

Figure 6: Dielectric pressure vs. R_a (constant rotation of 100 min^{-1})
Slika 6: Odvisnost tlaka dielektrične tekočine od hrapavosti površine R_a (pri konstanti hitrosti vrtenja 100 min^{-1})

test group (A) conducted with dielectric fluid mixed with 4 g/L carbon powder (column Di-2), the decreases were 4 % and 7 %, respectively (results for individual tests A-1, A-2, and A-3, under column Di-2). For the corresponding tests conducted with dielectric fluid mixed with 8 g/L carbon powder (column Di-3), the decreases were 3 % and 6 % (results for individual tests A-1, A-2, and A-3, under column Di-3).

When the same set of tests were repeated using 40 bar pressure, the observed decreases in R_a values were as follows: 7 % and 4 % (B-1, B-2 and B-3 under Di-0), 7 % and 7 % (B-1, B-2 and B-3 under Di-1), 5 % and 5 % (B-1, B-2 and B-3 under Di-2), and 2 % and 10 % (B-1, B-2 and B-3 under Di-3). For tests at 80 bar pressure, the observed decreases in R_a values were as follows: 2 % and 4 % (C-1, C-2 and C-3 under Di-0), 7 % and 7 % (C-1, C-2 and C-3 under Di-1), 2 % and 8 % (C-1, C-2 and C-3 under Di-2), and 4 % and 3 % (C-1, C-2 and C-3 under Di-3).

Normally, EDM processing results in craters being formed on the surface of the workpiece due to spark discharges, the presence of craters increasing the surface roughness. The decrease in surface roughness values observed here, in relation to increased rotational speeds of the electrode, is a significant outcome, as it proves that electrode rotation improves the process. The explanation for this outcome is that increased electrode rotation speeds reduce the force with which spark discharge occurs, as rotation of the electrode hinders the direct flow of spark to a single spot on the workpiece. Instead of a single spot, the spark is relayed to an area on the surface of the workpiece. As the spark is spread on the workpiece, crater depth is reduced, resulting in shallower craters.[2,7,10,18,30] As R_a values are directly related to the presence of craters on the workpiece, craters with less depth mean improved (lower) R_a values.

In addition to the electrode rotation speed, the study also looked at the effects of dielectric fluid spray pressure on surface roughness (**Figure 6**). It was observed that R_a values decreased as the dielectric fluid spray pressure was increased. For tests conducted with the electrode rotation speed kept constant at 100 min^{-1} and using pure distilled water dielectric fluid (individual tests A-1, B-1 and C-1 under column Di-0), increasing the spray pressure from 20 bar to 40 bar resulted in the R_a value decreasing by 6 %; increasing the spray pressure from 40 bar to 80 bar resulted in the R_a value decreasing by another 12 %. When the same tests were repeated for dielectric fluid concentration with 2 g/L carbon, the decreases were 4 % and 4 % (individual tests A-1, B-1 and C-1 under column Di-1); for dielectric fluid concentration with 4 g/L carbon, the results were 4 % and 6 % (same individual tests under column Di-2); and for dielectric fluid concentration with 8 g/L carbon, the results were 4 % and 2 % (same individual tests under column Di-3), respectively.

The decrease in R_a values as a result of the increase in dielectric fluid spray pressure is also a significant outcome for the study. It is interpreted that as the spray pressure is increased, the spark gap is flushed clean to a greater degree, allowing debris to be removed faster. By faster flushing, a continuous supply of clean dielectric fluid is maintained. This prevents the debris buildup from contributing to unwanted spark discharges, resulting in less damage to the workpiece surface. Controlling the spark discharge is very important to obtain the desired R_a values.[1–3,19,20,31] A spark gap region cluttered with debris also impedes the plunging action of the electrode, causing larger craters to be formed when the electrode's movement is obstructed; increasing the dielectric fluid spray pressure curtails this problem.

Another factor that affected R_a values was the carbon powder mixture (**Figures 5** and **6**). In test A-1 with dielectric fluid spray pressure of 20 bar and electrode rotation speed of 100 min^{-1}, conducted using distilled water with carbon powder at 2 g/L concentration (Di-1), R_a values were observed to decrease by 24 % compared to the same test conducted with pure distilled water (A-1 under Di-0).For the same test conducted using distilled water with carbon powder at 4 g/L concentration (Di-2), R_a values were observed to decrease by 34 % compared to the test with pure distilled water (A-1 under Di-0). When using distilled water with carbon powder mixed in at 8 g/L concentration (Di-3), R_a values were observed to decrease by 41 % compared to the same test conducted with pure distilled water (A-1 under Di-0). In test A-2 with electrode rotation speed of 200 min^{-1}, the observed decreases in R_a values were 25 %, 30 % and 37 %, respectively, for Di-1, Di-2, and Di-3, when compared to the R_a value for Di-0. In test A-3 with electrode rotation speed of 400 min^{-1}, the observed decreases in R_a values were 26 %, 31 % and 37 %, respectively, for Di-1, Di-2, and Di-3, when compared to the R_a value for Di-0.

In the case of a dielectric fluid spray pressure of 40 bar with electrode rotation at 100 min^{-1} (test B-1), the observed decreases in R_a values were 23 %, 33 % and 39 %, respectively, for Di-1, Di-2, and Di-3, when compared to the R_a value for Di-0. In the case of dielectric fluid spray pressure of 80 bar with electrode rotation at 100 min^{-1} (test C-1), the observed decreases in R_a values were 15 %, 28 % and 32 %, respectively, for Di-1, Di-2, and Di-3, when compared to the R_a value for Di-0.

In all of the tests conducted, it was observed that the carbon powder had a positive effect in decreasing R_a values. The cause is interpreted to be the wider discharge gap that is possible due to the use of the carbon powder mix. A wider discharge gap allows sparks to act on a larger workpiece surface area, leading to craters with less depth, and in turn, lower R_a values. During the hole drilling operation, loose debris from the workpiece increases the spark discharge between the electrode's lateral surfaces and the workpiece. This in turn leads to high points

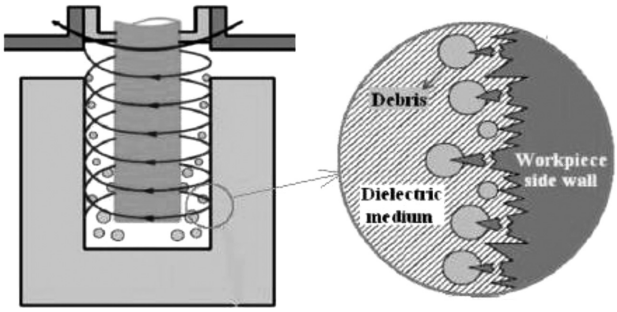

Figure 7: Debris in the spark gap region[18]
Slika 7: Drobci v področju reže[18]

on the workpiece surface being melted and vaporized (**Figure 7**), enabling lower R_a values to be attained.[21,26–28,32]

An additional reason for the observed decrease in R_a values when carbon powder mixes are used is the formation of low-power sparks among the carbon particulates and the workpiece surface. These low-power sparks cause shallow craters, which improve R_a values.[26,33]

The answer to whether further increasing carbon powder concentrations would help boost the observed decreases in R_a values was investigated through additional testing not included in this study. In the additional tests, carbon powder concentrations of 16 g/L and 20 g/L were used, but did not yield further improvements. Thus this study has been limited to reporting carbon powder mixed to an 8 g/L concentration. The interpretation for the limit reached in the efficiencies is two-fold: congestion within the electrode, and short circuits created within the spark gap. This study has demonstrated that specific carbon powder concentrations are highly effective on R_a and that an optimal carbon powder mix is an effective path to achieving low R_a values.

3.2 Analysis of the findings relating to average radial overcut (ARO)

The average radial overcut (*ARO*), an important parameter in describing the results obtained from EDM hole drilling operations, is the average difference between the diameter of the hole and the diameter of the electrode. The *ARO* value provides information on the hole profile; a lower value indicates that hole diameter is close to the electrode diameter. **Figures 8** and **9** present the *ARO* values attained in the study in relation to machining parameters as well as the carbon powder concentrations used.

The results presented in **Figures 8** and **9** indicate that increases in electrode rotation speed, dielectric fluid spray pressure and carbon powder concentrations, increase *ARO* values. In tests conducted using pure distilled water dielectric fluid (without carbon powder) (column Di-0) at 20 bar pressure (test group A), the *ARO* value increased by 14 % (from 42 μm to 48 μm) as electrode rotation speed was increased from 100 min^{-1} to 200 min^{-1}, and the *ARO* value increased by another 6 % (from 48μm to 51 μm) as electrode rotation speed was increased from 200 min^{-1} to 400 min^{-1} (corresponding to *ARO* results for individual tests A-1, A-2, and A-3, under column Di-0). For tests conducted with dielectric fluid of distilled water mixed with 2 g/L carbon powder (column Di-1) at 20 bar pressure (test group A), the increases were 5 % and 18 %, corresponding to the rotation speed increase from 100 min^{-1} to 200 min^{-1}, and from 200 min^{-1} to 400 min^{-1}, respectively (corresponding to *ARO* results for individual tests A-1, A-2, and A-3, under column Di-1). For the same test group (A) conducted with dielectric fluid mixed with 4 g/L carbon powder (column Di-2), the increases were 3 % and 6 %, respectively (results for individual tests A-1, A-2, and A-3, under column Di-2) and for tests conducted with 8 g/L carbon powder (column Di-3), the increases were 9 % and 6 % (results for individual tests A-1, A-2, and A-3, under column Di-3), respectively. Similar increases in *ARO* values at all electrode rotation speeds were observed for test groups B and C, corresponding to dielectric fluid spray pressures of 40 bar and 80 bar, respectively.

In addition to the electrode rotation speed, the study also looked at the effects of dielectric fluid spray pressure on *ARO* values. It was observed that *ARO* values increased as dielectric fluid spray pressure was increased. For tests conducted with the electrode rotation speed kept constant at 100 min^{-1} and using dielectric fluid of pure distilled water (individual tests A-1, B-1 and C-1 under column Di-0), increasing the spray pressure from 20 bar to 40 bar resulted in the *ARO* value increasing by 26 %; increasing the spray pressure from

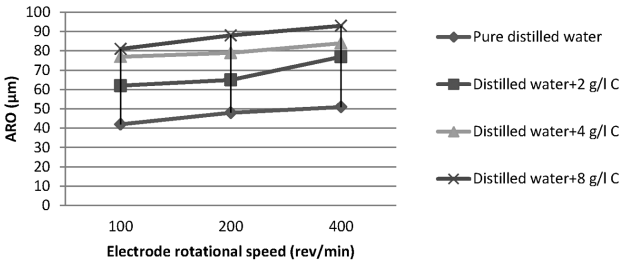

Figure 8: Electrode rotation speed vs. *ARO* (constant spray pressure at 20 bar)
Slika 8: Odvisnost hitrosti vrtenja elektrode od *ARO* (pri konstantnem tlaku curka 20 bar)

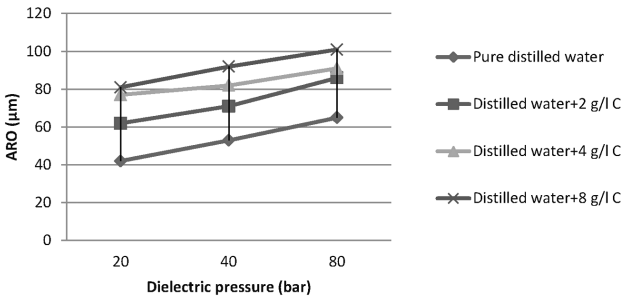

Figure 9: Dielectric pressure vs. *ARO* (constant rotation of 100 min^{-1})
Slika 9: Odvisnost med dielektričnim tlakom in *ARO* (konstantna hitrost rotacije 100 min^{-1})

40 bar to 80 bar resulted in the *ARO* value increasing by another 23 %. When the same tests were repeated for dielectric fluid concentration with 2 g/L carbon, the increases were 15 % and 21 % (individual tests A-1, B-1 and C-1 under column Di-1); for the dielectric fluid concentration of 4 g/L carbon, the results were 6 % and 11 % (same individual tests under column Di-2); and for dielectric fluid concentration of 8 g/L carbon, the results were 14 % and 10 % (same individual tests under column Di-3).

It is argued that better flushing of the machining area with increased circulation speed of the dielectric fluid and a more effective spark discharge, explain the increase in *ARO* values as electrode rotation speed and dielectric fluid spray pressures are increased. With faster flushing of the spark gap, the molten debris is better removed from the region, which leads to uninterrupted spark discharges.[1,2,7,16,32] With uninterrupted spark discharges, continuous arcing between the electrode lateral surfaces and cavity walls increases *ARO* values (depicted in **Figure 10**).

In EDM operations, debris inside the cavity may impede spark discharges, leading to a nonuniform hole profile in terms of diameter; large scale craters may also be formed.[1-3,33,34] In this study, fluctuations in the hole profile were prevented by the use of electrode rotation and dielectric fluid spray through the electrode itself. Through the selection of machining parameters, the creation of large depressions in the cavity were prevented; however, a certain increase in *ARO* values could not be avoided. This phenomena is related to electrode insulation, a current research topic with recent citations in literature, which requires further development, as research has demonstrated that insulating the lateral surfaces of the electrode helps to prevent increases in the *ARO* values.

Another factor that affected *ARO* values was the use of the carbon powder. In the A-1 test with dielectric fluid spray pressure of 20 bar and electrode rotation speed of 100 min^{-1}, conducted using distilled water with carbon powder at 2 g/L concentration (A-1 under Di-1), *ARO* values were observed to increase by 48 % compared to the same test conducted with pure distilled water (A-1 under Di-0). For the same test conducted using distilled water with carbon powder at 4 g/L concentration (A-1 under Di-2), *ARO* values were observed to increase by 83 % compared to the same test conducted with pure distilled water (A-1 under Di-0).When using distilled water with carbon powder at 8 g/L concentration (A-1 under Di-3), *ARO* values were observed to increase by 93 % compared to the same test conducted with pure distilled water (A-1 under Di-0). In test A-2 with electrode rotation speed of 200 min^{-1}, the observed increases in *ARO* values were 35 %, 65 % and 83 %, respectively, for Di-1, Di-2, and Di-3, compared to the *ARO* value for Di-0. In test A-3 with electrode rotation speed of 400 min^{-1}, the observed increases in *ARO* values were 51 %, 65 % and 82 %, respectively, for Di-1, Di-2, and Di-3, compared to the R_a value for Di-0.

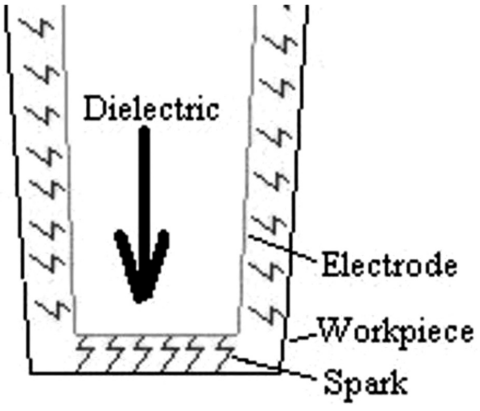

Figure 10: Increase in *ARO* values
Slika 10: Povečanje vrednosti *ARO*

In the case of dielectric fluid spray pressure of 40 bar, the observed increases in *ARO* values were 34 %, 55 % and 74 % for electrode rotation speed of 100 min^{-1} (test B-1), 32 %, 46 % and 66 % for electrode rotation speed of 200 min^{-1} (test B-2), and 30 %, 47 % and 63 % for electrode rotation speed of 400 min^{-1} (test B-3), respectively, for Di-1, Di-2, and Di-3, when compared to the *ARO* value for Di-0. In the case of dielectric fluid spray pressure of 80 bars, the observed increases in *ARO* values were 32 %, 40 % and 55 % for electrode rotation speed of 100 min^{-1} (test C-1), 22 %, 31 % and 46 % for electrode rotation speed of 200 min^{-1} (test C-2), and 24 %, 34 % and 47 % for electrode rotation speed of 400 min^{-1} (test C-3), respectively, for Di-1, Di-2, and Di-3, when compared to the *ARO* value for Di-0.

At higher dielectric fluid spray pressure, it is observed that the increase in *ARO* values slows down as the carbon powder concentration is increased. In the study, the lowest increase observed for *ARO* values as a result of an increase in carbon powder concentration was for the case of the spray pressure of 80 bar. Indeed, the increases of 22 %, 31 % and 46 % for test C-2 are the lowest figures for the study in terms of *ARO* increases with carbon powder concentrations. The interpretation for this surprising finding is that, as spray pressure is increased, the spark gap is flushed clean to a greater extent, allowing faster removeal of debris.[20,26,32–34] With faster flushing, a continuous supply of clean dielectric fluid is provided, preventing the debris from generating unwanted spark discharges and an excessive rise in the *ARO* values. It also results in a decreased machining duration. An increase in machining duration would have increased the hole diameter as well as the accompanying *ARO* values.

ARO values that increase in tandem with increases in carbon powder concentrations bring to the fore a fundamental problem in EDM hole drilling. Expulsion of carbon powders through the cavity as a result of dielectric flushing leads to spark generation between

electrode lateral surfaces and cavity walls. This has caused *ARO* values to increase in an accelerated fashion. The most significant result achieved in this study has been the low increases in *ARO* values observed at high dielectric fluid spray pressures for increasing powder concentrations, as decreased machining duration has positively influenced the *ARO* values. However, when the test results are considered in their entirety, it is clear that increased carbon powder concentrations in turn increase *ARO* values. While this outcome may in fact be exploited in certain applications, it is evident that carbon powder concentrations have a significant effect on hole profiles.

4 CONCLUSION

Using EDM, micro-holes with diameter of 0.5 mm and depth of 20 mm were drilled into an AISI 420 steel workpiece using four dielectric fluid concentrations, three electrode rotation speeds, and three dielectric fluid spray pressure settings. Effects of the machining parameters on the *ARO* values for hole profile and surface roughness (R_a) have been investigated. The results of the tests are presented below.

Significant reductions in R_a values were observed by mixing carbon powder with the dielectric fluid. As the carbon powder concentration was increased, R_a values decreased. In the study, R_a values were observed to decrease as electrode rotation speed was increased. As dielectric fluid spray pressure was increased, R_a values were again observed to decrease.

The study also investigated the hole profile (i.e. *ARO* values); as carbon powder concentrations, electrode rotation speeds and the dielectric fluid spray pressure were increased, *ARO* values were observed to increase. The findings were interpreted to be the result of a continuous spark discharge being enabled. It was determined that R_a and *ARO* values may be controlled by configuring the machining parameters and using an optimal mix of carbon powder with the dielectric fluid.

5 REFERENCES

[1] V. Yılmaz, Experimental investigation of drillability of micro holes using electro discharge machining, Ph. D. Thesis, Gazi University Graduate School of Naturel and Applied Sciences, Ankara 2013

[2] V. Yılmaz, M. Sarıkaya, H. Dilipak, Deep micro-hole drilling for Hadfield steel by electro-discharge machinig (EDM), Mater. Tehnol., 49 (**2015**) 3, 377–386, doi:10.17222/mit.2014.091

[3] V. Yılmaz, C. Y. Yılmaz, M. Sarıkaya, M. Özdemir, Modelling of performance output in the hole drilling process with different electrodes to X10CrAlSi24 sheet material, 3th International Symposium On Innovative Technologies In Engineering, Valencia, Spain, 2015, 1032–1041

[4] T. Kıvak, Optimization of surface roughness and flank wear using the Taguchi method in milling of Hadfield steel with PVD and CVD coated inserts, Measurement, 50 (**2014**), 19–28, doi:10.1016/j.measurement.2013.12.017

[5] G. F. Benedict, Nontraditional manufacturing processes, Marcel Dekker Inc. USA 1987, 1–250

[6] P. C. Pandey, H. S. Shan, Modern machining processes, Tata Mc Graw-Hill Publishing Company Limited, New Delhi 1980, 84–114

[7] V. Yılmaz, C. Y. Yılmaz, M. Özdemir, M. Sarıkaya, Examination of surface roughness in the hole drilling process with different electrodes, 3th International Symposium On Innovative Technologies In Engineering, Valencia, Spain 2015, 1024–1031

[8] R. K. Springborn, Non-traditional machining processes, American Society of Tool and Manufacturing Engineers, USA 1967

[9] T. Asokan, S. S. Reddy, P. D. E. Costa, Electrical discharge drilling of titanium alloys for aerospace applications, Proceedings of 19th AIMTDR conference, IIT Madras, Chennai 2000, 161–165

[10] D. T. Pham, S. S. Dimov, S. Bigot, A. Ivanov, K. Popov, Micro-EDM-recent developments and research issues, Journal of Materials Processing Technology, 149 (**2004**) 1–3, 50–57, doi:10.1016/j.jmatprotec.2004.02.008

[11] B. H. Yan, C. C. Wang, The machining characteristics of Al2O3/6061Al composite using rotary electro-discharge machining with a tube electrode, Journal of Materials Processing Technology, 95 (**1999**) 1–3, 222–231, doi:10.1016/S0924-0136(99)00322-2

[12] W. Yuangang, Z. Fuling, W. Jin, Wear-resist electrodes for micro-EDM, Chinese Journal of Aeronautics, 22 (**2009**) 3, 339–342, doi:10.1016/S1000-9361(08)60108-9

[13] E. Ferraris, V. Castiglioni, F. Ceyssens, M. Annoni, B. Lauwers, D. Reynaerts, EDM drilling of ultra-high aspect ratio micro holes with insulated tools, CIRP Annals-Manufacturing Technology, 62 (**2013**) 1, 191–194, doi:10.1016/j.cirp.2013.03.115

[14] P. Kuppan, A. Rajadurai, S. Narayanan, Influence of EDM process parameters in deep hole drilling of Inconel 718, International Journal of Advanced Manufacturing Technology, 38 (**2008**) 1–2, 74–84, doi:10.1007/s00170-007-1084-y

[15] V. Yilmaz, H. Dilipak, Method of electro discharge machining (EDM) micro hole drilling system design, IV. UTIS 2013, Kuşadası, Turkey, 2013, 151–159

[16] V. Yılmaz, M. Özdemir, M. Sarıkaya, C.Y. Yılmaz, H. Dilipak, Effect to hole profile of electrode selection in the micro deep holes processing drilling with electro discharge method, 2th International Iron and Steel Symposium, Karabük, Turkey 2015, 776–780

[17] Z. Y. Yu, K. P. Rajurkar, H. Shen, High aspect ratio and complex shaped blind micro holes by micro EDM, Annals of the CIRP, 51 (**2002**) 1, 359–362, doi:10.1016/S0007-8506(07)61536-4

[18] E. Bamberg, S. Heamawatanachai, Orbital electrode actuation to improve efficiency of drilling micro-holes by micro-EDM, Journal of Materials Processing Technology, 209 (**2009**) 4, 1826–1834, doi:10.1016/j.jmatprotec.2008.04.044

[19] F. N. Leao, Optimisation of EDM fast hole drilling through evaluation of dielectric and electrode materials, Proceedings of COBEM 2005, 18th International Congress of Mechanical Engineering, Ouro Preto, MG, 2005

[20] S. L. Chen, B. H. Yan, F. Y. Huang, Influence of kerosene and distilled water as dielectrics on the electric discharge machining characteristics of Ti-6Al-4V, Journal of Materials Processing Technology, 87 (**1999**) 1–3, 107–111, doi:10.1016/S0924-0136(98) 00340-9

[21] R. Teimouri, H. Baseri, Effects of magnetic field and rotary tool on EDM performance, Journal of Manufacturing Processes 14 (**2012**) 3, 316–322, doi:10.1016/j.jmapro.2012.04.002

[22] J. H. Jung, W. T. Kwon, Optimization of EDM process for multiple performance characteristics using Taguchi method and Grey relational analysis, Journal of Mechanical Science and Technology, 24 (**2010**) 5, 1083–1090, doi:10.1007/s12206-010-0305-8

[23] T. Endo, T. Tsujimoto, K. Mitsui, Study of vibration-assisted micro-EDM-The effect of vibration on machining time and stability of discharge, Precision Engineering, 32 (**2008**) 4, 269–277, doi:10.1016/j.precisioneng.2007.09.003

[24] H. S. Liu, B. H. Yan, C. L. Chen, F. Y. Huang, Application of micro-EDM combined with high-frequency dither grinding to improve micro-hole machining, International Journal of Machine Tools & Manufacture, 46 (**2006**) 1, 80–87, doi:10.1016/j.ijmachtools.2005.03.017

[25] L. Li, C. Diver, J. Atkinson, R. Giedl-Wagner, H. J. Helml, Sequential laser and EDM micro-drilling for next generation fuel injection nozzle manufacture, Annals of the CIRP 55 (**2006**) 1, 179–182, doi:10.1016/S0007-8506(07)60393-X

[26] Y. F. Tzeng, C. Y. Lee, Effects of powder characteristics on electro-discharge machining effiency, The International Journal of Advanced Manufacturing Technology, 17 (**2001**) 8, 586–592, doi:10.1007/s001700170142

[27] Y. S. Wong, L. C. Lim, I. Rahuman, W. M. Tee, Near-mirror-finish phenomenon in EDM using powder-mixed dielectric, Journal of Materials Processing Technology, 79 (**1998**) 1–3, 30–40, doi:10.1016/ S0924-0136(97)00450-0

[28] S. Singh, A. Bhardwaj, Review to EDM by using water and powder-mixed dielectric fluid, Journal of Minerals & Materials Characterization & Engineering, 10 (**2011**) 2, 199–230, doi:10.4236/jmmce.2011.102014

[29] H. M. Chow, L. D. Yang, C. T. Lin, Y. F. Chen, The use of SiC powder in water as dielectric for micro-slit EDM machining, Journal of Materials Processing Technology, 195 (**2008**) 1–3, 160–170, doi:10.1016/j.jmatprotec.2007.04.130

[30] T. Muthuramalingam, B. Mohan, A review on influence of electrical process parameters in EDM process, Archives of Civil and Mechanical Engineering, 15 (**2015**) 1, 87–94, doi:10.1016/j.acme.2014.02.009

[31] V. Yılmaz, H. Dilipak, M. Özdemir, G. Uzun, Examining the surface roughness while drilling micro-size deep holes with electro discharge technique on Hadfield steel, 2th International Symposium On Innovative Technologies In Engineering, Karabük, Turkey, 2014, 156-164

[32] X. Bai, Q. Zhang, J. Zhang, D. Kong, T. Yang, Machining efficiency of powder mixed near dry electrical discharge machining based on different material combinations of tool electrode and workpiece electrode, Journal of Manufacturing Processes, 15 (**2013**) 4, 474–482, doi:10.1016/j.jmapro.2013.09.005

[33] P. Huabei, Y. Deping, Z. Xun, W. Shanling, W. Yuhua, Fabrication of hollow nickel micro-spheres with high degree of hollowness by silicon powder-mixed spark erosion, International Journal of Machine Tools & Manufacture 85 (**2014**), 131–134, doi:10.1016/j.ijmachtools.2014.06.002

[34] M. P. Jahan, M. Rahman, Y. S. Wong, A review on the conventional and micro-electro discharge machining of tungsten carbide, International Journal of Machine Tools & Manufacture, 51 (**2011**) 12, 837–858, doi:10.1016/j.ijmachtools.2011.08.016

UDK 669.3:67.017:620.178.2
Original scientific article/Izvirni znanstveni članek

ISSN 1580-2949
MTAEC9, 50(5)677(2016)

THE PHENOMENON OF REDUCED PLASTICITY IN LOW-ALLOYED COPPER

POJAV ZMANJŠANJA PLASTIČNOSTI MALO LEGIRANEGA BAKRA

Wojciech Ozgowicz[1], Elżbieta Kalinowska-Ozgowicz[2], Barbara Grzegorczyk[1], Klaudiusz Lenik[2]

[1]Silesian University of Technology, Mechanical Engineering Faculty, Institute of Engineering Materials and Biomaterials, Konarskiego Str. 18A, 44-100 Gliwice, Poland
[2]Lublin University of Technology, Fundamentals of Technology, Nadbystrzycka Str. 38, 20-618 Lublin, Poland
kalinowska-ozgowicz@tlen.pl

Prejem rokopisa – received: 2015-05-19; sprejem za objavo – accepted for publication: 2015-10-12

doi:10.17222/mit.2015.101

This paper presents the results of investigations that allow us to determine the influence of the temperature of plastic deformation in the range from 20 °C to 800 °C during static tensile tests on the mechanical properties and structure of low-alloy copper alloys of the type CuCo2 and CuCo2B, completed by measurements of the microhardness and observations of the structure in a light microscope, and also of fractures in a scanning electron microscope. Based on the results of these investigations the temperature range for the occurrence of the reduced plasticity of the alloys CuCo2 and CuCo2B could be determined.

Keywords: low-alloy copper, plastic deformation, structure, mechanical properties, brittleness

Članek predstavlja rezultate preiskav, ki omogočajo opredelitev vpliva temperature na plastično deformacijo v območju od 20 °C do 800 °C s statičnimi nateznimi preizkusi na mehanske lastnosti in strukturo malo legiranih bakrovih zlitin, vrste CuCo2 in CuCo2B, izvedenih z merjenjem mikrotrdote ter opazovanjem mikrostrukture v svetlobnem mikroskopu in prelomov v vrstičnem elektronskem mikroskopu. Na osnovi rezultatov teh preiskav je bilo mogoče opredeliti temperaturno področje pojava zmanjšanja plastičnosti zlitin vrste CuCo2 in CuCo2B.

Ključne besede: malo legirani baker, plastična deformacija, struktura, mehanske lastnosti, krhkost

1 INTRODUCTION

Low-alloy copper is applied in various ways. However, most of it is applied in electrical engineering and electronics. It is also used in the production of welding electrodes, elements of bearings, non-sparking tools and chemical apparatus.[1–3] High-temperature brittleness results in a reduced plasticity at the given temperature of deformation, called the temperature of minimum plasticity (TMP).[4–6] The reason for this phenomenon concerning the brittleness of copper alloys has not been fully explained yet; it depends on many factors, mainly on the chemical composition, the structure of the alloy and the parameters of the deformation.[7–12]

The purpose of the present investigations was to determine the influence of the temperature of deformation on the mechanical properties, the structure, and particularly the range of temperature for the reduced plasticity of low-alloy copper, containing cobalt and boron of the type CuCo2 and CuCo2B.

2 MATERIALS AND METHODS

The investigations concerned low-alloy copper type CuCo2 and CuCo2B smelted in the laboratory in a crucible induction furnace with a frequency from 500 Hz to 4000 Hz and the mass of the charge up to 100 kg. In the course of smelting to liquid the CuCo2B alloy, boron was added in an amount of 0.005 %. The ready melts were passed to a graphite gate with a diameter of 30 mm. After cooling the obtained ingots, re-forged to rods, 15 mm in diameter, on a pneumatic forging hammer, the weight of its ram amounting to 200 t. For the chemical compositions of the investigated alloys CuCo2 and CuCo2B (**Table 1**).

Table 1: Chemical composition of the investigation alloys
Tabela 1: Kemijska sestava preiskovanih zlitin

Alloy type	Mass contents in mass fractions, (*w*/%)						
	Cu + Ag	Co	Si	Fe	Ni	P	B
CuCo2	96.71	2.76	0.29	0.16	0.01	0.05	–
CuCo2B	96.88	2.86	0.16	0.01	0.01	0.07	0.005

After forging the rods were supersaturated at 900 °C and cooled in water. The temperature during this procedure was determined based on an analysis of a binary system of the phase equilibrium of copper with cobalt.[11,12] The temperature of supersaturation was assumed to be 100 °C higher than the boundary temperature of the solubility of Co on Cu concerning the tested alloys. The

operation of supersaturation was carried out in an electric chamber furnace equipped with a controller ensuring measurements of the temperature with an accuracy of ±2 °C. After their supersaturation the rods were cut into segments, from which samples were used for testing the mechanical properties, applying a threaded grip.

The chemical compositions of the alloys CuCo2 and CuCo2B were tested on monolithic samples in the shape of disks with a thickness of about 5 mm and a diameter of 30 mm, cut out from the ingots.

The mechanical properties of the alloys CuCo2 and CuCo2B were tested on an Instron 1115 universal testing machine provided with a high-temperature resistance furnace, including a microprocessing system controlling the temperature. The procedure of heating was performed in a protective atmosphere containing 95 % nitrogen and 5 % hydrogen. Static tensile tests were accomplished in the temperature range 20 °C to 800 °C at a tensile rate of 20 mm/min, corresponding to the strain rate $\dot{\varepsilon} = 1.28\ 10^{-3}s^{-1}$. Based on the data on the curves of tension for the investigated alloys, the tensile strength (R_m) was determined, and the elongation (A) and the reduction of the area of the sample (Z) were calculated based on the geometrical features of the sample previous to and after the rupture. The result of the tests is the arithmetic mean of the three measurements.

Metallographic investigations were carried out on longitudinal microsections of the alloy CuCo2 and CuCo2B after supersaturation and hot tensile tests. The samples were immersed in self-hardening resin, and then mechanically polished. In order to reveal their structure the samples were etched in a reagent containing 5 g $FeCl_3$, 10 cm^3 HCl and 100 cm^3 C_2H_5OH. Metallographic observations were performed using an Olympus GX71 (Japan) light microscope with a magnifying power of up to 1000 times. The size of the grains was measured by applying the method of sections.

Fractographic tests of the fractions after decohesion in the tensile test were produced by means of a DSM940 scanning electron microscope by the firm Opton, accomplished at an accelerating voltage of 20 kV and magnifying power of up to 3000 times. The precipitation observed on the fractures was investigated by means of an EDAX X-ray microanalyzer. Prior to the fractographic test, the sample was ultra-sound cleaned in ethyl alcohol for 3 min.

The microhardness was measured on a Vickers sclerometer, applying a load of 50 g. These measurements were carried out on metallographic microsections of the alloys CuCo2 and CuCo2B after tension at a temperature of 20 °C to 800 °C.

3 RESULTS AND DISCUSSION

The results of the analysis of the chemical compositions of the investigated alloys have been gathered in **Table 1**. The analysis revealed that in these alloys there is a presence of cobalt and boron, as well as admixtures of silicon, iron, nickel and phosphorus. These elements affect mainly the electrical conductivity of copper, reducing it. Moreover, cobalt and iron increase the hardness of these alloys, and phosphorus is a de-oxidant, increasing their viscosity.

The results of the static tensile tests allowed us to determine the effect of temperature on the strength and plastic properties of the alloys CuCo2 and CuCo2B, and thus also to assess the range of temperature at which the plasticity of the investigated alloys decreases due to the dependence of elongation, contraction and strength on the temperature of deformation (**Figures 1** to **3**). Analyzing the dependence of the reduction of the area of the sample on the temperature of deformation of these alloys, it has been found to be more or less the same. In both these alloys the range of temperatures at which such a contraction attains its minimum value is quite evident.

The diagram of the dependence of elongation on the temperature of deformation of the alloy CuCo2 is characterized by a varying shape (**Figure 1**). At 20 °C the elongation of the alloy amounts to 34 %. An increase in the temperature of deformation is accompanied by a decrease in the value of A, reaching its minimum of 4.7 % at the temperature of 600 °C. A further rise in the temperature of deformation to 800 °C involves an increase of the elongation to 22 %. At 20 °C the elongation of the alloy $CuCo_2B$ amounts to 45.7 %. If the temperature of deformation rises from 20 °C to 550 °C, the elongation decreases, reaching its minimum of 10 % at 550 °C. A further rise of the temperature of deformation results in an elongation amounting to 53 % at 800 °C. The alloy CuCo2B is characterized by a much larger elongation in the range of the temperature of deformation from 700 °C to 800 °C than the alloy CuCo2. Analyzing the dependence of the course of contraction on the temperature of deformation of the alloys CuCo2 and CuCo2B, it has been found to be similar (**Figure 2**). In the case of both these alloys the range of temperature

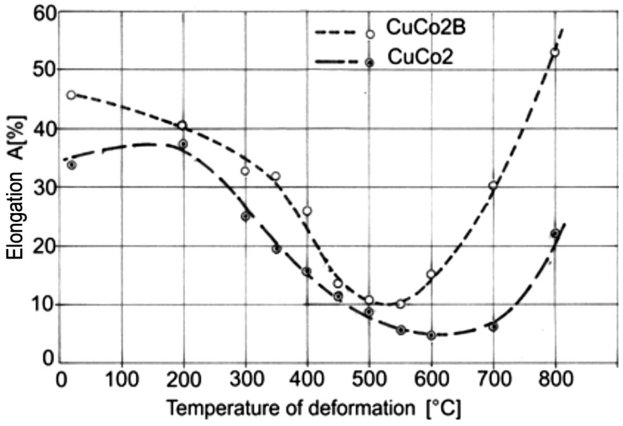

Figure 1: The influence of the temperature of plastic deformation in the tensile test on the elongation (*A*) of the alloys CuCo2 and CuCo2B
Slika 1: Vpliv temperature plastične deformacije pri nateznem preizkusu na raztezek (*A*) zlitin CuCo2 in CuCo2B

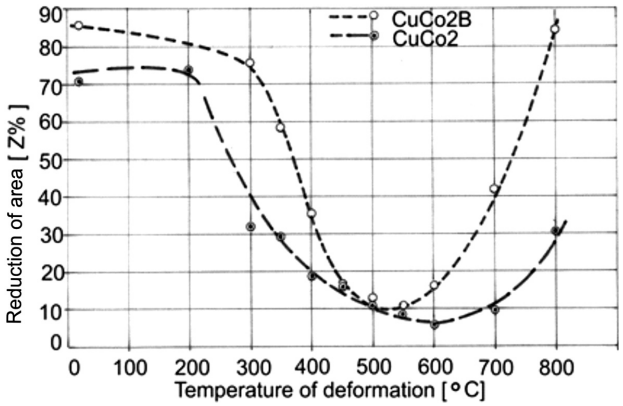

Figure 2: The influence of the temperature of plastic deformation in the tensile test on the reduction of area (Z) of the alloys CuCo2 and CuCo2B

Slika 2: Vpliv temperature plastične deformacije pri nateznem preizkusu na kontrakcijo (*Z*) zlitin CuCo2 in CuCo2B

characterized by a minimum contraction is quite distinct. The contraction of the alloy $CuCo_2$, deformed in the range of temperature from 20 °C to 600 °C, decreases, reaching its minimum at 600 °C (Z = 5.5 %). At a temperature of 600 °C to 800 °C the contraction increases up to a value of 30.6 %. At the temperature of deformation 20 °C the contraction of the alloy CuCo2 amounts to 71 % (**Figure 2**).

On the curve of the dependence of the contraction on the temperature of deformation of the alloy $CuCo_2B$ there occurs a local minimum (**Figure 2**). In the range of the temperature of deformation 20 °C to 550 °C the value of the contraction decreases from 85.7 % at 20 °C and attains its minimum Z = 10.9 % at 550 °C. A further rise of the temperature of deformation (to 800 °C) leads to an increase of the contraction to a value of 84.2 %.

Comparing the diagrams of the dependence of elongation and contraction on the temperature of deformation concerning the alloys CuCo2 and CuCo2B, we find that in both cases there exists a range of temperature in which these alloys indicate a minimum of the plastic properties,

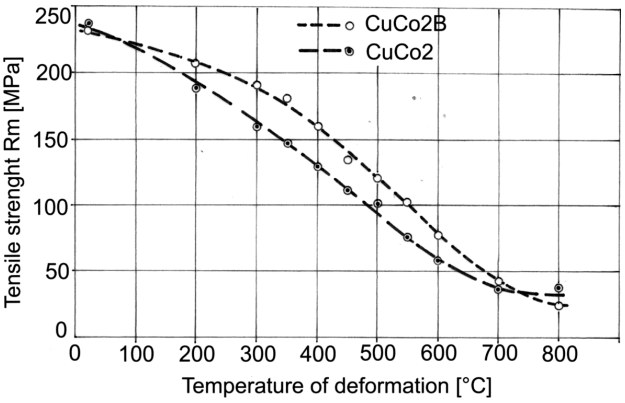

Figure 3: The influence of the temperature of plastic deformation in the tensile test on the strength (R_m) of the alloys CuCo2 and CuCo2B

Slika 3: Vpliv temperature plastične deformacije pri nateznem preizkusu na trdnost (R_m) zlitin CuCo2 in CuCo2B

characteristic for the phenomenon of brittleness (**Figures 1** and **2**). The alloy with the addition of boron is characterized by brittleness in the range of lower temperatures than the alloy without boron. The elongation and contraction of the alloy $CuCo_2B$ exceed those of the alloy CuCo2 in the entire range of the investigated temperature. The alloy CuCo2 displays a minimum plasticity in the range of temperature from 500 °C to 700 °C, and the alloy CuCo2B at a temperature of 450 °C to 600 °C.

Subjected to a static tensile test in the range of temperature from 20 °C to 800 °C, the investigated alloys display similar values of tensile strength (**Figure 3**). The curve in the diagram of the dependence of the tensile strength on the temperature of deformation concerning the alloys CuCo2 and CuCo2B is a decreasing function. The tensile strength of the alloy CuCo2, deformed at a temperature of 20 °C amounts to 237 MPa and drops to 38 MPa at 800 °C, where as in the case of the alloy CuCo2B it amounts, respectively, to 232 MPa and 34 MPa.

The results of the metallographic investigations allowed us to determine the influence of the temperature of deformation on the structure of the CuCo2 and CuCo2B in the range from 20 °C to 800 °C (**Figures 4** to **9**). After a hot tensile test the alloys $CuCo_2$ and $CuCo_2B$ have a variated structure in the zone of rupture and the central zone of the sample, with sliding bands. In the central part of the samples the grains have been found with a hardness of 71–93 HV and twins with straight and curve-linear boundaries. In the zone of rupture the structure of the alloy CuCo2, stretched at a temperature of 200 °C, is characterized by the occurrence of microcracks at the boundaries of elongated grains of the phase α (**Figure 4**), and the central part of the sample by axial grains α with twins (**Figure 5**). The alloy CuCo2B has a similar structure in the zone of rupture. The structures of

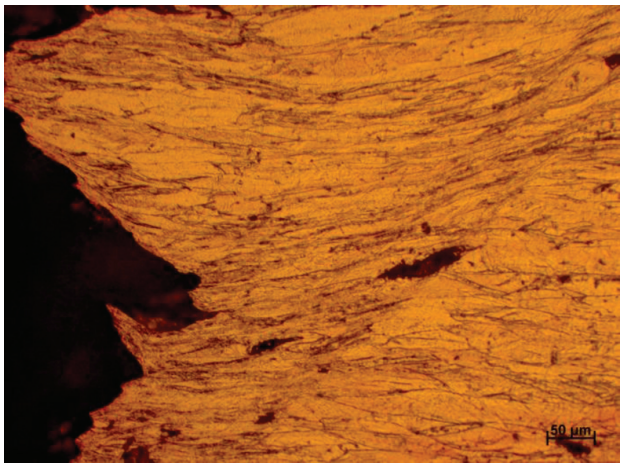

Figure 4: Elongated grains of the phase α with a micro-crack in the structure of the alloy CuCo2 after stretching at temperature of 200 °C (zone of rupture)

Slika 4: Razpotegnjena zrna α faze z mikrorazpokami v strukturi zlitine CuCo2, po nateznem preizkusu na temperaturi 200 °C (področje preloma)

Figure 5: Elongated grains of the phase α with twins and bands of deformation in the structure of the alloy CuCo2 after stretching at a temperature of 200 °C (central zone)

Slika 5: Razpotegnjena zrna α faze z dvojčki in deformacijskimi pasovi v strukturi zlitine CuCo2 po nateznem preizkusu na temperaturi 200 °C (sredina vzorca)

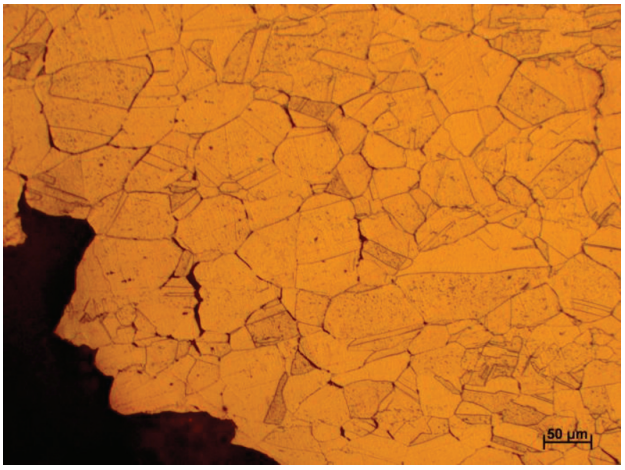

Figure 6: Recrystallized grains of the phase α and numerous cracks in the structure of the alloy CuCo2B after stretching at a temperature of 550 °C (zone of rupture)

Slika 6: Rekristalizirana zrna α faze in številne razpoke v strukturi zlitine CuCo2B po nateznem preizkusu na temperaturi 550 °C (področje preloma)

alloys stretched at elevated temperatures display a larger amount of microcracks occurring at the boundaries of the grains and at the contact of three grains and twin boundaries in the zone of rupture. In the central part of the sample a heterogeous structure was detected consisting of a diversified size of the grains (20 µm to 60 µm) depending on the temperature of the deformation and due to the process of recrystallization.

In alloys stretched at the temperature of minimum plasticity (550 °C) the structure in the zone of rupture is characterized by numerous micro-cracks. In the structure of the alloy $CuCo_2B$, stretched at the temperature 550 °C, the zone of rupture contains axial recrystallized grains of the phase α, 40 µm in diameter, and also many micro-cracks (**Figure 6**). Also in the central part of the sample there are micro-cracks at the boundary of the phase α (**Figure 7**). The structure of this part of the sample contains grains of the phase α with many twins with straight-lined boundaries as well as stepped boundaries, testifying to the advanced recrystallization of the alloy. In the central part the sample of the alloy CuCo2B there are grains of the phase α with micro-cracks and precipitations. After their deformation at 600 °C the investigated alloys display the structure of grains of the phase α, varying in their size, with twins and micro-cracks (**Figures 8** and **9**). The structure of the alloy CuCo2B, elongated at a temperature of 800 °C, displays numerous micro-cracks both in the zone of rupture and in the central part of the sample. In the structure of the central part of the sample the micro-cracks occurred in the front recrystallization due to the presence of large grains of the

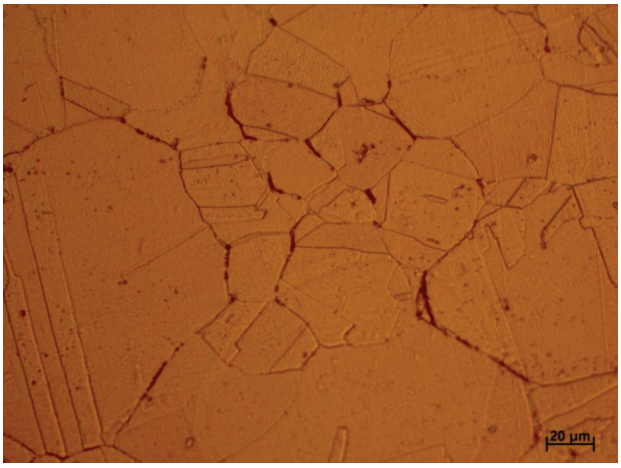

Figure 7: Micro-cracks at the boundaries of the phase α in the structure of the alloy CuCo2B after stretching at a temperature of 550 °C (central zone)

Slika 7: Mikrorazpoke na mejah α faze v strukturi zlitine CuCo2B po nateznem preizkusu na temperaturi 550 °C (sredina vzorca)

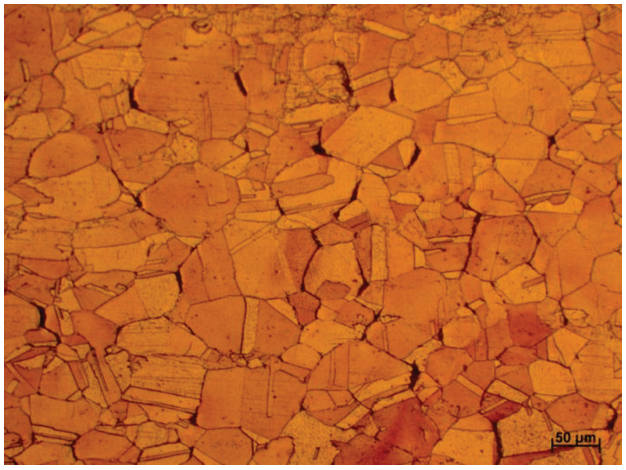

Figure 8: Differentiated grains of the phase α with the twins and micro-cracks in the structure of the alloy CuCo2B after stretching at the temperature 600 °C (central zone)

Slika 8: Diferencirana zrna α faze z dvojčki in mikrorazpokami v strukturi zlitine CuCo2B po nateznem preizkusu na temperaturi 600 °C (sredina vzorca)

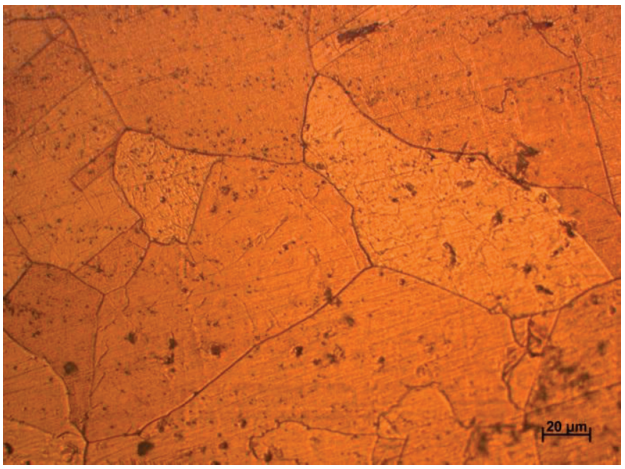

Figure 9: Coarse grains of the phase α with sub-grains in the structure of the alloy CuCo2B after stretching at a temperature of 800 °C (central zone)

Slika 9: Velika zrna α faze s podzrni v strukturi zlitine CuCo2B po nateznem preizkusu na temperaturi 800 °C (sredina vzorca)

phase (about 100 µm) with a hardness of about 60 HV and a revealed substructure (**Figure 9**). The size of the grains in the phase α of the structure of the alloy CuCo2B results from the way of recrystallization in the course of and after the plastic deformation during the tensile test.

The results of fractographic investigations allowed us to determine the influence of the temperature of deformation on the character of the fractures of the alloys CuCo2 and CuCo2B after decohesion in the tensile test in the range of temperature from 20 °C to 800 °C.

The fracture of the alloy CuCo2 and CuCo2B after the decohesion in the tensile test indicates a diversified character depending on the temperature of tension. At the temperature of deformation amounting to 200 °C, the investigated alloys are characterized by a transcrystalline ductile fracture with numerous craters differing in the

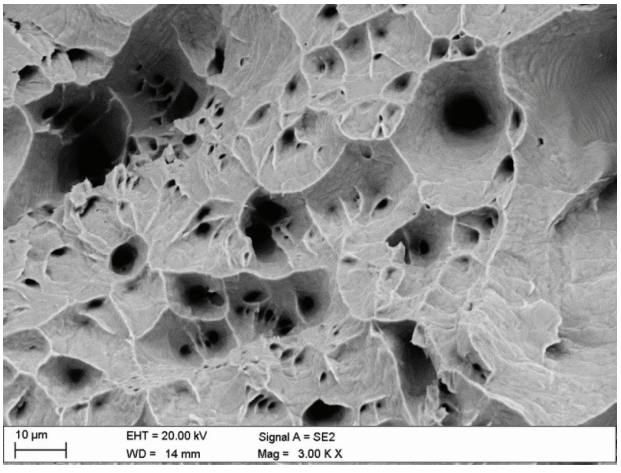

Figure 10: Transcrystalline ductile fracture in the alloy CuCo2 after a tensile test at 200 °C

Slika 10: Transkristalni žilav prelom zlitine CuCo2 po nateznem preizkusu na 200 °C

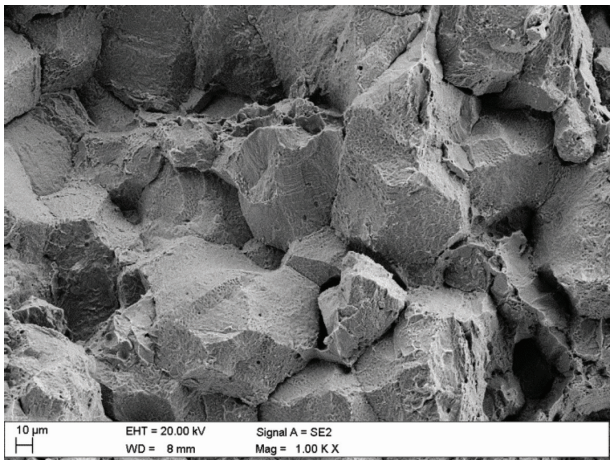

Figure 11: Intercrystalline brittle fracture in the alloy CuCo2B after a tensile test at 550 °C

Slika 11: Interkristalni krhki prelom zlitine CuCo2B, po nateznem preizkusu na 550 °C

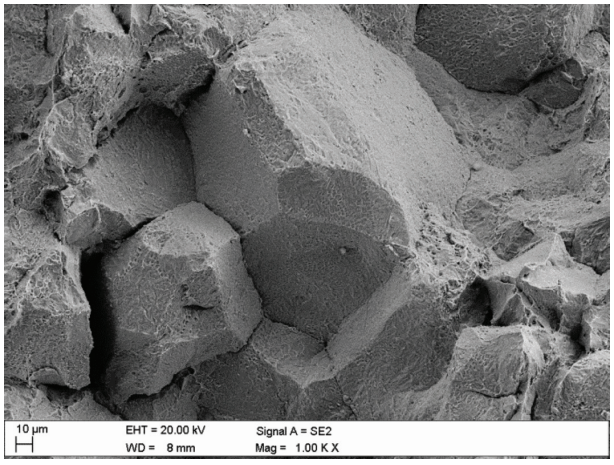

Figure 12: Intercrystalline brittle fracture in the alloy CuCo2 after a tensile test at 600 °C

Slika 12: Interkristalni krhki prelom zlitine CuCo2 po nateznem preizkusu na 600 °C

Element	Wt%	At%
CoK	03.30	03.55
CuK	96.70	96.45
Matrix	Correction	ZAF

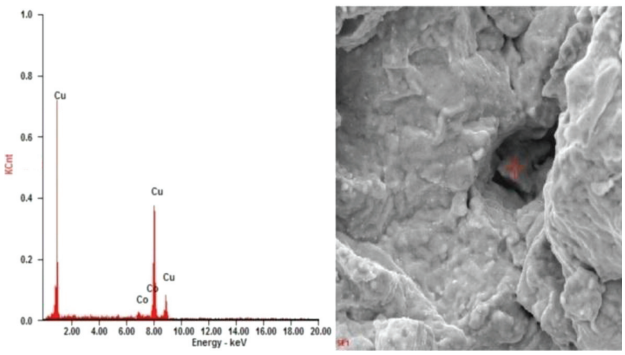

Figure 13: Result of the quantitative microanalysis of the chemical composition of a precipitate in the alloy CuCo2 after a tensile test at 550 °C

Slika 13: Rezultati kvantitativne mikroanalize kemijske sestave izločka v zlitini CuCo2 po nateznem preizkusu na 550 °C

diameters and precipitations in the bottom (**Figure 10**). The lateral planes of the craters are considerably corrugated.

At the temperature of deformation amounting to 550 °C and 600 °C, these alloys display brittle intercrystalline fractures with many micro-cracks and precipitations (**Figures 11** and **12**).

The planes of the cracks indicate the effects of plastic deformation. At the bottom of the crater on the fracture of the alloy CuCo2 precipitations were found, the chemical composition of which was determined by means of an X-ray analysis (EDAX) and proved to contain 96.55 % copper and 3.55 % cobalt (**Figure 13**). In the alloy CuCo2 deformed at 600 °C; an inter-crystalline brittle fracture was detected with micro-cracks at the boundaries (**Figure 12**), whereas in samples deformed at 800 °C a fracture mixed with cracks on the grain boundaries was observed.

4 CONCLUSIONS

The performed investigations and analyses of the obtained results allow us to draw the following conclusions:

1. The low-alloy copper type CuCo2 reaches its minimum plasticity in the tensile test at a temperature of deformation from 500 °C to 700 °C, whereas in the case of the alloy CuCo2B the minimum value is attained at a temperature of 450 °C to 600 °C.
2. An increase in the temperature of plastic deformation from 20 °C to 800 °C involves a decrease in the tensile strength of the alloy CuCo2 from about 240 MPa to about 40 MPa, and that of the alloy CuCo2B from about 230 MPa to about 25 MPa.
3. The temperature of the minimum plasticity (TMP) of the alloy CuCo2B from 20 °C to 800 °C is about 50 °C lower than the TMP of the alloy CuCo2. With a microaddition of boron the alloy is also more plastic (*A* and *Z* by about 5 %) in the range of TMP if compared with the alloy $CuCo_2$.
4. The structures of the investigated alloys of copper in the range TMP are characterized by homogeneous grains in the solution α, about 40 μm in size, with numerous micro-cracks at the grain boundaries.
5. The investigated plastically hot-deformed low-alloys beyond the region TMP have a typical structure of the solution α with a differing degree of deformation or dynamic or static recrystallization and a ductile fracture.
6. Low-alloy copper, in the range of TMP characterized by minimum plastic properties (*A* and *Z* about 5-10 %), displays after stretching a brittle intercrystalline fracture.
7. A micro-addition of boron involves increased plastic properties of the alloy CuCo2B in the entire range of the temperature of plastic deformation and changes the character of the fracture in the temperature interval from 550 °C to 800 °C.

5 REFERENCES

[1] M. Tokarski, An outline of physical metallurgy of metals and non-ferrous alloys, Silesian Publishing House, Katowice 1986

[2] Z. Górny, I. Sobczak, Modern casting materials based on non-ferrous, ZA-PIS Publishing House, Kraków 2005

[3] K. Kurski, Copper and its technical alloys, Silesian Publishing House, Katowice 1967

[4] W. Ozgowicz, Physico-chemical, structural and mechanical factor of intergranular brittleness, PhD Thesis, Silesian University of Technology, Gliwice, Poland 2004

[5] R. Nowosielski, Explication of minimum plasticity effect of mono-phase brasses, Mechanika, PhD Thesis, Silesian University of Technology, Gliwice, Poland 2000

[6] W. Ozgowicz, E. Kosek, Computer simulation of the diffusive segregation of impurities on the grain boundaries of metallic poly-crystals, Archive Science of Materials, 2 (**2004**), 93–112

[7] A. Maciejny, Brittleness of metals, Silesian Publishing House, Katowice 1973

[8] W. Ozgowicz, Structure and properties of copper and phosphorus tin bronzes zirconium modified in the process of hot deformation, Ore and Non-Ferrous Metals, 3 (**1995**), 96–103

[9] W. Ozgowicz, Analysis of intergranular embrittlement mechanisms of α-bronzes at elevated temperature, Part 1, Ores and Non-Ferrous Metals, 6 (**2005**), 320–327

[10] W. Ozgowicz, Analysis of intergranular embrittlement mechanisms of α-bronzes at elevated temperature, Part 2, Ores and Non-Ferrous Metals, 7 (**2005**), 377–391

[11] B. Massalski, Binary alloy phase diagrams, ASM, 1990

[12] W. Łoskiewicz, M. Orman, Equilibrium of binary metal alloys, PWN Publishing House, Warszawa 1956

UDK 621.926:621.763:67.017
Original scientific article/Izvirni znanstveni članek

ISSN 1580-2949
MTAEC9, 50(5)683(2016)

THE EFFECT OF HIGH-SPEED GRINDING TECHNOLOGY ON THE PROPERTIES OF FLY ASH

VPLIV TEHNOLOGIJE HITREGA MLETJA NA LASTNOSTI LETEČEGA PEPELA

Karel Dvořák, Iveta Hájková

Brno University of Technology, Faculty of Civil Engineering, Veveří 331/95, 602 00 Brno, Czech Republic
dvorak.k@fce.vutbr.cz

Prejem rokopisa – received: 2015-06-23; sprejem za objavo – accepted for publication: 2015-09-21

doi:10.17222/mit.2015.127

The aim of this work was to observe the impact of the milling technique employed by the DESI 11 disintegrator on the properties of fly ash. This type of mill is a high-speed pin mill with two counter rotors. The device selected for study allows the use of rotors with different working tools. In this case, two types of rotors were selected, identified as BR-AR and OR rotors. The OR rotor has cylindrical teeth, while the teeth on the AR-BR rotor can be described as rhomboidal. The fly ash was ground by 1, 2, 3, 5, and 10 passes through the mill. The Blaine specific surface area, particle size and particle size distribution were measured for each sample. The pozzolanic activity was also determined via a modified Chapelle test, and its influence on the shape of the grains was assessed by SEM. The results were compared together and with the original fly ash. There was a steep increase in the specific surface area and pozzolanic activity after the first pass through the mill. The second pass of ash through the mill did not increase the specific surface area due to strong aggregation, which gradually changes into agglomeration. However, the pozzolanic activity still increased during the aggregation phase. This phenomenon was clearly observable for both types of selected rotors. Based on the results, we can say that in the case of fly ash, a high-speed disintegrator can be a promising means of improving its properties via grinding and mechanical activation.

Keywords: high speed grinding, fly ash, pozzolanic activity

Namen dela je opazovati posledice uporabljene tehnike mletja, v DESI 11 mlinu, na lastnosti letečega pepela. To je mlin z veliko hitrostjo, z dvema nasprotnima rotorjema. Naprava, izbrana za študij, omogoča uporabo rotorjev z različnimi orodji. V tem primeru sta bila izbrana dva različna rotorja, označena kot AR-BR in OR rotor. OR rotor ima cilindričen zob, medtem ko je zob na AR-BR rotorju označen kot romboidalen. Leteči pepel je bil zmlet z 1, 2, 3, 5 in 10 prehodi skozi mlin. Za vsak vzorec so bile izmerjene Blainova specifična velikost površine ter velikost in razporeditev delcev. Pucolanska aktivnost je bila določena z modificiranim Chapelle testom. Vpliv na obliko zrn je bil določen s SEM. Rezultati so bili primerjani z originalnim letečim pepelom. Po prvem prehodu skozi mlin se je skokovito povečala specifična površina in pucolanska aktivnost. Drugi prehod pepela skozi mlin ni povečal specifične površine zaradi močne agregacije, ki se je postopoma spremenila v aglomeracijo. Vseeno pa je pucolanska aktivnost še naraščala med fazo agregacije. Ta pojav je bil jasno opažen pri obeh vrstah rotorjev. Na osnovi teh rezultatov lahko rečemo, da je v primeru letečega pepela dezintegrator z veliko hitrostjo obetajoče sredstvo, da z mletjem in mehansko aktivacijo izboljšamo njegove lastnosti.

Ključne besede: mletje z veliko hitrostjo, leteči pepel, pucolanska aktivnost

1 INTRODUCTION

One of the trends in the area of milling that have been intensively examined recently is high-energy milling (HEM). With HEM there are certain phenomena that have not been observed in conventional grinding. These phenomena can be summarized by the term mechanochemical activation.[1] The idea of mechanochemical activation is that an increase occurs in the value of the internal energy, consequently increasing the enthalpy and the formation of so-called active surfaces on the newly formed grains. To increase the level of enthalpy, it is not only necessary to supply a large amount of mechanical energy, but it is also important how that energy is transmitted to the material. Only if the material is capable of absorbing the energy can the internal structure of the substance be destabilized and new active surfaces be developed.[2] The effects of mechanical activation have been described for model materials such as dolomite[3] or clay minerals,[4–6] or, for example, for silica.[7] In the field of grinding and mechanical activation, research is focused on monitoring changes in the crystal structure and amorphization, [6,8] changes in the granularity and the aggregation and agglomeration of particles, [9,10] and changes in surface properties, especially the specific surface area and the zeta potential.[4,8] One type of HEM is high-speed grinding (HSG). HSG involves supplying large amounts of energy using very short and intense power pulses. The amount of energy that is effectively transferred to the material is higher in the case of HSG than with conventional grinding in mills with the same power input. One of the types of mills suitable for HSG is a high-speed pin mill with two counter-rotating rotors, known as a disintegrator.[11] This type of mill is particularly suitable for the grinding and activation of fine powder materials.[12] The material is refined by very intensive changes in the mechanical stress, which take place at a very high frequency. Another advantage is the variety of working tools that can be employed to affect the grinding process.[13] The disadvantage of this type of milling in the case of silicates is the significant electro-

static charging of the particles and their easy and quick aggregation.[1] One of the important silicate materials that are widely used in the construction industry is ash, various kinds of which exist. A number of authors describe the utilization and effects of pin mills on the physical and mechanical properties of both fluidized bed ashes[14,15] and ashes based on SiO_2.[16] In the case of fly ash, during traditional milling and even during HEM there is not only an increase in the specific surface area, but also an improvement in the reactivity. Different authors use a wide spectrum of methods for the assessment of reactivity, though it is typically done by FTIR and calorimetric methods during the hydration of cement pastes containing fly ash.[17,18] Increases in the reactivity are commonly achieved via the refinement of large porous particles of ash, i.e., plerospheres, which is relatively easy to do. The refinement of cenospheres is more difficult, and requires more grinding work, but leads to a further increase in the pozzolanic activity of the fly ash.[19] The particles remain in the chamber of the high-speed disintegrator for only a few seconds, which is because of the principle by which the pin mill operates. Repeating the passing of the material through the mill is the only effective way of extending the milling time. However, in the case of fly ash it entails the risk of grain agglomeration. The aim of this work was to describe and assess the effect of a HSG disintegrator's milling technique on the fly ash's properties, especially its pozzolanic properties, grain size, grain morphology and specific surface area.

2 MATERIALS AND METHODS

TEKO fly ash was used for monitoring the impact of the milling technique in question on the material properties. The fly ash was analyzed before the milling began, with its chemical composition being determined by traditional chemical analyses. The density was determined using a Micromeritics AccuPyc II 1340 automatic pycnometer. For the measurement of the Blaine specific surface area, a PC-Blaine-Star automatic device was used with a measurement cell capacity of 7.95 cm^3. The determination was performed three times to eliminate errors, and the resultant value was the average of these determinations. Milling of the samples was carried out in a DESI 11 disintegrator, which is a high-speed pin mill with two counter-rotating rotors. The total installed power of this mill is 4.1 kW. The rotors' rotation frequency is up to 200 Hz, and the maximum speed of impact is 240 ms^{-1}. The material is dispensed by a continuous feeder and enters the grinding chamber through the middle of the left rotor. To assess the effect of the selected milling technique, two rotor types were used for comparative purposes, i.e., types AR-BR and OR. The rotors were designed and manufactured by FF Service Ltd. Both types have two rows of teeth on the left-hand rotor and three rows of teeth on the right-hand rotor. The OR rotor has cylindrical teeth, while the shape of the teeth on the AR-BR rotor can be described as rhomboidal. With this kind of rotor, the tilt direction of the leading edge against the flow of material on the left-hand rotor is always opposite to that of the right-hand rotor. A continuous feeder was used for dosing the fly ash into the mill. The ash was always fed in at a dose of 0.5 kg and milled at the maximum Hz. The time required for all the material to pass through the mill was 180 s. The samples for both rotor variants were prepared for 1, 2, 3, 5 and 10 passes through the mill. Grinding was performed under standard laboratory conditions, at 22 °C and with a relative humidity of 56 %. Between the steps of grinding, the mill was cooled by an air stream so that the temperature of the working chamber did not exceed 70 °C. The Blaine specific surface area was determined for all the samples. All the fly ash samples, including the control sample, were subjected to particle size distribution measurements by laser granulometry. This analysis was performed on a Malvern Mastersizer 2000 with a Hydro 2000 G wet dispergation unit; 2-isopropanol was used as a dispersant. The effect of the milling technique on the morphology of the grains was observed and assessed by electron microscopy (SEM). A Tescan MIRA 3 XMU SEM with a secondary electron detector was used. The Chapelle test method[20] was used to determine the pozzolanic activity This test was done on the control sample of fly ash and the samples ground via one, three, and ten passes. The method was adapted for the needs of the experiment. The modified Chapelle test consists of allowing pozzolan and freshly annealed CaO to react together in an aquatic environment at 93 °C for 24 h. The reaction takes place in a tightly closed stainless-steel vessel and the suspension is stirred with an electromagnetic stirrer. The result is expressed as the amount of $Ca(OH)_2$ bound in mg per 1 g of pozzolan. The results were compared to each other and with those from the control sample of fly ash.

3 RESULTS

The results for the chemical composition of the control TEKO fly ash are shown in **Table 1**. Only selected oxides and loss on ignition are listed in the table.

Table 1: The chemical composition of the fly ash
Tabela 1: Kemijska sestava letečega pepela

Components	SiO_2	Al_2O_3	Fe_2O_3	CaO	SO_3	Loss on ign.	Others
Content % per mass	51.8	18.1	9.1	6.7	0.8	6	7.5

The specific surface area and density are then presented in **Table 2**.

Table 2: Density and specific surface area of the TEKO fly ash
Tabela 2: Gostota in specifična površina TEKO letečega pepela

Density (kg/m^3)	2423
Specific surface area (m^2/kg)	494

The chemical and physical properties are typical for conventional siliceous ash.

The specific surface area values were determined from the samples ground via the selected operating mode for both types of rotors immediately after passing through the mill. The specific surface area results for both types of rotors are shown in **Figure 1**.

After the first pass of the samples through the mill, a significant increase in the specific surface area is apparent in both cases. However, after the second pass through a significant decrease in the specific surface area can be seen. The decrease in specific surface area in the initial stages was greater in the case of the AR-BR rotors. Each additional pass through the mill led to a further reduction in the surface area. However, after ten cycles, the sample milled by the OR rotor had a lower specific surface area than the sample milled by the AR-BR rotor.

The granulometry of the control fly ash and of all the ground samples was analyzed by laser granulometry. Selected laser granulometry results for both types of rotor are shown in **Figures 2a** and **2b**.

The dependence of the grain size *d* (0.1), *d* (0.5) and *d* (0.9) on the number of passes of the material through the mill is summarized in **Table 3** in order to facilitate a comparison of the impact of the milling technique on the course of the grinding.

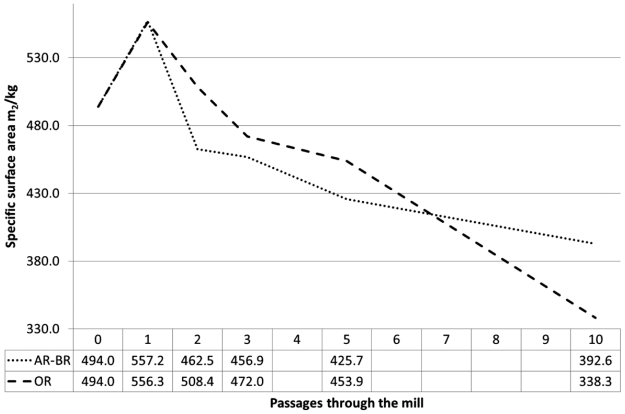

Figure 1: Specific surface area for all the samples
Slika 1: Specifična površina pri vseh vzorcih

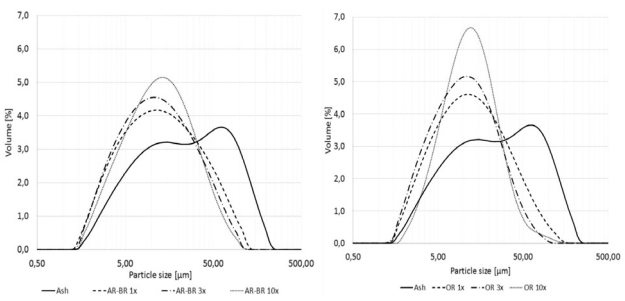

Figure 2: Particle size distribution: a) AR-BR and b) OR
Slika 2: Razporeditev velikosti delcev: a) AR-BR in b) OR

Table 3: The dependence of the grain size *d* (0.1), *d* (0.5) and *d* (0.9) on the number of passes of the material through the mill
Tabela 3: Odvisnost velikosti zrn *d* (0,1), *d* (0,5) in *d* (0,9) od števila prehodov materiala skozi mlin

	Number of passes through the mill						
	d/µm	0	1	2	3	5	10
AR-BR	0.1	4.90	3.52	3.66	3.53	3.99	3.99
	0.5	25.60	13.19	13.19	12.02	12.15	12.99
	0.9	108.083	52.87	47.80	43.86	37.57	40.08
OR	0.1	4.90	3.68	3.47	3.39	4.27	4.85
	0.5)	25.60	12.56	11.72	10.61	11.40	12.39
	0.9	108.083	46.59	38.90	32.45	33.01	30.91

In both cases, after the first pass there was a significant reduction in the proportion of coarse particles, with each additional grinding causing a further decline in the amount present. However, at the same time, there was also a decrease in the proportion of ultra-fine parti-

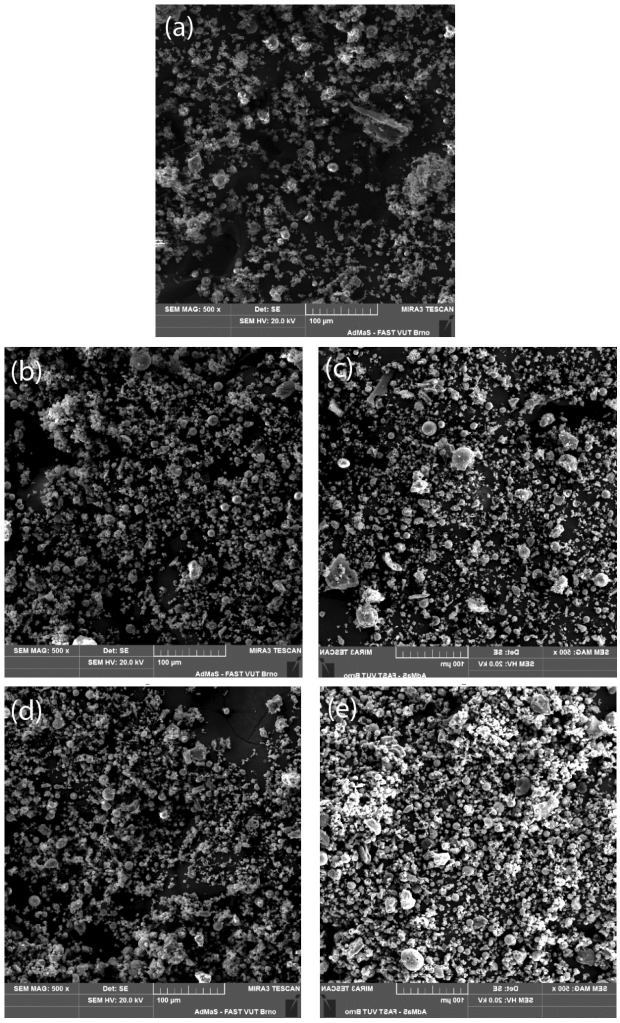

Figure 3: a) The morphology of the control fly ash, b) 1 pass, AR-BR rotors, c) 1 pass, OR rotors, d) 10 pass, AR-BR rotors and e) 10 pass, OR rotors
Slika 3: a) Morfologija kontrolnega letečega pepela, b) 1 prehod, AR-BR rotorji, c) 1 prehod, OR rotorji, d) 10 prehod, AR-BR rotorji in e) 10 prehod, OR rotorji

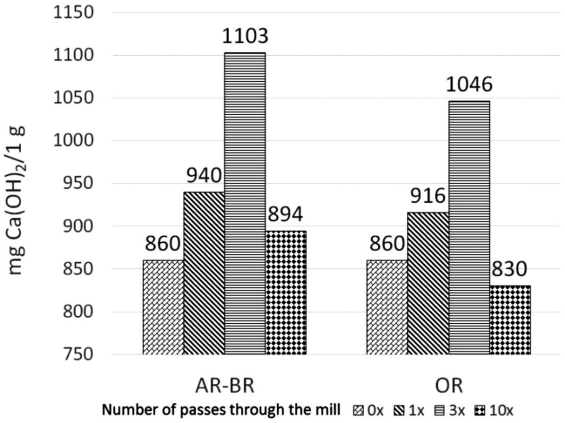

Figure 4: The impact of the technology of grinding on the pozzolanic activity
Slika 4: Vpliv tehnologije mletja na pucolansko aktivnost

cles. The distribution curves after 10 passes were significantly narrower. This phenomenon is more significant in the case of the OR rotor. The results of the effect of the rotors and the number of passes on the morphology of the grains after one and ten passes of fly ash through the mill are illustrated in **Figures 3a** to **3e**.

The SEM analysis shows that a clearly visible refining process is occurring, along with the subsequent agglomeration of particles. This effect is more distinctive in the case of the OR rotors.

Based on the evaluation of the specific surface area, samples were selected after one, three and ten passes through the mill for the purpose of determining the pozzolanic activity. The results of this determination are shown in **Figure 4**.

In both cases the first significant increase in evident pozzolanic activity did not occur until the third pass. A significant decrease occurred after the tenth cycle, this being mainly the case for the OR rotors.

4 DISCUSSION

A chemical composition with a high content of SiO_2 and a low content of SO_3 is typical for conventional siliceous ash. Morphologically, it is a mixture of spherical cenospheres and porous plerospheres, as is apparent from the SEM image. Its specific surface area of 494 m^2/kg is relatively high, which corresponds to the higher pozzolanic activity of fly ash at 860 mg of $Ca(OH)_2$/1g, as determined by the modified Chapelle test. The pozzolanic activity of fly ash tested by this method usually ranges from 700 to 850 mg $Ca(OH)_2$/1 g.[21] This fly ash can therefore be rated as reactive. In the case of both types of rotor, a step increase in the specific surface area occurred after the first pass of the ash through the mill. The specific surface area increased by about 60 m^2/kg to a final 557 m^2/kg in both cases. The growth in specific surface area is associated with a decrease in the grain sizes d (0.1), d (0.5) and d (0.9), which is clearly visible from the particle size distribution curves in **Figures 2a** and **2b**. As regards the rotors, the AR-BR curve is clearly wider than that for the OR type. At this stage, especially large, soft and porous plerospheres are milled very intensively, as evidenced by the SEM images above. However, the amount of pozzolanic activity is already different at this stage of the milling process. Fly ash ground on the AR-BR rotors showed pozzolanic activity that was 24 mg of $Ca(OH)_2$/1g higher for the same specific surface area than ash ground on the OR rotors. The results correspond well with the particle size distribution curves when the AR-BR sample contains more ultra-fine particles. A sharp decline in the specific surface area can be observed after the second and third passes. This phenomenon can be explained as being the result of the beginning of the aggregation process due to electrostatic forces. The lower decrease in the specific surface area value in the case of the OR rotors than for the AR-BR type can be explained by the cylindrical shape of the teeth on the OR rotors. The friction surface over which the particles roll is smaller with this tooth shape. The charging of the particles, which leads to aggregation, is thus smaller. The aggregation process can be clearly observed on the granulometric curves, which become narrower. However, in both cases, the pozzolanic activity increased significantly. This phenomenon can be explained as being just due to the formation of aggregates, which are only loosely bound together by electrostatic forces. Because the Chapelle test takes place in an aquatic environment, loosely bonded aggregates can easily disintegrate and the fine particles can react with the calcium ions very swiftly and easily. In the case of the AR-BR rotors, the increase in pozzolanic activity is significantly higher than in the case of the OR rotors. A possible explanation for this abnormality is simply that the AR-BR rotor teeth have a larger contact surface. They thus charge particles and accelerate the formation of aggregates more than the cylindrical teeth of the OR rotors, but may also create more defects on the surfaces of the fly ash particles, causing the particles to become more reactive. Between the third and the tenth passes, a gradual decline in specific surface area can be observed. The particle distribution curves become narrower and there is a significant increase in grain size d (0.1). At this point the aggregation phase has already changed to the stage of agglomeration, where the particles are bound by chemical bonds.[1] This confirms the results of the pozzolanic activity determination, and the SEM images. The specific surface area and pozzolanic activity results achieved by the OR rotors after ten passes are significantly worse than in the case of the AR-BR rotors. Because most of the grinding work in the phase of agglomeration is just consumed in the breakage of new agglomerates, the results indicate the AR-BR rotors have a higher efficiency compared to the OR rotors.

5 CONCLUSION

High-speed grinding in a high-speed disintegrator is very effective during the first pass of fly ash through the

mill, when there is a step increase in the specific surface area, and related pozzolanic activity. During the first pass there is no aggregation or agglomeration of the grains. Fly ash can thus be easily homogenized with the other components of the cement composite, and its properties can be improved at the same time. The disadvantage of this type of mill is the process of rapid aggregation and subsequent agglomeration, which makes it impossible to achieve a higher specific surface area. However, this phenomenon can be eliminated by adding grinding aids or using particle separators, for example. We can conclude based on all the achieved results that the use of the AR-BR rotor with rhomboid-shaped teeth for the grinding of fly ash is more advantageous in the case of a HSG disintegrator than using the OR rotor with its traditional cylindrical tooth shape. Higher pozzolanic activity was achieved for the same specific surface area. Based on the results, we can say that in the case of fly ash, a high-speed disintegrator can be a promising means of improving its properties via grinding and mechanical activation.

Acknowledgment

This work was financially supported by project No. LO1408 "AdMaS UP – Advanced Materials, Structures and Technologies", supported by the Ministry of Education, Youth and Sports under "National Sustainability Programme I" and by project No. 15-08755S: "Study of the effects of samples preparation on the final properties of inorganic binders".

5 REFERENCES

[1] P. Baláž, Mechanochemistry in Nanoscience and Minerals Engineering, Springer-Verlag, Berlin, Heidelberg 2008

[2] I. A. Massalimov, Materials processing in a disintegrator and their use for the improvement of chemical technologies, the Abstract of doctoral thesis, Ufa 2005, http://www.ogbus.ru/authors/Massalimov/Massalimov_1.pdf

[3] K. Tkáčková, Mechanical Activation of Minerals, Minerals Engineering, 11 (**1991**) 4, 185, doi:10.1016/0892-6875(91)90035-T

[4] N. Vdovic, I. Jurina, S. D. Skapin, I. Sondi, The surface properties of clay minerals modified by intensive dry milling-revisited, Applied Clay Science, 48 (**2010**) 4, 575–580, doi:10.1016/j.clay.2010.03.006

[5] F. Garcia, N. L. Bolay, J. L. Trompette, C. Frances, On fragmentation and agglomeration phenomena in an ultrafine wet grinding process: the role of polyelectrolyte additives, International Journal of Mineral Processing, 74 (**2004**) 10, S43–S54, doi:10.1016/j.minpro.2004.07.001

[6] J. Hrachova, P. Komadel, V. S. Fajnor, The effect of mechanical treatment on the structure of montmorillonite, Materials Letters, 61 (**2007**) 16, 3361–3365, doi:10.1016/j.matlet.2006.11.063

[7] N. Kotake, M. Kuboki, S. Kiya, Y. Kandac, Influence of dry and wet grinding conditions on fineness and shape of particle size distribution of product in a ball mill, Advanced Powder Technology, 22 (**2011**) 1, 86–92, doi:10.1016/j.apt.2010.03.015

[8] E. C. Sanchez, E. Torres, M. C. Diaz, F. Saito, Effects of grinding of the feldspar in the sintering using a planetary ball mill, Journal of Materials Processing Technology, 152 (**2004**) 3, 284–290, doi:10.1016/j.jmatprotec.2004.04.367

[9] F. Garcia, N. L. Bolay, C. Frances, Changes of surface and volume properties of calcite during a batch wet grinding process, Chemical Engineering Journal, 85 (**2002**) 2–3, 177–187, doi:10.1016/S1385-8947(01)00152-8

[10] C. Knieke, M. Sommer, W. Peukert, Identifying the apparent and true grinding limit, Powder Technology, 195 (**2009**) 1, 25–30, doi:10.1016/j.powtec.2009.05.007

[11] V. Hanykýř, J. Kutzendörfer, Technologie keramiky, Silis, Prague 2008

[12] V. V. Boldyrev, Mechanochemistry and mechanical activation of solids, Russian Chemical Reviews, 75 (**2006**) 3, 177–189, doi:10.1070/RC2006v075n03ABEH001205

[13] B. M. Kipnis, Analysis of prospects for the UDD - technology in the field of polymeric materials, UDD - Technology Abstracts II, (1983), 44–46

[14] M. Faltus, New types of hydraulic binders based on waste materials, 13th International Conference of Research Institute of Building Materials, 2009, 200–208

[15] M. Procházka, The test results of the new hydraulic binder DASTIT as a component of blended cements, 13th International Conference of Research Institute of Building Materials, 2009, 188–194

[16] R. Hela, D. Orsáková, The Mechanical Activation of Fly, Procedia Engineering, 65 (**2013**), 87–93, doi:10.1016/j.proeng.2013.09.016

[17] S. Kumar, R. Kumar, Mechanical activation of fly ash: Effect on reaction, structure and properties of resulting geopolymer, Ceramics International, 37 (**2011**) 2, 533–541, doi:10.1016/j.ceramint.2010.09.038

[18] N. Marjanović, M. Komljenović, Z. Baščarević, V. Nikolić, Improving reactivity of fly ash and properties of ensuing geopolymers through mechanical activation, Construction and Building Materials, 57 (**2014**), 151–162, doi:10.1016/j.conbuildmat.2014.01.095

[19] S. Aydin, C. Karatay, B. Baradan, The effect of grinding process on mechanical properties and alkali-silica reaction resistance of fly ash incorporated cement mortars, Powder technology, 197 (**2010**) 1–2, 68–72, doi:10.1016/j.powtec.2009.08.020

[20] R. Largent, Estimation de l'activité pouzzolanique, Bull Liaison Labo P et Ch, 93 (**1978**), 61–65

[21] J. Pokorný, M. Pavlíková, E. Navrátilová, P. Rovnaníková, Z. Pavnlík, R. Černý, Application of a-SiO_2 Rich Additives in Cement Paste, Applied Mechanics and Materials, 749 (**2015**), 362–367, doi:10.4028/www.scientific.net/AMM.749.362

UDK 620.1:67.017:669.055:669.21:669.872
Original scientific article/Izvirni znanstveni članek

ISSN 1580-2949
MTAEC9, 50(5)689(2016)

INVESTIGATION OF THE MECHANICAL PROPERTIES OF ELECTROCHEMICALLY DEPOSITED Au-In ALLOY FILMS USING NANO-INDENTATION

PREISKAVA MEHANSKIH LASTNOSTI ELEKTROKEMIJSKO NANEŠENEGA FILMA ZLITINE Au-In Z NANOVTISKOVANJEM

Sabina Cherneva[1], Roumen Iankov[1], Martin Georgiev[2], Tsvetina Dobrovolska[2], Dimitar Stoychev[2]

[1]Bulgarian Academy of Sciences, Institute of Mechanics, Acad. G. Bonchev str., Bl. 4, 1113 Sofia, Bulgaria
[2]Bulgarian Academy of Sciences, Institute of Physical Chemistry, Acad. G. Bonchev str., Bl. 11, 1113 Sofia, Bulgaria
sabina_cherneva@yahoo.com

Prejem rokopisa – received: 2015-06-26; sprejem za objavo – accepted for publication: 2015-09-09

doi:10.17222/mit.2015.129

Thin Au-In alloy films containing different amounts of In were electrochemically deposited on a CuZn substrate with a 500-μm thickness. The thicknesses of the obtained films varied from 0.4 μm to 2.7 μm. The chemical and phase compositions, as well as the structures of the films, were investigated by XRF, XRD and SEM analysis. The mechanical properties of the films and substrates were investigated using nano-indentation experiments. As a result, load–displacement curves were obtained and two mechanical characteristics of the substrate and investigated films – indentation hardness and indentation modulus – were calculated using the Oliver & Pharr approximation method. The dependence of the indentation modulus and the indentation hardness on the depth of the indentation and the content of In, the structure and the phase compositions of the films were investigated and discussed as well.

Keywords: gold-indium alloy, electrochemical deposition, mechanical properties, nano-indentation

Tanke plasti zlitine Au-In, z različno vsebnostjo In, so bile elektrokemijsko nanešene na podlago iz CuZn, debeline 500 μm. Debeline dobljene plasti so bile od 0,4 μm to 2,7 μm. Kemijska sestava in sestava faz, kot tudi mikrostruktura plasti, so bile preiskovane z XRF, XRD in s SEM analizami. Mehanske lastnosti preiskovanih plasti so bile preiskane s pomočjo preizkusa z nanovtiskovanjem. Kot rezultat so bile dobljene krivulje obremenitev-raztezek. Dve mehanski lastnosti podlage in preiskovanih plasti – trdota vtiskovanja in modul vtiskovanja – sta bili izračunani s pomočjo Oliver & Pharr metode približka. Preiskovana in prediskutirana je bila odvisnost modula vtiskovanja in trdota vtiskovanja na globino vtiska od vsebnosti In.

Ključne besede: zlitina zlato-indij, elektrokemijsko nanašanje, mehanske lastnosti, nanovtiskovanje

1 INTRODUCTION

The phase diagram of the gold–indium[1] system shows the presence of several intermetallic compounds existing at a temperature lower than the melting point of Indium (~ 156 °C), including stable AuIn and $AuIn_2$ phases with a cubic lattice, similar to the α-phase of gold. The indium phase starting from a 53 % mass fraction is tetragonal. The average microhardness obtained for the metallurgical alloy system Au–In is as follows: Au (99.999 %) = 0.660, α AuIn (8 % of amount fractions of In) = 1.700, ζ_1-phase = 3.68, AuIn = 2.73, $AuIn_2$ = 0.77 GPa and the alloy with 80 % of amount fractions of In = 2.07 GPa.[2] The microhardness in the hardened condition of the compound Au_3In_2 (ψ phase) is 1.83 GPa, and increases in the uniformity of the phase deviations in the stoichiometric composition.[3] In contrast to metallurgically obtained, the electrochemically deposited Au-In alloys are not well studied. At the same time, electrochemically deposited thin layers of Au–In alloys will find wide application (instead of pure gold coatings) in electrical engineering, micro-electronics, the manufacturing of various sensors, the jewelery industry, etc. The interest in studying the impact of the content of In in the Au–In alloy on a number of colors, decorative, optical, corrosion, mechanical and other properties, regardless of the method of their production, has also increased.[4–6] The aim of the present work is to investigate the indentation hardness and the indentation modulus of electrochemically deposited thin layers of Au–In alloys as a function of the indentation depth and considering the effect on them of the nature of the substrate, the content of In, the structure and phase composition of the alloy films as well as the surface roughness of the films.

2 EXPERIMENTAL PART

The Au-In alloy films with thicknesses between 0.4 μm and 2.7 μm were deposited onto brass sheet substrates (2 cm × 1 cm × 0.03 cm) in a standard electrochemical glass cell equipped with two Pt anodes as the counter electrodes. The standard preliminary treatment of the brass cathode-substrates includes a procedure for electrochemical decreasing, followed by pickling in a 20 % water solution of sulphuric acid at room temperature. The investigated Au–In alloy films were electrodeposited

in galvanostatic mode (in the range of cathodic current densities from 0.2 to 1.8 A dm^{-2}) of an acetate-citrate electrolyte (containing 1 g/L Au as a metal ($KAu(CN)_2$); 3 g/L In as a metal ($InCl_3$); 90 g/L CH_3COONa; 14 g/L citric acid). The electrolysis process was performed without any stirring of the electrolyte and at room temperature. The thickness, content of In and percentage composition (Au:In) of the thin alloy films were determined by X-ray fluorescence analysis (Fischerscope XDAL). The structure and morphology of the layer surface were investigated by scanning electron microscopy (SEM) using a JSM 6390 microscope. The phase composition was characterized by X-ray diffraction (XRD) using a PANalytical Empyrean Equipped with a multichannel detector (Pixel 3D) using Cu–K_α (45 kV-40 mA) radiation in the 20–115° 2θ range with a scan step of 0.01° per 20 s. The mechanical properties of the Au–In alloy films containing different amounts of In onto the CuZn substrate were investigated by means of nano-indentation experiments, using a Nano Indenter G200 (Keysight Technologies, USA), equipped with a Berkovich three-sided diamond pyramid with a centerline-to-face angle of 65.3° and a 20-nm radius at the tip of the indenter. We realized a series of 25 indentations on each sample probe. We used an indentation method that was proposed in [7]. The indentation hardness and indentation modulus are determined using the stiffness calculated from the slope of the load–displacement curve during each unloading cycle. As a result load–displacement curves were obtained and two mechanical characteristics of the substrate and the investigated films – indentation hardness (H_{IT}) and indentation modulus (E_{IT}) – were calculated using the Oliver & Pharr approximation method.[8]

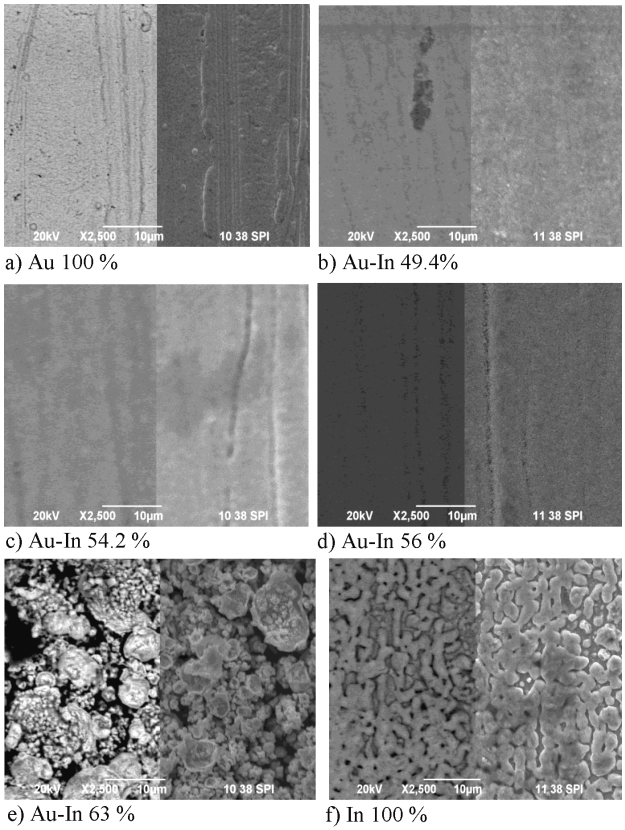

Figure 1: SEM microphotographs of deposited a) Au 100 %: f) In 100 % and Au–In alloy layers in which the content of indium (in mass fractions, (*w*/%) is: b) 49.4 % In, c) 54.2 % In, d) 56.0 % In and e) 63 % In (samples No. 2, 7, 3, 4, 5, 6 described in **Table 1**)

Slika 1: SEM-posnetek nanosa: a) Au 100 %, f) In 100 % in nanosi AuIn z različno vsebnostjo In (v masnih odstotkih, (*w*/%): b) 49,4 % In, c) 54,2 % In, d) 56,0 % In, e) 63 % In (vzorci št. 2, 7, 3, 4, 5, 6 opisani v **Tabeli 1**)

3 RESULTS AND DISCUSSION

Table 1 shows the results of the XRF analyses on the chemical composition, thickness (δ) and the micro roughness (R_z and R_a) of the tested alloy samples and the brass substrate on which they were deposited. From the results it can be seen that the interval of changes in content 49–63 % for the mass fractions of indium in the resulting thin alloy layers and changes of their micro roughness. Information about the surface morphology and the structure of the electrodeposited pure Au and In coatings of the working electrolyte for the preparation of the alloy coatings of which in the first case the presence of In ions is excluded, and in the second case, the presence of Au ions is excluded, give the microphotographs presented in **Figure 1a** and **1f**. While the Au coating is dense and uniform, formed by spherical crystallites having a size ~ 0.5–1.2 µm (**Figure 1a**), the coatings of In have an uneven thickness – over the fine crystal thin indium layer which covers the entire surface

Table 1: Chemical composition, thickness, R_z and R_a of the investigated Au–In alloy layers and the substrate on which they are deposited
Tabela 1: Kemijska sestava, debelina, R_z in R_a preiskovanih AuIn plasti in podlage, na katero so bile nanešene

No	Sample	Content in mass fractions, (*w*/%)	δ, µm	R_a, µm	R_z, µm	J, A dm^2 deposition time, min
1.	Brass substrate (pickled)	Cu – 65.80; Zn – 34.20	300	1.61	9.13	
2.	Au/Brass	Au – 100	0.64	1.13	4.77	1.0; 20
3.	AuIn/Brass	Au – 50.6; In – 49.4	0.56	1.14	4.90	1.8; 7
4.	AuIn/Brass	Au – 45.8; In – 54.2	0.75	1.40	5.37	1.2; 15
5.	AuIn/Brass	Au – 44.1; In – 56.0	1.42	1.15	5.00	0.6; 20
6.	AuIn/Brass	Au – 37.0; In – 63.0	2.76	1.50	8.93	0.2; 30
7.	In/Brass	In – 100	0.49	1.18	3.83	1.0; 20

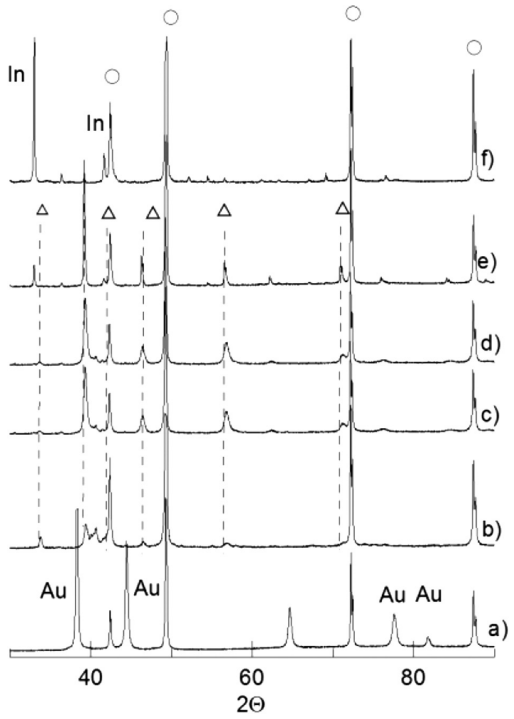

Figure 2: XRD patterns of the: a) Au 100 %, f) In 100 % and Au–In alloy layers, containing: b) 49.4 % In, c) 54.2 % In, d) 56.0 % In, e) 63 % In; (o) – reflections of CuZn substrates, (Δ) – reflections of $AuIn_2$

Slika 2: Rentgenogram: a) Au 100 %, f) In 100 % in AuIn nanosa z: b) 49,4 % In, c) 54,2 % In, d) 56,0 % In, e) 63 % In; (o) odboji CuZn podlage, (Δ) odboji $AuIn_2$

of the brass substrate, they grew, not fully coalesced, spheroidal agglomerates with size ~ 1–10 μm (**Figure 1f**). The influence of changes in the content of indium on the surface morphology and structure of the Au–In alloy layers is presented in **Figures 1b** to **1e**. From the microphotographs it is clear that at the lowest content of indium (49.4 %) (**Figure 1b**) the film has a morphology and structure that is different from that of the pure gold film. The alloy coating is formed by homogeneously distributed agglomerates of a size of the base several times

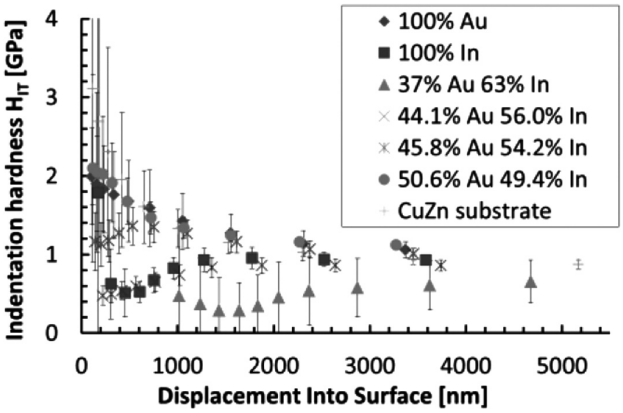

Figure 3: Dependence of the indentation hardness on the depth of the indentation

Slika 3: Odvisnost trdote vtiskovanja od globine vtiskovanja

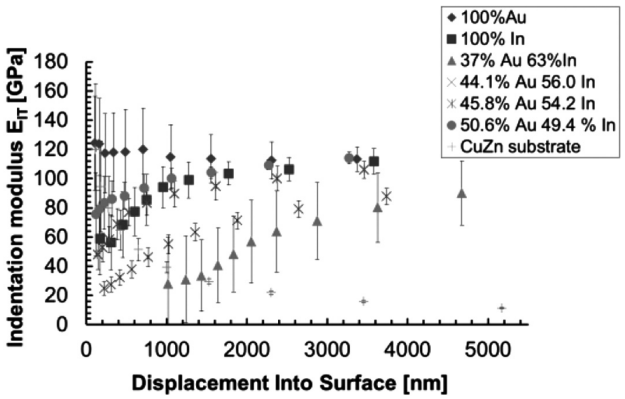

Figure 4: Dependence of indentation modulus on the depth of the indentation

Slika 4: Odvisnost modula vtiskovanja od globine vtiskovanja

larger than that of the spherical grains constituting the gold coating. Moreover, there was no phase heterogeneity in the regime of back scattering electrons. The reasons for this conclusion give the images on the left-hand side of the SPI electron microscopic image (**Figure 1b**), obtained in the regime of back scattering electrons (BEI), while the right-hand part of the photograph shows an image that was obtained in the regime of a secondary-electron image (SEI). With the same purpose (the recording of possible phase heterogeneity) are the SPI electron microscopic images for a higher content of In (**Figures 1c** to **1e**). Increasing the content of indium in the alloy layer to ~ 54 % (**Figure 1c**), leads to a levelling of the morphology, respectively, to a finer structure compared with those at a content of ~ 49 % (**Figure 1b**), in which an even greater degree was observed in the next amount (~ 56 %) of indium (**Figure 1d**). Obviously, the observed differences in morphology are not related to the phase, but are related to the topographic heterogeneity. When the content of co-deposited In, however, reached 63 %, the morphology and the structure drastically change; they are characterized by large aggregates (3–15 μm), composed of crystallites with dimensions of 0.5–1 μm. Moreover, the BEI image (left-hand side) of the electron microscopic micrograph, at this content (**Figure 1e**)

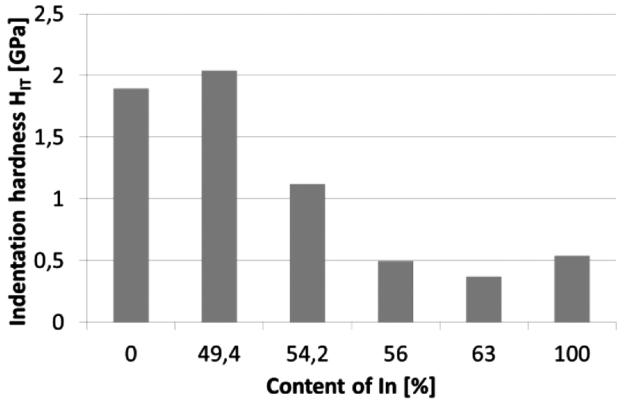

Figure 5: Dependence of the indentation hardness on the content of In

Slika 5: Odvisnost trdote vtiskovanja od vsebnosti In

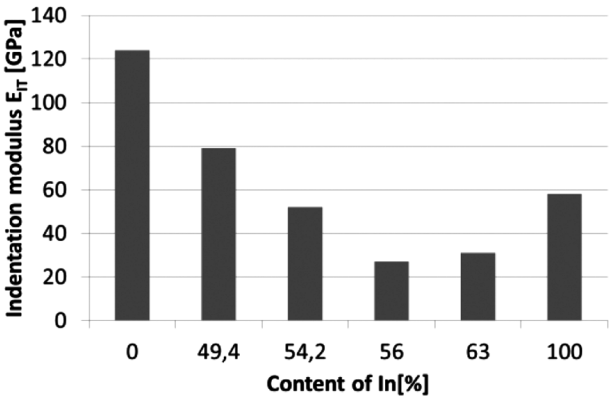

Figure 6: Dependence of the indentation modulus on the content of In
Slika 6: Odvisnost modula vtiskovanja od vsebnosti In

indicates the occurrence of phase heterogeneity. The X-ray phase analysis of the same alloy samples (**Figure 2**) showed that for electrodeposited samples of electrolyte containing only gold ions (in the absence of indium ions) the diffractogram showed the presence of reflections of the cubic lattice ($a = b = c = 4.08$) of the phase of gold (pdf 98-004-4362), and reflections of the brass substrate (pdf 98-062-9457) (**Figure 2a**). In the case of the electrodeposition of an indium film (in the absence of gold ions in the electrolyte), the diffractogram of the obtained sample indicates the presence of reflections of an In tetragonal phase (pdf 98 005-3091) with the lattice parameters $a = 0.3253$ nm, $b = 0.49455$ nm and reflections of the substrate made of brass (pdf 98-062-9457) (**Figure 2f**). Since the content of indium in the electrodeposited alloy film is in the range 49–63 % of mass fractions of In, then, according to the phase diagram for the system Au–In, they fall into the area of the phase $AuIn_2$. This is confirmed by the recorded reflections in the diffractograms presented in **Figures 2b** to **2e**. The $AuIn_2$ phase has a cubic lattice with highly expanded parameters regarding the α-phase of the gold ($a = b = c =$ 6.502). Only in the alloy composition containing over 63 % of mass fractions of In (**Figure 2e**) is there a presence of both the phase $AuIn_2$ and the tetragonal phase of In (pdf 98005-3091), which is the most likely cause for registered, strongly emphasized, morphological heterogeneity of the alloy coating (**Figure 1**). The dependence of the indentation hardness and the indentation modulus of the investigated alloy films on the depth of the indentation are shown in **Figures 3** and **4**. With an increasing depth of indentation, the indentation hardness and the modulus change a great deal. There are two possible reasons for this: the influence of the substrate and the effect of the difference in the structure with depth. The dependence of the indentation hardness and the indentation modulus of the investigated alloy films (at load = 1.15 mN, in order to be far enough from the influence of the substrate) on the content of In is shown in **Figures 5** and **6**. With an increase of the content of In from 0 to 49.4 %, the indentation hardness increases too, and after this (from 54.2 % to 63 % content of In) it starts to decrease. It is obvious from **Figure 6** that with an increase in the In content up to 56.0 % and 63 % the indentation modulus of the investigated Au–In films decreases. This could be explained by the influence of the simultaneously existing two phases on the surface electrode: In and $AuIn_2$. The effect of the non-regularity is very strong due to the different type of crystal lattice – tetragonal in case of the In phase and cubic in the case of the $AuIn_2$ phase. Most probably, the inhomogeneity of these two phases, as well as their roughness limit the accuracy, due to the randomly of both phases during the performed measurements.

4 CONCLUSIONS

In the present work the mechanical properties of electrochemically deposited thin layers of Au–In alloys as a function of the indentation depth and considering the effect on them of the nature of the substrate, the content of In, the structure and the phase composition of the alloy films as well as the surface roughness of the films were investigated. The results showed that with an increasing content of In from 0 % to 49.4 %, the indentation hardness increased too and after this (from 54.2 % to 63 % content of In) it starts to decrease. Moreover, with an increase in the In content up to 56.0 % and 63 % the indentation modulus of the investigated Au-In films decreases. This could be explained by the influence of the simultaneously existing two phases on the surface electrode: In and $AuIn_2$. The effect of the non-regularity is very strong due to the different types of crystal lattice: tetragonal in the case of the In phase and cubic in the case of the $AuIn_2$ phase.

Acknowledgments

Authors gratefully acknowledge the financial support of Bulgarian National Science Fund under Grant No. T02-22/12.12.2014.

5 REFERENCES

[1] T. Massalski, J. Murray, B. Lawrence, B. Hugh, Binary Alloy Phase Diagram, American Society for Metals, Metals Park, Ohio, 1 (**1986**) 90, 260–270

[2] G. W. Powell, J. D. Braun, Diffusion in the gold-indium system, Transactions of the Metallurgical Society of AIME, 230 (**1964**) 4, 694–699

[3] V. K. Nikitina, A. A. Babitsina, U. K. Lobanova, Phase diagrams of the system Au-In, Inorganic materials (in russian), Izvestia AN SSSR, 7 (**1971**) 3, 421–427

[4] L. C. Archibald, G. Sanderson, Electrodeposition of a White Gold-Indium Alloy from an Acid Cyanide Electrolyte, Transactions of the Institute of Metal Finishing, 55 (**1978**) 4, 149–154

[5] C. Cretu, E. Van der Lingen, Coloured Gold Alloys, Gold Bulletin, 32 (**1999**) 4, 115–126, doi: 10.1007/BF03214796

[6] U. E. Klotz, Metallurgy and processing of coloured gold intermetallics – Part I: Properties and surface processing, Gold Bulletin, 43 (**2010**) 1, 4–10, doi: 10.1007/BF03214961

[7] M. Datcheva, S. Cherneva, D. Stoychev, R. Iankov, M. Stoycheva, Determination of Anodized Aluminum Material Characteristics by Means of Nanoindentation Measurements, Materials Sciences and Applications, 2 (**2011**) 10, 1452–1464, doi:10.4236/msa.2011.210196

[8] W. Oliver, G. Pharr, Measurement of hardness and elastic modulus by instrumented indentation: Advances in understanding and refinements to methodology, Journal of Materials Research, 19 (**2004**) 1, 3–20

UDK 67.017:620.1:661.635.11
Original scientific article/Izvirni znanstveni članek

ISSN 1580-2949
MTAEC9, 50(5)695(2016)

GROWTH OF K_2CO_3-DOPED KDP CRYSTAL FROM AN AQUEOUS SOLUTION AND AN INVESTIGATION OF ITS PHYSICAL PROPERTIES

RAST KDP KRISTALOV Z DODATKOM K_2CO_3 IZ VODNE RAZTOPINE IN PREISKAVA NJIHOVIH FIZIKALNIH LASTNOSTI

Abrisham Rousta[1], Hamid Rezagholipour Dizaji[2]

[1]Islamic Azad University, Central Tehran branch, Faculty of Basic Sciences, Physics Department, Crystal Growth Laboratory, 2 Rasooli Alley, North Jamalzadeh st., Tehran, Iran
[2]Semnan University, Faculty of Physics, Semnan, Iran
hrgholipour@semnan.ac.ir

Prejem rokopisa – received: 2015-06-26; sprejem za objavo – accepted for publication: 2015-10-09

doi:10.17222/mit.2015.128

In this present work, KDP and 2M%-K_2CO_3-doped KDP crystals were grown by a slow-evaporation solution technique. The grown crystals were characterized by Fourier Transform Infrared (FT-IR) spectroscopy, X-ray diffractometry (XRD), UV-Vis spectroscopy, and laser damage threshold (LDT) analysis. The presence of the functional groups of the grown crystals was identified from the FT-IR spectra. The XRD tests showed that the grown crystals had a tetragonal structure. A comparison of the optical transmission of the grown crystals revealed that the K_2CO_3-doped KDP crystal had a higher transmission than the pure KDP crystal for the entire UV and visible region.

Keywords: growth from solution, slow-evaporation solution technique, KDP crystal, K_2CO_3 additive

V predstavljenem delu so KDP in z 2M % K_2CO_3 dopirani KDP kristali rasli s tehniko počasnega izhlapevanja tekočine. Dobljeni kristali so bili karakterizirani iz infrardečo spektroskopijo s Fourierjevo transformacijo (FT-IR), z rentgensko difrakcijo (XRD), z UV-Vis spektroskopijo in s pragom poškodbe z laserjem (LDT). Prisotnost funkcionalnih skupin kristalov v rasti je bila določena s FT-IR spektrom. XRD je pokazal, da imajo rastoči kristali tetragonalno zgradbo. Primerjava prepustnosti svetlobe v rastočih kristalih je odkrila, da imajo KDP kristali, dopirani s K_2CO_3, boljšo prepustnost kot pa čisti KDP v celotnem UV in v vidnem področju.

Ključne besede: rast iz raztopine, tehnika počasnega izparevanja raztopine, KDP kristal, dodatek K_2CO_3

1 INTRODUCTION

Potassium dihydrogen phosphate KH_2PO_4 (KDP) is a material that is soluble in water with a positive solubility coefficient. The crystal structure is tetragonal with the lattice parameters $a = b = 0.7448$ nm and $c = 0.6977$ nm. A KDP single crystal is piezoelectric at room temperature, and below 123 K (Curie point) it transforms to the ferroelectric phase and has an orthorhombic structure. This crystal is an excellent electro-optic and nonlinear optical (NLO) material, so it is used in optical modulators such as a second-harmonic generator. In addition, it is characterized by its good UV-visible transmission, high damage threshold, etc. Many attempts have been made to modify its properties, either by changing the growth condition or by adding different impurities.[1–7]

P. V. Dhanaraj et al.[8] showed that the addition of K_2CO_3 could make the KDP solution more stable than with other additives and enhanced the metastable zone width of the KDP solution for all temperatures.[8] They also found that the laser-induced damage threshold of a K_2CO_3-added KDP crystal was higher than that of the pure KDP crystal.

In the present study, pure and 2M%-K_2CO_3-doped KDP crystals were grown from an aqueous solution using the slow-evaporation method at room temperature. The grown crystals were then subjected to various characterization techniques.

2 EXPERIMENTAL PROCEDURE

KDP crystals, pure and with added 2M% K_2CO_3, were grown from an aqueous solution using the slow-evaporation method at room temperature. A saturated solution of KDP was prepared by dissolving an appropriate amount of commercially available KDP powder in double distilled water without any further purification. The solution was then stirred well for two hours using a magnetic stirrer, filtered using Whatmann filter paper and transferred into the growth container for the slow evaporation. In a similar way, a saturated solution of KDP with added 2 M% K_2CO_3 was prepared. Then each container was covered with a perforated cover and kept in a dust-free place. Within two weeks, transparent KDP crystals of both pure (22 mm × 21 mm × 8 mm) and with added 2 M% K_2CO_3 (24 mm × 20 mm × 14 mm) were

grown. **Figures 1a** and **1b** show the pure and doped crystals, respectively.

3 RESULTS AND DISCUSSION

3.1 X-ray diffraction analysis (XRD)

Both the pure and 2M%-K_2CO_3-added KDP crystals were subjected to powder X-ray diffraction (XRD) analysis using an X-ray diffractometer (Advance Model D8) with high-intensity Cu-K_α radiation (λ = 0.15406 nm). The grown crystals were ground using an agate mortar and pestle in order to determine the crystal phases by XRD. **Figure 2** shows the XRD patterns of the pure and doped KDP single crystals. From the data, both the crystals were found to crystallize in the tetragonal system. Comparing the two patterns, we found no extra peaks due to the doping; hence adding K_2CO_3 to KDP did not affect its crystal structure. The sharp peaks observed in both patterns indicate the good crystallinity of the grown crystals.

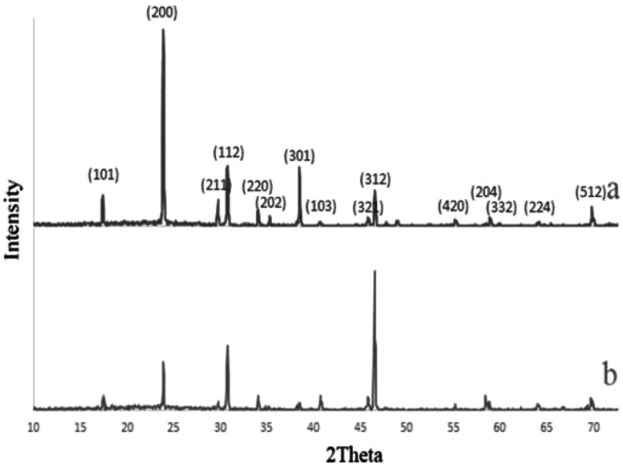

Figure 2: X-ray diffraction patterns of: a) pure KDP and b) 2 M%-K_2CO_3-added KDP single crystals

Slika 2: Rentgenograma: a) čisti KDP in b) KDP monokristali z dodatkom 2 M % K_2CO_3

3.2 Optical transmittance

The optical transmittance spectrum in the wavelength region 200–800 nm was recorded at room temperature using a Perkin Elmer model lambda25 UV-Vis-NIR spectro-photometer on a 1.8-mm-thick plate of the grown K_2CO_3-added KDP crystal in the (001) direction. This property is the most desirable one for an NLO material. **Figure 3** presents a comparison among the transmittance spectra of pure and 5M%-K_2CO_3-added KDP single crystals[7] and a 2 M%-K_2CO_3-added KDP single crystal (present work).

It is clear from the figure that the crystals are highly transparent across the entire UV-visible region. It is also obvious that the transmittance percentage of the doped KDP crystal is higher than that of the pure one. This improvement in the transparency of the KDP crystal after the addition of K_2CO_3 to the solution may be attributed to its ability to suppress the inclusions due to the heavy metals usually present in the starting material.

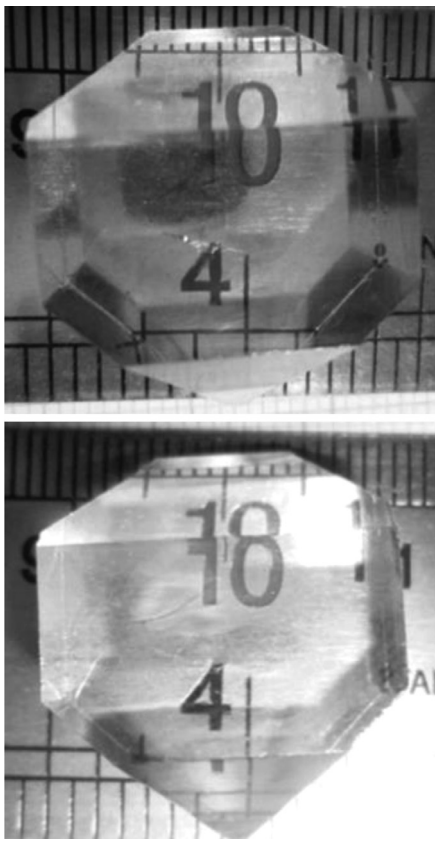

Figure 1: Photographs of: a) pure and b) 2 M%-K_2CO_3-doped KDP crystals

Slika 1: Posnetka: a) čistega in b) z 2 M% K_2CO_3 dopiranega KDP kristala

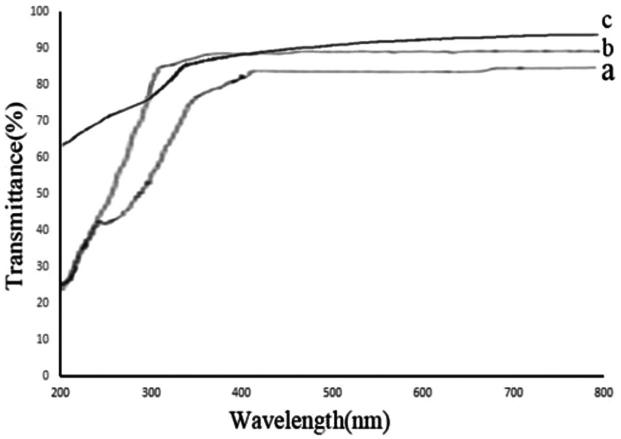

Figure 3: UV-visible transmittance spectra of: a) pure KDP and b) 5M%-K_2CO_3-added KDP single crystals[6], and c) 2 M%-K_2CO_3-added KDP single crystal

Slika 3: Spekter prepustnosti UV in vidne svetlobe: a) čisti KDP in b) monokristali KDP z dodatkom 5M % K_2CO_3[6] in c) monokristal KDP z dodatkom 2 M % K_2CO_3

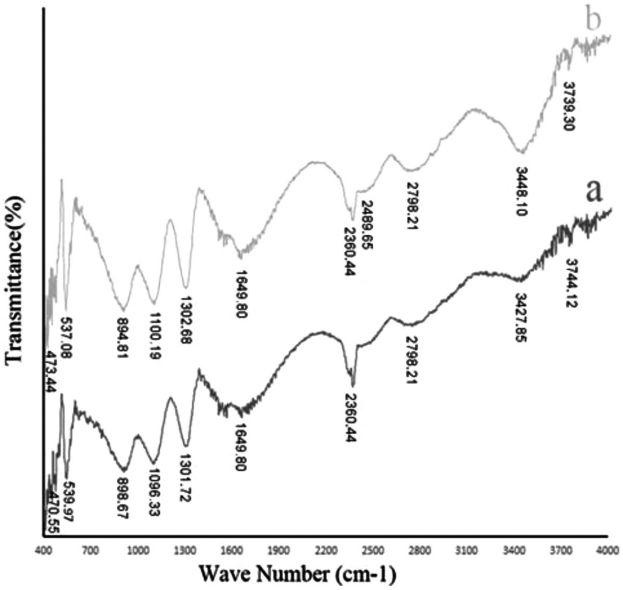

Figure 4: FT-IR spectra of: a) pure KDP and b) 2 M% K_2CO_3 added KDP single crystals

Slika 4: FT-IR-spektri: a) čisti KDP in b) KDP monokristal z dodatkom 2 M% K_2CO_3

3.3 Fourier-transform infrared (FT-IR) analysis

The FT-IR spectra of the pure and 2 M%-K_2CO_3-doped KDP crystals were recorded using a Perkin Elmer model 410 Jasco company spectrometer in the wavenumber range from 400 cm^{-1} to 4000 cm^{-1} using the KBr pellet technique. **Figure 4** represents the FT-IR spectra of the grown crystals. Also, the position of the peaks and their functional group assignments are given in **Table 1**.

Table 1: Observed FT-IR wave numbers (cm^{-1}) and their functional group assignments for the grown pure and 2M%-K_2CO_3-added KDP crystal

Tabela 1: Opažena FT-IR valovna števila (cm^{-1}) in dodeljene funkcionalne skupine pri čistem KDP kristalu in KDP kristalu z dodatkom 2M % K_2CO_3

Wave number (cm^{-1})		Functional group assignments
Pure KDP crystal	2M %K_2CO_3 added KDP crystal	
3739.30	3744.12	Free O-H stretching hydrogen bonded
3448.10	3427.85	O-H stretching hydrogen bonded
2489.65	–	O=P-OH asymmetric stretching
1649.80	1649.80	O-H bending out of plate
1302.68	1301.72	O-P=O stretching
1100.19	1096.33	P=O stretching
894.81	898.67	P-O stretching
537.08	539.97	O-P-O bending
473.44	470.55	PO_4 stretching

The broad band that appears in the range from 3800 cm^{-1} to 2500 cm^{-1} is due to free O-H stretching of the KDP. These functional groups arise at 3739 cm^{-1} and 3448 cm^{-1} in pure KDP and at 3744 cm^{-1} and 3427 cm^{-1} in doped KDP.

The peaks at 537 cm^{-1}, 1100 cm^{-1} and 2489 cm^{-1} in pure KDP and 539 cm^{-1} and 1096 cm^{-1} in doped KDP are due to the O-P-O bending, P=O stretching and O=P-OH asymmetric stretching of the KDP, respectively. The O-P=O stretching, P-O stretching and PO_4 stretching are found at 1302 cm^{-1}, 894 cm^{-1} and 473 cm^{-1} in pure KDP and 1301 cm^{-1}, 898 cm^{-1} and 470 cm^{-1} in doped KDP, respectively.

We can clearly see from the comparison of the FTIR spectrum of the two crystals that the presence of the dopant has led to a change in the intensity of the absorption of the IR frequencies and a slight shift in some of the frequencies. The strong similarities of the two graphs reveal the fact that the peaks corresponding to pure KDP crystal are predominant over those corresponding to the K_2CO_3-added KDP crystal, which may be due to the small amount of doped K_2CO_3 in the compound compared to the KDP.

3.4 Laser damage threshold (LDT)

One of the most important considerations when selecting a material for nonlinear optics applications is its ability to withstand high power intensities.[9]

The laser damage threshold (LDT) of nonlinear optical components depends on physical and chemical factors, particularly imperfections, defects and the concentration and type of the impurities, etc.[10]

The LDT of the grown pure and 2M%-K_2CO_3-doped KDP single crystals was carried out using a Nd:YAG laser with the wavelength 1064 nm and shot-to-shot mode, with an energy per pulse of 50 mJ, a repetition rate of 10 Hz, a pulse duration of 7 ns, a beam waist of 0.0841 mm and a spot diameter of 2.3 mm. The laser beam was focused on the sample with 1-m and 50-cm focal-length lenses. A Tektronic 2430A digital oscilloscope was used to record the energy of every pulse and save the data in a computer.

The damage threshold was calculated for the pure KDP and the 2 M%-K_2CO_3-doped KDP crystals and the value was found to be 12.1083 J/cm^2 and 19.1782 J/cm^2, respectively. It shows that, adding 2M% K_2CO_3 to the KDP solution increased the damage threshold of the KDP single crystal, which can be attributed to the ability of this additive to suppress the inclusions due to heavy-metal impurities like Cr^{3+}, Fe^{3+}, and Al^{3+} that are present in most of the commercially available chemicals.

4 CONCLUSIONS

In this work, pure KDP and 2M%-K_2CO_3-doped KDP crystals were grown by the slow-evaporation solution technique from an aqueous solution at room temperature. Structural studies indicate that both the grown

crystals have a tetragonal system with similar XRD patterns. Optical transmission studies showed that using 2 M% K_2CO_3 as an additive increased the optical quality of the KDP crystal compared to the pure crystal. Fourier transform infrared analysis revealed the functional groups of the samples. The laser-damage threshold of the 2 M%-K_2CO_3-added KDP crystal was found to be higher than that of the undoped crystal, indicating the suitability of K_2CO_3 as an additive to enable KDP to withstand high power intensities.

Acknowledgments

This work is based on a Master of Science thesis that was supported by the Islamic Azad University, Central Tehran Branch.

The authors are thankful to Dr. M. Nikpour, assistant Prof. of Chemistry Department and Mr. N. Madani faculty member of Physics Department, Islamic Azad University, Central Tehran Branch for their assistance.

5 REFERENCES

[1] K. D. Parikh, B. B. Parekh, D. J. Dave, M. J. Joshi, Nucleation Kinetics of L-Arginine, L-Lysine and L-Alanine Doped Potassium Dihydrogen Phosphate Crystals, Journal of Crystallization Process and Technology, 3 (**2013**), 92–96, doi:10.4236/jcpt.2013.33015

[2] S. Balamurugan, P. Ramasamy, Y. Inkong, P. Manyum, Effect of KCl on the bulk growth KDP crystals by Sankaranarayanan-Ramasamy method, Materials Chemistry and Physics, 113 (**2009**), 622–625, doi:10.1016/j.matchemphys.2008.07.102

[3] R. Kayalvizhi, G. Meenakshi, Growth And Characterisation Of Pure And Methyl Violet Dye Doped Potassium Dihydrogen Phosphate (KDP) Crystal, International Journal of Innovative Technology and Exploring Engineering (IJITEE), 3 (**2013**), 73–77, doi:10.9780/22315063

[4] Y. Shangfeng, S. Genbo, L. Zhengdong, J. Rihong, Rapid growth of KH2PO4 crystals in aqueous solution with additives, Journal of Crystal Growth, 197 (**1999**), 383–387, doi:10.1016/S0022-0248(98)00944-0

[5] O. V. Mary Sheeja, C. K. Mahadevan, Growth and characterization of CdS doped KDP single crystals, International Journal of Research in Engineering and Technology, 2 (**2013**), 738–748, doi:10.15623/ijret.2013.0212125

[6] A. Ghane, H. Rezagholipour Dizaji, Growth and Characterization of a Unidirectional EDTA Added KDP Single Crystal by the S-R Method, Chinese Journal of Physics, 50 (**2012**), 652–658, doi:10.6122/CJP

[7] X. G. Xu, X. Sun, Z. P. Wang, Z. S. Shao, Z. S. Gao, Abnormal optical properties in doped H_3BO_3 KDP crystals, Journal of Crystal Growth, 310 (**2008**), 5341–5346, doi:10.1016/S0030-4018(01)01130-0

[8] P. V. Dhanaraj, C. K. Mahadevan, C. K. Bhagavannarayana, P. Ramasamy, N. P. Rajesh, Growth and characterization of KDP crystals with potassium carbonate asadditive, Journal of Crystal Growth, 310 (**2008**), 5341–5346, doi:10.1016/j.jcrysgro.2008.09.019

[9] P. Rajesh, S. Sreedhar, K. Boopathi, S. Venugopal Rao, P. Ramasamy, Enhancement of the crystalline perfection of directed KDP single crystal, Current Applied Physics, 11 (**2011**), 1343–1348, doi:10.1016/j.cap.2011.03.076

[10] N. Balamurugan, P. Ramasamy, Investigation of the Growth Rate Formula and Bulk Laser Damage Threshold KDP Crystal Growth from Aqueous Solution by the Sankaranarayanan-Ramasamy (SR) Method, Crystal Growth & Design, 6 (**2006**), 1642–1644, doi:10.1021/cg050680n

UDK 621.7.015:621.78:669.721.5:669.715
Original scientific article/Izvirni znanstveni članek

ISSN 1580-2949
MTAEC9, 50(5)699(2016)

SURFACE TREATMENT OF HEAT-TREATED CAST MAGNESIUM AND ALUMINIUM ALLOYS

OBDELAVA POVRŠINE TOPLOTNO OBDELANIH MAGNEZIJEVIH IN ALUMINIJEVIH LIVNIH ZLITIN

Tomasz Tański, Maciej Wiśniowski, Wiktor Matysiak, Marcin Staszuk, Radosław Szklarek

Silesian University of Technology, Institute of Engineering Materials and Biomaterials, Konarskiego Str. 18A, 44-100 Gliwice, Poland
tomasz.tanski@polsl.pl

Prejem rokopisa – received: 2015-06-26; sprejem za objavo – accepted for publication: 2015-10-12

doi:10.17222/mit.2015.132

Modern coating systems deposited on surface layers of structural light materials are currently one of the most important issues in up-to-date material engineering, where vacuum deposition techniques are often used to improve the mechanical and functional properties of produced surface layers. Presented in this paper are gradient and monolithic coating types: Ti/Ti(C,N)/CrN, Ti/Ti(C,N)/(Ti,Al)N, Ti/(Ti,Si)N/(Ti,Si)N, Cr/CrN/CrN, Cr/CrN/TiN and Ti/DLC/DLC deposited onto magnesium and aluminium alloy substrates with the cathodic-arc-evaporation method (Arc PVD) and plasma-assisted process (PA CVD). Additionally, a thin metallic layer – in micrometers– (Cr and Ti) was deposited prior to the deposition of the final gradient coating to improve its adhesion to the substrate. This work presents the investigation results concerning the obtained surface-layer microstructures and mechanical properties of the obtained bi-layer coatings (gradient/multicompound) deposited onto light-alloy substrates using the chosen PVD and CVD methods, especially to meet the requirements needed for light-metal substrates – low temperature and duration. The structure investigations of the deposited coating were performed using a scanning electron microscopy (SEM) and glow discharge optical emission spectrometry (GDOES); the mechanical and functional properties were examined using the ball-on-disk method for the wear-resistance determination, and microhardness tests were performed for the functional usability of the coatings. The main finding is that the fracture morphology is characterized by a lack of columnar structures in the obtained coatings. The metallographic examinations carried out proved that the coatings were deposited uniformly over the whole sample, onto the investigated substrate materials; the measured thickness is characteristic for the produced coating type.It was also found that the particular layers adhere tightly to each other and to the light-metal substrate. The investigation results of the up-to-date PVD methods, together with light alloys, led to obtaining new applications, especially in the automobile and aviation industries.

Keywords: light alloys, PVD, CVD, structure, properties

Moderni sistemi nanosov na površinskih plasteh lahkih konstrukcijskih materialov so eden od najpomembnejših izzivov v inženiringu materialov, kjer se za izboljšanje mehanskih in funkcionalnih lastnosti plasti na površini pogosto uporabljajo tehnike vakuumske depozicije. V članku so predstavljeni gradientni in monolitni nanosi vrst: Ti/Ti(C,N)/CrN, Ti/Ti(C,N)/(Ti,Al)N, Ti/(Ti,Si)N/(Ti,Si)N, Cr/CrN/CrN, Cr/CrN/TiN in Ti/DLC/DLC ki so bili nanešeni z metodo katodnega izparevanja v obloku (Arc PVD) in s plazemskim postopkom (PA CVD). Dodatno je bila nanešena tanka kovinska plast (Cr in Ti), debelina v mikrometrih, in sicer pred nanosom končnega gradientnega nanosa, da bi se izboljšala njegova oprijemljivost na podlago. Članek predstavlja rezultate raziskave mikrostrukture površinskega nanosa in mehanske lastnosti dvoplastnega nanosa (gradient/multicompound), nanešenega na podlago iz lahke zlitine, s pomočjo izbranih metod PVD in CVD, da bi zagotovili zahtevam podlage iz lahke kovine – nizka temperatura in kratko trajanje. Preiskave zgradbe nanosa so bile izvedene s pomočjo vrstične elektronske mikroskopije (SEM) in z razelektritveno optično emisijsko spektrometrijo (GDOES), medtem ko so bile mehanske in funkcionalne lastnosti, preiskane z uporabo metode kroglica na plošči za določanje obrabne odpornosti ter mikrotrdote za funkcionalno uporabnost nanosov. Glavna ugotovitev je, da v morfologiji preloma nanosov ni stebraste zgradbe. Izvedene metalografske preiskave so pokazale, da so nanosi enakomerno nanešeni po vsej površini preiskovane podlage, izmerjene debeline so značilne za to vrsto nanosov in ugotovljeno je tudi, da se posamezni nanosi med seboj tesno stikajo, tudi s podlago iz lahke kovine. Rezultati raziskav kažejo, da uporaba sodobnih PVD metod, skupaj z lahkimi zlitinami, omogoča nove aplikacije, posebno v avtomobilski in letalski industriji.

Ključne besede: lahke zlitine, PVD, CVD, struktura, lastnosti

1 INTRODUCTION

Dynamic industry development introduces an escalation of requirements concerning new needs and working conditions, which facilitateand direct theprogress within material engineering, especially in the case of fabrication and examination of new materials.[1–3] Properties of many products and their elements depend not only on the possibility of transmitting mechanical loads through the whole active intersection or the material's physical and chemical properties, but also on the structure and properties of the surface layer. The use of surface layers, fulfilling thehigh requirements withsoft and cheap cores, is a great way of reducing expenses. A wide range of available layers and ways of theirmodification facilitate the design of thebest combination of core and layer properties possible. Modern surface-engineering techniques including the use of a corrosion- and abrasive-resistant hard material, despite the maintenance of accurate properties, should allow usto combine esthetic values and ecological production.[3]

With many available techniques of improving engineering materials, the physical vapordeposition (PVD),

chemical vapordeposition (CVD) and hybrid methods (which enable a full control of thechemical composition, structure and properties using characteristics of particular methods like CVD, PVD and conventional thermochemical treatments – thermal spraying + heat treatment, nitriding or cyaniding + pulsed-laser deposition (PLD), autocatalytic layer deposition + plasma-assisted processing) are essential.[4–20] Anotherimportant surface engineering technology, applied inlight-alloy processing, is the laser treatment including remelting and alloying.[3] These techniques allow us to make layers with special properties (high hardness and tribological resistance combined with constant substrate properties) and the thickness in a range from tenths of a millimeter to even a few millimeter scan be achieved. A layer obtained with the laser-alloying or remelting technique has a different structure and properties than those of the base or the alloying elements.[3] The morphology of a quasi-composite layer is homogeneous and exhibits a proper dispersion of the alloying elements into the whole depth except for a very thin diffusion-saturation layer.

The aim of this research was to obtain a hard coat for a soft core – such a material can resist different amounts of load (depending on many factors) because of the coating and thanks to the soft core, the internal forces are transferred and reduced inside. In some cases, the corrosion resistance is also observed, which is very desirable. An important part of the investigationdone on the material was the examination of the structures and mechanical properties of gradient/monolithic coatings deposited with the PVD and CVD methods onto magnesium and aluminum casting alloys after the heat treatment.[5,9,16,18]

2 EXPERIMENTAL PART

The materials used for the investigation includedcast magnesium and aluminium alloys, whosechemical compositions are presented in **Table 1**. The deposition of coatings Ti/Ti(C,N)/CrN, Ti/Ti(C,N)/(Ti,Al)N, Ti/(Ti,Si)N/(Ti,Si)N, Cr/CrN/CrN, Cr/CrN/TiN and Ti/DLC/DLC was made within a device based on the CAE PVD method in anatmosphere of Ar, N_2 and C_2H_2; moreover, the DLC coating wasdeposited using acetylene (C_2H_2) as the precursor and was produced with the PA CVD method. A gradient change in thechemical composition ofthe PVD coatings' cross-sections was achieved by changing the proportion of the reactive-gas dose or a variation in thearc-source current. The DLC coating was characterized byavariation in the silicon (Me) concentration, demonstrating that a gradient layer wasobtained. Silicon was supplied to the furnace chamber from the gas phase, Ti/a-C:H-Me/a-C:H. Cathodes containing pure metals (Cr, Ti) and alloys of TiAl and TiSi (50:50 % amount fractions) were used for the deposition of the coatings. The diameter of the used cathodes was 65 mm. The temperature was controlled with

Table 1: Chemical compositions oftheinvestigated alloys
Tabela 1: Kemijska sestava preiskovanih zlitin

Type of material	Mass concentration of the elements, in mass fractions (*w*/%)							
	Al	Zn	Mn	Si	Mg	Fe	Cu	Rest
Magnesium alloy – AZ91	9.09	0.77	0.21	0.04	89.8	0.011	–	0.079
Magnesium alloy – AZ61	5.92	0.49	0.15	0.04	93.3	0.007	–	0.093
Aluminium alloy – AlSi9Cu4	85.4	0.05	0.01	9.27	0.28	0.34	4.64	0.01
Aluminium alloy – AlSi9Cu	88.86	0.16	0.37	9.1	0.27	0.18	1.05	0.01

Table 2: Deposition parameters of the investigated coatings
Tabela 2: Parametri nanašanja preiskovanih nanosov

Coating parameters	Type of the achieved coating and the applied coating technique					
	PVD					CVD
	Ti/Ti(C,N)-gradient/CrN	Ti/Ti(C,N)-gradient/(Ti,Al)N	Cr/CrN-gradient/CrN	Cr/CrN-gradient/TiN	Ti/(Ti,Si)N-gradient/(Ti,Si)N	Ti/DLC-gradient/DLC
Base pressure (Pa)	5×10^{-3}	5×10^{-3}	5×10^{-3}	5×10^{-3}	5×10^{-3}	1×10^{-3}
Working pressure (Pa)	0.9/1.1-1.9/2.2	0.9/1.1-1.9/2.8	1.0/1.4-2.3/2.2	1.0/1.4-2.3/2.2	0.89/1.5-2.9/2.9	2
Argon flow rate (sccm)	80*	80*	80*	80*	80*	80*
	10**	10**	80**	80**	20**	–
	10***	10***	20***	20***	20***	–
Nitrogen flow rate (sccm)	225→0**	0→225**	0→250**	0→250**	0→300**	–
	250***	350***	250***	250***		
Acetylene flow rate (sccm)	0→170**	140→0**	–	–		230
Substrate bias voltage (V)	70*	70*	60*	60*	70*	500
	70**	70**	60**	60**	100**	
	60***	70***	60***	100***	100***	
Target current (A)	60	60	60	60	60	-
Process temperature (°C)	<150	<150	<150	<150	<150	<180

*during the metallic-layer deposition, **during the gradient-layer deposition, *** during the ceramic-layer deposition

thermocouples. To improve the adhesion of the coatings, a transition Cr, Ti interlayer was deposited. The working pressure during the deposition process was 2–4 Pa, depending on the coating type. The distance between the cathodes and the deposited substrates was 120 mm. Just before the coating-deposition process, the specimens were prepared with the standard procedures of grinding, polishing and chemical cleaning using multi-stage washing in an ultrasonic cleaner and a cascade washer, then dried in hot air. The next step was ion etching in the chamber to clean the surfaces atthe atomic scale and to activate them. The parameters used were asubstrate-polarization voltage of 800/200 V and a period of 20 min. The conditions of the coating deposition are presented in **Table 2**.

The investigations of the microstructures, micro-area qualitative and quantitative chemical compositionswere performed using a scanning electron microscope (SEM) ZEISS Supra 35. The cross-sectional atomic composition of the samples (coating and substrate) was obtained by using the glow discharge optical spectrometer GDOS-750 QDP from Leco Instruments.

The microhardness tests of the coatings were made with a SHIMADZU DUH 202 ultra-microhardness tester. The measurements were made with a 10 mN load, to eliminate the substrate influence on the coating hardness. Wear-resistance investigations were performed using the ball-on-disk method. A tungsten carbide ball with a diameter of 3 mm was used as the counter part. The tests were performed at room temperature overa defined time using the following test conditions: a load of F_n = 5N, a rotation of the disk of 200 min^{-1} 20.94 r/s, a wear radius of 2.5 mm and a sliding speed of 0.05 m/s.

3 RESULTS AND DISCUSSION

In order to determine the structures and relationships between the type of substrate and the types of hybrid layers, the metallographic investigation was done under the technological conditions (the soft substrate – the gradient intermediate layer able to easily change the concentration of one or a few components between the base and the surface – and the external layer) of the cathodic-arc deposition, Arc-PVD, and plasma-assisted chemical vapor deposition, PA-CVD processes.

The layers obtained with the CAE-PVD technique are heterogeneous, as many drop-shaped micro-sized molecules exist in their structures. This fact leads to changes in the mechanical, physical and chemical properties of the examined layers (**Figures 1** to **6**). The biggest surface heterogeneity, in comparison to the other examined layer surfaces, is visible within the Ti/Ti(C,N)/(Ti,Al)N and Ti/Ti(C,N)/CrN systems, in which a lot of precipitation of the evaporated, metal, clotty drops were identified (**Figures 1** and **2**). The occurrence of this morphological defect is related with the Arc-PVD process characteristics. Depending on the process parameters, including the kinetic energy transferred to the drops that are crashed due to the metallic base, and the type of the metal-vapor source used, particles varyingin shape and size are observed. It was confirmed that the clotty drops are spheroidal or irregular or they form agglomerates that often include a few equal drops (**Figures 1** to **6**). Moreover, characteristic hollows that form because of the clotty drops falling out, were observed after the PVD process wasfinished. On the basis of the metallographic observations it was confirmed that the hollows do not reach the surface. On the DLC layer obtained within the PACVD process fine drops, mostly spheroidal, were identified as well (**Figure 5**). The surface morphology of the DLC layer is different from that obtained with classical high-temperature CVD processes – no micro-gaps or wavy and globular-like surfaces were observed. The smallest amount of morphologic surface defects was obtained with the Cr/CrN/TiN layer (**Figure 4**).

A fractographic examination of magnesium- and aluminum-alloy samples with the applied layers, done with a scanning electron microscope, showed a sharp transi-

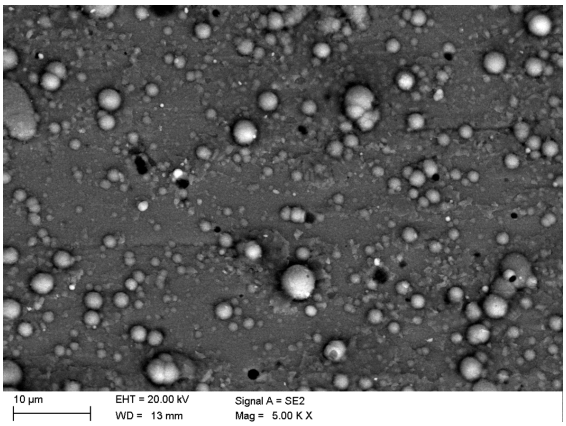

Figure 1: Surface topography of Ti/Ti(C,N)/CrN layer obtained on $AlSi_9Cu_4$ cast aluminum alloy

Slika 1: Topografija površine nanosa Ti/Ti(C,N)/CrN na $AlSi_9Cu_4$ aluminijevi livni zlitini

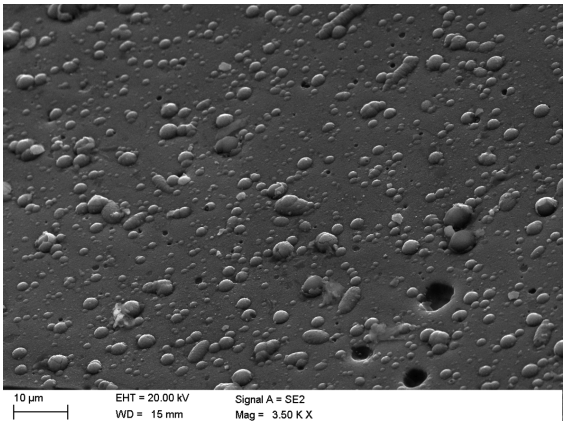

Figure 2: Surface topography of Ti/Ti(C,N)/(Ti,Al)N layer obtained on MCMgAl6Zn1 cast magnesium alloy

Slika 2: Topografija površine nanosa Ti/Ti(C,N)/(Ti,Al)N na $MCMgAl_6Zn_1$ livni magnezijevi zlitini

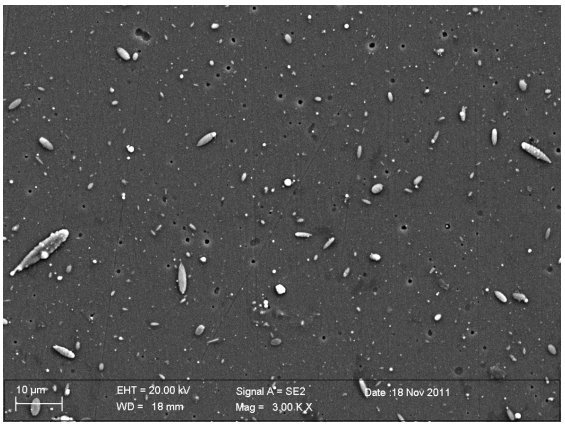

Figure 3: Surface topography of Cr/CrN/CrN layer obtained on $MCMgAl_9Zn_1$ cast magnesium alloy

Slika 3: Topografija površine nanosa Cr/CrN/CrN na $MCMgAl_9Zn_1$ livni magnezijevi zlitini

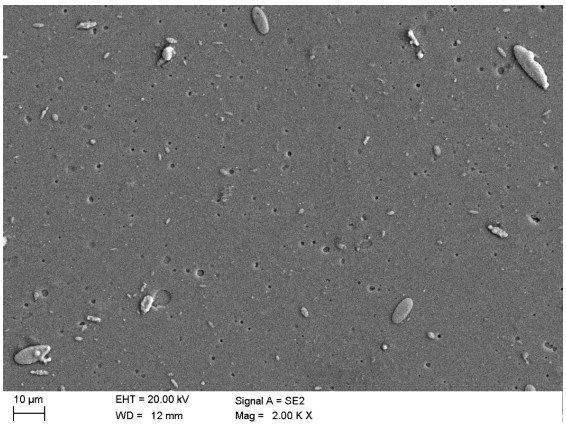

Figure 4: Surface topography of Cr/CrN/TiN layer obtained on $MCMgAl_9Zn_1$ cast magnesium alloy

Slika 4: Topografija površine nanosa Cr/CrN/TiN na $MCMgAl_9Zn_1$ livni magnezijevi zlitini

tion zone between the base and the layer. The layers are compact in structure with no visible delamination or defects. They are placed uniformly and they adhere to the

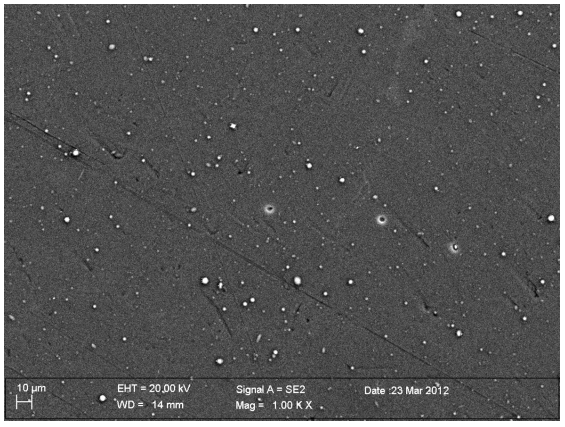

Figure 5: Surface topography of Ti/DLC/DLC layer obtained on $AlSi_9Cu_1$ cast aluminum alloy

Slika 5: Topografija površine nanosa Ti/DLC/DLC na $AlSi_9Cu_1$ livni aluminijevi zlitini

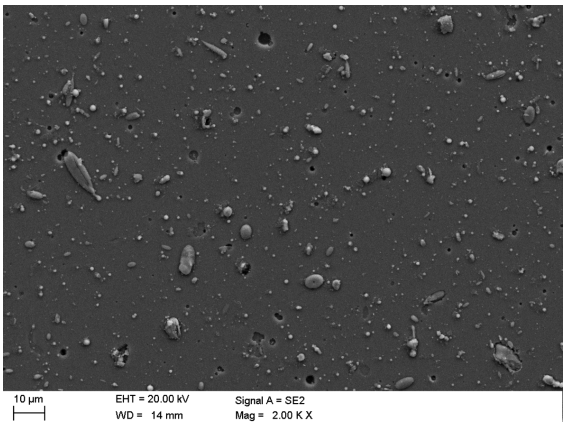

Figure 6: Surface topography of Ti/(Ti,Si)N/(Ti,Si)N layer obtained on $AlSi_9Cu_1$ cast aluminum alloy

Slika 6: Topografija površine nanosa Ti/(Ti,Si)N/(Ti,Si)N na $AlSi_9Cu_1$ livni aluminijevi zlitini

base hermetically (**Figures 7** to **10**). Observations of the fractures confirm that layers like Ti/Ti(C,N)/(Ti,Al)N and Ti/Ti(C,N)/CrN are laminar with a visible transition zone between the gradient and the anti-wear layers obtained with different metal-vapor sources (**Figure 7**). On the cross-section of the Cr/CrN/CrN, Ti/(Ti,Si)N/(Ti,Si)N layers, in which identical sets of chemical elements of gradient and anti-wear layers were used, no visible differences were observed (**Figure 8**). In addition, multi-layer carbon coats like Ti/DLC/DLC obtained with the CVD method, in which the gradient in the middle coating allows a variable silicon concentration, do not exhibit any visible transition zone between individual layers. Moreover, in the range of the thin adhesive layer (whose task is to improve the adhesion of the base and DLC layers) is was possible to identify a bright, continuous layer of titanium, which was also confirmed with theEDS spectrometry analysis (**Figure 9**). It was confirmed that the titanium nitride layer obtained with the Cr/CrN/TiN system has a close to columned rise character of crystallite that is characteristic for titanium

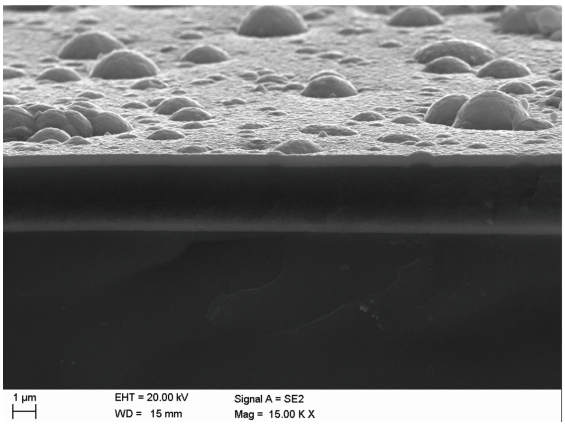

Figure 7: Fracture of Ti/Ti(C,N)/CrN layer obtained on $AlSi_9Cu_4$ cast aluminum alloy

Slika 7: Prelom nanosa Ti/Ti(C,N)/CrN na $AlSi_9Cu_4$ livni aluminijevi zlitini

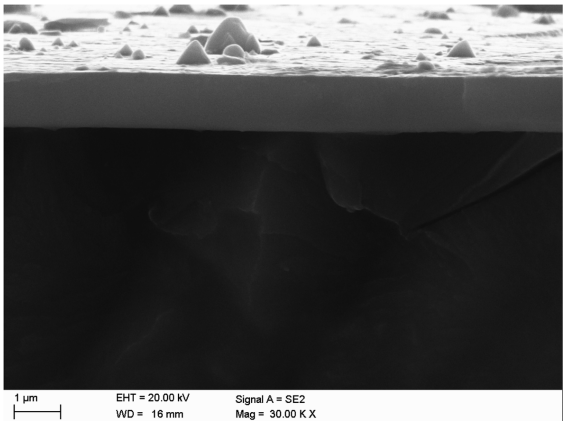

Figure 8: Fracture of Ti/(Ti,Si)N/(Ti,Si)Nlayer obtained on $MCMgAl_6Zn_1$ cast magnesium alloy

Slika 8: Prelom nanosa Ti/(Ti,Si)N/(Ti,Si)N na $MCMgAl_6Zn_1$ livni magnezijevi zlitini

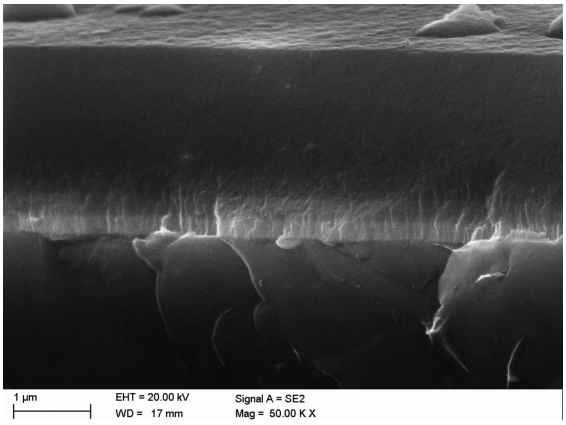

Figure 9: Fracture of Ti/DLC/DLC layer obtained on $AlSi_9Cu_1$ cast aluminum alloy

Slika 9: Prelom nanosa Ti/DLC/DLC na $AlSi_9Cu_1$ livni aluminijevi zlitini

nitride-based layers achieved with the Arc-PVD (**Figure 10**).

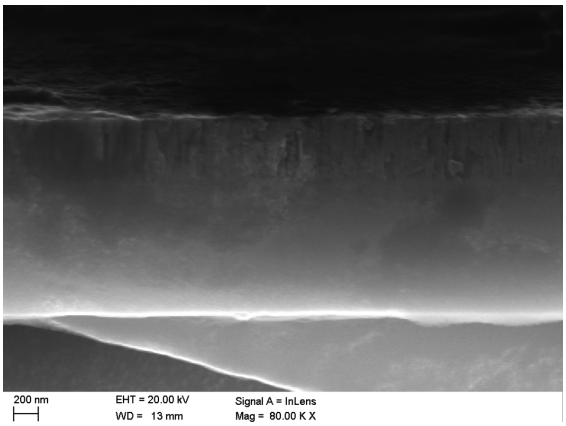

Figure 10: Fracture of Cr/CrN/TiN layer obtained on $MCMgAl_9Zn_1$ cast magnesium alloy

Slika 10: Prelom nanosa Cr/CrN/TiN na $MCMgAl_9Zn_1$ livni magnezijevi zlitini

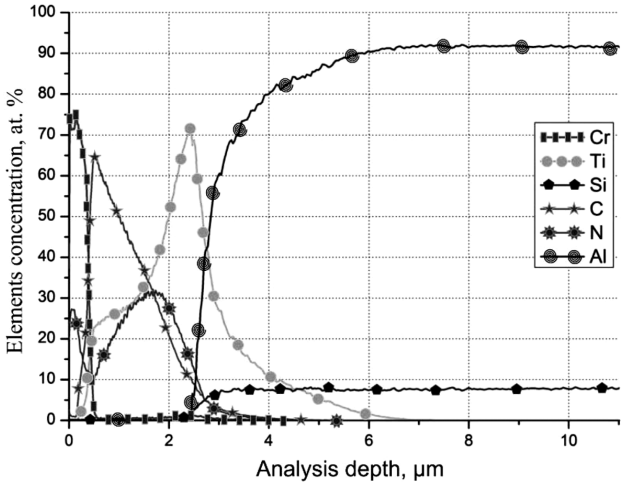

Figure 11: Variation in the concentration of Ti/Ti(C,N)/CrN layer chemical elementsobtained on $AlSi_9Cu_1$ magnesium alloy

Slika 11: Spreminjanje koncentracije elementov v Ti/Ti(C,N)/CrN nanosu na AlSi9Cu1 magnezijevi zlitini

The chemical-composition investigation carried out with GDOES and SEM confirmed the existence of the chemical elements of the obtained layers in a depth of 1.4–3.4 µm (**Figures 11** and **12**). The maximum thickness of the layers was measured to beas follows: Ti/Ti(C,N)/CrN ~3.3µm; Ti/Ti(C,N)/Ti(Al,N) ~3.4µm; Cr/CrN/CrN ~1.8µm; Cr/CrN/TiN ~1.7µm; Ti/Ti(Si,N)/Ti(Si,N) ~1.6µm; Ti/DLC/DLC ~2.5µm. The variation in the bonding-zone character – an increase in the chemical-element concentration of the base and a decrease in the chemical-element concentration of the layer – leads to the conclusion about the existence of a transitory diffusion zone between the base material and the layer, which improves their adhesion. Moreover, with the GDOES examination, the decrease zone of the linear concentration of the chemical elements of the layer was

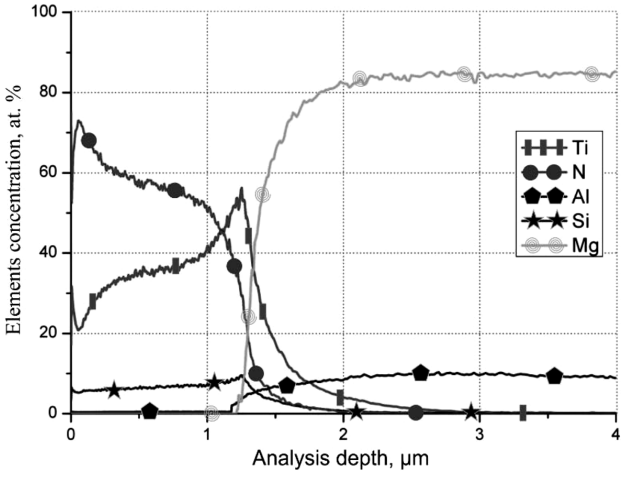

Figure 12: Variation in the concentration of Ti/(Ti,Si)N/(Ti,Si)N layer chemical elements obtained on $MCMgAl_6Zn_1$magnesium alloy

Slika 12: Spreminjanje koncentracije elementov v Ti/(Ti,Si)N/(Ti,Si)N nanosu na MCMgAl6Zn1 magnezijevi zlitini

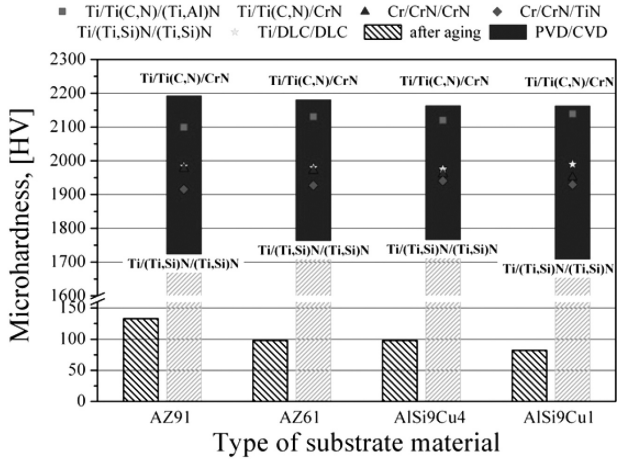

Figure13: Microhardness examination results forcast magnesium Mg-Al-Zn and aluminum Al-Si-Cu alloys after ageing, PVD and CVD processing

Slika 13: Rezultati meritev mikrotrdote na liti magnezijevi Mg-Al-Zn in aluminijevi Al-Si-Cu zlitini, po staranju ter PVD in CVD obdelavi

confirmed – it proves that the layers are gradient (**Figures 11** and **12**).

The layers obtained with Arc-PVD and PA CVD on the base of Mg and Al alloys significantly increased the microhardness compared to the base material (**Figure 13**). This phenomenon is caused by the chemical- and phase-concentration change, various conditions, the type of the method (PVD or CVD) and the combination of the layers.

The type of base material – Mg or Al alloys – has the least influence on the microhardness (**Figure 13**). A significant rise in the microhardness after the precipitation hardening, exceeding 100 % compared to the base material, took place due totheCr/CrN/CrN, Cr/CrN/TiN and

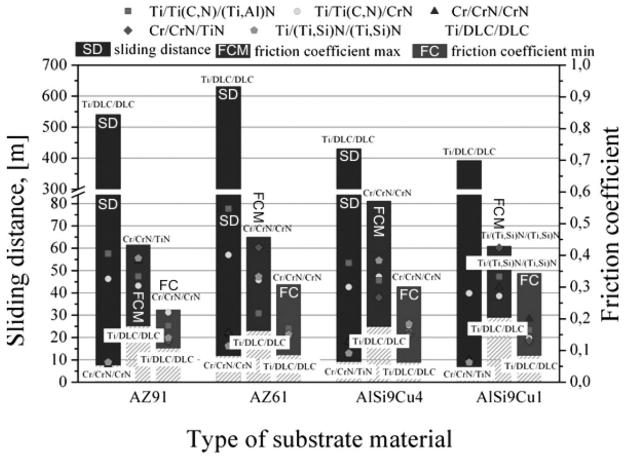

Figure14: Dependence of sliding distanceto the coating damage on the minimum and maximum friction coefficients intheball-on-disc test used on PVD and CVD layers obtained on aluminum and magnesium cast alloys

Slika 14: Odvisnost razdalje drsenja do poškodbe nanosa na minimalni in maksimalni koeficient trenja pri preizkusu kroglica na plošči, uporabljenem na PVD in CVD nanosih, na livnih aluminijevih in magnezijevih zlitinah

Ti/(Ti,Si)N/(Ti,Si)N layers obtained with the cathodic PVD process and N_2 as the protective gas. The layers' hardness does not exceed 2000 HV according to the microhardness test results, while the Ti/Ti(C,N)/CrN and Ti/Ti(C,N)/(Ti,Al)N layers obtained within the mixture of CH_4 and N_2 as the protective gas are even harder than 2000 HV.

In the case of the 5N load used in the examination, the average friction factor for theDLC coatings (done on Al and Mg) achieved with a 0.05 m/s slide velocity is in a range of 0.06–0.16 (**Figure 15**). Thisis a decrease in the whole order of magnitude in comparison to the other layers. This state is characteristic for the DLC layers that consist of graphite, which works like a lubricant during the abrasion process. Moreover, a high traverse speed, which causes heat accumulation, is responsible for an easier self-lubrication of the layer, resulting in a reduction in the friction coefficient (**Figures 14** and **15**). The sliding distance for the DLC coatings obtained on Mg is even 70 times higher than those measured for Cr/CrN/CrN or diamond-like layers (**Figure 14**). The sliding-distance values for all the examined layers were in a range of 6–630 m (**Figure 14**). When examining all the ball-on-disk test results, it was confirmed that the value

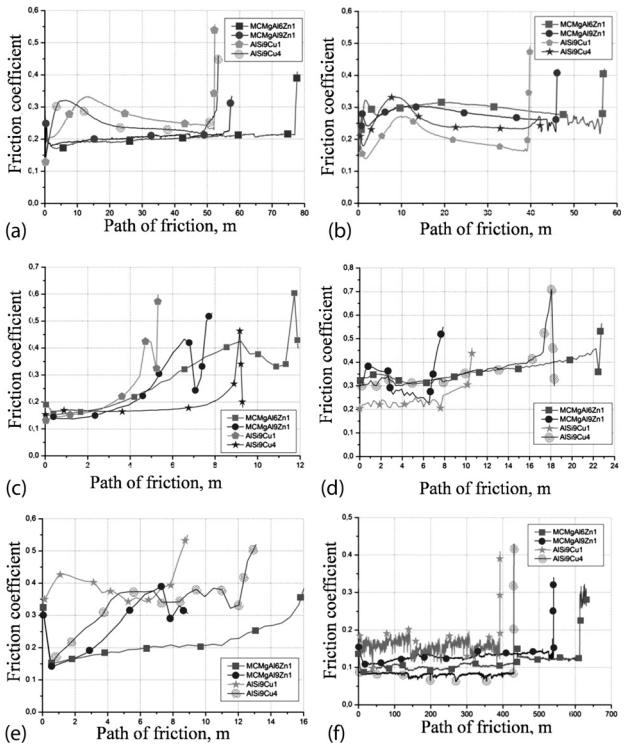

Figure 15: Dependence of layer friction coefficient on the counter-samplesliding distance achieved withtheball-on-disc method on: a) Ti/(Ti(C,N)/(Ti,Al)N, b) Ti/(Ti(C,N)/CrN, c) Cr/CrN/TiN, d) Cr/CrN/CrN, e) Ti/(Ti,Si)N/(Ti,Si)N, f) Ti/DLC/DLC, obtained on aluminum and magnesium cast alloys

Slika 15: Odvisnost koeficienta trenja od razdalje drsenja, dobljene pri metodi kroglica na plošči pri: a) Ti/(Ti(C,N)/(Ti,Al)N, b) Ti/(Ti(C,N)/CrN, c) Cr/CrN/TiN, d) Cr/CrN/CrN, e) Ti/(Ti,Si)N/(Ti,Si)N, f) Ti/DLC/DLC na livnih aluminijevih in magnezijevih zlitinah

of the sliding distance for magnesium coatings is larger than the sliding distance obtained with the aluminum-layer dual system; moreover, the results for the DLC coatings are even 30 % better (**Figure 14**).

For the tribological-resistance examination of the obtained layers, the charts demonstrating the rotation quantity or displacement of the countersample before the coating damage, depending on the friction coefficient and/or displacement of the countersample along the vertical axis were created. For all the registered friction coefficients dependingon the rotation quantity or the sliding distance, similar characteristic curves, which can be divided into two parts, were determined (**Figure 15**). In the first part, a significant increase in the friction coefficient with the sliding-distance increase was determined. It was accepted that it is the transient friction state. The second part of the chart is similar to the stationary state. Large changes in the friction coefficient measured during the examination were caused by a spallation of the sample and counter-sample surfaces.

4 CONCLUSION

Gradient and monolithic coatings including Ti/Ti(C,N)/CrN, Ti/Ti(C,N)/(Ti,Al)N, Ti/(Ti,Si)N/(Ti,Si)N, Cr/CrN/CrN, Cr/CrN/TiN and Ti/DLC/DLC were successfully deposited onto magnesium- and aluminum-alloy substrates using the cathodic-arc-evaporation method (Arc-PVD) and plasma-assisted process (PA CVD). The layers obtained with Arc-PVD and PA CVD on the base of Mg and Al alloys significantly increased the microhardness compared to the base material. The type of base material had the least influence on the microhardness. The fracture morphology was characterized by a lack of columnar structures in the obtained coatings. The metallographic examinations proved that the coatings were deposited uniformly over the whole sample onto the investigated substrate materials and that the measured thickness was characteristic for this coating type. It was also found that individual layers adhered tightly to each other and to the light metal substrate. The average friction factor of the DLC coatings (on Al and Mg) achieved at a 0.05 m/s slide velocity was in a range of 0.06–0.16, which was a decrease in the whole order of magnitude in comparison to the other layers. Examining all the ball-on-disk test results, it was confirmed that the value of the sliding distance for the magnesium coatings was higher than the sliding distance obtained with the aluminum-layer dual system; moreover, the results for the DLC coatings were even 30 % better. The investigation results obtained for the PVD method make it possible to obtain interesting solutions, which are very promising for the use in the automobile and aviation industries, for the production of the elements whose high functional properties like hardness and wear resistance are crucial for long-term service.

Acknowledgements

This publication was co-financed within the framework of the statutory financial grant providedby the Faculty of Mechanical Engineering of the Silesian University of Technology in 2015.

5 REFERENCES

[1] M. Avedesian, H. Baker (Eds.), ASM Specialty Handbook: Aluminium and Aluminium Alloys, ASM International, The Materials Information Society, USA 1999

[2] E. F. Horst, B. L. Mordike, Magnesium Technology, Metallurgy, Design Data, Application, Springer-Verlag Berlin, Heidelberg 2006

[3] T. Tański, A. D. Dobrzańska-Danikiewicz, K. Labisz, W. Matysiak, Long-term development perspectives of selected groups of engineering materials used in the automotive industry, Archives of Metallurgy and Materials, 59 (**2014**) 4, 1729–1740, doi:10.2478/amm-2014-0290

[4] M. Mattox, Handbook of Physical Vapor Deposition (PVD) Processing, Elsevier Science, <kraj izida manjka>2010

[5] L. Zeng, S. Yang, W. Zhang, Y. Guo, Ch. Yan, Preparation and characterization of a double-layer coating on magnesium alloy AZ91D, Electrochimica Acta, 55 (**2010**), 3376-3383, doi:10.1016/j.electacta.2010.01.041

[6] K. Mao, Y. Sun, A. Bloyce, T. Bell, Surface coating effects on contact stress and wear: an approach of surface engineering design and modelling, Surface Engineering, 26 (**2010**) 1–2, 142–148, doi:10.1179/174329409X446313

[7] M. Pellizzari, High temperature wear and friction behaviour of nitrided, PVD-duplex and CVD coated tool steel against 6082 Al alloy, Wear, 271 (**2011**), 2089–2099, doi:10.1016/j.wear.2011.01.067

[8] J. Eriksson, M. Olsson, Tribological testing of commercial CrN, (Ti,Al)N and CrC/C PVD coatings – Evaluation of galling and wear characteristics against different high strength steels, Surface and Coatings Technology, 205 (**2011**), 4045–4051, doi:10.1016/j.surfcoat.2011.02.053

[9] I. Endler, M. Höhn, M. Herrmann, H. Holzschuh, R. Pitonak, S. Ruppi, H. van den Berg, H. Westphal, L. Wilde, Aluminum-rich TiAlCN coatings by low pressure CVD, Surface and Coatings Technology, 205 (**2010**), 1307–1312, doi:10.1016/j.surfcoat.2010.09.002

[10] L. A. Dobrzański, L. W. Żukowska, J. Mikuła, K. Gołombek, D. Pakuła, M. Pancielejko, Structure and mechanical properties of gradient PVD coatings, Journal of Materials Processing Technology, 201 (**2008**) 1–3, 310–314, doi:10.1016/j.jmatprotec.2007.11.283

[11] K. Lukaszkowicz, J. Sondor, K. Balin, J. Kubacki, Characteristics of CrAlSiN + DLC coating deposited by lateral rotating cathode arc PVD and PACVD process, Applied Surface Science, 312 (**2014**) 1, 126–133, doi:10.1016/j.apsusc.2014.03.024

[12] M. W. Richert, A. Mazurkiewicz, J. A. Smolik, The deposition of WC-Co coatings by EBPVD technique, Archives of Metallurgy and Materials, 57 (**2012**) 2, 511–516, doi:10.2478/v10172-012-0053-0

[13] W. Gebarowski, S. Pietrzyk, Influence of the cathodic pulse on the formation and morphology of oxide coatings on aluminium produced by plasma electrolytic oxidation, Archives of Metallurgy and Materials, 58 (**2013**) 1, 241–245, doi:10.2478/v10172-012-0180-7

[14] G. R. dos Santos, D. D. da Costa, F. L. Amorim, R. D. Torres, Characterization of DLC thin film and evaluation of machining forces using coated inserts in turning of Al–Si alloys, Surface and Coatings Technology, 202 (**2007**), 1029–1033, doi:10.1016/j.surfcoat.2007.07.100

[15] Q. Wang, F. Zhou, Z. Zhou, Y. Yang, C. Yan, C. Wang, W. Zhang, L. Kwok-Yan Li, I. Bello, S. Tong Lee, Influence of Ti content on the structure and tribological properties of Ti-DLC coatings in water lubrication, Diamond & Related Materials, 25 (**2012**), 163–175, doi:10.1016/j.diamond.2012.03.005

[16] Y. S. Zou, Y. F. Wu, H. Yang, K. Cang, G. H. Song, Z. X. Li, K. Zhou, The microstructure, mechanical and friction properties of protective diamond like carbon films on magnesium alloy, Applied Surface Science, 258 (**2011**), 1624–1629, doi:10.1016/j.apsusc.2011.10.031

[17] J. Smolik, J. Walkowicz, T. Szubrycht, Ellipsometric characteristics of diamond-like a-C:H films obtained by the r.f. PACVD method, Surface and Coatings Technology, 174–175 (**2003**), 345–350, doi:10.1016/S0257-8972(03)00373-6

[18] T. Tański, Characteristics of hard coatings on AZ61 magnesium alloys, Journal of Mechanical Engineering, 59 (**2013**) 3, 165-174, doi:10.5545/sv-jme.2012.522

[19] T. Tański, K. Labisz, K. Lukaszkowicz, A. Śliwa, K. Gołombek, Characterisation and properties of hybrid coatings deposited onto magnesium alloys, Surface Engineering, 30 (**2014**) 12, 927–932, doi:10.1179/1743294413Y.0000000194

[20] M. Staszuk, L. A. Dobrzański, T. Tański, W. Kwaśny, M. Musztyfaga, The effect of PVD and CVD coating structures on the durability of sintered cutting edges, Archives of Metallurgy and Materials, 59 (**2014**) 1, 269–274, doi:10.2478/amm-2014-0044

UDK 620.1:67.017:621.318
Original scientific article/Izvirni znanstveni članek

ISSN 1580-2949
MTAEC9, 50(5)707(2016)

ANALYSIS OF THE STRUCTURAL-DEFECT INFLUENCE ON THE MAGNETIZATION PROCESS IN AND ABOVE THE RAYLEIGH REGION

ANALIZA VPLIVA STRUKTURNIH DEFEKTOV NA PROCES MAGNETIZACIJE V IN NAD RAYLEIGH PODROČJEM

Konrad Gruszka

Czestochowa University of Technology, Faculty of Production Engineering and Materials Technology, Institute of Physics, Armii Krajowej Av. 19, 42-200 Czestochowa, Poland
kgruszka@wip.pcz.pl

Prejem rokopisa – received: 2015-06-30; sprejem za objavo – accepted for publication: 2015-09-16

doi:10.17222/mit.2015.154

The paper presents studies of the structural-defect influence on the magnetization process in low magnetic fields ($H < 0.4\ H_c$) and above the Rayleigh range. The investigated $Fe_{62}Co_{10}Y_8B_{20}$ alloy samples were obtained with the injection casting method resulting in the amorphous-structure state, which was confirmed with XRD. The studies were conducted by analyzing the disaccommodation of the magnetic-susceptibility process and using Kronmüller's theory in the approach to the ferromagnetic saturation area. On the basis of the obtained results, it was found that the main factor responsible for the processes of magnetization in low magnetic fields are point defects, whereas in the case of high magnetic fields, the magnetization process depends mainly on second-type pseudo-dislocation dipoles.

Keywords: metallic glasses, defects, disaccommodation, Kronmüller's theory

Članek predstavlja študij vpliva strukturnih defektov na proces magnetizacije v šibkem magnetnem polju ($H < 0{,}4\ H_c$) in nad Rayleigh področjem. Vzorci preiskovane zlitine $Fe_{62}Co_{10}Y_8B_{20}$ so bili izdelani z metodo injekcijskega brizganja, kar je povzročilo amorfno strukturo, ki je bila potrjena z rentgensko analizo (XRD). Študije so bile izvedene z analizo procesa neustreznosti magnetne občutljivosti in z uporabo Kronmülerjeve teorije pri približevanju feromagnetno nasičenemu področju. Na osnovi dobljenih rezultatov je bilo ugotovljeno, da so pri procesu magnetizacije glavni faktor točkaste napake, medtem ko je v primeru magnetizacije v močnem magnetnem polju proces odvisen predvsem od druge vrste psevdodislociranih dipolov.

Ključne besede: kovinska stekla, napake, neustreznost, Kronmüllerjeva teorija

1 INTRODUCTION

Iron-based amorphous materials are extensively studied because of their excellent soft-magnetic properties.[1–3] For this reason, they have been widely used in the electrical industry, primarily as high-efficiency cores for power transformers and chokes and also as coatings due to their high corrosion resistance.[4,5]

In terms of topological structure, amorphous materials have properties similar to those of liquids. The atoms forming the material are scattered in a chaotic manner so that the observation of the long-range order is not possible. When the cooling rate of a liquefied alloy is sufficiently large, the kinetic energy of the atoms is taken so fast that they are trapped at higher energy positions. This results in the density and local chemical-composition fluctuations, and is the major cause of the areas with a deficiency of atoms. This type of local voids are called point defects (by analogy with the vacancies occurring in a crystal structure). In the cases where several point defects are located in a small local environment, a concentration to two-dimensional defects occurs and it is referred to as pseudo-dislocation dipoles.

Point defects and their conglomerates have a significant impact on the process of magnetization in high magnetic fields.[6,7] The presence of structural defects, which are the centers of internal stresses, causes a deformation of local magnetization vectors. The presence of structural defects in amorphous materials affects the magnetization process in the area called the approach to ferromagnetic saturation.[8] In close proximity to a point defect, the magnetization vectors are arranged in a "streamline" way[9,10] which is a potential cause of domain-wall anchors. A more complicated situation occurs in the presence of a pseudo-dislocation dipole, where the arrangement of individual vectors is not collinear and the centers of the deformation of these vectors are hooked at the dipole ends.[11–13]

Ferromagnetic materials, especially the ones based on the Fe-Co-B composition are well known for their great soft-magnetic properties, in particular a low coercive field and magnetostriction while they are not expensive and have a high sensitivity to alloying additives. In the compounds of this type, iron is typically the major part (more than a 50 % amount fraction) while Co, which has similar properties, allows an increase in the magnetization. Boron, due to a significant difference in the atomic radius, improves the glass-forming ability (GFA). In order to further increase the GFA, a small

amount of yttrium atoms are introduced. According to the literature, a concentration of up to a 4 % amount fraction has a positive effect on the GFA but exceeding this value brakes down good soft-magnetic properties. Using the studies on susceptibility-disaccommodation phenomena and approach to the ferromagnetic saturation area, it is possible to indirectly describe the structural defects existing in a material. This paper focuses on defects – the relations within a magnetization process and shows that despite an yttrium addition of up to 8 %, one can obtain reasonable results in terms of soft-magnetic parameters.

2 STUDIED MATERIAL AND METHODOLOGY

The investigated material comprises chemical elements of high purity (Fe – a 99.95 % amount fraction, the remaining component elements – 99.99 % amount fractions). A two-step preparation procedure was used. Initially, the ingredients were melted using a plasma arc (a working current of ~300 A) under a reduced pressure in a protective atmosphere of argon. The samples were melted several times to ensure a good homogeneity of the constituent distribution. Then the resulting ingot was melted, using an induction furnace, in a quartz tube and injected into a copper water-cooled mold, which was also under an argon atmosphere (at a pressure of 700 hPa). In the radial cooling process, good-quality amorphous solid samples with dimensions of 15 mm × 10 mm × 0.5 mm were obtained. The structure of the obtained samples was examined using an X-ray diffractometer (Bruker D8 Advance, Cu-K_α). The magnetic properties were determined with an analysis of the static hysteresis loop and the initial magnetization curve, which were obtained from the measurements of the magnetization as a function of the magnetic-field strength using a vibrating sample magnetometer (model Lakeshore 7301). Measurements of the initial permeability of the samples were taken over a wide temperature range of 300–650 K. The samples were suspended in a permalloy frame and placed in a quartz vacuum tube with a thermocouple, and the whole system was placed in an accumulative furnace. The disaccommodation-aftereffect intensity defined as $\Delta\left(\frac{1}{x}\right)=\frac{1}{\chi(t_1)}-\frac{1}{\chi(t_0)}$ was measured in time $(t_1 - t_0) = 118$ s

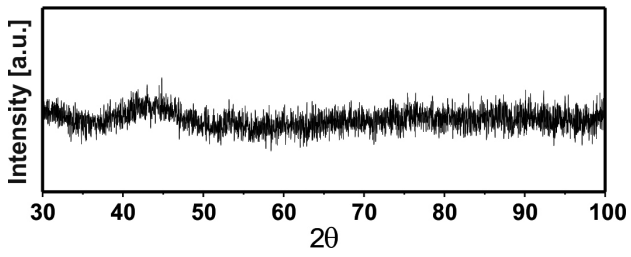

Figure 1: X-ray diffraction pattern of $Fe_{62}Co_{10}Y_8B_{20}$ in the as-quenched state
Slika 1: Rentgenska difrakcija $Fe_{62}Co_{10}Y_8B_{20}$ v kaljenem stanju

with the transformer method. The frequency of the ac field was set to 50 Hz. The samples were demagnetized by applying a sinusoidal decreasing magnetic field of 120 kHz.

3 RESULTS

Figure 1 shows the XRD of a sample after the solidification, measured for the 2θ angle in a range from 30° to 100°.

The diffraction pattern shows only the broad fuzzy maximum, located in a 2θ angle range from approximately 35° to 50°. This means that in a sample in the as-quenched state, there is no long-range order and the interactions between the atoms have a close- or medium-range character. Such a shape of a diffraction pattern is typical for the materials with an amorphous structure. Then measurements of the static magnetic hysteresis loop were carried out and the result is shown in **Figure 2**.

The observed shape of the curve is characteristic for a magnetic material with soft magnetic properties. Based on the analysis of the static magnetic hysteresis loop, the basic parameters for the magnetic sample were determined: magnetization saturation M_s = 1.27 (T), coercive field H_c = 289 (A/m). Next, an analysis of the primary magnetization curve in the approach to the ferromagnetic saturation area was carried out. **Figures 3** and **4** show magnetization curves as a function of $(\mu_0 H)^{-2}$ and $(\mu_0 H)^{1/2}$.

With respect to Kronmüller's theory, as a result of the analysis of the primary magnetization curve, it was found that in a $Fe_{62}Co_{10}Y_8B_{20}$ alloy sample the magnetization process in the area called "Ewing's knee" relates to the change in magnetization vector directions caused by the presence of free-volume conglomerates. The linear-defect size (D_{dip}) must therefore be larger than the exchange distance. Assuming that $D_{dip} > l_H$, the $a_2/(\mu_0 H)^2$ law of approach to the ferromagnetic saturation area is

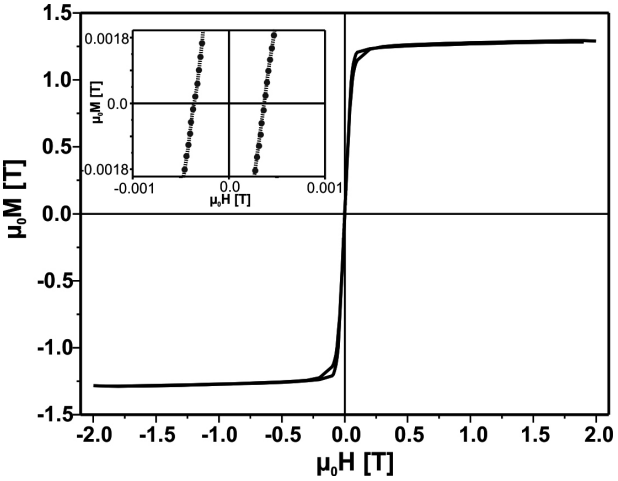

Figure 2: Static magnetic hysteresis loop for the $Fe_{62}Co_{10}Y_8B_{20}$ alloy
Slika 2: Statična magnetna histerezna zanka zlitine $Fe_{62}Co_{10}Y_8B_{20}$

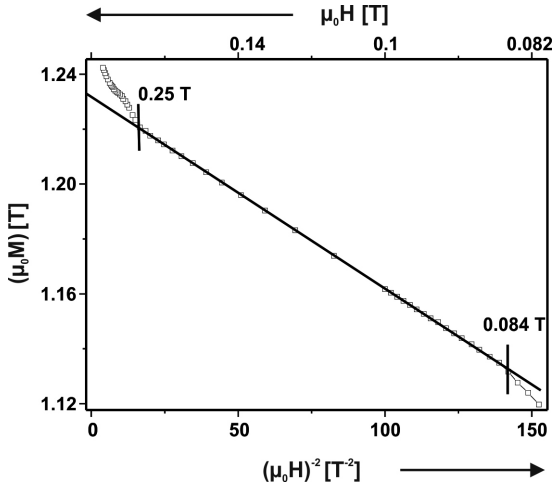

Figure 3: Magnetization as a function of $(\mu_0 H)^{-2}$ for the $Fe_{62}Co_{10}Y_8B_{20}$ alloy
Slika 3: Magnetizacija kot funkcija $(\mu_0 H)^{-2}$ zlitine $Fe_{62}Co_{10}Y_8B_{20}$

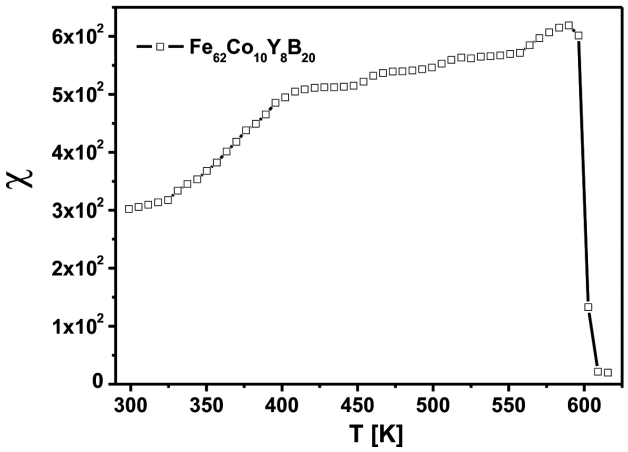

Figure 5: Dependence of the low-field magnetic susceptibility as a function of temperature for the $Fe_{62}Co_{10}Y_8B_{20}$ sample
Slika 5: Odvisnost magnetne občutljivosti v šibkem polju od temperature vzorca $Fe_{62}Co_{10}Y_8B_{20}$

fulfilled. Thus, these defects are the main source of stress in the magnetic-field strength from 0.084 (T) to 0.25 (T). Above the $(\mu_0 H)^{-2}$ dependence, Holstein-Primakoff's process intensifies, indicating that the further process of magnetization is associated with the damping of thermally excited spin waves with an external magnetic field (the b coefficient). The parameters obtained from the analysis of the primary magnetization curve are summarized in **Table 1**.

Table 1: Parameters obtained with the analysis of the primary magnetization curve
Tabela 1: Parametri, dobljeni z analizo primarne krivulje magnetizacije

a_2 (10^{-2} T^2)	b (10^{-2} T$^{1/2}$)	D_{sp} (10^{-2} meV nm^2)	A_{ex} (10^{-12} J m^{-1})	l_h (nm)
0.056	6.59	40.70	1.64	3.59

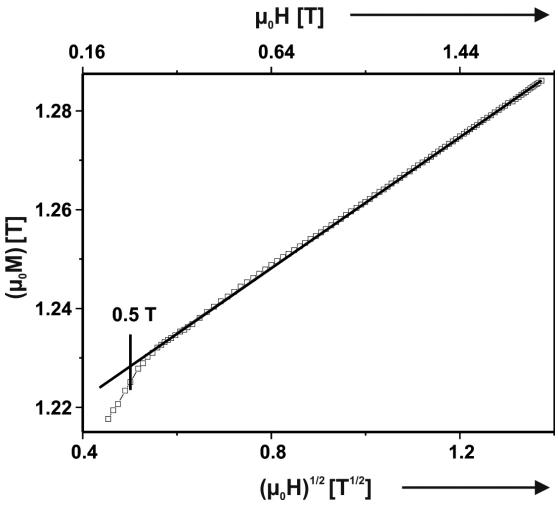

Figure 4: Magnetization as a function of $(\mu_0 H)^{1/2}$ for the $Fe_{62}Co_{10}Y_8B_{20}$ alloy. Holstein-Primakoff process
Slika 4: Magnetizacija kot funkcija $(\mu_0 H)^{1/2}$ zlitine $Fe_{62}Co_{10}Y_8B_{20}$. Proces Holstein-Primakoff

The absence of the $a_{1/2}$ and a_1 factors indicate that the point defects and linear defects of a smaller size had no effect on the magnetization process in magnetic fields greater than 0.4 H_c (above the Rayleigh region). This does not mean, however, that those defects are not present in the sample's structure but only that they are insignificant for the magnetization process. To investigate their potential impact on the magnetization at low fields, the susceptibility disaccommodation studies were conducted. According to Kronmüller's theory, it is possible to calculate the exchange distance of pseudo-dislocation dipoles (the l_h parameter) and the exchange-constant (A_{ex}) parameter. The latter is responsible for transferring magnetic interactions between the nearest neighbors (the energy of aligned spins) and the former describes the size of a defect's influence zone. The D_{sp} parameter, which describes the spin-wave stiffness (and, therefore, the ability to transfer the spin torque) is more than twelve times higher (D_{sp}/D_{Fe} = 12.96) than with pure Fe (the largest percentage share in the alloy), which is found to be between D_{Fe} = 2.8 meV nm^2 at 4.2 K[14] and D_{Fe} = 3.14 meV nm^2 at room temperature.[15] This parameter is connected with the atomic packing density (a higher D_{sp} means a higher surface density[16]) and it may indicate that linear defects should rather be considered as swellings of voids resulting in an increase in the local density around the defects, while keeping the overall material density low.

The thermal stability of the initial magnetic susceptibility was also investigated. This parameter is very important and often determines possible applications. For the studied sample, the shape of the dependency is shown in **Figure 5**.

Quite minor temperature-related changes in the value of the initial magnetic susceptibility were observed. A good stability and an almost linear growth may indicate that, in magnetic terms, the material is homogeneous and no other magnetic phases were formed (in accordance to

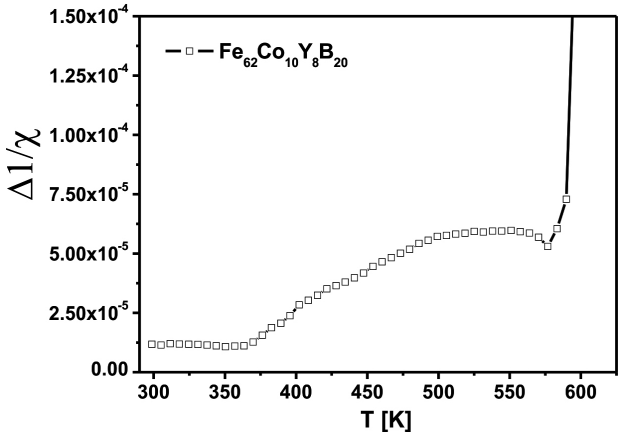

Figure 6: Magnetic-susceptibility disaccommodation curve for the $Fe_{62}Co_{10}Y_8B_{20}$ alloy after solidification

Slika 6: Neprimerna krivulja magnetne občutljivosti zlitine $Fe_{62}Co_{10}Y_8B_{20}$ po strjevanju

the XRD). Considering the rather low temperatures region, the conspicuous increase between 325 K and 400 K can be elucidated mainly with the sample's internal-tension relaxation processes, together with a minor contribution of the magnetic-anisotropy reduction. The sharp decline observed near 600 K is associated with the paramagnetic transition when the ferromagnetic order is destroyed.

The time dependence of the initial susceptibility after the demagnetization at various temperatures, or the magnetic-susceptibility disaccommodation curve for the investigated alloy, is presented in **Figure 6**.

As can be seen in **Figure 6**, the disaccommodation intensity linearly rises up to the broad maximum located at about 542 K. Above 542 K, the intensity decreases, which is directly connected with the decrease in the amount of the atom pairs reorienting in the point-defect vicinity. A pair reorientation can occur in two cases: the first one is associated with a reversible process, in which, through energy delivery, atom pairs near the point defects can swap their positions and return to the initial state after the energy reduction, and in the second one, this displacement is permanent due to the major changes in the local space involving a minimum of three atoms. Both processes can occur in the same time and the curve

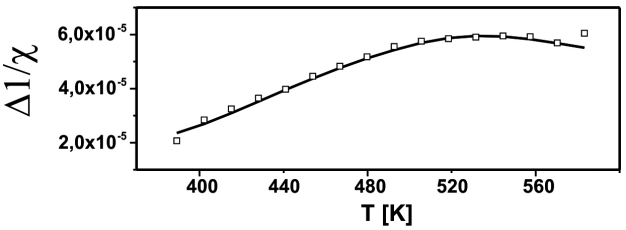

Figure 7: Theoretical magnetic-susceptibility disaccommodation curve (solid line) and experimental data for the $Fe_{62}Co_{10}Y_8B_{20}$ alloy after solidification

Slika 7: Teoretična krivulja neprimerne magnetne občutljivosti (polna linija) in eksperimentalni podatki za zlitino $Fe_{62}Co_{10}Y_8B_{20}$ po strjevanju

observed in **Figure 6** indicates the effect of the imposition of these two phenomena. The visible kink in the same temperature region as in the case of the stability of the initial-susceptibility curve (**Figure 5**) is presumably also caused by the relaxation processes. This phenomenon must therefore at least partially occur through the irreversible atomic-pair reorientation, clearly manifested between 325 K and 400 K (**Figure 6**). As the relaxation process of the material has to occur through the displacement of atoms into positions that lead to a lower total energy of the system, a part of these movements must therefore lead to the reorientation of atomic pairs visible as disaccommodation phenomena. Next, a numerical analysis of the disaccommodation curve was done (**Figure 7**).

The isochronal magnetic-susceptibility disaccommodation curve was numerically analyzed using the dependence given with Equation (1):

$$\Delta\left(\frac{1}{x}\right)=\sum_{i=1}^{I}\int_{-3\beta_{\tau i}}^{3\beta_{\tau i}}\beta_{\tau}^{-1}\pi^{-1/2}\frac{I_{pi}T_{pi}}{T}\cdot \left(e^{-\frac{t_1}{\tau_{mi}e^{z}}}-e^{-\frac{t_2}{\tau_{mi}e^{z}}}\right)e^{-\left(\frac{z}{\beta_{\tau i}}\right)^2}\mathrm{d}z \tag{1}$$

where the mean relaxation time τ_{mi} is given:

$$\tau_{mi}=\tau\exp\left(-\frac{Q_{mi}}{k}\left(\frac{1}{T}-\frac{1}{T_{pi}}\right)\right)$$

τ – the pre-exponential factor in the Arrhenius law, I_{pi} – the intensity of the i^{th} process at temperature T_{pi}, Q_{mi} – the mean activation energy, β – the distribution width and $z=\ln\tau/\tau_{mi}$.

The results of the analysis of the disaccommodation curve in function of temperature, based on the above formula done using the least squares method is presented in **Table 2**.

Table 2: Results obtained from the numerical analysis of disaccommodation curve

Tabela 2: Rezultati, dobljeni iz numerične analize neustrezne krivulje

a	$1.095*10^{-7}$	τ (s)
b	$-2.230*10^{-5}$	
T_p (K)	433.20	2.62×10^{-15}
I_p	$5.223*10^{-6}$	
Q (eV)	1.378	
β	6.9368	
T_p (K)	479.17	2.98×10^{-15}
I_p	$3.215*10^{-5}$	
Q (eV)	1.5189	
β	5.0638	
T_p (K)	542.87	5.26×10^{-15}
I_p	$2.52*10^{-5}$	
Q (eV)	1.6942	
β	3.7668	

The isochronal magnetic-susceptibility disaccommodation curve was decomposed into three elementary

processes (peaks). The first peak with the maximum localized at 433 K has the lowest activation energy (Q), the highest width (β) and the highest intensity (I_p). Most of the elementary-pair-reconfiguration processes therefore require a minimum activation energy of 1.38 eV. An analysis of **Table 2** reveals that the peak maximum temperature (T_p) increases together with the activation energy and relaxation time τ. At the same time, the distribution width and process intensity decrease. This phenomena is probably related with the atomic mass (and also the radius) of the ingredients. Thus, atom pairs with a higher mass or a bigger size require more energy and time for the relaxation to occur. On this basis, it can be concluded that the first elementary process is mostly caused by boron (a radius of 82 pm, a weight of 10.8 u), the second process mainly involves Fe (r. 126 pm, w. 55.9 u) and Co (r. 125 pm, w. 58.7 u) and the last process, which requires the largest activation energy, is caused due to an increasing involvement of yttrium (r. 180 pm, w. 88.9 u) atoms. Obviously, due to the smallest size and weight of B, this element probably has the largest share in each of the elementary processes, but it should be noted that the pair reorientation involving atoms with extreme size differences, tends to be irreversible.

4 CONCLUSIONS

In the radial cooling process, a good-quality bulk amorphous sample of the $Fe_{62}Co_{10}Y_8B_{20}$ composition was prepared. Studies of its magnetic properties showed that despite a notably large yttrium share, it is possible to make the material to be rather soft (H_c = 289 A/m). Susceptibility studies showed that in terms of magnetic properties, the material is homogeneous. Simultaneously, magnetic-susceptibility disaccommodation studies clearly revealed a presence of point defects, which are responsible for the magnetization process in the Rayleigh area. Therefore, point defects must also be distributed uniformly across the entire volume of the material. The decomposition of the susceptibility disaccommodation curve in three elementary processes was sufficient to completely describe the pair reorientation, showing the dependence of the activation energy, intensity and relaxation time on the mass (and radius) of the elements involved in the reorientation process. At $H > 0.4\ H_c$, in the approach to the ferromagnetic saturation area, the initial-magnetization-curve analysis, with respect to Kronmüller's theory, led to the conclusion that in the magnetization process, linear defects of the second type play the main role.

A detailed analysis of the parameters obtained on the basis of this theory showed that the defects of this type can be considered as swellings of voids, leading to an increase in the local density around them. On the other hand, as it is known, long-term annealing below the crystallization temperature leads to a decrease in disaccommodation phenomena[17] associated with the stress relaxation (due to the atom expansion) and defect diffusion to the sample's surface. There are no indications that the linear defects are not subjected to the same processes, leading to their decomposition into smaller point defects. At the same time, no increase in the intensity of disaccommodation phenomena is observed (directly related to the amount of point defects). This may suggest that the linear conglomerates of defects disappear because of collapse-like processes and not due to shredding. This is consistent with the conclusion about an increase in the structural stresses around the linear defects, pushing to fill the voids and, therefore, reduce the system energy. Considering that the range of the exchange interaction is smaller than the average size of a linear defect, the stress relaxation due to the annealing process should lead to a reduction in the number of defects, observed as a decrease in the D_{sp} parameter.

5 REFERENCES

[1] M. G. Nabiałek, P. Pietrusiewicz, M. J. Dospiał, M. Szota, K. Błoch, K. Gruszka, K. Ożga, S. Garus, Effect of manufacturing method on the magnetic properties and formation of structural defects in $Fe_{61}Co_{10}Y_8Zr_1B_{20}$ amorphous alloy, Journal of Alloys and Compounds, 615 (**2014**) S1, 51–55, doi:10.1016/j.jallcom.2013.12.163

[2] K. Błoch, M. Nabiałek, P. Pietrusiewicz, J. Gondro, M. Dośpiał, M. Szota, K. Gruszka, Time and Thermal Stability of Magnetic Properties in $Fe_{61}Co_{10}Y_8Nb_1B_{20}$ Bulk Amorphous Alloys, Acta Physica Polonica A, 126 (**2014**) 1, 108–109, doi:10.12693/APhysPolA.126.108

[3] K. Błoch, Structure and magnetic properties of bulk amorphous $(Fe_{0.61}Co_{0.10}Zr_{0.025}Hf_{0.025}\ W_{0.02}Ti_{0.02}B_{0.20})_{94}Y_6$ alloy, Archives of Materials Science and Engineering, 64 (**2013**) 2, 97–102

[4] W. J. Botta, J. E. Berger, C. S. Kiminami, V. Roche, R. P. Nogueira, C. Bolfarini, Corrosion resistance of Fe-based amorphous alloys, Journal of Alloys and Compounds, 586 (**2014**) 1, 105–110, doi:10.1016/j.jallcom.2012.12.130

[5] Y. Han, C. T. Chang, S. L. Zhu, A. Inoue, D. V. Louzguine-Luzgin, E. Shalaan, F. Al-Marzouki, Fe-based soft magnetic amorphous alloys with high saturation magnetization above 1.5 T and high corrosion resistance, Intermetallics, 54 (**2014**), 169–175, doi:10.1016/j.intermet.2014.06.006

[6] P. Pietrusiewicz, M. Nabiałek, M. Szota, M. Dośpiał, K. Gruszka, Influence of Low Temperature Annealing on the Magnetic and Structural Properties of $Fe_{61}Co_{10}Y_8W_1B_{20}$ Alloy, Acta Physica Polonica A, 126 (**2014**) 1, 110–111, doi:10.12693/APhysPolA.126.110

[7] K. Sobczyk, J. Świerczek, J. Gondro, J. Zbroszczyk, W. Ciurzyńska, J. Olszewski, P. Brągiel, A. Łukiewska, J. Rzącki, M. Nabiałek, Microstructure and some magnetic properties of bulk amorphous $(Fe_{0.61}Co_{0.10}Zr_{0.025}Hf_{0.025}Ti_{0.02}W_{0.02}B_{0.20})_{100-x}Y_x$ (x = 0, 2, 3 or 4) alloys, Journal of Magnetism and Magnetic Materials, 324 (**2012**), 540–549, doi:10.1016/j.jmmm.2011.08.038

[8] H. Kronmüller, Theory of magnetic after-effects in ferromagnetic amorphous alloys, Philosophical Magazine B: Physics of Condensed Matter, 48 (**1983**) 2, 127–150, doi:10.1080/13642818308226466

[9] H. Kronmüller, Micromagnetism and microstructure of amorphous alloys, Journal of Applied Physics, 52 (**1981**), 1859–1864, doi:10.1063/1.329552

[10] M. Hirscher, R. Reisser, R. Würschum, H. E. Schaefer, H. Kronmüller, Magnetic after-effect and approach to ferromagnetic saturation in nanocrystalline iron, Journal of Magnetism and Magnetic Materials, 146 (**1995**), 117–122, doi:10.1016/0304-8853(94)01643-7

[11] H. Kronmüller, Micromagnetism in Amorphous Alloys, IEEE Transactions on Magnetics, 15 (**1979**) 5, 1218–1225, doi:10.1109/TMAG.1979.1060343

[12] N. Lenge, H. Kronmüller, Low temperature magnetization of sputtered amorphous Fe-Ni-B films, Physica Status Solidi A, 95 (**1986**), 621–633, doi:10.1002/pssa.2210950232

[13] D. Goll, Handbook of Magnetism and Advanced Magnetic Materials 2, J. Wiley & Sons, 2007, doi: 10.1002/9780470022184.hmm203

[14] M. Pajda, J. Kudrnovsky, I. Turek, V. Drchal, P. Bruno, Ab initio calculations of exchange interactions, spin-wave stiffness constants, and Curie temperatures of Fe, Co, and Ni, Physical Review B, 64 (**2001**) 17, 174402: 1–9, doi:10.1103/PhysRevB.64.174402

[15] R. B. Muniz, J. d'Albuquerque e Castro, E. da Silva, Spin wave stiffness constant of iron, Journal de Physique Colloques, 49 (**1988**) C8, 89–90, doi:10.1051/jphyscol:1988831

[16] M. Nabiałek, P. Pietrusiewicz, M. Dośpiał, M. Szota, J. Gondro, K. Gruszka, A. Dobrzańska-Danikiewicz, S. Walters, A. J. Bukowska, Influence of the cooling speed on the soft magnetic and mechanical properties of $Fe_{61}Co_{10}Y_8W_1B_{20}$ amorphous alloy, Alloys and Compounds, 615 (**2015**), 56–60, doi:10.1016/j.jallcom.2013.12.236

[17] M. Hasiak, W. H Ciurzyńska, Y. Yamashiro, Microstructure and some magnetic properties of amorphous and nanocrystalline Fe–Cu–Nb–Si–B alloys, Materials Science and Engineering A, 293 (**2000**) 1–2, 261–266, doi:10.1016/S0921-5093(00)01030-3

UDK 67.017:549.3:620.193
Original scientific article/Izvirni znanstveni članek

ISSN 1580-2949
MTAEC9, 50(5)713(2016)

EFFECT OF SULPHIDE INCLUSIONS ON THE PITTING-CORROSION BEHAVIOUR OF HIGH-Mn STEELS IN CHLORIDE AND ALKALINE SOLUTIONS

VPLIV SULFIDNIH VKLJUČKOV NA JAMIČASTO KOROZIJO JEKEL Z VISOKO VSEBNOSTJO Mn V RAZTOPINAH KLORIDOV IN ALKALIJ

Adam Grajcar, Aleksandra Płachcińska

Silesian University of Technology, Institute of Engineering Materials and Biomaterials, Konarskiego Street 18a, 44-100 Gliwice, Poland
adam.grajcar@polsl.pl

Prejem rokopisa – received: 2015-07-01; sprejem za objavo – accepted for publication: 2015-09-02

doi:10.17222/mit.2015.169

The corrosion behaviour of the 27Mn-4Si-2Al- and 26Mn-3Si-3Al-type austenitic steels were evaluated in chloride 3.5 % NaCl and alkaline 0.1-M NaOH environments using potentiodynamic polarization tests. The type of non-metallic inclusions and their pitting-corrosion behaviour were investigated. In the chloride solution, both the steels exhibited a lower corrosion resistance in comparison to the alkaline solution. The high-Mn steels showed evidence of pitting and uniform corrosion, both in the chloride and alkaline solutions. SEM micrographs revealed that the corrosion pits are characterized by various shapes and an irregular distribution at the metallic matrix. Corrosion damage is more numerous in the chloride solution than in the alkaline solution. EDS analyses revealed that the corrosion pits nucleated on MnS inclusions or complex oxysulphides. The chemical composition of the steels (change in the Al and Si contents) does not affect the privileged areas of pit nucleation, whereas it influences the electrochemical behaviour of the steels in the chloride solution.

Keywords: high-Mn steel, austenitic steel, non-metallic inclusion, corrosion resistance, pitting corrosion, potentiodynamic polarization test

Korozijsko obnašanje avstenitnih jekel 27Mn-4Si-2Al in 26Mn-3Si-3Al je bilo ocenjeno v raztopini 3,5 % NaCl in v alkalni raztopini 0,1 M NaOH, s pomočjo potenciodinamičnih polarizacijskih preizkusov. Preiskovana je bila vrsta nekovinskih vključkov in njihovo ponašanje pri jamičasti koroziji. V raztopini kloridov sta obe jekli, v primerjavi z alkalno raztopino, pokazali manjšo korozijsko obstojnost. Jekla z visoko vsebnostjo Mn so pokazala jamičasto in splošno korozijo v obeh raztopinah, tako v kloridni kot v alkalični. SEM-posnetki so pokazali korozijske jamice različnih oblik in njihovo neenakomerno razporeditev po kovinski osnovi. Korozijske poškodbe so bolj številne v kloridni raztopini kot pa v alkalni raztopini. EDS-analize so pokazale, da korozijske jamice nastajajo na vključkih MnS ali na kompleksnih oksisulfidih. Kemijska sestava jekel (spremembe v vsebnosti Al in Si) ni vplivala na prednostna mesta nukleacije jamic, medtem ko je vplivala na elektrokemijsko ponašanje jekel v raztopini kloridov.

Ključne besede: jekla z veliko vsebnostjo Mn, avstenitno jeklo, nekovinski vključki, odpornost na korozijo, jamičasta korozija, potenciodinamični polarizacijski preizkus

1 INTRODUCTION

Pitting corrosion is a type of localized corrosion. It occurs mainly in the passive state of metals, in environments containing aggressive ions, i.e., chloride anions. The pits are often invisible during the formation stage, but their progressive local damage can lead to an element perforation.[1] It is well known that various factors – the chemical composition, microstructure, heat treatment and plastic deformation – affect the pitting potential.[2–4]

There are many reports that confirm the negative impact of non-metallic inclusions on the corrosion resistance of steel.[5–7] High-manganese austenitic steels have different types of inclusions, which form during melting and casting. These steels contain Mn, which combines with sulphur, and Si and Al additions with a high chemical affinity for oxygen (Al also to nitrogen).[8–10] Therefore, the presence of various sulphide and oxide inclusions in these steels can be expected.[11,12] I. J. Park et al.[7] observed MnS, AlN, Al_2O_3, $MnAl_2O_4$ and other complex inclusions in Mn-Al steels. Č. Donik et al.[5] and A. Pardo et al.[6] reported that the Mn additions to stainless steels have a detrimental effect on the pitting-corrosion resistance in a NaCl medium. Manganese favours the formation of MnS inclusions, which are vulnerable to the initiation of corrosion pits. Moreover, its presence drastically increases the corrosion current density of steel and displaces the E_{corr} values towards less noble potentials. K. J. Park and H. S. Kwon[13] found that the size of the MnS inclusions increased with an increase in the Mn concentration in Fe–18Cr–6Mn and Fe-18Cr-12Mn steels. The shape, composition and distribution of inclusions have significant effects on the corrosion resistance too.

The high-manganese alloys belong to a new, advanced group of steels that combine successively high strength and high plasticity due to the austenitic microstructure. Because of the homogeneous ductile micro-

structure they can be used for numerous elements of the energy-absorbing structures of cars.[14,15] These steels are used as a cheaper substitute for austenitic stainless steels. Manganese (austenite stabilizer) and aluminium can replace expensive nickel and chromium additions. The potential applications also include construction materials to transport different liquid gases with various pH values. However, their real application also depends on the corrosion behaviour. Therefore, the effect of non-metallic inclusions on the corrosion properties of the 27Mn-4Si-2Al and 26Mn-3Si-3Al steels in two environments, i.e., 3.5 % NaCl (neutral) and 0.1-M NaOH (alkaline), have been investigated in this study using electrochemical polarization tests.

2 EXPERIMENTAL PROCEDURE

The investigated materials were high-Mn austenitic steels with the chemical composition shown in **Table 1**. Both steels were treated using the same conditions. The steel ingots were prepared by vacuum melting, then they were hot-forged and roughly rolled to a thickness of 4.5 mm. The next step was their thermomechanical processing, consisting of the hot rolling of flat samples in three passes (relative reductions: 25 %, 25 % and 20 %) to a final sheet thickness of approximately 2 mm, obtained at 850 °C. Subsequently, the samples were rapidly cooled in water to room temperature.

The flat samples of the 27Mn-4Si-2Al and 26Mn-3Si-3Al steels with a 0.38 cm^2 exposed surface area were prepared for the electrochemical tests in 3.5 % NaCl (neutral) and 0.1-M NaOH (alkaline) solutions. The samples were mechanically ground with SiC paper up to 1200 grit. Prior to the experiments, all the samples were washed in distilled water and rinsed in acetone. The solutions were prepared using deionised water. The electrochemical cell comprised three electrodes. A stainless steel and a silver/silver chloride (Ag/AgCl) electrode (SSE) were used as the counter and the reference electrodes, respectively. The electrochemical measurements were performed using an Atlas 0531 Electrochemical Unit potentiostat/galvanostat driven by AtlasCorr05 software. The potentiodynamic polarisation measurements were conducted at a scan rate of 1 mV/s. The potentiodynamic scan data were collected to determine the electrochemical parameters: corrosion potential E_{corr} and corrosion current density I_{corr}.

The samples after the corrosion tests were polished using Al_2O_3 with a granularity of 0.1 μm for the scanning electron microscopy (SEM). To reveal the corrosion pits the cover formed on the pit surface has to be removed. Thus, the samples' surfaces were polished to obtain a uniform surface with pit-initiation sites. The corrosion damage was examined based on SEM observations and EDS techniques. Additionally, the depth of the corrosion damage on the cross-sectioned specimens was evaluated using a light microscope.

3 RESULTS AND DISCUSSION

Typical microstructures of the 27Mn-4Si-2Al and 26Mn-3Si-3Al steel specimens are shown in **Figures 1a** and **1b**, respectively. Both micrographs exhibit relatively coarse austenite grains elongated according to the direction of hot rolling. The mean grain size is approximately 80 μm. The microstructures reveal the presence of annealing twins, deformation effects and elongated sulphide inclusions.

Potentiodynamic curves of the 27Mn-4Si-2Al and 26Mn-3Si-3Al steels registered in 3.5 % NaCl (neutral – pH 7) and 0.1-M NaOH (alkaline – pH 14) solutions are illustrated in **Figures 2** and **3**. The average calculated values of the corrosion potential E_{corr} and the corrosion current density I_{corr} determined by the Tafel extrapolation are shown in **Table 2**. Both steels show lower corrosion resistance in the 3.5 % NaCl solution than in 0.1-M NaOH solution. The corrosion current density registered in the chloride solution was higher in comparison to the alkaline solution (**Table 2**). The obtained data are supported by the similar results of other authors[16,17], who reported that the high-Mn austenitic steels show a lower

Table 1: Chemical composition of investigated steels in mass fractions (*w*/%)
Tabela 1: Kemijska sestava preiskovanih jekel v masnih deležih (w/%)

Grade	Mn	Si	Al	S	P	Nb	Ti	N	O	Fe
27Mn-4Si-2Al	27.5	4.18	1.69	0.017	0.004	0.033	0.010	0.0028	0.0006	bal.
26Mn-3Si-3Al	26.0	3.08	2.87	0.013	0.002	0.034	0.010	0.0028	0.0006	bal.

Table 2: Average values of the electrochemical polarization data for the 27Mn-4Si-2Al and 26Mn-3Si-3Al steels obtained in the 3.5 % NaCl and 0.1-M NaOH solutions
Tabela 2: Srednje vrednosti podatkov elektrokemijske polarizacije 27Mn-4Si-2Al in 26Mn-3Si-3Al jekel, dobljene v raztopinah 3,5 % NaCl in 0,1 M NaOH

Grade	Statistics	3.5 % NaCl		0.1 M NaOH	
		E_{corr}/(mV)	I_{corr}/(mA/cm^2)	E_{corr}/(mV)	I_{corr}/(mA/cm^2)
27Mn-4Si-2Al	average value	–788	0.090	–392	0.007
	standard deviation	6.5	0.007	3.2	0.002
26Mn-3Si-3Al	average value	–785	0.009	–395	0.005
	standard deviation	11.2	0.005	4.3	0.003

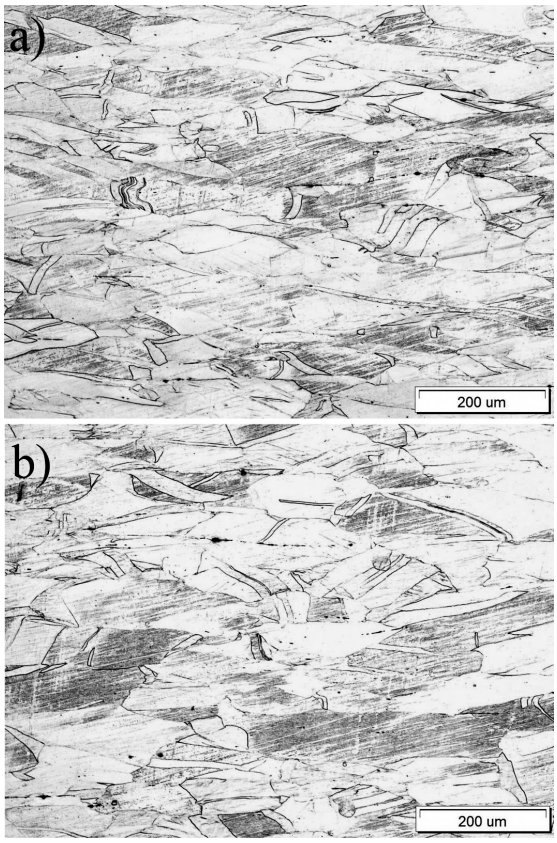

Figure 1: Austenitic microstructure of the thermomechanically processed: a) 27Mn-4Si-2Al and b) 26Mn-3Si-3Al steels

Slika 1: Avstenitna mikrostruktura termomehansko izdelanih jekel: a) 27Mn-4Si-2Al in b) 26Mn-3Si-3Al

corrosion resistance in the chloride medium than in the alkaline solution.

In the 3.5 % NaCl solution, the 27Mn-4Si-2Al steel specimens showed a much higher corrosion current density (0.09 mA/cm^2) than the 26Mn-3Si-3Al steel (0.009 mA/cm^2). This confirms our earlier results from the potentiodynamic polarisation tests.[3] It is related to the higher Al and lower Si contents in 26Mn-3Si-3Al steel in comparison to the steel containing 2 % Al (**Table 1**). It is reported[18] that a silicon addition decreases the corrosion resistance of steel. On the other hand, aluminium improves the corrosion resistance due to its tendency to form a protective Al_2O_3 passive layer on the steel surface in solutions of pH ~7 (Pourbaix diagrams).[19] All the specimens polarized in the 3.5 % NaCl solution show E_{corr} values shifted to less noble potentials (**Table 2**) when compared to the specimens polarized in the 0.1-M NaOH solution. The E_{corr} shift was about 400 mV towards the cathodic direction. The values of the corrosion-current density obtained in the 0.1-M NaOH were quite similar for both steels. The 27Mn-4Si-2Al steel specimens showed a corrosion current density of approximately 0.007 mA/cm^2, whereas it was 0.005 mA/cm^2 for the second steel. The better corrosion resistance of both steels in 0.1-M NaOH is related to the fact that in alkaline solutions, manganese precipitates as $Mn(OH)_2$, which is slightly soluble in solutions with pH>13, whereas in solutions of pH ~ 7 the manganese dissolves as Mn^{2+} (Pourbaix diagrams).[19]

The morphology of the corrosion pits after the electrochemical tests were studied using the SEM and

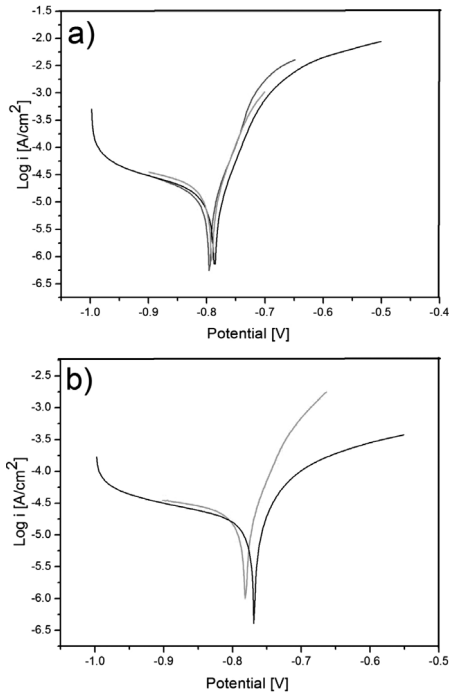

Figure 2: Potentiodynamic polarization curves of the: a) 27Mn-4Si-2Al and b) 26Mn-3Si-3Al steels obtained in 3.5 % NaCl solution

Slika 2: Krivulje potenciodinamične polarizacije jekel v raztopini 3,5 % NaCl: a) 27Mn-4Si-2Al in b) 26Mn-3Si-3Al

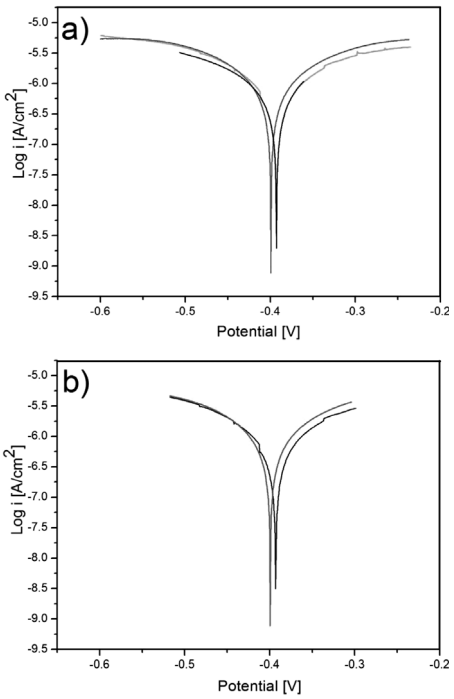

Figure 3: Potentiodynamic polarization curves of the: a) 27Mn-4Si-2Al and b) 26Mn-3Si-3Al steels obtained in 0.1-M NaOH solution

Slika 3: Krivulje potenciodinamične polarizacije jekel v raztopini 0,1 M NaOH: a) 27Mn-4Si-2Al in b) 26Mn-3Si-3Al

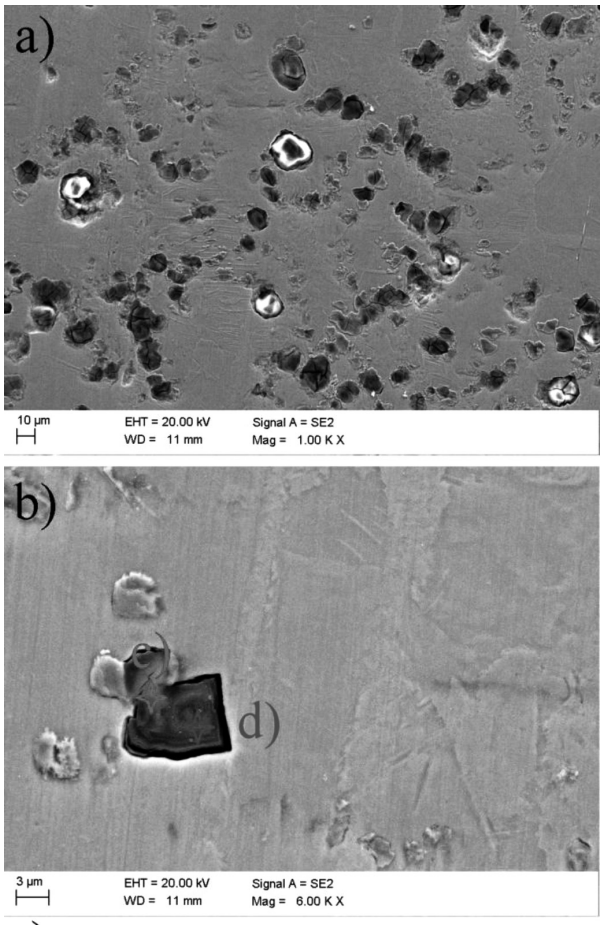

Element	Wt%	At%
OK	30.58	53.86
AlK	06.25	06.53
SiK	12.58	12.62
SK	00.49	00.43
MnK	06.75	03.46
FeK	41.16	20.77

Element	Wt%	At%
AlK	02.11	03.82
SiK	04.46	07.77
SK	09.25	14.12
MnK	33.28	29.66
FeK	50.90	44.63

Figure 4: a) SEM micrograph of the 27Mn-4Si-2Al steel surface, b) the individual pit interior, c) EDS analysis from point D, d) EDS analysis from point C after corrosion test in 3.5 % NaCl

Slika 4: a) SEM-posnetki površine jekla 27Mn-4Si-2Al, b) izgled posamezne jamice, c) EDS-analiza v točki D, d) EDS-analiza točke C po korozijskem preizkusu v 3,5 % NaCl

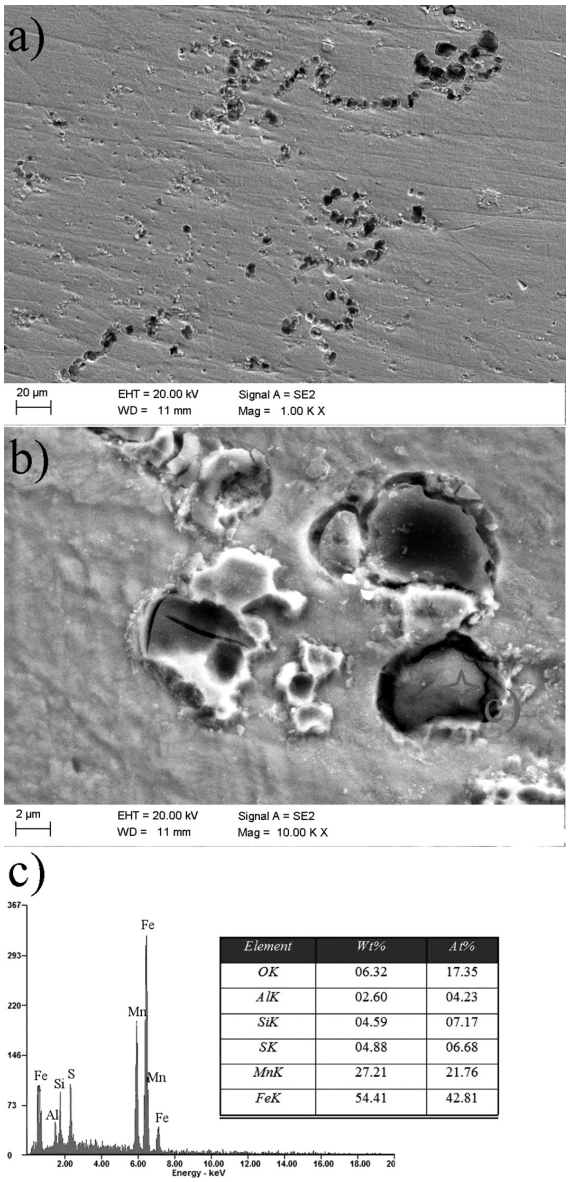

Element	Wt%	At%
OK	06.32	17.35
AlK	02.60	04.23
SiK	04.59	07.17
SK	04.88	06.68
MnK	27.21	21.76
FeK	54.41	42.81

Figure 5: a) SEM micrograph of the 26Mn-3Si-3Al steel surface, b) the individual pit interior, c) EDS analysis from point C after corrosion test in 3.5 % NaCl

Slika 5: a) SEM-posnetek površine jekla 26Mn-3Si-3Al, b) izgled posamezne jamice, c) EDS-analiza točke C po korozijskem preizkusu v 3,5 % NaCl

EDS techniques. The SEM images of the corrosion damage in both steels after the corrosion tests in 3.5 % NaCl are shown in **Figures 4** and **5**. The corrosion pits are characterized by various shapes and an irregular distribution at the metallic matrix (**Figures 4a** and **5a**). They are formed both at the grain boundaries and within the austenite grains. It is apparent that the pits are initiated at non-metallic inclusions. The EDS analysis revealed the variation of the chemical composition in the interior of the individual pits. For instance, the chemical composition of the particle inside the corrosion pit in **Figure 4b** showed a high content of manganese and sulphur (**Figure 4d**). This indicates that the privileged

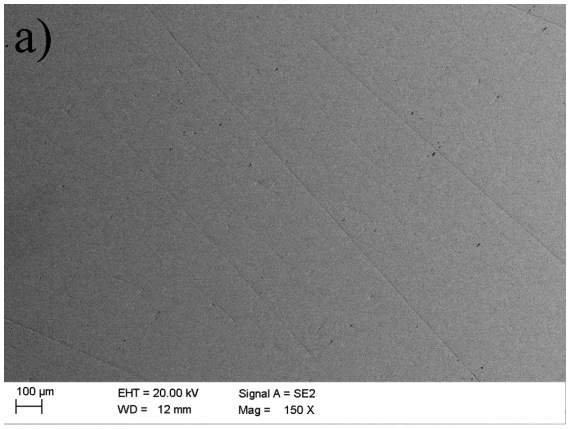

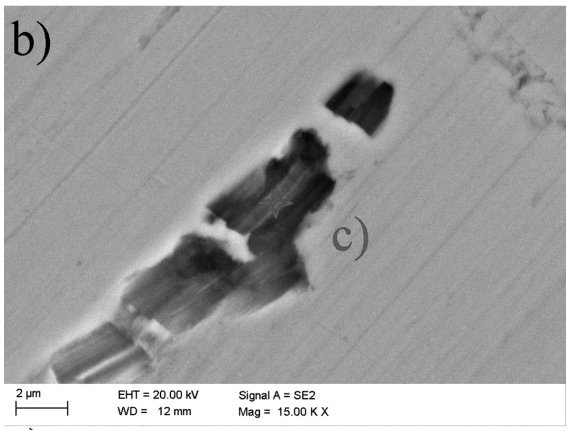

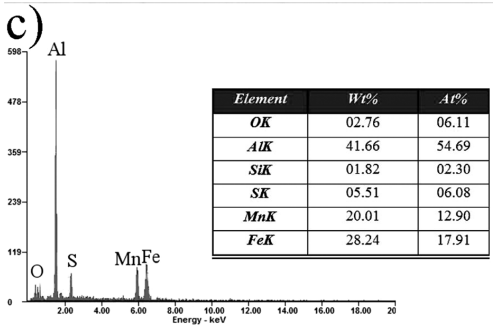

Element	Wt%	At%
OK	02.76	06.11
AlK	41.66	54.69
SiK	01.82	02.30
SK	05.51	06.08
MnK	20.01	12.90
FeK	28.24	17.91

Figure 6: a) SEM micrograph of the 27Mn-4Si-2Al steel surface, b) the individual pit interior, c) EDS analysis from point C after corrosion test in 0.1-M NaOH

Slika 6: a) SEM-posnetek površine jekla 27Mn-4Si-2Al, b) izgled posamezne jamice, c) EDS-analiza iz točke C po korozijskem preizkusu v 0,1 M NaOH

places for the pit initiation are MnS inclusions. There are many reports in the literature[5-7,20] that confirm that MnS inclusions are vulnerable for the initiation of corrosion pits. Their presence increases the corrosion current density and displaces the E_{corr} values towards less noble potentials. The chemical analysis of the corrosion damage shown in **Figure 4b** also revealed the presence of oxides containing Al and Si (**Figure 4c**).

Similar results were obtained for corrosion pits created in the steel containing the higher Al content (26Mn-3Si-3Al steel). The pits are preferentially initiated along the grain boundaries (**Figure 5a**). The EDS analysis showed the presence of corrosion pits at parti-

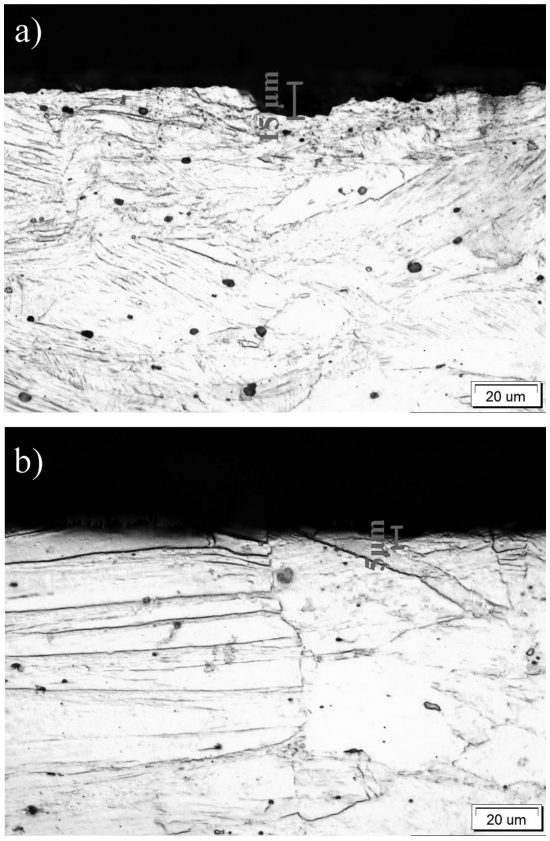

Figure 7: Light micrographs of the cross-section of 27Mn-4Si-2Al steel potentiodynamically polarized in: a) chloride solution and b) alkaline solution

Slika 7: Posnetek preseka jekla 27Mn-4Si-2Al potenciodinamično polariziranega v: a) kloridni raztopini in b) alkalni raztopini

cles with the high concentrations of manganese and sulphur, too (**Figures 5b** and **5c**). The resistance to pitting corrosion strongly depends on the quantity, size and type of non-metallic inclusions in the metallic matrix.[11] Park et al.[7] found that the size of the MnS inclusions increased with an increase in the Mn content from 6 to 12 % in the high-Cr steel. This is why both high-Mn steels contain a lot of corrosion damage.

The SEM images of both high-Mn steels after the corrosion tests in 0.1-M NaOH show good agreement with the results of the potentiodynamic tests. The observation of the steel surfaces (**Figure 6a**) confirmed a substantial reduction in the amount of corrosion damage. The EDS analyses of the individual pit in **Figures 6b** and **6c** revealed a high content of Mn, S, Al, Si and O, which indicates that complex oxysulphides containing Mn, Al and Si are also preferential sites for pit formation in the alkaline solution. According to I. J. Park et al.[21] Al_2O_3 particles have a higher resistance to pit formation than MnS particles.

The nature of the corrosion damage was evaluated on cross-sectioned specimens. In the chloride solution, the specimens showed evidence of uniform corrosion. In addition to uniform corrosion, pitting corrosion was also

observed (**Figure 7**). Other authors[5–7,16] observed corrosion pits in different high-manganese steels after polarization tests in chloride solution too. After the corrosion tests in 3.5 % NaCl the maximum depth of the corrosion pits in the steel containing 2 % Al was evaluated to be 15 µm (**Figure 7a**). Similar corrosion pits were also identified for the 26Mn-3Si-3Al steel. The corrosion damage formed in both steels in the alkaline medium is characterized by a small depth of 5 µm (**Figure 7b**). However, the quantity of corrosion damage was much lower when compared to the samples investigated in the chloride medium.

4 CONCLUSIONS

The morphology of corrosion damage after electrochemical tests in 3.5 % NaCl and 0.1-M NaOH supports the data registered in potentiodynamic tests. The high-Mn steels are characterized by a low corrosion resistance, especially in a chloride solution, where corrosion damage is more numerous. The corrosion pits are characterized by various shapes and are distributed irregularly both at grain boundaries and within the grains. EDS analyses confirmed that the corrosion pits nucleated preferentially on the MnS inclusions and complex oxysulphides containing Mn, Al and Si. The low density of corrosion damage in the alkaline solution is related to the fact that Mn precipitates as $Mn(OH)_2$, which is slightly soluble in solutions of pH>13, whereas in solutions of pH ~ 7 the manganese dissolves as Mn^{2+}. The concentration of the individual alloying elements was not strongly related to the corrosion behaviour of the steels in 0.1-M NaOH, in contrast to the 3.5 % NaCl solution. The increased contents of Mn and Si and the smaller content of Al are reflected in the lower corrosion resistance of the 27Mn-4Si-2Al, as registered during the potentiodynamic tests.

Acknowledgment

This work was financially supported with statutory funds of the Faculty of Mechanical Engineering of the Silesian University of Technology in 2015.

5 REFERENCES

[1] P. C. Pistorius, G. T. Burstein, Metastable pitting corrosion of stainless steel and the transition to stability, Philosophical Transactions of the Royal Society A, 341 (**1992**), 531–559

[2] A. Grajcar, A. Płachcińska, S. Topolska, M. Kciuk, Effect of thermomechanical treatment on the corrosion behaviour of Si- and Al-containing high-Mn austenitic steel with Nb and Ti micro-additions, Mater. Tehnol., 49 (**2015**) 6, 889–894, doi:10.17222/mit.2014.148

[3] A. Grajcar, A. Płachcińska, M. Kciuk, S. Topolska, Microstructure and corrosion behavior of hot-deformed and cold-strained high-Mn steels, Journal of Materials Engineering and Performance, 26 (**2016**) 6, 2245–2254, doi: 10.1007/s11665-016-2085-5

[4] S. Lasek, E. Mazancova, Influence of thermal treatment on structure and corrosion properties of high manganese triplex steels, Metalurgija, 52 (**2013**) 4, 441–444

[5] C. Donik, I. Paulin, M. Jenko, Influence of MnS inclusions on the corrosion of austenitic stainless steels, Mater. Tehnol., 44 (**2010**) 2, 67–72

[6] A. Pardo, M. C. Merno, A. E. Coy, F. Viejo, R. Arrabal, E. Matykina, Pitting corrosion behaviour of austenitic stainless steels – combining effects of Mn and Mo additions, Corrosion Science, 50 (**2008**), 1796–1806, doi:10.1016/j.corsci.2008.04.005

[7] I. J. Park, S. M. Lee, M. Kang, S. Lee, Y. K. Lee, Pitting corrosion behavior in advanced high strength steels, Journal of Alloys and Compounds, 619 (**2015**), 205–210, doi:10.1016/j.jallcom.2014.08.243

[8] A. Grajcar, M. Opiela, G. Fojt-Dymara, The influence of hot-working conditions on a structure of high-manganese steel, Archives of Civil and Mechanical Engineering, 9 (**2009**) 3, 49–58

[9] M. Jablońska, A. Śmiglewicz, Analysis of substructure of high-Mn steels in the context of dominant stress mechanism, Defect and Diffusion Forum, 334–335 (**2013**), 177–181, doi:10.4028/DDF.334-335.177

[10] L. A. Dobrzański, A. Grajcar, W. Borek, Microstructure evolution of C-Mn-Si-Al-Nb high-manganese steel during the thermomechanical processing, Materials Science Forum, 638-642 (**2010**), 3224–3229, doi:10.4028/MSF.638-642.3224

[11] A. Grajcar, U. Galisz, L. Bulkowski, Non-metallic inclusions in. high manganese austenitic alloys, Archives of Materials Science and Engineering, 50 (**2011**), 21–30

[12] A. Grajcar, M. Różański, M. Kamińska, B. Grzegorczyk, Study on non-metallic inclusions in laser-welded TRIP-aided Nb microalloyed steel, Archives of Metallurgy and Materials, 59 (**2014**) 3, 1163–1169, doi:10.2478/amm-2014-0203

[13] K. J. Park, H. S. Kwon, Effects of Mn on the localized corrosion behavior of Fe–18Cr alloys, Electrochimica Acta, 55 (**2010**), 3421–3427, doi:10.1016/j.electacta.2010.01.006

[14] M. Jabłońska, G. Niewielski, R. Kawalla, High manganese TWIP steel – technological plasticity and selected properties, Solid State Phenomena, 212 (**2014**), 87–90, doi:10.4028/SSP.212.87

[15] A. Grajcar, R. Kuziak, Softening kinetics in Nb-microalloyed TRIP steels with increased Mn content, Advanced Materials Research, 314-316 (**2011**), 119–122, doi:10.4028/AMR.314-316.119

[16] M. B. Kannan, R. K. S. Raman, S. Khoddam, Comparative studies on the corrosion properties of a Fe–Mn–Al–Si steel and an interstitial-free steel, Corrosion Science, 50 (**2008**), 2879–2884, doi:10.1016/j.corsci.2008.07.024

[17] Y. S. Zhang, X. M. Zhu, S. H. Zhong, Effect of alloying elements on the electrochemical polarization behavior and passive film of Fe–Mn base alloys in various aqueous solutions, Corrosion Science, 46 (**2004**), 853–876, doi:10.1016/j.corsci.2003.09.002

[18] S. Suzuki, E. Matsubara, T. Komatsu, Y. Okamoto, K. Kanie, A. Muramatsu, H. Konishi, J. Mizuki, Y. Waseda, Ex-situ and in-situ X-ray diffractions of corrosion products freshly formed on the surface of an iron–silicon alloy, Corrosion Science, 49 (**2007**), 1081–1096, doi:10.1016/j.corsci.2006.06.029

[19] N. Takeno, Atlas of Eh-pH diagrams, National Institute of Advanced Science and Technology, Tokyo 2005

[20] A. Abbasi Aghuy, M. Zakeri, M. H. Moayed, M. Mazinani, Effect of grain size on pitting corrosion of 304L austenitic stainless steel, Corrosion Science, 94 (**2015**), 368–376, doi:10.1016/j.corsci.2015.02.024

[21] I. J. Park, S. T. Kim, I. S. Lee, Y. S. Park, M. B. Moon, A study on corrosion behavior of DP-type and TRIP-type cold rolled steel sheet, Materials Transactions (JIM), 50 (**2009**), 1440–1447

UDK 620.193:621.793:67.017
Original scientific article/Izvirni znanstveni članek

ISSN 1580-2949
MTAEC9, 50(5)719(2016)

INFLUENCE OF Na_2SiF_6 ON THE SURFACE MORPHOLOGY AND CORROSION RESISTANCE OF AN AM60 MAGNESIUM ALLOY COATED BY MICRO ARC OXIDATION

VPLIV Na_2SiF_6 NA MORFOLOGIJO POVRŠINE IN KOROZIJSKO ODPORNOST MAGNEZIJEVE ZLITINE AM60, PREKRITE Z MIKROOBLOČNO OKSIDACIJO

Aysun Ayday

Sakarya University, Faculty of Engineering, Department of Metallurgical and Materials Engineering, 54187 Sakarya, Turkey
aayday@sakarya.edu.tr

Prejem rokopisa – received: 2015-07-01; sprejem za objavo – accepted for publication: 2015-09-09

doi:10.17222/mit.2015.176

Oxide coatings were formed by micro arc oxidation (MAO) on an AM60 magnesium alloy substrate. The effects of Na_2SiF_6 in an electrolytic solution on the micro arc oxidation process and the structure and mechanical properties of the oxide coatings were investigated. The results showed that the MAO coating produced in the electrolyte with Na_2SiF_6 was thicker and more uniform than that produced in the electrolyte without Na_2SiF_6. The pore diameter of the MAO coatings was reduced by the addition of Na_2SiF_6, while the coating density and surface roughness were increased. The coating formed in the electrolytic solution with or without the Na_2SiF_6 had a higher surface hardness than the AM60 alloy and the results of the corrosion behavior for including Na_2SiF_6 showed better resistance than that formed in the solution without Na_2SiF_6.

Keywords: magnesium alloy, micro arc oxidation (MAO), Na_2SiF_6, corrosion

Oksidne prevleke nastajajo pri oksidaciji v mikroobloku (MAO) podlage iz magnezijeve zlitine AM60. Preiskovan je bil vpliv Na_2SiF_6 v elektrolitni raztopini na proces oksidacije v mikroobloku in na mehanske lastnosti oksidne prevleke. Rezultati so pokazali, da je oksidna prevleka MAO, izdelana v elektrolitu z Na_2SiF_6, debelejša in bolj enakomerna, kot če je izdelana v elektrolitu brez Na_2SiF_6. Premer por v MAO prevleki se je zmanjšal z dodatkom Na_2SiF_6, medtem ko sta gostota prevleke in hrapavost površine narasli. Prevleka, nastala v elektrolitski raztopini, z ali brez Na_2SiF_6, ima večjo trdoto površine kot AM60 zlitina. Rezultati obnašanja pri koroziji, vključno z Na_2SiF_6, kažejo na boljšo odpornost kot pri prevleki, nastali v raztopini brez Na_2SiF_6.

Ključne besede: magnezijeva zlitina, oksidacija v mikro obloku (MAO), Na_2SiF_6, korozija

1 INTRODUCTION

Magnesium (Mg) alloys have been used in many industrial applications due to their high specific strength, low density and excellent mechanical properties. In recent years, Mg alloys are widely used in automotive production, with their low density, good castability and stiffness.[1–6] However, the poor corrosion resistance of Mg alloys is restricting their applications. That is why it is essential for magnesium alloy products to be protected with a surface treatment.[1,4,7] There are many techniques to improve the corrosion resistance of Mg alloys, such as electroless plating, conversion films, laser surface melting and organic coatings. Micro arc oxidation (MAO) is another efficient method to improve the properties of Mg alloys by producing ceramic films on their surface.[1,4,8] The MAO coatings have a strong adhesion to the Mg substrate, controllable thickness and other excellent properties, such as corrosion resistance, thermal shock resistance. However, the properties of MAO coatings are affected by the processing parameters, such as the composition of the electrolyte, voltage, current density, time, etc.[1,9] In this work, micro arc oxidation films have been coated on a Mg alloy with and without the Na_2SiF_6 in an electrolytic solution and the structure and corrosion resistance of the oxide coatings were investigated. The properties of the coatings were characterized by scanning electron microscopy (SEM), X-ray diffraction (XRD). The results were compared and correlated to understand the influence of the Na_2SiF_6 in the electrolytic solution on the coating-formation process, properties and corrosion behavior.

2 EXPERIMENTAL PART

2.1 Material and coating process

AM60 magnesium alloy was used as the substrate material in this study. The chemical composition of AM60 is given in **Table 1**.

Table 1: Chemical composition of AZ91D magnesium alloy (in mass fractions, *w*/%)
Tabela 1: Kemijska sestava magnezijeve zlitine AZ91D (v masnih deležih, *w*/%)

Al	Mn	Si	Fe	Mg
5.93	0.18	0.02 (max.)	0.013	Balance

Table 2: Concentration of the electrolyte solution
Tabela 2: Koncentracija elektrolitske raztopine

Sample code	Na_2SiO_3 (g/L)	NaOH (g/L)	Na_2SiF_6 (g/L)	Conductivity (mS/cm)	Roughness (μm)	Average thickness (μm)
AM60-%0	15	5	–	14.6	2.986	31.2±5
AM60-%1	15	5	1	15.1	3.532	32.6±5
AM60-%2	15	5	2	15.3	3.565	46.63±5
AM60-%4	15	5	4	17.4	3.920	47.63±5

The samples for all the tests were cut into cylinders with dimensions of 30 mm × 10 mm × 10 mm and mechanically polished with 600- and 1200-grit emery papers, rinsed with distilled water and dried in warm air. The MAO process of the sample was coated in alkali silicate electrolyte solution, which consisted of Na_2SiO_3 in distilled water with NaOH. After that 1%, 2%, and 4% Na_2SiF_6 was added to the electrolytic solution. The effects of the Na_2SiF_6 in the electrolytic solution on the MAO process and the structure and mechanical properties of the oxide coatings were investigated. The electrolyte composition is given in **Table 2**. The surface roughness (*R*a) of the MAO coatings was detected using a Mahr, Perthometer M1 surface roughmeter. The thicknesses of the coatings were measured using an SEM and the values of the conductivity for the electrolytes prepared with the base electrolyte and different concentrations of Na_2SiF_6 were measured and are shown in **Table 2**.

The oxide coatings were produced at a constant anodic voltage of 370 V for 30 min. The temperature of the electrolyte was kept at approximately 30 °C using a stirring and cooling system and the current density was varied in the range of 0.6–2 A cm^{-2}. The samples were rinsed in water and dried in hot air after the MAO process was finished.

2.2 Microstructure

The surface morphologies of the AM60 samples coated by MAO were characterized with scanning electron microscopy (SEM). The phase components of the coated samples were analyzed with X-ray diffraction (XRD) using Cu-K_α radiation.

2.3 Hardness test

The hardnesses of the AM60 and coated samples were measured using an FUTURE TECH-CORP.FM-700 microhardness tester at a load of 100 g for loading time of 10 s. The average of three measurements was reported.

2.4 Corrosion test

The immersion corrosion test was carried out in 10 % of mass fractions of NaOH solution for 10 d in an open system, the corrosion products were cleaned in distilled water with an ultrasonic cleaner, all the samples were weighed with a JA5003N electronic balance (accuracy: 1 mg) before and after the immersion test, and the corrosion rate was calculated from the weight-loss data. The PH of the solution was around 12±0.5.

3 RESULTS AND DISCUSSION

The SEM microstructures of the AM60 alloy after the MAO treatment for different electrolyte compositions are shown in **Figure 1**. It is clear that an increase in Na_2SiF_6 in the electrolytic solution changed the surface morphologies of the MAO coatings. The MAO coating processed for AM60-% 0, as shown in **Figures 1a** and **1b**, exhibits a relatively uniform surface appearance with large pores. **Figures 1c** to **1f** show the morphologies of the MAO coatings when adding 1 % and 4 % Na_2SiF_6, respectively, and the coatings are much rougher when compared with **Figure 1b**. Na_2SiF_6 can change the solution's properties, such as the solution conductivity, which

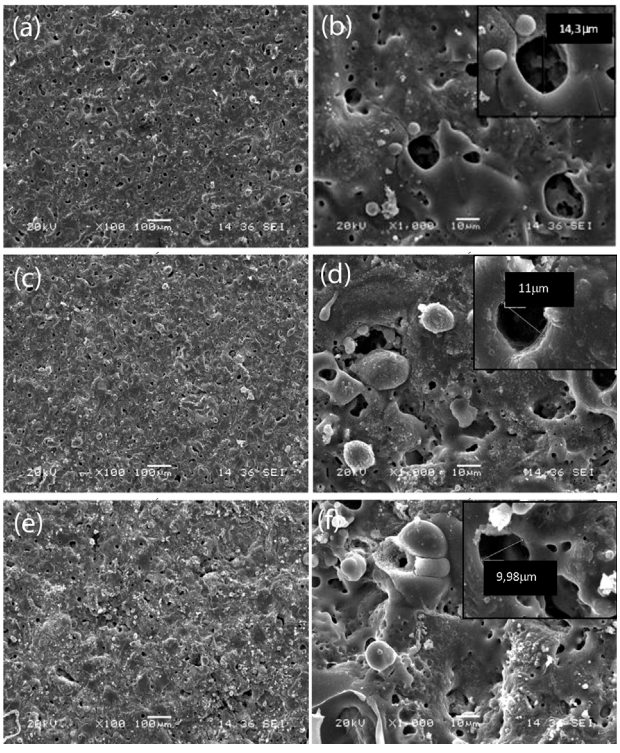

Figure 1: SEM images after the MAO treatment for: a), b) AM60–0 %, c), d) AM60–1 %, e), f) AM60–4 %
Slika 1: SEM-posnetki po MAO-obdelavi: a), b) AM60–0 %, c), d) AM60–1 %, e), f) AM60– 4 %

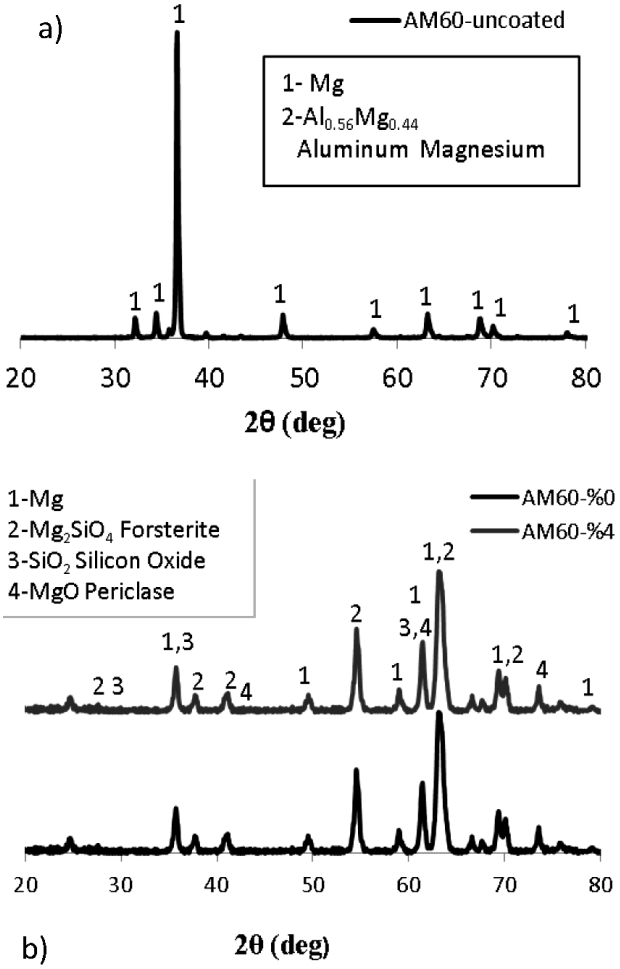

Figure 2: XRD patterns for: a) uncoated AM60, b) AM60-%0 and AM60-%4

Slika 2: Rentgenogram za: a) AM60 brez prevleke, b) AM60 0 % in AM60 4 %

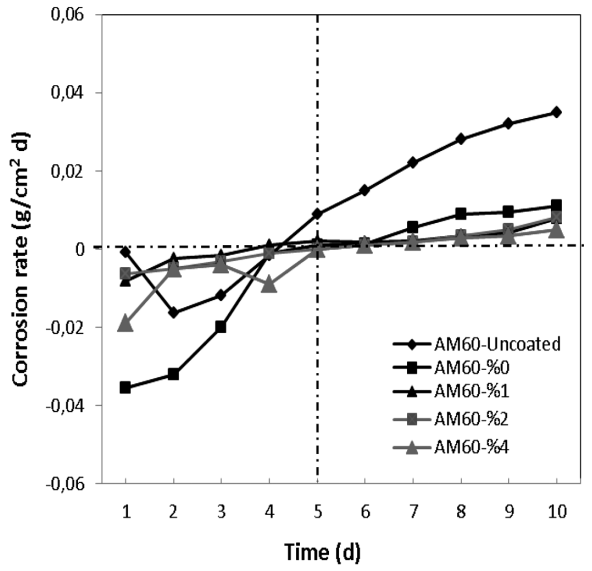

Figure 3: Variation of corrosion rate with immersion time in 10 % of mass fractions of NaOH

Slika 3: Spreminjanje hitrosti korozije s časom potapljanja v 10 % masnem deležu raztopine NAOH

plays an important role in determining the morphology and thickness. The sizes of certain pores decrease obviously with an increase of the Na_2SiF_6 solution, which is considered to be related to the increasing electrolyte conductivity.[10] According to **Table 2**, the electrolyte conductivity increased an increase in the concentration of Na_2SiF_6.

Table 2 reveals the roughness and average thickness of the MAO coatings on the AM60 alloy. It can be seen that the thickness and roughness increase with the concentration of the Na_2SiF_6, especially after 2%. The coating properties such as thickness and porosity are influenced by the final voltage, which is closely related to the solution conductivity. The electrical conductivity of the electrolytes increases with an increase of the Na_2SiF_6 concentration. The higher Na_2SiF_6 concentration corresponds to a higher current and thus a more intensive micro-arc discharge will occur on the surface.[11,12]

Before the coating, the average micro-hardness value is about 60±5 $HV_{0.1}$ for the AM60 alloy. After the MAO coating, the surface hardness increases with increasing Na_2SiF_6 concentration, and nearly all the coated samples have a hardness of approximately 479±5 $HV_{0.1}$ (AM60-%1). The surface hardness increases eight times when compared with the uncoated sample

The phases identified through the analysis of the XRD patterns for the uncoated AM60 alloy, AM60-%0 and AM60-%4 samples are presented in **Figure 2**. It is clear that the bulk material is formed of Mg and $Al_{0.56}Mg_{0.44}$ phases. However, the MAO coatings formed of Mg, Mg_2SiO_4 (Forsterite), SiO_2 (Silicon Oxide) and MgO (Periclase) phases. In addition, it can be seen from **Figure 2b** that the Mg_2SiO_4 (Fosterite) is the minor common phase that is present in all the coatings. This phase is formed due to the composition of Si in the Na_2SiO_3 (present as a constituent of the electrolyte) in the coating in the form of Mg_2SiO_4. Different phases were not seen on AM60-%4 sample surface when adding Na_2SiF_6.

Figure 3 shows the corrosion rate variation with the immersion time of the MAO coatings in 10 % mass fractions of NaOH solution. It is clear that three characteristics behaviors occur in the corrosion test, as can be seen from the curves. First of all, the corrosion rate values of the samples were negative at the initial periods. The mass gain phenomenon can result from the re-oxidation and attachment of the corrosion products. Then, the mass loss happened after immersion for about 5 d. After a long immersion period the coating layer and corrosion products began to exfoliate from the samples' surfaces. Thirdly, the corrosion rates of the MAO-coated samples were lower than the as-cast sample (AM60) for the whole immersion test. This indicates that the samples having the MAO coating with Na_2SiF_6 a have higher corrosion resistance.

4 CONCLUSIONS

Oxide coatings were produced on the AM60 alloy by micro arc oxidation in different solutions with and without Na_2SiF_6. The coatings produced with Na_2SiF_6 were thicker than the ones produced without Na_2SiF_6 for the same parameters. The pores on the surface decrease with an increasing Na_2SiF_6 concentration and the surface becomes rougher. The hardness improves nearly eight times when compared with uncoated sample. The corrosion resistance of the samples coated in the Na_2SiF_6 electrolyte solution can be attributed to the more uniform and compact structure of this coating, which acts as a barrier to the transfer of corrosive ion from the aggressive solution into the coating. The AM60-%4 sample shows the best corrosion resistance in 10 % mass fractions of NaOH solution.

5 REFERENCES

[1] K. Dong, Y. Song, D. Shan, E. Han, Formation mechanism of a self-sealing pore micro-arc oxidation film on AM60 magnesium alloy, Surface and Coatings Technology, 266 (**2015**), 188–196, doi:10.1016/j.surfcoat.2015.02.041

[2] H. Gao, M. Zhang, X. Yang, P. Huang, K. Xu, Effect of Na2SiO3 solution concentration of micro-arc oxidation process on lap-shear strength of adhesive-bonded magnesium alloys, Applied Surface Science, 314 (**2014**), 447–452, doi:10.1016/j.apsusc.2014.06.117

[3] Y. Ge, B. Jiang, M. Liu, C. Wang, W. Shen, Preparation and characterization of the micro-arc oxidation composite coatings on magnesium alloys, Journal of Magnesium and Alloys, 2 (**2014**), 309–316, doi:10.1016/j.jma.2014.11.006

[4] X. Cui, X. Lin, C. Liu, R. Yang, X. Zheng, M. Gong, Fabrication and corrosion resistance of a hydrophobic micro-arc oxidation coating on AZ31 Mg alloy, Corrosion Science, 90 (**2015**), 402–412, doi:10.1016/j.corsci.2014.10.041

[5] D. Veys-Renaux, E. Rocca, G. Henrion, Micro-arc oxidation of AZ91 Mg alloy: An in-situ electrochemical study, Electrochemistry Communications, 31 (**2013**), 42–45, doi:10.1016/j.elecom.2013.02.023

[6] A. L. Yerokhin, A. Shatrov, V. Samsonov, P. Shashkov, A. Leyland, A. Matthews, Fatigue properties of Keronite coatings on a magnesium alloy, Surface and Coatings Technology, 182 (**2004**), 78–84, doi:10.1016/S0257-8972(03)00877-6

[7] P. Wang, J. Li, Y. Guo, Z. Yang, Growth process and corrosion resistance of ceramic coatings of micro-arc oxidation on Mg-Gd-Y magnesium alloys, Journal of Rare Earths, 28 (**2010**) 5, 798–802, doi:10.1016/S1002-0721(09)60204-0

[8] F. Liu, Y. Li, J. Gu, Q. Yan, Q. Luo, Q. Cai, Preparation and performance of coating on rare-earth compounds-immersed magnesium alloy by micro-arc oxidation, Trans. Nonferrous Met. Soc. China, 22 (**2012**), 1647–1654, doi:10.1016/S1003-6326(11)61368-X

[9] D. A. Becerik, A. Ayday, L. C. Kumruoğlu, S. C. Kurnaz, A. Özel, The Effects of Na2SiO3 Concentration on the Properties of Plasma Electrolytic Oxidation Coatings on 6060 Aluminum Alloy, Journal of Materials Engineering and Performance, 21 (**2012**), 1426–1430, doi:10.1007/s11665-011-0022-1

[10] M. Tang, W. Li, H. Liu, L. Zhu, Preparation Al2O3/ZrO2 composite coating in an alkaline phosphate electrolyte containing K2ZrF6 on aluminum alloy by micro arc oxidation, Applied Surface Science, 258 (**2012**), 5869–5875, doi:10.1016/j.apsusc.2012.02.124

[11] R. F. Zhang, S. F. Zhang, J. H. Xiang, L. H. Zhang, Y. Q. Zhang, S. B. Guo, Influence of sodium silicate concentration on properties of micro arc oxidation coatings formed on AZ91HP magnesium alloys, Surface and Coatings Technology, 206 (**2012**), 5072–5079, doi:10.1016/j.surfcoat.2012.06.018

[12] Y. Yang, L. Zhou, Improving Corrosion Resistance of Friction Stir Welding Joint of 7075 Aluminum Alloy by Micro-arc Oxidation, J. Mater. Sci. Technol., 30 (**2014**) 12, 1251–1254, doi:10.1016/j.jmst.2014.07.017

UDK 67.017:621.315.614:677.494.675
Original scientific article/Izvirni znanstveni članek

ISSN 1580-2949
MTAEC9, 50(5)723(2016)

MECHANICAL PROPERTIES OF POLYAMIDE/CARBON-FIBER-FABRIC COMPOSITES

MEHANSKE LASTNOSTI KOMPOZITNE TKANINE IZ POLIAMID/OGLJIKOVIH VLAKEN

Cristina-Elisabeta Pelin[1,2], George Pelin[1,2], Adriana Ştefan[1], Ecaterina Andronescu[2], Ion Dincă[1], Anton Ficai[2], Roxana Truşcă[3]

[1]National Institute for Aerospace Research "Elie Carafoli" Bucharest- Materials Unit, 220 Iuliu Maniu Blvd, 061126 Bucharest, Romania
[2]University Politehnica of Bucharest, Faculty of Applied Chemistry and Materials Science, 1-7 Gh. Polizu St., 011061 Bucharest, Romania
[3]S.C. METAV Research & Development S.A., 31 C.A. Rosetti St., 020011 Bucharest, Romania
bancristina@gmail.com, ban.cristina@incas.ro

Prejem rokopisa – received: 2015-07-01; sprejem za objavo – accepted for publication: 2015-09-10

doi:10.17222/mit.2015.171

This paper presents the production of carbon-fiber-fabric-reinforced laminated composites based on a polyamide 6 matrix using a multiple-stages technique that involves polymer dissolution in formic acid followed by fabric impregnation and high-temperature pressing. The polyamide/solvent ratio's influence on the interface and mechanical properties is discussed, analyzing three PA6 weight contents of (10, 20, and 30) % in a formic acid solvent. The mechanical behavior of the obtained laminated composites is evaluated using tensile and 3-point bending tests and the fracture cross-section is analyzed using microscopy investigation techniques in order to evaluate the fiber-matrix interface and the composite fracture mechanism. The results show that the best mechanical performance is obtained when using a solution of 20 % mass fraction of polyamide in formic acid, as this leads to the formation of a uniform polymer layer that is able to completely embed the fibers that constitute the fabric and create a strong mechanical interface within the composite.

Keywords: polyamide 6, carbon fiber, mechanical properties, polymer/solvent ratio, mechanical interface

Članek predstavlja izdelavo laminatnega kompozita na osnovi poliamida 6, ojačanega s tkanino iz ogljikovih vlaken, z uporabo večstopenjske tehnike, ki vključuje raztapljanje poliamida v mravljinčni kislini ter impregnacijo tkanine in stiskanje pri visoki temperaturi. Razložen je vpliv razmerja poliamid/topilo na stik in mehanske lastnosti, z analizo treh masnih vsebnosti PA6 (10, 20, 30) % v mravljinčni kislini. Mehansko obnašanje dobljenega laminiranega kompozita je ocenjeno z nateznim preizkusom in s 3-točkovnim upogibnim preizkusom, presek preloma pa je analiziran z mikroskopsko tehniko, da bi ocenili stik z vlaknato osnovo in mehanizem preloma kompozita. Rezultati kažejo, da je najboljša mehanska zmogljivost dosežena pri uporabi raztopine z 20 % masnim deležem poliamida v mravljinčni kislini, ker to povzroči nastanek enakomernega polimernega sloja, ki lahko popolnoma obda vlakna tkanine in ustvari močan mehanski stik v kompozitu.

Ključne besede: poliamid 6, ogljikovo vlakno, mehanske lastnosti, razmerje polimer/topilo, mehanski stik

1 INTRODUCTION

In recent decades the use of composite structures in both aeronautic and automotive applications has increased tremendously. Nowadays, composites represent approximately 50 % of the structure of the Airbus A350 XWB and the Boeing 787 Dreamliner, resulting in 20–25 % reduction in fuel consumption.[1] Most composite structures are based on thermoset matrix fiber composites, but nowadays there is an increasing interest in replacing the thermoset with a thermoplastic matrix. This trend is due to problems arising from thermoset composites, such as the high costs of raw materials, high energy consumption, extended processing times, non-visible damage, complex repair procedures, recycling difficulties and significant amounts of scrap.[2–3] A thermoplastic matrix offers facile recycling possibilities, lower costs and more flexible processing routes[3–6], making them a promising solution for the shortcomings of thermoset composites.

Commercial carbon-fiber-fabric-based composites for the transport industry obtained using melt and solvent impregnation with thermoplastic matrixes use PEEK, PPS or PEI[7–8], which are high-performance polymers that require over 300 °C for the processing temperature, leading to high costs. This study focuses on an engineering polymer, with a high potential, i.e., polyamide 6. Most literature studies present polyamide 6 composites reinforced with short fibers (carbon, glass or aramid) processed by melt extrusion[9–12], a few studies present fabric-reinforced polyamide 6 composites[13–14], because of the technological processing difficulties arising from fabric-impregnation issues generated by the molten polymer and fiber wet out.[15] Moreover, the data concerning the optimum solution viscosity range and the optimum polymer/solvent ratio when using the solvent-impregnation method is very briefly discussed, although its importance is underlined[16–18], as the rheological properties of the matrix are important for establishing the composite's processing parameters. This paper presents the production of carbon-fiber-fabric-reinforced polyamide 6 matrix laminated composites using polymer dissolution followed by fabric solvent impregnation, solvent removal

and thermal pressing. The processing and final properties of fabric-reinforced composites depend on several factors, one of them being the viscosity of the matrix used to impregnate the fabric. In this context, the novelty of the study is represented by an optimization study concerning the PA6/formic acid (polymer/solvent) ratio's direct influence on the mechanical properties of the final composites, analyzing the solution's viscosity and its direct effect on the fiber/matrix interface and, consequently, on the failure mode of the composites. The mechanical behavior of the obtained laminated composites was evaluated using tensile and 3-point bending tests, the fracture cross-section being analyzed using microscopy techniques to evaluate the fiber-matrix interface and the composite fracture mechanism and to establish the optimum polymer content for the impregnation solution. The results indicate that at an optimum polymer/solvent ratio of 20 % of mass fractions, the obtained materials possess the highest tensile and flexural properties.

2 EXPERIMENTAL SECTION

2.1 Materials

The matrix was polyamide 6 (PA6) pellets supplied by SC ICEFS Săvineşti, while the solvent was formic acid 85 % analytical grade, purchased from Chemical Company, Romania. The reinforcing agent was a carbon-fiber-fabric twill weave (FC) produced by Chemie Craft, France, 3 K warp, with 193 g/m^2 fabric areal weight and 1.7 g/cm^3 fiber density.

2.2 Obtaining process

The procedure resembles a process involving fabric impregnation with thermoset resins, but it is adjusted to allow the use of polyamide pellets as the raw material. The dried polymer pellets were dissolved in 85 % formic acid in three different concentrations, i.e., 1(0, 20 and 30) % (polymer weight/solvent volume), under mechanical stirring for 4 h. Each ply of the carbon-fiber fabric was impregnated with the solution and stacked up in groups of five layers. The solvent was removed at room temperature for 48 h and additional traces were removed at 80–100 °C for 8 h. Each laminated composite was pressed using a CARVER hot platens press, following an established temperature program, with a linear temperature increase from 25 °C to 230 °C and 5 min dwell periods at (230, 235, 240 and 245) °C. Because the fabric layers were semi-impregnated with polymer after the solvent's removal, the high-temperature pressing did not generate impregnation difficulties that appear during standard polymer-melt impregnation because of the fiber wet-out difficulties.[19] The cooling took place under pressure down to room temperature. There were obtained laminated plates differing in the PA6 content solution used, referred to as PA6(10%)/5FC, PA6(20%)/5FC and PA6(30%)/5FC, with an average fiber volumetric ratio of 66 %, that were processed into tensile and flexural shape specimens.

2.3 Testing and characterization

The viscosity of the different concentration solutions used for the impregnation was measured using an Ubbelohde capillary-tube viscometer (Cannon CT-1000). The PA6 matrix was subjected to FTIR spectroscopy analysis (ThermoiN10 MX Mid Infrared FT-IR Microscope) operated in ATR mode and scanning electron microscopy (QUANTA INSPECT F). The carbon-fiber laminates were mechanically tested (INSTRON 5982 machine) in tensile conditions according to SR EN ISO 527-2[20] at a 5 mm/min tensile rate on dumbbell specimens and flexural tests, according to SR EN ISO 14125[21] at 2 mm/min, conventional deflection and span length on rectangular specimens. The fracture cross-section was analyzed using SEM and the fracture mode was evaluated using optical microscopy (Meiji 8500).

3 RESULTS AND DISCUSSION

3.1 Viscosity measurement

The solutions containing different contents of dissolved polymer used to impregnate the fabric has to have optimum viscosity, as it distributes the polymer through the fibers.[22] The effect of the PA6 content dissolved in formic acid on the kinematic viscosity of the solution was studied at room temperature. **Figure 1** presents the kinematic viscosity values of the solutions with three different PA6 weight contents, after 4 h of mechanical stirring. The viscosity increases dramatically with polymer content, from 34.1 mm^2/s for 10 % PA6 in formic acid to 173 mm^2/s for 20 % and 898 mm^2/s for 30 %. As the polymer content is increased, the viscosity increases exponentially by approximately five times compared to the

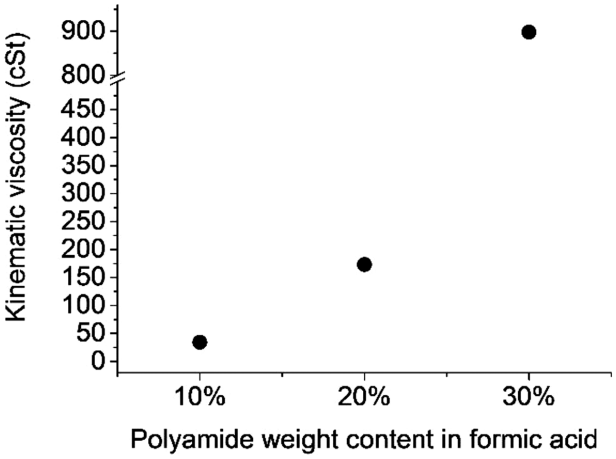

Figure 1: Kinematic viscosity as a function of polyamide 6 weight content in an 85 % formic acid solution

Slika 1: Odvisnost kinematične viskoznosti od vsebnosti poliamida 6 v raztopini 85 % mravljinčne kisline

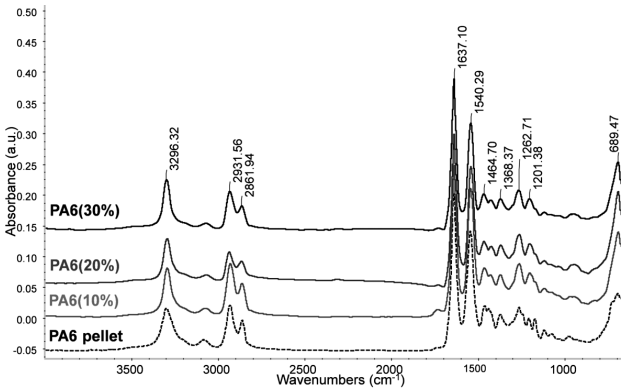

Figure 2: FTIR spectra of the pure PA6 pellet and dried samples based on different PA6 contents dissolved in 85 % formic acid: PA6 (10 %), PA6 (20 %), PA6 (30 %)

Slika 2: FTIR-spektri čistega peleta PA6 in posušenih vzorcev z različno vsebnostjo PA6, raztopljene v 85 % mravljinčni kislini: PA6 (10 %), PA6 (20 %), PA6 (30 %)

previous value. The dramatic increase for the 30 % content is due to the fact that this value is very close to the homogenous phase-formation limit of a polyamide/formic acid system.[23–27] The rheological properties affect the impregnation degree and the fiber/matrix interface. If the impregnating solution viscosity is too low, it will pass through the fabric, resulting in polymer coverings that are too thin, while a too high viscosity will not ensure uniform and large fiber-matrix contact surfaces, as any penetration through the fibers will be difficult.[28]

3.2 FTIR spectroscopy

FTIR spectroscopy was performed on polyamide films obtained after solvent removal from the three different solution concentrations to evaluate the chemical structure and the eventual solvent traces. **Figure 2** presents the spectra of the three PA6 samples compared to a pure PA6 pellet, all the spectra showing the characteristic peaks of polyamide 6.[29,30] There are no significant changes in the spectra of the samples compared with the pure pellet, as no supplementary peak appears, and there are no traces of unremoved solvent, confirming that the polyamide's chemical structure was not altered by the solvent's presence and it was fully dissolved. The small modification of the bands from (689.5, 1201.4 and 1464.7) cm^{-1} can be assigned to the restructuring of the polymer as a result of solubilization followed by crystallization.[31] The 1200 cm^{-1} and 1465 cm^{-1} peaks correspond to the amide V and CH_2 bending vibrations, respectively, in polyamide α or β form, which is commonly obtained when the processing of PA6 involves slow cooling[32], as is the case here.

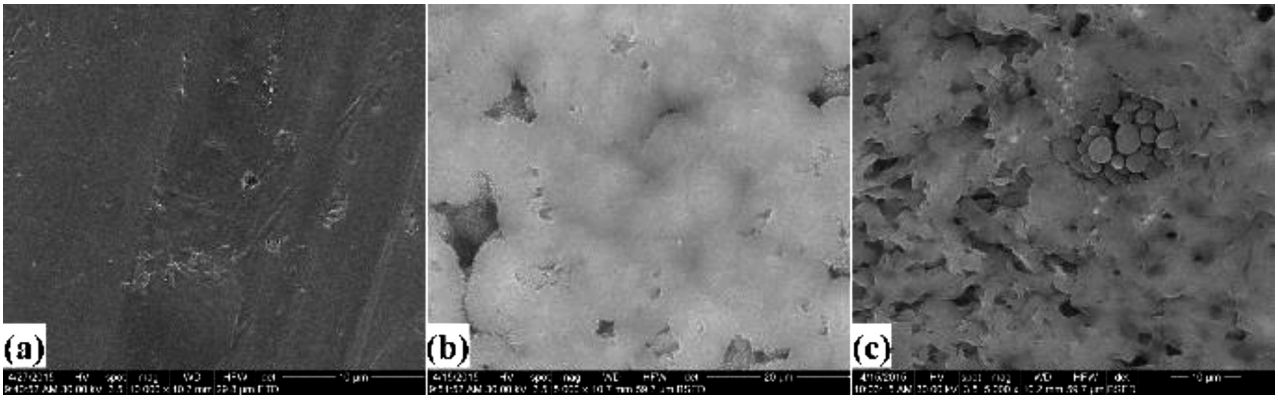

Figure 3: SEM images of matrix samples used to form the laminated composites: a) PA6(10 %), b) PA6(20 %), c) PA6(30 %)

Slika 3: SEM-posnetki osnove vzorcev, uporabljenih za laminiran kompozit: a) PA6 (10 %), b) PA6 (20 %), c) PA6 (30 %)

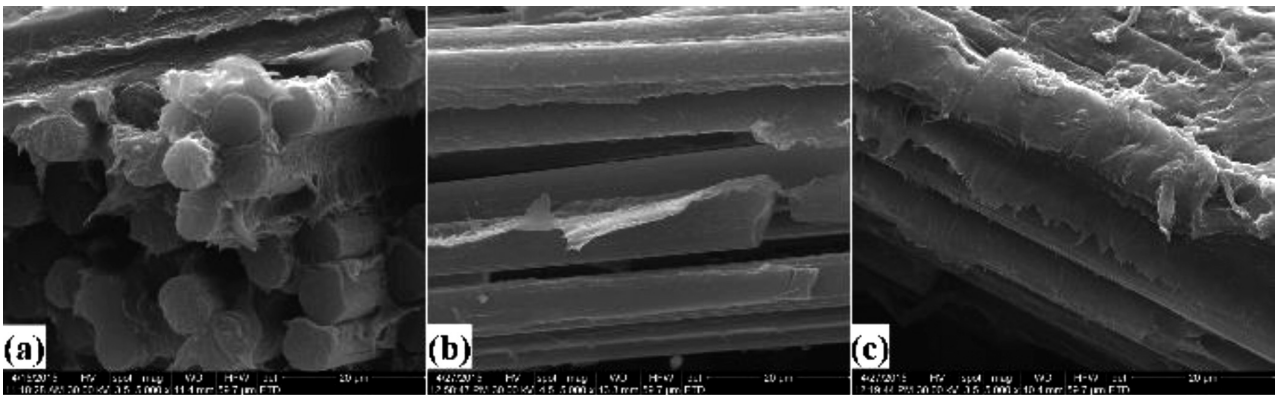

Figure 4: SEM images of the fracture cross-section of laminated composites: a), b) PA6(10%)/5FC, c) PA6(20%)/5FC

Slika 4: SEM-posnetki preseka preloma laminiranega kompozita: a), b) PA6 (10 %)/5FC, c) PA6 (20 %)/5FC

3.3 SEM analysis

SEM analyses were performed on the matrix samples in the form of films to evaluate the morphology and homogeneity. **Figure 3** presents the images of dried samples obtained after the dissolution of (10, 20 and 30) % PA6 into formic acid. As the PA6 content increased up to 30 %, there are visible areas of undissolved polymer; this higher concentration value being close to the weight content limit of PA6 in formic acid[23–26], it probably needs different process parameters for a complete dissolution (e.g., a longer homogenization time).

SEM investigations were performed on the fracture cross-section of the tensile tested laminates. **Figure 4** illustrates the samples with a matrix obtained by dissolving 10 % PA6 (**Figure 4a** and **4b**) and 20 % PA6 (**Figure 4c**). In PA6(10%)/5FC (**Figure 4a**) there are several areas where a thin polymer layer uniformly covers the fibers of the fabric, but there are also a few areas where the polymer layer is partially detached from the fiber surface and there are uncovered fibers (**Figure 4b**). The difference is significant for PA6(20%)/5FC, in which case the polymer is distributed in a solid layer that covers the entire fiber surface, but its thickness is not as uniform as in PA6(10%)/5FC. Each carbon fabric ply is covered with its own polymer layer. The polymer ductile fracture is distinguished from the fiber's fragile fracture.

3.4 Mechanical testing

Table 1 illustrates the average values of the strength and elasticity modulus, obtained after tensile and flexural testing of the obtained composites based on five carbon fabric plies. The highest mechanical performance in both the tensile and flexural testing is presented by the sample based on PA6(20%). PA6(20%)/5FC has a 60 % higher tensile strength compared to PA6(10%)/5FC, while the flexural strength is approximately 70% higher. These samples also have a superior rigidity, showing a modulus of elasticity that is higher by 35–40 %. The PA6(30%)/5FC samples showed lower tensile and flexural strengths and tensile moduli compared with PA6(20%)/5FC, but higher than the PA6(10%)/5FC, while the flexural modulus had the lowest average value for the entire series. These inconsistent results in PA6(30%)/5FC are most likely due to the high viscosity of the impregnating solution that was probably not able to uniformly distribute on the surface of the fiber fabric, supplemented by possible undissolved polymer sites, which although they were melted during thermal pressing, could also lead to non-uniform polymer layer sites at the microscopic level. These issues generate inhomogeneity and stress-concentration sites that decrease the rigidity.[33–34]

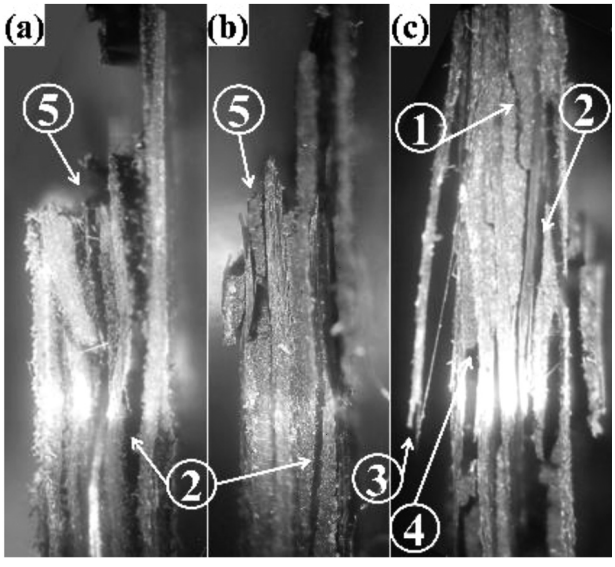

Figure 5: Fracture regions of tensile-tested specimens: a) PA6 (10 %)/5FC, b) PA6 (20 %)/5FC, c) PA6(30%)/5FC

Slika 5: Področja preloma nateznih preizkušancev: a) PA6 (10 %)/5FC, b) PA6 (20 %)/5FC, c) PA6 (30 %)/5FC

Table 1: Mechanical properties of composites based on PA6 (dissolved in different contents relative to the solvent) and five plies of carbon fiber fabric

Tabela 1: Mehanske lastnosti kompozita na osnovi PA6 (raztopljene različne količine v topilu) in petih plasti tkanine iz ogljikovih vlaken

Sample	Tensile strength (MPa)	Young's modulus (GPa)	Flexural strength (MPa)	Young's flexural modulus (GPa)
PA6(10%)/5FC	339.2	45.5	436.7	38.3
PA6(20%)/5FC	540.5	63.6	732.6	51.4
PA6(30%)/5FC	505	56.3	571.6	38.1

Overall, the mechanical results show that all the obtained carbon fabric/PA6 laminated samples are superior to the ones exhibited by long-carbon-fiber-reinforced PA6[35–37] that show a tensile strength between 240 and 300 MPa, a flexural strength between 330 and 500 MPa, and Young's modulus in the range 25–40 GPa for tensile and 20–30 GPa for flexural. Also, PA6(20%)/5FC mechanical properties are comparable with those presented by carbon-fiber-fabric-epoxy composites[38] with extended applications in aeronautics.

3.5 Fractography

Optical microscopy images were recorded on the fracture region of the laminated samples to establish the fracture mechanisms that led to the failure and to evaluate their behavior when tested under tensile and flexural loads. **Figure 5** presents the fracture region of representative specimens from each sample tested in tensile. The identified fracture mechanisms are marked, all of them being classified as classical mechanisms presented by [39–40]: (1) crack propagation, (2) layer de-bonding, (3) fiber breakage, (4) fiber pull-out, (5) ply breakage. The PA6(10%)/5FC and PA6(20%)/5FC fractures resemble as three layers are broken by fiber breakage in the same area, the fracture causing layer de-bonding to the next

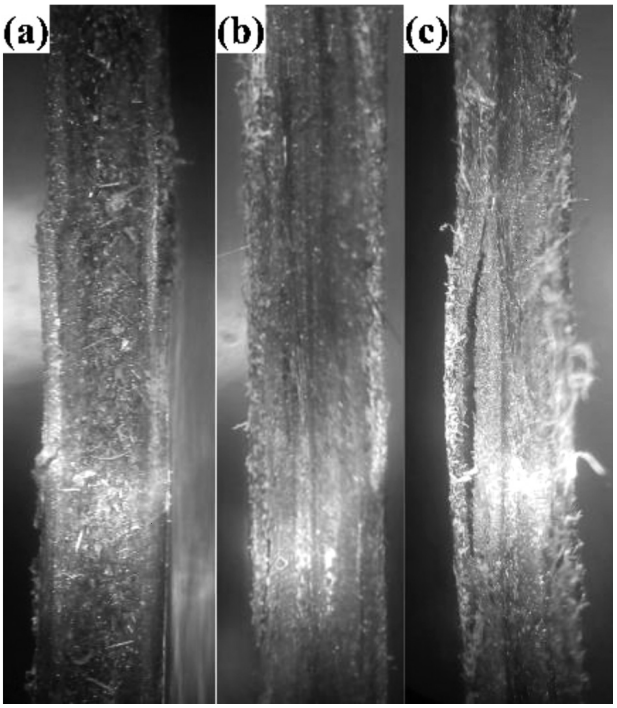

Figure 6: Fracture regions of flexural-tested specimens: a) PA6 (10 %)/5FC, b) PA6 (20 %)/5FC, c) PA6 (30 %)/5FC
Slika 6: Področje preloma upogibnih preizkušancev: a) PA6 (10 %)/5FC, b) PA6 (20 %)/5FC, c) PA6 (30 %)/5FC

layers, with more pronounced de-bonding in PA6(10%)/5FC. PA6(30%)/5FC presented the most destructive failure, involving several mechanisms including fiber pull out and interlayer crack propagation, leading to delaminated areas. This can be explained by the high viscosity of the solution that led to non-uniform matrix layers, creating stress-concentration sites. In flexural testing (**Figure 6**), PA6(10%)/5FC and PA6(20%)/5FC did not present any layer rupture until conventional deflection, but the PA6(30%)/5FC presented the rupture of one external layer that de-bonded on a longer length. It is important to mention that although PA6(10%)/5FC presented in general the lowest mechanical performance, its fracture mode was not as destructive as for PA6(30%)/5FC. The optical images complement both the mechanical test results and the SEM studies.

4 CONCLUSIONS

The study presents the production of carbon-fabric-reinforced laminated composites based on the engineering polymer polyamide 6 as the matrix using a multiple-stages technique that involves fabric solvent impregnation with a formic acid solution that contains different contents of dissolved polymer, solvent removal and high-temperature pressing. The aim of the study was to evaluate the polymer/solvent (PA6/formic acid) ratio's influence on the mechanical interface within the composite and on the mechanical properties. Three polymer contents in formic acid were used (10, 20 and 30) % weight/volume, with the rheology tests showing that the solution viscosity increases exponentially. A lower content solution led to a slightly uniform polymer layer that covered the fibers of the fabric, ensuring large contact areas, but because the thin layer was too weak, the laminates' mechanical performance was lower. The highest content solution (30 %) had an extremely high viscosity and most likely did not distribute uniformly, probably generating stress-concentration sites that resulted in a very destructive failure during the mechanical testing.

The study concludes that the optimum content is 20 % polymer dissolved into the solvent, as it leads to medium-viscosity solution that supports polymer penetration through the fibers and forms polymer layers with suitable thickness and uniformity on the fiber surface. This ensures high contact areas, a strong fiber-matrix interface and, consequently, an optimum fiber-matrix load transfer, leading to high mechanical performances in tensile and bending and failure modes that do not exhibit a high degree of delamination. The results show that at an optimum polymer/solvent ratio, these composites can represent potential solutions as materials for high mechanical performance in aeronautics and automotive applications.

Acknowledgments

This work was funded by the Sectoral Operational Programme Human Resources Development 2007-2013 of the Ministry of European Funds through the Financial Agreement POSDRU/159/1.5/S/132397 and by Romanian Ministry of Education through the PN-II-PT-PCCA-168/2012 project: "Hybrid composite materials with thermoplastic matrices doped with fibres and disperse nano fillings for materials with special purposes".

5 REFERENCES

[1] T. Chady, Airbus Versus Boeing-Composite Materials: The sky's the limit…, Le Mauricien, September 2013, http://www.lemauricien.com/, 15.6.2015

[2] M. Mrazova, Advanced composite materials of the future in aerospace industry, Incas Bulletin, 5 (**2013**) 3, 139–150, doi:10.13111/2066-8201.2013.5.3.14

[3] B. Money, Moving from thermosets to thermoplastics, Aerospace Engineering Magazine SAE International 2010, http://articles.sae.org/8547, 29.6.2015

[4] A. Pereira da Costa, E. C. Botelho, M. L. Costa, N. E. Narita, J. R. Tarpani, A review of welding technologies for thermoplastic composites in aerospace applications, Journal of Aerospace Technology and Management, 4 (**2012**) 3, 255–265, doi:10.5028/jatm.2012.04033912

[5] J. Dı´az, L. Rubio, Development to manufacture structural aeronautical parts in carbon fibre reinforced thermoplastic materials, Journal of Materials Processing Technology, 143-144 (**2003**), 342–346, doi:10.1016/S0924-0136(03)00450-3

[6] J. Pora, Composite Materials in the Airbus A380 – From History to Future, Proc. of the 13th International Conference on Composites (ICCM-13), Beijing, China 2001, 1–10

[7] A. C. Long, Composites Forming Technologies, 1st ed., CRC Press-Woodhead Publishing Ltd., Cambridge 2007, 261

[8] R. Vodicka, Thermoplastics for airframe applications: a review of the properties and repair methods for thermoplastic composites, Defense Science and Technology Organization – Australian Government of Defense, Report no. DSTO-TR-0424, 2006

[9] E. Lafranche, P. Krawczak, J. P. Ciolczyk, J. Maugey, Injection moulding of long glass fibre reinforced polyamide 6-6: guidelines to improve flexural properties, Express Polymer Letters, 1 (**2007**) 7, 456–466, doi:10.3144/expresspolymlett.2007.64

[10] H. M. Laun, Orientation effects and rheology of short glass fiber-reinforced thermoplastics, Colloid & Polymer Science, 262 (**1984**) 4, 257–269, doi:10.1007/BF01410464

[11] N. G. Karsli, A. Aytac, Tensile and thermomechanical properties of short carbon fiber reinforced polyamide 6 composites, Composites Part B, 51 (**2013**) 8, 270–275, doi:10.1016/j.compositesb.2013.03.023

[12] X. H. Zhang, H. Yang, H. Zhang, C. Y. Wang, A carbon fiber reinforced nylon 6 (CFRPA6) composite specialized for military field cooking task, Applied Mechanics and Materials, 224 (**2012**) 199–203, doi:10.4028/www.scientific.net/AMM.224.199

[13] C. E. Pelin, A. Stefan, I. Dincă, A. Ficai, G. Pelin, E. Andronescu, D. Constantinescu, G. Voicu, Polyamide 6/carbon fiber laminated composites, Journal of Optoelectronics and Advanced Materials, 17 (**2015**) 5–6, 750–756

[14] E. C. Botelho, L. Figiel, M. C. Rezend, B. Lauke, Mechanical behavior of carbon fiber reinforced polyamide composites, Composites Science and Technology, 63 (**2003**) 13, 1843–1855, doi:10.1016/S0266-3538(03)00119-2

[15] A. B. Strong, Fundamentals of composites manufacturing: materials, methods and applications, 2nd ed., Society of Manufacturing Engineers, Michigan 2008, 464

[16] S. Pillay, U. Vaidya, G. M. Janowski, Liquid molding of carbon fabric-reinforced nylon matrix composite laminates, Journal of Thermoplastic Composite Materials, 18 (**2005**) 6, 509–527, doi:10.1177/0892705705054412

[17] A. C. Long, Design and manufacture of textile composites, 1st ed., CRC Press-Woodhead Publishing Ltd., Cambridge 2006, 261

[18] S. P. Wilkinson, J. M. Marchello, N. J. Johnston, Composite Material Impregnation Unit- NASA Technical Memorandum, National Aeronautics and Space Adminstration Langley Research Center, Document no. 107751, 1993, 9–11

[19] K. K. C. Ho, S. R. Shamsuddin, S. Riaz, S. Lamorinere, M. Q. Tran, A. Javaid, A. Bismarck, Wet impregnation as route to unidirectional carbon fibre reinforced thermoplastic composites manufacturing, Plastics Rubber and Composites, 40 (**2011**) 2, 100–107, doi:10.1179/174328911X12988622801098

[20] European Standard SR EN ISO 527: Plastics – Determination of tensile properties, 2003

[21] European Standard SR EN ISO 14125: Fibre-reinforced plastics composites – Determination of flexural properties, 2001

[22] U. Vaidya, Composites for Automotive, Truck and Mass Transit: Materials, Design, Manufacturing, DEStech Publications, Pennsylvnia 2011, 82

[23] V. Gudkova, A. Krumme, Influence of addition of MWCNT on PA6 solubility in formic acid and solution viscosity properties, Functional Materials and Technologies Conference, University of Tartu and Tallinn University of Technology Doctoral School, 2013

[24] M. A. Calin, N. Khenoussi, L. Schacher, D. Adolphe, L. R. Manea, I. Gradinaru, I. Zetu, S. Stratulat, Morphological and broadband dielectric spectroscopy approaches on PA6 – CNT nanofibres, Materiale Plastice, 50 (**2013**) 4, 225–229

[25] S. S. Bhattacharya, A. Mandot, Polyamide/clay nanocomposites film, synthesis and mechanical testing, International Journal of Pure and Applied Sciences and Technology, 17 (**2013**) 2, 36–44

[26] María Monserrat de La Luz García Curiel, Polymer – Inorganic nanocomposites. Influence of colloidal silica, PhD Thesis, University of Twente, Netherlands 2004

[27] A. El-Gendi, H. Abdalla, S. Ali, Construction of ternary phase diagram and membrane morphology evaluation for polyamide/formic acid/water system, Australian Journal of Basic and Applied Sciences, 6 (**2012**) 5, 62–68

[28] T. Brocks, M. Y. Shiino, M. O. Hilário Cioffi. H. J. C. Voorwald, A. Caporalli Filho, Experimental RTM manufacturing analysis of carbon/epoxy composites for aerospace application: non-crimp and woven fabric differences, Materials Research, 16 (**2013**) 5, 1175–1182, doi:10.1590/S1516-14392013005000107

[29] K. Nishikida, J. Coates, Infrared and Raman analysis of polymers, in: Handbook of plastics analysis, Marcel Dekker Inc., New York 2003, 256–258

[30] J. Coates, Interpretation of infrared spectra, a practical approach, in: Encyclopedia of analytical chemistry, John Wiley & Sons Ltd, Chichester 2000, 10815–10837

[31] M. Porubska, O. Szöllos, A. Kónová, I. Janigová, M. Jasková, K. Jomová, I. Chodák, FTIR spectroscopy study of polyamide-6 irradiated by electron and proton beams, Polymer Degradation and Stability, 97 (**2012**) 4, 523–531, doi:10.1016/j.polymdegradstab.2012.01.017

[32] S. A. Curran, N. S. Murthy, S. M. Aharoni, H. Minor, Premelting crystalline relaxations and phase transitions in nylon 6 and 6,6, Macromolecules, 24 (**1991**) 11, 3215–3220, doi:10.1021/ma00011a027

[33] M. Dawood, M. Guddati, S. Rizkalla, Effective splices for a carbon fiber-reinforced polymer, Transportation Research Record: Journal of the Transportation Research Board, 2131 (**2009**), 125–133, doi:10.3141/2131-12

[34] D. Purslow, The shear properties of unidirectional carbon fibre reinforced plastics and their experimental determination Aeronautocal Research Council Current Papers, Paper No. 1381, 1977, 7–9

[35] Plasticomp, Product Data Sheet, Complēt® LCF50-PA6, Minnesota, USA 2014

[36] Plasticomp, Product Data Sheet, Complēt® LCF30-PA6, Minnesota, USA 2014

[37] RTP Company, Product Data Sheet & General Processing Conditions, RTP 287 A Nylon 6 (PA) Carbon Fiber, Minnesota, USA 2014

[38] M. C. Campos, C. A. Soufen, M. P. Bueno, M. Imaizumi, Comparative study of mechanical properties of woven of carbon fiber twill and plain weave in laminates with epoxy matrix, 2nd Brazilian Conference on Composite Materials – BCCM2, São José dos Campos-SP, Brazil 2014

[39] S. K. Deb & Chiranjeevee, Revealing of failure modes of FRP composite by microscopic technique, Bachelor's Degree Thesis, Department of Metallurgical and Materials Engineering, National Institute of Technology Rourkela 2008

[40] E. S. Greenhalgh, M. J. Hiley, Fractography of polymer composites: Current status and future issues, Proc. of the 13th European conference on composite materials (ECCM13), Stockholm, Sweden 2008

UDK 620.1:621.926:621.315.612:621.742.48
Original scientific article/Izvirni znanstveni članek

ISSN 1580-2949
MTAEC9, 50(5)729(2016)

EVALUATION OF THE GRINDABILITY OF RECYCLED GLASS IN THE PRODUCTION OF BLENDED CEMENTS

OCENA SPOSOBNOSTI DROBLJENJA RECIKLIRANEGA STEKLA PRI PROIZVODNJI MEŠANIH CEMENTOV

Karel Dvořák[1], Dušan Dolák[1], Dalibor Všianský[2], Petr Dobrovolný[1]

[1]Brno University of Technology, Faculty of Civil Engineering, Veveří 331/95, 602 00 Brno, Czech Republic
[2]Masaryk University, Faculty of Science, Kotlářská 267/2, 611 37 Brno, Czech Republic
dolak.d@fce.vutbr.cz

Prejem rokopisa – received: 2015-07-01; sprejem za objavo – accepted for publication: 2015-09-14

doi:10.17222/mit.2015.184

The replacement of primary raw materials in cement production is a current topic. Potentially usable raw materials include recycled glass. The disadvantage of glass is its tendency to aggregate. The conventional method for the production of blended cement is separate grinding and then homogenizing the components. However, in this case aggregated fine glass in the cement composites acts only physically and mechanically as a filler rather than as an active pozzolan. An interesting option to prevent the formation of aggregates formed from glass is co-grinding. This procedure is not very common in practice. Various ingredients of blended cements have widely different grindabilities, and it is therefore better to grind them separately. The aim is to compare the co-grinding and separate grinding of a combination of Portland clinker and recycled glass. The grindability was tested on clinker, glass, and blended cements prepared by co-grinding and by separate grinding. The results of the experiment show that by co-grinding the components of blended cement with the addition of 20 % of recycled glass as a pozzolan, a synergy effect caused by the various mechanical properties of the components occurs. The aggregation of grains is less significant than during separate grinding and it leads to a better grinding effect. This knowledge can by utilized in the design and processing of new blended cements. Also, co-milling the glass-cement system can eliminate the stage of homogenization, and, therefore save energy.

Keywords: grindability, Portland clinker, recycled glass

Tema članka je nadomeščanje primarnih surovin pri proizvodnji cementa. Potencialno uporabno surovino predstavlja reciklirano steklo. Pomanjkljivost stekla je, da ima nagnjenost k sprijemanju. Običajna metoda proizvodnje mešanega cementa je ločeno drobljenje in homogenizacija sestavin. V tem primeru drobnozrnato steklo v cementnih mešanicah deluje samo fizikalno in mehansko kot polnilo in ne kot aktiven pozolan. Dodatno mletje je pomembno za preprečevanje nastanka skupkov stekla. Vendar pa ta postopek ni tako pogost v praksi. Različne sestavine cementne mešanice se različno drobijo in je zato bolje, da se jih drobi ločeno. Namen študije je primerjati dodatno mletje in ločeno mletje kombinacije Portland klinkerja in recikliranega stekla. Mletje je bilo preizkušeno na klinkerju, steklu in mešanici cementov, pripravljenih z dodatnim mletjem in z ločenim mletjem. Rezultati preizkusov so pokazali, da se pri istočasnem mletju mešanic cementov z dodatkom 20 % recikliranega stekla kot pozolana, pojavi sinergijski pojav zaradi različnih mehanskih lastnosti sestavin. Združevanje zrn je manj izrazito kot pa pri ločenem mletju in povzroči boljši učinek mletja. To dejstvo je mogoče uporabiti pri načrtovanju in izdelavi novih mešanic cementov. Torej se lahko z istočasnim mletjem sistema steklo-cement, odpravi fazo homogenizacije in s tem prihrani energijo.

Ključne besede: sposobnost mletja, portlandski klinker, reciklirano steklo

1 INTRODUCTION

Secondary raw materials represent an ever more frequent replacement for primary raw materials in the production of building materials. The area of cement production is no exception. In current practice, blended cements are applied increasingly more often. In these cements, the Portland clinker is replaced by hydraulically active compounds or agents with pozzolanic properties.[1–3] Glass is chemically and mineralogically very close to traditional pozzolans. Therefore, various types of recycled glass may be potentially interesting raw materials for the production of blended cements. Various authors have described the behavior of finely ground glass in cement composites.[4,5] However, due to a considerable ability to agglomerate, the recycled glass used as an additive for the cement composite is not reactive enough and acts only physically-mechanically as a filler.[4] The common production process for blended cements is separate grinding of the individual components and their subsequent homogenization. This procedure is common in the production of blast-furnace slag cements. In this case the procedure is advantageous because Portland cement clinker and blast-furnace slag have very different grindabilities and it is therefore preferable to grind them separately, and subsequently to homogenize.[6] As noted above, fine glass powder exhibits a significant ability for aggregation, which greatly complicates the homogenization with Portland cement. Therefore, the traditional approach of separate grinding and subsequent homogenization seems to be less suitable in the case of a glass-cement system. An interesting option to prevent the formation of agglomerates with pure glass is co-grinding of the glass and clinker. The content of SiO_2 in recycled glass is only in amorphous form and the hardness is 7 on the Mohs scale. The standard alite

clinker contains four main minerals, and their weighted average hardness is between 6 and 7 on the Mohs scale.[7] However, the recycled glass is much more fragile, which means the grindability of both components could be very similar. Various authors have chosen different methods to assess grindability. Most methods are based on an evaluation of the ratio of the energy consumption and refinement of the material.[8–12] An interesting approach is to evaluate the grindability by using particle size distribution curves.[6] The aim was to assess whether in the case of a cement-glass system, co-grinding of the component is more advantageous than separate grinding with subsequent homogenization. The selected approach was to monitor and compare the grindability of the individual components as well as the mix. The method of monitoring the impact of the constant grinding time on the particle size distribution curves and specific surface area was chosen for the experiment.

2 MATERIALS AND METHODS

For monitoring the grindability, recycled glass and Portland cement were used. The chemical composition of the recycled glass was determined by traditional chemical analysis. The modified Chapelle test method[13] was used for the pozzolanic activity determination. The modified Chapelle test consists of the reaction of pozzolan and freshly annealed CaO in an aquatic environment at 93 °C for 24 h. The reaction takes place in a tightly sealed stainless-steel vessel and the suspension is stirred by an electromagnetic stirrer. The result is expressed as the amount of $Ca(OH)_2$ bound in mg per 1 g of pozzolan. The density of the recycled glass was determined by automatic pycnometer Micromeritics AccuPyc II 1340. For the measurement of the specific surface according to Blaine, an automatic PC-Blaine-Star device was used to measure the cell capacity of 7.95 cm^3. The determination was performed three times to eliminate errors. The morphology of the particles was determined by scanning electron microscope (SEM). A Tescan MIRA 3 XMU SEM with a secondary-electron detector was used. The Portland cement was prepared in a laboratory ball mill by co-grinding of the Portland clinker from cement plant Hranice and the chemo-gypsum Pregips in the ratio 95/5. Milling was carried out to the same specific surface area that was measured on the recycled glass. The chemical composition, the density, the specific surface area, and morphology of the particles were also determined. The blended cement was prepared by co-milling Portland clinker, gypsum and recycled glass in the ratio 76/4/20. Milling was carried out to the same specific surface area that was measured on the recycled glass. As in the previous case, chemical composition, density, specific surface area and morphology of the particles were also determined. The milling in this phase of the experiment was always carried out at a total dose of 5 kg in a Brio OM 20 ball mill at a speed of 40 min^{-1}. The grinding of the recycled glass, the Portland cement and the blended cement for determining the grindability was performed in a Fritsch Pulverisette 6 planetary mill at 500 min^{-1}. A steel vessel of 500 mL and 25 steel grinding balls of 20 mm diameter and a mass of 180 g of material were always used. The grinding times were (1, 2, 3 and 5) min. Then, the particle size distribution was performed on each of these samples using a Matest Air jet sieve. The sieves mesh size were (0.010, 0.020, 0.041, 0.063, 0.090 and 0.125) mm. The Blaine specific surface area and morphology of the particles by SEM were determined on all the samples ground for 5 min. A simple calculation using weighted-average values of the surface areas separately milled components was made to facilitate the grindability comparison, Equation (1):

$$S_{BC} = 0.8 \cdot S_{PC} + 0.2 \cdot S_{GR} \quad (1)$$

Where S_{BC} is the theoretical specific surface area of the blended cement, S_{PC} is the specific surface area of the Portland cement and S_{RG} is the specific surface area of the recycled glass. Subsequently, a sample of the blended cement was prepared by homogenization of the separately ground components in the same proportions. Homogenization of the sample was performed using a laboratory homogenizer for 1 h. On the resulting samples the specific surface area according to Blaine was determined. The results were compared with the calculation.

3 RESULTS

Chemical compositions of the clinker and gypsum are summarized in **Tables 1** and **2**.

Table 1: Partial chemical composition of clinker
Tabela 1: Parcialna kemijska sestava klinkerja

Component	SiO_2	CaO	Al_2O_3	Fe_2O_3	SO_3	Others
Content (%)	20.29	65.33	5.21	5.04	0.79	3.34

Table 2: Partial chemical composition of gypsum
Tabela 2: Parcialna kemijska sestava mavca

Component	$CaSO_4 \cdot 2H_2O$	H_2O	$CaSO_4$	Others
Content (%)	84.00	11.00	2.40	2.60

The chemical composition of the selected clinker is typical for Portland clinkers. In the case of gypsum, it is highly pure with a relatively high humidity; therefore, it should be dried for the cement preparation to reduce the humidity to under 5 % according to ČSN 721206.

Chemical composition of the recycled glass is summarized in **Table 3** and its pozzolanic activity is indicated in **Table 4**.

Table 3: Partial chemical composition of the recycled glass
Tabela 3: Parcialna kemijska sestava recikliranega stekla

Component	SiO_2	CaO	Al_2O_3	K_2O	Na_2O	Others
Content (%)	69.25	8.09	0.83	0.41	16.44	4.98

Table 4: Pozzolanic activity of recycled glass with different specific surface area
Tabela 4: Pozolanska aktivnost recikliranega stekla z različno specifično površino

Specific surface area (m^2 kg^{-1})	244
Pozzolanic activity (mg $Ca(OH)_2$/g pozzolan)	1112

The chemical and mineralogical compositions of the recycled glass resemble a classic pozzolan. The sample of recycled glass with a specific surface area of 244 m^2 kg^{-1} reached a pozzolanic activity of 1112 mg $Ca(OH)_2$/1 g in a modified Chapelle test.

An overview of the properties of the raw materials on the grindability are included in **Table 5**. All the pre-grinding was made on a ball mill to ensure roughly the same surface area as the recycled glass.

Table 5: Overview of input materials
Tabela 5: Pregled vhodnih materialov

Material	Compo-nents	(%)	Pre-ground	Density (kg/m^3)	Specific surface area (m^2 kg^{-1})
Portland cement	Clinker	95	Yes	3081	250
	Gypsum	5			
Glass	Glass	100	No	2458	244
Blended cement	Clinker	76	Yes	2952	247
	Gypsum	4			
	Glass	20			

All the input materials were then ground in a planetary mill for (1, 2, 3 and 5) min with a rotational speed of 500 min^{-1}. Each sample was then examined with a sieve analysis. The results are summarized in **Figures 1** to **5**.

From the size distribution curves of the input materials it is evident that although the specific surface area is similar, the recycled glass is much coarser. This is caused by the different shapes of the grains in the recy-

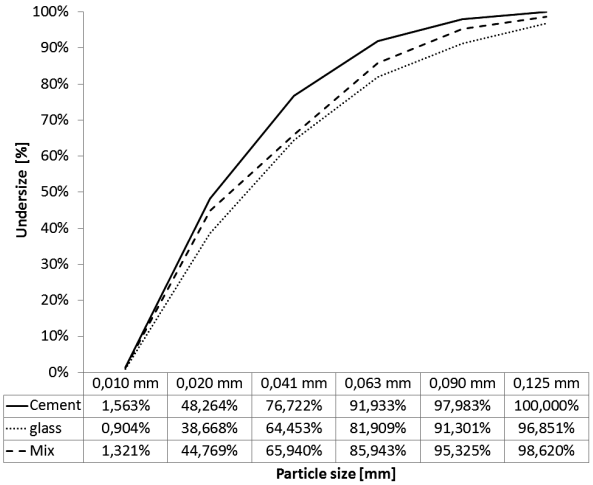

	0,010 mm	0,020 mm	0,041 mm	0,063 mm	0,090 mm	0,125 mm
Cement	1,563%	48,264%	76,722%	91,933%	97,983%	100,000%
glass	0,904%	38,668%	64,453%	81,909%	91,301%	96,851%
Mix	1,321%	44,769%	65,940%	85,943%	95,325%	98,620%

Figure 1: Size distribution of input materials
Slika 1: Razporeditev velikosti vhodnih materialov

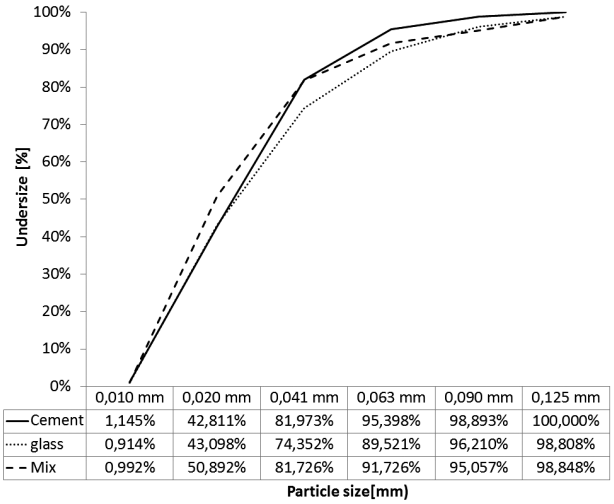

	0,010 mm	0,020 mm	0,041 mm	0,063 mm	0,090 mm	0,125 mm
Cement	1,145%	42,811%	81,973%	95,398%	98,893%	100,000%
glass	0,914%	43,098%	74,352%	89,521%	96,210%	98,808%
Mix	0,992%	50,892%	81,726%	91,726%	95,057%	98,848%

Figure 2: Size distribution after 1 min
Slika 2: Razporeditev velikosti po1 min

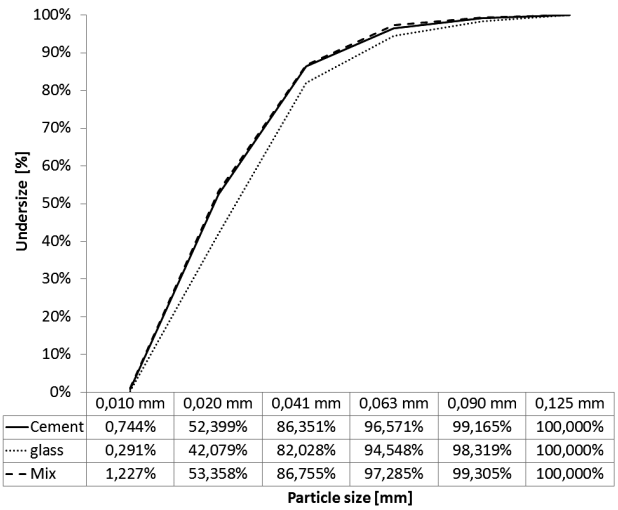

	0,010 mm	0,020 mm	0,041 mm	0,063 mm	0,090 mm	0,125 mm
Cement	0,744%	52,399%	86,351%	96,571%	99,165%	100,000%
glass	0,291%	42,079%	82,028%	94,548%	98,319%	100,000%
Mix	1,227%	53,358%	86,755%	97,285%	99,305%	100,000%

Figure 3: Size distribution after 2 min
Slika 3: Razporeditev velikosti po 2 min

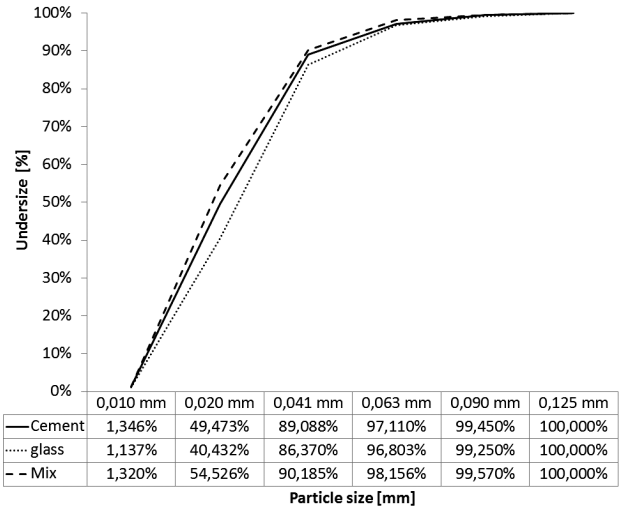

	0,010 mm	0,020 mm	0,041 mm	0,063 mm	0,090 mm	0,125 mm
Cement	1,346%	49,473%	89,088%	97,110%	99,450%	100,000%
glass	1,137%	40,432%	86,370%	96,803%	99,250%	100,000%
Mix	1,320%	54,526%	90,185%	98,156%	99,570%	100,000%

Figure 4: Size distribution after 3 min
Slika 4: Razporeditev velikosti po 3 min

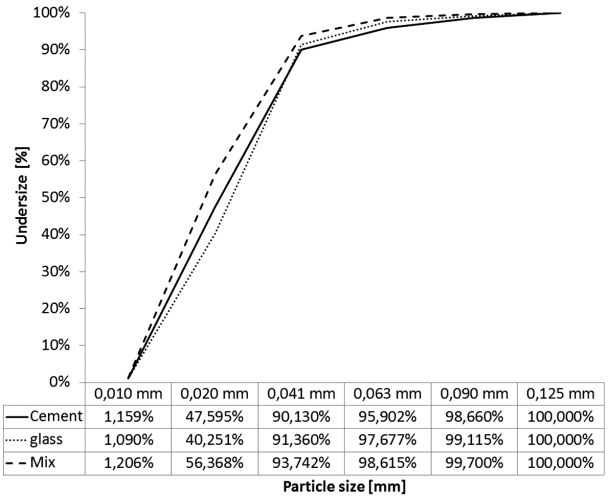

	0,010 mm	0,020 mm	0,041 mm	0,063 mm	0,090 mm	0,125 mm
Cement	1,159%	47,595%	90,130%	95,902%	98,660%	100,000%
glass	1,090%	40,251%	91,360%	97,677%	99,115%	100,000%
Mix	1,206%	56,368%	93,742%	98,615%	99,700%	100,000%

Figure 5: Size distribution after 5 min
Slika 5: Razporeditev velikosti po 5 min

cled glass, Portland cement and blended cement, as seen in **Figures 6** to **8**. The curves of the particle size distribution of the grinded materials indicate that the grindability of the recycled glass and the Portland cement is similar for selected time intervals. However, by co-grinding these materials, the grinding effect was stronger.

The images taken by scanning electron microscopy before and after the grinding of the components are

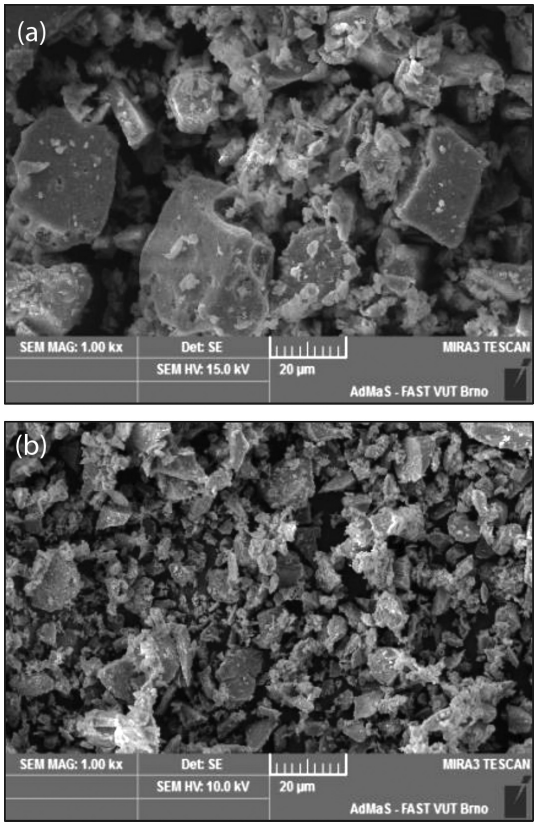

Figure 6: SEM image of BC: a) before and b) after grinding
Slika 6: SEM-posnetek BC: a) pred in b) po mletju

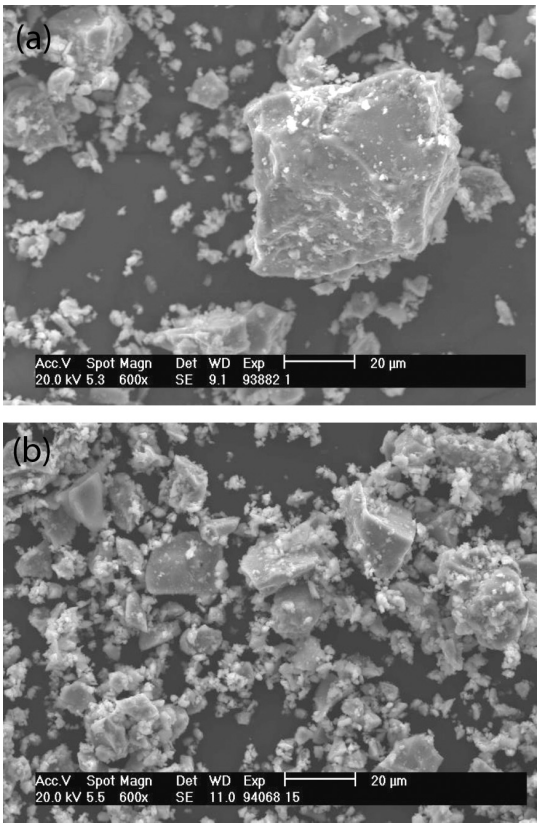

Figure 7: SEM image of PC: a) before and b) after grinding
Slika 7: SEM-posnetek PC: a) pred in b) po mletju

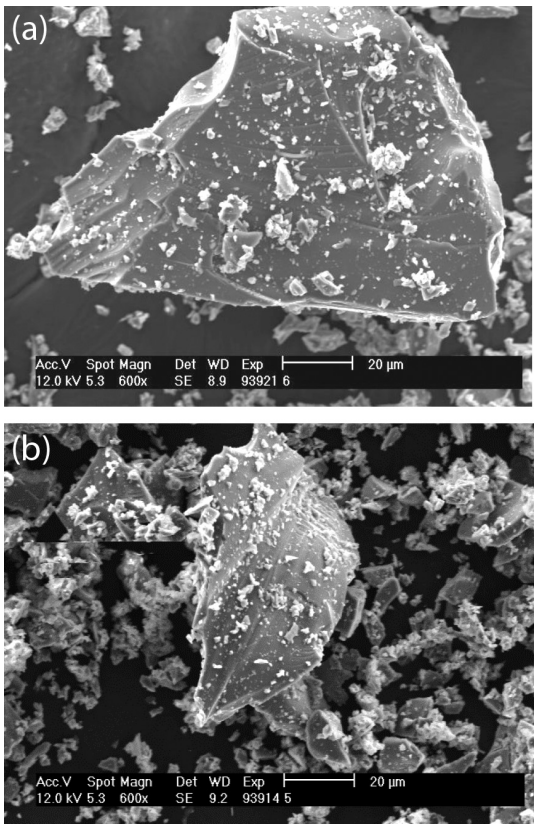

Figure 8: SEM image of RG: a) before and b) after grinding
Slika 8: SEM-posnetek RG: a) pred in b) po mletju

shown in **Figures 6** to **8**. BC is an abbreviation for blended cement, PC for Portland cement and RG for recycled glass.

The Blaine specific surface area was determined on all the samples ground for 5 min. The results of the measurement and the calculated specific surface area are summarized in **Table 6**.

$$S_{BC} = 0.8 \cdot S_{PC} + 0.2 \cdot S_{GR}$$

$$S_{BC} = 0.8 \cdot 500 + 0.2 \cdot 517 = 503.4$$

Table 6: Change of specific surface area before and after 5 min of grinding
Tabela 6: Sprememba specifične površine, pred in po 5 min mletju

Component	Cement	Glass	Blended c (together)	Blended c (separate)	Blended c (calculation)
Specific surface area before g (m^2/kg)	250	244	247	–	–
Specific surface area after g (m^2/kg)	500	517	532	504	503.4

Specific surface area of separate grinded blended cement corresponds with the calculation. In the case of co-grinded blended cement the specific surface area is considerably higher.

4 DISCUSSION

The chemical and mineralogical compositions of the recycled glass resemble a classic pozzolan. The sample of recycled glass with a specific surface area of 244 m^2 kg^{-1} reached a pozzolanic activity of 1112 mg $Ca(OH)_2$/1 g in a modified Chapelle test. The pozzolan activity of the chosen recycled material can be rated as high, because classic pozzolans such as fly ash reach values of 700 mg to 850 mg.[14] Therefore, it can be stated that this is a promising pozzolanic material. The chemical composition of the selected clinker is typical for Portland clinkers with a large amount of tricalcium silicate.[7] In the case of gypsum, it is a highly pure by-product gypsum from the production of titanium dioxide.

The grain morphology of the Portland cement and glass, which were adjusted to the same initial surface area and were used as the input for the grindability tests, are significantly different. Unlike Portland cement, recycled glass consists of grains with a substantially sharp-edged morphology. This grain shape can be explained by the high fragility and amorphous structure of the glass.[15] From the measured values of the balances of the raw materials on the sieves, the statement can be made that with a low surface area and larger grain size, Portland cement is milled the best. Glass is indeed fragile, but has a higher tendency to aggregate the particles.[15,16] This phenomenon can affect the outcome of the determination of the particle size distribution during the early stages of grinding. As shown in **Figures 2** to **5**, with increasing surface area, blended cement is ground more intensively than recycled glass or Portland cement. Increased efficiency co-milling is caused by the different mechanical properties of the clinker and the glass.[7,15] When recycled glass is milled separately, it preserves the delicate character and this leads to its rapid disintegration. Nevertheless, the distinctive ability of aggregation and agglomeration negatively affects the final particle size distribution, as evidenced in **Figure 8**. In the case of clinker, the ability to aggregate and agglomerate is lower.[17] Because of the chemical and mineralogical compositions of the grains they are more able to compensate for the impacts of the grinding elements. This affects the particle size distribution. The co-milling of cement and recycled glass leads to a better milling effect, since the above-described phenomena are compensated, plus the clinker grains are functioning as an additional grinding medium. This is reflected not only in the resulting particle size distribution obtained on specific surfaces, but also in a better homogeneity of mixed cement. The synergistic effect of co-milling in the case of cement glass was proved by the simple calculation model of weighted averages for the results of the separately ground materials' surface areas. The result of the calculation, 503.4 m^2 kg^{-1}, correlated well with the experimentally measured value of the specific surface area of the blended cement composed of separately milled components, i.e., 504 m^2 kg^{-1}. By joint grinding of the blended cement in same grinding conditions, a much larger specific surface area has been achieved, i.e., 532 m^2 kg^{-1}.

5 CONCLUSION

The pozzolanic activity of the fine recycled glass is relatively high. It reaches higher levels of pozzolanic activity than traditional ash, and on a significantly lower surface area. The distribution of particles of recycled glass and Portland cement measured by sieve analysis with separate grinding is similar. The synergistic effect of co-milling was demonstrated in comparison with a blended cement prepared by the homogenization of separately ground materials. This phenomenon is caused by the fact that the negatives associated with separate grinding of the individual materials are suppressed. Another advantage of co-milling the glass-cement system is energy saving, by eliminating the stage of homogenization. Based on the results obtained, recycled glass appears as a potentially useful pozzolan for the preparation of blended cements by co-milling with cement.

Acknowledgment

This work was financially supported by project number: 15-08755S "Study of effects of samples preparation on inorganic binders final properties" and project No. LO1408 "AdMaS UP – Advanced Materials, Structures and Technologies", supported by Ministry of Education,

Youth and Sports under the National Sustainability Programme I.

5 REFERENCES

[1] C. Meyer, Y. Xi, Use of recycled glass and fly ash for precast concrete, Journal of Materials in Civil Engineering, 11 (**1999**), 89–90, doi:10.1061/(ASCE)0899-1561(1999)11:2(89)

[2] D. Gazdič, Slag-Sulphate Binder Preparation, Advanced Materials Research, 818 (**2013**), 68–71, doi:10.4028/www.scientific.net/amr.818.68

[3] M. Keppert, P. Reiterman, Z. Pavlík, M. Pavlíková, M. Jerman, R. Černý, Municipal solid waste incineration ashes and their potential for partial replacement of Portland cement and fine aggregates in concrete, Cement Wapno Beton, 15/77 (**2010**) 4,187–193

[4] T. Melichar, J. Přikryl, P. Matulová, Substituce pojiva v cementových kompozitech jemně mletou recyklovanou sklovinou s ohledem na životní prostředí, Beton TKS, 9 (**2009**) 3, 50–55

[5] A. Khmiri, B. Samet, M. Chaabouni, A cross mixture design to optimise the formulation of a ground waste glass blended cement, Construction and Building Materials, 28 (**2012**) 1, 680–686, doi:10.1016/j.conbuildmat.2011.10.032

[6] M. Öner, A study of intergrinding and separate grinding of blast furnace slag cement, J. Cement and Concrete Research, 30 (**2000**), 473–480, doi:10.1016/S0008-8846(00)00197-6

[7] P. C. Hewlett, Lea's Chemistry of Cement and Concrete, 4 (**2003**), Elsevier

[8] F. C. Bond, Crushing and grinding calculations Part I, British Chemical Engineering, 6 (**1961**), 378-–385

[9] F. C. Bond, Crushing and grinding calculations Part II, British Chemical Engineering, 6 (**1961**), 543–634

[10] G. Mucsi, Fast test method for the determination of the grindability of fine materials, Chemical Engineering Research & Design, 18 (**2008**), 395–400, doi:10.1016/j.cherd.2007.10.015

[11] N. Magdalinovic, Calculation of energy required for grinding in a ball mill, Int J Miner Process, 25 (**1989**), 41–46, doi:10.1016/0301-7516(89)90055-0

[12] R. F. Yap, J. L. Sepulveda, R. Jauregui, Design And Installation Of Comminution Circuits, Chapter 12 – Determination of the bond work index using an ordinary laboratory batch ball mill (2008)

[13] R. Largent, Estimation de l'activité pouzzolanique. Bull. Liaison Labo. P. et Ch., 93, (**1978**), 61–65

[14] J. Pokorný, M. Pavlíková, E. Navrátilová, P. Rovnaníková, Z. Pavnlík, R. Černý, Application of a-SiO_2 Rich Additives in Cement Paste, Applied Mechanics and Materials, 749 (**2015**), 362–367, doi:10.4028/www.scientific.net/AMM.749.362

[15] E. Le Bourhis, Glass: Mechanics and Technology, Wiley VCH, 2007

[16] W. Pietsch, Agglomeration Processes: Phenomena, Technologies, Equipment, Wiley VCH, 2008

[17] S. Sohoni, R. Sridhar, G. Mandal, The effect of grinding aids on the fine grinding of limestone, quartz and Portland cement clinker, Powder technology, 67 (**1991**), 3, 277–286, doi:10.1016/0032-5910(91)80109-V

UDK 67.017:666.122.3:666.7
Original scientific article/Izvirni znanstveni članek

ISSN 1580-2949
MTAEC9, 50(5)735(2016)

RHEOLOGICAL PROPERTIES OF ALUMINA CERAMIC SLURRIES FOR CERAMIC SHELL-MOULD FABRICATION

REOLOŠKE LASTNOSTI GOŠČE IZ GLINICE ZA IZDELAVO KERAMIČNIH KALUPOV

Joanna Szymańska, Paweł Wiśniewski, Marcin Małek, Jarosław Mizera

Warsaw University of Technology, Faculty of Materials Science and Engineering, Woloska Street 141, 02-507 Warsaw, Poland
joanna.szymanska.pl@gmail.com

Prejem rokopisa – received: 2015-07-01; sprejem za objavo – accepted for publication: 2015-09-15

doi:10.17222/mit.2015.188

This research is about the properties of ceramic slurries prepared from hydrous nano-alumina-based binder and a corundum matrix used for fabricating the prime coat of ceramic shell moulds. Solid-state alumina powders with different granulations were used. The modification of the technological properties of the prepared slurries was based on additions of a polyacrylic binder with different amounts of polymer with respect to the alumina for different powder ratios. The slurries were prepared and tested in a mechanical mixer. During the slurry preparation (within 96 h), the plate weight, Zahn cup 4# viscosity and dynamic viscosity were controlled. The morphology and chemical properties of corundum powders and polymer were characterized with SEM and powder-grain-size distribution. The obtained results of the corundum-based ceramic slurries indicate that the application of a polymeric binder with various concentrations based on nano-alumina oxides causes different properties in comparison to the other commonly used binders.

Keywords: ceramic slurries, investment casting, shell moulds, alumina powder

Raziskava obsega lastnosti keramičnih gošč, pripravljenih iz nanogliničnega veziva na vodni osnovi in korundne osnove, uporabljenih za prvo prevleko pri izdelavi keramičnih tankostenskih form. Uporabljen je bil prah glinice v trdnem stanju, z različno zrnatostjo. Spreminjanje tehnoloških lastnosti pripravljene gošče je temeljilo na dodatku poliakrilnega veziva z različno vsebnostjo polimerov, glede na glinico pri različnih razmerjih praha. Gošče so bile pripravljene in preizkušene v mehanskem mešalniku. Med pripravo gošče (v okviru 96 h), je bila kontrolirana teža plošč, viskoznost 4# z Zahn potopnim viskozimetrom in dinamična viskoznost. Morfologija in kemijske lastnosti korundnih prahov in polimerov so bile določene s SEM in z razporeditvijo velikosti zrn. Dobljeni rezultati keramičnih gošč na osnovi korunda kažejo, da se z uporabo polimernega veziva in različne koncentracije nanoglinice, doseže različne lastnosti v primerjavi s standardno uporabljanimi vezivi.

Ključne besede: keramična gošča, precizijsko litje, tankostenska forma, glinica v prahu

1 INTRODUCTION

The investment-casting process is commonly applied in the manufacturing of the materials for the aviation, energy and military industries. The limiting components (flight safety parts) such as aircraft turbine blades characterized by complicated shapes are cast with the Bridgman method.[1] A commonly applied technique is the lost-wax processing including the use of ceramic shells. It determines the precise shape, dimensional accuracy, appropriate structure and metallurgic purity of designed parts. So far, ceramic shell moulds were fabricated on the basis of colloidal silica. However, the presence of SiO_2 in the prime coat during the Ni- or Co-superalloy casting causes a reaction with the liquid metal at a high temperature, inducing an oxidation of the reactive metal such as Hf. Such an adverse phenomenon reduces the quality of the properties of cast parts, affecting its exploitation time.[2]

The basic components for a ceramic slurry are binders and fillers in the form of ceramic powders and supportive materials. A commonly used binder is hydrolyzed tetraethylorthosilicate together with organic compounds of silicon.[3] However, pure ethyl silicate does not have the binding capacity. Water-based binders dry more slowly than alcohol-based ones. Consequently, there is a time elongation enabling the control of the surface smoothness, permeability, strength and dimensional stability of the model.[4,5]

A proper selection of powder for ceramic shell moulds and their parameters such as the kind, shape and size of particles affect the final characteristics of the cast elements.[6] Ceramic powders present a thermal resistance, a slight thermal expansion and a lack of polymorphic transitions.

Deflocculants, softeners and surfactants mainly determine the rheological properties of ceramic slurries.[3]

It was found that a nano-Al_2O_3-based binder does not react with Ni-alloy components. Moreover, such a binder demonstrates a higher melting point and a larger surface area than other inorganic solvents. It is also characterized by an improved dispersion of the particles in water, thus allowing the control of rheological properties by preventing the sedimentation of heavy particles in a ceramic slurry.[6,7] This is why such a binder can be applied instead of the colloidal silica-based binder.

The main aim of the following research was to examine and define the properties of a nano-aluminum-oxide-based binder and a corundum matrix using a polymeric binder with various concentrations.

2 MATERIALS AND EXPERIMENTAL METHODS

The subject of this research was a powder of Al_2O_3 with granulation of 0–30 and 200 mesh (Treibacher) characterized by the average size of 11.79 and 45.00 μm, respectively. Solvent, binder and a hydrous polymer were dispersed in colloidal Al_2O_3 with a particle size of 16 nm (Imerys, Evonik). The additive material applied to modify the rheological properties of the slurry was a poly acrylic polymer (Imerys, Evonik).

Ceramic slurries with a solid phase content of 72.5 % by weight and polymer amounts of (6, 10, 15) % mass fractions with respect to the alumina for different powder ratios of 35:65 and 65:35 (200:030 mesh) were prepared in a mechanical mixer within 96 h with a speed of 160 min^{-1}. During the slurry preparation, the pH (with the use of a pH meter), plate weight and Zahn cup 4# viscosity were checked every 24 h. These measurements are fundamental for the investment-casting industry. After 96 h of mixing, rheological properties such as dynamic viscosity were also defined with a *Brookfield DV-II* rheometer with the spindle rotating in a speed range of 1–200–1 min^{-1}. All the measurements were taken in an air-conditioned lab at 21 °C.

To characterize the morphology of the corundum powders and the polymer, SEM images were taken with a *Hitachi SU70* scanning electron microscope and a BSE detector at a voltage of 5 kV. A particle-size test was done using a *Horiba LA-950* laser diffraction device (Hitachi, Japan).

The plate test was based on immersing the plate (7.5×7.5 cm) in the moulding mass and estimating its weight after 120 s.

3 RESULTS AND DISCUSSION

The morphology of the powder based on the SEM analysis of #200 and #0–30 indicated typical structures of molten powders with angular-shaped particles.

The obtained results shown on **Figure 1** prove that the lowest plate values correspond to 6 % of mass fractions of the polymer content for a powder ratio of 35:65. The largest ones were noticed for the slurries with 6 and 15 % of mass fractions of the polymer content at a proportion of 65:35. The highest plate stability was obtained for the slurries with 15 % of mass fractions of polymer addition (65:35) and 10 % of mass fractions of polymer content (35:65). The values of the plate weight controlled on the last days of the measurements were in a range of 1.7–2.4 g. The measurements of the plate weight revealed a correlation with the polymer content: a 6 % of mass fraction of the polymer addition resulted in the highest weight value, equal to 2.40 g; this value was slightly lower in the case of a 15 % of mass fraction of the polymer content and the lowest for a 10 % of mass fraction of the polymer amount.

Zahn Cup 4# measurements showed (**Figure 2**) the lowest values (13–15 s) for the slurry with the 6 % of mass fraction of the polymer at the 35:65 ratio. The highest viscosity was noticed for the slurry with the 15 % of mass fraction at a powder ratio of 65:32. In this case, there was also a rapid viscosity change from 32 s (noticed on the first day) to 21 s after 96 h. The viscosity was stable during the whole ceramic-slurry preparation process for 6 (at 65:35) and 10 % of of mass fractions (at 35:65).

The obtained results shown on **Figure 3** indicate stability of all the measured slurries within the measurement time. The lowest values were noticed for the slurries with 10 % of mass fractions of the polymer content at the 65:35 ratio and for 6 of % of mass fractions of the polymer addition at the 35:65 powder proportion. The thickness values estimated after 96 h oscillated from 0.12 to 16 mm. Moreover, the slurries

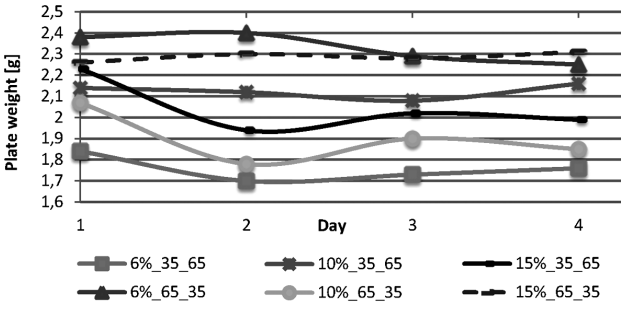

Figure 1: Relation between plate weight and stirring time for ceramic slurries with solid-content mass fraction of 72.5 % for different polymer contents at 35:65 and 65:35 powder ratios (200:030)

Slika 1: Razmerje med težo plošče in časom mešanja gošče z vsebnostjo 72,5 % trdnega masnega deleža, pri različnih vsebnostih polimera in razmerju prahov 35:65 in 65:35 (200:030)

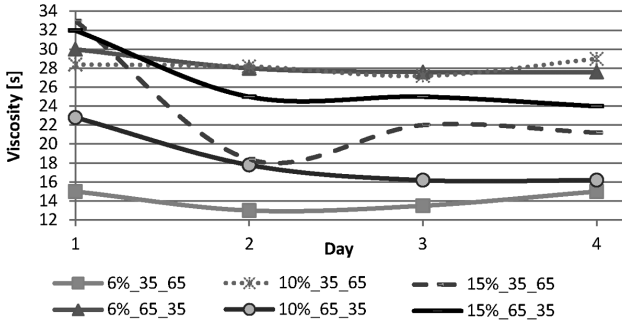

Figure 2: Relation between Zahn cup 4# viscosity and stirring time for ceramic slurries with 72.5 % of mass fractions of solid content for different polymer contents at 35:65 and 65:35 powder ratios (200:030)

Slika 2: Razmerje med Zahn viskoznostjo 4# in časom mešanja keramične gošče z 72,5 % trdnega masnega deleža, pri različni vsebnosti polimera in razmerju prahov 35:65 in 65:35, mreža (200:030)

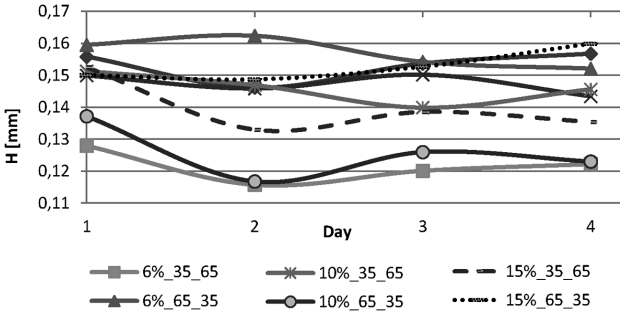

Figure 3: Coating thickness (H) dependence on time for the slurries with 72.5 % of mass fractions of solid content for (6, 10, 15) % of mass fractions of polymer content at two powder ratios, 35:65 and 65:35 (200:030 mesh)

Slika 3: Debelina nanosa (H) v odvisnosti od časa pri gošči z 72, 5 % masnim deležem trdnega in pri vsebnosti (6, 10 , 15) % masnega deleža polimera, pri dveh razmerjih prahov 35:65 in 65:35, mreža (200:030)

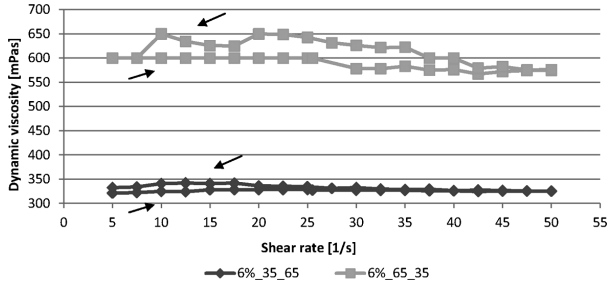

Figure 4: Relation between viscosity and shear rate of Al_2O_3 ceramic slurries with 72.5 % of mass fractions of solid content for 6 % of mass fractions of polymer content at two powder ratios, 35:65 and 65:35 (200:030 mesh)

Slika 4: Odvisnost med viskoznostjo in strižno hitrostjo Al_2O_3 keramične gošče z 72,5 % deležem trdnega pri 6 % masnega deleža polimera, pri dveh razmerjih zrnatosti prahov 35:65 in 65:35, mreža (200:030)

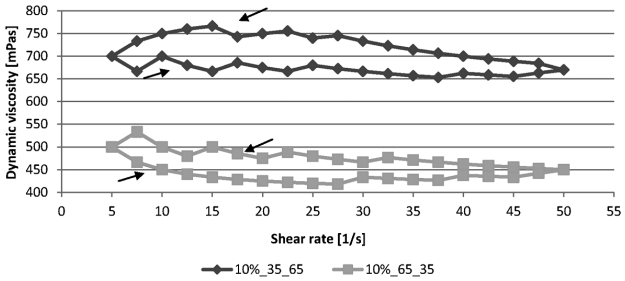

Figure 5: Relation between viscosity and shear rate of Al_2O_3 ceramic slurries with 72.5 % of mass fractions of solid content for 10 % of mass fractions of polymer content at two powder ratios, 35:65 and 65:35 (200:030 mesh)

Slika 5: Odvisnost med viskoznostjo in strižno hitrostjo Al_2O_3 keramične gošče z 72,5 % masnim deležem trdnega pri 10 % masnega deleža polimera, pri dveh razmerjih zrnatosti prahov 35:65 in 65:35, mreža (200:030)

with 6 and 10 % of mass fractions of the polymer content were characterized as similar according to the viscosity level.

The measurements of the ceramic-slurry dynamic viscosity are shown on **Figures 4** do **6** where the rela-

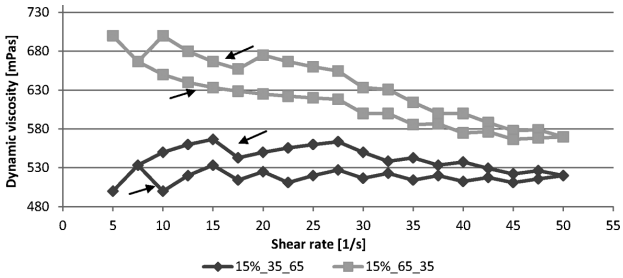

Figure 6: Relation between viscosity and shear rate of Al_2O_3 ceramic slurries with 72.5 % of mass fractions of solid content for 15 % of mass fractions of polymer content at two powder ratios, 35:65 and 65:35 (200:030 mesh)

Slika 6: Odvisnost med viskoznostjo in strižno hitrostjo Al_2O_3 keramične gošče z 72,5 % masnim deležem trdnega pri 15 % masnega deleža polimera, pri dveh razmerjih zrnatosti prahov 35:65 in 65:35, mreža (200:300)

tionship between the shear rate and viscosity is presented. As seen on the diagrams, additions of different concentrations of polymers to the ceramic slurries of Al_2O_3, with two powder ratios, determine their viscosity. The obtained results indicate that the application of 10 % of mass fractions of polymer at the 35:65 powder ratio causes the largest increase in the dynamic viscosity where the maximum value is 763 MPa s. The most effective was the addition of 6 % of mass fraction of polymer at the 35:65 powder ratio resulting in the lowest dynamic-viscosity value of 321.12 MPa s.

4 CONCLUSION

The Al_2O_3 powder characterized by irregularly shaped particles with sharp edges demonstrates the ability to agglomerate, resulting in a non-uniform particle-size distribution. The Zahn cup viscosity (7.35 s) is slightly larger in comparison to water viscosity (5.83 s), thus the Al_2O_3 particle dispersion in the binder is facilitated.

In addition, a relatively large content of the solid phase in a slurry reduces the coat shrinkage during the drying process and enhances its strength. The properties of the coating surface may be improved by increasing the plate weight. An addition of a poly acrylic polymer at the lowest content to the alumina powders with various granulation values allows a regulation of the rheological properties of the ceramic slurry towards more effective ceramic shell-mould fabrication.

The investigated slurries show standard features in the investment-casting process on an industrial scale. They are prospective for future shell-mould fabrication.

Acknowledgement

The financial support from the Structural Funds for the Operational Programme Innovative Economy (IE OP) provided by the European Regional Development Fund – Project "Modern material technologies in aero-

space industry", Nr POIG.01.01.02-00-015/08-00, is gratefully acknowledged.

5 REFERENCES

[1] S. Roskosz, Relationship between mould's technology and structure of investment cast nickel based superalloys, Inżynieria Materiałowa, 29 (**2008**) 4, 375–379, doi:bwmeta1.element.baztech-article-BPL8-0006-0070

[2] H. Matysiak, J. Ferenc, J. Michalski, Z. Lipiński, G. Jakubowicz, K. J. Kurzydłowski, Porosity and strength of ceramic shell moulds used in investment casting process by Bridgman method, Inżynieria Materiałowa, 32 (**2011**) 1, 17–21, doi:bwmetal.element.baztech-cle4cb00-4f01-476e-8401-81df9ad0e967

[3] J. Raabe, E. Bobryk, Functional Ceramics, Oficyna Wydawnicza Politechniki Warszawskiej, 1997

[4] R. Haratym, Investment casting processes for ceramic shell moulds, Warszawa 1997

[5] S. Jones, C. Yuan, Advances in shell moulding for investment casting, Journal of Materials Processing Technology, 135 (**2003**) 2–3, 258–265, doi:10.1016/S0924-0136(02)00907-X

[6] M. Zagórska, P. Wiśniewski, H. Matysiak, K. Kwapiszewska, J. Ferenc-Dominik, J. Michalski, K. J. Kurzydłowski, The influence of polymer binder, based on nano-Al_2O_3 dispersion, on the properties of ceramic slurries used in the investment casting, Euromat, 2011

[7] M. R. Ismael, R. D. Dos Anjos, R. Salomao, V. C. Pandolffelli, Colloidal silica as a nanostructured binder for refractory castables, Refractories Applications and News, 11 (**2006**) 4, 16–20

UDK 67.017:621.762:669.721:661.862'027
Original scientific article/Izvirni znanstveni članek

ISSN 1580-2949
MTAEC9, 50(5)739(2016)

EFFECT OF MECHANICAL ACTIVATION ON THE SYNTHESIS OF A MAGNESIUM ALUMINATE SPINEL

VPLIV MEHANSKE AKTIVACIJE NA SINTEZO MAGNEZIJ-ALUMINATNEGA ŠPINELA

Derya Kırsever, Nilgün Kaya Karabulut, Nuray Canikoğlu, Hüseyin Özkan Toplan

Sakarya University, Metallurgy and Materials Engineering, 54187 Sakarya, Turkey
dkirsever@sakarya.edu.tr

Prejem rokopisa – received: 2015-07-08; sprejem za objavo – accepted for publication: 2015-09-09

doi:10.17222/mit.2015.209

A magnesium aluminate spinel powder (72 % Al_2O_3 & 28 % MgO) was prepared with mechanical activation. Samples were sintered in a temperature range of 1400–1750 °C. The final sintered products were characterized with densification, phase and microstructural analyses and a hardness measurement to evaluate the influence of mechanical activation on the synthesis of a magnesium aluminate spinel.

Keywords: mechanical activation, magnesium aluminate spinel, ceramic, sintering, densification, mechanical properties

Prah magnezij aluminatnega špinela (72 % Al_2O_3 & 28 % MgO) je bil pripravljen z mehansko aktivacijo. Sintranje vzorcev je bilo izvedeno v temperaturnem območju 1400–1750 °C. Na končnih sintranih vzorcih je bila določena zgostitev, opravljena je bila analiza faz in mikrostrukture ter meritev trdote, da bi ocenili vpliv mehanske aktivacije na sintezo magnezij- aluminatnega špinela.

Ključne besede: mehanska aktivacija, magnezij-aluminatni špinel, keramika, sintranje, zgoščevanje, mehanske lastnosti

1 INTRODUCTION

Magnesium aluminate spinel ($MgAl_2O_4$, MA) is a widely used refractory material due to its high-temperature properties, mechanical resistance, thermal-shock resistance and high corrosion resistance to acidic and basic slags.[1,2] MA spinel has a high melting point (2135 °C), high hardness (16.1 GPa), relatively low density (3.58 g/cm^3), high strength (180 MPa) at room and at elevated temperatures, high chemical inertness, a low thermal-expansion coefficient (9×10^{-6}/°C between 30 °C and 1400 °C) and high thermal-shock resistance.[3]Also, MA spinel refractories are very attractive due to their environmental friendliness, contrary to magnesium chromite refractories. However, aspinel formation is accompanied by a 5–7 % volume expansion which does not allow it to densify in a single-stage firing.[4] Therefore, the synthesis of spinel and fabrication of spinel refractories were not feasible with commercial methods due to the difficulty with sintering.[1,2] High-purity spinel was synthesized mostly with hydrothermal techniques, sol-gel, spray plasma, cool drying, controlled hydrolysis, co-precipitation, mechanical activation and the aerosol method.[1]

Mechanical activation is a method, which can induce changes tothe solid-state properties, such as the distortion of the structure, accompanied by the accumulation of energy and the formation of active centers on the newly formed surfaces.[5] Different processes can remarkably influence the reactivity of solids. Mechanical treatments are particularly important as long as they can help to produce changes to the texture and structure of the solids. In many cases, these alterations tothe structure cause certain modifications to the phases formed due to the thermal treatment of the solids, which were mechanochemically treated.[6]

The main aim of this study was to prepare a magnesium aluminate spinel by firing between 1400–1750 °C and to analyze the effect of mechanical activation. Investigations of the phases, crystal morphology and densification of the fired products were carried out. In addition, the hardness values of the samples for different sintering temperatures were studied.

2 EXPERIMENTAL DETAILS

Al_2O_3 (72 % of mass fractions) and MgO (28 % of mass fractions) powders were ball milled with alumina balls in a polyethylene bottle for 1 h. The mixture was made in a high-energy planetary ball mill (Fristch) at a rotation speed of 600 min^{-1}. The ball-to-powder weight ratio was adjusted to 20. Milling of the precursor was carried out for 1 h. Activated and non-activated powders were uniaxially pressed to form pellets at 255 MPa. The pellets were sintered in the temperature range of 1400–1750 °C for 1 h. An X-ray diffraction analysis was performed using a Rigaku Ultima X-ray diffractometer. A Joel 6060 LV scanning electron microscope was used for the morphological analysis of the non-activated and activated powders and sintered samples. The hardness

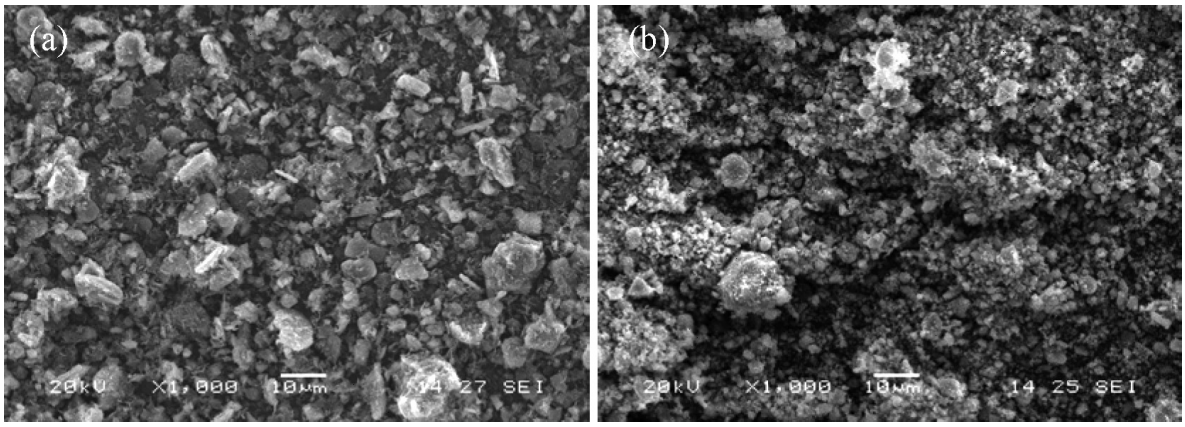

Figure 1: SEM micrographs of powder mixtures: a) non-activated, b) activated for 1 h
Slika 1: SEM-posnetka mešanice prahu: a) neaktiviran, b) aktiviran 1 h

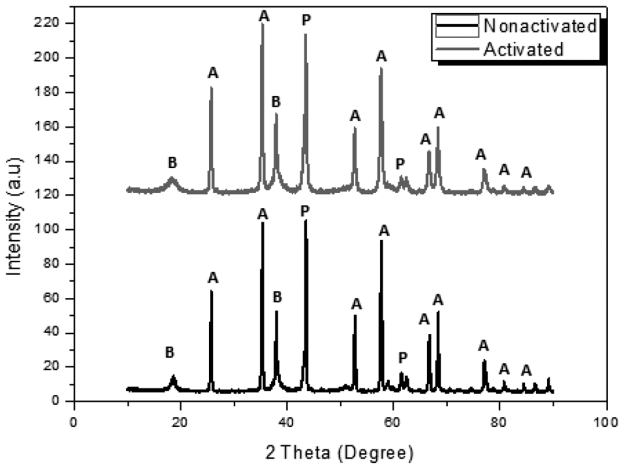

Figure 2: XRD patterns of non-activatedand activated powder mixtures of MgO and Al_2O_3(A: Al_2O_3, B: $Mg(OH)_2$, P: MgO)
Slika 2: Rentgenograma neaktivirane in aktivirane mešanice prahu MgO in Al_2O_3 (A: Al_2O_3, B: $Mg(OH)_2$, P: MgO)

measurements of the samples were done using Leica Microsysteme GmbH. The apparent porosity and bulk density of the sintered samples were measured with the liquid-displacement method using Archimedes'principle. Water absorption was alsoinvestigated.

3 RESULTS AND DISCUSSION

Figure 1 shows SEM micrographs of non-activated and activated powder mixtures. The non-activated powder mixture has well-defined faces and edges. However, the particle size decreases and the particle shape becomes round with mechanical activation.

Figure 2 shows XRD patterns of the non-activated and activated powder mixtures of MgO and Al_2O_3. As a result, $Mg(OH)_2$, Al_2O_3 and MgO peaks are observed.

SEM micrographs of the fractured surfaces of all the samples sintered in the temperature range of 1400–1750 °C for 2 h are shown in **Figure 3**. It can be seen that all the samples appear to be relatively dense

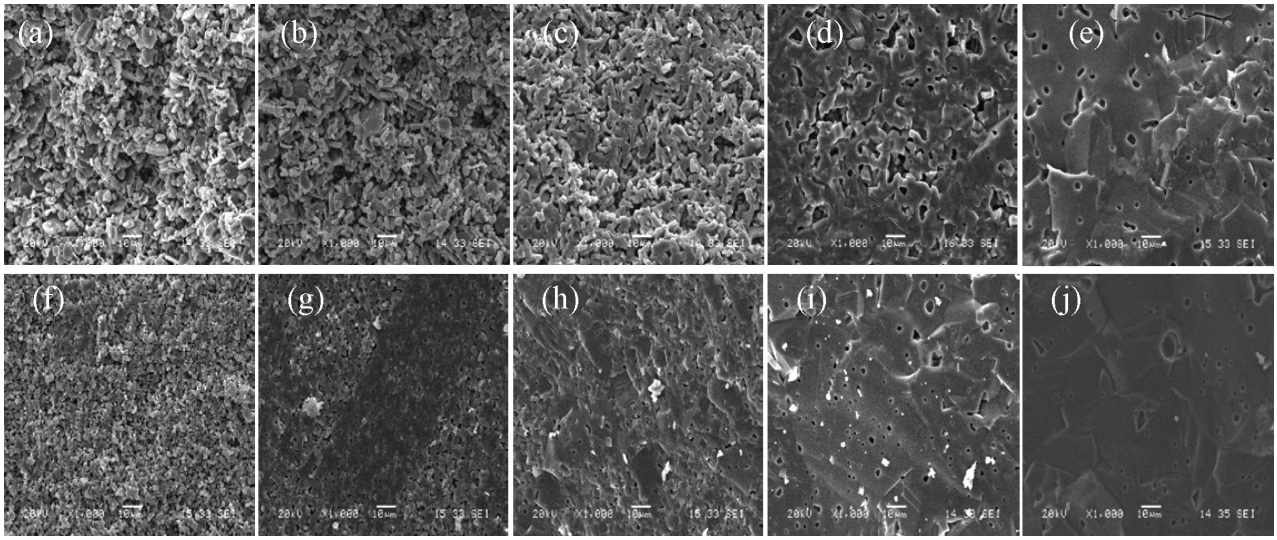

Figure 3: SEM micrographs of all sintered samples prepared from: a), b), c), d), e) non-activated and f), g), h), i), j) activated powder mixtures
Slika 3: SEM-posnetki vseh sintranih vzorcev pripravljenih iz: a), b), c), d) , e) neaktivirana in f), g), h), i), j) aktivirana mešanica prahu

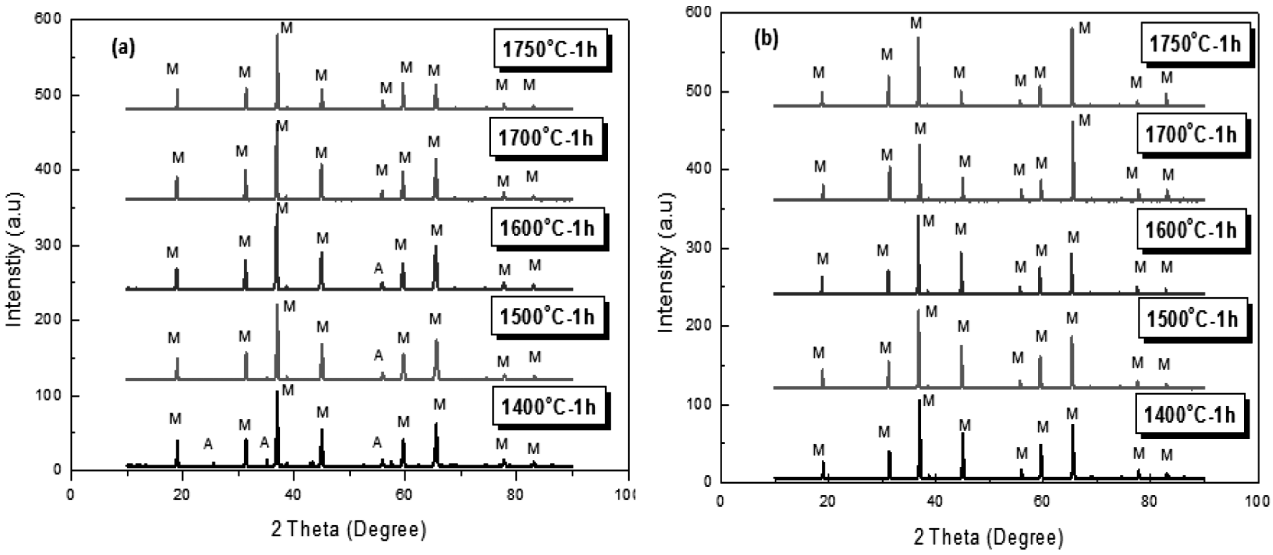

Figure 4: XRD patterns of: a) non-activated and b) activated samples sintered at different temperatures for 2 h(M: $MgAl_2O_4$, A: Al_2O_3)
Slika 4: Rentgenogrami: a) neaktivirani in b) aktivirani vzorci sintrani 2 h na različnih temperaturah (A: Al_2O_3, M: $MgAl_2O_4$)

with the increasing sintering temperature and mechanical activation. After the sintering at 1700 °C, spinel grain growth was found for the non-activated and activated samples. However, porosity levels seem relatively higher for the non-activated samples.

Figure 4 shows the XRD patterns of the non-activated and activated samples after the sintering in the temperature range of 1400–1750 °C for 2 h. These confirm that the Mg-Al spinel is the only phase of the activated samples. However, Al_2O_3 peaks are also present at 1400 °C for the non-activated samples.

Figure 5 summarizes the bulk density and apparent porosity of all the sintered samples. A general trend in the increasing bulk density and decreasing apparent porosity with the increasing sintering temperature was observed. The mechanically activated samples showed relatively higher density values compared to those of the non-activated samples. On the other hand, the mechanically activated samples obtained a lower apparent porosity than the non-activated samples. The sintered bulk density and apparent porosity ofthenon-activated and activated samples are 3.76 g/cm^3 and 3.1 g/cm^3, respectively.

The reduction of the particle size decreases the distance between the vacancy sites (or betweenthegrain boundaries) and enhances the vacancy diffusion to the surface, thus increasing the densification. The reduction of the particle size is obtained with mechanical activation.[7]

Figure 6 shows the water absorption of all the sintered samples. It can be seen that the water absorption decreases with the sintering temperature and mechanical activation. For the activated samples, there is no relative water absorption above 1600 °C.

Figure 7 shows the hardness resultsfor the non-activated and activated samples with respect to the sintering temperature. The highest hardness value of an activated sample is 1623 HV at 1650 °C. Also, the hardness values of the activated samples arehigher than those for the

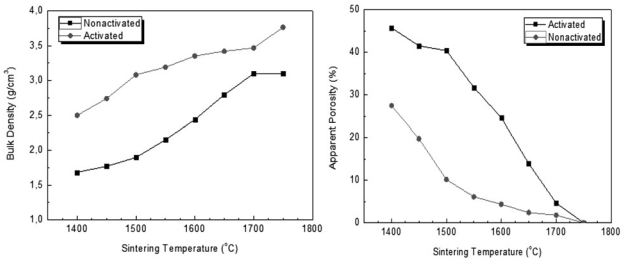

Figure 5: Bulk-density and apparent-porosity plots for all the sintered samples
Slika 5: Diagrama gostote osnove in navidezne poroznosti vseh sintranih vzorcev

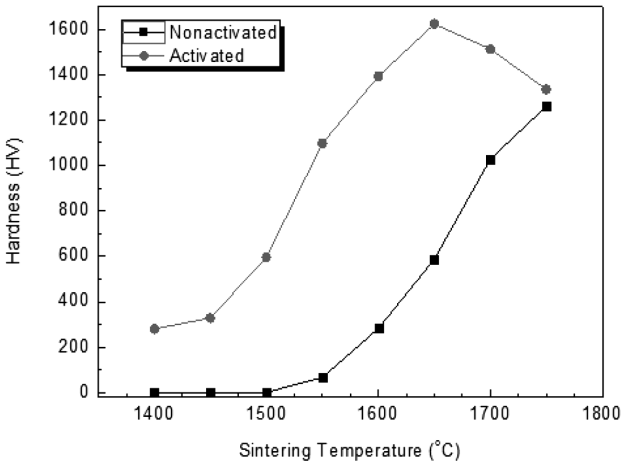

Figure 6: Hardness measurements forall the sintered samples
Slika 6: Meritve trdote vseh sintranih vzorcev

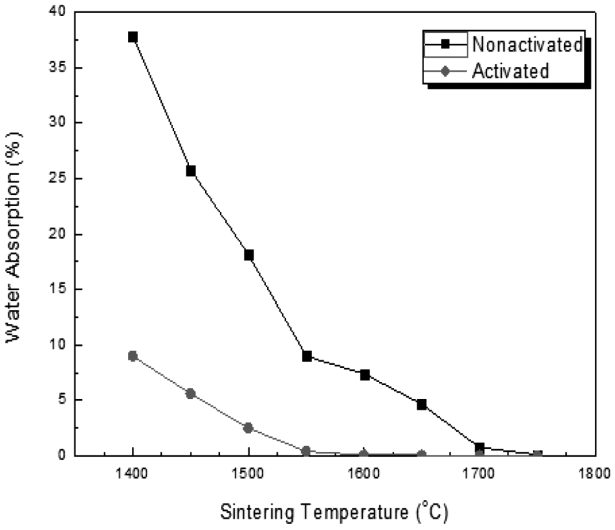

Figure 7: Water absorption of all the sintered samples
Slika 7: Absorpcija vode vseh sintranih vzorcev

non-activated samples. These results arerelated to thedensification and a low porosity level.

4 CONCLUSIONS

Magnesium aluminate spinel samples were synthesized using mechanical activation. The activated samples resulted in higher density and hardness values in comparison with the non-activated samples. In addition, theactivated samples exhibited dense grains and a low porosity. So, mechanical activation can facilitate a single-stage sintering process and greatly influence the costs of the production.

5 REFERENCES

[1] P. Orosco, L. Barbosa, M. C. Ruiz, Synthesis of magnesium aluminate spinel by periclase and alumina chlorination, Materials Research Bulletin, 59 (**2014**), 337–340, doi:10.1016/j.materresbull.2014.07.026

[2] P. G. Lampropoulou, C. G. Katagas, Effects of zirconium silicate and chromite addition on the microstructure and bulk density of magnesia–magnesium aluminate spinel-based refractory materials, Ceramics International, 34 (**2008**), 1247–1252, doi:10.1016/j.ceramint.2007.03.015

[3] I. Ganesh, Fabrication of magnesium aluminate ($MgAl_2O_4$) spinel foams, Ceramics International, 37 (**2011**), 2237–2245, doi:10.1016/j.ceramint.2011.03.068

[4] H. S.Tripathi, B. Mukherjee, S. Das, M. K. Haldar, S. K. Das, A.Ghosh, Synthesis and densification of magnesium aluminate spinel: effect of MgO reactivity, Ceramics International, 29 (**2003**), 915–918, doi:10.1016/S0272-8842(03)00036-1

[5] E. Turianicová, A. Obut, Ľ. Tuček, A. Zorkovská, İ. Girgin, P. Baláž, Interaction of natural and thermally processed vermiculites with gaseous carbon dioxide during mechanical activation, Applied Clay Sci., 88–89 (**2014**), 86–91, doi:10.1016/j.clay.2013.11.005

[6] S. Koç, N. Toplan, K. Yýldız, H. Ö. Toplan, Effects of mechanical activation on the non-isothermal kinetics of mullite formation from kaolinite, J. Therm. Anal. Calorim., 103 (**2010**), 791–796, doi:10.1007/s10973-010-1154-5

[7] R.Sarkar, S.Kumar Das, G.Banerjee, Effect of attritor milling on the densification of magnesium aluminate spinel, Ceramics International, 25 (**1999**), 485–489, doi:10.1016/S0272-8842(98)00065-0

UDK 67.017:661.8'02:621.3.032.22:537.533
Original scientific article/Izvirni znanstveni članek

ISSN 1580-2949
MTAEC9, 50(5)743(2016)

PHASE AND MICROSTRUCTURE DEVELOPMENT OF LSCM PEROVSKITE MATERIALS FOR SOFC ANODES PREPARED BY THE CARBONATE-COPRECIPITATION METHOD

RAZVOJ KRISTALNIH FAZ IN MIKROSTRUKTURE LSCM PEROVSKITNIH MATERIALOV ZA SOFC ANODE, PRIPRAVLJENIH S KARBONATNO METODO KOPRECIPITACIJE

Klementina Zupan, Marjan Marinšek, Tina Skalar

University of Ljubljana, Faculty of Chemistry and Chemical Technology, Večna pot 113, 1000 Ljubljana, Slovenia
klementina.zupan@fkkt.uni-lj.si

Prejem rokopisa – received: 2015-07-21; sprejem za objavo – accepted for publication: 2015-10-09

doi:10.17222/mit.2015.232

Most SOFC development has been based on nickel yttria-stabilized zirconia anodes. Such materials have excellent catalytic properties for fuel oxidation, high electrical conductivity, good mechanical strength and an appropriate thermal expansion coefficient compatible with other cell components. Unfortunately, cermet anodes based on doped zirconia exhibit some disadvantages, e.g., the catalysing side reaction of carbon deposition during hydro-carbon fuel oxidation and a susceptibility to sulphur poisoning. Perovskite-type compounds based on lanthanum-strontium-manganese-chromium oxide (LSCM) can serve as an alternative material. Since the optimal perovskite composition is still not known, $La_{1-x}Sr_xMn_yCr_{1,y}O_{3\pm\delta}$ (x from 0 to 0.3 and y from 0.4 to 0.6) ceramics were prepared with the co-precipitation method. Crystalline phase formation was followed by X-ray powder diffraction and Rietveld refinement. Quantitative microstructure analysis of the samples sintered at various temperatures was performed on SEM micrographs using Axiovision 4.8 software.

Keywords: co-precipitation, oxide LSCM anode, phase development, microstructure

Večina razvoja visokotemperaturnih gorivnih celic je temeljila na anodnih materialih na osnovi niklja in cirkonijevega dioksida, stabiliziranega z itrijem. Ta ima odlične katalitske lastnosti pri reakciji oksidacije goriva, visoko električno prevodnost, dobro mehansko trdnost in temperaturni razteznostni koeficient, skladen z ostalimi komponentami celice. Žal so ti materiali med delovanjem podvrženi neželenim reakcijam izločanja ogljika in zastrupljanja z žveplom, zato jih poskušamo nadomestiti z oksidnimi spojinami perovskitnega tipa, z lantan-stroncij-mangan-krom oksidom (LSCM). Optimalna sestava teh materialov še ni znana, zato smo z metodo soobarjanja pripravili keramiko $La_{1-x}Sr_xMn_yCr_{1,y}O_{3\pm\delta}$ (x od 0 do 0,3 in y od 0,4 do 0,6). Z rentgensko praškovno analizo in Rietveldovim prilagajanjem smo spremljali razvoj kristalnih faz. Z analizo SEM posnetkov vzorcev po sintranju pri različnih temperaturah smo mikrostrukture pripravljenih materialov kvantitativno ovrednotili z uporabo programa Axiovision 4.8.

Ključne besede: kopercipitacija, oksidna LSCM anoda, razvoj faz, mikrostruktura

1 INTRODUCTION

Fuel cells can be considered as devices that electrochemically convert fuels into electricity or, more precisely, batteries with permanent fuel supplies. Solid-oxide fuel cells (SOFCs), based on an ion-conducting electrolyte, have several advantages over other types of fuel cells, including their potential fuel flexibility and very high chemical-to-electrical conversion efficiency due to the absence of Carnot limitations. Further energy gains can be achieved in SOFC systems when cogenerated heat is used for the internal reforming of methane or other hydrocarbon fuels directly on the anode.[1]

Porous Ni/YSZ-based materials are conventionally used as SOFC anodes due to their high electrical conductivity, activity for electrode electro-chemical oxidation, stability under reduced environmental conditions, appropriate thermal expansion and a chemical compatibility with other cell components.[2] Despite the many advantages they possess, there are some drawbacks, such as a low tolerance to sulphur impurities[3] and a tendency to coke when hydrocarbons are used as fuels[4].

Alternative cermet anode materials have been extensively studied, such as Cu-CeO_2-YSZ. Researchers have demonstrated their operation using various fuels.[5,6] Recently, another alternative approach aiming to prepare all-oxide anode materials has been proposed in order to develop electrodes that exhibit catalytic, electron- and ion-conducting properties. Many problems with all-oxide anodes have been overcome with the introduction of novel perovskite-structure materials with the general formula $ABO_{3-\delta}$. The A element is typically lanthanide, while the B element is the transition metal. In principle, catalytic activity toward fuel oxidation, electron- and ion-conductivity can be tailored by a wide range of doping elements. The oxidation states of the A-site and B-site cations determine the oxygen vacancy concentration δ.[2] Among various perovskites, a particularly complex metal oxide with the composition $La_{0,75}Sr_{0,25}Mn_{0,5}Cr_{0,5}O_{3-\delta}$ has attracted much attention as a

promising anode material, due to its good catalytic activity, excellent redox stability, reduced carbon deposition susceptibility and improved sulphur-poisoning stability.[7] An introduction of alkaline earth ions, i.e., Mg^{2+}, Ca^{2+}, and Sr^{2+}, into the A site of lanthanum chromite can enhance the electrical conductivity by two orders of magnitude.[7] L. Deleebeck et al.[9] first demonstrated that the removal of Sr from $La_{1-x}Sr_xMn_{1-y}Cr_yO_{3\pm\delta}$ improves the thermo-chemical stability and the electronic conductivity in a humidified H_2 atmosphere. In their second study, they reported that the catalytic activity toward H_2 oxidation decreases with increasing Cr content (y = 0.4–0.6), while the relatively high Sr content (x = 0.2) shows a lower catalytic activity.[10] The optimal LSCM material composition is not yet known.

Various chemical routes to prepare LSCM powders have been reported, including the solid-state reaction,[7] the chelating method,[11] gel casting,[12] and combustion synthesis.[13–16] However, the synthesis of single-phase LSCM composed of fine powders requires a further improvement. Co-precipitation is a promising and simple chemical method to prepare well-defined and less-agglomerated perovskite powders. It was reported that the most significant synthesis parameter for LSCM preparation via co-precipitation is the pH value of the reaction mixture, which should be maintained slightly below 8 in order to ensure that all the cations precipitate.[17] In addition to an appropriate chemical composition of the LSCM material, the electrode performance in an operating SOFC is also essentially dependent on the electrode microstructure, final porosity and potential presence of secondary phases.

In this work, we applied the "reverse strike" carbonate co-precipitation method for batch $La_{1-x}Sr_xMn_{1-y}Cr_yO_{3\pm\delta}$ perovskite preparation in which the Sr content and the Cr-to-Mn molar ratio were varied. The aim of this work is to describe the relationship between the microstructure parameters and the LSCM composition using various analytical techniques.

2 EXPERIMENTAL PROCEDURE

$La_{1-x}Sr_xMn_{1-y}Cr_yO_{3\pm\delta}$ (x = 0, 0.1, 0.2 or 0.3 and y = 0.4, 0.5 or 0.6) oxides were prepared using co-precipitation synthesis (**Table 1**). $La(NO_3)_3{\cdot}6H_2O$ (99 %), $Sr(NO_3)_2$ (98 %), $Cr(NO_3)_3{\cdot}9H_2O$ (98.5 %) and $Mn(NO_3)_2{\cdot}4H_2O$ (98 %), all from Alfa Aesar, were used as the source of metal ions. The carbonate precursors were prepared using the "reverse strike" method in which a mixed metal nitrate solution is added to a precipitant carbonate solution to achieve a more uniform cation distribution by instantaneous precipitation. A total of 600 mL of 0.125-M aqueous solution of $(NH_4)_2CO_3$ was poured into a jacket glass reactor (1.25 L); 0.5-M metal nitrates solutions were prepared, as were adequate volumes of each LSCM component regarding the desired final LSCM composition. The solutions were mixed together and dripped into a stirring precipitant solution. The precipitating solution was kept at 60 °C under a CO_2 protective atmosphere to prevent manganese oxidation during synthesis. The pH inside the jacket glass reactor was kept at 7.8±0.1 by the periodic addition of ammonia (25 %, aq.). Afterwards, the precipitate was filtered off under a CO_2 environment and washed three times (50 mL) with a 0.125-M solution of $(NH_4)_2CO_3$, dried for 6 h at 110 °C and finally calcined at 1000 °C in an air atmosphere.

Table 1: Compositions and sample notations
Tabela 1: Sestave in poimenovanje vzorcev

Sample composition	Sample name
$La_{0,7}Sr_{0,3}Cr_{0,5}Mn_{0,5}O_{3-d}$	La7Cr5
$La_{0,8}Sr_{0,2}Cr_{0,5}Mn_{0,5}O_{3-d}$	La8Cr5
$La_{0,9}Sr_{0,1}Cr_{0,5}Mn_{0,5}O_{3-d}$	La9Cr5
$La_1Cr_{0,5}Mn_{0,5}O_{3-d}$	La10Cr5
$LaCr_{0,6}Mn_{0,4}O_3$	La10Cr6
$La_{0,9}Sr_{0,1}Cr_{0,6}Mn_{0,4}O_3$	La9Cr6
$La_{0,9}Sr_{0,1}Cr_{0,4}Mn_{0,6}O_3$	La9Cr4
$LaCr_{0,4}Mn_{0,6}O_3$	La10Cr4

The synthesized powders were milled in an agate mortar and un-axially pressed into pellets (100 MPa) and sintered at various temperatures (1250 °C, 1300 °C, 1400 °C and 1500 °C) for 1 h. The calcined and sintered samples were analysed with a PANalytical X'Pert PRO MPD apparatus. For the determination of the microstructure, the sintered tablets were polished (diamond pastes of 3 μm and 0.25 μm), thermally etched, and subsequently analysed with a FE-Zeiss ULTRA Plus SEM. The quantitative analyses of the microstructures were performed on digital images (images were digitized into pixels with 255 different grey values) using Axiovision 4.8 image-analysis software.

3 RESULTS AND DISCUSSION

The carbonate co-precipitation route is an appropriate method for the preparation of complex metal oxides, such as $La_{1-x}Sr_xMn_{1-y}Cr_yO_{3\pm\delta}$ (LSCM). When the "reversed strike" co-precipitation method is used and the mixed solution of metal ions drips into the concentrated precipitant solution, the various cations within each droplet precipitate almost instaneously.[18] Lanthanum carbonate precipitated at pH > 4.2, manganese carbonate at pH > 5 and strontium carbonate at pH > 7.3. Chromium precipitates as a hydroxide in a very narrow pH range from 6.6 to 7.3; however, $Cr(OH)_3$ starts to dissolve at a pH value of 7.9.[17] Therefore, the precipitation of mixed metal oxide should be carried out carefully in the tiny pH range from 7.3 and 7.9. If we take into account only simple carbonate and hydroxide species (Equations (1) to (4)) for the calculation for the stoichiometric amount of ammonium carbonate as a precipitant agent, we can conclude that an excess of 50 % is used during the precipita-

tion process. Thus, the super-saturation ratio in the case of the LSCM synthesis calculated from the molar ratio of ammonium carbonate and total metal ions is 1.5.

$$3(NH_4)_2CO_3 + 2La^{3+} \rightarrow La_2(CO_3)_3 + 6NH_4^+ \quad (1)$$

$$(NH_4)_2CO_3 + Sr^{2+} \rightarrow SrCO_3 + 2NH_4^+ \quad (2)$$

$$3(NH_4)_2CO_3 + Cr^{3+} + H_2O \rightarrow Cr(OH)_3 + 6NH_4^+ + 3HCO_3^- \quad (3)$$

$$(NH_4)_2CO_3 + Mn^{2+} \rightarrow MnCO_3 + 2NH_4^+ \quad (4)$$

According to **Figure 1**, the perovskite LSCM phase formation for all the samples is practically complete after calcination at 1000 °C for 1 h (the perovskite peaks are denoted with a letter "P"). The main perovskite phase is quite well crystallised. In the sample La7Cr5, with the highest Sr content and equal amounts of chromium and manganese, the XRD analysis revealed a small amount of strontium secondary phase $SrCrO_4$ (denoted with the letter "S"). It is described in the literature that in the humidified hydrogen atmosphere $SrCrO_4$ further transforms into the Ruddlesden-Popper phase Sr_2CrO_4.[9] Additionally, the X-ray powder diffraction indicates that in samples with the lowest Cr content (0.4), a lanthanum-rich secondary phase La_2CrO_6 is formed (denoted with the letter "L"). Varying the Sr content in this Cr-poor sample reveals that in the Sr-free and Sr = 0.1 samples the La_2CrO_6 content determined according to the Rietveld refinement is 3.1 % and 7.6 %, respectively. Multiple RTG peaks observed in some patterns are a consequence of a perovskite lattice superstructure. This lattice superstructure is formed due to the octahedron tilting, which has its origin in the random Sr-incorporation into the perovskite structure.[19,20] By doping lanthanum-manganite with Sr and Cr, the symmetry of the structure is lowered due to the different sizes of the introduced cations compared to the original ions. Consequently, octahedrons defined by a central cation (B-site cation) and the surrounding oxygen ions are slightly tilted and the repeating structure pattern is defined by eight original unit cells.

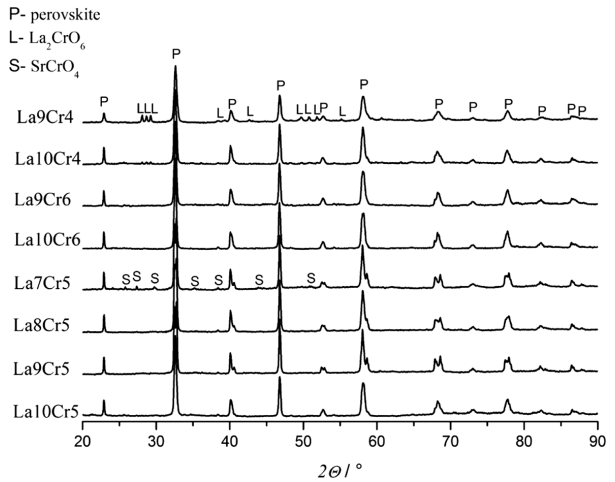

Figure 1: X-ray diffraction patterns of prepared samples after calcination at 1000 °C

Slika 1: Rentgenogram pripravljenih vzorcev po kalcinaciji pri 1000 °C

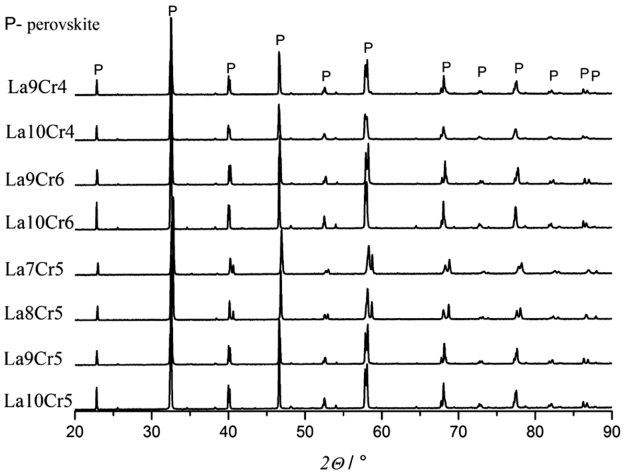

Figure 2: X-ray diffraction patterns of all samples after calcination at 1250 °C

Slika 2: Rentgenogram vseh vzorcev po kalcinaciji pri 1250 °C

The secondary phases are highly undesired in the final LSCM since they result in the so-called layered perovskite structure with additional layers of Sr-oxide, La-oxide, or a mixture of both separating the LSCM at temperatures around 1100 °C and in a H_2 atmosphere. Furthermore, the secondary phases decrease the thermochemical stability, catalytic activity and electrical conductivity of the LSCM.[9,12]

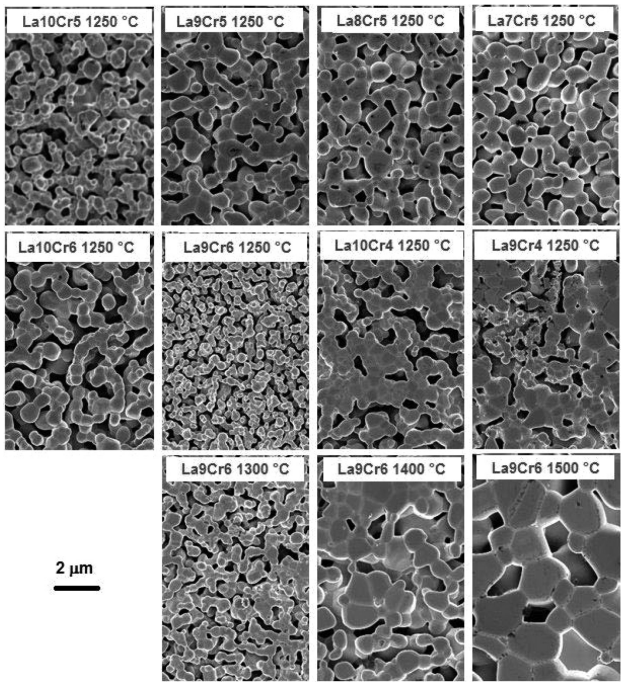

Figure 3: SEM micrographs of all samples sintered at 1250 °C and sample La9Cr6 sintered at 1250 °C, 1300 °C, 1400 °C and 1500 °C

Slika 3: SEM-posnetki vseh vzorcev po sintranju pri 1250 °C in vzorca La9Cr6, sintranega pri 1250 °C, 1300 °C, 1400 °C in 1500 °C

Table 2: Results of quantitative microstructure analysis of the sintered samples
Tabela 2: Rezultati kvantitativne analize mikrostrukture sintranih vzorcev

	T/°C	ε/%	d_y/μm	d_x/μm	$\bar{d}$/μm	ψ	S_{pore}/μm^2	$FERET_{MAX}$ /μm	ρ_{teor} / g cm^{-3}	ρ_{rel} /%
La10Cr5	1250	51.9	0.30	0.31	0.28	0.67	0.44	1.02	6.71	48.1
	1300	50.9	0.43	0.44	0.41	0.74	0.86	1.66		49.1
	1400	40.1	1.00	1.01	0.92	0.73	1.31	2.03		59.9
	1500	27.4	1.85	1.91	1.70	0.70	1.27	1.82		72.6
La9Cr5	1250	44.6	0.52	0.53	0.48	0.70	0.77	1.69	6.60	55.4
	1300	41.5	0.60	0.61	0.55	0.71	0.72	1.60		58.5
	1400	25.4	1.10	1.11	1.02	0.74	0.58	1.26		74.6
	1500	9.9	2.89	2.92	2.67	0.69	0.39	0.65		90.1
La8Cr5	1250	43.7	0.50	0.49	0.45	0.70	0.36	1.05	6.56	56.3
	1300	40.3	0.62	0.60	0.55	0.67	0.20	0.76		59.7
	1400	27.0	1.22	1.25	1.14	0.74	0.77	1.46		73.0
	1500	16.0	2.54	2.65	2.35	0.72	0.65	1.12		84.3
La7Cr5	1250	45.9	0.56	0.58	0.53	0.72	0.37	0.80	6.45	54.1
	1300	42.1	0.86	0.86	0.79	0.76	0.74	1.04		57.9
	1400	31.2	1.23	0.86	1.14	0.75	0.66	1.47		68.8
	1500	21.8	1.94	2.00	1.79	0.73	0.39	0.87		78.2
La10Cr6	1250	54.2	0.44	0.45	0.42	0.72	1.12	1.42	6.72	45.8
	1300	48.1	0.76	0.77	0.72	0.75	1.33	1.92		51.9
	1400	37.9	1.20	1.21	1.13	0.77	1.33	2.06		62.1
	1500	23.4	1.97	1.96	1.84	0.76	1.94	2.31		76.6
La9Cr6	1250	54.0	0.24	0.23	0.22	0.79	0.37	1.07	6.57	46.0
	1300	50.5	0.39	0.39	0.36	0.79	3.10	2.73		49.5
	1400	40.7	0.67	0.69	0.63	0.76	2.54	2.94		59.3
	1500	38.6	1.70	1.73	1.60	0.78	1.35	2.02		61.4
La10Cr4	1250	44.5	0.40	0.41	0.38	0.78	0.59	1.11	6.73	55.5
	1300	39.2	0.77	0.78	0.72	0.71	0.36	1.01		60.8
	1400	31.6	1.21	1.19	1.11	0.72	0.83	1.42		68.4
	1500	24.0	2.15	2.09	1.94	0.70	1.11	1.47		76.0
La9Cr4	1250	54.1	0.43	0.43	0.40	0.72	2.63	2.76	6.59	45.9
	1300	50.7	0.69	0.67	0.64	0.73	1.65	2.43		49.3
	1400	34.1	1.43	1.44	1.33	0.76	2.30	2.65		65.9
	1500	22.5	2.68	2.60	2.44	0.75	1.13	1.18		77.5

After the sintering at 1250 °C, the only phase present in all the samples is the LSCM perovskite, as shown in **Figure 2**. The absence of secondary phases indicates that they re-dissolve in the main LSCM phase when the sintering temperature is increased. This discovery also gives a very effective tool for controlling the amount of secondary phases in LSCM or even eliminates them completely. Due to the possibility of eliminating the secondary phases from the LSCM, it is reasonable to conclude that the co-precipitation method offers an essential advantage over the synthesis processes that are based on the solid-state reactions in which local inhomogeneity in chemical composition are quite common.

One of the major challenges in applying LSCM material as an anode in ceramic fuel cells is achieving the continuity of the electrode material as well as the continuity of the pores. Good contact between the particles is critical for forming continuous paths throughout the formed anode, reaching a high conductivity. The sintering behaviour of all the samples after sintering at 1250 °C is demonstrated in **Figure 3**. Since all the microstructure parameters that are important for an exact anode analysis are sometimes difficult to deduce simply from the SEM micrographs, a detailed quantitative microstructure analysis of sintered samples is performed. For statistically reliable data in each case, 5 to 10 different regions were analyzed. The results of the quantitative microstructure analysis are summarized in **Table 2**. The parameters $\bar{d}$, d_x, d_y and ψ are represented as the diameter of the area-analogue circle – D_{circle}, the intercept lengths in the x and y directions – $FERET_X$, $FERET_Y$ and the Shape factor f_{circle}. S_{pore} and $FERET_{MAX}$ are determined as the pore areas and maximum intercept lengths of the pore while ρ_{rel} and ε are determined from the geometric densities of the tablets and the theoretical densities that were calculated using the Rietveld refinement.

SEM micrographs sintered at 1250 °C reveal that the microstructure parameters greatly depend on the sample composition. When comparing samples with equal amounts of Cr and Mn with various Sr contents we can observe that the presence of strontium promotes sintering. It is also evident that the grains are larger in samples

that contain Sr than in the Sr-free sample. Although no secondary phases are detected in the Sr-free sample (La10Cr5), the microstructure is composed of regions with larger and smaller grains. All Sr-free samples with a lower Cr-content behave similarly. The presence of a secondary phase $SrCrO_4$ in the sample with the highest Sr content (La7Cr5) evidently does not have a significant effect on the LSCM grain size distribution. In contrast, the presence of a lanthanum-rich secondary phase La_2CrO_6 in samples with a lower Cr content (La10Cr4 and La9Cr4) causes non-homogenous microstructures with the denser regions containing larger grains and the less dense regions containing smaller grains. In the phase-pure LSCM sample with a Cr content $y = 0.6$ (La9Cr6), a very interesting microstructure is formed after sintering at 1250 °C. In this sample, the formation of well-connected fine grains is observed.

The results of a quantitative microstructural analysis are in good agreement with optical observations. The relative sintered density increases and the porosity decreases with the increasing sintering temperature. Samples with a Sr content $x = 0.1$, 0.2 or 0.3 and equal contents of Cr and Mn sinter at the lowest sintering temperature of 1250 °C to somewhat higher densities than the Sr-free sample (La10Cr5). At the same sintering temperature, ρ_{rel} reaches 48.1 %, 55.4 %, 56.3 % and 54.1 % for the samples La10Cr5, La9Cr5 La8Cr5 and La7Cr5, respectively. The addition of strontium to the perovskite also results in grain growth, during which grains reach an average size of 0.28 μm at 1250 °C in a Sr-free sample, while for the highest Sr content in sample $x = 0.3$ the average grain size grew to 0.53 μm. At the highest sintering temperature (1500 °C), $\rho_{rel.}$ reaches 90.1 %, 72.6 %, 84.3 % and 78.2 % for the samples La9Cr5, La10Cr5, La8Cr5 and La7Cr5, respectively. From this fact, it can be deduced that the addition of Sr to some amount $x = 0.1$ accelerates sintering, while adding Sr to perovskite above a certain concentration $x = 0.2$ and 0.3 supresses the densifying process. At a lower Sr concentration, $SrCrO_4$ (according to phase diagram $SrO–Cr_2O_3$) forms a liquid phase due to eutectic and peritectic reactions[21] that promote sintering.[22] In principle, a higher Sr-content increases the amount of $SrCrO_4$ phase which reacts to the liquid phase and secondary solid phase through a peritectic transformation. This secondary solid phase hinders sintering. A higher sintering temperature also results in pronounced grain growth in which originally sub-micrometre grains grow to almost ~2.7 μm in size at 1500 °C. With this pronounced growth the grains become less similar to an ideal sphere, which is manifested as a slight decrease in the shape factor. Similar behaviour was observed for the sintering of a combustion-derived LSCM ceramic.[23]

In the LSCM phase, with a pure sample (La9Cr6) with Cr content $y = 0.6$ and a low Sr-addition, the formation of well-connected grains is observed after sintering at 1250 °C. With increasing sintering temperature, the densification process normally advances and the grains grow; however, the grain growth is somehow less pronounced than that in other samples. The average grain size for sample La9Cr6 sintered at various temperatures 1250 °C, 1300 °C, 1400 °C and 1500 °C is 0.22 μm, 0.36 μm, 0.63 μm and 1.6 μm, respectively. Furthermore, for the sample La9Cr6, a calculation of the average $FERET_{MAX}$ of pores versus the grain diameter gives the highest value among all the samples. Since the average pore diameter is comparable at sintering temperature 1250 °C in all samples, this value somehow indicates a low average LSCM grain size and pore appearance in the sample, which contribute mainly to the open porosity. This fact together with the absolute value of porosity is very important from the practical point of view if such material is to be used as an anode layer in the operating SOFC. In order to form a continuous phase of pores in sintered samples, the porosity should be at least 30 vol.%, while the pore appearance should contribute to open porosity to keep the LSCM anode layer permeable for gases.

Several very important findings arise from the quantitative microstructure analysis of LSCM samples. Regarding sintering optimisation, a lower Sr content ($x = 0.1$) with a somewhat higher chromium content ($y = 0.6$) (sample La9Cr6) leads to proper microstructure formation at 1250 °C, where the grain-to-grain contact area is enlarged, making it progressively easier to find a solid continuous path of LSCM throughout the sample. At the same time, the appropriate porosity is preserved and the average grain size is the smallest, thus enlarging the interface area where gaseous reactants meet the electrocatalytic solid surface in a potential fuel cell. With additional information from the literature[10] regarding LSCM catalytic activity toward H_2 oxidation, it can be concluded that $La_{0,9}Sr_{0,1}Cr_{0,6}Mn_{0,4}O_3$ is the most appropriate LSCM chemical composition, which will also ensure the desired microstructure characteristics at the relatively low sintering temperature of 1250 °C.

4 CONCLUSIONS

$La_{1-x}Sr_xMn_{1-y}Cr_yO_{3\pm\delta}$ perovskite materials (x from 0 to 0.3 and y from 0.4 to 0.6) were prepared using the "reverse strike" carbonate co-precipitation method, which has been shown to be an appropriate method since it allows good control over the reaction system and the preparation of LSCM materials with various compositions.

After calcination of the precipitated mixed carbonate-hydroxide precursors at 1000 °C, the main crystalline phase in all the samples is LSCM perovskite. In the sample with the highest Sr content ($x = 0.3$) and equal amounts of chromium and manganese ($y = 0.5$), a strontium secondary phase $SrCrO_4$ was detected, while in samples with a lower Cr content ($y = 0.4$) a lanthanum-rich secondary phase La_2CrO_6 is formed. After sintering at 1250 °C, the secondary phase re-dissolved into the perovskite.

Microstructure parameters for the LSCM ceramics greatly depend on the sample composition. In samples with equal contents of Cr and Mn, a slight addition of Sr ($x = 0.1$) accelerates the sintering, while adding Sr to the perovskite above a concentration of $x = 0.2$ supresses the densifying process. In samples with a lower Cr content ($x = 0.4$), the presence of a lanthanum-rich secondary phase La_2CrO_6 causes non-homogenous microstructures to form.

Samples with a lower Sr content ($x = 0.1$) and a somewhat higher chromium content ($y = 0.6$) (La9Cr6) lead to appropriate microstructure formation at sintering temperatures as low as 1250 °C. Such a composition and sintering temperature are also recognized as the most appropriate parameters for suitable LSCM material.

5 REFERENCES

[1] A. Atkinson, S. Barnett, R. J.Gorte, J. T. D. Irvine, A. J. McEvoy, M. Mogensen, S. C. Singhal, J. Vohs, Advanced anodes for high temperature fuel cells, Nat. Materials, 3 (**2004**), 17–24, doi:10.1038/nmat1040

[2] C. Sun, U. Stimming, Recent anode advances in solid oxide fuel cells, J. Pow. Sources, 171 (**2007**), 247–260, doi:10.1016/j.jpowsour.2007.06.086

[3] H. Hurokawa, T. Z. Sholklaper, C. P. Jacobson, L. C. De Jonghe, S. J. Visco, Ceria nanocoating for sulphur tolerant Ni-based anodes of solid oxide fuel calls, Electrochem.Solid State, 100 (**2007**), 135–138, doi:10.1149/1.2748630

[4] S. Macintosh, R. J. Gorte, Direct hydrocarbon solid oxide fuel cells, Chem. Rev., 104 (**2004**), 4845–4865, doi:10.1021/cr020725g

[5] S. Tao, J. T. S. Irvine, A redox-stable efficient anode for solid-oxide fuel cells, Nat. Mater., 2 (**2003**), 320–322, doi:10.1038/nmat871

[6] W. Zhu, D. Ding, C. Xia, Enhancement in Three-Phase Boundary of SOFC Electrodes by an Ion Impregnation Method: A Modeling Comparison, Electrochem. Solid-State Lett., 11 (**2008**), B83–B86, doi:10.1149/1.2895009

[7] S. Tao, J. T. S. Irvine, Synthesis and characterization of $La_{0.75}Sr_{0.25}Cr_{0.5}Mn_{0.5}O_{3-\delta}$, a redox stable, efficient perovskite anode for SOFCs, J. Electrochem. Soc., 151 (**2004**), 252–259, doi:10.1149/1.1639161

[8] C. Lu, W. L. Worrell, J. M. Vohs, R. J. Gorte, A Comparison of Cu-Ceria-SDC and Au-Ceria-SDC Composites for SOFC Anodes, J. Electrochem. Soc., 150 (**2003**), A1357–A1359, doi:10.1149/1.1608003

[9] L. Deleebeeck, J. L. Fournier, V. Birss, Comparison of Sr-doped and Sr-free $La_{1-x}Sr_xMn_{0.5}Cr_{0.5}O_{3\pm\delta}$ SOFC Anodes, Solid State Ionics, 181 (**2010**), 1229–1237, doi:10.1016/j.ssi.2010.05.027

[10] L. Deleebeeck, J. L. Fournier, V. Birss, Catalysis of the hydrogen oxidation reactions by Sr-doped $LaMn_{1-y}Cr_yO_{3\pm\delta}$ oxides, Solid State Ionics, 203 (**2011**), 69–79, doi:10.1016/j.ssi.2011.07.017

[11] J. Wan, J. H. Zhu, J. B. Goodenough, $La_{0.75}Sr_{0.25}Cr_{0.5}Mn_{0.5}O_{3-d}$ + Cu composite anode running on H_2 and CH_4 fuels, Solid State Ionics, 177 (**2006**), 1211–121, doi:10.1016/j.ssi.2006.04.046

[12] S. P. Jiang, L. Zhang, Y. Zhang, Lanthanum strontium manganese chromite cathode and anode synthesized by gel-casting for solid oxide fuel cells, J. Mater. Chem., 17 (**2007**), 2627–2635, doi:10.1039/b701339f

[13] M. A. Raza, I. Z. Rahman, S. Beloshapkin, Synthesis of nanoparticles of $La_{0.75}Sr_{0.25}?Cr_{0.5}Mn_{0.5}$ $O_{3-\delta}$ (LSCM) perovskite by solution combustion method for solid oxide fuel application, Journal of Alloys and Compounds, 485 (**2009**), 593–597, doi:10.1016/j.jallcom.2009.06.059

[14] S. Zha, P. Tsang, Z. Cheng, M. Liu, Electrical properties and sulfur tolerance of $La_{0.75}Sr_{0.25}Cr_{1-x}Mn_xO_3$ under anodic conditions, J. Solid State Chem, 178 (**2005**), 1844–1850, doi:10.1016/j.jssc.2005.03.027

[15] D. M. Bastidas, S. Tao, J T. S. Irvine, A symmetrical solid oxide fuel cell demonstrating redox stable perovskite electrodes. J. Mater. Chem., 16 (**2006**), 1603–1605, doi:10.1039/b600532b

[16] B. Huang, S. R. Wang, R. Z. Liu, X. F. Ye, H. W. Nie, X. F. Sun, T. L. Wen, Performance of $La_{0.75}Sr_{0.25}Cr_{0.5}Mn_{0.5}O_{3-\delta}$ perovskite-structure anode material at lanthanum gallate electrolyte for IT-SOFC running on ethanol fuel, J. Power Sources, 167 (**2007**), 39–46, doi:10.1016/j.jpowsour.2007.02.022

[17] R. Pelosato, C. Cristiani, G. Dotelli, M. Mariani, A. Donazzi, I. N. Sora, Co – precipitation synthesis of SOFC electrode materials, International Journal of Hydrogen Energy, 38 (**2013**), 480–491, doi:10.1016/j.ijhydene.2012.09.063

[18] B. H. Sang, C. Pyeong-Seok, H. C. Yoon, L. Dokyol, L. Jong-Heun, Preparation of $La_{0.75}Sr_{0.25}Cr_{0.5}Mn_{0.5}O_{3-\delta}$ fine powders by carbonate coprecipitation for solid oxide fuel cells, J. Power Sources, 195 (**2010**), 124–129, doi:10.1016/j.jpowsour.2009.06.078

[19] A. M. Glazer, The Clasisification of Tilted octahedra in Perovskites, Acta Cryst., B28 (**1972**), 3384–3392

[20] Noel W. Thomas, A. Beitollahi, Inter-Relationship of Octahedral Geometry, Polyhedral Volume Ratio and Ferroelectric Properties in Rombohedral Perovskites, Acta Cryst., B50 (**1994**), 549–560

[21] E. M. Levin, H. F. McMurdie, Phase Diagrams for Ceramists, The American Ceramic Society, 1975, p. 29

[22] P. H. Duvigneaud, Factors Affecting the Sintering and the Electrical Properties of Sr-Doped $LaCrO_3$, J. European Cer. Soc., 14 (**1994**), 359–367, doi:10.1016/0955-2219(94)90073-6

[23] K. Zupan, M. Marinšek, Combustion Derived $La_{1-x}Sr_xMn_{0.5}Cr_{0.5}O_{3\pm\delta}$ ($x = 0.20, 0.25$) Perovskite: Preparation, Properties, Characterization, Mater. Tehnol., 48 (**2014**), 885–891

UDK 67.017:622.411.52:621.762.3
Original scientific article/Izvirni znanstveni članek

ISSN 1580-2949
MTAEC9, 50(5)749(2016)

ARTIFICIAL AGGREGATE FROM SINTERED COAL ASH

UMETNI AGREGAT IZ SINTRANEGA PEPELA PREMOGA

Vit Cerny, Rostislav Drochytka

Brno University of Technology, Faculty of Civil Engineering, Veveri 95, 602 00 Brno, Czech Republic
cerny.v@fce.vutbr.cz

Prejem rokopisa – received: 2015-07-22; sprejem za objavo – accepted for publication: 2015-09-23

doi:10.17222/mit.2015.235

Fly ash is one of the most commonly used secondary raw materials in the Czech Republic. It is used predominantly for re-cultivation, roads and additions to cement or plasters. The use of fly ash in the technology of sintering-based artificial aggregate was tested in the 1980s. However, the production was stopped for various technological and economic reasons. Nowadays, possibilities for the production of artificial aggregate are tested with fly ash produced in the Czech Republic and could be promising for future technologies, mainly with respect to the stability of production. The paper presents part of the study describing the possibilities of using microsilica and Fe_2O_3 for the optimization of a raw-material mix and fly-ash body. Three samples of high-temperature lignite combustion fly ash were selected from prospective sources in the Czech Republic. The fly ash was mixed with 5 % or 10 % additions. Then, samples were fired at temperatures of 1150 °C and 1200 °C. After firing, the physico-mechanical properties of the fly-ash bodies and microstructure were evaluated. The results imply that the addition of microsilica unambiguously improves the quality of the fly-ash body. The addition of Fe_2O_3 did not take part in the formation of the melt and weakened the fly-ash body's structure.

Keywords: fly ash, ash body, firing, microsilica, sintering, iron trioxide

Leteči pepel sodi k najpogosteje uporabljanim sekundarnim surovinam na Češkem. Predvsem se uporablja za rekultivacijo, za ceste in za cementne omete. Uporaba letečega pepela v tehnologiji izdelave sintranih agregatov je bila preizkušena v osemdesetih letih prejšnjega stoletja. Vendar je bila proizvodnja ustavljena iz različnih tehnoloških in ekonomskih razlogov. Dandanes se preizkušajo možnosti za izdelavo umetnih agregatov iz letečega pepela nastalega na Češkem, kar je lahko perspektivno za bodoče tehnologije, predvsem iz stališča stabilnosti izdelave. Članek predstavlja del študije o možnosti uporabe mikrosilike in Fe_2O_3 za optimizacijo mešanice surovin na osnovi letečega pepela. Trije vzorci letečega pepela pri visokotemperaturnem zgorevanju lignita, so bili izbrani iz obetavnih virov, ki so na voljo na Češkem. Leteči pepel je bil zmešan s 5 % ali 10 % dodatka. Nato so bili vzorci žgani pri temperaturi 1150 °C in 1200 °C; po žganju so bile določene fizikalno-mehanske lastnosti teles iz letečega pepela in ocenjena je bila mikrostruktura. Rezultati kažejo, da dodatek mikrosilike nedvomno izboljša kvaliteto kosov iz letečega pepela. Dodatek Fe_2O_3 ni sodeloval pri nastanku taline in je oslabil zgradbo kosov letečega pepela.

Ključne besede: leteči pepel, kos letečega pepela, žganje, mikrosilika, sintranje, železov trioksid

1 INTRODUCTION

Power plants producing electrical energy create energetic by-products during the combustion of pulverized lignite. The dominant proportion of the by-products is fly ash. Ecological and economic reasons motivate technological innovations focusing on using solid waste. The production of artificial fly-ash aggregate is a suitable construction material, which could be made from fly ash. Artificial, sintered, fly-ash aggregate is one of the few construction materials that can be produced only with fly ash. European and worldwide trends of newly developed building technologies accentuate the demand for the production of high-quality, sintered, artificial, fly-ash aggregate. If the character of the fly ash is optimal, no further treatment is needed. However, not every sample of fly ash has an optimal composition. The quality of fly ash has an influence on the composition of the mix, the technological parameters and the quality of the produced aggregate. For enhancing the properties of sintered fly-ash aggregate, additions commonly used in the ceramics industry could be used. The main candidates are microsilica and oxides of iron.

Microsilica is an amorphous SiO_2, which is commonly obtained from separators during the production of ferrosilicon and silicium in electric arc furnaces. The application of microsilica in fire-resistant materials has been known for more than 40 years. The main task of microsilica in fire-resistant ceramic materials is the reaction in the system of binders, including the reaction mechanism at various temperatures. Various temperatures can be critical as regards the reactions. Microsilica consists of spheroidal particles with a mean diameter of around 0.15 microns. These spheroidal particles are a construction unit of primary agglomerates, which are bound to one another by strong bonds. The large specific surface and the wide distribution of microsilica increases the effectiveness of the encapsulation of the grains and the functionality of the fire-resistant ceramic materials compared to a narrow fraction. Microsilica is usually the finest part of the system with a specific surface of around 20 m^2 g. The surface properties and possible impurities are important for a determination of the properties of the

final product. Microsilica can add more than 50 % to the total surface area of the particles in the mix.[1]

Oxides of iron influence the formation of a ceramic body in various atmospheres[2], temperatures and firing cycles in furnaces There are three main forms of iron used in ceramics: red iron trioxide (Fe_2O_3), black iron monoxide oxide or magnetite (FeO or Fe_3O_4) and yellow hydrated iron oxide (FeO(OH)). Iron trioxide is considerably influenced by a reducing atmosphere, in which it can act as a melting agent at high temperatures. The presence of iron reduces the temperature of melting.[3] From the point of view of a reduction of the firing temperature, oxides of iron can be used as effective melting agents for the production of sintered fly-ash aggregate.

The optimal mix of appropriate raw materials for the production of artificial aggregate is mixed with water and granulated on a cylindrical or plate granulator, which makes the appropriate shape of the sintered fly-ash aggregate. After granulation, the bodies are fired at a maximum temperature of around 1200 °C. After sufficient firing and cooling, the mix is crushed and screened for the final fractions.

For the production of aggregate of good quality, the granulometry of the input materials, their structure and chemical composition are also important. The produced sintered fly-ash aggregate is used for filtration layers, back filling and lightweight concrete.[4–6]

2 EXPERIMENTAL PART

Three samples representing prospective sources in the Czech Republic were selected for verification of the appropriateness of high-temperature lignite combustion fly ash for the production of artificial aggregate.

From the physico-mechanical and physico-chemical parameters we selected the loss on ignition (CSN 72 0103) showing unburned residues, the bulk density (CSN 72 2071), the specific surface area and the rest on the 0.045-mm sieve (CSN 72 2072-6). We also conducted the chemical and mineralogical analyses.

The parameters listed in **Table 1** imply that fly ash produced in the Czech Republic has a minimal unburnt content and fulfills the requirements of the standard (CSN 72 2072-6, 2013) for a maximum loss on ignition of 15 %. For self-firing, it will be necessary to mix the fly ash with pulverized coal to achieve an optimal value of 8 % combustibles by weight. The greater coarseness of the fly ash FA3 evaluated with respect to the rest on the 0.0045-mm sieve and specific surface is evident. This fly ash also has a larger content of iron and lime, which can cause a reduction of the melting temperature of a batch. All the values of the high-temperature fly-ash samples fulfill the requirements of the Standard CSN 72 2072-6, 2013 for a minimal value of 800 kg m^{-3}.

As is clear from **Table 2** FA1 has the highest percentage of mullite and a lower content of amorphous phase in comparison with FA2 and FA3. The mineralogical analysis further confirms that FA2 contains more minerals with a lower melting point and a low content of mullite.

Table 2: Mineralogy of tested ashes, in mass fractions (*w*/%)
Tabela 2: Mineralogija preizkušenih pepelov, v masnih odstotkih (*w*/%)

Sample	Quartz	Mullite	Hematite	Magnetite	Amorphous phase
	SiO_2	$Al_6Si_2O_{13}$	Fe_2O_3	Fe_3O_4	–
FA1	7.0	39.3	1.2	0.1	39.5
FA2	7.2	19.1	2.5	3.1	55.2
FA3	7.8	32.3	–	0.2	58.1

As an addition for the experimental work, microsilica (96 % SiO_2) and Fe_2O_3 (powder, 97 % cleanliness) were selected. As a reference, samples from pure fly ash were used, which were then modified with a 5 % or 10 % addition. The mixtures were mixed with water to reach the limit of fluidity. Samples of size 20 mm × 20 mm × 100 mm were made, which were next day dried at 60 °C for 2 h and then fired in a muffle kiln. The firing was characterized by an initial temperature of 25 °C and the rate of firing the muffle kiln of 300 °C/h and an isothermal dwell at 1150 °C (resp. 1200 °C) for 10 min. After firing and natural cooling, the specimens were taken out of the kiln and placed in a desiccator. After thermal stabilization, their density (CSN EN 1015-10), compressive strength (CSN EN 14617-15) and water-absorbing capacity (CSN EN 1097-6) were determined. Then, the samples were analyzed with a scanning electron microscope using a sensing element in an environmental form. Primarily, the structure was analyzed and the influence of the addition on the fly ash body.

3 RESULTS AND DISCUSSION

After firing in a laboratory furnace and sufficient cooling to laboratory temperature 20±5 °C, the following

Table 1: Main parameters of the tested ashes
Tabela 1: Glavni parametri preizkušenih pepelov

Sample	Loss on ignition (%)	Bulk density (compacted) (kg/m^3)	Rest on the sieve 0.045 mm (%)	Specific surface (m^2/kg)	Chemical composition (%)				
					SiO_2	Al_2O_3	Fe_2O_3	SO_3	CaO
FA1	1.19	990	58.5	329	47.7	28.2	5.6	0.13	1.1
FA2	1.15	1010	72.0	234	50.0	23.4	14.5	0.26	3.4
FA3	1.07	1110	53.1	299	54.6	29.5	5.5	0.10	1.8

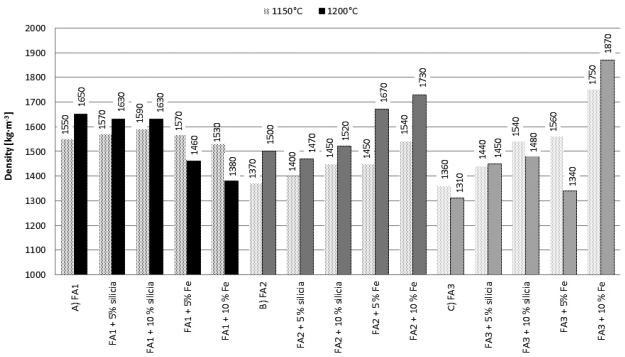

Figure 1: Density of fired samples
Slika 1: Gostota žganih vzorcev

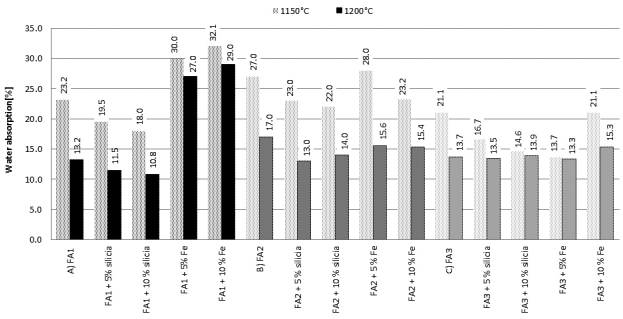

Figure 3: Water absorption of fired samples
Slika 3: Absorpcija vode žganih vzorcev

physico-mechanical parameters of the test specimens were determined.

Figure 1 shows the results of the determination of density. In general, it can be stated that the density grows slightly with an increasing temperature of firing. The samples based on FA1 showed the highest values of density, while the samples based on FA3 showed the lowest density.

A determination of the compressive strength (**Figure 2**) showed that the strengths at the firing temperature 1200 °C were considerably higher than the strengths at 1150 °C. The addition of silica had a very positive effect on the strength of the fly ash body – samples with as little as 5 % showed considerably higher strengths. In contrast, the addition of Fe_2O_3 weakened the fly-ash body and the measured strengths were often lower than those of the reference samples based on pure fly ash.

An evaluation of the results of the determination of the water-absorbing capacity (**Figure 3**) in some cases shows the influence of firing temperature on the quality of the fly-ash body. The water-absorbing capacity of the samples fired at 1150 °C was often much higher. This can be caused by insufficient sintering of the fly-ash body and a higher proportion of open porosity. The influence of the type of addition on the results of the water-absorbing capacity is most marked for the samples based on FA with the addition of Fe_2O_3.

To clarify the results determined during the evaluation of the physico-mechanical parameters, the samples

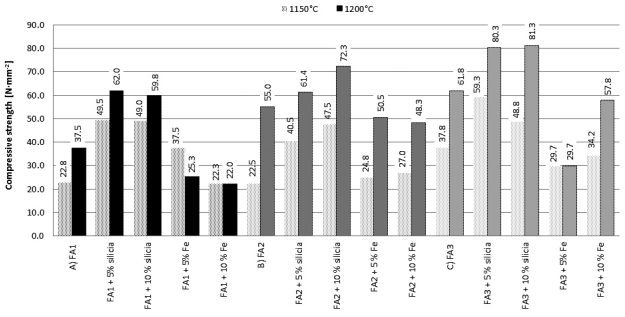

Figure 2: Compressive strength of fired samples
Slika 2: Tlačna trdnost žganih vzorcev

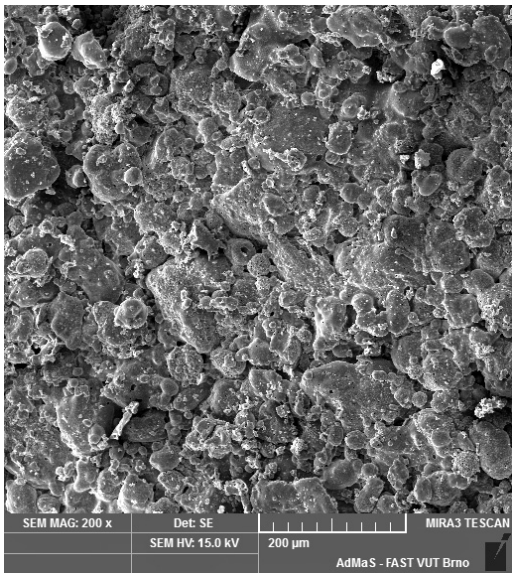

Figure 4: Structure of fly-ash body with 5 % of mass fractions of Fe_2O_3
Slika 4: Struktura kosa letečega pepela s 5 % masnega deleža Fe_2O_3

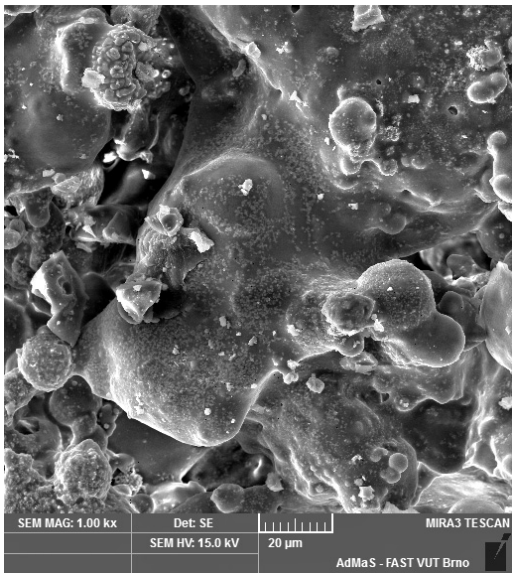

Figure 5: Detail of structure of fly-ash body with 5 % of mass fractions of Fe_2O_3
Slika 5: Detajl strukture kosa letečega pepela s 5 % masnega deleža Fe_2O_3

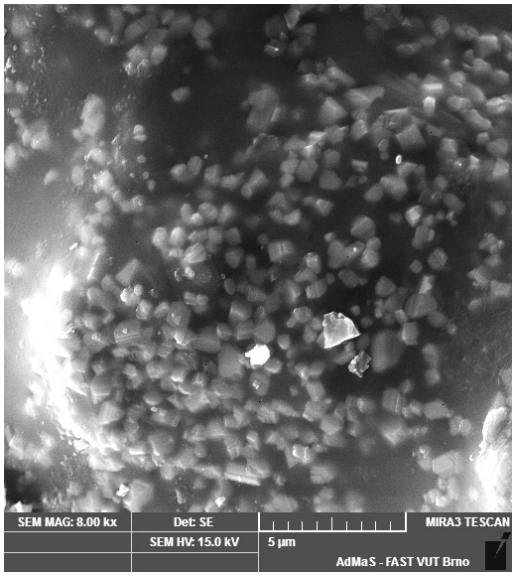

Figure 6: Non-reacted proportion of Fe_2O_3 in fly-ash body
Slika 6: Nereagiran delež Fe_2O_3 v kosu letečega pepela

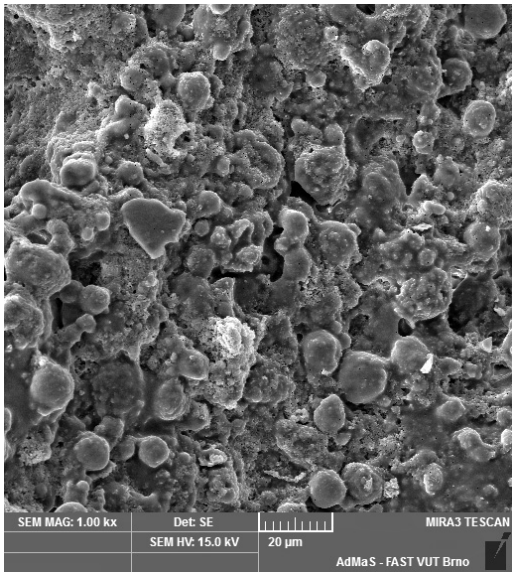

Figure 8: Structure of fly-ash body with 10 % of mass fractions of silica
Slika 8: Struktura kosa letečega pepela z 10 % masnega deleža kremena

were examined under a scanning electron microscope with a sensing element in an environmental form. The aim was an evaluation of the influence of firing temperature and additions on the structure of the fly-ash body.

Figures 4 to **7** show the structure of a surface of a test specimen based on FA3 with a 5 % addition of Fe_2O_3 and fired at 1200 °C. **Figure 4** shows a low proportion of sintered structure and visible grains of fly ash. **Figure 5** shows a part of a sample with melted material at higher magnification, where non-reacted grains of Fe_2O_3 are visible. **Figure 6** shows a closer detail of the same place grains of Fe_2O_3 and **Figure 7** an analysis of the elements in a larger area where the dominant Fe is evident in the grains. This fact proves that Fe_2O_3 did not take part in the formation of a solid structure, and that it weakened the fly-ash body.

Figures 8 and **9** show the structure of the test specimens based on FA3 with a 10 % addition of silica. **Figure 8** shows a sample fired at 1150 °C, where the grains of fly ash and a minimal proportion of melted material are clear. **Figure 9** shows a sample fired at 1200 °C, where the proportion of melted material is more con-

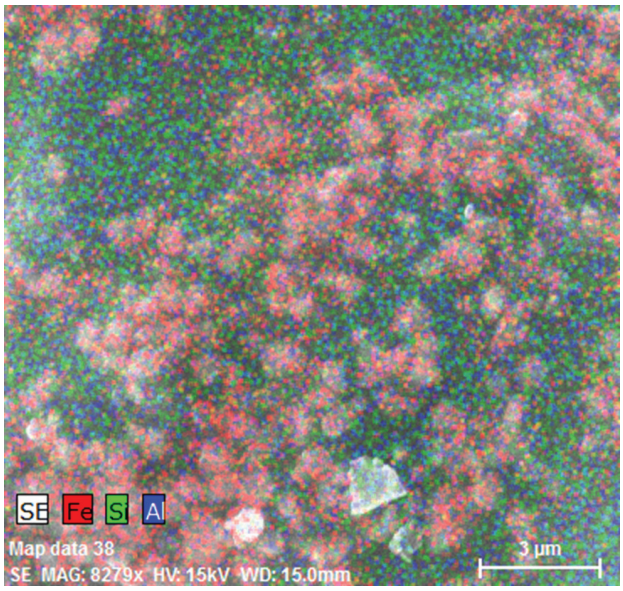

Figure 7: Marked composition of elements of sample with non-reacted Fe_2O_3
Slika 7: Razporeditev elementov v vzorcu, ki ni reagiral z Fe_2O_3

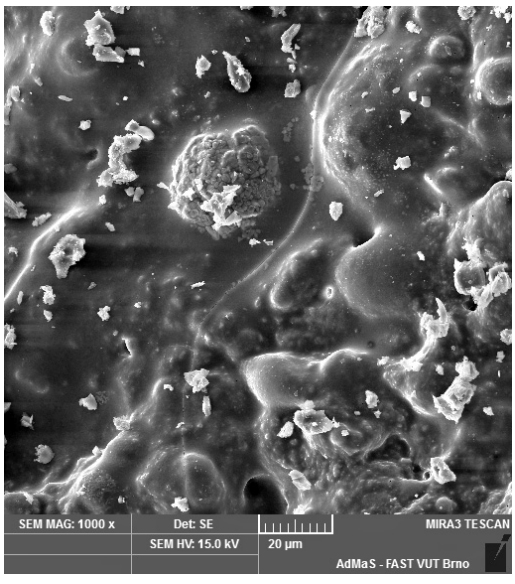

Figure 9: Detail of structure of fly-ash body with 5 % of mass fractions of silica
Slika 9: Detajl strukture kosa letečega pepela s 5 % masnega deleža kremena

siderable and the grains have a stronger and more homogeneous structure.

4 CONCLUSIONS

The manufacture of artificial aggregate from fly ash is one of the options for using the maximum proportion of this raw material in construction materials. The character of the fly ash and good control of the technology for producing the aggregate by self-firing also brings savings for traditional raw materials. The paper described the experimental testing of possibilities for the modification of fly ash with the addition of microsilica or Fe_2O_3 in order to achieve better quality of the fly-ash body with a lower energy demand of the process. The results show how important it is to set the firing temperature at 1200 °C, which makes sure it is possible to achieve considerably higher strengths in the system. An evaluation of the influence of the used additions showed that the addition of microsilica unambiguously improves the quality of the fly-ash body. Higher strengths and a lower water-absorbing capacity were achieved compared to use of pure fly ash. The addition of Fe_2O_3 did not take part in the formation of the melt, and stayed almost unchanged and weakened the fly-ash body structure.

Acknowledgements

This paper has been worked out under the project No. LO1408 "AdMaS UP – Advanced Materials, Structures and Technologies", supported by Ministry of Education, Youth and Sports under the "National Sustainability Programme I".

5 REFERENCES

[1] B. Sandberg, B. Myhre, Microsilica A Versatile Refractory Raw Material, Indian Refractories Congress, Jamshedpur, India 1994, 1–7

[2] R. Magrla, M. Fridrichova, K. Kulisek, K. Dvorak, O. Hoffmann, Utilisation of Fluidised Fly Ash for Reduction of CO_2 Emissions at Portland Cement Production, Advanced Materials Research, 1054 (**2014**), 168–171, doi:10.4028/www.scientific.net/AMR.1054.168

[3] J. Britt, All about iron: Iron is everywhere in many different forms, but that doesn't mean it has to be boring-or even brown, Cmtechnofileiron, 2011

[4] J. Brozovsky, Influence of Moisture of Light-Weight Concrete Containing Lightweight Expanded Clay Aggregate on Test Results Obtained by Means of Impact Hammer, Advanced Materials Research, 753–755 (**2013**), 663–667, doi:10.4028/www.scientific.net/AMR.753-755.663

[5] B. Yun, I. Ratiyah, P. A. M. Basheer, Properties of lightweight concrete manufactured with fly ash, furnace bottom ash, and Lytag, International Workshop on Sustainable Development and Concrete Technology, Beijing 2004, 77–88

[6] T. Melichar, J. Bydzovský, Study of the parameters of lightweight polymer-cement repair mortars exposed to high temperatures, Applied Mechanics and Materials, 395 (**2013**) 8, 429–432, doi:10.4028/www.scientific.net/AMM.395-396.429

[7] R. Sokolar, Keramika, Publishing house VUTIUM, Brno, Czech Republic 2006

UDK 620.19:620.178.16:621.793.8
Original scientific article/Izvirni znanstveni članek

ISSN 1580-2949
MTAEC9, 50(5)755(2016)

INVESTIGATION STUDIES INVOLVING WEAR-RESISTANT ALD/PVD HYBRID COATINGS ON SINTERED TOOL SUBSTRATES

PREISKAVE OBRABNE ODPORNOSTI HIBRIDNEGA NANOSA ALD/PVD NA SINTRANEM ORODJU

Marcin Staszuk, Daniel Pakuła, Tomasz Tański

Silesian University of Technology, Institute of Engineering Materials and Biomaterials, Konarskiego Street 18A, 44-100 Gliwice, Poland
marcin.staszuk@polsl.pl

Prejem rokopisa – received: 2015-07-22; sprejem za objavo – accepted for publication: 2015-10-13

doi:10.17222/mit.2015.236

This paper is an important research contribution to the development of PVD coatings, in particular, on ceramic substrates, which, due to their dielectric properties, are difficult materials to coat using this technique. In order to satisfy the desired expectations relating to the PVD coatings, one of the basic properties must be provided for, the adherence to the substrate. The main aim of this research is to investigate the structure and mechanical properties of the coatings deposited in a hybrid process, comprising the atomic-layer deposition (ALD) and cathodic-arc evaporation (CAE-PVD) on sintered carbides and multipoint ceramic cutting tools. The concept of this research study involves an execution and investigation of ALD + PVD hybrid coatings on sintered carbides and a sialon-ceramic substrate, and defining the influence of the ALD interlayer on the adherence of the investigated coatings. The critical load L_c, which is the adhesion measure of coats, was determined with the scratch-test method and a tribological test made with a pin-on-disk tester. Observations of the surface topography and wear mechanism were performed using a scanning electron microscope and atomic-force microscopy. The investigation studies showed that an ALD layer considerably improves the adherence of the PVD layer to the tool-ceramic substrate. The research of the coatings on sintered-carbide substrates showed that the adherence of the PVD coating to the substrate deteriorates in the case of applying an ALD interlayer.

Keywords: PVD, ALD, hybrid coatings, tool ceramics, sintered carbides

Članek je pomemben raziskovalni prispevek k razvoju PVD nanosov, še posebno na keramični podlagi, ki je zaradi dielektričnih lastnosti zahteven material za nanašanje s to tehniko. Da bi zadovoljili pričakovanja na delu s PVD nanosom, je oprijemljivost na podlago osnovna lastnost, na katero je potrebno biti pozoren. Glavni namen raziskave je preiskati strukturo in mehanske lastnosti nanosa, nanešenega s hibridnim postopkom, ki obsega nanos atomskih plasti (ALD) in katodno izparevanje v obloku (CAE-PVD) na sintrane karbide in večtočkovno keramično rezilno orodje. Koncept te raziskave vključuje izvedbo in preiskavo hibridnega nanosa ALD + PVD na podlago iz sintranih karbidov in sialon keramike ter določitev vpliva vmesne plasti ALD na oprijemljivost preiskovanih nanosov. Kritična obremenitev L_c, ki je merilo oprijemljivosti nanosov, je bilo določeno s preizkusom razenja in s tribološkim preizkusom trn na plošči. S pomočjo vrstičnega elektronskega mikroskopa in mikroskopa na atomsko silo je bilo izvedeno opazovanje topografije površine in mehanizma obrabe. Izvedene preiskave kažejo, da ALD nanos močno izboljša oprijemljivost PVD nanosa na orodno keramiko. Pri nanosu na podlago iz sintranega karbida je raziskava pokazala, da je pri uporabi ALD vmesne plasti, oprijemljivost PVD nanosa slabša.

Ključne besede: PVD, ALD, hibridni nanosi, keramika za orodja, sintrani karbidi

1 INTRODUCTION

Sialon-tool ceramics are a group of tool materials combining the mechanical properties of silicon nitride Si_3N_4 and the chemical properties of Al_2O_3. Ceramic sinters are fabricated with powder-metallurgy methods, but in contrast to sintered carbides, they do not contain a metallic binder. The use of tool ceramics as compared to sintered carbides is still considerably small but it is growing, also due to the application of thin wear-resistant layers PVD and CVD.[1,2]

Surface engineering technologies play a significant role in material engineering and are viewed as the fundamental scope of knowledge in this field of engineering. The research entities working in this field try to investigate and identify the phenomena taking place on the surfaces of the machined materials. In order to improve the operating properties of products, various surface-machining technologies are applied.[2–6] The advantages arising from the application of PVD coatings on cutting tools such as a high microhardness and resistance to abrasion, a low friction coefficient of the tool covered with the coat, the resistance to oxidation or to the formation of build-up edges on the tool, combined with the possibility to machine materials without liquid cooling lubricants are important contributions advocating the development of this technological field. However, in order to improve the desired properties of PVD coatings, one of the basic properties must be taken care of, which is the adherence to the substrate. The coating of ceramic materials in PVD processes, including also tool ceramics, is difficult due to dielectric properties, since the inability of the substrate polarization during the coating

process makes it difficult to obtain coatings with a good adherence to ceramic substrates.[2,7–11]

The fabrication technology of stratified coatings of the type "adhesive layer/PVD layer" using the multi-stage surface machining is one of the most modern methods to modify the properties of the surface layer and it consists, in a successive application, of two (or more) technologies of surface engineering. In terms of material effects, we obtain multilayer systems whereof one part is made up of an appropriately selected adhesive layer fabricated on the surface of the substrate, which protects the "proper" PVD layer against a loss of internal cohesion and an insufficient adhesion to the substrate. And on the other end of the system, we obtain a PVD coating which efficiently insulates the substrate, limiting the impact of the external harmful factors encountered in the operating process.[2,12]

The coatings of the (Ti,Al)N type are isomorphic, with titanium nitride which is still widely applied. The presence of aluminum in the coatings of this type brings about the situation where the service-life temperature of these coatings exceeds 970 K, and in such operating conditions of raised temperature, a layer of Al_2O_3 is formed on the surface, which forms a diffusive barrier for the atmospheric oxygen.[13,14]

Zinc oxide is a semiconductor characterized by a high energy gap (3.4 eV), high exciton binding energy (60 meV) and easy n-type doping.[15,16] Zinc oxide, ZnO, obtained with the use of the ALD technique on a sialon-ceramic substrate enables the polarization of this substrate during the technological process of PVD and, hence, the objective of this paper is to investigate the impact of the ZnO layer obtained with the use of the ALD technique on the adhesion of the hybrid coating ALD/PVD of the ZnO/(Ti,Al)N type to the sialon substrate. For the sake of comparison, we also investigated the coatings on sintered carbide substrates.

2 MATERIALS AND METHOD

The research studies were carried out on multipoint cutting tools made of sintered carbides WC-Co and sialon-tool ceramics covered in the PVD and ALD/PVD processes. The tools were covered during the cathodic-arc evaporation process CAE-PVD with the (Ti,Al)N coating type and in the ALD/PVD hybrid process using the ZnO/(Ti,Al)N coating type.

The topography of the surfaces and wear mechanisms of the coatings was viewed with a Supra 35 scanning electron microscope from Zeiss. The secondary-electron (SE) detection was used to obtain the images of the tested samples, with an acceleration voltage of 5–20 kV.

The topography of the coatings was tested using a Park Systems XE-100 atomic-force microscope. The tests were carried out in the non-contact mode.

The adherence of the coatings to the substrate was assessed with a scratch test on a Revetest device from CSEM. The method consists of moving a Rockwell C diamond indenter through the surface of a tested sample at a constant speed, with the applied force growing linearly. The ranges of the applied load were 0–100 N and 0–200 N. The L_c critical load, at which the coating adhesion is lost, was determined according to the acoustic-emission value registered during the measurement and by observing the scratches formed during the scratch test.

The abrasive-wear-resistance tests and the wear-factor tests for the tested coatings were performed with the pin-on-plate method using a CSEM Tribometer (THT). A 6 mm Al_2O_3 ball was used as the counter specimen. The tests were made at room temperature. The following test conditions were applied: a normal force of F_N = 10 N and a movement speed of v = 0.1 m/s. The total distance of 1 km was set for all the tested specimens.

3 DISCUSSION AND TEST RESULTS

The value of critical load L_c, being the adherence measure for the investigated coatings on sintered-carbide substrates or sialon-tool ceramic substrates, was determined using a scratch test (**Figure 1**). The research studies show that the ALD/PVD hybrid coat has a much

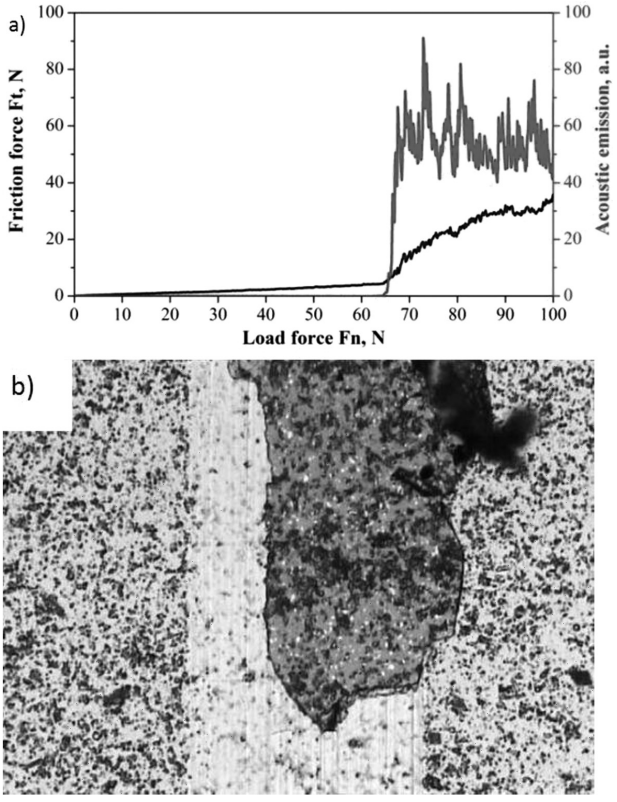

Figure 1: a) Acoustic emission (AE) and friction force F_t depending on load F_n for the ZnO/(Ti,Al)N coating on sialon ceramics, b) scratch failure at L_c (opt) = 65 N, magnified 200×

Slika 1: a) Akustična emisija (AE) in sila trenja F_t v odvisnosti od obremenitve F_n pri ZnO/(Ti,Al)N nanosu na sialon keramiko, b) poškodba z razo pri L_c (opt) = 65 N, povečano 200×

higher adherence to the sialon-ceramic substrate than the PVD coating without the adhesive layer (**Table 1**). A reverse situation takes place in the case of coatings on sintered-carbide substrates. Due to high adhesion of the PVD coating to the sintered-carbide substrate, the ALD layer causes a drop in the critical load from 109 N to 55 N.

Table 1: Critical loads L_c of the investigated coatings
Tabela 1: Kritične obremenitve L_c preiskovanih nanosov

Type of coating	Critical load L_c, N	
	Sialon substrate	Cemented-carbide substrate
(Ti,Al)N	21	109
ZrO/(Ti,Al)N	64	55

The damage done to the coats during the performed adhesion/scratch tests was identified on the basis of observations with the scanning electron microscope. The studies carried out show that it is the delamination, which is the principle mechanism of the coat damage on the sialon-ceramic substrate after the critical load L_c has been exceeded. In the case of the PVD coat, which is characterised by a low adherence to the ceramic substrate, a total delamination with vast chipping was identified. Furthermore, a low adherence of the PVD coat to the ceramic substrate indicates a considerable morphological non-homogeneity and, in particular, the presence of chippings found on the whole surface of the coat (except for the scratch area) (**Figure 2**). A low adherence of the coat to the substrate results in its unprompted chipping due to the internal strain of the coat. In the case of the ZnO/(Ti,Al)N hybrid coat on the sialon substrate, delamination was identified on both sides of the sample (**Figure 3**). The chipping on both sides of the scratched sample is definitely less vast than that observed in the case of the (Ti,Al)N coat on the same substrate. The only morphological defects of the hybrid coat are the drop-shaped microparticles, inseparably connected with the cathodic-arc evaporation process (**Figure 4**). In the case

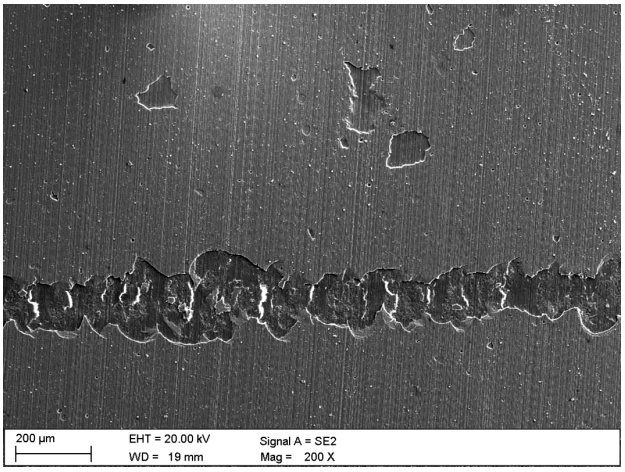

Figure 2: Characteristic failure obtained with the scratch test of the (TiAl)N coating deposited on the sialon-ceramic substrate
Slika 2: Značilna poškodba pri preizkusu z razenjem nanosa (Ti,Al)N, nanešenega na podlagi iz sialonske keramike

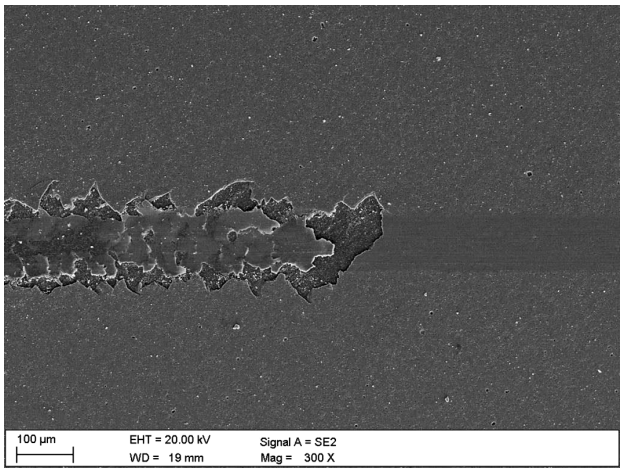

Figure 3: Characteristic failure obtained with the scratch test of the ZnO/(TiAl)N coating deposited on the sialon-ceramic substrate
Slika 3: Značilna poškodba pri preizkusu razenja ZnO/(Ti,Al)N nanosa, nanešenega na podlago iz sialonske keramike

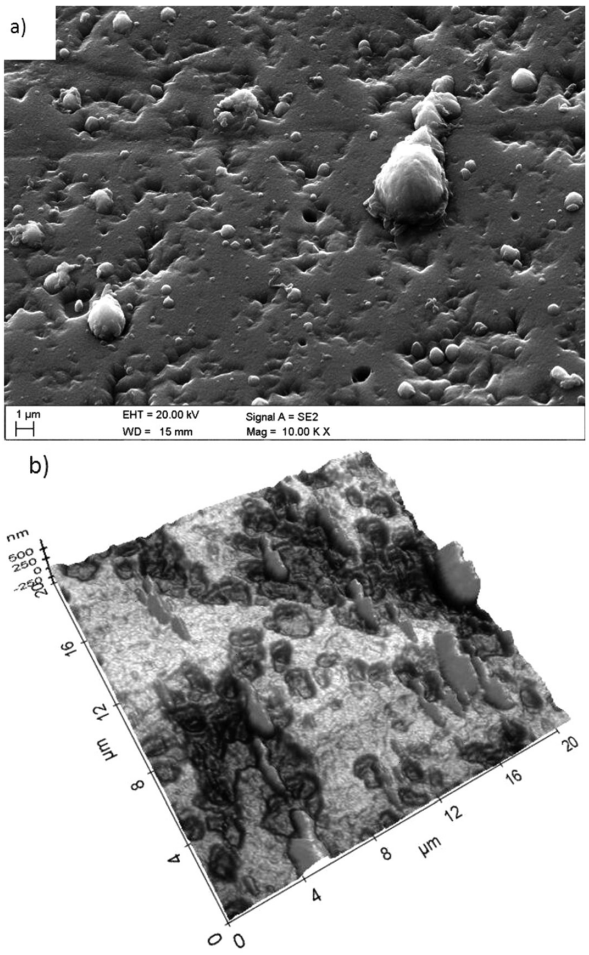

Figure 4: Surface topography of the ZnO/(Ti,Al)N coating deposited onto the sialon-ceramic substrate: a) SEM, b) AFM
Slika 4: Topografija površine ZnO/(Ti,Al)N nanosa, nanešenega na podlago iz sialonske keramike: a) SEM, b) AFM

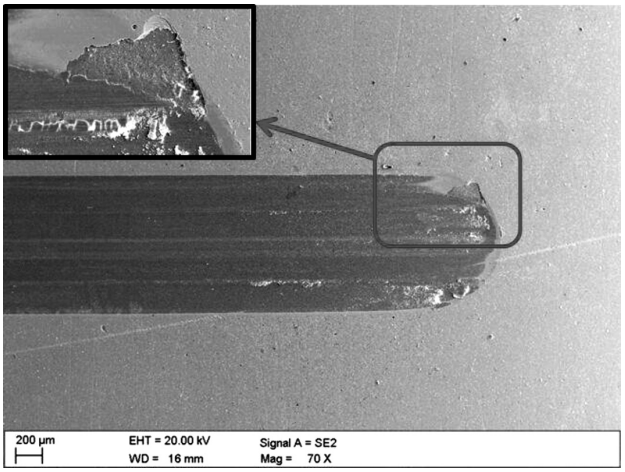

Figure 5: Trace of tribological damage on the surface of the (Ti,Al)N coat deposited on the sialon-ceramic substrate

Slika 5: Sled tribološke poškodbe na površini (Ti,Al)N nanosa, nanešenega na podlago iz sialonske keramike

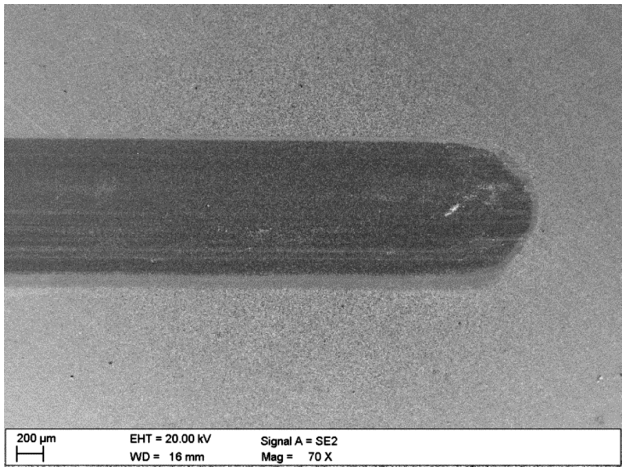

Figure 6: Trace of tribological damage on the surface of the ZnO/(Ti,Al)N coat deposited on the sialon-ceramic substrate

Slika 6: Sled tribološke poškodbe na površini ZnO/(Ti,Al)N nanosa, nanešenega na podlago iz sialonske keramike

of the coats on sintered-carbide substrates, friction is the dominant mechanism. In the case of the PVD coat on the sintered-carbide substrate, which is characterised by the highest adherence among the investigated samples, no abrasion deep down in the substrate was identified until the maximum load was reached during the scratch test. However, numerous cohesive cracks were identified after surpassing the critical load L_c. In the ZnO/(Ti,Al)N coat on the same substrate, we identified a uniform abrasion spreading down into the substrate after the critical load was exceeded.

With the tests on the abrasive-wear resistance of the coats deposited on sialon ceramics and on sintered carbides using the pin-on-plate method, we found that in almost all the cases where the coats were applied the coats were damaged down to the substrate zone (**Figures 5** and **6**). The dominant wear mechanism of the investigated coats was attrition. We also found that in some cases the damaged coat sticks onto the material of the counter specimen, which has a direct impact on the changing values of the friction coefficient. The research studies also confirm a positive impact of the ZrO layer on the attrition resistance as compared to the specimen without such a layer. At one end of the scratch, we observed a lot of damage to the coat deposited on the sialon substrate without the ZrO layer. The damage is of adhesive character – we can observe stratifications and cracks of the layer (**Figure 5**). And in the case of the coat deposited with the ZrO layer, the end of the scratch is uniformly grated without any adhesive damage (**Figure 6**).

4 CONCLUSION

Nowadays, the improvement of the wear resistance of cutting tools mainly involves surface machining, while the selection of the technology or coating material aims at ensuring the proper resistance of a tool to dominant wear mechanisms. The operating properties of the coats resistant to the wear are the results of many components, primarily the microhardness, the grain size and the adherence to the substrate. Especially the last property is of key importance, and in view of the performed research studies[2], the grain size, the thickness and the microhardness of the obtained coats have smaller impacts than the adhesion on the durability of cutting tools since the changes in these properties have smaller impacts on service life.

The paper presents the results of research studies involving the application of an ALD layer to obtain a better adhesion of the PVD coat to the tool sialon-ceramic substrate or sintered-carbide substrate. We investigated the (Ti,Al)N coat deposited on both substrates, with the ZnO layer and without it. On the basis of the investigation studies, we can state that zinc oxide considerably improves the adherence of the PVD coat to the ceramic substrate, which was confirmed with scratch tests and observations of the damage made during the tests, using a scanning electron microscope. The critical load, being the adherence measure of the PVD coat on the ceramic substrate, increased due to the application of the adhesive layer by over 200 %. With respect to the investigated coats on sintered carbides, the adherence of the PVD coat to the ALD layer decreased as compared to the coat without ALD.

The improvement in the adherence of the PVD coat to the ceramic substrate is undaubtly connected with the possibility to polarize the substrate during the coating process involving the application of the ZnO layer. The results of the research studies are important since the deposition of ceramics in PVD processes is hindered due to the dielectric properties of ceramics.

Acknowledgements

The publication was co-financed by the statutory grant of the Faculty of Mechanical Engineering of the Silesian University of Technology in 2015.

5 REFERENCES

[1] M. Sopicka-Lizera, M. Tańcula, T. Włodek, K. Rodak, M. Hüller, V. Kochnev, E. Fokina, K. MacKenzie, The effect of mechanical activation on the properties of β-sialon precursors, Journal of the European Ceramic Society, 28 (**2008**) 279–288, doi:10.1016/j.jeurceramsoc.2007.05.003

[2] M. Staszuk, L.A. Dobrzański, T. Tański, W. Kwaśny, M. Musztyfaga-Staszuk, The effect of PVD and CVD coating structures on the durability of sintered cutting edges, Archives of Metallurgy and Materials, 59(1) (**2014**), 269–274, doi:10.2478/amm-2014-0044

[3] D. Janicki, High Power Diode Laser Cladding of Wear Resistant Metal Matrix Composite Coatings, Solid State Phenomena, Mechatronic Systems and Materials V, 199 (**2013**), 587–592, doi:10.4028/www.scientific.net/SSP.199.587

[4] A. Lisiecki, Titanium Matrix Composite Ti/TiN Produced by Diode Laser Gas Nitriding, Metals, 5 (**2015**), 54–69, doi:10.3390/met5010054

[5] A. Kurc-Lisiecka, W. Ozgowicz, W. Ratuszek, J. Kowalska, Analysis of Deformation Texture in AISI 304 Steel Sheets, Sol. St. Phenomena, 203–204 (**2013**), 105–110, doi:10.4028/www.scientific.net/SSP.203-204.105

[6] T. Tański, Characteristics of Hard Coatings on AZ61 Magnesium Alloys, Strojniski Vestnik-Journal Of Mechanical Engineering, 59(3) (**2013**), 165–174, doi:10.5545/sv-jme.2012.522

[7] L.A. Dobrzański, D. Pakuła, Comparison of the structure and properties of the PVD and CVD coatings deposited on nitride tool ceramics, Journal of Materials Processing Technology, 164–165 (**2005**), 832–842, doi:10.1016/j.matprotec.2005.02.094.

[8] L.A. Dobrzański, L.W. Żukowska, J. Mikuła, K. Gołombek, D. Pakuła, M. Pancielejko, Structure and mechanical properties of gradient PVD coating, Journal of Materials Processing Technology, 201 (**2008**), 310–314, doi:10.1016/j.matprotec.2007.11.283

[9] K. Lukaszkowicz, A. Czyzniewski, W. Kwasny, M. Pancielejko, Structure and mechanical properties of PVD coatings deposited onto the X40CrMoV5-1 hot work tool steel substrate, Vacuum, 86 (**2012**), 1186–1194, doi:10.1016/j.vacuum.2011.10.031

[10] L. Żukowska, J. Mikuła, M. Staszuk, M. Musztyfaga-Staszuk, Structure And Properties Of PVD Coatings Deposited On Cermets, Archives of Metallurgy and Materials, 60(2) (**2015**), 727–733, doi:10.1515/amm-2015-0198

[11] B. Podgornik, V. Leskovšek, Wear mechanisms and surface engineering of forming tools, Mater. Tehnol., 49 (**2015**) 3, 313–324, doi:10.17222/mit.2015.005

[12] Z. Gronostajski, M. Kaszuba, M. Hawryluk, M. Marciniak, M. Zwierzchowski, A. Mazurkiewicz, J. Smolik, Durability of Hot Forging Tools by Applying Hybrid Layers, Metalurgija, 54 (**2015**) 4, 687–690

[13] Guo-an Cheng, Dong-yan Han, Chang-lin Liang, Xiao-ling Wu, Rui-ting Zheng, Influence of residual stress on mechanical properties of TiAlN thin films, Surface & Coatings Technology, 228 (**2013**), S328–S330, doi:10.1016/j.surfcoat.2012.05.108

[14] Hongfei Shang, Jian Li, Tianmin Shao, Mechanical properties and thermal stability of TiAlN/Ta multilayer film deposited by ion beam assisted deposition, Applied Surface Science, 310 (**2014**), 317–320, doi:10.1016/j.apsusc.2014.03.099

[15] Jian Zhang, Hui Yang, Qi-long Zhang, Shurong Dong, J.K. Luo, Forming-free resistive switching of tunable ZnO films grown by atomic layer deposition, Applied Surface Science, 282 (**2013**), 390–395, doi:10.1016/j.apsusc.2013.05.141

[16] V. Subramanian, T. Bakhishev, D. Redinger, S.K. Volkman, Solution processed zinc oxide transistors for low cost electronic applications, Journal of Display Technology, 5/12 (**2009**), 525–530, doi:10.1109/JDT.2009.2029124

UDK 621.791.76/.79:691.714:621.791.05
Original scientific article/Izvirni znanstveni članek

ISSN 1580-2949
MTAEC9, 50(5)761(2016)

DISSIMILAR SPOT WELDING OF DQSK/DP600 STEELS: THE WELD-NUGGET GROWTH

TOČKASTO VARJENJE JEKEL DQSK/DP600: RAST JEDRA ZVARA

Seyed Pirooz Hoveida Marashi

Amirkabir University of Technology, Mining and Metallurgical Engineering Department, Tehran, Iran
pmarashi@aut.ac.ir

Prejem rokopisa – received: 2015-07-30; sprejem za objavo – accepted for publication: 2015-10-12

doi:10.17222/mit.2015.241

The weld-nugget size is the key issue in determining the mechanical properties of resistance spot welds. This paper aims at investigating the weld-nugget growth of dissimilar-resistance spot welding of ferrite-martensite DP600 and drawing-quality special-killed (DQSK) low-carbon steel. It was revealed how the weld-nugget size is influenced by the main welding parameters: welding current, welding time and electrode force. The weldability lobe was established and proper welding conditions for the welds with a sufficient size and without an expulsion were determined. Using the experimental data, an empirical relationship between the weld-nugget size and the welding parameters was developed.

Keywords: resistance spot welding, dual-phase steel, dissimilar welding, weld-nugget growth

Velikost jedra zvara je ključnega pomena pri določanju mehanskih lastnosti uporovnih točkastih zvarov. Namen tega članka je preiskava rasti jedra zvara pri točkastem uporovnem varjenju feritno-martenzitnega DP600 in pomirjenega malogljičnega jekla DQSK za globoki vlek. Ugotovljeno je bilo, kako na velikost jedra zvara vplivajo glavni parametri varjenja: varilni tok, čas varjenja in pritisk elektrode. Vzpostavljen je bil varilni kiln in določeni so bili pravilni varilni pogoji za izdelavo dovolj velikih zvarov, brez izgonov taline. Z uporabo eksperimentalnih podatkov je bila postavljena empirična odvisnost med velikostjo jedra zvara in parametri varjenja.

Ključne besede: uporovno točkasto varjenje, dvofazno jeklo, varjenje različnih materialov, rast jedra zvara

1 INTRODUCTION

Resistance spot welding is considered as the dominant process for joining sheet metals in the automotive industry. Simplicity, low cost, high speed (low process time) and automation possibility are the advantages of this process. The quality and mechanical behavior of spot welds significantly affect the durability and crash-worthiness of a vehicle.[1–3] To ensure and maintain the structural integrity of a finished component under a wide range of operating conditions, e.g., a crash situation, a remotest possibility of producing even one or two defective welds in a critical component needs to be eliminated. These requirements, coupled with the uncertainties about the weld quality due to the difficulty of applying non-destructive tests to spot welds, are responsible for the practice of making more spot welds than needed for maintaining the structural integrity. Typically, there are about 2000–5000 spot welds in a modern vehicle. Around 20–30 % of these spot welds are due to the uncertainty of the quality of spot welds. A significant cost associated with over-welding provides a considerable driving force for optimizing this process.[4]

Resistance spot welding is a process of joining two or more metal parts using fusion at discrete spots at the interface of workpieces. The resistance to the current flow through the metal workpieces and their interface generates heat; therefore, the temperature rises at the interface of the workpieces. When the melting point of the metal is reached, the metal will begin to fuse and a nugget begins to form. The current is then switched off and the nugget is cooled down to solidify under pressure.[5,6]

It is well established that the geometrical attributes of spot welds, particularly the weld-nugget size, are the most important controlling factors determining the mechanical strength of RSWs.[7–12] In this regard, the weld-nugget size was included in several empirical relations. For example, J. Heuschkel[13] developed empirical relations among the tensile-shear strength (P), weld-nugget diameter (D), base-metal tensile strength (σ_{BM}), sheet thickness (t) and base-metal chemical composition (C, Mn):

$$P = Dt\left[\alpha - \beta(C + 0.05\text{Mn})\right]\sigma_{BM} \quad (1)$$

where α and β are material-dependent coefficients. Similar relations were developed by other researchers. For example, the following relation was developed by J. M. Sawhil and J. C. Baker[14] for the tensile-shear strength of spot welds:

$$P = ftD\sigma_{BM} \quad (2)$$

where f is a material-dependent coefficient, with a value between 2.5 and 3.1.

Considering the importance of the weld-nugget size for the quality of spot welds, there is a need to study the

effects of RSW parameters such as welding current, electrode force and welding time on this key physical weld attribute. Moreover, an increased use of advanced high-strength steels (AHSS), particularly ferrite-martensite DP steels, led to a wider range of possible material combinations in the resistance spot welding (RSW) of body-in-white assemblies. Therefore, there is clearly a practical need for the study of the weld-nugget growth during the RSW of dissimilar steel grades. In this paper, weld-nugget growth characteristics of dissimilar RSW of ferrite-martensite DP600 and drawing-quality special-killed (DQSK) low-carbon steel are investigated. The aim of this paper is to reveal how the weld-nugget size is influenced by the main welding parameters: welding current, welding time and electrode force.

2 EXPERIMENTAL PROCEDURE

2-mm-thick drawing-quality special-killed (DQSK) low-carbon steel and 2-mm-thick DP600 dual-phase steel sheets were used as the base metals. The chemical compositions of the base metals are shown in **Table 1**. Resistance spot welding was performed using a PLC-controlled, 120 kVA AC pedestal-type resistance-spot-welding machine. The welding was conducted using a 45-deg truncated-cone RWMA Class 2 electrode with an 8-mm face diameter.

Table 1: Chemical compositions of steels used in this study
Tabela 1: Kemijska sestava jekel, uporabljenih v študiji

Base metal	C	Mn	Si	S	P
DP600	0.035	1.08	0.388	0.004	0.038
LCS	0.065	0.204	0.095	0.017	0.018

To study the effects of the welding conditions (welding current, welding time and electrode force) on the weld failure mode, several welding schedules were used. **Figure 1** shows a schematic of the welding schedules used in this study. A total of 60 combinations of the welding current, the welding time and the electrode force were performed.

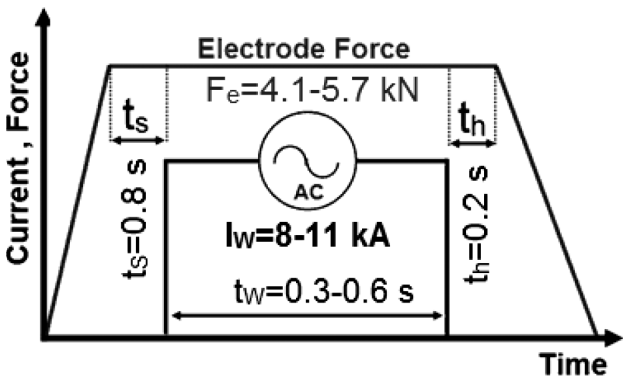

Figure 1: Schematic of the welding schedules used in this study
Slika 1: Shema časovnega poteka varjenja v tej študiji

Samples for the metallographic examination were prepared using the standard metallographic procedure. Light microscopy was used to examine the macrostructures and microstructures and to measure the weld fusion zone (weld nugget). The samples for the metallographic examination were prepared using the standard metallographic procedure. A 4 % Nital etching reagent was used to reveal the macrostructures of the samples. The FZ size is defined as the width of the weld nugget at the sheet/sheet interface in the longitudinal direction. The indentation depth is expressed as the percentage of the sheet thickness.

3 RESULTS AND DISCUSSION

3.1 Weld macrostructure

Figure 2 shows the macrostructure of a weld joining DP600 and low-carbon steel indicating that there are three distinct microstructural zones:

1) The weld nugget (WN) or fusion zone (FZ) which is melted during the welding process and then resolidified showing a cast structure. The macrostructure of the weld nugget consists of columnar grains.
2) The heat-affected zone (HAZ) which does not melted but undergoes microstructural changes.
3) The base metal (BM).

3.2 Effects of the welding parameters on the weld-nugget growth

The effects of welding parameters on the weld-nugget size are shown in **Table 2**. Contour plots for the weld-nugget size versus the welding current and the welding time at three levels of the electrode force are shown in **Figure 3**. According to these results, the following points can be drawn:

1) The welding current has a profound effect on the weld-nugget growth. Increasing the welding current increases the weld-nugget size.
2) Increasing the welding time increases the weld-nugget size.
3) Increasing the electrode force decreases the weld-nugget size. Indeed, when applying electrode force,

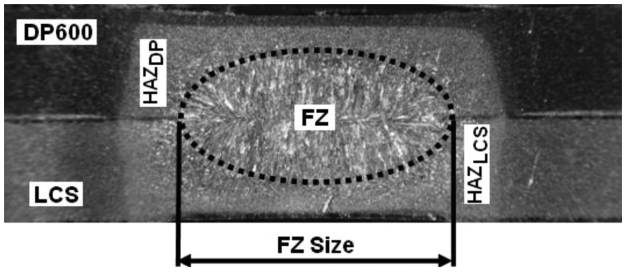

Figure 2: Macrostructure of a weld of DP600 and low-carbon steel: FZ size is defined as the width of the weld nugget at the sheet/sheet interface in the longitudinal direction
Slika 2: Makrostruktura zvara DP600 in malooglјičnega jekla: FZ je širina pretaljenega jedra na stiku pločevin v vzdolžni smeri

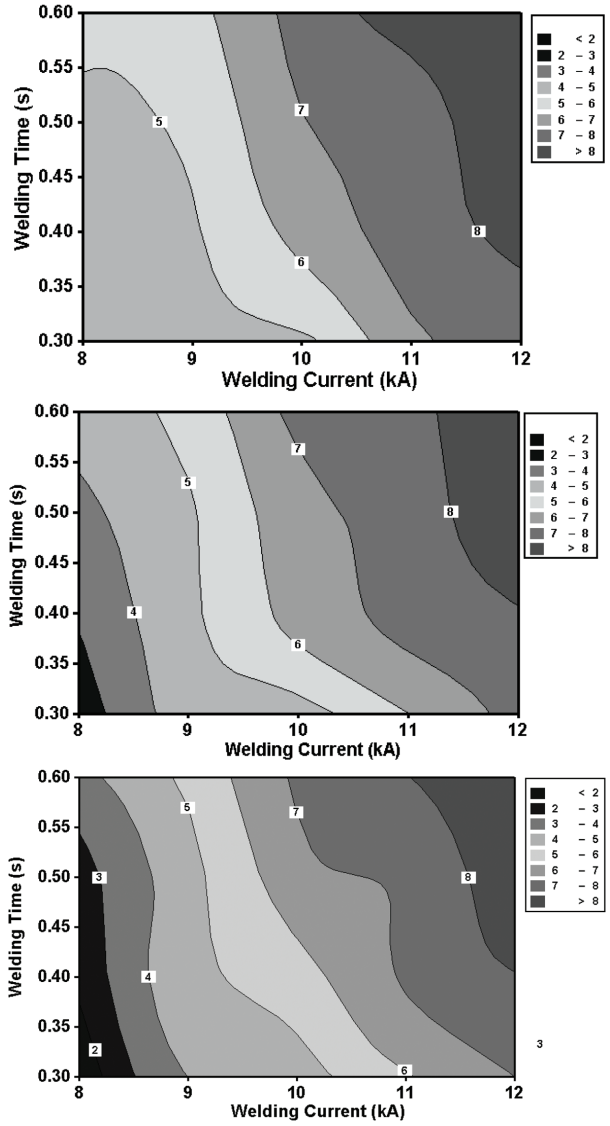

Figure 3: Weld-nugget size versus welding time and welding current at electrode forces of: a) 4.1 kN, b) 5.1 kN and c) 5.7 kN

Slika 3: Velikost pretaljenega jedra zvara v odvisnosti od časa varjenja in varilnega toka pri sili elektrode: a) 4,1 kN, b) 5,1 kN in c) 5,7 kN

there is need to use higher welding current and welding time to obtain a specific weld-nugget size.

The amount of heat generated at the sheet-to-sheet interface during the spot-welding process is the main reason for the nugget formation and its strength. The heat generated during the resistance spot welding can be expressed as follows:

$$Q = RI_{\mathrm{W}}^{2} t_{\mathrm{W}} \tag{3}$$

where Q, R, I_{W} and t_{W} are the generated heat, the electrical resistance, the welding current and the welding time, respectively.

Therefore, the three main parameters affecting the weld-nugget growth are the welding current, the welding time and the electrical resistance. The heat varies directly with the interface resistance, the welding time and the

Table 2: Effects of welding current and welding time on the weld-nugget size at three different electrode forces (S: small, A: acceptable, E: expulsion)

Tabela 2: Vpliv varilnega toka in časa varjenja na velikost pretaljenega jedra pri treh različnih pritiskih elektrod

Welding current (kA)	Welding time (s)	Weld-nugget size (mm)		
		F=4.1 kN	F=5.1 kN	F=5.7 kN
8	0.3	4.35 (S)	2.3 (S)	1.2 (S)
8	0.4	4.67 (S)	3.15 (S)	2.2 (S)
8	0.5	4.9 (S)	3.8 (S)	2.6 (S)
8	0.6	5.12 (S)	4.24 (S)	3.7 (S)
9	0.3	4.8 (S)	4.4 (S)	4 (S)
9	0.4	4.9 (S)	4.8 (S)	4.65 (S)
9	0.5	5.25 (S)	4.9 (S)	4.67 (S)
9	0.6	5.73 (A)	5.4 (S)	5.22 (S)
10	0.3	4.85 (S)	4.55 (S)	4.55 (S)
10	0.4	6.3 (A)	6.35 (A)	5.6 (A)
10	0.5	6.95 (A)	6.65 (A)	6.6 (A)
10	0.6	7.35 (A)	7.25 (A)	7.1 (A)
11	0.3	6.75 (A)	6 (A)	5.9 (A)
11	0.4	7.5 (A)	7.3 (A)	7.1 (A)
11	0.5	7.55 (A)	7.5 (A)	7.2 (A)
11	0.6	8.5 (A)	7.75 (A)	7.95 (A)
12	0.3	7.65 (E)	7.35 (E)	7 (E)
12	0.4	8.2 (E)	7.95 (E)	7.95 (E)
12	0.5	9 (E)	8.95 (E)	8.75 (E)
12	0.6	8.8 (E)	8.9 (E)	8.9 (E)

second power of the welding current. Again, this contact (interface) resistance varies in a complex manner and it is influenced by the electrode force, the surface conditions of the sheets used and also by the geometry of the electrode tip.

Increasing the welding current and the welding time increases the heat generation, which in turn, causes an enlargement of the weld nugget.

The static electrical resistance (i.e., the contact resistance) is mainly governed by the electrode force, which in turn controls the weld-nugget formation.[15] On a ductile material, where a normal force is applied across the contact interface, the number of surface asperities supporting the applied load gradually increases due to their successive yielding. In other words, the true contact area will initially be a relatively small fraction of the macroscopic, or apparent, contact area. Later, the true contact area will increase with the application of load and, in the limit, approach the apparent contact area.[8] Therefore, an increase in the electrode force decreases the electric resistance and thus reduces the generated heat at the sheet/sheet interface.

Since the generated heat is proportional to the squared current, the current to the duration and the contact resistance is inversely proportional to the electrode force, another parameter, the so-called heat factor, can be defined as follows:

$$\text{Heat factor} = \frac{I_{\mathrm{W}}^{2} t_{\mathrm{W}}}{F_{\mathrm{e}}} \tag{4}$$

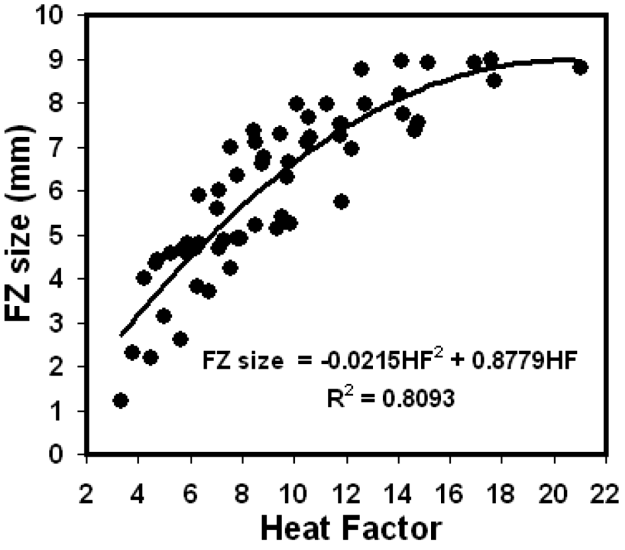

Figure 4: Weld-nugget size versus heat factor (HF)
Slika 4: Velikost pretaljenega jedra zvara v odvisnosti od faktorja toplote (HF)

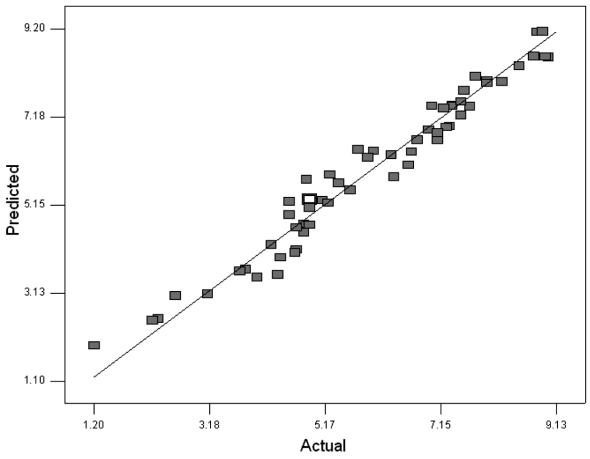

Figure 5: Scatter plot for the weld-nugget size
Slika 5: Diagram raztrosa velikosti staljenega jedra zvara

where F_e is the electrode force. It is expected that the higher the heat factor, the higher is the weld-nugget size. As it can be seen in **Figure 4**, the weld-nugget growth is proportional to the heat factor, with the exception of high heat factors. This can be explained with the fact that increasing the heat factor increases the probability of expulsion. Expulsion can increase the heat losses. Therefore, increasing the heat factor beyond the critical value does not increase the weld-nugget size. Therefore, it can be concluded that there is not a proportional relationship between the heat factor and the weld-nugget size. This is important when selecting the optimum welding condition to obtain a larger weld-nugget size.

3.3 Quantitative relation between welding parameters and the weld-nugget size

To establish a relationship between the weld-nugget size and the welding parameters, viz., the welding time, the welding current and the electrode force, the following relation was developed using multiple regression:

$$\text{Weld Nugget Size} = 0.62524 + 1.182121 I_w + \\ + 5.69533 t_w - 3.07395 F_e + 0.2568 I_w F_e - 0.063452 I_w^2 \quad (5)$$

In **Figure 5**, the values of the weld-nugget size obtained experimentally are plotted against the weld-nugget size predicted with Equation (5). As can be seen, there is very little scatter of the points from the proposed equation. Deviations are well within the 95 % confidence limit.

The ability to make a weld, based on the welding parameters and under production conditions, is best defined in terms of a 'weldability lobe'. The weldability lobe defines the available tolerances for producing a weld of a defined quality. In this way, it is possible to determine the welding parameters that allow an acceptable weld quality as defined with precise physical limits, such as the weld size, or non-marking or aesthetic qualities, associated with the amount of surface indentation.[4] According to the AWS D8.1M standard[16] for automotive weld-quality resistance spot welding of steels, the lower limit of a lobe diagram corresponds to the welding condition leading to the welds with the nugget size larger than $4t^{0.5}$, where t is the sheet thickness. The upper limits outlining the tolerance box for acceptable welding are generally defined in terms of the weld-nugget expulsion.

In **Table 2,** the range of the welding parameters producing reliable spot welds is highlighted in blue. The welding condition producing small welds is in gray. Also, the expulsion occurrence is highlighted in red. The suitable welding-current range is from the current, under which the minimum nugget diameter (for example, $4t^{0.5}$) is formed to that, under which the expulsion occurs. A wide suitable welding-current range is desirable because it is possible to control the nugget diameter within a prescribed range even if the welding current fluctuates. The welding range for each welding time is about 2 kA, which is a proper welding-current range indicating good weldability.

4 CONCLUSIONS

Understanding the influence of RSW parameters on the weld-nugget growth during resistance spot welding is a prerequisite for the development of the optimum welding conditions, ensuring high levels of joint quality in auto-body manufacture. The results of the present research revealed how the weld-nugget size is influenced by the main welding parameters, viz., the welding current, the welding time and the electrode force:

1) Increasing the heat input caused by increasing the welding current and the welding time led to an enlargement of the weld nugget due to increasing the heat generated at the sheet/sheet interface.

2) Increasing the electrode force can increase the initial sheet/sheet contact areas and therefore decrease the sheet/sheet interfacial electrical resistively, which in turn leads to a reduction in the generated heat at the sheet/sheet interface. In other words, increasing the electrode force increases the welding current and welding time required to melt the sheet/sheet interface.
3) We determined a relation involving the weld-nugget size and the welding parameters, viz., the welding current, the welding time and the electrode force. This helped us to evaluate the combined effect of the welding parameters on the weld-nugget size. Using such a quantitative relation, the selection of the optimum welding condition becomes straightforward.
4) Another factor, the heat factor = I^2t/F, was defined to evaluate the combining effect of the welding parameters on the weld-nugget size.
5) The weldability lobe for dissimilar-resistance spot welding of DP600 and low-carbon steel was determined using the established criteria of the AWS standard. A wide welding-current range was established indicating good weldability.

5 REFERENCES

[1] M. Pouranvari, H. R. Asgari, S. M. Mosavizadeh, P. H. Marashi, M. Goodarzi, Effect of weld nugget size on overload failure mode of resistance spot welds, Sci. Technol. Weld. Joining, 12 (**2007**), 217–225, doi:10.1179/174329307x164409

[2] M. Pouranvari, Susceptibility to interfacial failure mode in similar and dissimilar resistance spot welds of DP600 dual phase steel and low carbon steel during cross-tension and tensile-shear loading conditions, Mater. Sci. Eng. A, 546 (**2012**), 129–138, doi:10.1016/j.msea.2012.03.040

[3] M. Pouranvari, E. Ranjbarnoodeh, Dependence of Fracture Mode on Welding Variables in Resistance Spot Welding of DP980 Advanced High Strength Steel, Mater. Tehnol., 46 (**2012**), 665–671

[4] N. T. Williams, J. D. Parker, Review of resistance spot welding of steel sheets, Part 1: Modelling and control of weld nugget formation, International Materials Reviews, 49 (**2004**), 45–75, doi:10.1179/095066004225010523

[5] J. C. Feng, Y. R. Wang, Z. D. Zhang, Nugget growth characteristic for AZ31B magnesium alloy during resistance spot welding, Sci. Technol. Weld. Joining, 11 (**2006**), 154–162, doi:10.1179/174329306x84364

[6] M. Pouranvari, S. P. H. Marashi, Critical review of automotive steels spot welding: process, structure and properties, Sci. Technol. Weld. Joining, 18 (**2013**), 361–403, doi:10.1179/1362171813y.0000000120

[7] H. Zhang, J. Senkara, Resistance welding: fundamentals and applications, Taylor & Francis CRC Press, ... 2005

[8] A. De, O. P. Gupta, L. Dorn, An experimental study of resistance spot welding in 1 mm thick sheet of low carbon steel, Proc. Inst. Mech. Engrs., Part B: Journal of Engineering Manufacture, 210 (**1996**), 341–347, doi:10.1243/pime_proc_1996_210_126_02

[9] M. Pouranvari, S. P. H. Marashi, On the failure of low carbon steel resistance spot welds in quasi-static tensile-shear loading, Materials & Design, 31 (**2010**), 3647–3652, doi:10.1016/j.matdes.2010.02.044

[10] M. Pouranvari, S. P. H. Marashi, S. M. Mousavizadeh, Failure mode transition and mechanical properties of similar and dissimilar resistance spot welds of DP600 and low carbon steels, Science and Technology of Welding & Joining, 15 (**2010**), 625–631, doi:10.1179/136217110x12813393169534

[11] M. Pouranvari, S. P. H. Marashi, Failure mode transition in AISI 304 resistance spot welds, Welding Journal, 91 (**2012**), 303–309

[12] M. Pouranvari, S. P. H. Marashi, Factors affecting mechanical properties of resistance spot welds, Materials Science and Technology, 26 (**2010**), 1137–1144, doi:10.1179/174328409x459301

[13] J. Heuschkel, The expression of spot-weld properties, Welding Journal, 31 (**1952**), 931–943

[14] J. M. Sawhill, J. C. Baker, Spot weldability of high-strength sheet steels, Welding Journal, 59 (**1980**), 19–30

[15] Q. Song, W. Zhang, N. Bay, An experimental study determines the electrical contact resistance in resistance, Welding Journal, 85 (**2005**), 73–76

[16] Specification for automotive weld quality resistance spot welding of steel, AWS D8:1M, New York, American National Standard, 2007

UDK 620.17:623.445.1:67.017
Original scientific article/Izvirni znanstveni članek

ISSN 1580-2949
MTAEC9, 50(5)767(2016)

ARMOUR PLATES FROM KOZLOV ROB – ANALYSES OF TWO UNUSUAL FINDS

OKLEPNI PLOŠČI S KOZLOVEGA ROBA – ANALIZE DVEH NENAVADNIH NAJDB

Tomaž Lazar[1], Primož Mrvar[2], Martin Lamut[3], Peter Fajfar[2]

[1]National Museum of Slovenia, Prešernova cesta 20, 1000 Ljubljana, Slovenia
[2]University of Ljubljana, Faculty of Natural Sciences and Engineering, Department of Material Science and Metallurgy, Aškerčeva cesta 12, 1000 Ljubljana, Slovenia
[3]Slovenian centre of excellence for space sciences and technologies, Aškerčeva cesta 12, 1000 Ljubljana, Slovenia
peter.fajfar@omm.ntf.uni-lj.si

Prejem rokopisa – received: 2015-07-30; sprejem za objavo – accepted for publication: 2015-10-13

doi:10.17222/mit.2015.242

During archaeological excavations of the fortifications on Kozlov rob, two perforated steel plates were discovered, the purposes of which had never been explained satisfactorily. Detailed examinations and scientific analyses confirmed that in one case at least we were dealing with fragments of armour from the late Middle Ages or the early Modern Period that had later been reworked into an entirely unrelated object having, in all possibility, a non-warlike function.

Keywords: armour, weapons, archaeometallurgy, metallography, nano-indentation, Kozlov rob

Med arheološkimi izkopavanji utrdbe na Kozlovem robu sta bili odkriti dve preluknjani, jekleni plošči, katerih namembnost ni bila nikoli zadovoljivo pojasnjena. Natančne preiskave in znanstvene analize so potrdile, da gre v vsaj enem primeru za fragment oklepa iz poznega srednjega veka ali iz zgodnjega novega veka. Ta je bil naknadno predelan v predmet, ki po vsej verjetnosti ni služil vojaškemu namenu.

Ključne besede: oklep, orožje, arheometalurgija, metalografija nanovtiskovanje, Kozlov rob

1 INTRODUCTION

Kozlov rob is a lone hill of almost rectangular form reaching an altitude of 426 m above sea-level overlooking the town of Tolmin. Due to the strategic importance of the location, a castle was built on Kozlov rob in the 12th Century. The castle remained in use until the mid-17th Century.[1]

Archaeological excavations at Kozlov rob were carried out in 1964/5 and 1996/7. The excavations revealed various finds.[2] As elsewhere in Central Europe,[3,4,5] the finds consisted mostly of small, often fragmentary objects. Among those related to warfare, the largest group is represented by crossbow bolts.[6] In addition to other fragments of arms and armour, two steel plates were found, both perforated with rows of holes. One of them was first reported on in 2008.[1,7]

The unclear purposes of the plates soon stimulated lively discussion. The first plate evidently represents the upper half of a breastplate. The second plate is made from much thicker steel sheet but lacks any recognisable features. The two fragments have little in common apart from the more or less symmetrically distributed holes. This is an indication that both objects had performed an identical function during their last period of working life. At least three hypotheses have been suggested as to their intended purpose:

1. Fragments of armour were used by the castle garrison for target practice with crossbows.
2. The perforated breastplate with vent holes is an example of extremely rare tournament armour for foot combat.
3. Worn-out fragments of armour were recycled and modified into something else, perhaps a grate or vent.

In 2010 the plates from Kozlov rob were submitted to in-depth research for the first time. Four small samples were removed from each plate and subjected to metallographic analysis. The results indicated that both plates were made from relatively high-quality steel containing approximately 0.3 % to 0.8 % carbon with a ferritic-pearlitic structure.[8,9]

These preliminary results underlined the need for additional analyses and a more detailed publication about the plates from Kozlov rob. The following paper has been compiled to present a comprehensive overview of the analytical methods used as well as an interdisciplinary discussion of the latest findings.

2 EXPERIMENTAL PART

The fragment of breastplate No. 1 (**Figure 1**) is heavily corroded. It represents the upper half of a steel cuirass reaching up to the folded rim of the neck and armpit cut-out. The fragment originally belonged to a

Figure 1: Fragment of breastplate showing the locations of the samples (Photo: T. Lazar), Goriški muzej, Nova Gorica, s. n.
Slika 1: Odlomek prsne plošče z mesti odvzema vzorcev (foto: T. Lazar), Goriški muzej, Nova Gorica, s. n.

breastplate of comparatively plain construction, possibly of North Italian manufacture, in the style typical for the period around 1500 AD.[8,10] It is made from one piece of steel sheet, approximately 1.5 mm to 3 mm thick. The length of the plate is 252 mm, the width is 286 mm, and its weight is 778 g. Due to a progressive state of corrosion, the original thickness of the sheet metal is difficult to measure precisely, but can be estimated at around 2 mm on average. The convex-shaped steel sheet is perforated along two thirds of its width on the right-hand side with 18 holes arranged in more or less symmetrical rows. The holes are mostly of uniform, square shaped, pierced from the inner side of the breastplate.[1,9]

The fragment of steel plate No. 2 (**Figure 2**) is shaped as an irregular parallelogram. It is made from a massive steel sheet with a multi-layered anisotropic microstructure. The plate is perforated with 16 square and round holes pierced from both sides. Due to advanced corrosion the metal sheet has largely disintegrated longitudinally into multiple layers. The surface is covered with a thick layer of corrosion products. The thickness of the steel sheet is approximately 3.5 mm to 7 mm, with an average of around 4.5 mm. The length of the plate is 245 mm, the width 244 mm, and its weight is 1.504 g.[8,9]

For the microstructural characterization and the mechanical analysis three small samples were removed from each steel plate. The locations of the samples of fragment No. 1 are shown in **Figure 1**, and their shapes are shown in **Figure 3**, and the locations of the samples of fragment No. 2 are shown in **Figure 2**, and their shapes are shown in **Figure 4**. The obtained samples were embedded in resin, ground, polished and etched using a solution of 2 % nital. The microstructural characterization was performed using light optical microscopy (Olympus Microscope BX61). The tests for mechanical analysis were conducted on an Agilent G200 Nanoindenter using the continuous stiffness measurement (CSM) option. The CSM technique allows the contact stiffness together with the projected area of hardness impressions to be measured at any point along the loading curve.[11,12] This instrument monitors and records the dynamic load and displacement of the indenter during indentation with a force resolution of approximately 50 nN and a displacement resolution of approximately 0.01 nm.

3 RESULTS

3.1 Metallographic analysis

Sample 1 originates from the edge of a heavily corroded hole. The examined surface runs along the plane of the plate. The sample is corroded, hence the microstructure of the metal is invisible on the macro photograph (**Figure 3a**). Sample 2 was removed from the lower, broken part of the plate. The examined surface

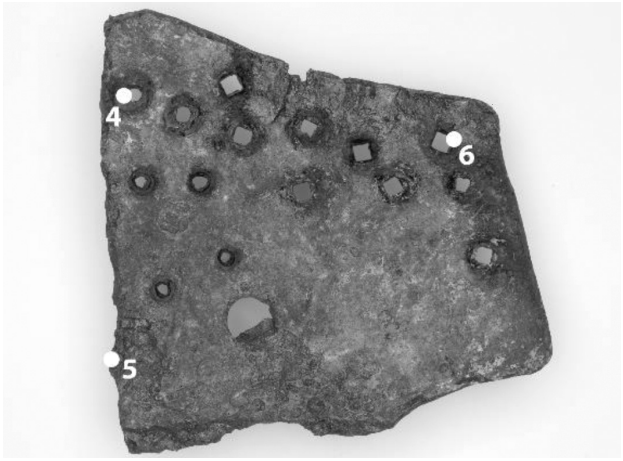

Figure 2: Fragment of steel plate showing the locations of the samples (Photo: T. Lazar), Goriški muzej, Nova Gorica, s. n.
Slika 2: Odlomek jeklene plošče z mesti odvzema vzorcev (Photo: T. Lazar), Goriški muzej, Nova Gorica, s. n.

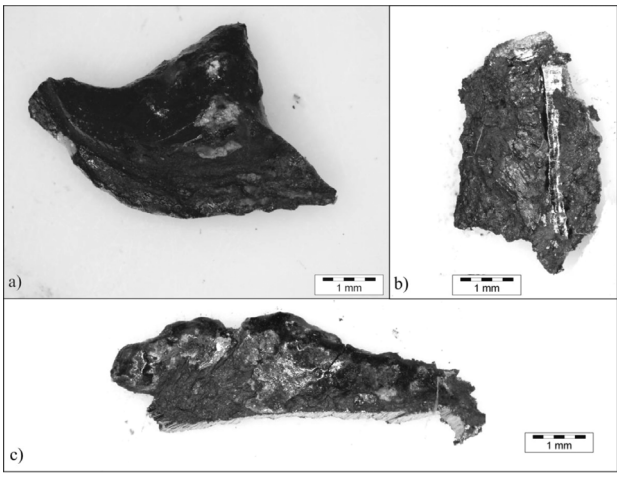

Figure 3: Samples from the plate No. 1: a) sample 1, b) sample 2, c) sample 3
Slika 3: Vzorci plošče št. 1: a) vzorec 1, b) vzorec 2, c) vzorec 3

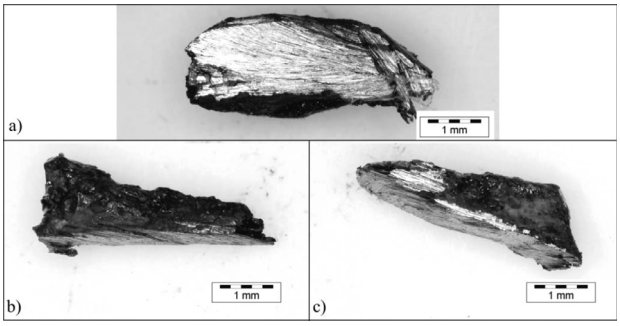

Figure 4: Samples from plate No. 2: a) sample 4, b) sample 5, c) sample 6
Slika 4: Vzorci plošče št. 2: a) vzorec 4, b) vzorec 5, c) vzorec 6

runs perpendicular to the plane of the plate (**Figure 5**). The microstructure contains mostly pearlite (darker microstructural areas of the grain) with a small proportion of ferrite (white microstructural areas). On the lower edge of the sample the grain is finely formed within a directional structure. Also, the proportion of ferrite is markedly larger. The dark area along the left edge represents the corroded surface. Sample 3 was taken from the right edge of the plate. The examined surface runs along the plane of the plate (**Figure 6**). The microstructure contains mostly pearlite with a small proportion of ferrite. On the upper edge of the sample (the outside edge of the plate) the grain is smaller and the proportion of ferrite larger. The dark area around the right edge represents the corroded surface. The existing corrosion products are formed mostly on the basis of Fe_2O_3 and Fe_3O_4.

Within the narrow band along the lower right edge, the microstructure of sample 2 is directed along the flow of material produced during the perforation process (**Figure 5**). The grain is plastically deformed, non-recrystallized, as is typical of cold working. Given that the edge layers contain a significantly higher portion of recrystallized ferrite grain, it can be estimated that the

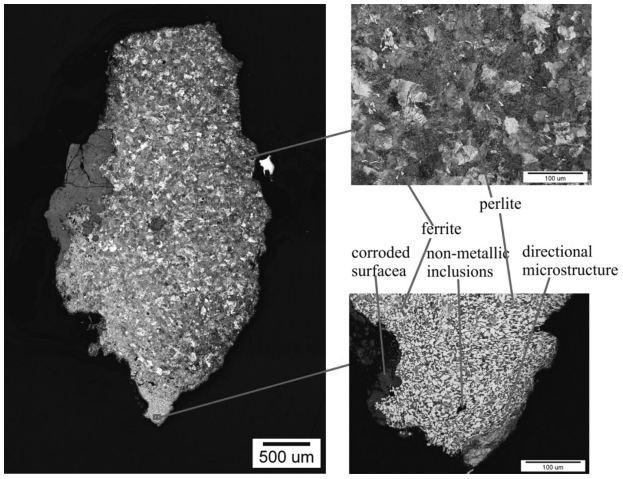

Figure 5: Sample 2, plate No. 1
Slika 5: Vzorec 2, plošča št. 1

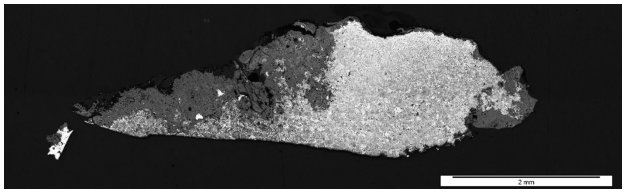

Figure 6: Sample 3, plate No. 1
Slika 6: Vzorec 3, plošča št. 1

steel plate was heated to a temperature between 700 °C and 900 °C prior to the perforation process. At that temperature and a suitable time of heating the steel plate was partly decarburised on the surface. This is confirmed by the microstructure containing an increased proportion of ferrite. The narrow band of non-recrystallized grain may have been formed during a later repair of the hole done cold.

Sample 4 originates from the edge of a round hole. The examined surface runs perpendicularly along the plane of the plate (**Figure 7**). In the centre of the sample the microstructure contains mostly pearlite with a small proportion of ferrite. In the outer layers the grain is formed more finely and there is an increased content of ferrite. Sample 5 was removed from the left edge of the plate. The examined surface runs perpendicular to the plane of the plate (**Figure 8**). Along the entire cross-section pearlite can be observed, indicating that the steel has a composition containing 0.8 % carbon. Sample 6 was taken from the edge of a square hole. The examined surface runs perpendicular to the plane of the plate (**Figure 9**). The microstructure is fine grained, containing pearlite and ferrite. The edges of the sample contain ferrite and the grain is larger, too.

The microstructure of sample 5 is predominantly pearlitic. The examined surface is directed towards the interior of the plate. Such a microstructure is typical of hot working. The micro photographs demonstrate that

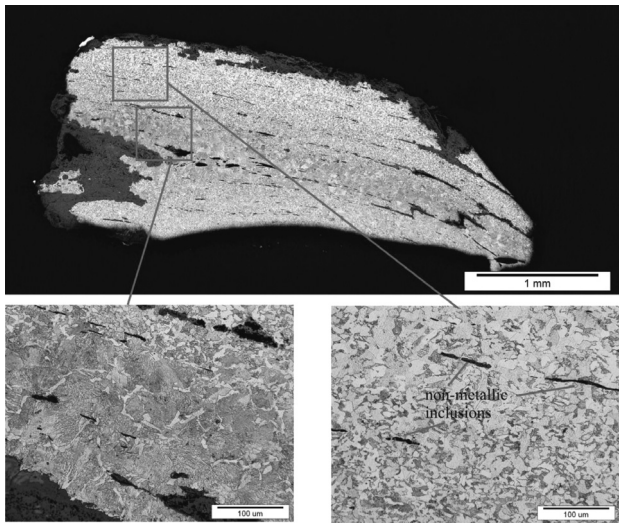

Figure 7: Sample 4, plate No. 2
Slika 7: Vzorec 4, plošča št. 1

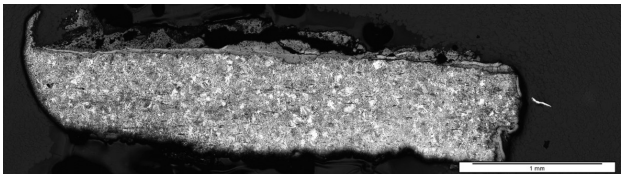

Figure 8: Sample 5, plate No. 2
Slika 8: Vzorec 5, plošča št. 1

the plate was formed by hot forging, then slowly air cooled. The holes on the second plate were punched hot as well. This is confirmed by the compositions of samples 4 and 6 that contain fine-grained microstructures with an increased ferrite content in the outer layers, which are partly decarburised. The grain is larger than is the case with the first plate. The proportion of ferrite is larger, too. Assuming that both plates were heated to the same temperature during the manufacture, the larger grain size may be attributed to a longer heating time, as plate No. 2 is twice as thick as No. 1.

The examined samples also contain non-metallic inclusions that were oriented perpendicularly to the direction of deformation during the sequences of hot forging.[13,14]

Figure 7 demonstrates that these inclusions are relatively soft and therefore were deformed considerably.

3.2 Mechanical analysis

In order to obtain a deeper insight into the origin of the archaeological finds in the form of two perforated steel plates it was decided to obtain some mechanical data. Since the archaeologists and museum curators are not in favour of any material being detached from museum objects, the amount material to work with is usually fairly small, hence it is difficult to extract its mechanical properties. Due to such constraints the nanoindentation technique was used, which can provide a Young's modulus and a hardness from very small samples.

The penetration depth of 1 μm was carefully chosen in order to avoid the influences of the indentation size effect, the surface roughness or the surface inclination and to reach a constant value or plateau region. At each

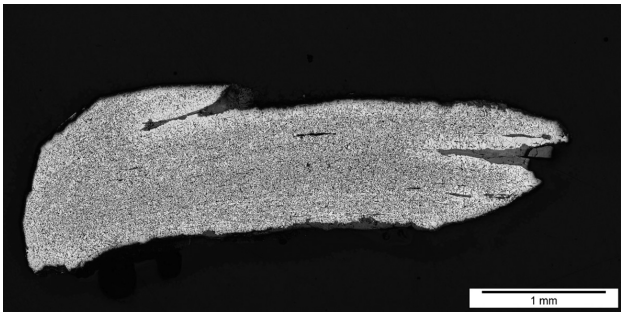

Figure 9: Sample 6, plate No. 2
Slika 9: Vzorec 6, plošča št. 1

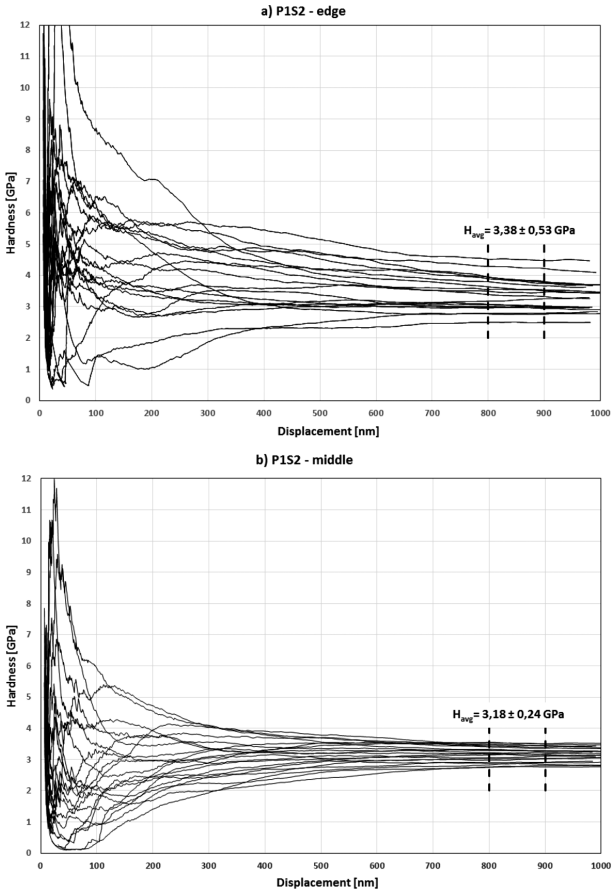

Figure 10: Hardness as a function of contact depth for P1S2: a) the edge and b) the middle
Slika 10: Trdota v odvisnosti od kontaktne globine za P1S2: a) rob in b) sredina

point at least 6 measurements were taken. In spots where the results showed extensive dissipation, the number of measurements was increased considerably.

The first point of interest was plate No. 1, sample 2 (P1-S2), removed from the area next to a hole, where at the edge finely formed grains are found with an increased portion of ferrite and in the middle part larger grains with a predominantly pearlitic microstructure. The results are presented in **Table 1**. In order to eliminate point fluctuations in the load-displacement curve the values are averages at depths between 800 nm and 900 nm from each test. (Note that for the nanoindentation range the hardness values are greater than for the micro or macro scale[11,12]). The hardness measurements of P1-S2 (**Figure 10**) show a large dissipation at the edge in comparison to the area in the middle. It shows a slightly larger mean hardness (**Table 1**), but considering the dissipation it all falls into the margin of error. Since ferrite has a smaller hardness than pearlite it is assumed that the influence of cold-worked smaller grains is minimized by a greater ferrite share in the microstructure. Furthermore, the tests were made separately at the ferritic and pearlitic grains, but the results overlapped, most likely due to effects from adjacent grains, so it was

hard to draw any sound conclusions. Sample 3 (P1-S3), taken away from the afterwards induced holes, shows a considerably smaller hardness. The grains remained in the original state and no plastic deformation occurred, which agrees well with the above hypothesis.

Table 1: Hardness tests statistics on the first plate
Tabela 1: Statistika preizkusov trdote za prvo ploščo

	P1-S2 middle	P1-S2 edge	P1-S3
Mean	3.18	3.38	2.29
Std. Dev.	0.24	0.53	0.15
% COV	7.48	15.82	6.36

In **Table 2** the hardness results from plate No. 2 are given. Samples 4 and 6 (P2-S4, P2-S6), taken from the vicinity of a hole, show higher hardness where the grains are smaller with a lower share of ferrite, which in these cases is in the middle of the samples. Where the grains are larger and a higher share of ferrite is observed, the hardness is lower, comparable with the samples P1-S3 and P2-S5, taken from the area with no subsequent reworking of the plates.

Table 2: Hardness tests statistics on the second plate
Tabela 2: Statistika preizkusov trdote za drugo ploščo

	P2-S4 middle	P2-S4 edge	P2-S5	P2-S6 middle	P2-S6 edge
Mean	3.05	2.69	2.82	2.97	2.57
Std. Dev.	0.08	0.09	0.3	0.3	0.23
% COV	2.56	3.24	10.53	10.1	9

4 DISCUSSION

Fragments of armour were used by the castle garrison for target practice with crossbows.

Both steel plates are perforated with holes, mostly of a square shape, measuring approximately 10 mm × 10 mm (**Figures 11** and **12**). Such dimensions correspond to the typical late-medieval crossbow bolt with a square- or diamond-shaped head. A sizeable group of bolt heads of that same type was unearthed on Kozlov rob[6,7], seemingly supporting the idea that the plates had been used for marksmanship practice.

However, several arguments speak against such an explanation. On both plates the holes are placed quite neatly in straight rows. Such precise shot placement would be difficult to achieve even by a skilled marksman. At any rate, the arrangement of holes is much more symmetrical than might be expected from a random dispersion of hits.

The penetration of late medieval crossbows should not be overestimated. The spanning force of a "one-foot" military crossbow was within the range of 1500 N, or 2100 N in the case of the heavier "two-foot" type. In the 15th century, even more powerful crossbows were developed with draw weights up to 5000 N.[16–20] However, their efficiency was low. At point-blank range, the maximum penetration of a typical crossbow bolt weighing 70 g might reach up to 60 mm of pinewood. Documented cases of projectiles stuck within the wooden structures of medieval castles show a degree of penetration averaging only 20 mm in seasoned softwood.[16]

The kinetic energy of a crossbow bolt[21] at point-blank range may be estimated at around 200 J.[16] The latter is clearly superior to a yew longbow with a kinetic energy of 120 J at a draw weight of 670 N.[22] However, it would be barely sufficient to penetrate even the relatively thin plate No. 1. The second plate, at least twice as thick, would prove entirely resistant to crossbow bolts. In fact, it would be proof against a musket ball possessing at least ten times greater kinetic energy.[23]

Therefore, it seems highly unlikely that the two steel plates from Kozlov rob were pierced by crossbow bolts. The final answer is provided by the metallographic analysis. Had the holes been made by the impact of crossbow bolts the samples would show evidence of mechanical deformation and cold work hardening of the microstructure.

The perforated breastplate with vent holes is an example of extremely rare tournament armour for foot combat.

In the late Middle Ages, new types of armour were developed specifically for tournament use. The famous

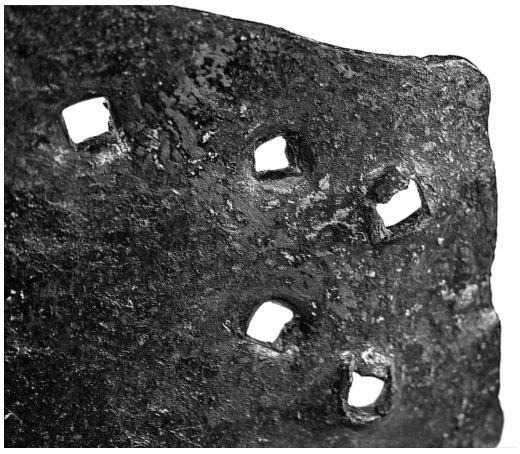

Figure 11: Square-shaped holes of plate No. 2 (Photo: D. Todorović)
Slika 11: Luknje kvadratne oblike na plošči št. 2 (foto: D. Todorović)

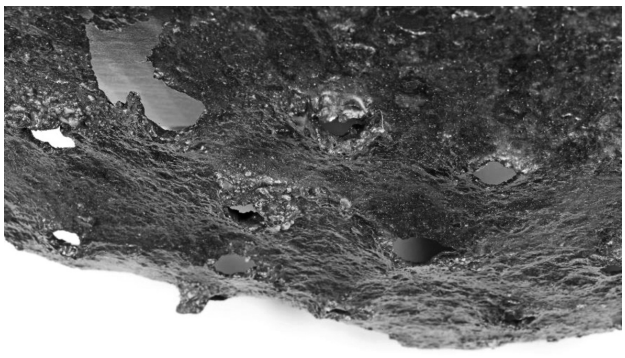

Figure 12: Holes on plate No. 1 (Photo: T. Lazar)
Slika 12: Luknje na plošči št. 1 (foto: T. Lazar)

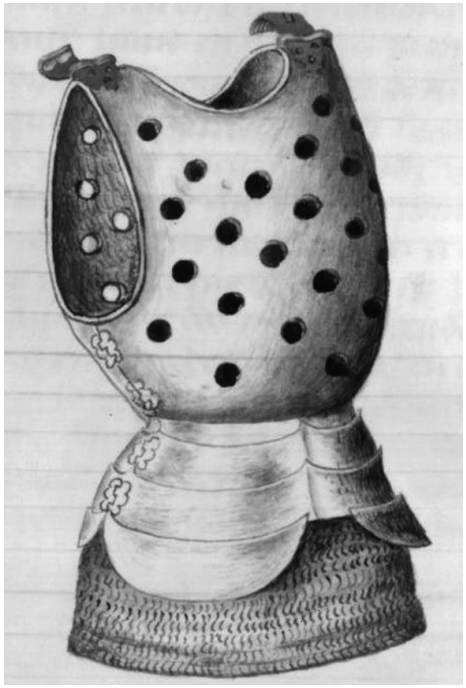

Figure 13: Armour for foot combat as depicted in René of Anjou's tournament book (Bibliothèque Nationale, Paris, MS Fr 2695, fol. 25v)
Slika 13: Oklep za pehotni dvoboj iz turnirske knjige Renéja Anžujskega (Bibliothèque Nationale, Paris, MS Fr 2695, fol. 25v)

tournament book of René of Anjou from ca. 1460 depicts a cuirass with numerous vent holes for fighting on foot (**Figure 13**).[24,25] Recent archaeological excavations at the Haus Herbede in the Ruhr district have revealed a breastplate of the exact same type.[26,27] The discovery of a perforated breastplate at Kozlov rob gave rise to speculation that it might have belonged to a similar suit of tournament armour designed to prevent overheating.[1,7]

Nonetheless, a closer examination of the breastplate disproved such a possibility. The holes are crudely made, which is clearly inconsistent with the workmanship of late-medieval tournament armour. At any rate, the breastplate would be very uncomfortable to wear due to the sharp perforations. The second perforated plate is an even less sophisticated product. The holes were struck into the steel sheet from both sides, in many cases, forming crude bulges up to a centimetre deep. Such a plate could never have belonged to armour worn on one's person (**Figure 14**).

Worn-out fragments of armour were recycled and reworked into something else, perhaps a grate or vent.

Steel was an expensive commodity in the past, hence recycling of old or damaged steel products was part of everyday life. Provided that a damaged fragment of armour had to be scrapped, it seems plausible that it was reworked into a new product, even something as mundane as a fireplace grate or a vent. Two very similar plates used for that purpose were spotted coincidentally in 2010, built into a modern brick structure on the island of Rab (**Figures 15a** and **15b**).

The perforations on the plates were clearly made using a massive chisel or punch. Due to the thickness of the metal sheet, particularly on plate No. 2., it can be

Figure 14: Side view of plate No. 2 (Photo: D. Todorović)
Slika 14: Stranski pogled plošče št. 2 (foto: D. Todorović)

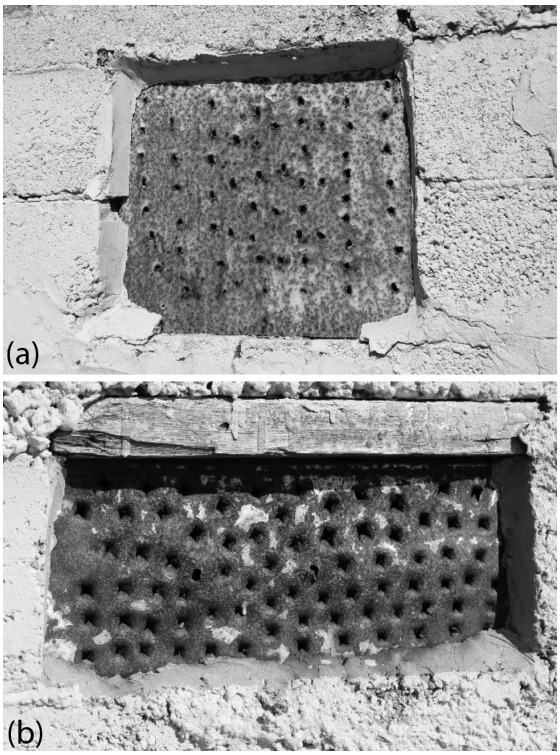

Figure 15: a), b): Unexpected analogy from the Adriatic coast: two simple steel vents, designed in the same manner, built into a modern outbuilding on the island Rab (Photo: T. Lazar)
Slika 15: a), b): Nepričakovana podobnost z Jadranske obale: dva preprosta jeklena zračnika, oblikovana na enak način in vgrajena v moderno zgradbo na otoku Rab (foto: T. Lazar)

assumed that the punching was performed while the plate was heated in a forge. Even so, the process would have necessitated heavy hammer blows, causing severe deformation of the material. Further explanation of the work process may be provided by scientific analyses, in particular metallography.[13,14,28,29]

5 CONCLUSION

The fragmentary breastplate No. 1 was a quality product made of steel with a relatively high carbon content.[16] The latter also holds true for plate No. 2, even though, based on its shape alone, it is impossible to determine what sort of object it had belonged to originally. One cannot exclude the possibility that it was merely a steel semi-product.[8]

The results of the metallographic analyses proved that both plates had been reworked in a similar manner. As could be expected given the technological capabilities of the pre-industrial era, the holes were made by hot punching. Only later on, as indicated by the non-recrystallization, the directional structure of the part of sample 2 (**Figure 5**), some of the holes may have been repaired or reworked slightly by cold working. The mechanical analyses show that in the case of small samples the nanoindentation technique can provide useful additional data. The results confirm the metallographic analyses and further reveal the material properties as well as the methods of making and processing the plates.

Based on the above observations, it is clear that once the holes had been punched and formed, at least plate No. 1 was not exposed to temperatures in excess of approximately 400 °C that would have caused recrystallization of the cold-worked areas. Therefore, it is possible to conclude that the perforated plates were most likely used as simple grates, vents or were put to some other similar uses.

The reworking of the steel plates seems all the more plausible considering the gradual decline of armour in Europe during the 17th century. From that standpoint it might be easier to understand why on Kozlov rob a breastplate was reworked into a new product, no longer having anything in common with the armour's original purpose.

6 REFERENCES

[1] B. Žbona Trkman, F. Bressan, Orožje z gradu Kozlov rob; Vojske, orožje in utrdbeni sistemi v Posočju, Tolminski muzej, Tolmin 2008, 58

[2] B. Žbona Trkman, A. Kruh, Stanje raziskav gradov in dvorcev na območju historične Goriške I. Dobrovo, Kozlov rob, Rihemberk, Štanjel, Goriški letnik, Nova Gorica, 33–34 (**2010**), 195–217

[3] K. Predovnik, Trdnjava Kostanjevica na Starem gradu nad Podbočjem, Filozofska fakulteta, Ljubljana 2003, 240

[4] C. Krauskopf, Plemstvo in predmeti iz njegovega vsakdanjika. Raziskave materialne kulture 13. in 14. stoletja, Arheo, Ljubljana, 23 (**2005**), 47–62

[5] T. Lazar, Bojišča visokega in poznega srednjega veka kot izziv slovenski arheologiji, Arheo, Ljubljana, 28 (**2011**), 119–130

[6] F. Bressan, Le cuspidi di freccia nel Friuli medievale, Università degli Studi di Trieste, Trieste 1996, 275

[7] T. Lazar, Vojaška zgodovina slovenskega ozemlja od 13. do 15. stoletja, Filozofska fakulteta, Ljubljana 2009, cat. no. M 315–346, 442

[8] A. Williams: Metalurške značilnosti poznosrednjeveških oklepov iz srednje Evrope, Vitez, dama in zmaj; Dediščina srednjeveških bojevnikov na Slovenskem, 1, Razprave, Ljubljana 2011, 233–247

[9] T. Lazar, T. Nabergoj, P. Bitenc, Vitez, dama in zmaj; Dediščina srednjeveških bojevnikov na Slovenskem. 2, Katalog predmetov, Narodni muzej Slovenije, Ljubljana 2013, cat. no. 256, 257

[10] J. Mann, Wallace Collection Catalogues, European Arms and Armour, Vol I., Armour, The Trustees of the Wallace Collection, London 1962, cat. no. A 214

[11] W. C. Oliver, G. M. Pharr, An Improved Technique for Determining Hardness and Elastic Modulus Using Load and Displacement Sensing Indentation Experiments, J. Mater. Res., 7 (**1992**), 1564–1583, doi:10.1557/JMR.1992.1564

[12] R. Rodríguez, I. Gutierrez, Correlation Between Nanoindentation and Tensile Properties. Influence of the Indentation Size Effect, Materials Science and Engineering, A361 (**2003**), 377–384, doi:10.1016/S0921-5093(03)00563

[13] M. Nečemer, T. Lazar, Ž. Šmit, P. Kump, B. Žužek, Study of the Provenance and Technology of Asian Kris Daggers by Application of X-Ray Analytical Techniques and Hardness Testing, Acta Chim. Slov., 351 (**2013**) 60, (2), 351–357

[14] Fajfar, J. Medved, G. Klančnik, T. Lazar, M. Nečemer, P. Mrvar, Characterization of a Messer – the late-Medieval single-edged sword of Central Europe, Materials Characterization, 86 (**2013**), 232–241, doi:10.1016/j.matchar. 2013.10.005

[15] E. Duka, H. Oettel, T. Dilo, Connection Between Micro and Macro Hardness. Pearlitic-Ferritic Steel, AIP Conference Proceedings 1476, 2012, 47–5, doi:10.1063/1.4751563

[16] E. Harmuth, Die Armbrust, Akademische Druck- und Verlaganstalt, Graz 1986, p. 232

[17] W. F. Paterson, A Guide to the Crossbow, Society of Archer-Antiquaries, Burnham 1990, 132

[18] J. Alm, European Crossbows, Royal Armouries, Leeds 1996, 25

[19] J. Liebel, Springalds and Great Crossbows, Royal Armouries, Leeds 1998, 23

[20] H. Richter, Die Hornbogenarmbrust, Hoernig Angelika, Ludwigshafen 2006, 190

[21] A. Williams, The Knight and the Blast Furnace, Brill, Leiden, Boston 2003, 954

[22] M. Strickland, R. Hardy, The Great Warbow; From Hastings to the Mary Rose, Sutton, Stroud 2005, 538

[23] P. Krenn, Von alten Handfeuerwaffen, Landeszeughaus, Graz 1989, 149

[24] Bibliothèque Nationale, Paris, MS Fr 2695

[25] J. Heers, F. Robin, René d'Anjou, Traité des Tournois, Lengenfelder, München 1993, 30

[26] H. W. Peine, 2004: Ein Blick in die Waffenkammer des Hauses Herbede an der Ruhr, Das Brigantinen-Symposium auf Schloss Tirol/Il simposio sulla brigantina a Castel Tirolo, Innsbruck, 2004, 51–53

[27] C. Blair, European Armour, B. T. Batsford Ltd., London 1958, 248

[28] D. A. Scott, Metallography and Microstructure of Ancient and Historic Metals, The J. Paul Getty Trust, Los Angeles 1991, 155

[29] T. Lazar, N. Nemeček, Interdisciplinary Research of Museum Objects. Practical Experience with Various Analytical Methods, RMZ: Materials and geoenvironment, 60 (2013) 4, 249–261

UDK 519.6:620.179:67.017
Original scientific article/Izvirni znanstveni članek

ISSN 1580-2949
MTAEC9, 50(5)775(2016)

NUMERICAL AND EXPERIMENTAL INVESTIGATION OF THE EFFECT OF HYDROSTATIC PRESSURE ON THE RESIDUAL STRESS IN BOILER-TUBE WELDS

NUMERIČNA IN EKSPERIMENTALNA PREISKAVA VPLIVA HIDROSTATIČNEGA TLAKA NA ZAOSTALE NAPETOSTI V ZVARU NA KOTLOVSKI CEVI

Daryoush Danyali, Eslam Ranjbarnodeh

Amir Kabir of University of Technology, Department of Mining and Metallurgical Engineering, Tehran, Iran
islam_ranjbar@yahoo.com, islam_ranjbar@aut.ac.ir

Prejem rokopisa – received: 2015-08-13; sprejem za objavo – accepted for publication: 2015-10-09

doi:10.17222/mit.2015.255

A tube to tube-sheet weld joint is a critical section in many boilers. Leakage and failure are two common problems that can occur with this type of joint. The tensile residual stresses associated with welding can play a major role in these problems. In the present study, the Finite-Element Method is used to predict the residual stresses in a tube to tube-sheet weld and the effect of hydrostatic pressure on the residual stresses' redistribution. Investigations were performed by numerical analyses and experimental methods. The joint included a circumferential fillet weld in one pass using a gas tungsten arc welding process. The thermomechanical behavior of the joint is simulated with a two-dimensional axisymmetric model and a subroutine developed in ANSYS software. The thermography method is used for the thermal verification and the hole-drilling strain gauge under post-weld heat treatment is used for the mechanical analysis verification. The numerical and experimental results showed that applied hydrostatic pressure can reduce, by about 58 %, the axial residual stress.

Keywords: hydrostatic test, residual stress, boiler tubes, tube-sheet, finite element method (FEM)

Kritični področji v kotlih sta zvarjen spoj cevi in cevne predelne stene. V tej vrsti spoja sta glavna problema, ki se pojavljata, puščanje in porušitev. Zaostale natezne napetosti povezane z varjenjem so glavni dejavnik pri teh problemih. V študiji je bila uporabljena metoda končnih elementov za napovedovanje zaostalih napetosti v zvarih cevi in cevne predelne stene in vpliv hidrostatičnega tlaka na razporeditev zaostale napetosti. Raziskave so bile izvedene z numerično analizo in z eksperimentalnimi metodami. Spoj je vključeval obodni zvar izdelan v obloku z volframovo elektrodo in zaščito s plinom. Termomehansko obnašanje spoja je bilo simulirano z uporabo dvodimenzijskega osnosimetričnega modela in programa razvitega z ANSYS programsko opremo. Termografska metoda je uporabljena za preverjanje toplote in pri toplotni obdelavi zvarov je bila uporabljena metoda z merilnimi lističi na izvrtini za preverjanje mehanske analize. Numerični in eksperimentalni rezultati so pokazali, da uporabljen hidrostatični tlak, lahko za 58 % zmanjša osne zaostale napetosti.

Ključne besede: hidrostatični preizkus, zaostala napetost, kotlovske cevi, cevna predelna stena, metoda končnih elementov (FEM)

1 INTRODUCTION

Boilers are a very important part of many industries, such as power generation, food, hospitals, and hotels. Boilers are the most troublesome components of electrical power generation plants. It costs the US utility industry over $5 billion per year in unscheduled shutdowns, repairs and power replacements.[1] In general, the safety and structural integrity of a boiler are of paramount importance. Welding is common method in the boiler-manufacturing process and the process of welding has a direct influence on the integrity of the components and their thermal and mechanical behaviors during service. Micro-cracking in tube to tube-sheet welds, in both the radial and circumferential directions, is commonplace.[2]

The nature of failures in the vicinity of the tube to tube-sheet interfaces is particularly difficult to determine because of the large temperature gradients as well as the relatively high pressures. Due to the high temperatures introduced during welding and the subsequent cooling of the welded metal, welding can produce undesirable residual stresses and deformations. Radial cracking is more likely to occur, but circumferential cracking also occurs and results from the thermal cycling, which is exacerbated by a high residual stress.[3] The thermal stress, mechanical stress and welding residual stress of tube to tube-sheet has received a lot of attention in recent years.

B. Yildrim and H. F. Nied[4] investigated the residual stress and distortion in boiler-tube panels with welded overlay cladding. X. Qingren[5] reported that residual stress in the circumferential weld in pipes is reduced when hydrostatic pressure is increased. To the best of the knowledge of the author, a very limited number of FEM models have been proposed for predicting the residual stresses in a tube to tube-sheet weld and the effect of hydrostatic pressure test on the residual stresses in this type of joint. The present study uses a two dimensional

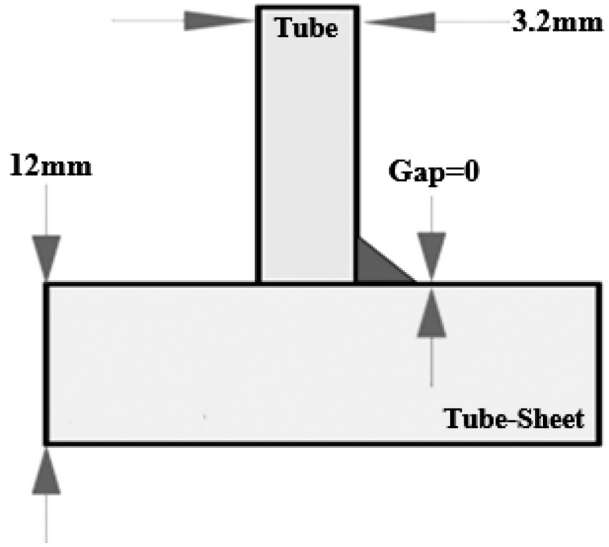

Figure 1: Schematic of geometrical model for verification
Slika 1: Shematski prikaz geometrijskega modela za preverjanje

axisymmetric FEM model for the calculation and distribution of the residual stresses in a tube to tube-sheet joint. The Thermography Method is used for the thermal verification and the hole-drilling strain gauge under post-weld heat treatment is used for the mechanical analysis verification and then the effect of hydrostatic pressure on the redistribution residual stresses is investigated by numerical analyses and experimental methods.

2 FEM AND VERIFICATION PROCEDURES

2.1 Welding verification procedures

To verify the results of the FEM method, an experimental test with the same geometry, material and welding parameters was produced, as shown in **Figure 1**.

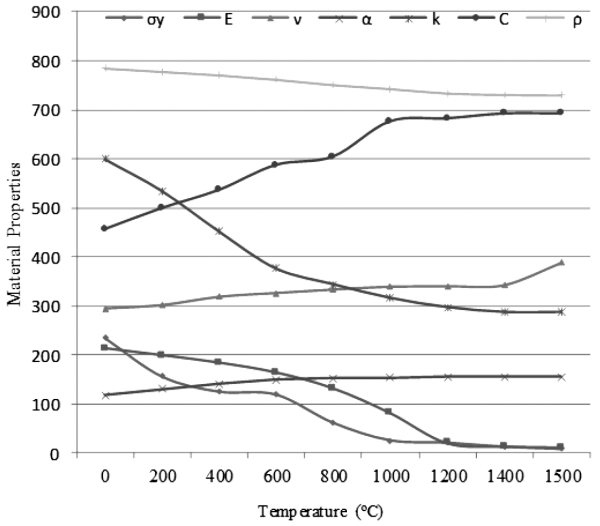

Figure 2: Thermo-physical and mechanical properties
Slika 2: Termofizikalne in mehanske lastnosti

2.2 Material properties

The base metal of the tube was steel St35.8 and tube-sheet was steel 17Mn4. The chemical compositions are listed in **Table 1**.

Table 1: Chemical composition in mass fractions (*w*/%)
Tabela 1: Kemijska sestava v masnih odstotkih (*w*/%)

Composition	C	Si	Mn	P	S	Cr
St35.8	0.17	0.35	0.60	0.03	0.03	–
17Mn4	0.20	0.20	0.120	0.03	0.025	0.30

For the thermal and mechanical analyses, the relationship between the thermo-physical and the thermo-mechanical properties of the materials with temperature is incorporated, as shown in **Figure 2**.

The welding parameters used were exactly as same as the boiler-repair parameters. The dimensions of the welded parts are presented in **Table 2**.

Table 2: The dimensions of the pieces used
Tabela 2: Dimenzije uporabljenih kosov

Material	Diameter (mm)	Width (mm)	Width (mm)	Thickness (mm)
Tube	51.8	–	200	3.2
Tube-sheet	–	80	80	12

2.3 Thermal verification procedure

To verify the thermal model, thermography was used. In this study, the welding temperature was monitored with a model T8 thermography camera. It helps to record the temperature during the welding and after the weld cooling.

2.4 Mechanical model verification procedure

To verify the weld profile obtained using the FEM method, a section was prepared for macroscopic examination of the welded samples. The section was prepared, polished and etched in a solution with 50 mL of 37 % hydrochloric acid and 50 ml of distilled water for 30 minutes. After the etching period it was examined macroscopically.

2.5 Residual stress verification procedure

The hole-drilling strain gauge under post-weld heat treatment is based on the principle that if a hole in a piece is created, stresses around the hole and the hole will be released. When this amount increases, the mobility of the hole will increase. The strain and thus the amount of residual stresses can be calculated by determining the displacement of the hole. This procedure is based on Tait's research.[3]

The amounts of axial residual stresses were produced by the drilling under post-weld heat treatment technique.

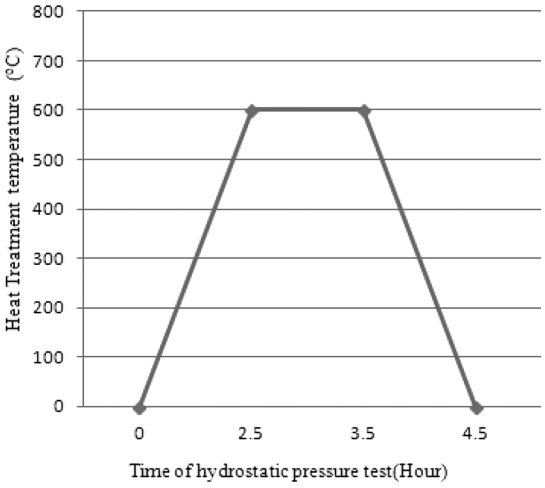

Figure 3: Heat-treatment cycle
Slika 3: Potek toplotne obdelave

The samples were drilled using a TOSKURIM drilling machine.

The high-speed steel drill was 2 mm in diameter, known as the drill chuck. The rotation speed was 2743 min^{-1} and the forward speed of the drill was 0.05 mm/min. After drilling, the distances between the holes were measured and recorded with a MITUTOYO micrometer type with an accuracy of up to 0.02 mm. After measuring the distance between the holes, the samples were heat treated according to the guidelines for heat treatment.[5]

The applied heating rate was 220 °C/h. The welded parts were held at 620 °C for an hour and then they were allowed to cool with a cooling rate of about 275 °C/h, cooled in furnace to 300 °C and after that in air. **Figure 3** shows the applied heat-treatment cycle for the welded parts in this study.[6]

After that the samples were cooled, the distances between the holes were measured and recorded again in the same manner using the same micrometer. The residual stresses in the specimens are released by drilling the specimens, and the axial strain, e_x, and transverse released strain, e_y, are measured. Using the measured strains, the axial residual stress, σ_x, can be obtained from Equation (1):[7]

$$\sigma_x = [-E/(1 - v^2)](e_x + ve_y) \quad (1)$$

where E is Young's modulus and v is Poisson's ratio.

2.6 Hydrostatic test verification procedure

Before applying hydrostatic pressure, the distances between holes were measured and recorded again. The drilling apparatus and procedure were the same as used in the calculation of the residual stresses. **Figure 4** shows a hydrostatic test setup and **Figure 5** shows the sample drilled to investigate the behavior of residual stresses after the hydrostatic pressure.

To create the real conditions, like hydrostatic test conditions, the welded part was restrained between the fixed jaws of a clamp. The fittings for the pressure-testing machine were installed and water with a temperature of about 15 °C was injected into the welded part. When the air bubbles exit completely, a pressure equal to 1.5 times the boiler's design pressure was applied to the welded part.[6] Due to the design the pressure of the investigated boiler in this study was 0.4 MPa, while the

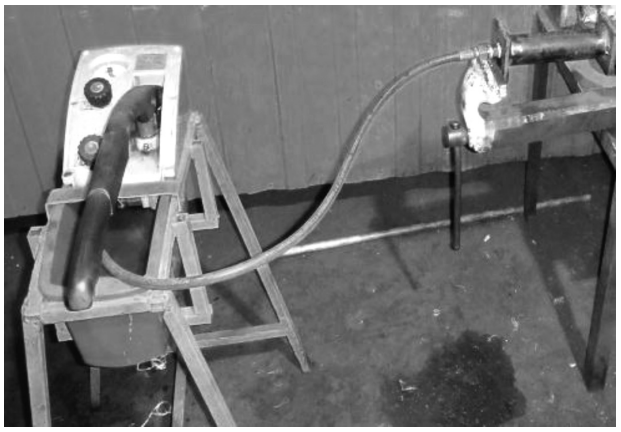

Figure 4: Hydrostatic test setup
Slika 4: Sestav za hidrostatični preizkus

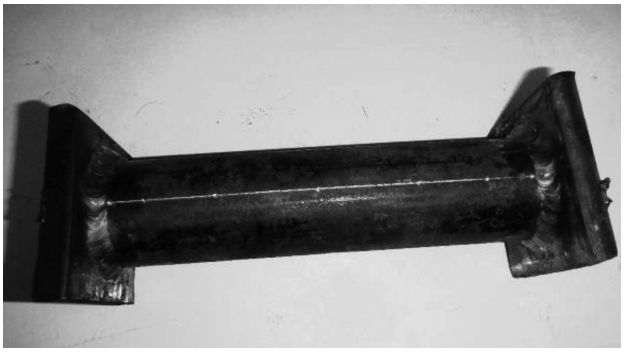

Figure 5: The sample drilled for axial residual stress measurement and hydrostatic tests
Slika 5: Zvrtan vzorec za merjenje aksialnih zaostalih napetosti in hidrostatični preizkus

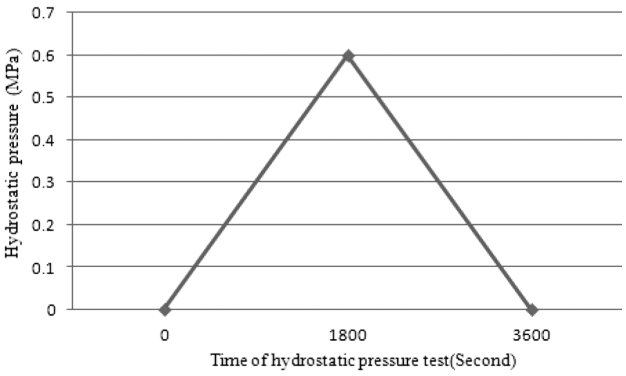

Figure 6: Applied hydrostatic pressure as a function of time
Slika 6: Uporabljen hidrostatični tlak v odvisnosti od časa

applied hydrostatic pressure to the welded part was about 0.6 MPa.

Figure 6 shows the applied hydrostatic pressure as a function of time. After 1800 s, the hydrostatic pressure was removed. After the completion of the hydrostatic testing procedure, the distances between the drilling locations were measured and recorded with the same micrometer.

2.7 FEM meshed model

The FEM model of the welding process is performed on the St35.8 steel tube with an outer diameter of 51 mm and a wall thickness of 3 mm, and 17Mn4 steel tube-sheet with a wall thickness of 12 mm using a single pass. There was no gap between the tube and tube-sheet. The welding process used was gas tungsten arc welding. For a more convenient calculation, a part of the tube-sheet was selected for the FEM analysis. Although the real welding is a three-dimensional procedure, it is often considered sufficient to represent a circumferential weld with a two-dimensional axisymmetric FEM model.[7] The two-dimensional axisymmetric FEM model is much faster and easier to perform.[8,9] Therefore, the methodology described here is based on a two-dimensional axisymmetric model.

The meshed model is shown in **Figure 7**. For the meshing, plane55 and Surf151 elements were used for thermal analysis and the plane82 element was used for the mechanical analysis. In total, 346 nodes and 303 elements were generated. The welding of the tube to tube-sheet was performed with a single pass weld. In the weld adjacent, the meshing was very fine due to the high thermal gradient of this region during the welding process.

2.8 Thermal analysis

The heat equation is a parabolic partial differential equation that describes the distribution of heat (or variations in temperature) in a given region over the time and is generally describes by Fourier's relation, Equation (2):[6]

$$\rho c_{\mathrm{p}}\left(\frac{\partial}{\partial t}\right)=\frac{\partial}{\partial x}\left[K_x\frac{\mathrm{d}T}{\mathrm{d}x}\right]+\frac{\partial}{\partial y}\left[K_y\frac{\mathrm{d}T}{\mathrm{d}y}\right]+\frac{\partial}{\partial z}\left[K_z\frac{\mathrm{d}T}{\mathrm{d}z}\right]+Q \quad (2)$$

where ρ is the density (kg/m^3), C_{p} is the specific heat capacity (J/kg K), K (W/m K) is the thermal conductivity, Q is the heat input (W), and T is the temperature (K).

The Gaussian function is calculated by following Equation (3):[6,10]

$$q(r)=\left(\frac{3Q}{\pi r_0^2}\right)\exp\left[-3\left(\frac{r}{r_0^2}\right)\right] \quad (3)$$

where $q(r)$ is the heat flux (W/m^2), r_0 is the radius of the welding heat source that is estimated to be about one half of the Gaussian curve width, r is the distance from the middle point of the heat source to the center, and Q is the heat input (W) that is calculated using Equation (4):[6]

$$Q = V{\cdot}I{\cdot}\eta \quad (4)$$

where V is the welding voltage, I is the welding current, and ç is the welding efficiency. In this paper V, I, η and r_0 were 10 V, 120 A, 0.85 and 10 mm, respectively. The filler metal, welding speed and gas flow rate were ER70S-6, 5cm/min and 15 L/min, respectively.

The fluid flow in the welding pool increases the heat-transfer rate, which has an important effect on the temperature field in the welding process. The effect of fluid flow on the weld pool temperature for the whole temperature field is considered by the heat-transfer coefficient, h. In this study, as in a previous study, h = 15

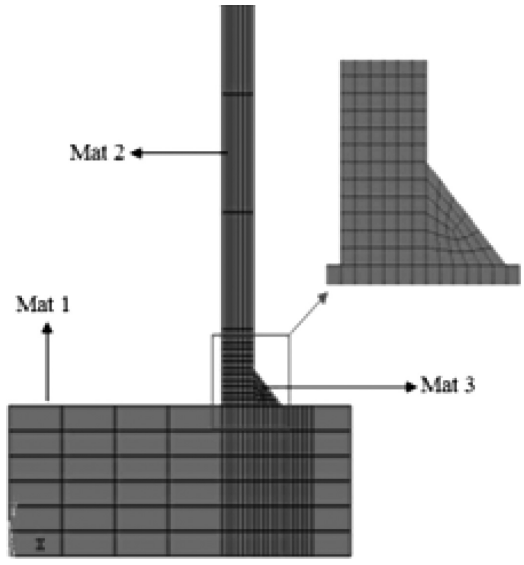

Figure 7: FEM meshed model
Slika 7: Model mreže za FEM

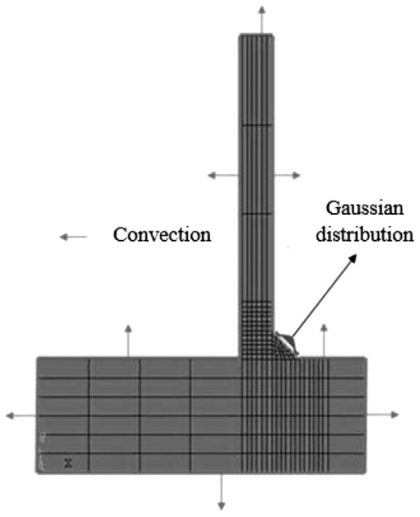

Figure 8: The applied thermal boundary conditions
Slika 8: Uporabljeni toplotni robni pogoji

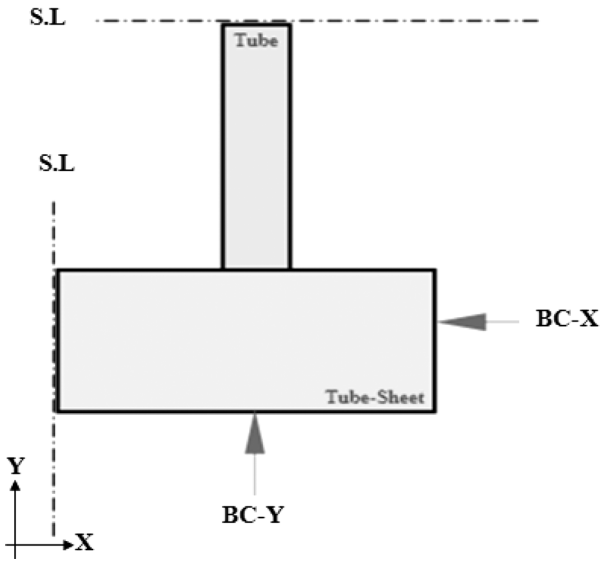

Figure 9: The mechanical boundary conditions
Slika 9: Mehanski robni pogoji

W/K m^2.[11] Due to the small thickness of the parts, preheating before welding is not done and the initial temperature of the welded parts was assumed to be 27 °C. **Figure 8** shows the applied thermal boundary conditions.

2.9 Mechanical analysis

The residual stress was calculated by using the temperature distribution obtained from the thermal analysis as input data. The material properties relevant to the residual stress are the Young's modulus, the yield strength, the Poisson's ratio, and the coefficient of thermal expansion. The total strain can be decomposed into three components, as in Equation (5):[11]

$$\varepsilon^{\text{thotal}} = \varepsilon^{\text{e}} + \varepsilon^{\text{p}} + \varepsilon^{\text{th}} \quad (5)$$

where ε^{e}, ε^{p}, and ε^{t} are the elastic strain, plastic strain and thermal strain, respectively. The elastic strain was modeled using the isotropic Hooke's law with a temperature-dependent Young's modulus and Poisson's ratio. During the mechanical analysis, boundary conditions were applied to prevent the rigid-body motion. **Figure 9** shows the applied mechanical boundary conditions. Because of the tube-sheet rigidity, BC-X is constrained in the X-direction and BC-Y is constrained in the Y-direction. The S.L lines are axisymmetric lines.

3 RESULTS AND DISCUSSION

3.1 Thermal results

The thermal contour recorded by the experimental method is shown in **Figure 10** and the thermal results recorded by experiment and the FEM are shown in **Figure 11**. The weld-pool peak temperatures of the FEM model and the experiments are 1900 °C and 1716 °C,

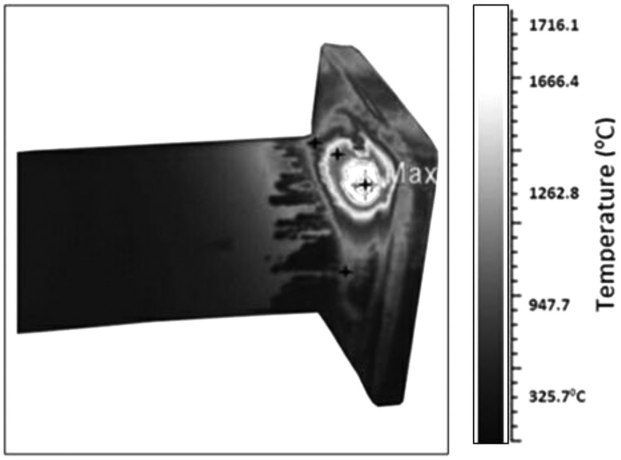

Figure 10: Contours of the thermal history
Slika 10: Plastnice termične zgodovine

respectively. This 10 % difference shows the good agreement between the experimental results and the FEM model. This difference could be due to changes in thermo-physical properties of the materials as a function of the temperature, the difference in the thermal conductivity. In the same way, Majzobi and colleagues conducted a study in which a thermography technique was used to record the thermal history.[12] The thermal history

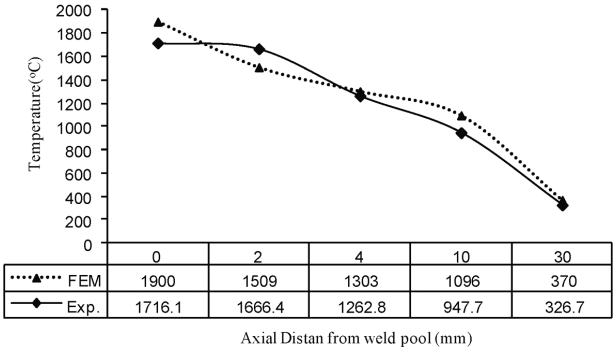

Figure 11: Curves of the thermal history
Slika 11: Krivulji toplotne zgodovine

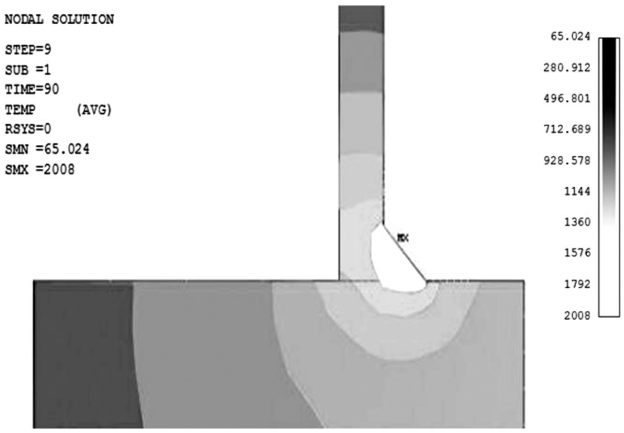

Figure 12: Temperature contours for the FEM model during welding
Slika 12: Razporeditev temperature pri FEM modelu med varjenjem

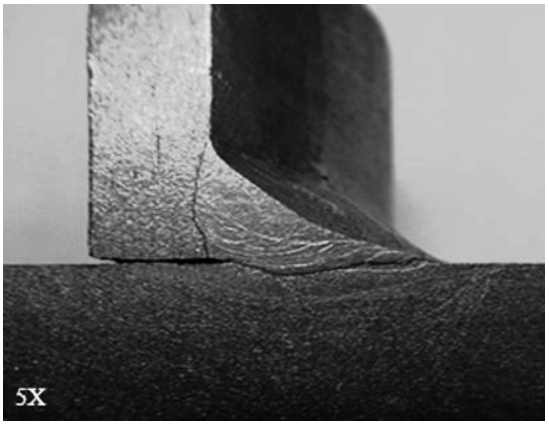

Figure 13: The weld profile using the experimental method
Slika 13: Profil zvara pri preizkusu

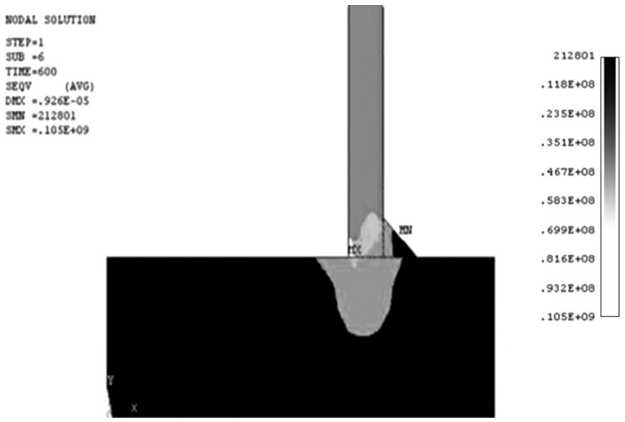

Figure 14: Residual stresses results in axial direction using the FEM method, before the hydrostatic test
Slika 14: Zaostale napetosti v osni smeri po FEM metodi, pred hidrostatičnim preizkusom

of the contours recorded by the other researches also shows a difference of about 11 %, which confirms the results of the present study.

The weld profile that is created with the FEM is shown in **Figure 12**. The peak of the weld's penetration is 1.06 mm into the tube. The weld profile that is created using the experimental method is shown in **Figure 13**. The peak of the weld penetration is 1.2 mm into the tube.

Comparing these two sets of results shows that greatest difference in the amount of weld penetration into the tube-sheet is about 12 %. The results are proved to be in a logical agreement for the FE method and experimental results.

3.2 Mechanical behavior under hydrostatic effect

The residual stresses contour in the axial direction is shown in **Figure 14**. The axial residual stress calculated by the FEM and experimental methods is shown in **Figure 15**. The peak axial residual stress of 105 MPa is located in the weld root zone. The peak axial residual stress calculated by the experimental method was 85.94

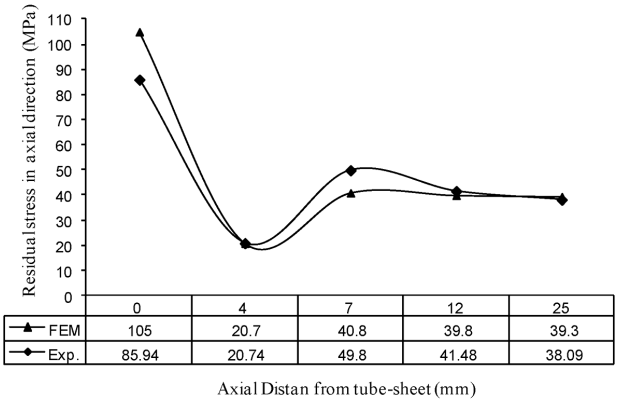

	0	4	7	12	25
FEM	105	20.7	40.8	39.8	39.3
Exp.	85.94	20.74	49.8	41.48	38.09

Figure 15: Residual stresses results in axial direction using the FEM method, before the hydrostatic test
Slika 15: Zaostale napetosti v smeri osi, po FEM metodi, pred hidrostatičnim preizkusom

MPa. The axial residual stresses first decrease from the peak value, and then start to increase. All the axial residual stresses decrease along the weld and the outer surface of the tube. The axial residual stress values are

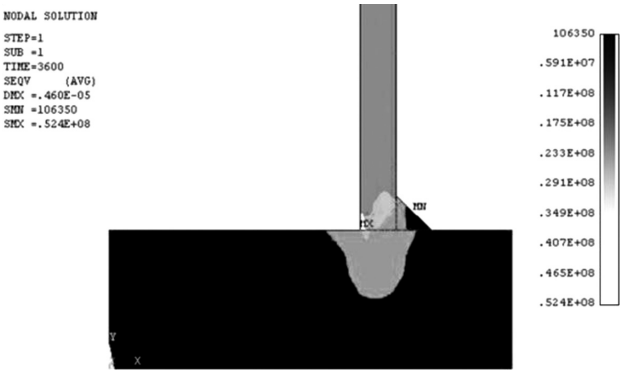

Figure 16: Residual stresses in axial direction using the FEM and experimental methods, after the hydrostatic test
Slika 16: Zaostale napetosti v smeri osi po FEM in eksperimentalni metodi, po hidrostatičnem preizkusu

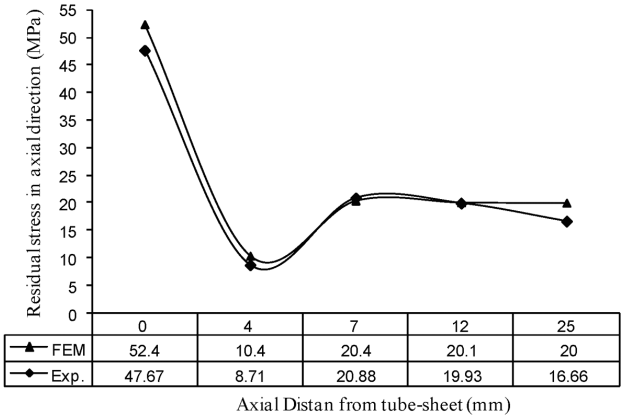

	0	4	7	12	25
FEM	52.4	10.4	20.4	20.1	20
Exp.	47.67	8.71	20.88	19.93	16.66

Figure 17: Residual stresses in axial direction using the FEM and experimental methods, after the hydrostatic test
Slika 17: Zaostale napetosti v osni smeri po FEM in po eksperimentalni metodi, po hidrostatičnem preizkusu

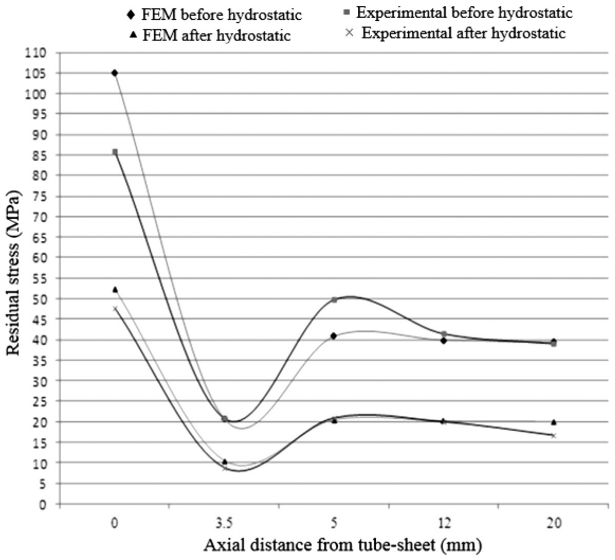

Figure 18: Residual stresses in the axial direction using the FEM and experimental methods, before and after the hydrostatic test

Slika 18: Zaostale napetosti v osni smeri po FEM in po eksperimentalni metodi, pred in po hidrostatičnem preizkusu

reasonable, compared to Sattari-Far's research results.[13,14] The maximum difference between the two methods is 18 % and the lowest is 2 %. As compared to Tait's results[2], the findings of the present study are acceptable. The peak axial tensile residual stress is 105 MPa in the root of the joint, which caused the initiation and growth of fatigue cracks under cyclic loading in this boiler joint.

In order to investigate the effect of the hydrostatic test on the residual stress in the axial direction in a boiler-tube weld, hydrostatic pressure is applied using the FEM and experimental methods. **Figure 16** shows the curve of the residual stress results in the axial direction using the FEM and experimental methods, before the hydrostatic test. It is clear that the hydrostatic pressure affects the residual stress in the axial direction, as shown in **Figure 17**. The maximum difference between the two methods is about 9 %. The results of the FE method show a peak in the residual stress in the axial direction after the application of the hydrostatic pressure is 52.4 MPa. The results of the experimental method show that the peak residual stresses in the axial direction after the application of hydrostatic pressure is 47.7 MPa.

The residual stresses in the axial direction calculated by the FEM method in the weld root are shown in **Figure 18**. The residual stresses in the axial direction calculated by the FEM method in weld root show that the application of a hydrostatic test pressure after the welding process can reduce the tensile residual stresses in the axial direction from 105 MPa to of 52.4 MPa, i.e., by approximately 51 %. The results of the residual stresses in the axial direction calculated using the FEM method in the weld toe shows that hydrostatic pressure can reduce the tensile residual stresses in the axial direction from 40.8 MPa to 20.4 MPa, i.e., a reduction of about 50 %. The residual stresses in the axial direction calculated using the experimental method in the weld shows that applying a hydrostatic test pressure after the welding process can reduce the tensile residual stresses in the axial direction from 20.74 MPa to 8.71 MPa. This means a reduction of about 58 %. The reason for this reduction can be sought in the accumulation of the hydrostatic pressure and the previous residual stresses that were caused by plastic deformation. In the plastically deformed region, the total stresses exceeded the yield strength and partial relaxation of the residual stresses can be occurred.

4 CONCLUSIONS

This study predicted the axial residual stresses and their behavior under hydrostatic pressure using the FEM and experimental methods. The results of this study can be summarized as follows:

1. The root of tube to tube-sheet joint and the weld toe were two critical points with the maximum axial tensile residual stress.
2. Applying a hydrostatic pressure after the welding process could reduce the axial tensile residual stresses in the weld by about 58 %.
3. Applying a hydrostatic pressure after the welding process could reduce the axial tensile residual stresses in the root of tube to tube-sheet joint by about 50 %.
4. Applying hydrostatic pressure after the welding process could reduce the axial tensile residual stresses in the weld toe by about 51 %.
5. It was easier and cheaper to calculate the residual stresses in the design of a complex geometry in connection with a corner joint with a very low thickness using the technique of strain measurement accuracy of the hole under the heat treatment.
6. The results of the present study could be generalized for other critical boiler joints, such as the shell to furnace joint and the furnaces to tube-sheet joint.
7. The results of the present study could be generalized to other high-pressure equipment including heat exchangers, hot-water boilers, hot-oil boilers and any other equipment that has a tube to tube-sheet joint.

5 REFERENCES

[1] X. Shugen, W. Weiqiang, Numerical investigation on weld residual stresses in tube to tube sheet joint of a heat exchanger, Int. J. Pres. Ves. Pip., 101 (**2013**), 37–44, doi:10.1016/j.ijpvp.2012.10.004

[2] R. Tait, J. Press, Investigation An experimental study of the residual stresses, and their alleviation, in tube to tube-sheet welds of industrial boilers, Engineering Failure Analysis, 8 (**2001**), 15–27, doi:10.1016/j.engfailanal.2013.04.01

[3] K. Abouswa, F. Elshawesh, A. Abuargoub, Stress corrosion cracking (caustic embrittlement) of super heater tubes, Desalination, 222 (**2008**), 682-688, doi:10.1016/j.desal.2007.02.073

[4] B. Yildrim, H. F. Nied, Residual Stress and Distortion in Boiler Tube Panels with Welded Overlay Cladding, Journal of Pressure Vessel Technology – Transactions of ASME, 126 (**2004**), 426–431, doi:10.2320/matertrans.126.426

[5] X. Qingren, F. Yaorong, H. Chun-Yong, The measurement and control of residual Stress in spiral submerged arc welded pipe, Proceedings of 4th International pipeline conference, Calgary, 2002, 615–622

[6] British Standards Institute, BS2790, Design and manufacturing of shell boilers of welded construction, 1992, 80–100

[7] C. Lee, K. Chang, Numerical investigation of residual stresses in Strength mismatched dissimilar steel butt welds, J. Strain Analysis, 43 (**2008**), 55–66, doi:10.1243/03093247JSA313

[8] T. Soanes, W. Bell, A. Vibert, Optimizing residual stresses at a repair in a steam header to tube plate weld, Int. J. Pres. Ves. Pip., 82 (**2005**), 311–318, doi:10.1016/j.ijpvp.2004.08.009

[9] D. Deng, H. Murakawa, Numerical simulation of temperature field and residual stress in multi-pass welds in stainless steel pipe and comparison with experimental measurements, Comp. Mater. Sci., 37 (**2006**), 269–277, doi:10.1016/j.commatsci.2005.07.007

[10] X. Shugen, Z. Yanling, Using FEM to determine the thermo mechanical stress in tube to tube–sheet joint for the SCC failure analysis, Engineering Failure Analysis, 34 (**2013**), 24–34, doi:10.1016/j.engfailanal.2013.07.01

[11] T. Tso-Liang, F. Chin-Ping, C. Peng-Hsiang, Y. Wei-Chun, Analysis of residual stresses and distortion in T-joint fillet welds, Int. J. Pres.Ves. Pip., 78 (**2001**), 523–538, doi:10.1016/j.ijpvp.2000.07.008

[12] J. Otegui, P. Fazzini, Failure analysis of tube–tubesheet welds in cracked gas heat exchangers, Engineering Failure Analysis, 11 (**2004**), 903–913, doi:10.1016/j.engfailanal.2004.01.003

[13] I. Sattari-Far, Y. Javadi, Influences of welding sequence on welding distortion in pipes, Int. J. Pres. Ves. Pip., 85 (**2008**), 265–274, doi:10.1016/j.engfailanal.2007.02.004

[14] I. Sattari-Far, M. Farahani, Effect of the weld groove shape and pass number on residual stresses in butt-welded pipes, Int. J. Pres. Ves. Pip., 86 (**2009**), 769–777, doi:10.1016/j.ijpvp.2009.07.007

UDK 621.78.08:67.017:691.714
Original scientific article/Izvirni znanstveni članek

ISSN 1580-2949
MTAEC9, 50(5)783(2016)

EFFECT OF DIRECT COOLING CONDITIONS ON THE MICROSTRUCTURE AND PROPERTIES OF HOT-FORGED HSLA STEELS FOR MINING APPLICATIONS

VPLIV POGOJEV OHLAJANJA NA MIKROSTRUKTURO IN LASTNOSTI VROČE KOVANIH HSLA JEKEL ZA UPORABO V RUDARSTVU

Piotr Skubisz, Łukasz Lisiecki, Tadeusz Skowronek, Artur Żak, Władysław Zalecki

[1]AGH University of Science and Technology, Department of Metals Engineering and Industrial Computers Science, 30A Mickiewicz Ave, Kracow, Poland
[2]Ferrous Metals Institute, 12-14 K. Miarki, Gliwice, Poland
pskubisz@metal.agh.edu.pl

Prejem rokopisa – received: 2015-09-18; sprejem za objavo – accepted for publication: 2015-10-26

doi:10.17222/mit.2015.298

The article presents hot deformation and controlled direct cooling of hardened medium-carbon HSLA steel with micro-additions of alloying elements Ti and/or V. It also contains a study of the effect of thermomechanical-processing conditions on grain refinement and precipitation kinetics in the replacement of the conventional reheating-requiring heat treatment with a cost-effective technology. Controlled cooling with accelerated air and mist adjusted to lower carbon and hardenability-related alloying elements by means of employing experimentally designed heats, varying in the Mo content, was designed to meet the mining-industry requirements for mechanical properties. Besides microstructural-property relations, the vital problem of non-uniformity of the obtained properties is addressed with regard to within-part variances in the cooling rate of the as-forged, undeformed and dynamically recrystallized material. The strength and plasticity versus the microstructure of the produced fine pearlite/bainite structure with grain-boundary ferrite were evaluated. Microstructure-property relations allowed the formulation of the conclusions on the effect of direct-cooling conditions on the microstructure and grain substructure, their mutual synergic effect in controlling the microstructure, as well as guidelines for the transfer of the locally established process parameters into technological conditions.

Keywords: thermomechanical processing, drop forging, accelerated cooling, grain refinement, tempered martensite

Članek predstavlja vročo deformacijo in kontrolirano ohlajanje srednjeogljičnega HSLA jekla z mikrododatkom legirnih elementov Ti in/ali V. Vsebuje tudi študijo vpliva pogojev termomehanske obdelave na udrobnjenje zrn in kinetiko izločanja pri nadomeščanju običajnega režima ogrevanja za toplotno obdelavo s cenejšo tehnologijo. Da bi dosegli zahteve rudarske industrije in mikrostrukturne lastnosti, je bilo vzpostavljeno kontrolirano ohlajanje s tokom zraka in mešanice zraka ter vode, prilagojeno nižjemu ogljiku in drugim elementom. Ti vplivajo na prekaljivost z uporabo eksperimentalnih talin, v katerih se je spreminjala vsebnost Mo. Poleg odvisnosti lastnosti od mikrostrukture, je glavni problem neenakost dobljenih lastnosti, kar je delno povezano z razlikami pri ohlajanju v kosu kovanega, nedeformiranega ali dinamično rekristaliziranega materiala. Ocenjeni sta bili trdnost in plastičnost v odvisnosti od nastale drobnozrnate perlitno/bainitne mikrostrukture s feritom po mejah zrn. Odvisnost mikrostrukture od lastnosti omogoča postavitev zaključkov o vplivu pogojev pri neposrednem ohlajanju na mikrostrukturo in zrna substrukture ter njihov medsebojni vpliv pri kontroli mikrostrukture, kot tudi navodila za prenos lokalno ugotovljenih procesnih parametrov v tehnološke pogoje.

Ključne besede: termomehanska obdelava, kovanje s padalnim kladivom, pospešeno ohlajanje, zmanjšanje zrn, popuščen martenzit

1 INTRODUCTION

Forging has long been more than a mere shaping technique. In addition to the accuracy requirements, such as allowances and yield, mechanical properties must be fulfilled. As an alternative to the traditional quenching and tempering (Q&T) heat treatment, thermomechanical processing (TMP) in controlled conditions of forging and direct cooling is increasingly used on an industrial scale, offering a good combination of strength and ductility at a lower cost.[1–3]

The strength levels obtained with TMP are often lower as compared to a traditional Q&T material[4], due to an excessive surplus of indices in the case of the latter. Furthermore, some mechanical properties of TMP microalloyed grades, such as the fatigue strength, are second to those treated with Q&T.[5] The key issue is to control the chemistry and processing cycle so as to achieve the sustainable strength, plasticity, cracking and/or fatigue resistance required by the end user of a finished product.

Thus, numerous microalloyed grades for specific applications have been designed over the decades. So have the technologies of forging and subsequent cooling.[6,7] This work is devoted to the design or modification of a microalloyed steel grade exhibiting as-forged air-cooled mechanical properties suitable for a mining application. The target application of this combination is a miners' linking hook for coal transport, which, after a

controlled hot-forging and direct heat treatment, involving quenching and self-tempering, is expected to provide a yield strength (*YS*) of 800 MPa, the ultimate tensile strength (*UTS*) of 1050 MPa, an elongation to fracture of *A* 15 % and/or an impact strength at room temperature of KCV 60 J/cm^2 to substitute C45 or SJ355 heat-treatable structural steel grades.

2 EXPERIMENTAL METHODS

The research plan included testing the effect of forging temperature on the microstructure and mechanical properties obtained after direct cooling in forced air and atomizers, applied to designed microalloyed grades, hot deformed in an inconvenient high-speed hammer-forging process. The goal of the study was both the investigation of the effect of material-process conditions on the final (as-forged) properties, and its applicability to drop-forging industrial conditions with respect to the uniformity of the properties.

Eight different sets of alloying elements were composed on the basis of the computation in Thermocalc under equilibrium thermodynamics conditions. Diagrams were established on the basis of a volumetric-change analysis (dilatometer DIL 805 with probe LVDT) CTT, followed by an examination of the microstructures obtained with different cooling rates of 0.17 °C/s, 0.42 °C/s, 1 °C/s, 2 °C/s, 4 °C/s, 10 °C/s, 20 °C/s, 40 °C/s, 50 °C/s and 100 °C/s, taking into consideration the cooling rates predicted in the modeling of physical cooling of the target geometry. Having had selected two grades, further described as A and B, laboratory tests of rolling and direct cooling with water and air were conducted, as well as forging on a hydraulic press of 5 MN with a ram velocity of 50 mm/s.

To estimate the amount of deformation and the actual forge-end temperature in the bulk of the part, a numerical calculation of an equivalent strain and temperature progression in hot forging was carried out. Since the forging temperature should be high enough to dissolve carbides and carbonitrides so as to enable their precipitation during the post-forging direct cooling, a soaking temperature of 1190 °C was established and forging temperatures ranging between (1100, 1000 and 900) °C were assumed. The cooling rate – fast enough to provide harder microstructural components during the subsequent cooling[8] – was realized with atomizers.

Numerical modeling was conducted with the finite-element method (FEM) in code QForm3D. Besides supplying the data for the prediction of transformation products or microstructural development, and carbide and carbonitride precipitation kinetics, the results of the calculation formed the basis for experimental controlled cooling tests on a laboratory continuous cooling line, QuenchTube Duo (**Figure 1**).

The laboratory cooling line simulated an industrial cooling line, providing a forced stream of mist with intervals resulting from the transfer of a part between consecutive cooling zones. All runs involved the same cycle, irrespective of the forging temperature and the alloy. Cooling was conducted at a cooling rate adapted to the temperature changes, calculated for a drop-forged miners' link hook (**Figure 2**), which formed a case study for an evaluation of the effectiveness of the selected processing conditions with respect to the forging temperature and chemical composition.

3 MATERIALS

The study involved experimentally designed steel grades, which were to provide directly cooled forgings with the mechanical properties comparable to typical mining-industry grades, such as C45, 41Cr, 36CrNiMo4 and 23MnNiCrMo5.

Eight grades were made, based on the assumption of a reduction of carbon and the major alloying elements, and micro-additions of Ti, V and Nb, with or without Mo. The heating was performed in an induction-heating vacuum furnace, VSG-100, with a 100 kg nominal capacity of the melting pot. Thermodynamic stability and volume fractions of phase components and precipitates were calculated in Thermocalc and confirmed with a dilatometric analysis. Upon the investigation of the primary and transformed austenite grain size, the predicted or calculated yield and impact strength, two grades were

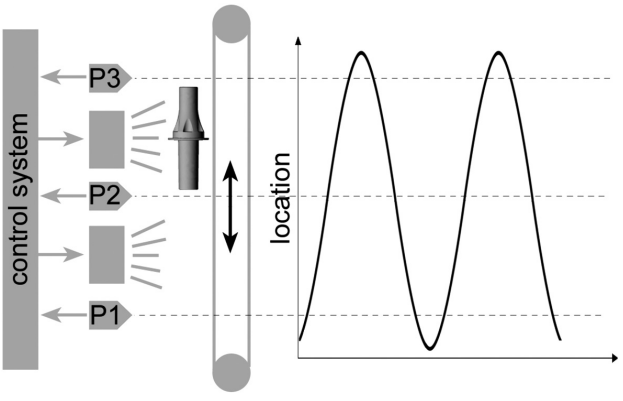

Figure 1: Laboratory simulation of the cooling line
Slika 1: Laboratorijski simulator linije ohlajanja

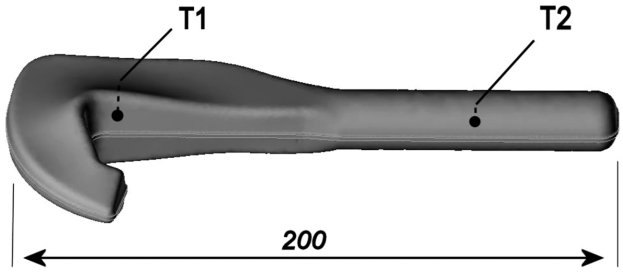

Figure 2: Geometry of the target application; T1, T2 – thermocouple locations
Slika 2: Geometrija preizkušanca; T1, T2 – lokacija termoelementov

Table 1: Chemical compositions of experimental heats of microalloyed steels used in the study
Tabela 1: Kemijska sestava eksperimentalnih talin mikrolegiranih jekel, uporabljenih v študiji

Steel	% C	% Mn	% Cr	% Si	% Mo	% Ti	% V	% Nb	% N	Ac_1,°C	Ac_3,°C
A	0.30	1.50	0.42	0.26	0	0.011	0.09	0.039	0.011	809	785
B	0.28	1.24	0.42	0.27	0.2	0.019	0.067	0.047	0.010	728	727

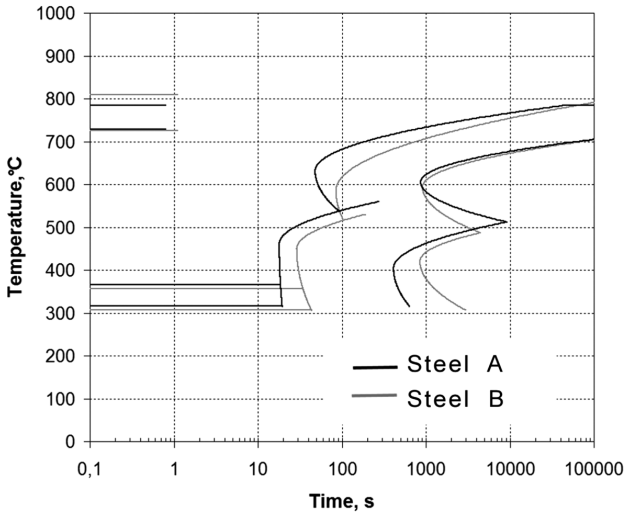

Figure 3: Continuous-cooling diagrams calculated with TTSteel code, modified with theoretical equations[9]
Slika 3: Diagram kontinuiranega ohlajanja, izračunan s TTSteel kodo in spremenjen s teoretičnimi enačbami[9]

selected (**Table 1**), indicating the smallest grain size and a potential combination of strength and ductility. Utilizing the deformed material from plastometric tests with formulas for characteristic times,[9] continuous-cooling-transformation diagrams (CCT) of non-recrystallized materials were made, as shown in **Figure 3**.

4 RESULTS AND EVALUATION

4.1 Analysis of the target forging technology

Forging-machine kinematics has an enormous impact on thermomechanical parameters for a hot-forged piece. As could be expected, hammer forging produces an increased amount of generated heat and temperature gradients, which influence the flow stress and metal displacement. Numerical modeling with FEM allowed for an estimate of the level, variance and gradients of the temperature and strain development during the forging. This information made it possible to evaluate the obtained results of direct cooling where, unlike for the traditionally heat-treated material, the as-forged steel inherits the aftermath of dynamic processes. Thus, to fit the laboratory-test results to the target application, we carried out an insightful analysis of the development of the thermomechanical indicators of the changes influencing the final microstructure and properties.

The results of the FEM analysis are summarized in **Table 2**.

Table 2: Evolution of thermo-mechanical conditions in the forged part (in locations shown in **Figure 2**)
Tabela 2: Razvoj termo-mehanskih pogojev v kovanem kosu (na mestih prikazanih na **Sliki 2**)

Operation		1	2	3	4	5
Effective strain	T1	0.62	0.62	0.62	0.84	0.88
	T2	0.62	1.25	2.51	2.75	2.81
Temp., °C	T1	1115	1107	1089	1105	1090
	T2	1115	1130	1136	1144	1140

4.2 Effect of the cooling rate

To assess the dependence of the structural components and the grain size on the cooling rate, the microstructure derived from a dilatometric investigation of normalized material was examined. Micrographs obtained for both alloys are shown in **Figures 4** and **5**.

4.3 Physical modeling of forging and cooling

The effect of the run-out table temperature on the kinetics of austenite restoration and precipitation of carbides and carbonitrides, and the resulting strengthening

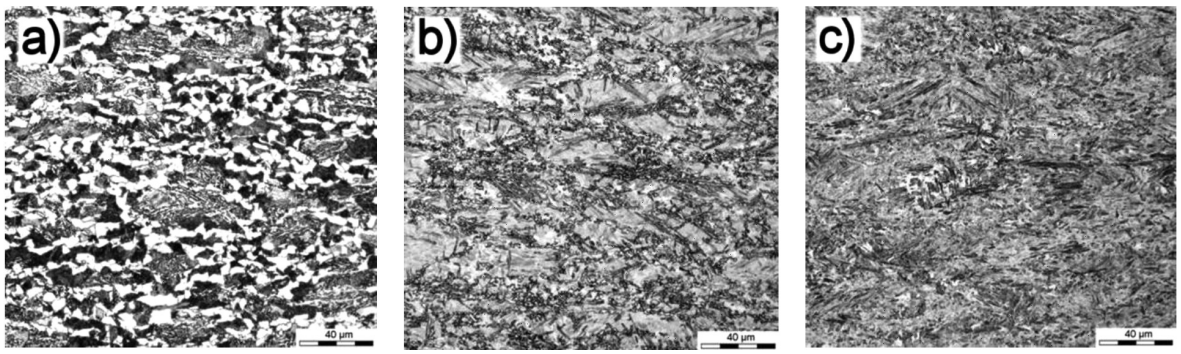

Figure 4: Microstructure of as-received (hot-rolled) alloy A after anisothermal cooling at rates: a) 1 °C/s, b) 10 °C/s, c) 50 °C/s
Slika 4: Mikrostruktura izhodne (vroče valjane) zlitine A, po anizotermnem ohlajanju s hitrostjo: a) 1 °C/s, b) 10 °C/s, c) 50 °C/s

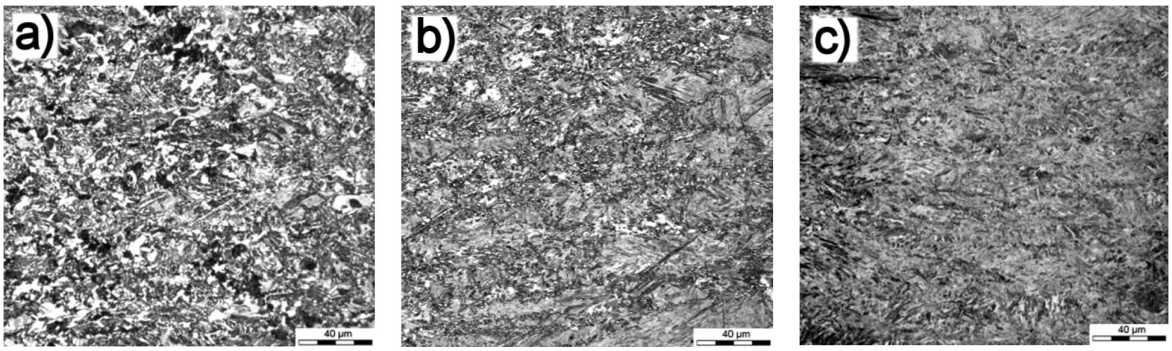

Figure 5: Microstructure of as-received (hot-rolled) alloy B after anisothermal cooling at rates: a) 1 °C/s, b) 10 °C/s, c) 50 °C/s
Slika 5: Mikrostruktura izhodne (vroče valjane) zlitine B, po anizotermnem ohlajanju s hitrostjo: a) 1 °C/s, b) 10 °C/s, c) 50 °C/s

efficiency was investigated by varying the forging temperature while employing the same cooling conditions after the deformation.

According to the plots of temperature measured during the experiments, the assumed temperatures changed during the deformation and therefore the forge end temperature was not exactly the same as expected. Due to a non-uniform distribution of strain in the bulk, the amount of generated deformation heat varied with the location (**Table 2**). However, the assumed temperatures of forging, (1100, 1000 and 900) °C, allowed an analysis of the material response in the representative ranges in relation to the temperatures of the dynamic-recrystallization stop and the solution of carbonitrides/carbides. The highest temperature, assumed for the total content of carbon and microalloying elements, was found in the solution, available for precipitation. The lowest forging temperature of 900 °C dropped to 880 °C due to the material transfer and die cooling; it was meant to provide the alloys with a reasonable amount of accumulated strain, based on the calculated recrystallization stop temperature. The forging at 1000 °C was to show the effect of the precipitates formed prior to forging on the evolution of dynamically recrystallized grains. As alloy B did not contain Mo, this test was conducted for alloy A only.

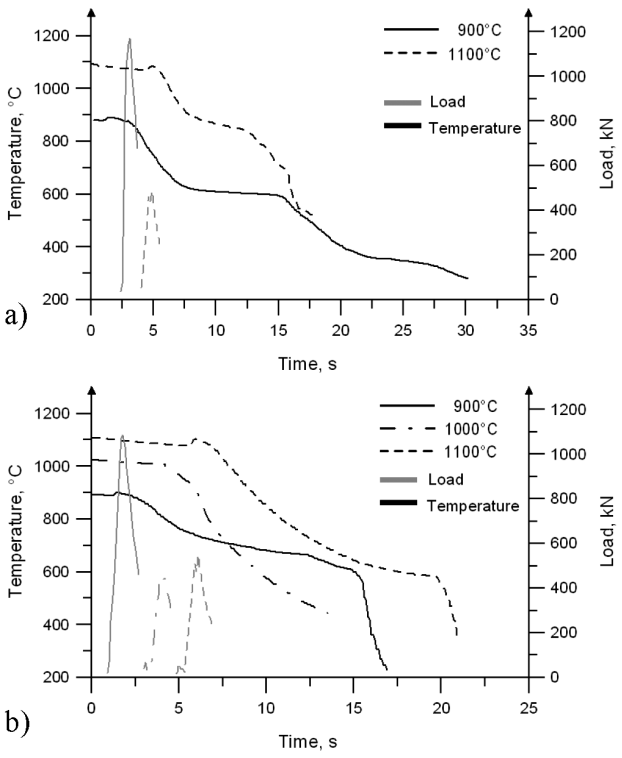

Figure 6: Experimental cooling-curve plots for: a) steel A, and b) steel B; load peaks (grey) indicate forge-end points
Slika 6: Diagrami eksperimentalnih krivulj ohlajanja: a) jeklo A in b) jeklo B; konice obremenitve (siva barva) kažejo konec kovanja

The obtained cooling curves are shown in **Figure 6** for steels A and B, respectively. For clarity, the plots were shifted and the moment of deformation was indicated by plotting the forging load (in grey). This was also an opportunity to indicate unexpected dependence of the load extreme on the temperature for steel B, which shows a higher value at 1000 °C than at 900 °C. The experiment conducted showed that the deformation temperature is high enough to avoid ferrite nucleation, which adversely affects the strength properties.[10,11] The load observed at 900 °C implies there is no occurrence of ferrite dynamic precipitation, while incomplete softening can be found with the aid of a metallographic analysis (**Figures 7** and **8**).

5 MICROSTRUCTURE AND MECHANICAL PROPERTIES

The microstructure obtained using accelerated cooling with mist is composed of martensite and bainite, depending on forging temperature portions of fine and narrow-spaced pearlite, differing in the fractions of the constituents. The cooling rate of 20 °C/s is sufficient to omit the high-temperature onset of a diffusion-driven transformation into recrystallized austenite. Industrial-like conditions of direct cooling (based on the assumption of quenching directly after deformation) caused an increased amount of ferrite, with a simultaneous increase in the fraction of martensite instead of bainite or Widmanstätten ferrite. As indicated in the physical simulation included in the study, 80° s^{-1} in a range of

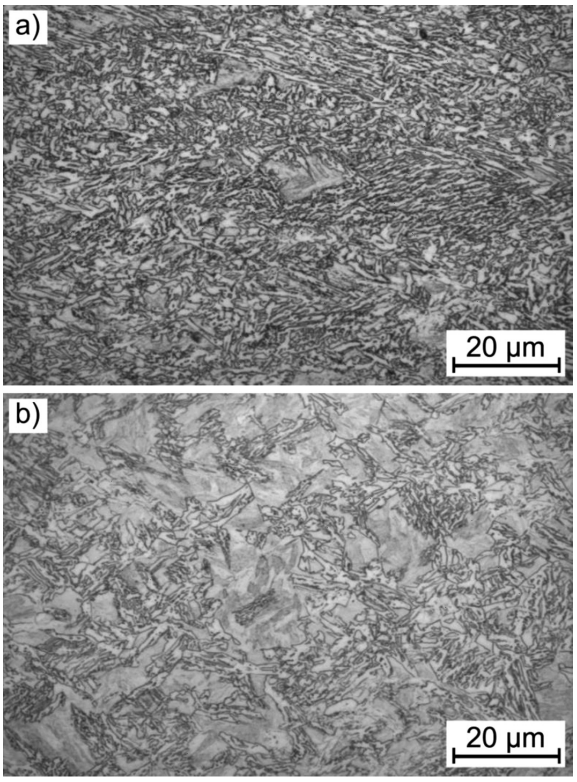

Figure 7: Microstructures of alloy A in as-forged direct-cooling conditions, after forging at: a) 1100 °C, b) 900 °C

Slika 7: Mikrostruktura zlitine A, ohlajene takoj po kovanju: a) 1100 °C, b) 900 °C

Table 3: Mechanical properties of the microalloyed steels after accelerated cooling

Tabela 3: Mehanske lastnosti mikrolegiranih jekel po pospešenem ohlajanju

Alloy	Forging temperature, °C	*YS*, MPa	*UTS*, MPa	Elongation at fracture, A_{10} %	Area reduction, %
Steel A	1100 °C	1104	1688	3.2	6
	900 °C	915	1486	5.8	20
Steel B	1100 °C	706	1208	9.4	44
	1000 °C	1043	1514	7.5	38
	900 °C	757	1012	11.0	59

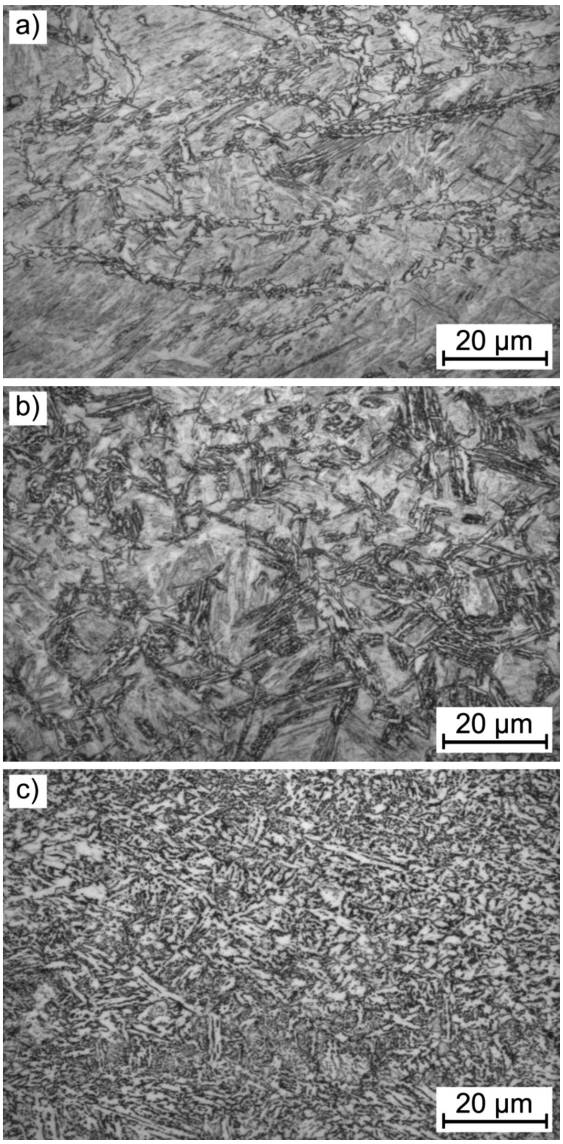

Figure 8: Microstructures of alloy B in as-forged direct-cooling conditions, after forging at: a) 900 °C, b) 1000 °C, c) 1100 °C

Slika 8: Mikrostruktura zlitine B, ohlajene takoj po kovanju na: a) 900 °C, b) 1000 °C, c) 1100 °C

800–500 °C suffices to produce a 50 % martensite transformation after the post-forging operations like trimming the flash and transfer on air. As shown in **Figure 7**, by forging at 900 °C, we obtained non-recrystallized microstructures with a high density of crystallographic defects, such as shearing bands and sub-cells with very fine grains at the grain boundaries, illustrating the increment of the total strength enhancement due to the reduction of the forging regime.

Based on comparable cooling conditions, the microstructure analysis indicated a strong effect of forging conditions on the grain size and morphology, which is reflected by mechanical properties. Steel A exhibits a higher strength, with *UTSs* of 1688 MPa after the forging at 1100 °C and 1486 MPa for 900 °C (**Table 3**). Steel B shows a better ductility associated with the Mo addition. Furthermore, directly cooled steel A showed a 5 % elongation while steel B indicted an 8 % elongation, which is a satisfactory result, taking into account that no tempering was carried out, while auto-tempering, enabling a ductility enhancement, could be utilized in industrial processes.

6 CONCLUSIONS

Deformation at a varied temperature, in connection with direct cooling, indicates a strong influence of hammer-forging conditions on the resultant mechanical properties. This gave us an opportunity for investigating

the possibilities of controlling microstructural properties and comparing them.

According to the prevailing studies of the TMP utilization in combination with microalloyed steels, detrimental hammer-forging conditions and the required final properties make big differences. Nevertheless, hammer-forging plants, as well as those employing high-speed-press forging, are quite numerous and the control and design of the TMP process in such conditions are still challenging.

Both the chemical compositions of the designed alloys and the technology based on the concept of direct cooling from the forge-end condition assure simplicity and attractiveness to the forging industry, offering reduced costs and making it possible for steelworks to keep the imposed limits of alloying elements. Moreover, the predefined cooling conditions are easily transferable to forge-plant conditions. The contents of the micro-alloying elements in alloys are kept within reasonable limits required from the standpoint of control of the grain-structure evolution due to the interactions of the precipitates with microstructural defects during forging and the subsequent cooling.[12]

The incremental character of forging, the thin end, optionally allows continuous-cooling deformation modeling. However, it may be noticed that the hook undergoes a double reduction: during the flattening and finishing of the impression. Hence, a simple compression of a 25 mm flat bar ensures appropriate geometrical and, more importantly, phenomenological similarity conditions. Thus, the forging tests reflected the industrial processes of both forging and cooling. Having passed the 800–500 °C range, the cooling rate was slowed down producing a type of the equalizing hold (**Figures 6** and **7**), reducing thermal stresses on the one hand and the time for the Nb carbide precipitation[13] on the other hand.

Precipitates greatly contribute to the hardening of an alloy; however, the efficiency of their strengthening depends on the volume fraction and size of the precipitates. Depending on the particle relation to the dislocation parameters, it can pile up and loop the dislocations or be sheared by it.[14] In the case of the analyzed alloys, both instances were witnessed. The produced carbides and carbonitrides TiC and Ti(C,N) are of the largest size among the occurring precipitates. They are reported to take on the form of cube-like shapes, reaching a micrometer in diameter, which enabled an observation with the immersion technique using an optical microscope. On the other hand, Nb carbides have smaller particle diameters. They are found to have a spherical shape and the size of dozens of nanometers. Their contribution to the total strength enhancement reaches 90 MPa[13,15], which causes high effectiveness in pinning grain boundaries during deformation and grain-restoration processes.

The volume of these precipitates allow for a significant microstructural controllability brought about by Nb(C,V), provided the whole Nb content dissolves at temperatures of 1170–1190 °C. The applied Nb content is supposed to retard recrystallization, which calls for a lower forging temperature.

The overall level of the strength properties results from the grain refinement, which contributes up to 250 MPa.[14] It is enhanced by the presence of N and Al, lowering the tendency for coagulation of the V(C,N) precipitates. In addition to reducing the amount of vanadium dissolved in the austenite[16] by decreasing the self-diffusion of iron, N reduces the grain-growth tendency[17], as long as it is below the content necessary for the VN formation.[18]

Besides the precipitates, the grain is refined due to the grain-structure restoration during the forging, which greatly influences the concentration of nucleation sites. Decreasing the forging temperature from 1180 °C to 1000 °C resulted in lowering the forge-end point from about 1210 °C to 1034 °C, producing a fine-grained structure, which formed a base for fine colonies of pearlite or bainite during the cooling. The produced microstructure exhibits a grain size decreasing with the lowering forging temperature. However, contrary to higher temperature trials, a microstructure abundant in crystallographic defects was obtained during the forging at about 900 °C, such as shearing bands and non-recrystallized sub-cells with particularly fine grains at the grain boundaries, which can be attributed to discontinuous dynamic recrystallization, resulting in a selective renovation of the grains, typical of a low-temperature deformation.[19,20] The presence of such grains confirms that the deformation was completed below the temperature, at which the recrystallization and/or the strain-induced precipitation inhibiting static recrystallization can occur. [21]

The mixture of fine recrystallized and strain-hardened grains produced a significant strengthening, resulting in an *UTS* of 1700 MPa, similar to the related studies.[22] On the other hand, a low plasticity, reaching at most 11 % of A_{10} elongation to fracture was obtained. However, in an industrial practice, higher plasticity indices should be expected as, in contrast to small laboratory samples, massive parts allow the auto-tempering effect to occur, enabling a ductility improvement. It must be noted that the flat specimens did not have a privileged grain-flow direction. On the contrary, the grain-flow orientation in the gauge area of the tensile specimens was perpendicular to the tension direction. In the considered part, the situation was different – the metal flow pattern produced an evident longitudinal grain flow, allowing the ductility enhancement.

Acknowledgements

Financial assistance of NCBiR within project PBS2/B5/29/2013 agreement 19.19.110.86730, is acknowledged.

7 REFERENCES

[1] W. Von Karl-Wilhelm, Werkstoffentwicklung für Schmiedeteile im Automobilbau, ATZ Automobiltechnische Zeitschrift, 100 (**1998**) 12, 918–927, doi:10.1007/BF03223434

[2] S. Engineer, B. Huchtemann, V. Shueler, A Review of the Development and Application of Microalloyed Medium-Carbon Steels, Proceedings of an International Symp. Fundamentals of Microalloying Forging Steels, Golden, Colorado 1986, 19–37

[3] A. A. Petrunenkov, K. Hulka, Niobium Technical Report, NbTR, 15 (**1990**), 1–22

[4] R. Lagneborg, O. Sandberg, W. Roberts, Fundamentals of Microalloying Forging Steels, Warrendale, 187 (**1986**), 39–51

[5] D. J. Naylor, Microalloyed Forging Steels, Materials Science Forum, 284–286 (**1998**), 83–94, doi:10.4028/www.scientific.net/MSF.284-286.83

[6] P. E. Reynolds, Alternatives to conventional heat treatment for engineering steel components, Heat Treatment of Metals, 3 (**1990**), 69–72

[7] C. I. Garcia, A. K. Lis, T. M. Maguda, A. J. DeArdo, A new microalloyed, multi-phase steel for high strength forging applications, Proc. of the International Conference on Processing, Microstructure and Properties of Microalloyed and Other Modern High Strength Low Alloy Steels, Pittsburgh 1991, 395–400

[8] X. X. Xu, B. Z. Bai, D. Y. Liu, Y. Yuan, Effect of Thermomechanical Treatment Temperature on Structure and Properties of CFB/M Ultra-High Strength Steel, J. Iron and Steel Res. Int., 17 (**2010**) 4, 66–72, doi:10.1016/S1006-706X(10)60088-X

[9] H. K. D. H. Bhadeshia, Driving force for martensitic transformation in steels, Met. Sci., 15 (**1981**) 4, 175–177, doi:10.1179/030634581790426714

[10] M. Mukherjee, U. Prahl, W. Bleck, Modelling of Microstructure and Flow Stress Evolution during Hot Forging, Steel Res. Int., 81 (**2010**), 1102–1116, doi:10.1002/srin.201000114

[11] P. Skubisz, Ł. Lisiecki, Warm-forging characteristics and microstructural response of medium carbon high-strength steels for high-duty components, Key Eng. Mat., 611–612 (**2014**), 167–172, doi:10.4028/www.scientific.net/KEM.611-612.167

[12] P. Skubisz, A. Żak, M. Burdek, Ł. Lisiecki, P. Micek, Design of controlled processing conditions for drop forgings made of microalloy steel grades for mining industry, Arch. Metall. Mat., 60 (**2015**) 1, 445–453, doi:10.1515/amm-2015-0073

[13] A. G. Kostryzhev, A. Al Sharami, C. Zhu et al., Effect of niobium clustering and precipitation on strength of an NbTi-microalloyed ferritic steel, Mat. Sci. and Eng. A, 607 (**2014**), 226–235, doi:10.1016/j.msea.2014.03.140

[14] T. Gladman, Precipitation hardening in metals, Mat. Sci. Tech., 15 (**1999**) 1, 30–36, doi:10.1179/026708399773002782

[15] R. D. K. Misra, H. Nathani, J. E. Hartmann, F. Siciliano, Microstructural evolution in a new 770MPa hot rolled Nb–Ti microalloyed steel, Mat. Sci. Eng. A, 394 (**2005**), 339–352, doi:10.1016/j.msea.2004.11.041

[16] E. Głowacz, H. Adrian, W. Osuch, The nitrogen content effect on carbonitride coagulation in 40Cr8 steel with micro-additions V and V+Al, Arch. Met. Mater., 58 (**2013**) 2, 607–611, doi:10.2478/amm-2013-0045

[17] H. Adrian, E. Głowacz, The effect of nitrogen and microalloying elements (V and V+Al) on austenite grain growth of 40Cr8 steel, Arch. Met. Mater., 55 (**2010**) 1, 107–116

[18] J. Adamczyk, E. Kalinowska-Ozgowicz, W. Ozgowicz, R. Wusatowski, Interaction of carbonitrides V(C,N) undissolved in austenite on the structure and mechanical properties of microalloyed V-N steels, J. Mat. Proc. Techn., 53 (**1995**) 1–2, 23–32, doi:10.1016/0924-0136(95)01958-H

[19] P. R. Spena, D. Firrao, Thermomechanical warm forging of Ti–V, Ti–Nb, and Ti–B microalloyed medium carbon steel, Mat. Sci. Eng. A, 560 (**2013**), 208–215, doi:10.1016/j.msea.2012.09.058

[20] G. Gao, Ch. Feng, B. Bai, Effects of Nb on the Microstructure and Mechanical Properties of Water-Quenched FGBA/BG Steels, J. Mat. Eng. Perf., 21 (**2012**) 3, 345–352, doi:10.1007/s11665-011-9903-6

[21] J. Kliber, R. Fabik, I. Vitez, K. Drozd, Hot forming recrystallization kinetics in steel, Metalurgija, 49 (**2010**) 1, 67–71

[22] X. Kong, L. Lan, Optimization of mechanical properties of low carbon bainitic steel using TMCP and accelerated cooling, Proc. Eng., 81 (**2014**), 114–119, doi:10.1016/j.proeng.2014.09.136

UDK 621.663:67.017:621.791.05:669.3
Original scientific article/Izvirni znanstveni članek

ISSN 1580-2949
MTAEC9, 50(5)791(2016)

INFLUENCE OF THE TOOL ROTATIONAL SPEED ON THE MICROSTRUCTURE AND JOINT STRENGTH OF FRICTION-STIR SPOT-WELDED PURE COPPER

VPLIV HITROSTI VRTENJA ORODJA NA MIKROSTRUKTURO IN TRDNOST TORNO VRTILNO TOČKASTO ZVARJENEGA SPOJA ČISTEGA BAKRA

Isaac Dinaharan, Esther T. Akinlabi

University of Johannesburg, Department of Mechanical Engineering Science, Auckland Park, Kingsway Campus, Johannesburg 2006, South Africa
dinaweld2009@gmail.com

Prejem rokopisa – received: 2015-09-21; sprejem za objavo – accepted for publication: 2015-10-05

doi:10.17222/mit.2015.301

Copper is very difficult to be spot welded with conventional fusion-welding techniques due to a high thermal diffusivity. Friction-stir spot welding (FSSW) is a novel solid-state welding process, suitable and effective for spot welding copper. Commercially pure copper sheets of 3 mm thickness were spot welded using an industrial friction-stir welding machine. The spot welds were made by varying the tool rotational speed at three levels. The spot welds were characterized using light microscopy. The shear-fracture load was evaluated using a computerized tensile-testing machine. The results revealed that the tool rotational speed remarkably influenced the microstructure, the shear-fracture load and the mode of fracture.

Keywords: copper, friction-stir spot welding, microstructure, shear load

Zaradi velike toplotne prevodnosti se baker zelo težko točkasto vari pri običajnih postopkih varjenja z zlivanjem. Torno vrtilno točkasto varjenje (FSSW) je nov način varjenja v trdnem stanju, ki je primerno in primerljivo s torno vrtilnim točkastim varjenjem bakra. Bakrene pločevine, debeline 3 mm, iz čistega komercialno dostopnega bakra, so bile točkasto zvarjene s torno vrtilnim točkastim varjenjem, z uporabo industrijske naprave za tovrstno varjenje. Točkasti zvari so bili izdelani pri treh hitrostih vrtenja orodja. Karakterizirani so bili z uporabo svetlobne mikroskopije. Strižna trdnost je bila ocenjena z uporabo računalniško vodenega nateznega stroja. Rezultati so pokazali, da hitrost vrtenja orodja močno vpliva na mikrostrukturo, strižno trdnost in način preloma.

Ključne besede: baker, torno vrtilno točkasto varjenje, mikrostruktura, strižna obremenitev

1 INTRODUCTION

Pure copper is extensively used in the optical and electronic industries owing to its excellent properties such as good ductility, high electrical, thermal conductivity and good corrosion resistance. The welding of copper is often encountered in the electrical, nuclear and automobile industries.[1,2] Spot welding of pure copper is generally hard to do with conventional fusion welding because of the high thermal diffusivity, which is about 10 to 100 times higher than in many steels and nickel alloys. The heat input required is much higher than in almost any other material. Further, pure copper is susceptible to solidification cracking and blowhole formation.[3,4] Friction-stir spot welding (FSSW) is a novel solid-state welding technique, promising for spot welding copper without the problems associated with fusion-welding techniques.[5]

FSSW is a derivative process based on friction-stir welding (FSW) which was developed at The Welding Institute in 1991. There are several differences between FSSW and FSW. One distinct difference is that there is no translation of tool during FSSW. FSW is commonly employed to join metallic plates in a butt configuration along the line of contact. On the other hand, FSSW is performed on thinner plates kept in a lap configuration. A rotating, non-consumable, cylindrical-shouldered tool with a pin is plunged, at a predetermined feed rate, into the overlapping plates to a depth slightly shorter than the total thickness of both plates. Frictional heat is generated between the plate material and the rotating tool, which plasticizes the material. The rotating action of the pin induces the material flow in both the circumferential and axial directions. The axial force applied along the tool axis forges the plasticized material and forms an annular, solid-state bond around the pin. At this moment, the rotating tool is retracted, leaving the exit hole behind. The major process parameters, which influence the joint strength, are the tool geometry, the tool rotational speed, the tool penetration depth and the dwell time. FSSW exhibits key advantages such as excellent mechanical properties, a low distortion, ease of handling, low cost, and clean working environment.[6–8]

The FSSW technique has been successfully used to spot weld aluminum[9], magnesium[10], steel[11] and plastics.[12] Both similar and dissimilar spot welds were reported in

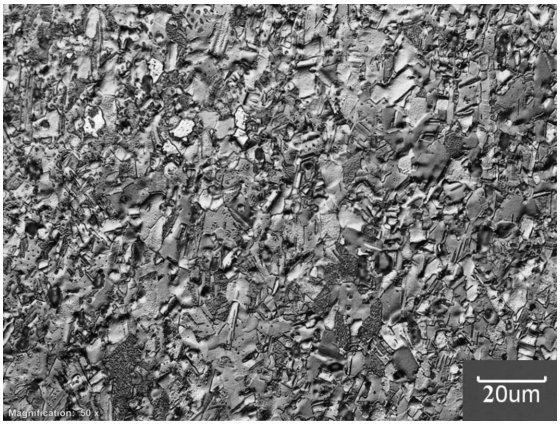

Figure 1: Light micrograph of pure copper
Slika 1: Svetlobni posnetek mikrostrukture čistega bakra

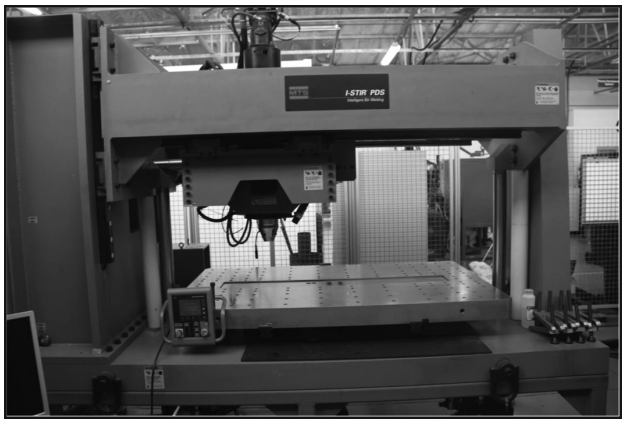

Figure 2: I-STIR friction-stir welding machine
Slika 2: I-STIR naprava za torno vrtilno varjenje

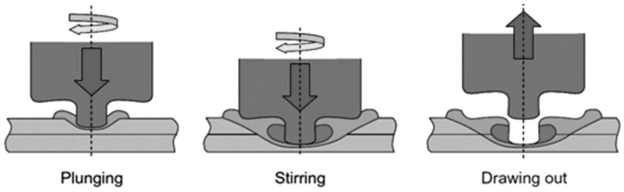

Figure 3: Schematic illustration of the friction-stir spot-welding process
Slika 3: Shematski prikaz postopka torno vrtilnega točkastega varjenja

the literature[13,14]. FSSW of copper and its alloys is least explored. Z. Barlas[15] spot welded pure copper and brass sheets using FSSW and analyzed the influences of the tool rotational speed, dwell period and material location on the microstructure and the tensile shear-fracture load (TSFL). He found that the welding parameters had an important influence on the TSFL and the failure mode. The TSFL increased with an increase in the tool rotational speed and dwell time. R. Heideman[16] spot-welded AA6061 and pure-copper sheets and studied the effects of the tool pin length, the shoulder plunge depth, the welding time and the tool rotational speed on the TSFL. Literature on FSSW of pure copper is scantily. Therefore, the present work focuses on spot welding copper sheets of 3 mm using FSSW and analyzes the influence of the tool rotational speed on the TSFL.

2 MATERIALS AND METHODS

Commercially available pure copper sheets of 3 mm were used in this study. The optical photomicrograph of the as-received copper sheet is shown in **Figure 1**. Lap joint configuration was used to fabricate the spot welds where the rolling direction of the material was kept parallel to the loading directions and the joint was initially obtained by securing the sheets in position using mechanical clamps. A non-consumable tool made of high-carbon steel was used to fabricate the joints. The tool had a shoulder of 18 mm and a conical profile of a diameter varying from 5 mm to 3 mm along the length of pin. The pin length was 5.7 mm. An industrial-purpose FSW machine (I-STIR), depicted in **Figure 2**, was used for FSSW. The FSSW procedure and the welding cycle are depicted in **Figure 3**. The tool rotational speed was varied at three levels of 1200 min^{-1}, 1600 min^{-1} and 2000 min^{-1}. Other parameters were kept constant. The dwell period and axial force were 3 s and 10 kN, respectively. Spot welds were made on two sheets clamped in the lap configuration. Sufficient cooling was allowed between successive spot welds. The spot-welded copper sheet is shown in **Figure 4**. Six spot welds were made for each set of the process parameters. Specimens were machined from the welded sheets and polished semi-automatically in a polishing machine (Struers LaboPol 25). The mirror-polished specimens were etched with a color etchant containing 20 g of chromic acid, 2 g of sodium

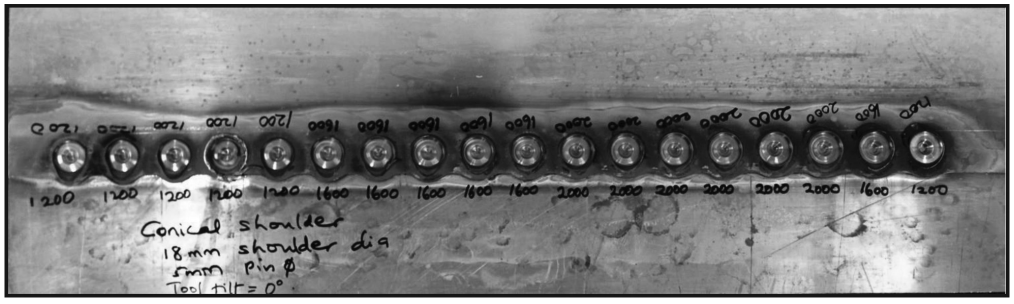

Figure 4: Friction-stir spot-welded sheet
Slika 4: Torno vrtilno točkasto zvarjena pločevina

sulfate and 1.7 mL of HCl (35 %) in 100 mL distilled water. The macrostructure was recorded using a stereo microscope (OLYMPUS SZX16). The microstructure was observed using a metallurgical microscope (OLYMPUS BX51M). The TSFL was evaluated using a computerized tensile tester (INSTRON 1195) at a crosshead speed of 2 mm/min.

3 RESULTS AND DISCUSSION

Macrographs of the copper friction-stir spot-welded as a function of the tool rotational speed are presented in **Figure 5**. It is possible to spot weld successfully using the chosen parameters. The weld zones are almost symmetrical with respect to the axis of the keyhole. The tool rotation generates frictional heat, which plasticizes the copper. The force applied along the axis of the tool promotes the vertical motion of the plasticized copper. The axial force further consolidates the plasticized copper and a spot joint is formed. The joint width is clearly visible on all the joints. Considerable areas of both the top and bottom sheets are bonded together. The hook does not extend to the keyhole area, which indicates bonding between the sheets. The bond width was measured and was found to be (7.5, 8.5 and 10) mm, respectively, at the selected tool rotational speeds. An increase in the tool speed improves the bond width because the frictional-heat generation depends upon the tool rotational speed.[17] The higher the tool rotational speed, the higher is the heat generation. Hence, more copper is plasticized and the bond width increases.

Regions with different microstructures were observed on these macrographs. They are the stir zone (SZ), the thermomechanically affected zone (TMAZ), the heat-affected zone (HAZ) and the base copper. These regions are presented in the micrographs in **Figure 6** as a function of the tool rotational speed. The stir zone is adjacent to the keyhole area and displays very fine grains. FSSW was derived from FSW. The plasticized material in FSW undergoes dynamic recrystallization, which results in the formation of fine grains. The width of the stir zone reduces as the tool rotational speed is increased due to a higher heat input. The TMAZ region presents slightly elongated grains with an array of oxide particles. The shearing of the plasticized material from the advancing side to the retreading side causes the grains in this region to elongate. The width of the TMAZ is found to reduce with an increase in the tool rotational speed. The third

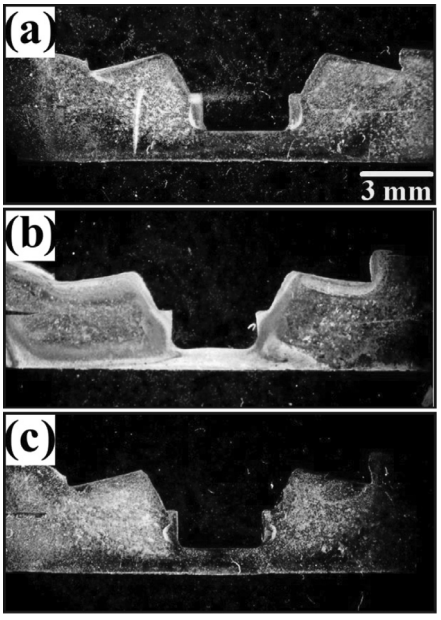

Figure 5: Macrographs of friction-stir spot-welded copper at: a) 1200 min^{-1}, b) 1600 min^{-1} and c) 2000 min^{-1}

Slika 5: Makro posnetek torno vrtilno točkasto zvarjenega bakra pri: a) 1200 min^{-1}, b) 1600 min^{-1} in c) 2000 min^{-1}

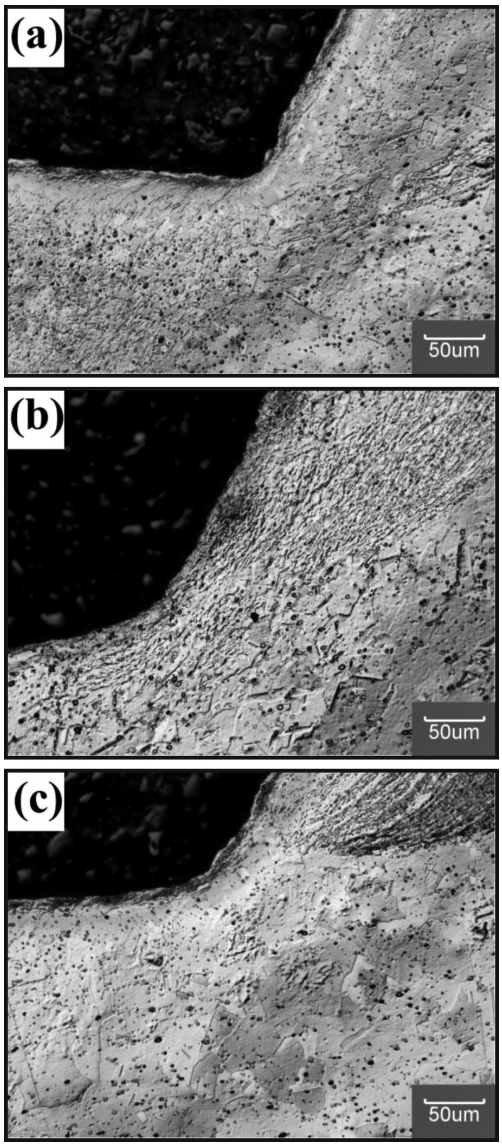

Figure 6: Light micrographs of the transition zone of friction-stir spot-welded copper at: a) 1200 min^{-1}, b) 1600 min^{-1} and c) 2000 min^{-1}

Slika 6: Svetlobni posnetki mikrostrukture prehodne cone torno vrtilno točkasto zvarjenega bakra pri: a) 1200 min^{-1}, b) 1600 min^{-1} in c) 2000 min^{-1}

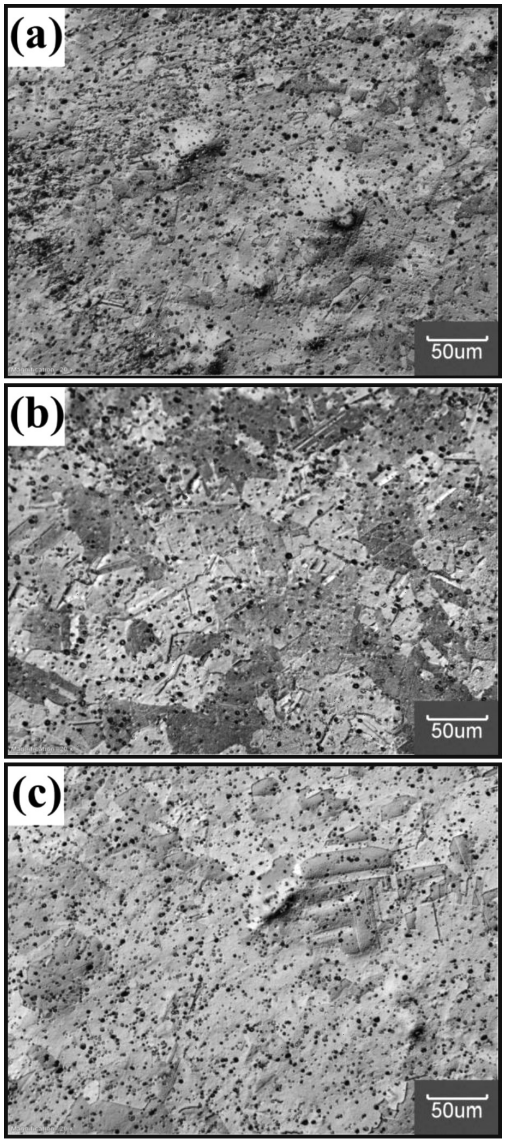

Figure 7: Light micrographs of the heat-affected zone of friction-stir spot-welded copper at: a) 1200 min^{-1}, b) 1600 min^{-1} and c) 2000 min^{-1}

Slika 7: Svetlobni posnetki mikrostrukture toplotno vplivane cone torno vrtilno točkasto zvarjenega bakra pri: a) 1200 min^{-1}, b) 1600 min^{-1} in c) 2000 min^{-1}

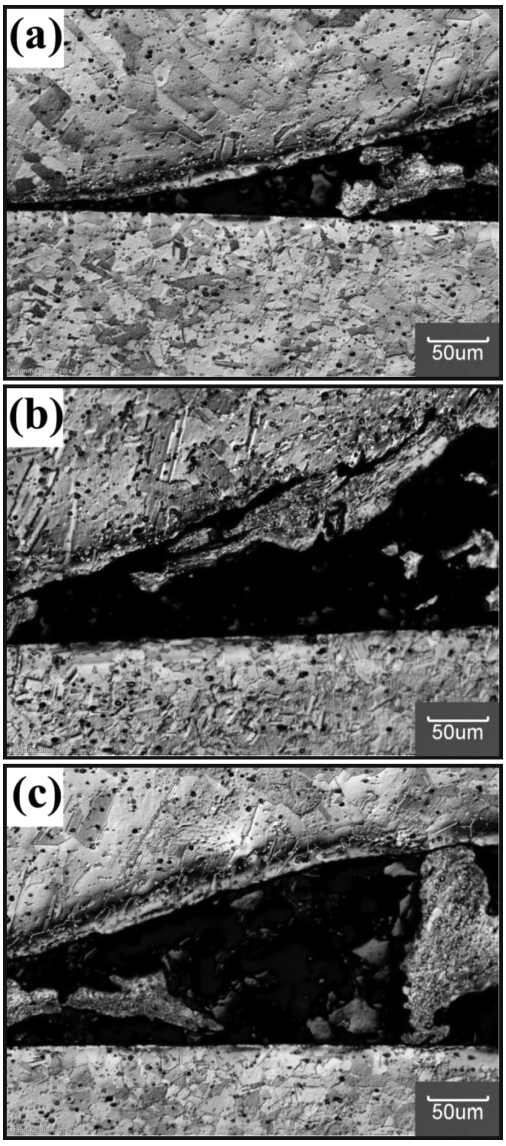

Figure 8: Light micrographs of the unbonded zone of friction-stir spot-welded copper at: a) 1200 min^{-1}, b) 1600 min^{-1} and c) 2000 min^{-1}

Slika 8: Svetlobni posnetki nezvarjenega področja torno vrtilno točkastega zvara bakra pri: a) 1200 min^{-1}, b) 1600 min^{-1} in c) 2000 min^{-1}

region, the HAZ, contains coarse grains. The coarseness of the grains increases with an increase in the tool rotational speed as presented in **Figure 7**.

A higher frictional heat causes the grains to become coarse. The grain size in the HAZ region is higher compared to the grain size of the as-received pure copper in **Figure 1**. This region is clearly influenced by the frictional heat generated during FSSW, leading to the grain growth. The stir zone is very thin at the higher tool rotational speed of 2000 min^{-1}. The higher heat causes the recrystallized grains to grow further and diminishes the width of the stir zone. The microstructure of the unbonded zone is presented in **Figure 8**. The grains of the upper and lower sheets are not uniform. The grains in the upper sheet are coarser than those in the lower sheet. This can be attributed to the proximity of each sheet to the tool shoulder. The upper sheet receives more heat input compared to the lower sheet, causing the grains to become coarser.

The influence of the tool rotational speed on the TSFL is depicted in **Figure 9**. It is evident from the figure that the increase in the tool rotational speed increased the TSFL. Although the increase in the tool rotational speed caused grain growth in different regions across the joint, the TSL improved upon the increased tool rotational speed because the TSFL depends upon the joint width and the hook position from the stir-zone area. A hook is formed in a FSSW joint as the material from the bottom sheet flows upwards during the process. The distance of the hook from the stir-zone area determines the load-carrying capacity of the joint. The hook is not

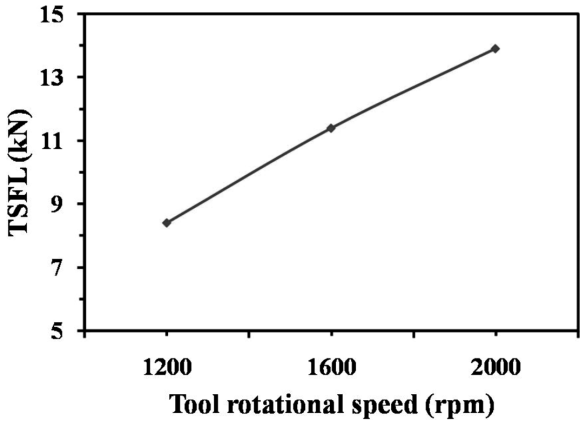

Figure 9: Effect of tool rotational speed on tensile shear load of friction-stir spot-welded copper

Slika 9: Vpliv hitrosti vrtenja orodja na natezno strižno obremenjenega torno vrtilno zvarjenega bakra

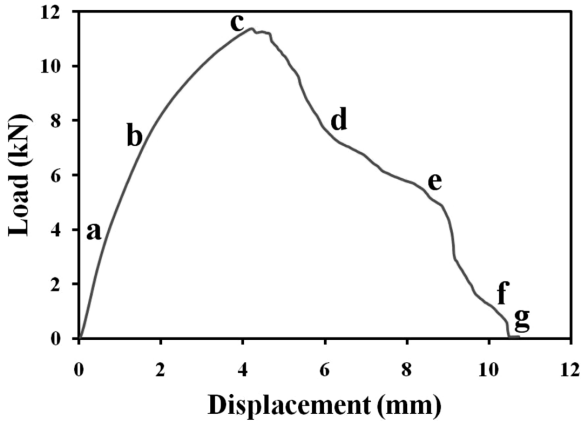

Figure 11: Load-versus-displacement graph for a tensile shear-tested specimen at the tool rotational speed of 1600 min^{-1}

Slika 11: Odvisnost obremenitve in raztezka pri nateznem strižnem preizkusu vzorcev pri hitrosti vrtenja orodja 1600 min^{-1}

clear in the macrograph in **Figure 1** due to the annealing effect of copper during FSSW.

The other factor is the bond width. The bond width increased with an increase in the tool rotational speed. This provided more tangential area to resist the external load. Hence, the TSFL increased as the tool rotational speed was increased. The photographs of failed specimens are shown in **Figure 10**. The failed specimens demonstrate different modes of failure. The nugget pull-out failure is observed at the tool rotational speeds of 1200 min^{-1} and 1600 min^{-1}. It can be inferred from the

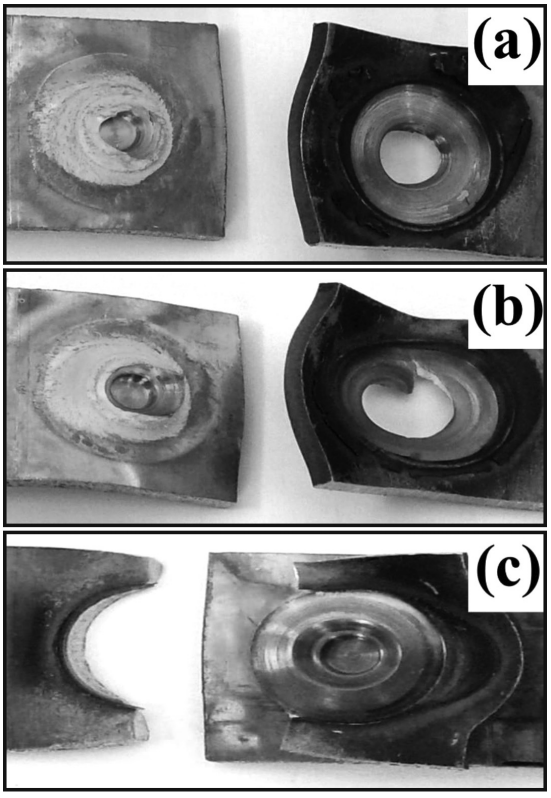

Figure 10: Images of failed sheets at tool rotational speeds of: a) 1200 min^{-1}, b) 1600 min^{-1} and c) 2000 min^{-1}

Slika 10: Posnetki porušenih pločevin pri hitrosti vrtenja orodja: a) 1200 min^{-1}, b) 1600 min^{-1} in c) 2000 min^{-1}

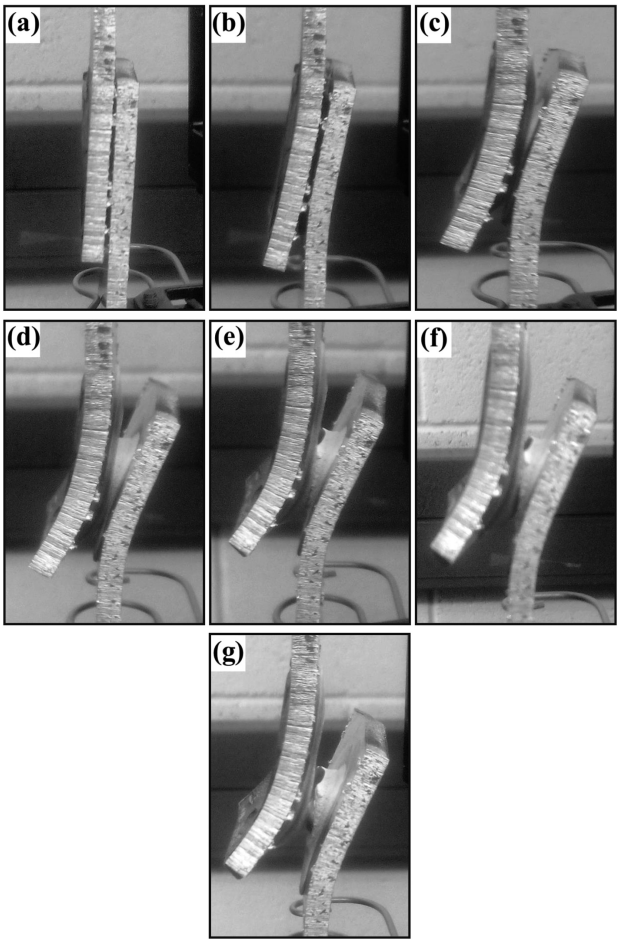

Figure 12: Images of tensile shear specimens during loading as marked in **Figure 11**

Slika 12: Posnetki nateznih strižnih vzorcev med obremenjevanjem, kot je prikazano na **Sliki 11**

photographs (**Figures 10a** and **10b**) that the nugget pull-out originated from the bottom of the keyhole area. The diameter of the hole in the upper failed sheet is higher at 1500 min^{-1} than 1200 min^{-1}. This is due to an increase in bond width, which provided a wider metallurgical bonding. The mode of failure at the tool rotational speed of 2000 min^{-1} is tearing. The tearing started circumferentially around the unbonded region and could not pull the nugget out because the higher bond width at 2000 min^{-1} caused the sheet to tear like a tensile specimen.

The load-versus-displacement curve for the tensile shear-tested specimen at the tool rotational speed of 1600 min^{-1} is presented in **Figure 11**. The load increases with a constant slope until point 'c' is reached. Corresponding photographs in **Figure 12** show details of the points marked in **Figure 11**. As the load is increased to point 'b', the specimen bends. The axis of the normal load does not coincide with the centre of the tested specimen, which creates a small moment causing the bending. The specimen starts to yield, i.e., the nugget pull-out commences at point 'c'. The load does not drop sharply to zero, unlike in the cases of tensile failures, because the nugget pull-out is not instant. The nugget pulls out gradually as the separation increases until point 'g' is reached. The load drops to zero, which indicates a complete separation of both sheets.

4 CONCLUSIONS

Commercially pure copper sheets were successfully spot welded using the novel FSSW technique. The influence of the key processing parameter, the tool rotational speed, on the microstructure and TSFL was analyzed. The increase in the tool rotational speed increased the bond width and coarsened the grains in the stir zone and HAZ. The TSFL improved as the tool rotation increased. The nugget pull-out failure took place at 1200 min^{-1} and 1600 min^{-1} and the tear-out failure took place at 2000 min^{-1}.

5 REFERENCES

[1] K. Surekha, A. Els-Botes, Development of high strength, high conductivity copper by friction stir processing, Materials and Design, 32 (**2011**), 911–916, doi:10.1016/j.matdes.2010.08.028

[2] P. Xue, B. L. Xiao, Q. Zhang, Z. Y. Ma, Achieving friction stir welded pure copper joints with nearly equal strength to the parent metal via additional rapid cooling, Scripta Materialia, 64 (**2011**), 1051–1054, doi:10.1016/j.scriptamat.2011.02.019

[3] R. M. Leal, N. Sakharova, P. Vilaca, D. M. Rodrigues, A. Loureiro, Effect of shoulder cavity and welding parameters on friction stir welding of thin copper sheets, Science and Technology of Welding and Joining, 16 (**2011**), 146–152, doi:10.1179/1362171810Y.0000000005

[4] W. B. Lee, S. B. Jung, The joint properties of copper by friction stir welding, Materials Letters, 58 (**2004**), 1041–1046, doi:10.1016/j.matlet.2003.08.014

[5] M. I. Khan, M. L. Kuntz, P. Su, A. Gerlich, T. North, Y. Zhou, Resistance and friction stir spot welding of DP600: a comparative study, Science and Technology of Welding and Joining, 12 (**2007**), 175–182, doi:10.1179/174329307X159801

[6] J. Jeon, S. Mironov, Y. S. Sato, H. Kokawa, S. H. C. Park, S. Hirano, Friction stir spot welding of single-crystal austenitic stainless steel, Acta Materialia, 59 (**2011**), 7439–7449, doi:10.1016/j.actamat.2011.09.013

[7] Y. F. Sun, H. Fujii, N. Takaki, Y. Okitsu, Microstructure and mechanical properties of mild steel joints prepared by a flat friction stir spot welding technique, Materials and Design, 37 (**2012**), 384–392, doi:10.1016/j.matdes.2012.01.027

[8] S. Bozzi, A. L. H. Etter, T. Baudin, B. Criqui, J. G. Kerbiguet, Intermetallic compounds in Al 6016/IF-steel friction stir spot welds, Materials Science and Engineering A, 527 (**2010**), 4505–4509, doi:10.1016/j.msea.2010.03.097

[9] G. Buffa, L. Fratini, M. Piacentini, Journal of Materials Processing Technology, 208 (**2008**), 309–317, doi:10.1016/j.jmatprotec.2008.01.001

[10] Y. H. Yina, N. Sun, T. H. North, S. S. Hu, On the influence of tool path in friction stir spot welding of aluminum alloys, Journal of Materials Processing Technology, 210 (**2010**), 2062–2070, doi:10.1016/j.jmatprotec.2010.07.029

[11] C. C. P. Mazzaferro, T. S. Rosendo, M. A. D. Tiera, J. A. E. Mazzaferro, J. F. Dos Santos, T. R. Strohaecker, Microstructural and Mechanical Observations of Galvanized TRIP Steel after Friction Stir Spot Welding, Materials and Manufacturing Processes, 30 (**2015**), 1–14, doi:10.1080/10426914.2015.1004699

[12] P. H. F. Oliveira, S. T. A. Filho, J. F. dos Santos, E. Hage, Preliminary study on the feasibility of friction spot welding in PMMA, Materials Letters, 64 (**2010**), 2098–2101, doi:10.1016/j.matlet.2010.06.050

[13] M. Yamamoto, A. Gerlich, T. H. North, K. Shinozaki, Science and Technology of Welding and Joining, 13 (**2008**), 583–592, doi:10.1179/174329308X349520

[14] V. X. Tran, J. Pan, T. Pan, Fatigue behavior of spot friction welds in lap-shear and cross-tension specimens of dissimilar aluminum sheets, International Journal of Fatigue, 32 (**2010**), 1022–1041, doi:10.1016/j.ijfatigue.2009.11.009

[15] Z. Barlas, Effect of friction stir spot weld parameters on Cu/CuZn30 bimetal joints, International Journal of Advanced Manufacturing Technology, 80 (**2015**), 161–170, doi:10.1007/s00170-015-6998-1

[16] R. Heideman, C. Johnson, S. Kou, Metallurgical analysis of Al/Cu friction stir spot welding, Science and Technology of Welding and Joining, 15 (**2010**), 597–604, doi:10.1179/136217110X12785889549985

[17] R. S. Mishra, Z. Y. Ma, Friction stir welding and processing, Materials Science and Engineering R, 50 (**2005**), 1–78, doi:10.1016/j.mser.2005.07.001

UDK 621.317.33:616.833.58:599.323.452:543.42
Original scientific article/Izvirni znanstveni članek

ISSN 1580-2949
MTAEC9, 50(5)797(2016)

MEASUREMENT OF BIO-IMPEDANCE ON AN ISOLATED RAT SCIATIC NERVE OBTAINED WITH SPECIFIC CURRENT STIMULATING PULSES

MERITEV BIOIMPEDANCE NA IZOLIRANEM ŽIVCU ISCHIADICUS PRI PODGANI, VZBUJENEM S POSEBNIMI TOKOVNIMI STIMULACIJSKIMI IMPULZI

Janez Rozman[1,3], Monika C. Žužek[2], Robert Frangež[2], Samo Ribarič[3]

[1]Center for Implantable Technology and Sensors, ITIS d. o. o., Lepi pot 11, 1000 Ljubljana, Slovenia
[2]Institute of Physiology, Pharmacology and Toxicology, Veterinary Faculty, University of Ljubljana, Gerbičeva 60, 1000 Ljubljana, Slovenia
[3]Institute of Pathophysiology, University of Ljubljana, ZaMedical Faculty, loška 4, 1000 Ljubljana, Slovenia
samo.ribaric@mf.uni-lj.si

Prejem rokopisa – received: 2015-09-30; sprejem za objavo – accepted for publication: 2015-10-26

doi:10.17222/mit.2015.307

In this study we designed and tested a four-probe, bio-impedance measurement set-up for peripheral nerves, based on the Red Pitaya open-source measurement and control tool. The set-up was tested on an isolated rat sciatic nerve (RSN) while it was stimulated with specific current stimulating pulses. The measurements tested the hypothesis that the specific waveform of a stimulating pulse elicits current differences at the double layer (DL) interface between the platinum (Pt) stimulating electrode and the nerve tissue. Impedance spectroscopy was used to electrically characterize the interface between the Pt electrode and the nerve tissue and measure the interface electrical impedance (*Z*). An analysis of the frequency response and the impedance, with specific current stimulating pulses, characterised the structure and the composition-related electrical properties of the RSN. An analysis of the voltage responses (VRs), measured at the same time, showed that the maximum negative polarization across the electrode-electrolyte interface (E_{mc}) and the maximum positive polarization across the electrode-electrolyte interface (E_{ma}) did not exceed the safety limits for water electrolysis. We conclude that the voltage and current changes, elicited at the DL of the interface between the Pt stimulating electrode and the nerve tissue, do not lead to tissue damage. Based on the obtained electrophysiological results we conclude that the developed stimulating electrodes and the stimulus pattern could act as a useful tool for developing nerve-stimulating electrodes.

Keywords: electrical impedance, electrical impedance spectroscopy, bio-impedance, voltage response, current source, platinum, rat sciatic nerve, electrode-nerve tissue interface

Izdelali in preizkusili smo napravo za štiri-točkovno merjenje električne impedance (*Z*) perifernih živcev, katere osnova je odprtokodna merilna in kontrolna konzola (Red Pitaya). Naprava je bila preizkušana na izoliranem živcu ischiadicus pri podgani (RSN) tako, da smo živec lahko dražili z izbranimi tokovnimi stimulacijskimi impulzi. Preverili smo hipotezo, da izbrani stimulacijski impulzi izzovejo razlike na dvojni plasti (DL) prehoda med platinovo (Pt) stimulacijsko elektrodo in živčnim tkivom. Z metodo impedančne spektroskopije smo izmerili *Z* na prehodu med Pt elektrodo in živčnim tkivom. Analiza frekvenčnega odgovora RSN, medtem ko je bil stimuliran s posebnimi tokovnimi stimulacijskimi impulzi, je podala od sestave in zgradbe odvisne električne lastnosti živca. Nadalje je analiza sočasno merjenega napetostnega odgovora (VR) pokazala, da nobena od obeh, tako največja negativna polarizacija E_{mc} kot tudi največja pozitivna polarizacija E_{ma}, na prehodu med elektrodo in elektrolitom, ni presegla varne meje pri kateri lahko pride do elektrolize vode. Zaključujemo, da napetostne in tokovne razlike, ki so nastale na DL prehodu med Pt stimulacijsko elektrodo in živčnim tkivom, nimajo škodljivega učinka na živčno tkivo. Končni sklep raziskave je, da je mogoče pridobljene elektrofiziološke rezultate koristno uporabiti pri nadaljnem načrtovanju in razvoju stimulacijskih elektrod.

Ključne besede: električna impedanca, električna impedančna spektroskopija, bioimpedanca, napetostni odgovor, tokovni vir, platina, kolčni živec podgane, prehod med elektrodo in živčnim tkivom

1 INTRODUCTION

Tissue-characterizing techniques based on electrical impedance (*Z*) are being used to study the *Z* variations of biological tissues over a range of frequencies. Some of these analysing techniques provide *Z* values of the tissue sample as a lumped estimation at a suitable frequency range and the information on several complex bioelectrical phenomena occurring in cells and tissues under an alternating (AC) electric current signal.[1,2] In this regard, a measurement of the complex *Z* in biological systems is one of the developing technologies for monitoring and determining the pathological and physiological status of biological tissues.[3] Namely, with AC electrical stimulation, biological tissues produce a complex *Z* that depends on the tissue composition, structures, health status, and applied stimulus frequency.[4]

In biological tissues, plasma membranes of the cells are composed of electrically non-conducting lipid bilayers and an ion-conducting proteins channels.[5,6] This structure provides a capacitance to the applied AC signal and contributes to the overall response of the biological tissues by producing a complex *Z*, which is a function of the tissue composition as well as the frequency of the applied AC signal. *Z* is a measurement of the overall

ability of a medium to conduct electrical current, defined as the ratio of the voltage in an object to the current in a conductive medium. *Z* is a complex quantity, which consists of a real part (resistance) and an imaginary part (reactance).[7] Its units are ohms (Ω). In this regard, Wtorek et al.[8] presented the construction of a probe for immittance spectroscopy based on the four-electrode technique. They tested the probe in "in-vivo" measurements on swine gluteal tissue.

The simplest set-up for measuring *Z* is the so-called two-probe set-up, where a current source is used in order to feed a known current (*I*) into the unknown *Z*. A voltage measurement using a voltage-measurement device determines the voltage drop, which is assumed to be proportional to the unknown *Z*. However, the resistivity of cables and the contact resistance also fully contribute to the voltage drop and to the measured voltage. As a result, the measurement result *Z* is actually higher than the true *Z*.

In the diagnosis of neuromuscular diseases, for instance, the *Z* of muscles can be measured to monitor patients with amyotrophic lateral sclerosis, muscular dystrophy and inflammatory myopathies. In clinical practice, a surface-electrode *Z* measurement is used for *Z* measurements of the skin tissue, which can be used for monitoring various conditions relating to the physical or medical state of a patient. The accuracy of a *Z* measurement with surface electrodes can be degraded by unknown contact impedances.

In order to avoid the disadvantages of the two-probe, *Z* measurement set-up, the four-probe, *Z* measurement set-up employs an additional pair of electrodes. In the four-probe, *Z* measurement set-up, the current is fed through two feeding electrodes[1,4] (considered as drive terminals) within the line of four equidistantly placed electrodes, while the voltage drop is measured between two measurement electrodes[2,3] (considered as measurement terminals). The voltage is measured with an instrument that has a very high input *Z*, so that almost no current flows through the measurement electrodes, i.e., their cables and contact resistance play almost no role in the measurement. Therefore, the measured voltage is almost identical to the voltage drop at the unknown *Z*.[9] For many applications, the four-probe, *Z* measurement set-up thus provides sufficient accuracy.

The measurement of *Z* in biological systems, such as nerve tissue, with the four-probe measurement set-up, eliminates the influence of the *Z* of the electrode/nerve tissue interface on the nerve tissue *Z*. Namely, electrode polarization is avoided and the contact *Z* is eliminated from the measurement.[10,11] However, the *Z* measurement error cannot be fully eliminated due to current flow through the measurement electrodes. As the use of Pt electrodes in selective nerve-stimulation applications (SNS) became indispensable, significant research was dedicated to understanding the electrode-electrolyte interface in “in vivo” and the electrode-nerve tissue interface in "in vivo". Of particular importance to SNS is Schwan’s limit of linearity: the voltage at which the electrode system’s *Z* becomes nonlinear and is often exceeded during SNS.[12,13]

The main goal of this study was to use the electrical impedance spectroscopy (EIS) and voltage response (VR) experimental results to enhance our understanding of the effect of physical processes at the interface *Z*, with the expressed purpose of improving the interface design of future multi-electrode stimulating systems for SNS. The measurements were performed to test the hypothesis that a specific waveform of current stimulating pulse elicits controlled and tissue-safe voltage differences at the double layer (DL) of the interface between the Pt stimulating electrode and the nerve tissue. These repetitive voltage differences are potentially harmful since over time they can prevent effective excitation of the nerve tissue at the stimulating electrode due to electrolysis-induced nerve-tissue damage.

2 MATERIAL AND METHODS

2.1 Experimental design and set-up

Among the several custom-designed pieces of equipment, the most important was a temperature-controlled measuring chamber and proprietary stimulation/recording cables (**Figure 1d**). The chamber was developed for the two-probe and the four-probe electrophysiological measurements. The bulk body of the chamber was machined out of Plexiglas, using a computerized numerical control milling machine. The main part of the chamber was a ladder with seven Pt hook-shape electrodes mounted horizontally over the chamber aperture and filled with a Krebs-Ringer solution (154-mM NaCl, 5-mM KCl, 2-mM $CaCl_2$, 1-mM $MgCl_2$, 5-mM HEPES, 11-mM D-glucose, pH 7.4). The distance between the electrodes was 4.8 mm.

The hook-shape electrodes were manufactured from a cold-drawn Pt wire (99.99 % purity) with a thickness of 1 mm. Pure Pt is commonly used as a stimulating electrode material because it can effectively supply high-density electrical charge to activate the neural tissue. Pt is normally used in the form of a pure metal because impurities and alloying elements may adversely affect its mechanical characteristics, working characteristics and its stability against corrosion in physiological media. Pt also has many physical properties that are of great value for their use in the technology of implantable stimulating electrodes. The contact surface of the Pt electrodes was increased, relative to the electrodes’ geometric area, by sanding with a metallurgical grade sandpaper number 1000.

Consequently, in the developed measuring system, the two Pt hooks (electrode 1 and 7) of the ladder, representing the first two points of the four-probe measuring set-up, are used as shown in **Figure 1d**. For measurements of the voltage drop elicited by the current

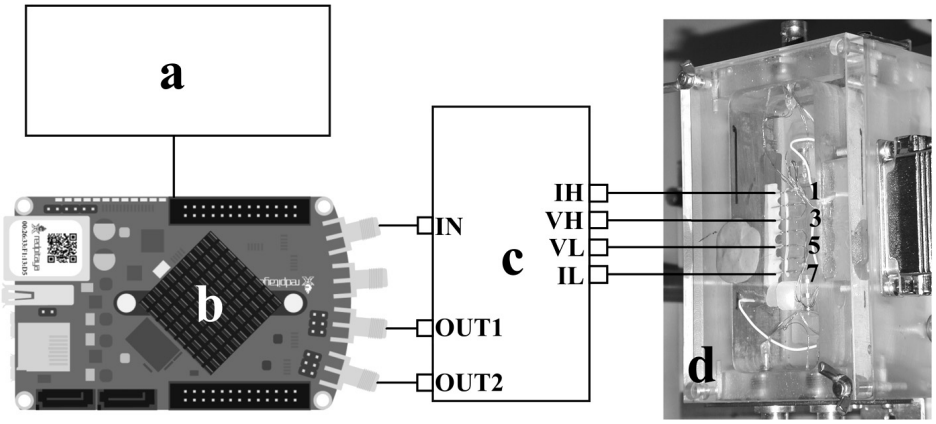

Figure 1: Schematic diagram of the stimulating/measuring set-up: a) programming part of the *Z* measurement set-up, b) Red Pitaya, c) *Z* front-end device, d) 3D view of the measuring chamber with a ladder of electrodes

Slika 1: Shematski prikaz stimulacijsko/merilne naprave: a) programska enota naprave za merjenje *Z*, b) Red Pitaya, c) vhodno izhodna naprava *(Z)*, d) tridimenzionalna slika merilne celice z lestvico elektrod

pulse, the two hooks (electrode 3 and 5) representing the second two probes of the four-probe measuring set-up, were used. The hook electrode 1 is connected to the high current source output (I_H) of the bio-impedance front-end device (**Figure 1c**), while the hook electrode 7 is connected to the low current source output (I_L) of the bio-impedance front-end device. Electrode 3 was connected to the high-voltage input (V_H) of the bio impedance front-end device and electrode 5 was connected to the low-voltage input (V_L) of the bio impedance front-end device. Before the rat's sciatic nerve (RSN) was placed on the ladder of electrodes, the chamber canal was filled with saline to prevent the drying out of the RSN. To reduce the polarization and voltage shifts, the electrodes were soaked for 15 min to 30 min.

2.2 Nerve dissection and preparation

Z measurements were performed on two isolated RSNs harvested from adult male Wistar rats, weighing 300 g to 350 g, purchased from Charles River. Animal handling complied with the Prevention of Cruelty to Animals law, which is consistent with the European Community Directive 2010/63/EU and was approved by the Institutional Review Board. The rats are euthanized by CO_2 and exsanguination. Dissection began with an incision through the skin on the lateral side of the hind limb from the knee to the hip region. To expose the RSN, the superficial layer of the thigh muscle is carefully dissected between the m. gluteus superficialis and m. biceps femoris. The length of RSN available for measurement depends on the point at which the RSN divides into the peroneal, tibial and sural nerves. To prevent nerve injury during handling, a thread was tied around the distal end of the RSN. After the attached tissue was removed from the RSN, the RSN was cut as close to the knee joint as possible. Similarly, at the proximal end, the RSN was cut as close as possible to the spinal column. By doing so, the RSN obtained was long enough (between 30 mm and 35 mm) to be in contact with all the electrodes in the ladder.

Afterwards, the RSN was placed in a glass silicon-lined Petri dish filled with Krebs-Ringer solution. As the buffer was used for cell physiology experiments, it was gassed with 100 % oxygen for 10–20 min, so that the RSN could recover from the dissection. The RSN was transferred from the Petri dish into the chamber and placed on the ladder so that it touched all the electrodes. The RSN was kept moist with saline to prevent it from drying out and rendering it useless for the experiment. Finally, to prevent evaporation and drying of the tissue the chamber was covered with a lid. All of the recordings were made at an ambient temperature of 22–23 °C.

2.3 Measuring system

The Red Pitaya (Red Pitaya, Solkan, Slovenia) development platform was used for the stimulating/measuring set-up shown schematically in **Figure 1**. This platform enables signal generation, signal acquisition and signal processing.

The set-up used two built in D/A and A/D converter inputs enabling measurements with a 14-bit resolution at a 125 MHz/s sampling rate. This sampling rate could be adjusted with a decimal/dividing factor to 1, 8, 64, 1024, 8192 and 65536, respectively. Red Pitaya was attached to the *Z* front-end device as shown in **Figure 1c**. This device was composed of a voltage-controlled current source (VCCS) based on the Howland method. The VCCS was designed to provide a constant current signal (i_c), up to 4 mA, independent of the value of the attached load within a frequency range from 1 Hz to 1 MHz. The *Z* front-end device enabled simultaneous, four- and two-probe *Z* measurements.[3,7]

2.4 Bio-impedance spectroscopy measurements

The EIS-based frequency response studies of *Z*, of any material, can provide the material's structure- and

composition-dependent electrical properties as well as its frequency response.[14] In this study, EIS was used to estimate the complex ($Z(f)$) and phase angle ($\theta(f)$) of the RSN at different frequencies f_i (f_i: f_1, f_2, f_3,..., f_n) by measuring the surface voltage ($V(f)$) developed for a constant low-amplitude, low-frequency alternating sinusoidal current ($I(f)$) injected into a RSN using both the two- and four-probe methods.[15–18] Afterwards, the frequency-dependent electrical bio-impedance $Z(f_i)$ was found as the transfer function of the RSN, and thus the $Z(f_i)$ was calculated by dividing the voltage data ($V(f_i)$) measurement by the applied current ($I(f_i)$), as shown in the following Equation (1):

$$Z(f_i) = V(f_i)/I(f_i) \quad (1)$$

The programming part of the Z measurement set-up, shown in Figure 1a, was performed with a Lenovo T420 portable computer (Lenovo, Singapore) and MATLAB R2007a software (The Mathworks Inc., USA). In this way, communication and concomitant functional control of the Red Pitaya was made and monophasic and biphasic voltage pulses to drive (driving pulse) a VCCS within the front-end device, having a specific waveform shown in **Figures 2a** and **2b**, were generated. An aforementioned waveform of the stimulating pulse was adopted from a recent study where this waveform was tested by selective nerve stimulation of the isolated porcine left cervical vagus nerve segment.[19] Afterwards, driving pulses were delivered to the VCCS, where they were converted into constant current pulses by means of the high-output-impedance current generator. To avoid a measurement error in developing the presented Z measurement set-up, it was essential that a high-output Z was maintained over the operating frequency range so that the injected current was constant and that the current source did not load the sample.[20] The stimulating current pulses, having precisely the same waveform as the driving pulses that were delivered to the VCCS, were constant current, biphasic, partially charge-balanced and asymmetric, composed of a precisely determined quasi-trapezoidal cathodic phase with a square leading edge of intensity i_c, a plateau of the cathodic phase with the width of t_c, followed by an exponentially decaying phase with the width of t_{exp} and the time constant $\hat{\boldsymbol{o}}_{exp}$, and ended by a wide, rectangular, anodic phase with the width t_a and intensity of i_a.

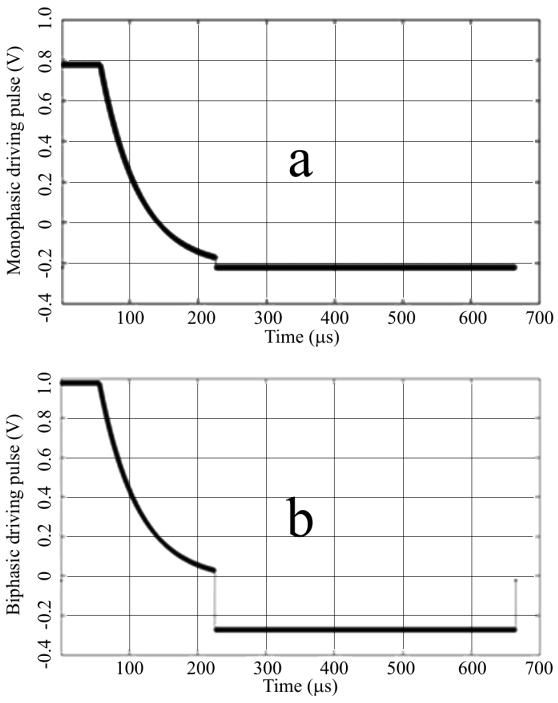

Figure 2: Voltage driving pulses to control the VCCS current source: a) a monophasic pulse and b) a biphasic pulse

Slika 2: Napetostna krmilna pulza za kontrolo VCCS tokovnega vira: a) monopolarni pulz in b) bipolarni pulz

In the four-probe measurement, the generated current stimulating pulse waveform i_c was applied to an isolated RSN via the two outer hook electrodes within the ladder, electrode number 1 and electrode number 7 that served as current feeding probes I_H and I_L. They were separated from the electrodes number 3 and 5 that served as voltage probes V_H and V_L, respectively. In the two-probe measurement, the generated current stimulating pulse was applied on an isolated RSN via the electrode number 1, serving as a current feeding probe I_H, and connected to the electrode number 3 that served as a voltage probe V_H and via the electrode number 7, that served as a current feeding probe I_L and was connected to electrode number 5 that served as a voltage probe V_L.

These measurements were used to obtain the Bode and Nyquist diagrams with which the equivalent circuit model elements could be calculated for each of the samples. The Nyquist diagram consists of a Zimaginary vs. Zreal plot, representing the imaginary and real values for the Z. This paper however, only reports an "in-vitro" study of RSN samples conducted using EIS to find the frequency-dependent Z.

2.5 Voltage-response (VR) measurements

The presented set-up also enabled measurements of *VR*s that were elicited in the RSN using generated quasi-trapezoidal monophasic and biphasic pulses. The generated stimulating pulse was measured indirectly as a voltage drop at the reference resistor with a trains impedance amplifier to assess the value of the phase angle θ. Later on, this value was used in the processing of data for the Z calculation. The aforementioned stimulating pulse was used for excitation of the RSN that represented a floating load; therefore, the elicited voltage drop was measured differentially using an instrumental amplifier.

The RSN was stimulated with the generated current pulses while information on the *VR* and stimulating current was recorded simultaneously. In this regard, i_c was 1.8 mA while t_c was 60 μs. In each measurement, where 50 pulses were generated, the last pulse was saved and a time to gap of 250 μs was introduced. The EIS was per-

formed using current sinusoidal signals with an amplitude of 400 μA that were generated at frequencies evenly distributed within the frequency range between 1 Hz and 500 kHz and delivered to the RSN. While the RSN was stimulated with the aforementioned current sinusoidal signals, the stimulating current and *VR* were saved again. All of the data were analysed off-line and *Z* was calculated with the lock-in method.

3 RESULTS

3.1 Bio-impedance spectroscopy

Figure 3a shows the Bode diagram of the absolute value of *Z*, measured on the RSN, using the two- and four-probe set-ups while the RSN is stimulated with two specific monophasic and biphasic excitation pulses, respectively. **Figure 3b** shows the θ obtained with the two- and four-probe set-ups expressed in the Bode diagram during RSN stimulation with monophasic and biphasic stimuli. **Figure 3c** shows the *Z* spectrum measured with the two- and four-probe set-ups, presented with the Nyquist diagram (Cole-Cole diagram), while the RSN is stimulated with monophasic and biphasic stimuli.

The absolute *Z* value, expressed in the Bode diagram while the RSN is stimulated with monophasic and biphasic stimuli and measured using the two-probe set-up, decreased almost exponentially from approximately 60 kΩ measured at 1 Hz to slightly below 800 Ω measured at 20 kHz (**Figure 3a**). At frequencies between 20 kHz and 100 kHz, *Z* remained almost unchanged; at frequencies above 100 kHz, however, *Z* began to decrease rapidly. It was noted that traces of *Z* belonging to stimulation with monophasic and biphasic stimuli were almost identical.

Figure 3b, representing the θ expressed in the Bode diagram, shows that for the two-probe measurement, the capacitive nature of an interface between RSN and platinum electrodes prevailed at frequencies below 500 Hz. Namely, a corresponding θ measured at 1 Hz was –60 °C and θ measured at 500 Hz was –10 °C, respectively. At frequencies between 500 Hz and 30 kHz, the nature of the interface remained still slightly capacitive, expressing the same value of the phase angle θ, i.e., –10 °C. Within this frequency range, the ohmic nature of the interface between the RSN and platinum electrodes prevailed. At frequencies above 100 kHz, however, the nature of the interface between the RSN and the platinum electrodes started to be progressively capacitive again, expressing the sharp decrease of θ towards negative values. The traces of θ, belonging to the stimulation with the monophasic and biphasic stimuli, were almost identical.

In **Figure 3c**, the *Z* spectra measured with two- and four-probe set-ups expressed in a Nyquist diagram (Cole-Cole diagram) while the RSN is stimulated with monophasic and biphasic stimuli differ considerably. This diagram represents the relationship between the imaginary and the real component of *Z,* as measured at the interface between the RSN and the particular platinum electrodes using the two- versus four-probe set-up and monophasic versus biphasic stimuli. In other words, this diagram represents the relationship between capacitive and ohmic natures of the interface between the RSN and the platinum electrodes. The difference was not significant for monophasic versus biphasic stimuli but was for the two- versus four-probe measurements. Traces of *Z* spectra, belonging to stimulation with monophasic and biphasic stimuli, were almost identical for the two- as well as for the four-probe measurements. For the two-

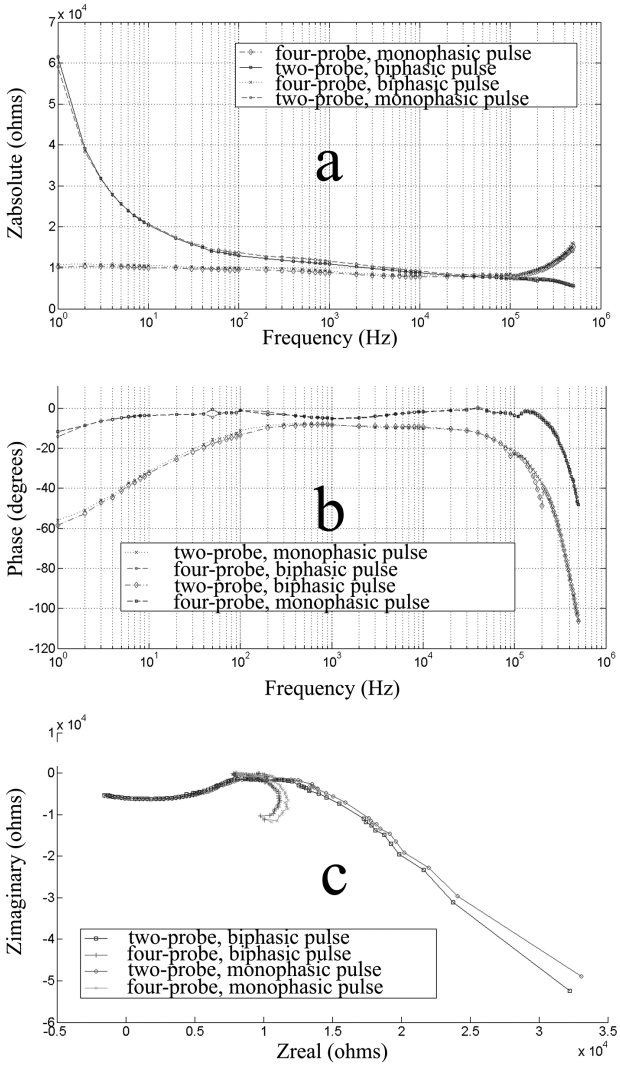

Figure 3: Results of *Z* spectroscopy measurements while the RSN is stimulated with monophasic and biphasic stimuli: a) Absolute *Z* value measured with a two- and four-probe set-ups expressed in a Bode diagram, b) θ obtained with a two- and four-probe set-ups expressed in a Bode diagram, c) *Z* spectrum measured with two- and four-probe set-ups expressed in a Nyquist diagram (Cole-Cole diagram)

Slika 3: Rezultati spektroskopskih meritev *Z*, medtem, ko je bil RSN stimuliran z monofaznimi in bifaznimi pulzi: a) absolutna vrednost *Z* merjena z dvo in štiritočkovno metodo, prikazana z Bodejevim diagramom, b) θ merjen z dvo in štiritočkovno metodo, prikazan z Bodejevim diagramom, c) spekter *Z* merjen z dvo in štiritočkovno metodo prikazana z Nyquistovim diagramom (Cole-Cole diagram)

and four-probe measurement, the *Z* spectrum below 10 kΩ of the real/ohmic component, showed an almost identical relationship between the imaginary/capacitive and the real/ohmic nature of the interface between the RSN and the Pt electrodes. Above 10 kΩ of real/ohmic component, however, the two-probe measurement showed an almost linear decrease of an imaginary/capacitive nature and, at the same time, an almost linear increase of the real/ohmic nature, while the four-probe measurement showed no further increase in the real/ohmic nature.

3.2 Voltage-response (VR) measurements

*VR*s, during the excitation of the RSN with the quasi-trapezoidal monophasic and biphasic pulses using the two- and four-point measurement set-ups, are shown in the **Figures 4a** to **4c**. **Figure 4a** shows the VRs elicited with a monophasic pulse and measured with the two- and four-point set-ups. VRs measured with the four-point set-up follow the quasi-trapezoidal pulse more accurately than the VRs measured using the two-point set-up. This was in accordance with **Figure 3** where the real/ohmic nature of the interface between the RSN and the Pt electrode in the four-point measurement prevails over the imaginary/capacitive nature of the interface between the RSN and the Pt electrode.

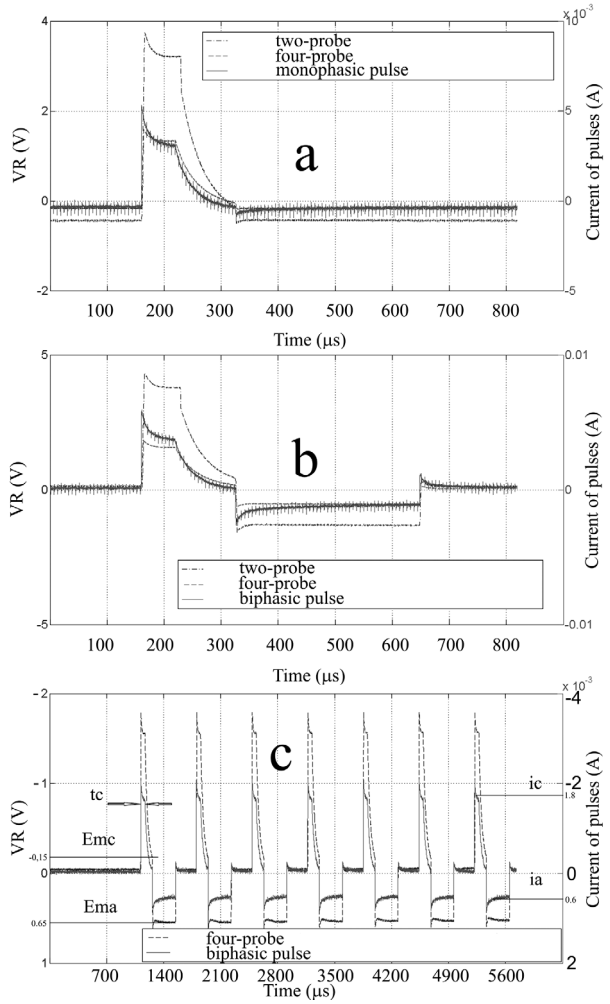

Figure 4: Stimulation pulses and corresponding *VR*s: a) *VR*s measured using a two- and four-point measurements elicited with a monophasic pulse, b) *VR*s measured using a two- and four-point measurements elicited with a biphasic pulse, c) *VR*s measured using a four-point measurement elicited with a train of biphasic pulses

Slika 4: Stimulacijski pulzi in pripadajoči *VR*-ji: a) *VR*-ji merjeni z dvo in štiritočkovno metodo, izzvani z monofaznim pulzom, b) *VR*-ji merjeni z dvo in štiritočkovno metodo, izzvani z bifaznim pulzom, c) *VR*-ji merjeni z dvo- in štiritočkovno metodo, izzvani z vlakom bifaznih pulzov

Figure 4b shows VRs measured with the two- and four-point set-ups elicited with the biphasic pulse. VRs measured with the two-point set-up follow the quasi-trapezoidal pulse more accurately than the VRs measured with the four-point set-up. This is in accordance with **Figure 3** where the real/ohmic nature of the interface between the RSN and the Pt electrode in the four-point measurement prevails over the imaginary/capacitive nature of the interface between the RSN and the Pt electrode.

As seen in all three panels of **Figure 3**, the leading edge of the cathodic phase i_c and the plateau of the cathodic phase with the width t_c of the generated stimulating current pulses were not of exactly the same shape as the waveform of pulses that were delivered to the VCCS. Other parts of the generated current pulses, such as exponentially decaying phase with the width of t_{exp} and the time constant τ_{exp} in both monophasic and biphasic pulses as well as the rectangular, anodic phase with the width t_a and intensity of i_a in the biphasic pulse, are almost identical. It was presumed that in calculations of *Z*, after a monophasic and biphasic pulse, the aforementioned dissimilarity did not influence *Z* significantly.

Figure 4c shows *VR*s measured using the four-point set-up, elicited with a train of generated biphasic pulses with a cathodic intensity (i_c) of 1.8 mA and the elicited *VR*s with the entire voltage drop of ΔV = 1.7 V. As shown in **Figure 4c**, an onset of i_c elicited the near-instantaneous voltage increase with the same time course. However, when i_c was terminated, the course of the voltage in the exponential decay region where i_c exponentially approached the lowest value, the voltage also exponentially approached the value of approximately -0.15 V. Almost at the same time as the cathodic pulse i_c was terminated, the onset of an anodic intensity (i_a) of 0.6 mA elicited the near-instantaneous positive voltage of approximately 0.65 V, having a slightly different course.

As in the VR of the tested stimulation pulse, the maximum negative polarization across the electrode-nerve tissue interface (E_{mc}) and the maximum positive polarization across the electrode-nerve tissue interface (E_{ma}) reached -0.15 V and 0.65 V, respectively. None of them exceed the safety limit range for water electrolysis, from -0.60 V to +0.85 V.[21]

4 DISCUSSION

The presented work demonstrates the feasibility of a *Z* measurement on an isolated RSN with quasi-trapezoidal current biphasic stimulating pulses. The feasibility of the stimulating paradigm, where the specific stimulus waveform was used to selectively stimulate different types of nerve fibres within the cervical segment of porcine vagus nerve, has already been published.[19]

In the last two decades, particular attention has been paid to vagus nerve stimulation techniques that are used to treat, among others, a number of nervous-system disorders, neuropsychiatric disorders, eating disorders, sleep disorders, cardiac disorders, endocrine disorders, and pain.[22–25] Considerable scientific and technological efforts have been devoted to developing systems of electrodes that interface the human vagus nerve with electronic implantable devices.[26,27]

The *Z* characterization of the electrode-electrolyte interface is of paramount importance in the field of neuroprotheses, where small electrodes are required for SNS and recording of superficial regions of peripheral nerves via multi-electrode systems. The electrode-electrolyte interface is determined from the known electrode Z, which should be as low as possible to avoid nerve tissue damage. A high *Z* would result in a large applied electrode voltage leading to undesirable electrochemical reactions that damage the nerve tissue.[28] As shown in the presented study, neither the maximum negative polarization across the electrode-electrolyte interface (E_{mc}), nor the maximum positive polarization across the electrode-electrolyte interface (E_{ma}), exceeded the safety limits for water electrolysis.[21]

Nevertheless, large surface area stimulating electrodes (due to a roughened surface), with a relatively much smaller geometric surface area and thus a much lower Z than current designs, could be beneficial, especially where a larger number of stimulating electrodes within the multi-electrode system[29] is needed. The authors demonstrated "in vitro" that by increasing the real surface area of stimulating electrodes, a significantly lower polarization impedance and electrode impedance, as well as a low residual direct current, could be obtained. Also, all three electrical parameters, electrode impedance, access resistance and polarization, could be calculated from the current and voltage measurements. Thus, a theoretical equivalent circuit model of the interface between the RSN and Pt electrodes could be modelled by fitting the equivalent circuit model elements to the EIS-based frequency-response spectroscopy experimental results.[28,30,31]

5 CONCLUSIONS

The first conclusion is that at frequency range between 0 kHz and 2.5 kHz, which confines the power spectrum density of the proposed quasi-trapezoidal stimulating pulse (power spectrum density not shown in this paper), the ohmic nature of the interface between RSN and Pt electrodes prevailed over the imaginary/capacitive nature, yielding the relative low *Z* of approximately 1 kΩ.

The second conclusion is that the differences elicited at the DL of the interface between the Pt stimulating electrode and the nerve tissue, while the RSN was stimulated using biphasic quasi-trapezoidal stimuli, have not exceeded the voltage range considered safe for nerve tissue.

The third conclusion is that the designed and tested four-probe bio-impedance measurement set-up, based on the Red Pitaya open-source measurement and control tool, provided data on the structure- and composition-related electrical properties of the RSN tissue that contribute to the development of multi-electrode nerve stimulating systems.

Definitions of field-specific terms

SNS – selective nerve stimulation
RSN – segment of a rat sciatic nerve
AC – alternating current
Z – electrical impedance
VCCS – voltage controlled current source
driving pulse – voltage pulses to drive a VCCS
EIS – Electrical impedance spectroscopy
Pt – platinum
chamber – temperature-controlled measuring chamber
CNC – computerized numerical control
i_c – intensity of the cathodic phase
t_c – width of the cathodic phase
t_{ex}p – width of the cathodic exponential decay
τ_{exp} – time constant of the exponential decay
i_a – intensity of the anodic phase
t_a – width of the anodic phase
I_H and IL – current feeding probes
V_H and VL – voltage probes
VR – voltage response
R – reference resistor
θ – phase angle
DL – double layer
E_{ma} – maximum positive polarization across the electrode-electrolyte interface
E_{mc} – maximum negative polarization across the electrode-electrolyte interface

Acknowledgement

This work was financed by the research grant P3-0171 and P4-0053 from the Slovenian Research Agency (ARRS), Ministry of Education, Science and Sport, Ljubljana, Republic of Slovenia. The authors acknowledge Professor Dejan Križaj from the Faculty of Electrical Engineering, University of Ljubljana, for the

useful discussion and enabling us to use a measuring set up developed in his laboratory.

Ethical approval

The neural tissue was treated in accordance with the approval guidelines of the ethics committee of the Veterinary Administration, Ministry of Agriculture, Forestry and Food, Republic of Slovenia.

Conflict of interest statement

The authors declare that there are no conflicts of interest regarding the publication of this paper. None of the authors received any financial or other compensation for undertaking this study or during its execution. No personal relationships with other people or organizations inappropriately influenced the work.

6 REFERENCES

[1] T. K. Bera, J. Nagaraju, Electrical impedance spectroscopic study of broiler chicken tissues suitable for the development of practical phantoms in multifrequency EIT, J Electr Bioimp, 2 (**2011**), 48–63, doi:10.5617/jeb.174

[2] H. P. Schwan, Electrical properties of tissue and cell suspensions, Adv Biol Med Phy, 5 (**1957**), 147–209

[3] H. Solmaz, Y. Ülgen, M. Tümer, Design of a Cole-Cole Meter for Complex Impedance Measurement of Living Tissues, Biomedical Engineering, 7 (**2010**), doi:10.2316/Journal.216.2010.7.680-137

[4] J. J. Ackmann, Complex bioelectric impedance measurement system for the frequency range from 5 Hz to 1 MHz, Ann Biomed Eng, 21 (**1993**) 2, 135–146

[5] R. W. Griffiths, M. E. Philpot, B. J. Chapman, K. A. Munday, Impedance cardiography: non-invasive cardiac output measurement after burn injury, Int J Tissue React, 3 (**1981**) 1, 47–55

[6] C. J. Schuster, H. P. Schuster, Application of impedance cardiography in critical care medicine, Resuscitation, 11 (**1984**) 3–4, 255–274

[7] H. Solmaz, Y. Ülgen, M. Tümer, Design of a microcontroller based Cole-Cole impedance meter for testing biological tissues, World Congress on Medical Physics and Biomedical Engineering, 2009, doi:10.1007/978-3-642-03885-3_135

[8] J. Wtorek, A. Bujnowski, A. Poliński, L. Józefiak, B. Truyen, A probe for immittance spectroscopy based on the parallel electrode technique, Physiol Meas, 25 (**2004**) 5, 1249–1260, doi:10.1088/0967-3334/25/5/014

[9] R. Pinter, R. Schmidt, Impedance Measurement Circuit and Method. U.S. Patent No. 8831898, 2010 URL:http://patft.uspto.gov/netacgi/nphParser?Sect1=PTO1&Sect2=HITOFF&d=PALL&p=1&u=%2Fnetahtml%2FPTO%2Fsrchnum.htm&r=1&f=G&l=50&s1=8831898.PN.&OS=PN/8831898RS=PN/8831898

[10] T. Palko, F. Bialokoz, J. Weglarz, Multifrequency device for measurement of the complex electrical bio-impedance – design and application, Proc. of the Engineering in Medicine and Biology Society, 1995 and 14th Conference of the Biomedical Engineering Society of India, An International Meeting, the first regional conference, New Delhi, 1995, doi:10.1109/RCEMBS.1995.508682

[11] Y. Yang, J. Wang, G. Yu, F. Niu, P. He, Design and preliminary evaluation of a portable device for the measurement of bioimpedance spectroscopy, Physiol Meas, 27 (**2006**) 12, 1293–1310

[12] H. P. Schwan, Electrode polarization impedance and measurements in biological materials, Ann N Y Acad Sci, 148 (**1968**), 191–209

[13] H. P. Schwan, Linear and nonlinear electrode polarization and biological materials, Ann Biomed Eng, 20 (**1992**), 269-288

[14] E. Barsoukov, J. R. Macdonald, Impedance spectroscopy: theory, experiment and applications, 2nd ed., John Wiley & sons, Hoboken, New Jersey 2005

[15] A. J. Bard, L. R. Faulkner, Electrochemical methods: fundamentals and applications, 2nd ed., John Wiley & sons, New York 2001

[16] J. O'M. Bockris, A. K. N. Reddy, Modern Electrochemistry, vol. 2, Plenum publishing corporation, New York 1970

[17] J. R. Macdonald, Impedance spectroscopy, John Wiley & sons, New York 1987

[18] T. K. Bera, Bioelectrical impedance methods for noninvasive health monitoring: a review, Journal of Medical Engineering, 2014 (**2014**), Article ID 381251, 28 pages, doi:10.1155/2014/381251

[19] P. Pečlin, J. Rozman, Alternative paradigm of selective vagus nerve stimulation tested on an isolated porcine vagus nerve, Scientific World Journal, 2014 (**2014**), 310283, doi:10.1155/2014/310283

[20] A. A. Silverio, A. A. Silverio, A high output impedance current source for wideband bioimpedance spectroscopy using 0.35μM TSMC CMOS technology, International Journal of Engineering and Applied Sciences, 1 (**2012**) 2, 68–75

[21] E. M. Hudak, J. T. Mortimer, H. B. Martin, Platinum for neural stimulation: voltammetry considerations, J Neural Eng, 7 (**2010**) 2, 26005, doi:10.1088/1741-2560/7/2/026005

[22] T. A. Anholt, S. Ayal, J. A. Goldberg, Recruitment and blocking properties of the CardioFit stimulation lead, J Neural Eng, 8 (**2011**) 3, 034004, doi:10.1088/1741-2560/8/3/034004

[23] A. M. Bilgutay, I. M. Bilgutay, F. K. Merkel, C. W. Lillehei, Vagal tuning: a new concept in the treatment of supraventricular arrhythmias, angina pectoris, and heart failure, J Thorac Cardiovasc Surg, 56 (**1968**), 71–82

[24] C. Heck, S. L. Helmers, C. M. DeGiorgio, Vagus nerve stimulation therapy, epilepsy, and device parameters: scientific basis and recommendations for use, Neurology, 59 (**2002**), S31–S37

[25] D. M. Labiner, G. L. Ahern, Vagus nerve stimulation therapy in depression and epilepsy: therapeutic parameter settings, Acta Neurol Scand, 115 (**2007**), 23–33

[26] J. D. Sweeney, D. A. Ksienski, J. T. Mortimer, A nerve cuff technique for selective excitation of peripheral nerve trunk regions, IEEE Trans Biomed Eng, 37 (**1990**) 7, 706–715

[27] A. Q. Choi, J. K. Cavanaugh, D. M. Durand, Selectivity of multiple-contact nerve cuff electrodes: asimulation analysis, IEEE Trans Biomed Eng, 48 (**2001**), 165–172

[28] W. Franks, I. Schenker, P. Schmutz, A. Hierlemann, Impedance characterization and modeling of electrodes for biomedical applications, IEEE Trans Biom Eng, 52 (**2005**) 7, 1295–1302

[29] M. Tykocinski, Y. Duan, B. Tabor, R. S. Cowan, Chronic electrical stimulation of the auditory nerve using high surface area (HiQ) platinum electrodes, Hear Res, 159 (**2001**) 1-2, 53–68

[30] D. R. Merrill, The electrochemistry of charge injection at the electrode/tissue interface, In: D. Zhou, E. Greenbaum, Implantable Neural Prostheses 2, Springer, New York 2010, 85–138, doi:10.1007/978-0-387-98120-8_4

[31] L. A. Geddes, Historical evolution of circuit models for the electrode–electrolyte interface, Ann Biomed Eng, 25 (**1997**), 1–14

UDK 620.1/.2:669.056:67.017
Original scientific article/Izvirni znanstveni članek

ISSN 1580-2949
MTAEC9, 50(5)805(2016)

INFLUENCE OF DIFFERENT PRODUCTION PROCESSES ON THE BIODEGRADABILITY OF AN FeMn17 ALLOY

VPLIV RAZLIČNIH PROCESOV IZDELAVE NA BIORAZGRADLJIVOST ZLITINE FeMn17

Aleksandra Kocijan, Irena Paulin, Črtomir Donik, Matej Hočevar, Klemen Zelič, Matjaž Godec

Institute of Metals and Technology, Lepi pot 11, 1000 Ljubljana, Slovenia
aleksandra.kocijan@imt.si

Prejem rokopisa – received: 2016-03-31; sprejem za objavo – accepted for publication: 2016-04-06

doi:10.17222/mit.2016.055

The purpose of this research was to evaluate the biodegradability of a cast FeMn17 alloy that was processed by hot rolling and annealing, which influenced both the mechanical and corrosion properties of the FeMn17 alloy. The corrosion behaviour and in-vitro biodegradability were investigated by light microscopy, scanning electron microscopy, X-ray diffraction and immersion tests in Hank's solution. Compared to pure Fe, the cast FeMn17 alloy has a better biodegradability (higher corrosion rate). We showed that hot rolling additionally improves the biodegradability, while the annealing process lowers the biodegradability of the FeMn17 alloy.

Keywords: biodegradability, FeMn alloy, corrosion, XRD, SEM

Namen raziskave je bil oceniti biorazgradljivost zlitine FeMn17 s predelavo z vročim valjanjem in žarjenjem. Vroče valjanje in žarjenje vplivata na mehanske in korozijske lastnosti zlitine FeMn17. Korozijske lastnosti in biorazgradljivost smo preverjali s svetlobno mikroskopijo, vrstično elektronsko mikroskopijo, rentgensko difrakcijo in s testi potapljanja v Hankovo raztopino. V primerjavi s čistim Fe, ima zlitina FeMn17 veliko boljšo biorazgradljivost (večjo korozijsko hitrost). Pokazali smo, da vroče valjanje dodatno izboljša biorazgradljivost, z žarjenjem pa se biorazgradljivost zlitine FeMn17 poslabša.

Ključne besede: biorazgradljivost, FeMn zlitina, korozija, XRD, SEM

1 INTRODUCTION

Biodegradable metallic materials represent a novel class of bioactive biomaterials that can temporarily support tissue healing and should progressively degrade completely without a negative effect on the healing process.[1–3] Potential applications of these biomaterials are paediatric, orthopaedic (fixation screws and pins) and cardiovascular implants (coronary stents).[1,4] Biodegradable polymers were first investigated as bioactive biomaterials; however, in recent years biodegradable metallic materials, especially Fe and Mg alloys, have received more attention due to their superior mechanical properties and their cytocompatibility.[1–3,5] Compared with Mg-based materials, Fe-based materials possess similar mechanical properties to stainless steel and are more attractive for applications that require high strength and ductility.[1] Despite the immense potential of Fe and Mg alloys, experiments and clinical trials also exposed their weaknesses: too rapid degradation rates, poor mechanical properties and significant hydrogen evolution during the corrosion process of Mg-based alloys and a too slow degradation of Fe-based alloys.[5–8]

Fe-based alloys may also present problems with certain imaging devices (magnetic resonance imaging, for example) due to the Fe's ferromagnetic nature. However, alloying and heat treatment can modify the mechanical, corrosion, and ferromagnetic properties of pure Fe.[1,2] The choice and the amount of alloying element is important with respect to the toxicity and degradation behaviour of the Fe alloy.[2] Mn represents a suitable alloying element based on microstructural, magnetic, corrosion, and toxicological considerations.[2] Mn (austenite-forming element) transforms Fe into a nonmagnetic material, lowers the standard electrode potential of Fe and thus enhances the degradation of the material, which represents an essential trace element necessary in many enzymatic reactions. Newly developed Fe-Mn-based alloys containing up to 35 % of mass fractions of Mn have comparable mechanical properties to stainless steel, faster degradation and improved MRI compatibility.[1,2] Despite this, the low corrosion rate still represents the major problem fornewly developed Fe–Mn-based alloys.

Non-conventional processing techniques such as powder metallurgy, electrodeposition and inkjet 3D-printing can achieve the faster degradation of Fe–Mn alloys.[1,2] However, these techniques are rather complex and expensive, therefore it is necessary to further investigate conventional methods, such as casting with additional steel-processing techniques in order to find an economically favourable solution. Research has rarely been made on the influence of subsequent processing and heat treatment on the properties of any conventional, cast,

Table 1: Chemical composition in mass fractions, *w*/%
Tabela 1: Kemijska sestava v masnih deležih, *w*/%

Material	Mo	Ni	Mn	Cu	Ti	Si	C	Fe
Pure Fe	<LOD	0.14	0.262	0.043	<LOD	0.051	0.19	balance
FeMn17 alloy	0.021	0.182	17.08	0.446	0.058	0.167	0.08	balance

biodegradable, metallic materials, including Fe–Mn-based alloys. The aim of the present study was to investigate the influence of three basic steel-processing methods (casting, hot rolling and annealing) on the corrosion behaviour of the biodegradable Fe–Mn-based alloy due to the formation of less-corrosion-resistant deformational martensite.[9]

2 EXPERIMENTAL PART

Material preparation – The investigated Fe-based alloy with 17 % of mass fractions of Mn (FeMn17) was produced from relatively pure Fe and Mn. Both materials were melted in an induction furnace under air atmosphere at approximately 1700 °C and cast into two iron moulds. One mould was left to cool down in air atmosphere and the other one was after casting in mould, hot rolled at approximately 1000 °C for a 33 % reduction. Parts of both samples were annealed at 1050 °C for 1 h and then furnace cooled. The materials were analysed and the results were compared with pure Fe. The chemical compositions of the alloy and the pure Fe were determined using an X-ray fluorescence spectrometer XRF (Thermo Scientific Niton XL3t GOLDD+) and arepresented in **Table 1**.

Metallographic investigation – Samples were cut with a water-cooled saw and cross-sections of the samples were prepared by the standard metallographic techniques of grinding and polishing. The samples were etched with 3 % Nital, an ethanol solution of $HCl_{(aq)}$ and an ethanol solution of $HNO_{3(aq)}$. The characterization of the material was performed using a light microscope (LM, Microphot FXA Nikon with Olympus DP73) and a scanning electron microscope coupled with an energy-dispersive spectrometer (SEM, JEOL JSM-6500F, EDS INCA ENERGY 400) for analyses of the inclusions and phases.

X-ray Powder Diffraction – The samples were measured using a Panalyitical XPERT Pro PW 3040/60 goniometer 2θ between 15–90° with a step size of 0.002° and a scan step time of 100 s on each step. Cu with (K_α = 0.154 nm) anode was used with a current of 40 mA and a potential of 45 kV.

Mechanical properties – The microhardness was measured by Vickers HV5 (5 kg load, 11s -Instron Tukon 2100B).

Electrochemical measurements – Were performed on prepared specimens, ground with SiC emery paper down to 1200 grit. The experiments were carried out in a simulated physiological Hank's solution, containing 8 g/L NaCl, 0.40 g/L KCl, 0.35 g/L $NaHCO_3$, 0.25 g/L $NaH_2PO_4 \times 2H_2O$, 0.06 g/L $Na_2HPO_4 \times 2H_2O$, 0.19 g/L $CaCl_2 \times 2H_2O$, 0.41 g/L $MgCl_2 \times 6H_2O$, 0.06 g/L $MgSO_4 \times 7H_2O$ and 1 g/L glucose, at pH = 7.8. All chemicals were from Merck, Darmstadt, Germany. The measurements were performed using a three-electrode, flat BioLogic corrosion cell (volume 0.25 L). The test specimen was employed as the working electrode (WE). The reference electrode (RE) was a saturated calomel electrode (SCE, 0.242 V vs. SHE) and the counter electrode (CE) was a platinum net. Electrochemical measurements were recorded by using a BioLogic Modular Research Grade Potentiostat/Galvanostat/FRA Model SP-300 with an EC-Lab®software V10.44. The specimens were immersed in the solution 1 h prior to the measurement in order to stabilize the surface at the open-circuit potential (OCP). *The potentiodynamic curves* were recorded after 1 h of sample stabilisation at the open-circuit potential (OCP), starting the measurement at 250 mV vs. SCE more negative than the OCP. The potential was then increased, using a scan rate of 1 mV s^{-1}, until the transpassive region was reached. The *linear polarisation* measurements were performed at ±25 mV according to the OCP, using a scan rate of 0.01 mV s^{-1}.

3 RESULTS AND DISSCUSION

3.1 Microstructure characterization

The microstructures of all four samples, i.e., cast, hot rolled and both samples after annealing at 1050 °C and furnace cooled down, are shown in **Figure 1**. There is no difference in the chemical composition, where as there are some differences in the microstructure. In the cast sample, the cast structure occurs upon cooling, though the cooling rate is too high for equilibrium phase transformation, as predicted from the Fe–Mn phase diagram. We observed some boundary segregations rich in Mn and inclusions of MnS and TiN, which were also confirmed by the EDS analyses. The observed average grain size for these samples was approximately 350 μm. There was also some smaller porosity present in the microstructure. The cast + annealed sample (**Figure 1b**) has a similar microstructure with the same precipitations and inclusions that are ubiquitous at grain boundary and in the grains. The difference is in the much larger grain sizes (average of approx. 1200 μm) and more segregation of Mn at the grain boundaries according to the prolongation of the time available for the cooling after annealing.

In the hot-rolled sample was observed, beside austenite, also traces of strain-induced martensite and deformation twins. Due partly to the recrystallization, the microstructure consists of large and small grains. The

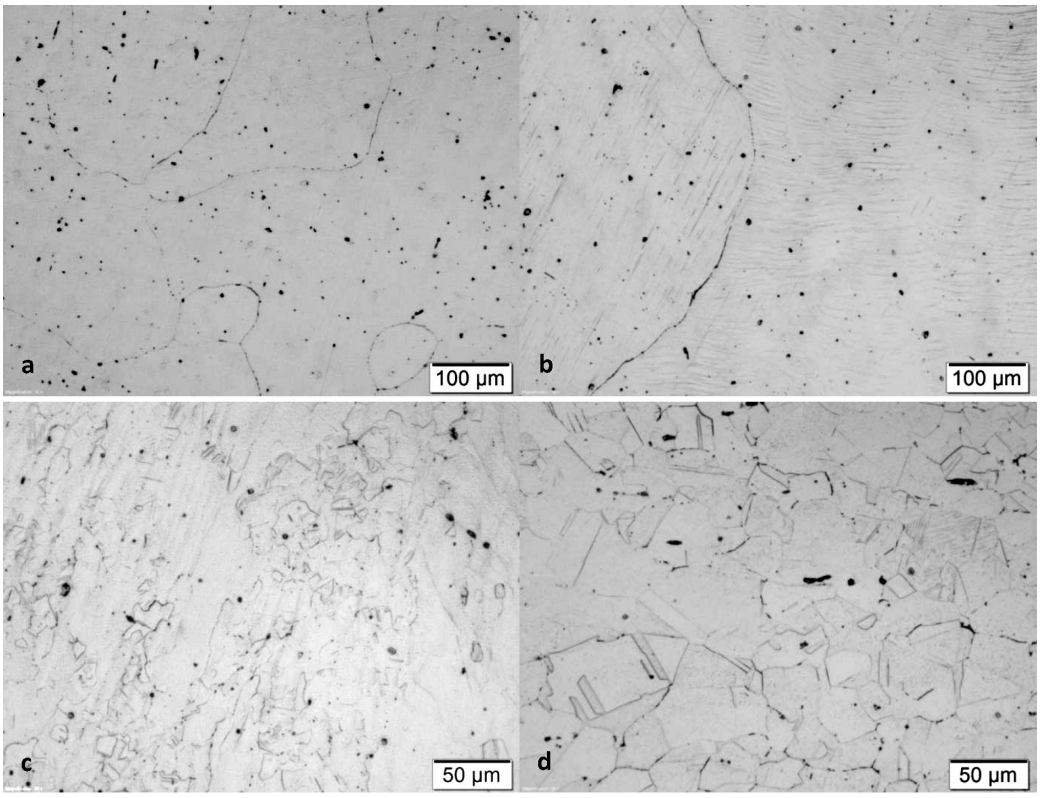

Figure 1: LM images of microstructure: a) cast sample, b) cast + annealed sample, at 1050 °C c) hot-rolled sample, and d) hot-rolled + annealed sample
Slika 1: LM-posnetki mikrostruktur: a) ulit vzorec, b) ulit + žarjen na 1050 °C, c) vroče valjan vzorec in d) vroče valjan + žarjen vzorec

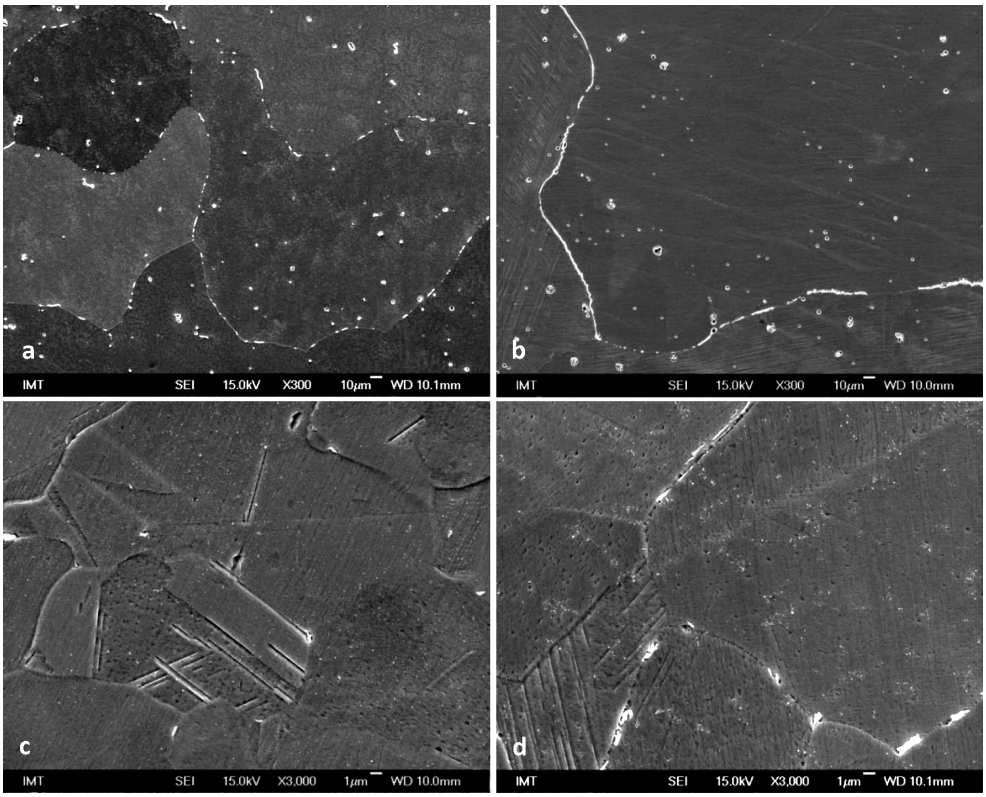

Figure 2: SEM images of microstructure: a) cast sample, b) cast + annealed sample, at 1050 °C, furnace cooled down, c) hot-rolled sample and d) hot-rolled + annealed at 1050 °C
Slika 2: SEM-posnetki mikrostruktur: a) ulit vzorec, b) ulit + žarjen na 1050 °C, c) vroče valjan vzorec in d) vroče valjan + žarjen vzorec

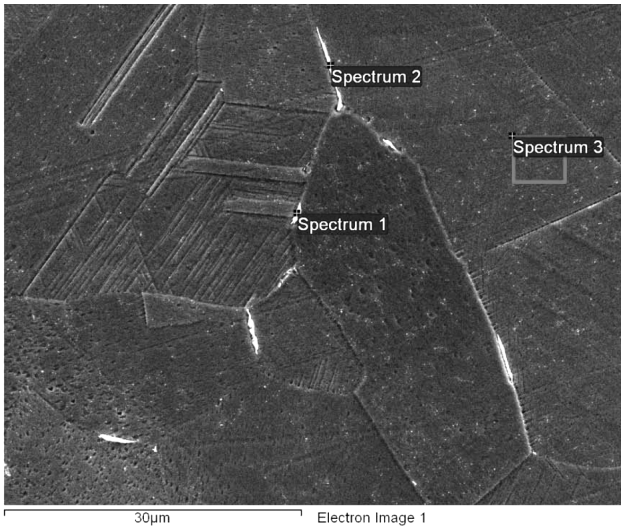

Figure 3: SEM image of microstructure and areas of EDS measurements on the hot-rolled sample
Slika 3: SEM-posnetek mikrostrukture z mesti EDS-analiz vroče valjanega vzorca

increased concentration of Mn was observed on the grain boundaries well as the MnS and TiN inclusions in the matrix as determined by the EDS analyses.

After annealing the sample has a recrystallized microstructure with smaller grains, an average of approximately 40 µm and the strain-induced martensite is still present in the microstructure. This means the annealing temperature was too low or the annealing time was too short for complete recrystallization. The SEM imaging was performed at higher magnification for details of the microstructures (**Figure 2**). In the microstructures of the hot rolled and the hotrolled + annealed FeMn17 samples the similar mixture of martensitic and austenitic microstructure was observed, similar to those previously described by Y. K. Lee at al.[10], J. Martinez at al.[11] and M. Schinhammer at al.[12] However, there was no literature presenting only cast FeMn17 material. The EDS analyses were performed for a determination of the precipitations and inclusions in the microstructure (**Figure 3**).

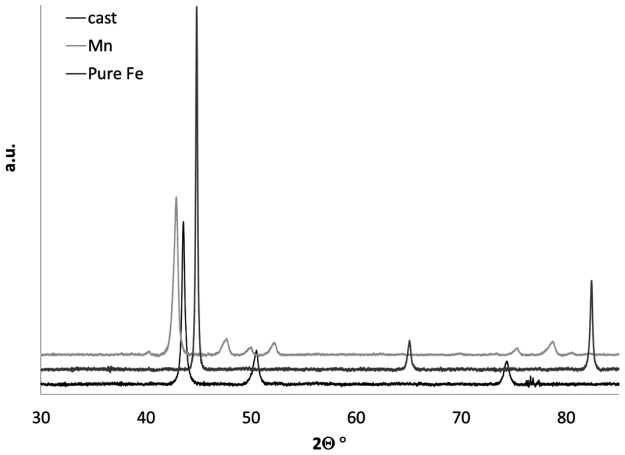

Figure 4: The XRD patterns for specimens – the two original materials,pure Fe and Mn, and the specimen of cast FeMn17 alloy
Slika 4: XRD-spektri dveh osnovnih materialov, čistega Fe in Mn, ter ulite zlitine FeMn17

3.2 Microhardness

Microhardness by Vickers (HV) was measured with a 5-kg load for 11 s. The results are in **Table 2**. The pure Fe has, as expected, the lowest microhardness. The higher microhardness is achieved in the hot-rolled samples, whereas the HV decreases with the annealing of the samples. In cast sample, the HV is not different according to the sample cast + annealed and cooled down with the furnace. On the other hand, all the HVs are lower thanthe one of the hot-rolled samples.

Table 2: Microhardness HV 5
Tabela 2: Mikrotrdota po HV5

Samples	Pure Fe	Cast	Hot rolled	Cast + annealed	Hot rolled + annealed
HV 5	110	181	240	180	210

3.3 X-ray powder diffraction

Diffraction peaks of the FeMn17 specimens correspond to the phases previously observed in FeMn17. These phases are similar to those observed by Y. K. Lee et al.[10], J. Martinez et al.[11] and H. Hermawan et al.[13] in various Fe–Mn binary alloys at room temperature. **Figure 4** shows observed peaks for the FeMn17 alloy and two starting materials, pure Fe and Mn. The highest peak at $2\theta = 43.6°$ corresponds to (111), the next peak at 50.5° to (002) and the last peak, at 74.4°, corresponds to (022). The results correspond to a cubic crystal system, with the space group F m –3 m and space group number 225, the cubic cell unit is face centred (fcc). The XRD spectrum shows peaks at different 2θ for pure Fe and Mn, which proves that all the starting materials were melted in a new alloy with a different cell unit and different chemical composition and mechanical properties was prepared.

The highest intensity peak forthe pure Fe, as a starting material, is observed at 44.8° and corresponds to (011), the next peak is observed at 82.4° corresponding to (112) and the peak with lowest intensity was at 65.1°, which corresponds to (002). This is also a cubic crystal system with a different space group, I m –3 m, and the space number is 229. The cell unit for used pure Fe, as the main alloying material is body centred cubic (bcc).

The other starting material used for the alloying was Mn. The XRD spectrum for the Mn shows main peaks at 43.0°, which corresponds to (330), next peak at 47.8° corresponds to (332) and two peaks with similar intensities at 52.3° and 78.9° that correspond to (510) and (721), respectively. This is also a cubic crystal system with the space group I –4 3 m and the corresponding space group number 217, the cubic cell unit is body centred cubic (bcc).

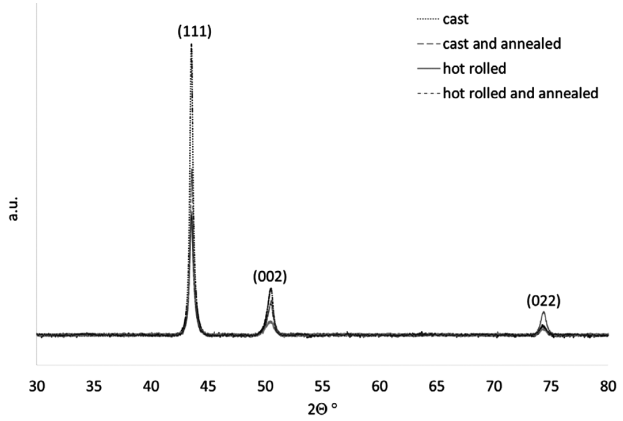

Figure 5: XRD patterns for specimens of differently produced FeMn17 alloy
Slika 5: XRD-spekter različno obdelane zlitine FeMn17

From the observed results it can be concluded that the alloy consists of just one phase, FeMn and some non-metallic inclusions. Any other potential phases in the alloy are below 2 %, which is also the limit of detection of the XRD technique. This corroborates SEM/EDS and LM results where onlysome additional non-metallic inclusions and Mn-rich grain-boundaries are present in the matrix of the investigated FeMn17 alloy.

Figure 5 shows the comparison of XRD spectra between differently processed FeMn17 alloys. The only difference between the spectra is in the intensities of the peaks and not in the peak positions, which corroborates the fact that the only difference between these specimens was just the thermal and mechanical treatments. The most intense peak was for the first peak at 43.6° of FeMn17 that was cast in a metal mould, and hot rolled, while the preferential orientation was observed due to the hot rolling, which explains the decrease of the intensity of the peak at 74.4° in comparison to the other specimens. The annealing of the specimens reduces the preferential orientation so that the intensities in the XRD spectrum are shifted to lower values and become very similar to the samples just cast in a metal mould.

3.4 Electrochemical measurements

Figure 6 represents the potentiodynamic behaviour of the investigated materials in a simulated physiological Hank's solution at pH = 7.8. The influence of different production parameters on the corrosion behaviour of the tested materials compared to pure Fe was investigated. After 1 h of stabilization at the OCP, the corrosion potential (E_{corr}) for pure Fe in Hank's solution was approximately –0.67 V vs. SCE. Hot rolled + annealed FeMn17 as well as cast + annealed FeMn17 alloys exhibited similar potentiodynamic behaviour as pure Fe, with E_{corr} at approximately –0.68 V vs. SCE. In the case of cast + hot-rolled FeMn17 alloys the corrosion stability decreased compared to other three specimens and the Tafel region was shifted to higher corrosion-current densities and E_{corr} was –0.74 V vs. SCE. None of the investigated samples in Hank's solution exhibited typical potentiodynamic behaviour with a passive region followed by a transpassive region.

Figure 7 represents linear polarisation curves for the investigated samples in a simulated physiological Hank's solutionat pH = 7.8. The calculations were performed from linear polarization measurements using Equation (1):

$$R_p = \beta_a\beta_c/(2.3\ I_{corr}\ (\beta_a + \beta_c)) \quad (1)$$

The polarization resistance, R_p, is evaluated from the linear polarization curves by applying a linear least-squares fit of the data around ±10 mV E_{corr}. The corrosion current, I_{corr}, is calculated from R_p, the least-squares slope, and the Tafel constants, β_a and β_c, of 120 mV decade^{-1}. The value of $E_{(I\ =\ 0)}$ is calculated from the least-squares intercept. The corrosion rate was calculated by using the following conversion equation (2):

$$v_{corr} = C(EW/d)(I_{corr}/A) \quad (2)$$

where EW is the equivalent weight of the sample in g, A is the sample area in cm^2, d is its density in g/mL, and C is a conversion constant, which is dependent upon the desired units. The results demonstrated steeper linear polarisation curves and therefore a lower corrosion resistance of cast + hot-rolled FeMn17 alloys compared to pure Fe, cast + annealed FeMn17 and hot rolled + annealed FeMn17 alloys. The corrosion parameters calculated from the linear polarisation and potentiodynamic measurements in a simulated physiological Hank's solution indicated that the corrosion stability of the cast + hot rolled FeMn17 alloys was lower compared to pure Fe, cast + annealed and hot rolled + annealed FeMn17 alloys. This was proven by the higher corrosion currents (I_{corr}), the higher corrosion rates (v_{corr}) and the lower polarization resistances (R_p), compared to pure Fe, cast + annealed and hot rolled + annealed FeMn17 alloys (**Table 3**).

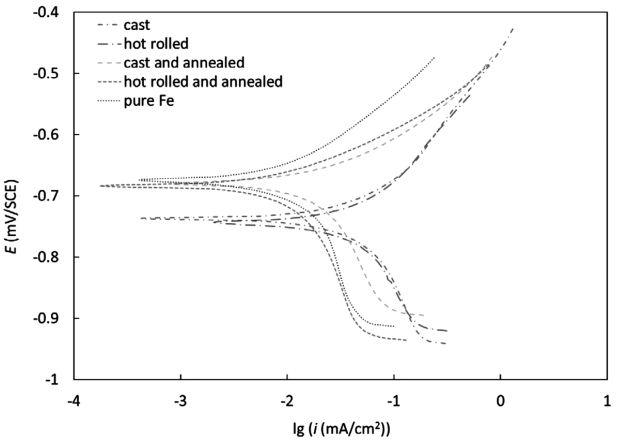

Figure 6: Potentiodynamic curves for pure Fe, cast, hot rolled, cast + annealed and hot rolled + annealed FeMn17 alloy in a simulated physiological Hank's solution
Slika 6: Potenciodinamske krivulje za čisto Fe, ulito in vroče valjano, ulito + žarjeno in vroče valjano + žarjeno FeMn17 zlitino

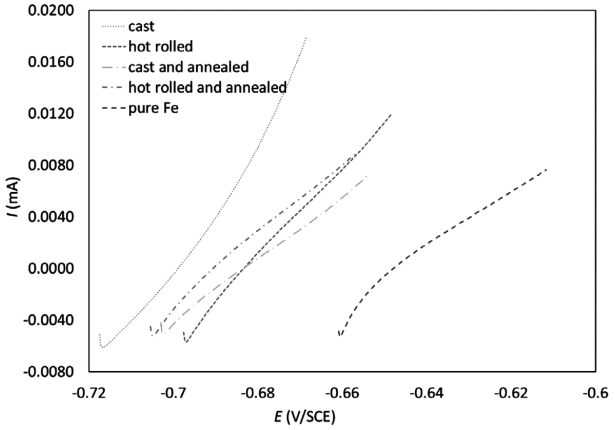

Figure 7: Linear polarisation curves for pure Fe, cast, hot rolled, cast + annealed and hot rolled + annealed FeMn17 alloy in a simulated physiological Hank's solution.

Slika7: Linearne polarizacijske krivulje za čisto Fe, ulito in vroče valjano, ulito + žarjeno in vročevaljano + žarjeno zlitino FeMn17

A wide variety of biodegradability/corrosion studies have been made using the electrochemical testing of the desired designed materials due to aconvenient and easy method to evaluate the corrosion property by testing theOCP (open-circuit potential), polarization curves and EIS(electrochemical impedance spectroscopy) via a three-electrode system.[6–8,12,13,15–17] Very similar results of corrosion testing with potentiodynamic testing were observed by H. Hermawan[13] with one distinctive difference, our pure Fe behaved biodegradability much more similar to the FeMn17 alloy than theirs.

In the present biodegradable material design study, the three design criteria as listed by H. Hermawan[1] have been considering fordeveloping a new alloy for biodegradability: a) mechanical properties that approach to those of AISI 316L; b) degradation rate that matches with the remodelling period (6–12 months) A. Schomig et al.[14] and complete disappearance of the implant material within a reasonable period (corrosion rate in the range of 0.1 mm/year); and c) no toxic substances are released during the degradation process (just pure Fe and Mn with minor non-metallic inclusions).

Table 3: Corrosion parameters calculated from the electrochemical measurements

Tabela 3: Korozijski parametri izračunani iz elektrokemijskih meritev

Material	$E_{(I=0)}$ (mV)	I_{corr} (μA)	R_p (kΩ)	v_{corr} (nm/year)
Pure Fe	–675	8.7	4.8	102
Cast	–737	40.6	2.4	486
Cast + hot rolled	–742	44.7	2.1	537
Cast + annealed	–676	18.0	3.7	216
Cast + hot rolled + annealed	–682	14.3	4.3	172

4 CONCLUSIONS

In the present study, we focused on a comparison of the biodegradability of a produced FeMn17 alloy after different preparation processing, i.e., casting, hot rolling and annealing. All the prepared specimens were compared to pure Fe.

With additions of Mn the mechanical properties increase and the corrosion resistance decreases. The process parameters influenced the biodegradability as well as the mechanical properties. The produced material, cast and hot rolled, has interior stress and that increases the biodegradability, though the annealing process increases the stability of the material and the corrosion resistance. The microstructure differences of the material are notable in the grain growth of the annealed sample and the recrystallization in the annealed hot-rolled sample.

The electrochemical investigation confirmed the enhanced biodegradability of the developed FeMn17 alloy compared to pure Fe. We confirmed that cast as well as additionally hot-rolled specimens exhibited a pronounced corrosion instability compared to the annealed material.

Acknowledgement

This work was carried out within the framework of the Slovene programme P2-0132, "Fizika in kemija površin kovinskih materialov" of the Slovenian Research Agency, whose support is gratefully acknowledged by the authors.

5 REFERENCES

[1] H. Hermawan, Biodegradable Metals, From Concept to Applications, 1st ed., Springer, Berlin 2012, 69, doi:10.1007/978-3-642-31170-3

[2] Y. F. Zheng, X. N. Gu, F. Witte, Biodegradable metals, Materials Science and Engineering: R, Reports, 77 (**2014**) 1–34, doi:10.1016/j.mser.2014.01.001

[3] H. Hermawan, D. Dubé, D. Mantovani, Developments in metallic biodegradable stents, Acta Biomaterialia, 6 (**2010**) 5, 1693–1697, doi:10.1016/j.actbio.2009.10.006

[4] H. Hermawan, D. Mantovani, Degradable metallic biomaterials: the concept, current developments and future directions, Minerva Biotecnologica, 21 (**2009**) 4, 207–216

[5] M. P. Staiger, A. M. Pietak, J. Huadmai, G. Dias, Magnesium and its alloys as orthopedic biomaterials: A review, Biomaterials, 27 (**2006**) 9, 1728–1734, doi:10.1016/j.biomaterials.2005.10.003

[6] Z. Zhen, T. Xi, Y. Zheng, A review on in vitro corrosion performance test of biodegradable metallic materials, Transactions of Nonferrous Metals Society of China, 23 (**2013**) 8, 2283–2293, doi:10.1016/S1003-6326(13)62730-2

[7] B. Liu, Y. F. Zheng, Effects of alloying elements (Mn, Co, Al, W, Sn, B, C and S) on biodegradability and in vitro biocompatibility of pure iron, Acta Biomaterialia, 7 (**2011**) 3, 1407–1420, doi:10.1016/j.actbio.2010.11.001

[8] D. Vojtěch, J. Kubásek, J. Čapek, I. Pospíšilová, Comparative mechanical and corrosion studies on magnesium, zinc and iron alloys as biodegradable metals, Mater. Tehnol., 49 (**2015**) 6, 877–882, doi:10.17222/mit.2014.129

[9] L. L. Shreir, R. A. Jarman, G.T. Burstein, Corrosion Volume 1, Metal/Environment Reactions, 3rd ed., Oxford 1994, 3184, doi:10.1016/B978-0-08-052351-4.50001-7

[10] Y. K. Lee, J. H. Jun, C. S. Choi, Damping capacity in Fe-Mn bi- nary alloys, ISIJ International, 37 (**1997**) 10, 1023–1030, doi:10.2355/isijinternational.37.1023

[11] J. Martinez, S. M. Cotes, A. F. Cabrera, J. Desimoni, A. Fernández Guillermet, On the relative fraction of ε martensite in γ-Fe-Mn alloys, Materials Science and Engineering A, 408 (**2005**), 26–32, doi:10.1016/j.msea.2005.06.019

[12] M. Schinhammer, A. C. Hänzi, J. F. Löffler, P. J. Uggowitzer, Design strategy for biodegradable Fe-based alloys for medical applications, ActaBiomaterialia, 6 (**2010**) 5, 1705–1713, doi:10.1016/j.actbio.2009.07.039

[13] H. Hermawan, D. Dubé, D. Mantovani, Degradable metallic biomaterials, Design and development of Fe–Mn alloys for stents, Journal of Biomedical Materials Research Part A, 93 (**2010**) 1, 1–11, doi:10.1002/jbm.a.32224

[14] A. Schömig, A. Kastrati, H. Mudra, R. Blasini, H. Schühlen, V. Klauss, G. Richardt, F. J. Neumann, Four-year experience with Palmaz-Schatz stenting in coronary angioplasty complicated by dissection with threatened or present vessel closure, Circulation 90 (**1994**) 6, 2716–2724, doi: 10.1161/01.CIR.90.6.2716

[15] M. Schinhammer, P. Steiger, F. Moszner, J. F. Löffler, P. J. Uggowitzer, Degradation performance of biodegradable Fe-Mn-C(-Pd) alloys, Materials Science and Engineering: C, 33 (**2013**) 4, 1882–1893, doi:10.1016/j.msec.2012.10.013

[16] F. Moszner, Fe–Mn–Pd maraging steels for biodegradable implant applications, PhD thesis, ETH-Zürich 2014, doi.org/10.3929/ethz-a-010211762

[17] B. Liu, Y. F. Zheng, L. Ruan, In vitro investigation of Fe30Mn6Si shape memory alloy as potential biodegradable metallic material, Materials Letters, 65 (**2011**) 3, 540–543, doi:10.1016/j.matlet.2010.10.068

UDK 67.017:621.763:621.745.4
Professional article/Strokovni članek

ISSN 1580-2949
MTAEC9, 50(5)813(2016)

EFFECT OF A COMBINATION OF FLY ASH AND SHRINKAGE-REDUCING ADDITIVES ON THE PROPERTIES OF ALKALI-ACTIVATED SLAG-BASED MORTARS

VPLIV KOMBINACIJE LETEČEGA PEPELA IN DODATKA ZA ZMANJŠANJE KRČENJA NA LASTNOSTI MALTE IZ Z ALKALIJAMI AKTIVIRANE ŽLINDRE

Vlastimil Bílek, Lukáš Kalina, Jan Koplík, Miroslava Mončeková, Radoslav Novotný

Brno University of Technology, Faculty of Chemistry, Materials Research Centre, Purkyňova 118, 612 00 Brno, Czech Republic
xcbilekv@fch.vutbr.cz, bilek@fch.vut.cz

Prejem rokopisa – received: 2015-06-29; sprejem za objavo – accepted for publication: 2015-10-26

doi:10.17222/mit.2015.133

This study is aimed at reducing the drying shrinkage of alkali-activated slag (AAS) through the use of low-calcium fly ash (FA) and commercially available shrinkage-reducing additives (SRAs) originally developed for OPC-based binders, since there are no such admixtures tailored for AAS systems. Generally, all the SRAs tested are based on modified alcohols. All the mortars were based on slag activated by waterglass, with the water-to-slag ratio equal to 0.40 and the sand-to-binder ratio 2:1. In the first step, the effect of the partial replacement of slag by FA (25, 50 and 75) % of mass fractions on the drying shrinkage and compressive strength was investigated. On the basis of the obtained results a mortar with 50 % FA in the binder was chosen for subsequent experiments, where the influence of three types of SRAs on the drying-shrinkage behaviour was examined. It was observed that while 25 % of the FA did not affect the drying shrinkage significantly, 50 % and 75 % of FA in the binder decreased the drying shrinkage by 57 % and 78 %, respectively. However, with an increasing content of FA, the compressive strength markedly decreased. All the tested SRAs had a similar effect on the drying shrinkage of the slag/fly ash (50/50) mortar: at a dose of 0.50 % (by mass of slag) the shrinkage was reduced only slightly, whereas 1.0–3.0 % of SRA resulted in a decrease by 49–66 %. Also, the drying shrinkage rate during the first days of drying was modified. However, all the SRAs reduced the compressive strength as compared to the neat slag-FA mortar, especially when the doses were higher than 0.50 %.

Keywords: alkali-activated slag, fly ash, shrinkage reducing additives, shrinkage, strength

Namen študije je zmanjšanje krčenja pri sušenju z alkalijami aktivirane žlindre (AAS) z uporabo letečega pepela (FA), z majhno vsebnostjo kalcija in komercialno dostopnega dodatka za zmanjšanje krčenja pri sušenju (SRA), originalno razvitega za veziva na osnovi OPC, ker do sedaj ni bilo takega dodatka primernega za AAS sisteme. Na splošno so vsi preizkušeni SRA temeljili na modificiranih alkoholih. Vse malte so bile iz žlindre, aktivirane z vodnim steklom, z razmerjem voda:žlindra (0,40) in pesek:vezivo v razmerju 2:1. Na prvi stopnji je bil preiskovan vpliv delne nadomestitive žlindre s FA (25, 50 in 75) % masnih odstotkov, na krčenje pri sušenju in na tlačno trdnost. Na osnovi dobljenih rezultatov je bila za nadaljevanje preizkusov izbrana malta s 50 % FA v vezivu, kjer se je preiskoval vpliv treh vrst SRA na skrček pri sušenju. Opaženo je bilo, da medtem ko 25 % FA ni vplivalo pomembno na skrček pri sušenju, je 50 % in 75 % FA v vezivu, zmanjšalo skrček pri sušenju za 57 % oziroma 78 %. Vendar pa se je z naraščajočim deležem FA tlačna trdnost opazno zmanjšala. Vse preizkušene SRA so imele podoben vpliv na krčenje pri sušenju malte, z razmerjem žlindra:leteči pepel (50:50), pri količini 0,50 % (masa:žlindra) se je skrček zmanjšal samo delno, medtem ko se je pri 1,0–3,0 % SRA skrček zmanjšal za 49–66 %. V prvih dneh se je spremenila tudi hitrost krčenja pri sušenju. Vendar pa je SRA zmanjšala tlačno trdnost, v primerjavi z maltami iz žlindre in FA, še posebno, če sta bila njuna deleža večja od 0,5 %.

Ključne besede: z alkalijami aktivirana žlindra, leteči pepel, dodatki za zmanjšanje krčenja, skrček, trdnost

1 INTRODUCTION

Concretes based on Portland cement (PC) provide a very good mechanical performance for arelatively low cost. Besides some durability problems that may occur, PC production is connected with the significant emissions of greenhouse gases such as CO_2 and NO_x and a high energy consumption. It is estimated that the PC industry contributes 7 % to the global CO_2 emissions. The utilization of some industrial wastes or by-products such as blast-furnace slag (BFS) and fly ash (FA) may be a possible way to partially solving the above-mentioned problems. BFS and/or FA can be activated by an alkaline activator to formulate so-called alkaline cements with similar or even better properties than PC-based materials.[1]

Alkali-activated slag (AAS), especially when the activator is waterglass, shows similar mechanical properties to PC-based materials.[2] However, a high shrinkage, leading to cracking, usually occurs,[3] which is considered to be the most serious complication for the use of AAS in practice.[4] The fact that the drying shrinkage of AAS concrete is several times higher thana that of PC-based concrete is often associated with a higher mesopore volume in the AAS matrix, which results in substantial capillary tensile forces at the water-air meniscii and the material shrinks.[5]

One possible way to mitigate shrinkage is the use of shrinkage-reducing admixtures (SRAs). Generally, SRAs belong to the group of chemical substances called surfactants. The molecules of surfactants are composed of a polar head (ionic or non-ionic) and a non-polar tail. Considering the water-vapour interface, the polar head is attracted to the water phase, while the non-polar tail is oriented towards the gaseous phase, which means that surface tension is reduced and thus the capillary stresses decreas.[6] On the other hand, there are several doubts about the importance of surface tension and capillary stresses on shrinkage. For example, F. Wittmann[7] stated that even a significant reduction in the surface tension of the pore solution did not noticeably affect the shrinkage of a cementitious system and found the disjoining pressure to be more important. Also, M. J. Setzer[8] emphasized the role of the disjoining pressure and changes in the surface energy. Nevertheless, SRAs are successfully used in concrete production and a reduction in shrinkage of up to 50 % was reported.[6]

A limited number of studies concerning the use of SRAs in AAS are available. C. Bilim et al.[9] and also M. Palacios and F. Puertas[10] reported a reduction in shrinkage through the use of an SRA based on polypropylene glycol, especially in the case of moist curing. T. Bakharev et al.[11] achieved a lower shrinkage thanks to some non-standard SRA and also when using some air-entraining agent.

2 EXPERIMENTAL WORK

2.1 Materials and sample preparation

Ground granulated BFS with specific surface area of 400 m^2/kg was used as a reference binder and siliceous sand as a fine aggregate. The sand-to-binder ratio was 2:1. The BFS was activated by liquid sodium silicate with a SiO_2/Na_2O ratio of 1.85 at the doses of 4.2 % by binder mass. The water-to-binder ratio was 0.40.

In the first series the BFS was partially replaced by low-calcium FA. The weight ratios of the S/FA were 100/0 (marked as *S*), 75/25 (FA25), 50/50 (FA50) and 25/75 (FA75). The mortar FA50 was additionally modified using three commercially available SRAs in doses of 0.50, 1.0, 2.0 and 3.0 % by mass of BFS + FA. Based on the safety data sheets, these SRAs were generally a mixture of alcohols and glycols. The first one (A) was a mixture of 5-ethyl-1,3-dioxane-5-methanol, 2-ethylpropane-1,3-diol and 2-ethyl-2-(hydroxymethyl)propane-1,3-diol, the second one (B) was based on 2,2-dimethylpropane-1,3-diol and 2-butylaminoethanol and the third one (C) consisted mainly of 2-methoxymethylenoxy propanol and propane-1,2-diol.

At the beginning of the mixing procedure, all the liquid components were combined and the BFS + FA were added. After 30 s of mixing the sand was added. The total mixing procedure took 4 min. Then the fresh mortar was cast into the moulds. After 24 h of moist curing, the specimens were de-moulded and the strength or shrinkage testing followed.

2.2 Compressive strength testing

In the case of the first series (BFS partially replaced by FA), the compressive strength was tested on broken parts of the specimens (from the three-point bending test) with the dimensions 20 mm × 20 mm × 100 mm, while the influence of the different dosages of SRAs was studied on broken parts of the specimens with the dimensions 40 mm × 40 mm × 160 mm. All these tests were performed for 24 h, 7 d and 28 d after the mixing. After their de-moulding, all the specimens were submerged in water until the start of the test.

2.3 Shrinkage tests

The drying shrinkage was measured as length changes on the basis of the procedure described in ASTM C596. After the de-moulding the specimens were immersed in water, in which they were stored for 3 d. Then they were taken out to the laboratory conditions (approximately 50 % relative humidity and 23 °C), their surfaces were dried with a wet towel and measurements of their length changes began. Also, their mass changes during drying were measured and evaluated.

3 RESULTS

The results obtained for the first series, i.e., the influence of the partial replacement of BFS by FA on the compressive strength development, the drying shrinkage and the mass changes during drying, are presented in **Figures 1** to **3**, respectively. On the basis of these data, the mortar FA50 with a relatively low drying shrinkage and a concurrently satisfactory compressive strength was

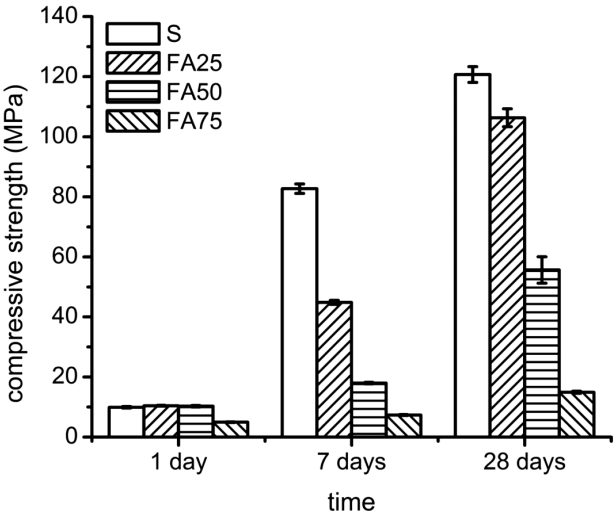

Figure 1: Effect of fly ash on the compressive strength of alkali-activated slag mortar

Slika 1: Vpliv letečega pepela na tlačno trdnost malte iz z alkalijami aktivirane žlindre

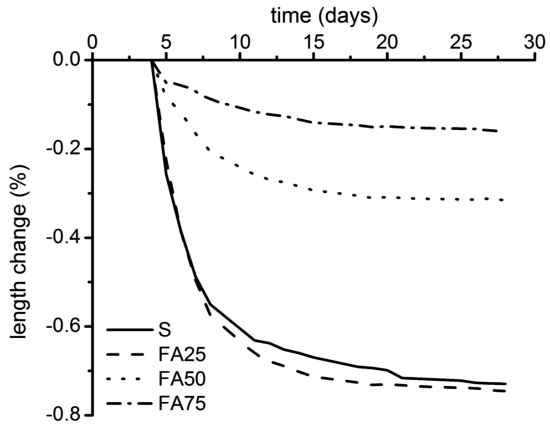

Figure 2: Effect of fly ash on the drying shrinkage of alkali-activated slag mortar
Slika 2: Vpliv letečega pepela na skrček pri sušenju malte iz z alkalijami aktivirane žlindre

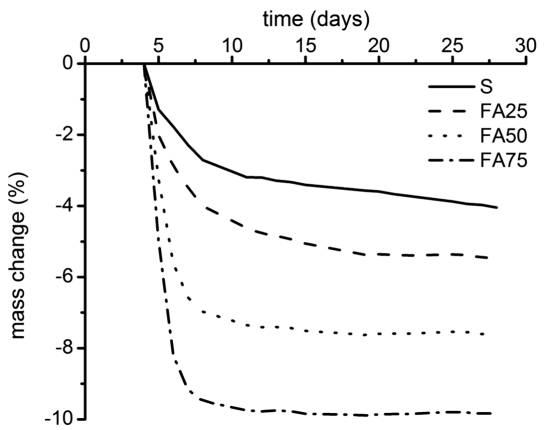

Figure 3: Effect of fly ash on the mass changes during drying of alkali-activated slag mortar
Slika 3: Vpliv letečega pepela na zmanjšanje mase med sušenjem malte iz z alkalijami aktivirane žlindre

chosen for further experiments, where the effect of different dosages of different SRAs on the compressive strength (**Table 1**), the drying shrinkage (**Figure 3**) and the mass loss during drying (**Figure 4**) was investigated. In order to compare the compressive strengths of the mortars containing SRAs with the reference mortar FA50 by using the specimens of the same dimensions, the FA50 mortar was prepared once more. Thus, the designation R for the FA50 mortar was used in the second part of this study.

4 DISCUSSION

As can be seen from **Figures 1** and **2**, the partial replacement of the BFS in the binder by FA led to a gradual decrease in the compressive strength, but also to a significant shrinkage reduction in the case of mortars with 50 % and 75 % of FA in the binder. These results correspond with those reported by M. Marjanović et al.[12], where the compressive strength of mortars with a predominant content of BFS in the binder were significantly higher than those with a predominant content of FA. Also, the slightly higher shrinkage of the mortar with a BFS/FA ratio of 75/25 than that of the 100/0 mortar was recorded in the same study. The increasing content of FA led to a substantial increase in the mass loss during the drying process under laboratory conditions, as can be seen from **Figure 3**. This could imply that a smaller quantity of hydration products was formed in the specimens with higher doses of FA, because the alkali activation of FA is generally favoured by an elevated temperature and a larger amount of Na_2O in the mixture.[12] Moreover, the main hydration product of FA activation, the N-A-S-(H) phase, does not chemically bind water,[13] which may also affect the mass changes during drying.

Table 1 shows the impact of SRAs on the compressive strength on the reference mortar R, whose composition was the same as the mortar FA50. The difference was only in the size of the specimens for compressive strength testing, as stated in Section 2.2. However, similar results for the compressive strength were obtained, when compared **Table 1** and **Figure 2**. Regardless of the type of SRA used, the compressive strength of the reference mortar was markedly reduced when SRAs were applied. Generally, the compressive strength decreased with the increasing dose of SRAs. The exception was the mortar with 3 % of SRA C, where a noticeably higher strength than that of the mortars with 1 % and 2 % of this additive were observed during the whole testing period.

The effect of SRAs on drying shrinkage of the reference mortar is shown in **Figure 4**. It is clear that all the SRAs tested modified the drying shrinkage development in a similar way. If only 0.5 % of SRA was used, the drying shrinkage slightly decreased, while a significant decrease in shrinkage was observed when the dose of SRA was raised from 0.5 % to 1.0 %. A further increase in the SRA dosage only led to a minor decrease in the drying shrinkage. A noticeably different situation was observed for the mass loss during the drying of these mortars (**Figure 5**), which exhibited a rather gradual

Table 1: Effect of SRAs (A, B, C) on the compressive strength development (in MPa) of alkali-activated BFS/FA 50/50 (*R*) mortar
Tabela 1: Vpliv SRA (A, B, C) na razvoj tlačne trdnosti malte BFS/FA 50/50 (R), aktivirane z alkalijami

Mixture	*R*	A				B				C			
SRA dose (%)	0	0.5	1.0	2.0	3.0	0.5	1.0	2.0	3.0	0.5	1.0	2.0	3.0
1 d	8.1	4.4	5.0	–	–	4.7	3.0	–	–	4.1	3.8	1.2	5.7
7 d	16	9.9	9.1	2.7	1.5	11	5.7	2.4	1.9	7.9	5.7	4.0	11
28 d	54	40	16	3.6	2.8	44	19	2.2	2.2	40	7.6	4.2	14

increase in the mass loss with the increasing content of SRAs. The reason for such an increase in the mass loss is likely to be associated with some retardation effect of all the SRAs used on the hydration of alkali-activated BFS/FA mortars, which is indicated by its compressive strength development. The SRAs also modified the shrinkage rate during the first days of drying, where a significant reduction as compared with the reference mortar was observed. After this the period of most intensive shrinkage followed, while since approximately the 10th day of exposure to a dry climate, all the mortars had almost the same shrinkage profile.

Although its porosity was not measured, we can expect a significant decrease in the amount of hydration products of the mortars containing 1.0 % and more SRA and therefore a higher volume of larger pores filled with easily evaporable water before the start of the drying. This raises considerable doubts about the compatibility

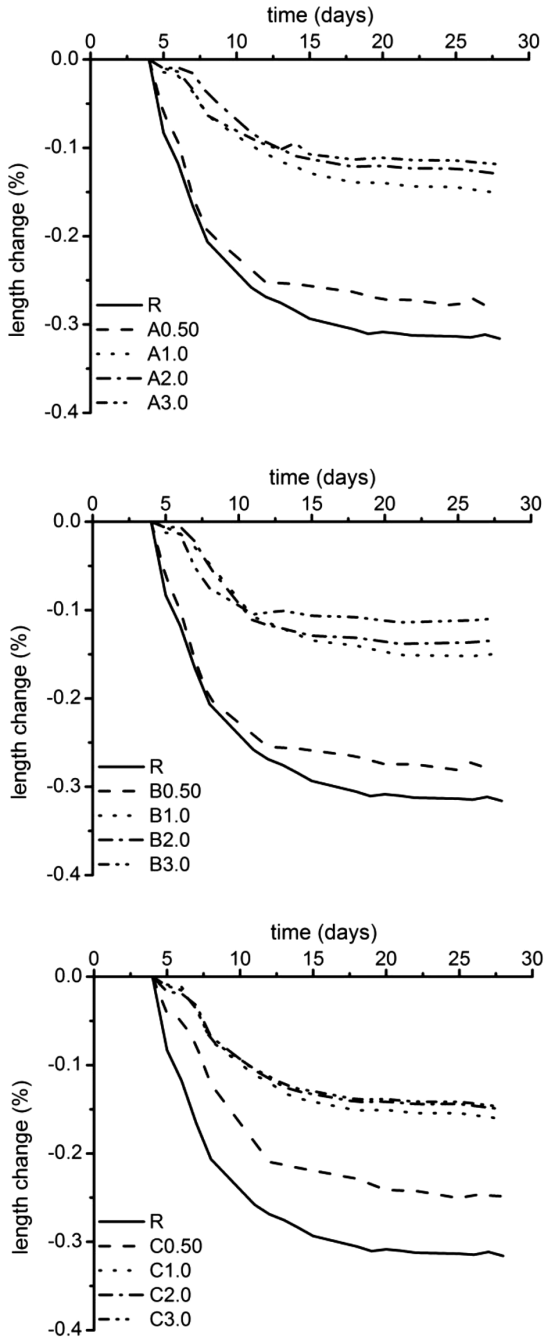

Figure 4: Effect of SRAs (A, B, C) on the drying shrinkage of alkali-activated BFS/FA 50/50 (R) mortar

Slika 4: Vpliv SRA (A, B, C) na krčenje pri sušenju malte BFS/FA 50/50 (R), aktivirane z alkalijami

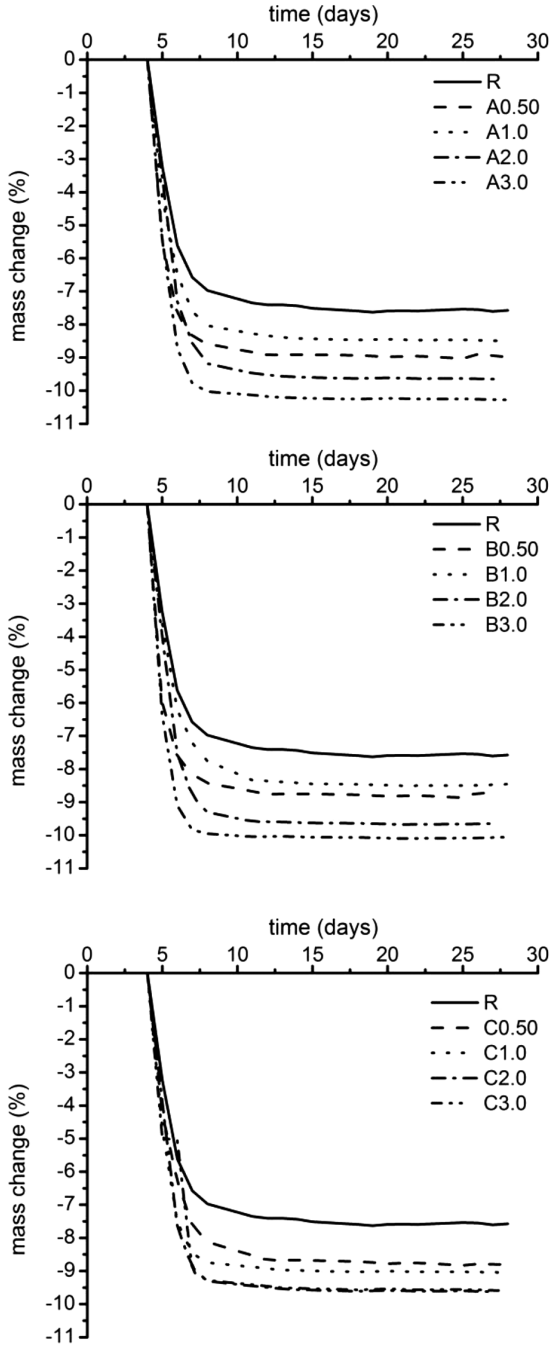

Figure 5: Effect of SRAs (A, B, C) on the mass loss of alkali-activated BFS/FA 50/50 (R) mortar during drying

Slika 5: Vpliv SRA (A, B, C) na zmanjšanje mase pri sušenju malte BFS/FA 50/50 (R), aktivirane z alkalijami

of the tested SRAs with the studied alkali-activated system. Some of the authors mentioned in the introduction achieved a significant reduction of the drying shrinkage without any significant changes in the AAS hydration, but they used SRAs based on polypropylene glycol, while the SRAs used in this study mainly comprised low-molecular-weight diols.

5 CONCLUSIONS

This paper looks at the possibilities of drying-shrinkage reduction for mortars based on AAS by FA and SRAs. The compressive strength and mass changes during the drying were also evaluated. From the results obtained it can be concluded that despite a certain strength decrease the FA can be successfully used for the shrinkage reduction of AAS. Considering both the compressive strength and the drying shrinkage, the mortar with the ratio of BFS/FA 50/50 seems to be the most favourable FA. A further decrease in the shrinkage of this mortar was achieved through the application of commercial SRAs based mainly on diols and designed for Portland-cement-based systems. However, all these SRAs had a very negative impact on the compressive-strength development, which makes them unsuitable for the studied alkali-activated BFS/FA system.

Acknowledgement

This outcome was achieved with the financial support by the project: Materials Research Centre at FCH BUT-Sustainability and Development, REG LO1211, with financial support from National Programme for Sustainability I (Ministry of Education, Youth and Sports).

6 REFERENCES

[1] A. Férnandez-Jiménez, A. Palomo, D. Revuelta, Alkali activation of industrial by-products to develop new earth-friendly cements, Proc. of the 11th Inter. Conf. on Non-Conventional Materials and Technologies Bath, UK 2009, 1–15

[2] F. Puertas, M. Palacios, H. Manzano, J. S. Dolado, A. Rico, J. Rodríguez, A Model for the C-A-S-H gel Formed in Alkali-Activated Slag Cements, Journal of the European Ceramic Society, 31 (**2011**), 2043–2056, doi:10.1016/j.jeurceramsoc.2011.04.036

[3] F. G. Collins, J. G. Sanjayan, Cracking tendency of alkali-activated slag concrete subjected to restrained shrinkage, Cement and Concrete Research, 30 (**2000**), 791–798, doi:10.1016/S0008-8846(00)00243-X

[4] A. A. M. Neto, M. A. Cincotto, W. Repette, Drying and autogenous shrinkage of pastes and mortars with activated slag cement, Cement and Concrete Research, 38 (**2008**), 565–574. doi:10.1016/j.cemconres.2007.11.002

[5] F. Collins, J. G. Sanjayan, Effect of pore size distribution on drying shrinking of alkali-activated slag concrete, Cement and Concrete Research, 30 (**2000**), 1401–1406, doi:10.1016/s0008-8846(00)00327-6

[6] F. Rajabipour, G. Sant, W. J. Weiss, Interactions Between Shrinkage Reducing Admixtures (SRA) and Cement Paste's Pore Solution, Cement and Concrete Research, 38 (**2008**), 606–615, doi:10.1016/j.cemconres.2007.12.005

[7] F. Wittmann, Heresies On Shrinkage And Creep Mechanisms (Keynote Lecture), Proc. of the Eighth International Conference on Creep, Shrinkage and Durability of Concrete and Concrete Structures (CONCREEP 8), London 2009, 3–10, doi:10.1201/9780203882955.pt1

[8] M. J. Setzer, The solid-liquid gel-system of hardened cement paste, Proc. of the Eighth International Conference on Creep, Shrinkage and Durability of Concrete and Concrete Structures (CONCREEP 8), London 2009, 237–243, doi:10.1201/9780203882955.ch28

[9] C. Bilim, O. Karahan, C. D. Atiş, S. İlkentapar, Influence of admixtures on the properties of alkali-activated slag mortars subjected to different curing conditions, Materials and Design, 44 (**2013**), 540–547, doi:10.1016/j.matdes.2012.08.049

[10] M. Palacios, F. Puertas, Effect of shrinkage-reducing admixtures on the properties of alkali-activated slag mortars and pastes, Cement and Concrete Research, 37 (**2007**), 691–702, doi:10.1016/j.cemconres.2006.11.021

[11] T. Bakharev, J. G. Sanjayan, Y. B. Cheng, Effect of Admixtures on Properties of Alkali-Activated Slag Concrete, Cement and Concrete Research, 30 (**2000**), 1367–1374, doi:10.1016/S0008-8846(00)00349-5

[12] N. Marjanović, M. Komljenović, Z. Baščarević, V. Nikolić, R. Petrović, Physical-mechanical and microstructural properties of alkali-activated fly ash–blast furnace slag blends, Ceramics International, 41 (**2015**), 1421–1435, doi:10.1016/j.ceramint.2014.09.075

[13] J. L. Provis, R. J. Myers, C. White, V. Rose, J. S. J. Van Deventer, X-ray Microtomography Shows Pore Structure and Tortuosity in Alkali-Activated Binders, Cement and Concrete Research, 42 (**2012**), 855–864, doi:10.1016/j.cemconres.2012.03.004

UDK 620.168:621.926:678.077
Professional article/Strokovni članek

ISSN 1580-2949
MTAEC9, 50(5)819(2016)

CUTTING-TOOL PERFORMANCE IN THE END MILLING OF CARBON-FIBER-REINFORCED PLASTICS

ZMOGLJIVOST REZILNEGA ORODJA PRI REZKANJU PLASTIKE, OJAČANE Z OGLJIKOVIMI VLAKNI

Ondřej Bílek, Soňa Rusnáková, Milan Žaludek

Faculty of Technology, TBU Zlín, Nám. T.G.M 5555, 760 01 Zlín, Czech Republic
bilek@ft.utb.cz

Prejem rokopisa – received: 2015-06-30; sprejem za objavo – accepted for publication: 2015-09-09

doi:10.17222/mit.2015.153

Carbon-fiber-reinforced plastics (CFRPs) are no longer the exclusive domain of aerospace industries and nowadays find more applications in the automotive and consumer industries. The growing volume of these materials increases the need for their efficient machining. However, the machinability of CFRPs is a rather complex task due to the heterogeneity and the considerable number of parameters influencing the cutting process. The cutting tool has long been recognized as an important factor influencing both surface quality and dimensional accuracy. Hence, in this paper, tool performance is investigated in the end milling of CFRPs. The effect of tool geometry and coatings on the cutting forces, dimensional accuracy and surface quality were experimentally examined for side and slot milling.

Keywords: CFRP, composites, end mill, surface quality, cutting forces

Plastika, ojačana z ogljikovimi vlakni (CFRP), dosedaj ekskluzivna domena letalske industrije, se v zadnjem času bolj pogosto uporablja tudi v strojništvu, v avtomobilski industriji in v potrošništvu. Z naraščanjem uporabe teh materialov, narašča tudi potreba po učinkoviti strojni obdelavi. Vendar pa je strojna obdelava CFRP-a precej kompleksna naloga zaradi heterogenosti in številnih parametrov, ki vplivajo na proces rezanja. Že dolgo je znano, da je rezilno orodje pomemben faktor, ki vpliva na kvaliteto površine in dimenzijsko natančnost. Zato je v članku preiskovana zmogljivost orodja pri rezkanju plastike, ojačane z ogljikovimi vlakni. Pri bočnem in utorovnem rezkanju je bil preiskovan vpliv geometrije orodja in površinske prevleke na sile rezanja, dimenzijsko zanesljivost in na kvaliteto površine.

Ključne besede: CFRP, kompoziti, čelni rezkar, kvaliteta površine, sile rezanja

1 INTRODUCTION

Milling is the key manufacturing operation for the successful machining of fiber-reinforced plastic parts, which ensures dimensional and qualitative requirements. Milling is used, as a rule, as an edge-trimming operation, or a slotting/routing process to produce complex contours.

Composite materials such as carbon fiber-reinforced plastics (CFRPs) are heterogeneous materials composed of dissimilar constituents, where the resulting mechanical properties are more than the sum of the characteristics of the individual components. A plastic matrix of CFRPs is reinforced by carbon fibers entirely, resulting in a high specific strength and stiffness throughout the lifetime of the components, together with electrical and magnetic resistance. This makes them interesting for applications in the automotive and aircraft industries, in railway and ship building, medical applications and the space industry.[1,2]

CFRP composites replace traditional metallic materials; however, their machinability is fundamentally different and the cutting mechanism is still under investigation. The machining properties are influenced by the heterogeneity and anisotropy of the composite material. The mechanical properties of the matrix are strongly

Table 1: Characteristics of the end mill
Tabela 1: Značilnosti steblastih rezkarjev

	Tool cutting zone	Cutting diameter (mm)	Helix angle (°)	Rake angle (°)	Coating
T1	Down-cut spiral with chip-breaker	5.81±0.07	15	0	PCD
T2	Four flute up-cut spiral	5.96±0.02	10	6	PCD
T3	Cross-pitch spiral	5.92±0.01	25 and 27	7	PCD
T4	Cross-pitch spiral	5.91±0.02	25 and 27	7	uncoated
T5	Up-cut spiral with chip-breaker	5.96±0.03	47	10	Multilayered
T6	Right- and left-hand spiral	5.94±0.02	13	30	Multilayered
T7	Cross-pitch spiral	5.97±0.02	10	0	PCD
T8	Three flute upcut spiral	5.91±0.03	15	30	PCD

temperature dependent, while the carbon fibers can withstand temperatures up to 3000 °C, and during machining cause considerable tool wear.[3]

Machining CFRPs brings with it certain difficulties, such as layer delaminations, fiber pull-out, uncut fibers, degradation and burning of the plastic matrix.[4–7] Tool manufacturers and scientists recommend carbide tools with a polycrystalline diamond (PCD) coating for CFRP material machining. These tools ensure high productivity with a sufficient tool life. Unfortunately, the cost of PCD tools is six times higher than uncoated tools, whereas tool life is only three times longer.[8] End mills usually have a very special design suitable for the milling of CFRPs.[9] Helical end mills with two flutes are suitable for rigid or back-supported parts.[10] Compression end mills with two sets of left-hand and right-hand flutes limit the delamination and burrs on the cut edges.[11] Furthermore, the machining of flexible parts by multi-tooth end mills eliminates the cutting force along the *Z*-axis, thereby reducing the deflection and vibration of the part.[8] In-between are helical mills with a chip-breaker geometry[12] that shears fibers and shortens chips with the simultaneous reduction of vibrations.

In this work we compare the performance of end mills on the resulting surface quality, dimensional accuracy and cutting forces in the slotting and side milling of CFRPs.

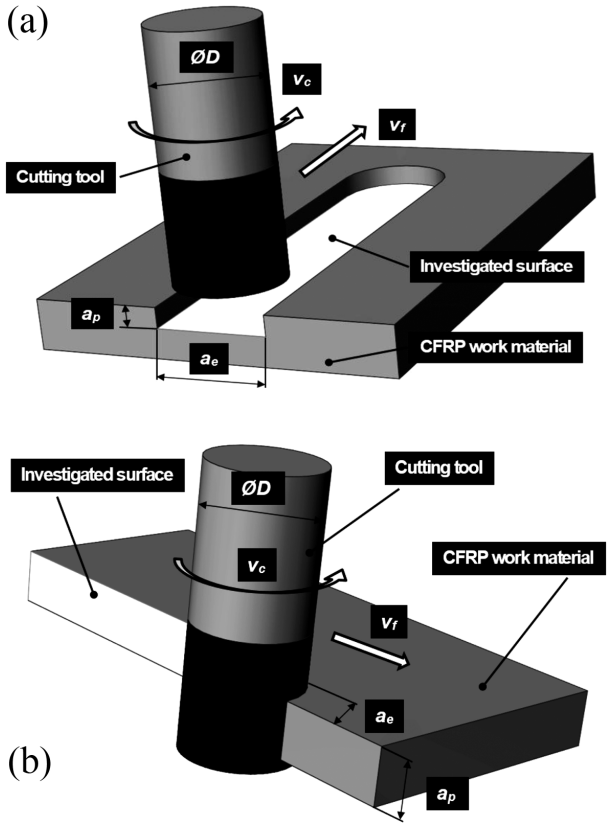

Figure 1: a) slot milling and b) side milling
Slika 1: a) rezkanje utora in b) bočno rezkanje

2 EXPERIMENTAL PROCEDURE

The composite samples used in the experimental investigation were produced by vacuum infusion technology. The carbon fiber and the epoxy were supplied by KORDCARBON CZ. The fabric was Toray HS 3K 200 tex, a balanced twill bidirectional (0–90°) weave and 380 μm thick. The epoxy used in the fabrication was the commercially available Havel L285 epoxy system.

Fourteen layers of fabric were used to fabricate the work samples with an average thickness of 4 mm. Overall, the CFRP composite average flexure strength was 501 MPa, the modulus of elasticity was 43,300 GPa and the tensile strength was 378 MPa.

The experiment was carried out by using eight carbide end mills acquired from different producers (SECO, WNT, KTOOLS). The required tool cutting diameter was 6 mm. In this article the end mills are referred to as T1-T8 and were concerned for special applications such as the milling of composites with a wide range of compositions. Their geometry is summarized in **Table 1**. Except for the T4 tool, the end mills were coated to withstand the machining of a highly abrasive work material.

A CNC milling machine C-442 HWT with a 1.0-kW spindle power and high-speed spindle of 416.16 Hz was used to perform the experiments. Part of the program was created to ensure the repeatability and accuracy of the experiment. The machining was divided into two consecutive methods, first slot milling (**Figure 1a**) and next upcut side milling (**Figure 1b**) of the CFRP work material. The machining conditions are given in **Table 2** for both methods. A coolant was not used and the tool cutting length was 150 mm in both methods. A tool-wear evaluation was carried out at the end of every set of experiments. First, each tool was milling a slot and subsequently a side of work material, so that the tool displacement towards the bottom surface of the work material was 2 mm.

Table 2: Cutting conditions
Tabela 2: Pogoji rezanja

Method	Cutting speed v_c (m/min)	Feed rate v_f (mm/min)	Depth of cut a_p (mm)	Width of cut a_e (mm)
Slot milling	100	550	1.25	$a_e = D$
Side milling	100	550	2.0	4.0

Cutting forces were measured on the strain-gauge dynamometer in the direction of the feed-rate vector (force *Ff*) and perpendicularly to *Ff* (force *Ffn*). The signal from dynamometer was processed by a Spider8 data-acquisition system and the evaluations were made through a PC with Conmes Spider software, as illustrated in **Figure 2**.

The dimensional accuracy of the machined slot was evaluated using a Mitutoyo caliper. The surface quality was measured with a portable surface-roughness tester Mitutoyo SJ-301, according to ISO 4287 on the high-

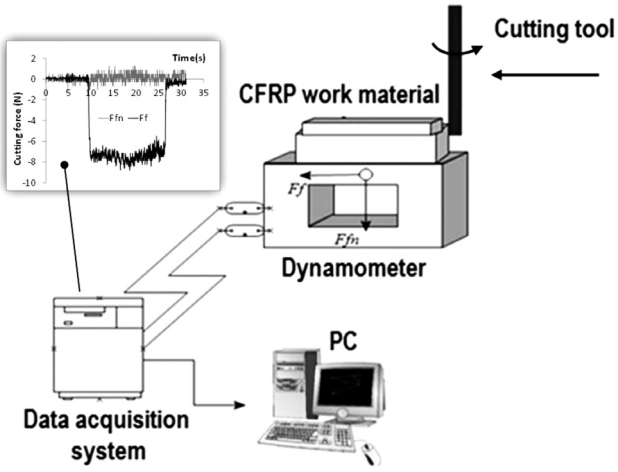

Figure 2: Experimental set up for milling CFRPs
Slika 2: Eksperimentalni sestav za rezkanje CFRP

lighted areas at the bottom of the slot (**Figure 1a**) and the side surface (**Figure 1b**). The measurements repeated were 15 times at different surface locations in the direction of the feed-rate vector that was identified as the direction of highest roughness. The roughness parameter *Ra* was considered as an evaluation parameter for the surface quality according to ISO.

3 RESULTS AND DISCUSSION

3.1 Cutting forces

All the force measurements were worth a maximum of 4.86 % of variance. The results were graphically summarized in **Figure 3** and **4**. There is a significant difference between the end mills, moreover not the only one is suitable both as side and slot milling. Tool T6 with right- and left-hand spirals reached the lowest values *Ff* when slot milling (**Figure 3**) and the second best value as for T4 tool without coating. Higher values of *Ff* and *Ffn* were achieved by the same T3 tool with the coating. This may be due to increased adhesion of work material to the PCD coating material.

Tools T1, T3, T8 keep along the average. Conversely, the highest values of *Ff* achieved tool T2 and T7,

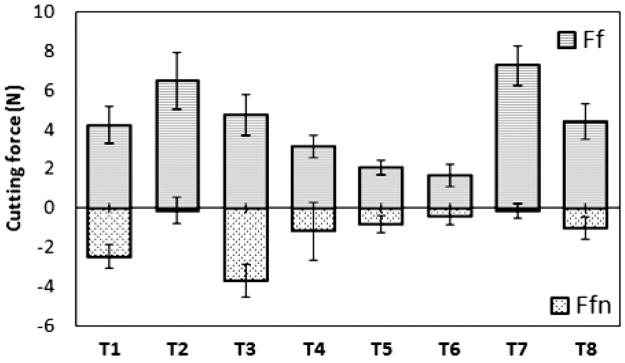

Figure 3: Cutting forces for slot milling of CFRP work material
Slika 3: Sile rezanja pri rezkanju utora v CFRP obdelovanec

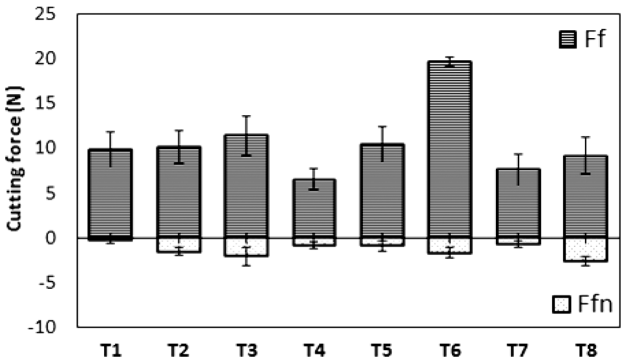

Figure 4: Cutting forces for side milling of CFRP work material
Slika 4: Sile rezanja pri bočnem rezkanju CFRP obdelovanca

although with different flute geometries, but with the same helix angle of 10°, despite the normal force *Ffn* was the lowest one. The helix angle probably improves the chip removal at the bottom of the slot; however, the tool is more power loaded in the feed direction. In the case of higher cutting depths we can expect a higher tool bend, but without a buckling effect.

When side milling, the non-significant *Ffn* force was not evaluated, yet was mentioned in **Figure 4**. The force *Ff* is more than 2 times higher than when slot milling. The smallest *Ff* value comes from the T4 tool without coating, the worst was the T6 tool with a right- and left-hand hand spiral. The reason for this may be in the compression effect of contra-rotating spirals, becoming for these tools. Although the flutes' geometry for the T1, T2, T5 and T8 tools was dissimilar, the feed-force characteristics were almost identical and quite balanced.

3.2 Surface roughness

The dynamometric investigation was followed by surface-roughness measurements of the R_a parameter.

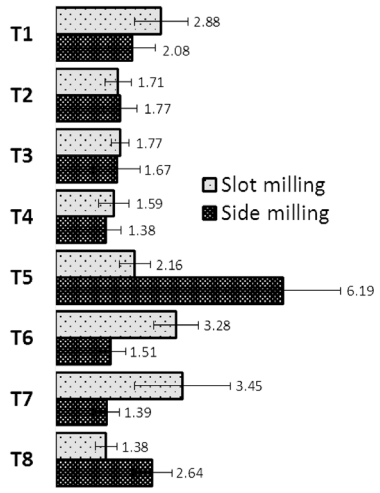

Figure 5: Surface roughness R_a for slot and side milling
Slika 5: Hrapavost površine R_a pri rezkanju utora in pri bočnem rezkanju

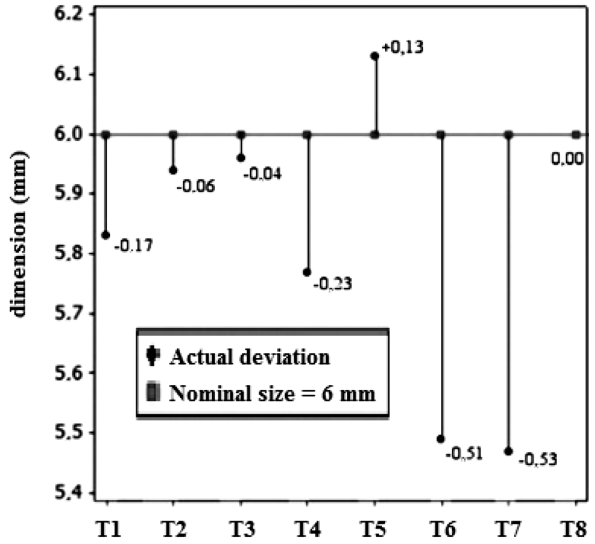

Figure 6: Dimensional accuracy of the width of the slot
Slika 6: Dimenzijska natančnost širine utora

The results are shown in **Figure 5** for the side and slot milling.

The lowest average value of R_a = 1.38±0.40 μm was on the side surface made by the uncoated T4 tool and the same value R_a = 1.38±0.29 μm is at the bottom of the slot by the T8 tool. The T5 tool had the highest and most unsatisfactory effect for side milling, where the roughness value was R_a = 6.19±1.57 μm. It is the only tool with an upcut spiral in the experiment and is actually a production tool recommended for rough machining. Approximately half values of R_a = 3.45±1.30 μm, but highest for slot milling, was made with the cross-pitched T7 tool with a 0° rake angle.

3.3 Dimensional accuracy

Since end mills should have a 6 mm diameter, it was expected that the resulting dimension of the slot would be given with a certain accuracy close to that value. As it turned out, this was not entirely true for slot milling of CFRP work material, as can be seen in **Figure 6**.

In most cases, the resulting dimension of the slot is smaller than the desired nominal size. On the one hand, it could be given by the true tool diameter (**Table 1**) that was smaller than the producer specification. In contrst, for the T5 tool with an upcut spiral we found that the slot was about 0.13 mm wider. This excludes the eventuality that a smaller tool diameter was made on purpose, taking into account the CFRP material's behavior. Finally, the T8 tool made it possible to achieve a superior slot accuracy, but otherwise lagged behind in terms of cutting efficiency and surface quality.

4 CONCLUSIONS

In this work the cutting performance of the end mills in the CFRPs milling has been presented, taking into account the force, surface roughness and dimensional measurements. After the testing of eight end mills several conclusions can be drawn:

- an upcut spiral can cause considerably worse surface quality together with an increment of the slot dimension,
- PCD-coated tools for CFRPs machining has a lower cutting efficiency due to a different friction characteristic than the uncoated tools,
- tools with left-hand and right-hand spirals recommended for side milling, result in up to twice the cutting force,
- to ensure compliance with the required dimensions, accuracy and stability it is necessary to include an offset (by part program, cutting conditions, thermal field) for the CFRPs tool individually.

5 REFERENCES

[1] E. Uhlmann, F. Sammler, S. Richarz, F. Heitmüller, M. Bilz, Machining of Carbon Fibre Reinforced Plastics, Procedia CIRP, 24 (**2014**), 19–24, doi:10.1016/j.procir.2014.07.135

[2] S. Rusnakova, L. Fojtl, M. Zaludek, V. Rusnak, Design of material composition and technology verification for composite front end cabs, Manufacturing Technology, 14 (**2014**), 607–611

[3] O. Pecat, R. Rentsch, E. Brinksmeier, Influence of milling process parameters on the surface integrity of CFRP, Procedia CIRP, 1 (**2012**), 466–470, doi:10.1016/j.procir.2012.04.083

[4] M. H. El-Hofy, S. L. Sooa, D. K. Aspinwalla, W. M. Simb, D. Pearsonc, P. Hardend, Factors affecting workpiece surface integrity in slotting of CFRP, Procedia Eng., 19 (**2011**), 94–99, doi:10.1016/j.proeng.2011.11.085

[5] W. Hintze Wolfgang, D. Hartmann, C. Schütte, Occurrence and propagation of delamination during the machining of carbon fibre reinforced plastics (CFRPs) - An experimental study, Compos. Sci. Technol., 71 (**2011**), 1719–1726, doi:10.1016/j.compscitech.2011.08.002

[6] Y. Karpat, O. Bahtiyar, B. Deer, Mechanistic force modeling for milling of unidirectional carbon fiber reinforced polymer laminates, Int. J. Mach. Tools Manuf., 56 (**2012**), 79–93, doi:10.1016/j.ijmachtools.2012.01.001

[7] R. Teti, Machining of Composite Materials, CIRP Annals – Manufacturing Technology, 51 (**2002**), 611–634, doi:10.1016/S0007-8506(07)61703-X

[8] L. N. López de Lacalle, A. Lamikiz, F. J. Campa, A. Fdz. Valdivielso, I. Etxeberria, Design and Test of a Multitooth Tool for CFRP Milling, J. Compos. Mater., 43 (**2009**), 3275–3290, doi:10.1177/0021998309345354

[9] Y. G. Wang, X. P. Yan, X. G. Chen, C. Y. Sun, G. Liu, Cutting Performance of Carbon Fiber Reinforced Plastics Using PCD Tool, Advanced Materials Research, 215 (**2011**), 14–18, doi:10.4028/www.scientific.net/AMR.215.14

[10] J. P. Davim, P. Reis, Damage and dimensional precision on milling carbon fiber-reinforced plastics using design experiments, J. Mater. Process. Technol., 160 (**2005**), 160–167, doi:10.1016/j.jmatprotec.2004.06.003

[11] P. Masek, P. Zeman, Effective milling of composites with thermoplastic matrix, MM Prumyslove spektrum, 6 (**2013**), 60–64

[12] S. Legutko, G. Krolczyk, J. Krolczyk, Quality evaluation of surface layer in highly accurate manufacturing, Manuf. Technol., 14 (**2014**), 50–56

UDK 620.1:66.017:621.78
Professional article/Strokovni članek

ISSN 1580-2949
MTAEC9, 50(5)823(2016)

INFLUENCE OF SOLIDIFICATION SPEED ON THE STRUCTURE AND MAGNETIC PROPERTIES OF $Nd_{10}Fe_{81}Zr_1B_6$ IN THE AS-CAST STATE

VPLIV HITROSTI STRJEVANJA NA STRUKTURO IN MAGNETNE LASTNOSTI ZLITINE $Nd_{10}Fe_{81}Zr_1B_6$ V LITEM STANJU

Marcin Dośpiał, Marcin Nabiałek

Czestochowa University of Technology, Institute of Physics, Armii Krajowej Av. 19, 42-200 Czestochowa, Poland
mdospial@wp.pl

Prejem rokopisa – received: 2015-07-01; sprejem za objavo – accepted for publication: 2015-09-15

doi:10.17222/mit.2015.174

The paper presents results of the structure and magnetic properties of the $Nd_{10-x}Tb_xFe_{81}Zr_1B_6$ (x = 0, 2) alloy in the as-cast state. The samples were produced using the melt-spinning method. The solidification speed was controlled indirectly by changing the linear velocity of a copper drum. Based on magnetic and structural studies, it was found that samples obtained while the linear velocity of the copper drum was equal to 20 m/s had good hard-magnetic properties. The substitution of 2 % of Nd by Tb led to grain growth of both the α-Fe (9 nm and 24 nm for x = 0 and x = 2) and $Nd_2Fe_{14}B$ phases (41 nm and 70 nm for x = 0 and x = 2, respectively). The grain growth to sizes higher than the exchange interaction distance in the sample with Tb resulted in a bimodal shape of the demagnetization curve. The samples obtained at higher linear speeds of the copper drum were composed of amorphous matrices with small amounts of crystalline phases and had weak, soft-magnetic properties.

Keywords: permanent magnets, nanocomposities, X-ray diffraction, exchange interactions

Članek predstavlja rezultate študije strukturnih in magnetnih lastnosti zlitine $Nd_{10-x}Tb_xFe_{81}Zr_1B_6$ (x = 0, 2) v litem stanju. Vzorci so bili pripravljeni z ulivanjem na hitro vrtečem se valju. Hitrost strjevanja je bila posredno kontrolirana s spreminjanjem linearne hitrosti bakrenega valja. Magnetne in strukturne študije so pokazale, da imajo vzorci, dobljeni pri linearni hitrosti bakrenega valja 20 m/s, dobre trdomagnetne lastnosti. Nadomestilo z 2 % atomskega deleža Nd s Tb, je povzročilo rast zrn obeh faz α-Fe (9 nm in 24 nm pri x = 0 in x = 2) in $Nd_2Fe_{14}B$ (41 nm in 70 nm pri x = 0 in x = 2). Rast zrn, do velikosti, večje od izmenjalne interakcijske razdalje v vzorcu s Tb, se je pokazala v bimodalni obliki demagnetizacijske krivulje. Vzorci, dobljeni pri večjih linearnih hitrostih bakrenega valja, so bili sestavljeni iz amorfne osnove z majhnim deležem kristalnih faz in so imeli slabe mehko magnetne lastnosti.

Ključne besede: permanentni magneti, nanokompoziti, rentgenska difrakcija, izmenjalne interakcije

1 INTRODUCTION

Alloys based on rare earths, iron and boron are currently some of the most popular groups of materials with hard magnetic properties. These materials are widely used in the electro-engineering industry. In recent years, many scientific and industrial units have been carrying out research on methods for curing their magnetic properties.[1–5] The studies were mainly focused on slight modifications to the chemical composition and modifications to the production process parameters.

The most effective process, which guarantees repeatability of the functional properties of produced alloys, is producing amorphous ribbons and then tailoring their properties by an appropriately matched heat treatment.[6] However, the application of the heat treatment generates additional costs. An alternative approach is solidification of the liquid alloy with a slow speed. This leads to a material with hard magnetic properties in the as-cast state. A drawback of this method is the poor repeatability of the functional parameters.

Modifications to the composition by a partial substitution of Nd by Tb can lead to two outcomes: if an excess amount of Tb is used, it can result in the formation of an amorphous matrix dividing the $Nd_2Fe_{14}B$ grains, thereby leading to a higher coercivity and also a significantly reduced remanence;[7,8] if smaller amounts of rare earths with respect to the stoichiometric $Nd_2Fe_{14}B$ composition are used, it may result in the formation of nanocomposites consisting of both $Nd_2Fe_{14}B$ and α-Fe grains. The proper selection of the production process parameters leads to grains of soft magnetic phase with sizes similar or smaller than the exchange-interaction length. This allows obtaining hard magnetic materials with high saturation magnetization and a significant remanence.[8,9]

Motivated by the above idea, we studied the influence of cooling rate on the curing of magnetic properties and the structure of $Nd_{10-x}Tb_xFe_{81}Zr_1B_6$ (x = 0 and x = 2) alloys, in the as-cast state, and the results of the study we report in this paper.

2 EXPERIMENTAL DETAILS

The research material, i.e., $Nd_{10-x}Tb_xFe_{81}Zr_1B_6$ (x = 0, 2) melt, was obtained from components of the following

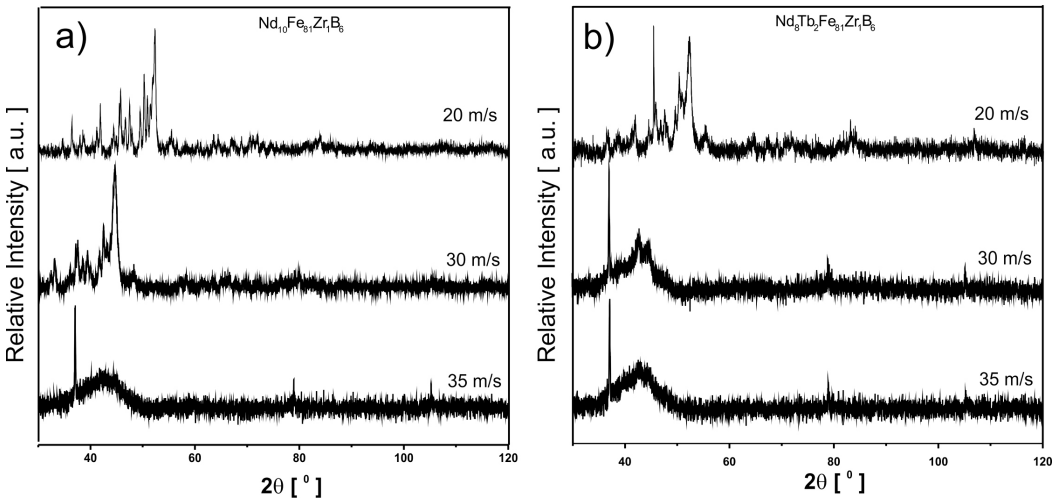

Figure 1: X-ray diffraction patterns of: a) $Nd_{10}Fe_{81}Zr_1B_6$, b) $Nd_8Tb_2Fe_{81}Zr_1B_6$ alloys obtained at different cooling rates, for samples in the as-cast state

Slika 1: Rentgenska difrakcija: a) $Nd_{10}Fe_{81}Zr_1B_6$, b) $Nd_8Tb_2Fe_{81}Zr_1B_6$ zlitin, dobljenih pri različnih hitrostih ohlajanja, za vzorce v litem stanju

purity: Fe – 99.99 %; Zr – 99.99 %; Nd – 99.95 %, Tb – 99.95 %, B – 99.99 %. The crystalline ingots were several times remelted to ensure the best mixing of elements constituting the investigated material. Thin tapes were produced by a unidirectional solidification of liquid metal on a rotating copper cylinder, with three different linear velocities (20, 30 and 35) m/s. The microstructure of the samples, in the as-cast state, was examined using a Bruker D8 Advance X-ray diffractometer with a characteristic Cu-K_α radiation source (0.154056 nm). The samples were scanned in the 2θ angle range from 30° to 120° with a resolution of 0.02° and an exposure time of 3 s per step. Two samples were chosen for further analyses, both qualitative and quantitative. Phase-composition analysis was performed using the Rietveld method. The magnetic studies were performed using a LakeShore vibrating-sample magnetometer in an external magnetic field up to 2 T. The demagnetization coefficient dependent on the shape of the sample was not taken into account. All the measurements were performed at room temperature.

3 RESULTS AND DISCUSSION

Figure 1 shows the X-ray diffraction patterns obtained for $Nd_{10-x}Tb_xFe_{81}Zr_1B_6$ (x = 0, 2) samples in the form of tapes, in the as-cast state.

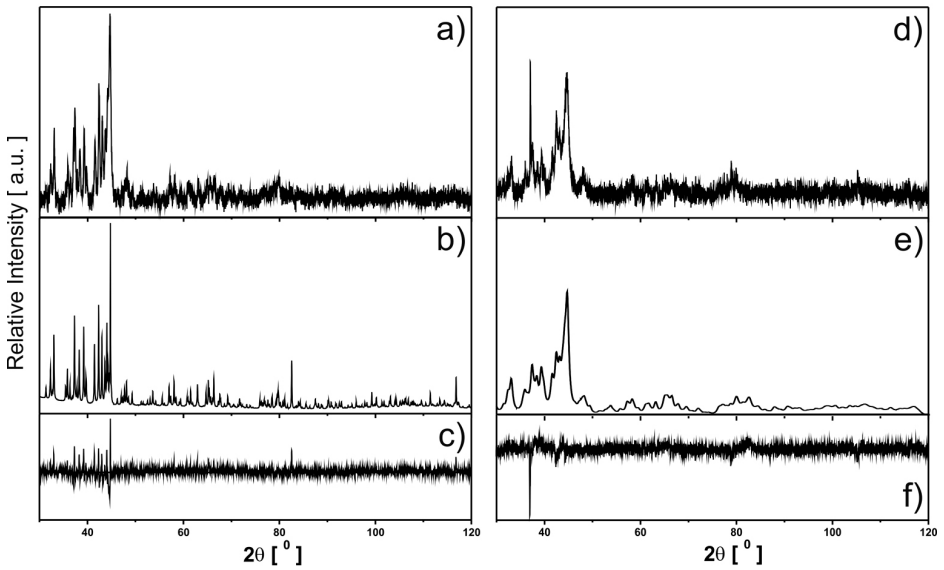

Figure 2: Quantitative match of the phase composition obtained using the Rietveld refinement method for: a), c) $Nd_{10}Fe_{81}Zr_1B_6$, d), f) $Nd_8Tb_2Fe_{81}Zr_1B_6$ alloys solidified at 20 m/s linear velocity of copper drum, where a), d) experimental curve, b), e) matched pattern and c), f) difference plot

Slika 2: Kvantitativno ujemanje sestave faz, dobljene z Rietveldovo metodo izpopolnitve: a), c) $Nd_{10}Fe_{81}Zr_1B_6$, d), f) $Nd_8Tb_2Fe_{81}Zr_1B_6$ zlitini strjeni pri linearni hitrosti bakrenega valja 20 m/s, kjer sta a), d) eksperimentalni krivulji, b), e) ujemanje in c), f) diagram razlik

In all the diffraction patterns obtained for the samples cooled at higher rates, corresponding to the drum linear speeds of 30 m/s and 35 m/s, at a 2θ angle of about 43° a broad, diffused halo characteristic for materials containing an iron-based amorphous phase is present. Also, it is possible to distinguish the presence of narrower peaks originating from small inclusions of crystalline phases. Similar patterns were described in the literature as semi-crystalline structures.[10,11]

The diffraction patterns of the samples solidified at a drum speed of 20 m/s were composed of a number of narrow peaks characteristic for a crystalline structure. In this case, no diffused halo was observed, which indicates the absence of any amorphous phase. A comparison of the experimental diffraction peaks with the EVA database let us conclude that two crystalline phases were present in the sample: α-Fe and $Nd_2Fe_{14}B$. These results are in agreement with other reports concerned on $Nd_2Fe_{14}B$ alloys with an over-stoichiometric iron content.[7,12–13]

To ascertain quantitatively the phase compositions of the samples without an amorphous matrix, Rietveld analysis was performed (**Figure 2**), and the matching results are summarized in **Tables 1** and **2**.

Table 1: The qualitative phase composition of $Nd_{10-x}Tb_xFe_{81}Zr_1B_6$ (where x = 0 or 2) samples solidified with the linear velocity of the copper drum of 20 m/s, determined using the Rietveld refinement method

Tabela 1: Kvalitativna sestava faz $Nd_{10-x}Tb_xFe_{81}Zr_1B_6$, (kjer je x = 0 ali 2), strjenih vzorcev z linearno hitrostjo bakrenega valja 20 m/s, določena z uporabo Rietveldove metode izpopolnitve

Phase composition		
Alloy	α-Fe (% vol)	$RE_2Fe_{14}B$ (% vol)
$Nd_{10}Fe_{81}Zr_1B_6$	19.15	80.85
$Nd_8Tb_2Fe_{81}Zr_1B_6$	19.40	80.60

Table 2: Matching coefficients of the quantitative phase composition of $Nd_{10-x}Tb_xFe_{81}Zr_1B_6$ (where x = 0 or 2) samples solidified with the linear velocity of the copper drum of 20 m/s, determined using the Rietveld refinement method

Tabela 2: Koeficienti ujemanja kvantitativne sestave faze $Nd_{10-x}Tb_xFe_{81}Zr_1B_6$ (kjer je x = 0 ali 2) strjenih vzorcev z linearno hitrostjo bakrenega valja 20 m/s, določeno z uporabo Rietveldove metode izpopolnitve

R – match parameters			
Alloy	R_p	R_{wp}	R_{exp}
$Nd_{10}Fe_{81}Zr_1B_6$	46.11	197.03	0.18
$Nd_8Tb_2Fe_{81}Zr_1B_6$	44.15	192.79	0.11

The average grain size was determined on the basis of Bragg's equation for the 10 and 3 most intense peaks of the $Nd_2Fe_{14}B$ and α-Fe, respectively:[14]

$$\Delta^{hkl}(2\theta)\cdot\cos(\theta_B^{hkl}) = \frac{K\cdot\lambda}{D} + 2\frac{\Delta d}{d}\cdot\sin(\theta_B^{hkl}) \qquad (1)$$

where D is the average grain size, K is a shape factor of 0.89, λ is the X-ray wavelength, and Δ^{hkl} is the half-width of the peak, $\Delta d/d$ is the relative deformation of the crystalline lattice and θ_B^{hkl} is the Bragg angle.

The above-presented equation describes the effect of the grain size and the relative deformation of the crystalline lattice resulting from diffraction-peak broadening. This relationship is linear and the grain size is determined from the intersection of the ordinate axis.

The average grain size of the α-Fe and $Nd_2Fe_{14}B$ phases was 9 nm and 41 nm, respectively, for $Nd_{10}Fe_{81}Zr_1B_6$, and 24 nm and 70 nm for the alloy $Nd_8Tb_2Fe_{81}Zr_1B_6$ for samples solidified at a drum linear velocity of 20 m/s. Due to the low intensity of the peaks originating from the crystalline phases, for samples solidified at higher linear velocities of the copper drum, the particle size was not determined.

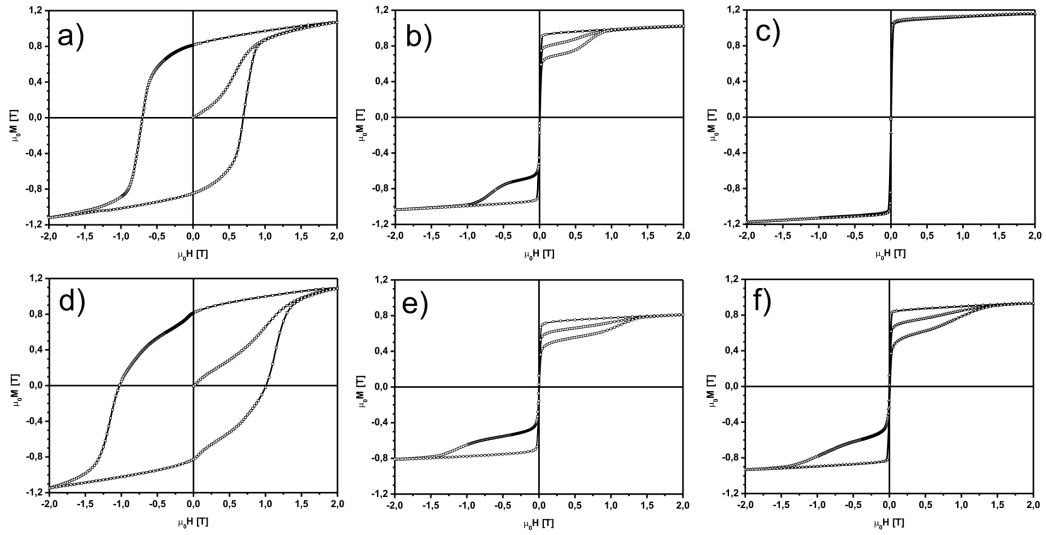

Figure 3: The magnetic hysteresis loops and the initial magnetization curves for the: a), c) $Nd_{10}Fe_{81}Zr_1B_6$ and d), f) $Nd_8Tb_2Fe_{81}Zr_1B_6$ alloys, solidified at linear speeds of the copper drum equal to: a), d) 20 m/s, b), e) 30 m/s, c), f) 35 m/s

Slika 3: Magnetne histerezne zanke in začetne krivulje magnetizacije pri zlitinah: a), c) $Nd_{10}Fe_{81}Zr_1B_6$ in d), f) $Nd_8Tb_2Fe_{81}Zr_1B_6$, strjenih pri linearni hitrosti bakrenega valja: a), d) 20 m/s, b), e) 30 m/s, c), f) 35 m/s

Figure 3 shows the magnetic hysteresis loops and the initial magnetization curves for all the studied samples.

From the analysis of the initial magnetization curves and the main hysteresis loops the magnetic parameters, such as coercivity ($_JH_C$), remanence ($\mu_0 M_R$) and saturation of the magnetization ($\mu_0 M_s$), were determined (**Table 3**). Additionally, for the materials with the best hard magnetic properties the ratio M_R/M_S was also calculated. It allows estimating the extent to which, in the nanocomposite, the phases with hard and soft magnetic properties are coupled by means of exchange interactions.[12,15,16] An additional indicator proving information about the existence of such interactions in the nanocomposite comprising the phases of different magnetic hardness can be the shape of the magnetic hysteresis loop in combination with the results of the phase composition and grain size studies.[15–17]

Table 3: The basic magnetic parameters of the studied $Nd_{10-x}Tb_xFe_{81}Zr_1B_6$ (where x =0 or 2) tapes in the as-cast state, determined from the initial magnetization curves and magnetic hysteresis loops

Tabela 3: Osnovne magnetne lastnosti proučevanih $Nd_{10-x}Tb_xFe_{81}Zr_1B_6$ (kjer je x = 0 ali 2) trakov v litem stanju, določenih iz začetnih magnetizacijskih krivulj in magnetnih histereznih zank

Linear velocity v (m/s)	coercivity $_JH_C$ (T)	remanence $\mu_0 M_R$ (T)	M_R/M_S ratio (a.u.)	Saturation of the magnetization $\mu_0 M_S$ (T)
$Nd_{10}Fe_{81}Zr_1B_6$				
20	0,7	0,82	0,77	1,06
30	9×10^{-4}	–	–	1,02
35	4×10^{-4}	–	–	1,15
$Nd_8Tb_2Fe_{81}Zr_1B_6$				
20	1,03	0,81	0,73	1,10
30	54×10^{-4}	–	–	0,81
35	13×10^{-4}	–	–	0,93

Based on the data collected in **Table 3**, it was found that the material solidified at higher linear speeds of the rotating copper drum (30 m/s and 35 m/s) was characterized by poor, soft-magnetic properties, which was related to the polycrystalline structure. Inclusions of nanocrystalline grains in the amorphous matrix led to the formation of additional pinning sites, which increases the coercivity of the sample. Tapes produced with the lowest cooling rates (20 m/s drum speed) were characterized by good hard magnetic properties. The substitution of Nd by Tb in the $Nd_{10-x}Tb_xFe_{81}Zr_1B_6$ alloy, quenched with the lowest cooling rate resulted in an improvement of the saturation magnetization and in a significant increase in the coercivity. The increase in the saturation magnetization was associated with a slightly higher content of α-Fe phase in the alloy composition.

The shape of the magnetic hysteresis loop of a $Nd_{10}Fe_{81}Zr_1B_6$ sample with hard magnetic properties was smooth, in spite of the presence of the two phases with different magnetic hardnesses. Additionally, a high M_R/M_S ratio (greater than 0.5) and a moderate grain size of both phases are evidence of a strong coupling between the grains of different phases, through exchange interactions. The change of 2 % in the fractions of Nd by Tb in the atomic composition, while maintaining the same cooling rate, caused the formation of a bimodal shape of the hysteresis loop. Juxtaposing this with the much larger average grain size of both phases (almost two times higher) and a lower M_R/M_S ratio, it can be concluded that not all the soft magnetic α-Fe grains were covered by exchange interactions. In this case, an increase in the cooling rate by increasing the linear speed of the rotating copper drum to 22 m/s should result in hardening of the magnetic properties, because a $Nd_8Tb_2Fe_{81}Zr_1B_6$ alloy with smaller grain sizes would be obtained and phases with different magnetic hardnesses would interact with each other by exchange coupling.

The hysteresis loops for the samples solidified at higher cooling speeds were of a wasp shape, typically encountered in materials containing small inclusions of hard magnetic phase distributed in the amorphous matrix. The exception was the hysteresis loop obtained for the $Nd_{10}Fe_{81}Zr_1B_6$ alloy that was solidified at the fastest cooling rate. It had a typical shape characteristic for a magnetically soft material. In this case, the low content of crystalline phase only slightly affected the shape of the hysteresis loop, mainly by increasing the coercivity field (relative to a fully amorphous alloy).

4 CONCLUSIONS

On the basis of X-ray studies, it was found that the samples made with the 20 m/s linear velocity of the copper cylinder were crystalline and consisted of two phases: α-Fe and $RE_2Fe_{14}B$. A qualitative analysis of the phase composition showed that the contents of both phases were 19.15 and 19.40 of α-Fe phase, 80.85 and 80.60 of $Nd_2Fe_{14}B$ phase, for $Nd_{10}Fe_{81}Zr_1B_6$ and $Nd_8Tb_2Fe_{81}Zr_1B_6$ alloys, respectively. The grain size analysis based on Bragg's equation showed that the grains in the alloy containing Tb were almost two times larger. Alloys obtained with higher linear speeds of the copper drum (30 m/s and 35 m/s) were mainly amorphous and contained only small amounts of crystalline phase precipitates.

From the magnetic studies it was found that the tapes produced with the lowest cooling rate were characterized by the best hard magnetic properties. The application of higher speeds of the copper drum resulted in their deterioration.

The hysteresis loop of $Nd_{10}Fe_{81}Zr_1B_6$ (obtained at 20 m/s) was smooth due to presence of strong exchange coupling between the phases of different magnetic hardness. The substitution of Nd by Tb in these samples resulted in an improvement of the saturation magnetization and in a significant increase in the coercivity, but also resulted in the formation of a bimodal shape for the hysteresis loop. The reason for this was decoupling of

the exchange interaction due to an increase of the grain sizes of both phases. Summarizing, for alloy with Tb addition, an increase in the linear speed of the rotating copper drum from 20 m/s to 22 m/s should result in a hardening of the magnetic properties.

5 REFERENCES

[1] Y. Sen, S. Xiaoping, D. Youwei, Exchange coupled $Nd_2Fe_{14}B/\alpha$-Fe nanocomposite magnets with fine α-Fe grains, Microelectron. Eng., 66 (**2003**), 121–127, doi:10.1016/S0167-9317(03)00035-2

[2] R. Fischer, T. Schrefl, H. Kronmuller, J. Fidler, Phase distribution and computed magnetic properties of high-remanent composite magnets, J. Magn. Magn. Mater., 150 (**1995**), 329–344, doi:10.1016/0304-8853(95)00298-7

[3] E. F. Kneller, R. Hawig, The Exchange-Spring Magnet: A new material principle for permanent magnets, IEEE Trans. Magn., 27 (**1991**) 4, 3588

[4] C. Wang, M. Yan, Q. Li, Effects of Nd and B contents on the thermal stability of nanocomposite $(Nd,Zr)_2Fe_{14}B/\alpha$-Fe magnets, Mater. Sci. Eng. B, 150 (**2008**) 77, doi:10.1016/j.mseb.2008.02.007

[5] B. Xiaoqian, Z. Jie, L. Wei, G. Xuexu, Z. Shouzeng, Influence of zirconium addition on microstructure, magnetic properties and thermal stability of nanocrystalline $Nd_{12.3}Fe_{81.7}B_{6.0}$ alloy, Journal of Rare Earths, 27 (**2009**), 843, doi:10.1016/S1002-0721(08)60347-6

[6] Z. Tian, S. Li, K. Peng, B. Gu, J. Zhang, M. Lu, Y. Du, The microstructure and magnetic properties of NdFeB magnets directly solidified at a low cooling rate, Mater. Sci. Eng. A, 380 (**2004**), 143, doi:10.1016/j.msea.2004.03.077

[7] A. Ceglarek, D. Płusa, P. Pawlik, M. Dośpiał, Influence of heat treatment on magnetic properties of nanocrystalline $Nd_9Fe_{84}Zr_1B_6$ ribbons received by rapid solidification method, Arch. Metall. Mater., 57 (**2012**), 229–232, doi:10.2478/v10172-012-0015-6

[8] H. Sheng, X. Zeng, D. Fu, F. Deng, Differences in microstructure and magnetic properties between directly-quenched and optimally-annealed Nd–Fe–B nanocomposite materials, Physica B, 405 (**2010**), 690, doi:10.1016/j.physb.2009.09.088

[9] A. E. Ceglarek, D. Plusa, M. J. Dospial, M. G. Nabialek, P. Pietrusiewicz, Investigation of the Magnetization Reversal Process of High-Remanent $Nd_{10}Fe_{83}Zr_1B_6$ Alloy in the As-Cast State, Acta Phys. Polon. A, 121 (**2012**), 1279–1281

[10] J. C. Martínez-García, J. A. García, M. J. Rias, Asymmetric magnetization reversal of partially devitrified $Co_{66}Si_{15}B_{14}Fe_4Ni_1$, Non-Cryst. Solids, 354 (**2008**), 5123–5125, doi:10.1016/j.jnoncrysol.2008.05.059

[11] M. Dośpiał, J. Olszewski, M. Nabiałek, P. Pietrusiewicz, T. Kaczmarzyk, The microstructure and magnetic properties of $Nd_{8.5}Tb_{1.5}Fe_{83}Zr_1B_6$ ribbons obtained at various cooling ratek, Nukleonika, 60 (**2015**) 1, 15–18, doi:10.1515/nuka-2015-0005

[12] M. Dospial, D. Plusa, B. Ślusarek, Study of the magnetic interaction in nanocrystalline Pr–Fe–Co–Nb–B permanent magnets, J. Magn. Magn. Mater., 324 (**2012**), 843–848, doi:10.1016/j.jmmm.2011.09.029

[13] H. Kronmüller, M. Fähnle, Micromagnetism and the microstructure of ferromagnetic solids, Cambridge University Press, Cambridge, United Kingdom 2003

[14] G. K. Williampson, W. H. Hall, X-ray line broadening from filed aluminium and wolfram, Acta Metallurgica, 1 (**1953**) 22, doi:10.1016/0001-6160(53)90006-6

[15] J. D. Livingston, The history of permanent-magnet material, Journal of Metals, 2 (**1990**), 30-34

[16] M. Dospial, D. Plusa, Magnetization reversal processes in bonded magnets made from a mixture of Nd-(Fe,Co)-B and strontium ferrite powders, J. Magn. Magn. Mater., 330 (**2013**), 152–158, doi:10.1016/j.jmmm.2012.10.022

[17] R. W. Gao, D. H. Zhang, W. Li, X. M. Li, J. C. Zhang, Hard magnetic property and $\delta M(H)$ plot for sintered NdFeB magnet, J. Magn. Magn. Mater., 208 (**2000**), 239, doi:10.1016/S0304-8853(99)00562-4

UDK 620.1:691.714.018.8:621.791.053
Professional article/Strokovni članek

ISSN 1580-2949
MTAEC9, 50(5)829(2016)

METALOGRAFSKA PREISKAVA IN KOROZIJSKA ODPORNOST ZVAROV FERITNEGA NERJAVNEGA JEKLA

METALLOGRAPHIC INVESTIGATION AND CORROSION RESISTANCE OF WELDS OF FERRITIC STAINLESS STEELS

Matjaž Torkar, Aleksandra Kocijan, Roman Celin, Jaka Burja, Bojan Podgornik

Inštitut za kovinske materiale in tehnologije, Lepi pot 11, 1000 Ljubljana, Slovenija
matjaz.torkar@imt.si

Prejem rokopisa – received: 2016-04-04; sprejem za objavo – accepted for publication: 2016-05-12

doi:10.17222/mit.2016.059

Preiskovani so bili vzorci zvarov feritnega nerjavnega jekla X6Cr17 (W.Nr. 1.4016). Prikazane so metalografske značilnosti prečnega in krožnega zvara. Določena je bila hitrost korozije v dveh korozijskih medijih in pri dveh temperaturah. Predstavljeni so rezultati osnovnega materiala, dveh zvarov in dveh primerjalnih materialov, jekla X2CrTi17 in maloogljičnega jekla DC01 EN10130. Rezultati preiskave so pokazali, da se v zvaru poveča velikost zrn, po mejah zrn pa je izločena martenzitna faza, oboje pa vpliva na korozijsko obstojnost. Nobeden od preiskovanih vzorcev ni pokazal izrazite pasivacije površine pri elektrokemijskem korozijskem preizkusu.

Ključne besede: feritno nerjavno jeklo, metalografija, zvar, korozijska odpornost

Samples of welds made from the ferritic stainless steel X6Cr17 (W.Nr. 1.4016) were investigated. Here we present the results of the metallographic charaterisations of these welds. We determined the corrosion rate in two corrosion media at two temperatures. The results from the base material and two welds are presented and compared with the steel X2CrTi17 and the low-carbon steel DC01 EN10130. The results revealed enlarged grains in the weld and martensite at the grain boundaries, both have an influence on the corrosion resistance. None of the investigated samples showed distinctive passivation of the surfaces during the electrochemical corrosion tests.

Keywords: ferritic stainless steel, metallography, weld, corrosion resistance

1 UVOD

Feritna nerjavna jekla so poceni, cenovno stabilna in korozijsko odporna jekla. Uporaba teh nerjavnih jekel je pogosta v avtomobilski industriji, pri izdelavi kuhinjskih pripomočkov in naprav ter tudi na drugih področjih. Feritna nerjavna jekla se zaradi njihove dobre toplotne prevodnosti in majhnega toplotnega raztezka uporabljajo tako za izdelavo dimnikov, glušnikov, izpušnih sistemov, pritrdilnih elementov, kot tudi za grelne elemente, ki se jih uporablja v kopelih staljene soli za toplotno obdelavo, v konstrukcijske namene in podobno.[1–5]

Pri visokih temperaturah iz taline nastaja faza delta ferita (δ), ki se potem ko kristalizira, pri ohlajanju ne spremeni. Te popolnoma feritne mikrostrukture se ne da toplotno obdelati. Neprisotnost fazne premene razloži, zakaj so pri ogrevanju ta jekla nagnjena k rasti zrn.

Feritna faza v zvaru in toplotno vplivana cona sta občutljivi na intersticijske elemente, kot sta ogljik in dušik, ki pri visokih temperaturah z difuzijo spremenita feritno fazo v avstenit. Ta avstenit pa se pri ohlajanju po mejah zrn pretvori v martenzit (krhek). Dodaten problem je tudi z rastjo zrn v toplotno vplivani coni in v zvaru.[6,7] Za zadržanje duktilnosti feritne strukture, ki vsebuje tudi martenzit, je potrebno izvršiti toplotno obdelavo čim prej po zaključnem varjenju. Ta obdelava za odpravo napetosti se izvede pri maksimalni temperaturi 750-800 °C, kar je malo pod temperaturo nastanka avstenita v področjih bogatih z ogljikom. Namen te obdelave je popustiti martenzit, zmanjšati zaostale napetosti v zvaru ter povečati žilavost zvarnega spoja in toplotno vplivane cone.

Za preprečitev rasti zrn in pojava avstenitizacije je potrebno varjenje izvršiti z majhnim vnosom toplote (1 kJ/mm).[8]

Študija korozijske odpornosti zvarov je izredno pomembna za uspešno uporabo feritnih nerjavnih jekel. Poleg obnašanja samega materiala v korozijskem mediju, je pomembna tudi korozijska odpornost zvarnih spojev. Literatura[9], navaja, da je korozijska odpornost zvarov odvisna tudi od velikosti zrn in prisotnosti različnih faz v mikrostrukturi zvara.

Namen predstavljene preiskave je z metalografsko preiskavo ugotoviti mikrostrukturne značilnosti dveh vrst zvarov ter napraviti primerjavo s preizkusom korozijske odpornosti osnovnega materiala, zvarov in primerjalnih materialov v dveh korozijskih medijih.

Dobljeni podatki naj bi služili optimiranju tehnologije varjenja feritnega nerjavnega jekla in naj bi prispevali k podaljšanju zdržljivosti zvarov v danem korozijskem mediju.

2 OPIS VZORCEV

Vzorci, prikazani na **Sliki 1**, so bili odrezani iz kadi in označeni kot "prečni zvar", izveden prečno na dno kadi in "krožni zvar", izveden po obodu kadi. Obod in dno kadi sta izdelana iz enakega feritnega nerjavnega jekla X6Cr17, prečni in krožni zvar pa sta izdelana z različnimi varilniki, zaradi česar je potrebno napraviti tudi primerjavo med posameznimi zvari. Dno kadi se na sliki 1 vidi slabo, ker je pravokotno na obod kadi in je označen z belo puščico.

Za primerjavo korozijskih hitrosti sta bila dodatno preizkušena še vzorec malo ogljične pločevine kvalitete DC01 po standardu EN10130 in vzorec pločevine feritnega nerjavnega jekla X2CrTi17. Nominalna kemijska sestava za preiskovana jekla je podana v **Tabeli 1**.

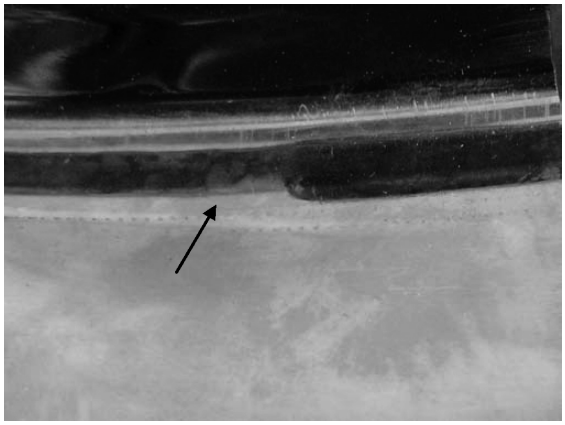

Slika 2: Detajl krožnega zvara z razširitvijo, ki jo kaže puščica
Figure 2: Detail of circular weld with enlargement shown by arrow

3 EKSPERIMENTALNO DELO

Zvari so bili izdelani po postopku TIG (Tungsten inert gas welding), brez dodajanja materiala.

Odrezani so bili vzorci zvarov (jeklo X6Cr17) in pripravljeni so bili za metalografsko preiskavo po standardnem postopku z zalivanjem v maso, brušenjem in poliranjem. Za metalografsko preiskavo so bili vzorci jedkani z Vilella jedkalom (5 cm^3 HCl, 2 g pikrinske kisline in 100 cm^3 etil alkohola).

Izvedena je bila metalografska preiskava obeh vrst zvarov; prečnega in krožnega zvara. Mikrostruktura je bila pregledana s pomočjo svetlobne mikroskopije, s svetlobnim mikroskopom Nikon Microphot FXA, opremljenim z videokamero Olympus DP73 in računalniškim programom za analizo Stream Motion.

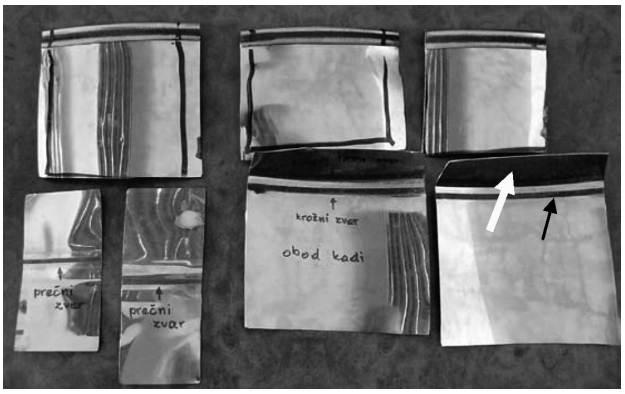

Slika 1: Vzorci s prečnim in krožnim zvarom. Jeklo X6Cr17. Svetla puščica označuje dno kadi, črna puščica pa krožni zvar.
Figure 1: Samples with cross and circular weld. Steel X6Cr17. White arrow indicates the bottom of the tub, the black arrow indicates the circular weld.

Korozijske meritve so potekale na potenciostatu/galvanostatu EG&G PAR Model 273 s trielektrodno korozijsko celico, pri čemer je bila uporabljena tehnika potenciodinamske polarizacije. Korozijsko so bile preizkušene tri osnovne pločevine (**Tabela 1**) in dve vrsti zvara (prečni in krožni zvar).

4 REZULTATI

4.1 Metalografski pregled zvarov

Iz vzorcev sta bila pripravljena prečna prereza obeh vrst zvarov, prečnega zvara in krožnega zvara.

Pregled izgleda površine zvara je pokazal, da se pri obeh vrstah zvarov na začetku zvara oziroma na mestu združevanja zvarov pojavi razširjeno področje (**Slika 2**).

V prečnem preseku prečnega zvara je opazna črta, ki izgleda kot nezveznost v zvaru (**Slika 3**). Črta se prične na površini, teče pod kotom 45° do sredine zvara, nato teče vzporedno s površino in se nato zopet pod kotom 45° obrne proti nasprotni površini zvara.

Metalografski pregled je pokazal, da gre za nespojeno področje med pločevinama in da se kristalna zrna na prehodu v zvar povečajo. Pri feritnem nerjavnem jeklu se v zvaru zrna lahko povečajo, ker to jeklo nima faznih premen pri ohlajanju in ogrevanju, zato je potrebno pazljivo izvajati proces varjenja.

Na **Sliki 4** je prikazan prehod iz zvara v toplotno vplivano cono na preseku prečnega zvara, na **Sliki 5** pa mikrostruktura v sredini enojnega (čelnega) prečnega zvara. Iz **Slike 5** je razvidno, da so zrna v zvaru večja kot

Tabela 1: Nominalna kemijska sestava za preiskovana jekla
Table 1: Nominal chemical composition for investigated steels

Jeklo	C (max.)	Si (max.)	Mn (max.)	P (max.)	S (max.)	Cr	N (max.)	Ti (max.)	Al (max.)
X6Cr17	0,08	1,0	1,0	0,040	0,015	16 – 18	/	/	/
X2CrTi17	0,025	0,50	0,5	0,040	0,015	16-18	0,015	0,3-0,6	/
DC01	0,12	0,03	0,6	0,045	0,045	/	/	/	0,02-0,06

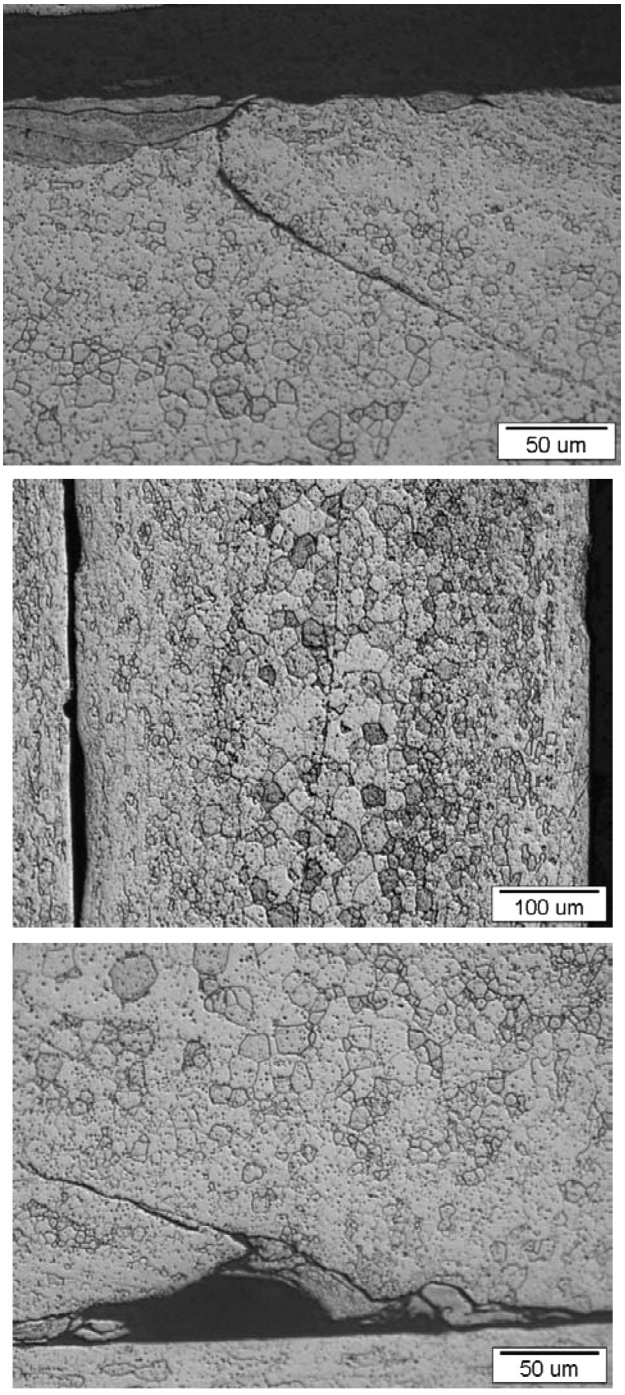

Slika 3: Detajl preseka skozi prečni zvar: a) zgornja površina, b) sredina in c) spodnja površina. Jeklo X6Cr17, jedkano z Vilella jedkalom.

Figure 3: Detail of cross-section of cross weld: a) upper surface, b) middle and c) lower surface. Steel X6Cr17, etched with Vilella's reagent.

v osnovni mikrostrukturi jekla X6Cr17, ki je prikazana na **Sliki 6**.

Značilnosti mikrostrukture krožnega zvara so prikazane na **Slikah** od **7** do **9**.

V posameznih delih zvara so opazne nezveznosti, kjer ni prišlo do popolne pretalitve vsega materiala.

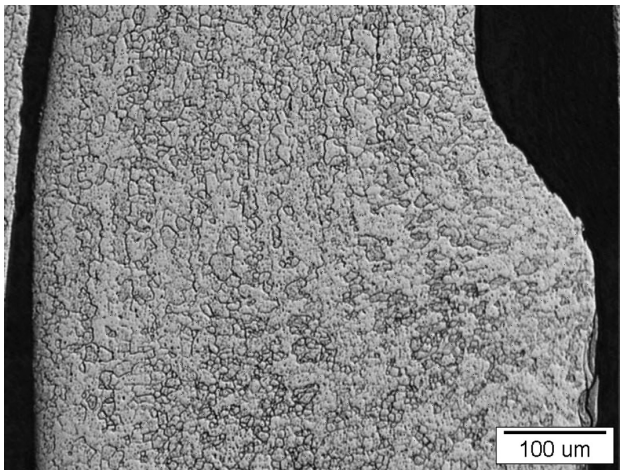

Slika 4: Presek prečnega zvara. Prehod iz zvara v toplotno vplivano cono. Jeklo X6Cr17, jedkano z Vilella jedkalom.

Figure 4: Cross-section of the cross weld. Transition from weld to heat-affected zone. Steel X6Cr17, etched with Vilella's reagent.

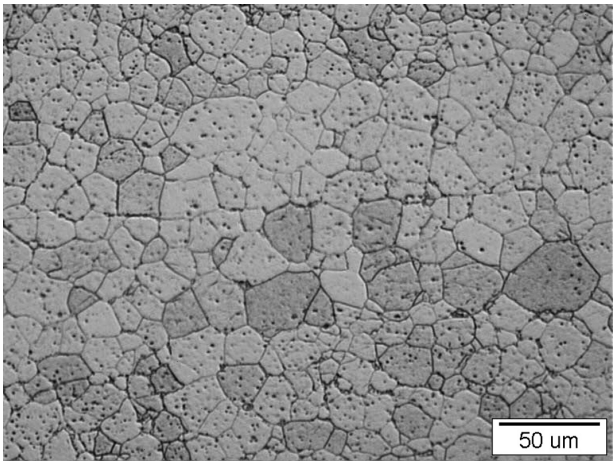

Slika 5: Mikrostruktura v sredini prečnega zvara. Jeklo X6Cr17, jedkano z Vilella jedkalom.

Figure 5: Microstructure in the middle of the cross weld. Steel X6Cr17, etched with Vilella's reagent.

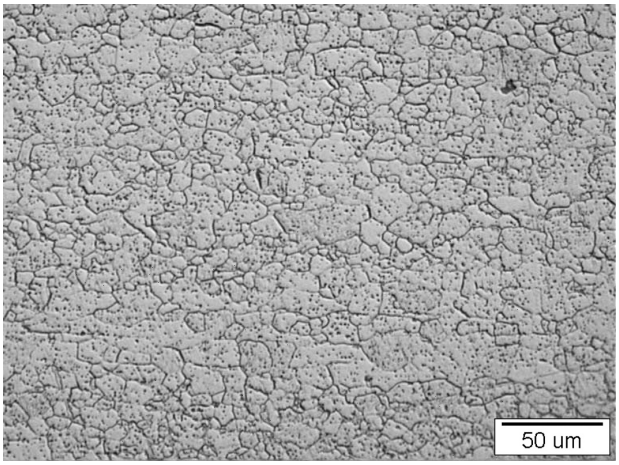

Slika 6: Mikrostruktura osnovne pločevine. Jeklo X6Cr17, jedkano z Vilella jedkalom.

Figure 6: Microstructure of base sheet material. Steel X6Cr17, etched with Vilella's reagent.

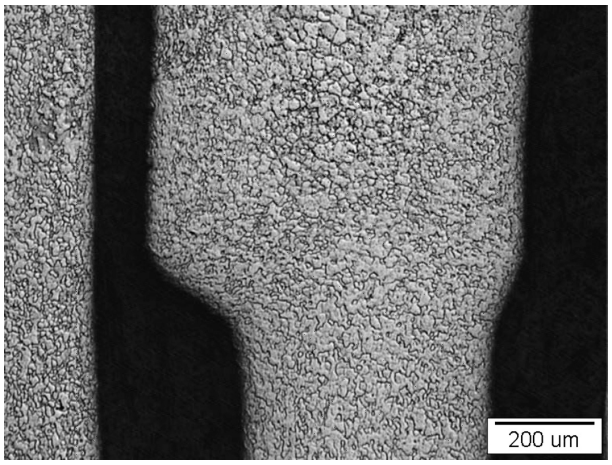

Slika 7: Prerez prehoda v krožni zvar. Jeklo X6Cr17, jedkano z Vilella jedkalom
Figure 7: Cross-section of transition to a circular weld. Steel X6Cr17, etched with Vilella's reagent

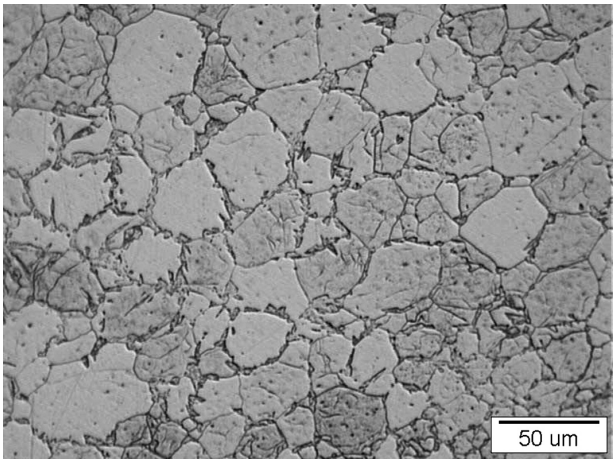

Slika 9: Mikrostruktura krožnega zvara z izločenim martenzitom po mejah zrn. Jeklo X6Cr17, jedkano z Vilella jedkalom
Figure 9: Microstructure of circular weld with a martensite phase on the grain boundaries. Steel X6Cr17, etched with Vilella's reagent

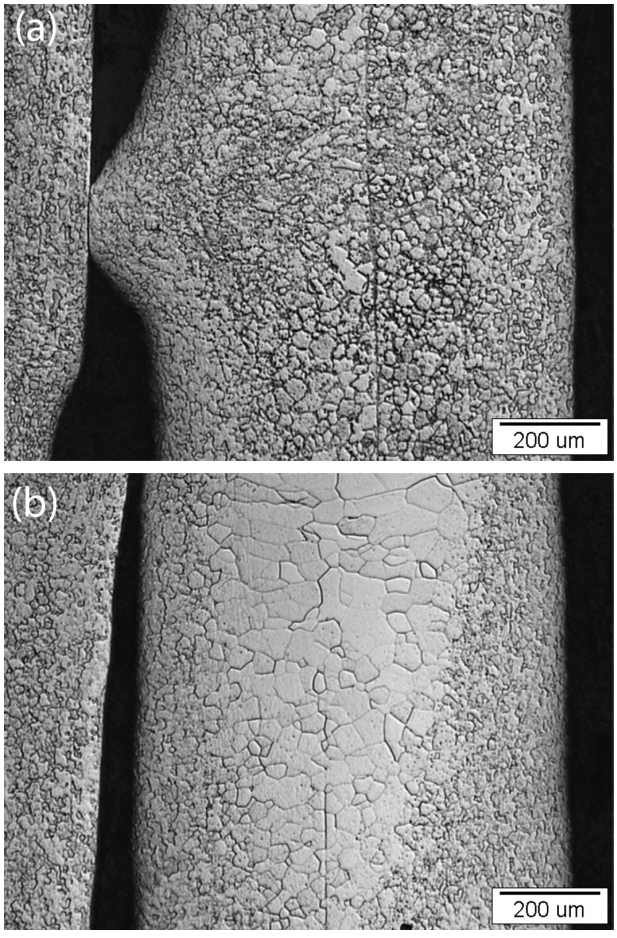

Slika 8: a) Napaka v sredini krožnega zvara in b) rast zrn. Jeklo X6Cr17, jedkano z Vilella jedkalom
Figure 8: a) Failure in the central part of a circular weld and c) grain growth. Steel X6Cr17, etched with Vilella's reagent

Poleg tega so v področju krožnega zvara, na posameznih mestih, opazna tudi povečana zrna in izločena martenzitna faza po mejah zrn. Spreminjanje mikrostrukture zvara pomeni, da so se spreminjali parametri med postopkom varjenja.

Značilnosti obeh vrst zvarov kažeta, da bi bilo potrebno izboljšati, oziroma optimirati izvedbo varjenja.

4.2 Korozijske preiskave

Korozijski preskusi so bili izvedeni v dveh medijih, ki se jih uporablja pri funkcionalnih meritvah na feritnem nerjavnem jeklu, pri temperaturah 60 °C in 90 °C. Korozijski medij oz. raztopino smo pripravili iz dveh praškov z oznako IEC-A base in Na-perborate tetrahydrate in to na naslednji način:

Raztopina 1: 10 g IEC/L H_2O s pH 10,5 pri temperaturi 60 °C

Raztopina 2: 8 g IEC + 2 g Na-perborata/L H_2O pH 11, pri temperaturi 90 °C

Vse korozijske meritve so potekale na potenciostatu/galvanostatu z uporabo tehnike potenciodinamske polarizacije. Ta tehnika postopnega dvigovanja potenciala na enoto časa, k bolj pozitivnim vrednostim, spreminja korozijsko stabilnost kovine. Z naraščanjem potenciala postaja material termodinamsko vedno manj stabilen, kar pomeni, da narašča tudi korozijski tok, ki je merilo za stopnjo korozije. Tako spoznamo splošno kvalitativno sliko o obnašanju materiala v nekem mediju. Iz oblike anodnega dela krivulje lahko sklepamo o korozijski odpornosti, morebitni pasivaciji, potencialu preboja in podobno.[10] Iz Taflovega dela krivulje (±250 mV glede na E_{kor}) lahko izračunamo tudi korozijsko hitrost in polarizacijsko upornost, s tem pa stopnjo korozije.

Za delovno elektrodo so bili uporabljeni naslednji vzorci:

Vzorec 1 (dno kadi – X6Cr17)
Vzorec 2 (krožni zvar – X6Cr17)
Vzorec 3 (prečni zvar – X6Cr17)
Vzorec 4 (malo ogljično jeklo kvalitete DC01)

Vzorec 5 (jeklo X2CrTi17).

Izpostavljena površina elektrodne reakcije na delovni elektrodi je bila 1 cm^2, referenčna elektroda je bila nasičena kalomelova elektroda in pomožna elektroda je bila grafitna palica.

V **Tabeli 1** so podani rezultati potenciodinamskih meritev za korozijsko hitrost, korozijski potencial, korozijski tok in polarizacijska upornost petih preiskovanih vzorcev v raztopini 1, v **Tabeli 2** pa rezultati za raztopino 2.

Na **Slikah 10** in **11** so prikazane potenciodinamske polarizacijske krivulje preiskovanih vzorcev v raztopini 1 pri 60 °C in raztopini 2 pri 90 °C.

Tabela 1: Rezultati potenciodinamskih meritev petih vzorcev v raztopini 1, pri 60 °C

Table 1: Results of potentiodynamic measurements of five samples in solution 1, at 60 °C

Vzorec	Korozijska hitrost	E (I = 0)	I_{corr}	R_p
1 (dno kadi) X6Cr17	0,0013 mm/leto	–151,3 mV	120,0 nA	277,0 kΩ
2 (krožni zvar) X6Cr17	0,036 mm/leto	–242,1 mV	3282 µA	13,16 kΩ
3 (prečni zvar) X6Cr17	0,015 mm/leto	–281,5 mV	1399 µA	27,26 kΩ
4 (DC01)	0,059 mm/leto	–340,5 mV	6132 µA	5382 kΩ
5 (X2CrTi17)	0,0013 mm/leto	–240,8 mV	116,1 nA	310,5 kΩ

Preiskave potenciodinamske polarizacije petih preiskovanih vzorcev so pokazale, da sta vzorec 1 (dno kadi – X6Cr17) in vzorec 5 (X2CrTi17) v raztopini 1 pri 60 °C korozijsko najbolj odporna, kar je razvidno iz najnižjih vrednosti korozijskih hitrosti (1,3 µm/leto) in najvišjih

Tabela 2: Rezultati potenciodinamskih meritev petih vzorcev v raztopini 2 pri 90 °C

Table 2: Results of potentiodynamic measurements of five samples in solution 2 at 90 °C

Vzorec	Korozijska hitrost	E (I = 0)	I_{corr}	R_p
1 (dno kadi) X6Cr17	0,059 mm/leto	–21,62 mV	5442 µA	6063 kΩ
2 (krožni zvar) X6Cr17	0,411 mm/leto	–40,08 mV	37,77 µA	1137 kΩ
3 (prečni zvar) X6Cr17	0,351 mm/leto	–78,87 mV	32,22 µA	781,1 Ω
4 (DC01)	8,167 mm/leto	–434,4 mV	847,4 µA	56,51 Ω
5 (X2CrTi17)	0,049 mm/leto	–4851 mV	4568 µA	7700 kΩ

vrednosti polarizacijske upornosti R_p (277–310 kΩ). Pričakovano je korozijsko najmanj stabilen vzorec 4 (malo ogljično jeklo), s 45- do 60-krat slabšo korozijsko odpornostjo, medtem ko sta vzorca 2 in 3 (krožni zvar – X6Cr17 in prečni zvar –X6Cr17) dokaj primerljiva, a še vedno za en velikostni razred manj korozijsko odporna kot osnovni material. Domnevamo, da je to posledica razlike v velikosti zrn in značilnosti strjevalne strukture zvarov ter pojava martenzitne faze po mejah zrn. Vidimo lahko tudi, da je prečni zvar ∼2-krat korozijsko bolj odporen kot krožni zvar, kjer se opazi v zvaru martenzitna faza po mejah zrn. V raztopini 2 pri 90 °C so vrednosti korozijske hitrosti 10-krat višje, kar je posledica bolj agresivnega medija. V primeru vzorca 4 (malo ogljično jeklo) je ta pojav še posebej izrazit, kjer se ocenjena korozijska hitrost poveča kar za dva velikostna razreda na približno 8 mm/leto. Tudi v raztopini 2 sta korozijsko najbolj stabilna vzorca 1 (X6Cr17) in 5 (X2CrTi17) z ocenjeno korozijsko hitrostjo 50–60

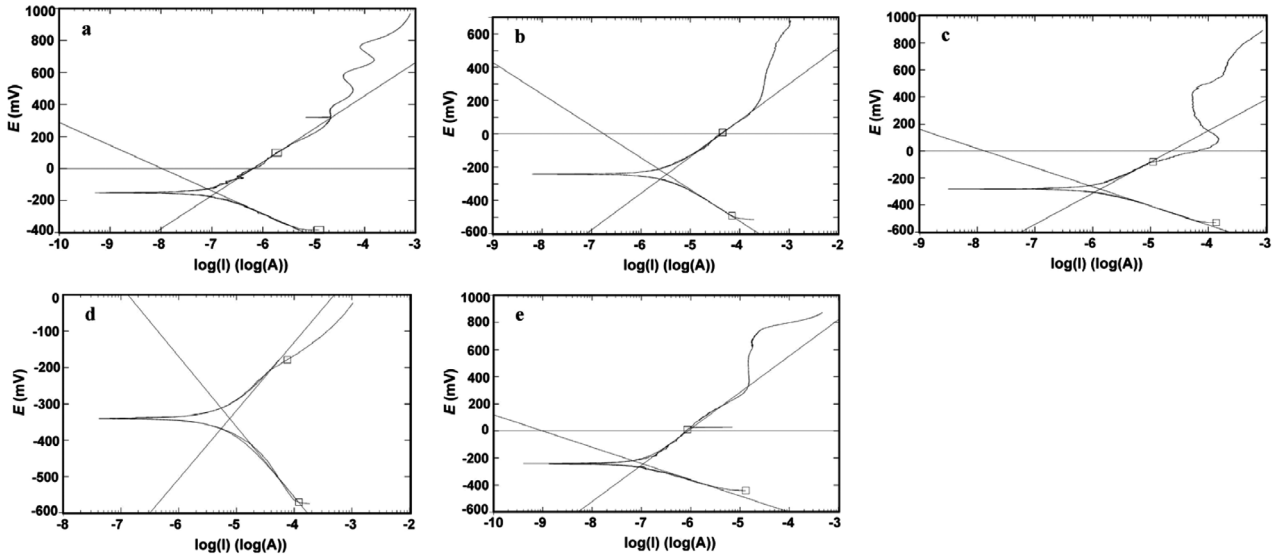

Slika 10: Potenciodinamska krivulja v raztopini 1 pri 60 °C: a) X6Cr17 – dno kadi, b) X6Cr17 – krožni zvar, c) X6Cr17 – prečni zvar, d) malo-ogljično jeklo CD01, EN10130 in e) primerjalno jeklo X2CrTi17

Figure 10: Potentiodynamic curve in solution 1 at 60 °C: a) X6Cr17 – bottom of the tub, b) X6Cr17 – circular weld, c) X6Cr17 – cross weld, d) low-carbon steel CD01, EN10130 and e) X2CrTi17 comparative steel

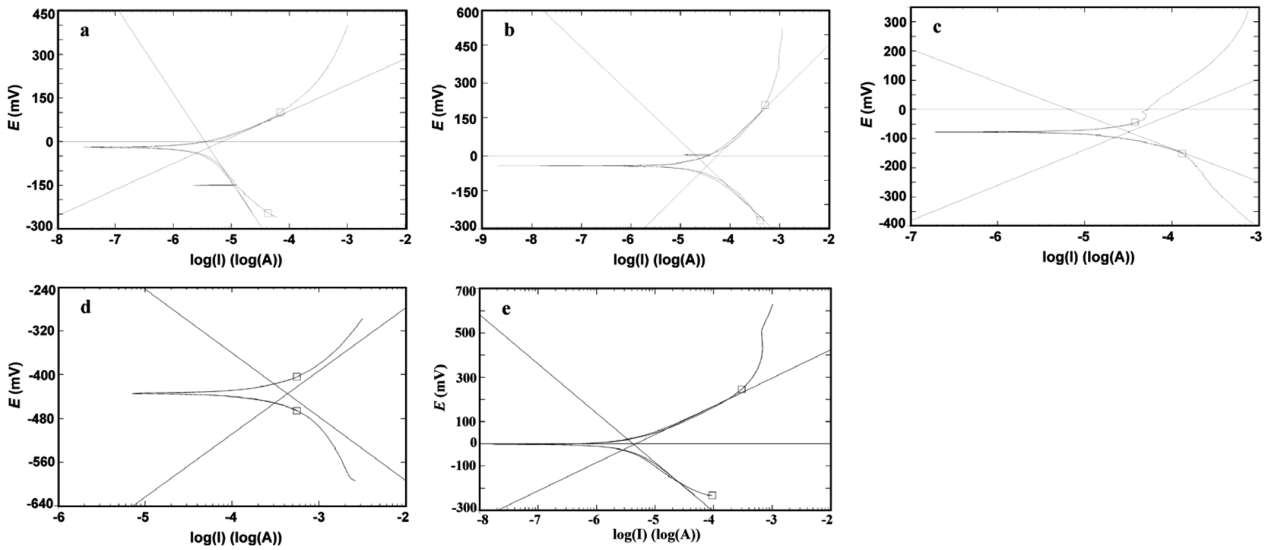

Slika 11: Potenciodinamska krivulja v razopini 2 pri 90 °C: a) X6Cr17 – dno kadi, b) X6Cr17 – krožni zvar, c) X6Cr17 – prečni zvar, d) malo-ogljično jeklo CD01 po standardu EN10130 in e) primerjalno jeklo X2CrTi17

Figure 11: Potentiodynamic curve in solution 2 at 90 °C: a) bottom of the tub, b) circular weld, c) cross weld, d) low-carbon steel CD01, EN10130 and e) X2CrTi17 comparative steel

μm/leto in polarizacijsko upornostjo 6–7 MΩ, najmanj pa vzorec 4. Med vzorcema 2 in 3 pa v raztopini 2 praktično ni razlik, še vedno pa ne dosegata korozijske odpornosti osnovnega materiala (vzorec 1).

Med korozijskim preskusom nobeden od preiskovanih vzorcev ni pokazal izrazite pasivacije površine.

5 ZAKLJUČKI

Na podlagi primerjave narejenih raziskav zvarov in pločevin lahko postavimo naslednje zaključke:

Zvari, tako prečni kot krožni, so izvedeni slabo, saj material ni pretaljen po vsej dolžini zvara. Potrebno bo tehnološko optimiranje tehnologije izvedbe varjenja.

Razlike v mikrostrukturi in velikosti zrn ter nespojena mesta v zvaru kažejo, da so se procesni parametri med varjenjem spreminjali.

Izvršene korozijske preiskave v dveh medijih in pri dveh temperaturah so pokazale, da sta na korozijo v obeh primerih najbolj odporna dno kadi iz feritnega nerjavnega jekla X6Cr17 in primerjalno jeklo X2CrTi17. Na mestu zvara se korozijska odpornost materiala zmanjša za cel velikostni razred.

Slabša korozijska odpornost krožnega zvara je posledica nastanka martenzitne faze po mejah zrn v zvaru.

Od preiskovanih vzorcev je korozijsko najmanj stabilen vzorec maloogljičnega jekla.

Pri nobenem od preiskovanih vzorcev se med korozijskim preizkusom v dveh korozijskih medijih ni pokazala izrazita pasivacija površine.

6 LITERATURA

[1] A. Talja, M. Torkar, Lap shear tests of bolted and screwed ferritic stainless steel connections, Thin-walled Structures, 83 (**2014**), 157–168, doi:10.1016/j.tws.2014.01.016

[2] Structural design of cold worked austenitic stainless steel, Final Report, Technical Steel Research, Steel products and application for building construction and industry, Directorate – General for Research, European Commission, Contract No. 7210-PR/318, 2006

[3] K. H. Jo, J. H. Kim, K. M. Kim, I. S. Lee, S. J. Kim, Development of a new cost effective Fe-Cr ferritic stainless steel for SOFC interconnect, International Journal of Hydrogen Energy 40 (**2015**) 30, 9523 – 9529, doi:10.1016/j.ijhydene.2015.05.125

[4] I. Arrayagon, F. Picci, E. Mirambell, E. Real, Interaction of bending and axial load for ferritic stainless steel RHS columns, Thin-Walled Structures, 91 (**2015**), 96–107 doi:10.1016/j.tws.2015.02.012

[5] M. Cortie, M. du Toit, Stainless Steels, Ferritic, Reference Module in Materials Science and Materials Engineering, (2016), doi:10.1016/B978-0-12-803581-8.02501-7

[6] G. M. Reddy, S. D. Meshran, Grain refinement in ferritic stainless weld through magnetic arc oscillations and its effect on tensile property, Indian Welding Journal, 39 (**2006**) 3, 35–41

[7] G. M. Reddy, T. Mohandas, Explorative studies on grain refinement of ferritic stainless steel welds, Journal of Materials Science Letters, 20 (**2001**) 8, 721–723

[8] M. O. H. Amuda, S. Mridha, An Overview of Sensitization Dynamics in Ferritic Stainless Steel Welds, International Journal of Corrosion, Volume 2011 (**2011**), 1–9, doi:10.1155/2011/305793

[9] A. K. Lakshminarayanan, K. Shanmugam, V. Balasubramanian, Effect of Autogenous Arc Welding Processes on Tensile and Impact Properties of Ferritic Stainless Steel Joints, Journal of Iron and Steel Research, International, 16 (**2009**) 1, 62–68

[10] Corrosion Mechanisms in Theory and Practice, 3rd Ed., Ed. Philippe Marcus, 2012